

Springer Series in Biomaterials Science and Engineering 6

Zhifei Dai *Editor*

Advances in Nanotheranostics I

Design and Fabrication of Theranostic
Nanoparticles

 Springer

Springer Series in Biomaterials Science and Engineering

Volume 6

Series editor

Prof. Min Wang

Department of Mechanical Engineering

The University of Hong Kong

Pokfulam Road, Hong Kong

e-mail: memwang@hku.hk

Aims and scope

The Springer Series in Biomaterials Science and Engineering addresses the manufacture, structure and properties, and applications of materials that are in contact with biological systems, temporarily or permanently. It deals with many aspects of modern biomaterials, from basic science to clinical applications, as well as host responses. It covers the whole spectrum of biomaterials – polymers, metals, glasses and ceramics, and composites/hybrids – and includes both biological materials (collagen, polysaccharides, biological apatites, etc.) and synthetic materials. The materials can be in different forms: single crystals, polycrystalline materials, particles, fibers/wires, coatings, non-porous materials, porous scaffolds, etc. New and developing areas of biomaterials, such as nano-biomaterials and diagnostic and therapeutic nanodevices, are also focuses in this series. Advanced analytical techniques that are applicable in R & D and theoretical methods and analyses for biomaterials are also important topics. Frontiers in nanomedicine, regenerative medicine and other rapidly advancing areas calling for great explorations are highly relevant.

The Springer Series in Biomaterials Science and Engineering aims to provide critical reviews of important subjects in the field, publish new discoveries and significant progresses that have been made in both biomaterials development and the advancement of principles, theories and designs, and report cutting-edge research and relevant technologies. The individual volumes in the series are thematic. The goal of each volume is to give readers a comprehensive overview of an area where new knowledge has been gained and insights made. Significant topics in the area are dealt with in good depth and future directions are predicted on the basis of current developments. As a collection, the series provides authoritative works to a wide audience in academia, the research community, and industry.

More information about this series at <http://www.springer.com/series/10955>

Zhifei Dai
Editor

Advances in Nanotheranostics I

Design and Fabrication of Theranostic
Nanoparticles

 Springer

Editor
Zhifei Dai
Department of Biomedical Engineering
College of Engineering
Peking University
Beijing, China

ISSN 2195-0644 ISSN 2195-0652 (electronic)
Springer Series in Biomaterials Science and Engineering
ISBN 978-3-662-48542-2 ISBN 978-3-662-48544-6 (eBook)
DOI 10.1007/978-3-662-48544-6

Library of Congress Control Number: 2015957361

Springer Berlin Heidelberg New York Dordrecht London
© Springer-Verlag Berlin Heidelberg 2016

This work is subject to copyright. All rights are reserved by the Publisher, whether the whole or part of the material is concerned, specifically the rights of translation, reprinting, reuse of illustrations, recitation, broadcasting, reproduction on microfilms or in any other physical way, and transmission or information storage and retrieval, electronic adaptation, computer software, or by similar or dissimilar methodology now known or hereafter developed.

The use of general descriptive names, registered names, trademarks, service marks, etc. in this publication does not imply, even in the absence of a specific statement, that such names are exempt from the relevant protective laws and regulations and therefore free for general use.

The publisher, the authors and the editors are safe to assume that the advice and information in this book are believed to be true and accurate at the date of publication. Neither the publisher nor the authors or the editors give a warranty, express or implied, with respect to the material contained herein or for any errors or omissions that may have been made.

Printed on acid-free paper

Springer-Verlag GmbH Berlin Heidelberg is part of Springer Science+Business Media (www.springer.com)

Preface

Recent advances in nanotechnology have produced a variety of functional nanoparticles such as magnetic nanoparticles, quantum dots, metallic nanoparticles, silica nanoparticles, liposomes, polymersomes, dendrimers, etc. A key feature of these nanoparticles is they are easier to accumulate in the tumor than in healthy tissues. It has been found that the small size of nanoparticles can have profound impact on their mode of endocytosis, cellular trafficking, and processing. Due to the unique attributes such as electronic, magnetic, optical, and structural properties, nanoparticles have been shown to be capable of functioning either as carriers for chemotherapeutic drugs to improve their therapeutic efficacy or as therapeutic agents in photodynamic, gene, thermal, and photothermal therapy or as molecular imaging agents to detect and monitor cancer progression.

The successful integration of diagnosis and therapy on a single agent using multifunctional nanoparticles has led to the birth of a new, highly interdisciplinary research field named “nanotheranostics,” which has given hope in developing innovative strategies to enable “personalized medicine” to diagnose, treat, and follow up patients with cancer.

Nanotheranostic agents may offer us a powerful tool for the *in vivo* assessment of drug biodistribution and accumulation at the target site, for the minimally invasive *in vivo* visualization of the drug release from a provided nanovehicle, and for the prediction and real-time monitoring of therapeutic outcome. Thus, constructing compact nanoformulations with highly integrated modalities is of the essence in nanotheranostics. Yet, it has been proven to be a big challenge to fuse multiple components on a single nanoscale particle for combined diagnostics and therapy.

Although efficient cancer therapy is still problematic, currently nanotheranostics develops very fast with significant achievements, fostering a new avenue for cancer therapy and diagnosis. To translate these applications into clinical use, the nanotheranostic agents must be optimized by starting with small-animal models and scaling up to nonhuman primate models. This should lay a solid foundation for the long-term development of nanotheranostics into clinical medical practice.

A survey of the recent advances and basic principles of nanotheranostics with a particular emphasis on the design and fabrication of various multifunctional

nanoparticles for cancer imaging (diagnosis) and therapy is summarized in two volumes of books entitled *Advances in Nanotheranostics I: Design and Fabrication of Theranostic Nanoparticles* and *Advances in Nanotheranostics II: Cancer Theranostic Nanomedicine*.

The volume *Advances in Nanotheranostics I: Design and Fabrication of Theranostic Nanoparticles* has three parts: Part I Gold Nanostructure-Based Theranostics, Part II Theranostic Luminescent Nanoparticles, and Part III Dendrimers and Liposomes for Theranostics. Part I includes three chapters, summarizing synthesis, surface modification, and functionalization of gold nanostructures and their use as therapeutic components, imaging contrast agents, and theranostic platforms for imaging-guided therapy. Part II contains four chapters, each focusing on one of the following: fabrication of lanthanide-doped upconversion nanoparticles, quantum dots, and organic dye-loaded nanoparticles, as well as their applications for multimodal imaging and imaging-guided drug delivery and therapy. Part III consists of three chapters, reviewing dendrimers and liposome-based nanodevices, nanoscale imaging agents, drug delivery systems, and theranostic nanosystems for cancer treatment, respectively.

The volume *Advances in Nanotheranostics II: Cancer Theranostic Nanomedicine* has the following structure: Part I Magnetic Nanoparticles for MRI-Based Theranostics, Part II Ultrasonic Theranostic Agents, and Part III Nanoparticles for Cancer Theranostics. Part I contains three chapters, describing controlled synthesis and surface modification of magnetic nanoparticles, molecular imaging of tumor angiogenesis, and MRI-based theranostics with magnetic nanoparticles. Part II consists of three chapters, summarizing ultrasound contrast agent-based multimodal imaging, drug delivery and therapy, and hollow mesoporous silica nanoparticles for magnetic resonance/ultrasound imaging-guided tumor therapy. Part III includes four chapters, demonstrating multifunctional nanoprobe for multimodality imaging and therapy of gastric cancer, nanoparticles for molecular imaging-guided gene delivery and therapy, silica nanoparticles, and micelles for cancer nanotheranostics, respectively.

It is hoped that these books will be of great interest for readers who want to follow up the exciting new development in theranostic nanomedicine. Each chapter was written by well-recognized experts in the related field. I would like to thank the authors most sincerely for their excellent contributions and congratulate them for the brilliant efforts that have resulted in these superb volumes. I also want to express my thanks to Professor Min Wang at the Department of Mechanical Engineering, University of Hong Kong, who is the Series Editor of Springer Series in Biomaterials Science and Engineering, and Springer Beijing office for providing me such a wonderful opportunity to edit these books, especially Ms. June Tang and Ms. Heather Feng for their support in publishing these volumes.

Contents

Part I Gold Nanostructures Based Theranostics

- 1 **Near-Infrared Light-Mediated Gold Nanoplatfoms for Cancer Theranostics** 3
Liming Wang, Yingying Xu, and Chunying Chen
- 2 **Gold Nanostructures for Cancer Imaging and Therapy** 53
Yongping Gao and Yongsheng Li
- 3 **Gold Nanorods for Biomedical Imaging and Therapy in Cancer** 103
Zhenzhi Shi, Yu Xu, and Aiguo Wu

Part II Theranostic Luminescent Nanoparticles

- 4 **Lanthanide-Doped Upconversion Nanoparticles for Imaging-Guided Drug Delivery and Therapy** 139
Zhanjun Li, Yuanwei Zhang, and Gang Han
- 5 **Engineering Upconversion Nanoparticles for Multimodal Biomedical Imaging-Guided Therapeutic Applications** 165
Wenpei Fan, Jianlin Shi, and Wenbo Bu
- 6 **Multifunctional Quantum Dot-Based Nanoscale Modalities for Theranostic Applications** 197
Bowen Tian
- 7 **Organic Dye-Loaded Nanoparticles for Imaging-Guided Cancer Therapy** 217
Zonghai Sheng and Lintao Cai

Part III Dendrimers and Liposomes for Theranostics

8 Dendrimer-Based Nanodevices as Contrast Agents for MR Imaging Applications	249
Wenjie Sun, Jingchao Li, Mingwu Shen, and Xiangyang Shi	
9 Functional Dendritic Polymer-Based Nanoscale Vehicles for Imaging-Guided Cancer Therapy	271
Yanhong Zhang, Kui Luo, and Zhongwei Gu	
10 Multifunctional Liposomes for Imaging-Guided Therapy.....	301
Xiuli Yue and Zhifei Dai	

Part I
Gold Nanostructures Based Theranostics

Chapter 1

Near-Infrared Light-Mediated Gold Nanoplatfoms for Cancer Theranostics

Liming Wang, Yingying Xu, and Chunying Chen

Abstract In the past decade, great advances have been achieved for the biomedical application of gold (Au) nanostructures. Due to their unique physicochemical properties, Au nanostructures have been extensively explored for their use in cancer cell imaging, photothermal therapy, as well as drug/gene delivery. The facile control of synthesis and surface functionalization help the construction of multifunctional Au nanostructures for cancer diagnosis and treatment. Recently, Au nanostructure-based theranostic platforms have been extensively explored, and great advantages have been demonstrated. This chapter summarizes the recent progress of Au nanostructures as contrast agents for cancer imaging, as therapeutic composites for photothermal therapy and drug/gene delivery, and as multifunctional theranostic platform for cancer. The surface functionalization of Au nanostructures including noncovalent and covalent modification will also be discussed. We focus on the near-infrared (NIR) light-mediated cancer theranostics using Au nanostructures including Au nanoshells (AuNSs), Au nanorods (AuNRs), hollow Au nanospheres (HAuNSs), and Au nanocages (AuNCs).

Keywords Au nanostructures • Imaging • Photothermal therapy • Surface plasmon resonance • Cancer theranostics

L. Wang

CAS Key Laboratory for Biomedical Effects of Nanomaterials and Nanosafety,
Institute of High Energy Physics, Chinese Academy of Sciences, Beijing 100049, China

Y. Xu • C. Chen (✉)

CAS Key Laboratory for Biomedical Effects of Nanomaterials and Nanosafety,
National Center for Nanoscience and Technology of China, Beijing 100190, China
e-mail: chenchy@nanoctr.cn

1.1 Introduction

At present, cancer remains one of the major causes of human death in the world. Traditional cancer treatments, including surgery, chemotherapy, and radiotherapy, usually fail to radical cure because of the recurrence and metastasis of cancer. Chemotherapy, one of the most commonly used cancer treatments, has contributed greatly to reductions in cancer mortality. However, chemotherapeutic agents often cause adverse effects such as liver and kidney damage, hair loss, nausea, and cardiac toxicity [1–3]. These systemic hazards are generally due to the lack of drug specificity toward tumorigenic cells [4]. What's more, chemotherapy usually leads to drug resistance and causes treatment failure [5]. Therefore, there is an urgent need for the development of novel anticancer strategy.

Over the past decade, nanostructure-based cancer therapy and diagnosis have been largely explored. Among them, various types of Au nanostructures have been synthesized by scientists with tunable size and shapes (Fig. 1.1) [6–16]. These gold (Au) nanostructures are promising candidates for cancer theranostics because of their intrinsic physicochemical properties [17, 18]. Several unique features make Au nanostructures particularly suitable for cancer treatment and diagnosis. First, the small size of Au nanostructures enables them to preferentially accumulate at tumor sites either via passive targeting (i.e., the enhanced permeability and retention effect) or active targeting facilitated by tumor-targeting ligands conjugation. Second, the near-infrared (NIR, 650–900 nm) light absorption and scattering of Au nanostructures makes them excellent candidates as contrast agents for NIR imaging such as light scattering imaging, two-photon luminescence imaging, and photoacoustic tomography. Third, efficient light absorption and rapid heat conversion make Au nanostructures efficient photothermal conducting agents used in cancer photothermal ablation therapy. Last, the facile surface chemistry of Au nanostructures eases the simultaneous delivery of drugs, ligands, or imaging contrast agents, which enables the design of multifunctional theranostic nanoplatforms.

In this chapter, we review the recent progress on the NIR light-mediated Au nanoplatforms for cancer theranostics. We first summarize the recent progress on Au nanostructures used for NIR light-triggered optical imaging for cancer and then the hyperthermia therapy of cancer with Au nanostructures by the means of their photothermal effects. The functionalization of Au nanostructures including noncovalent and covalent chemical modification will also be discussed. We emphasize on the researches of NIR light-mediated theranostics application of Au nanoshells (AuNSs), Au nanorods (AuNRs), hollow Au nanospheres (HAuNSs), and Au nanocages (AuNCs).

1.2 Near-Infrared Light-Mediated Cancer Imaging by Au Nanostructures

One of the most dramatic and useful properties distinguishing nanoscale Au from its bulk form is the interaction between gold and light. When an Au nanoparticle is irradiated with light, strong absorption and/or scattering will occur at specific

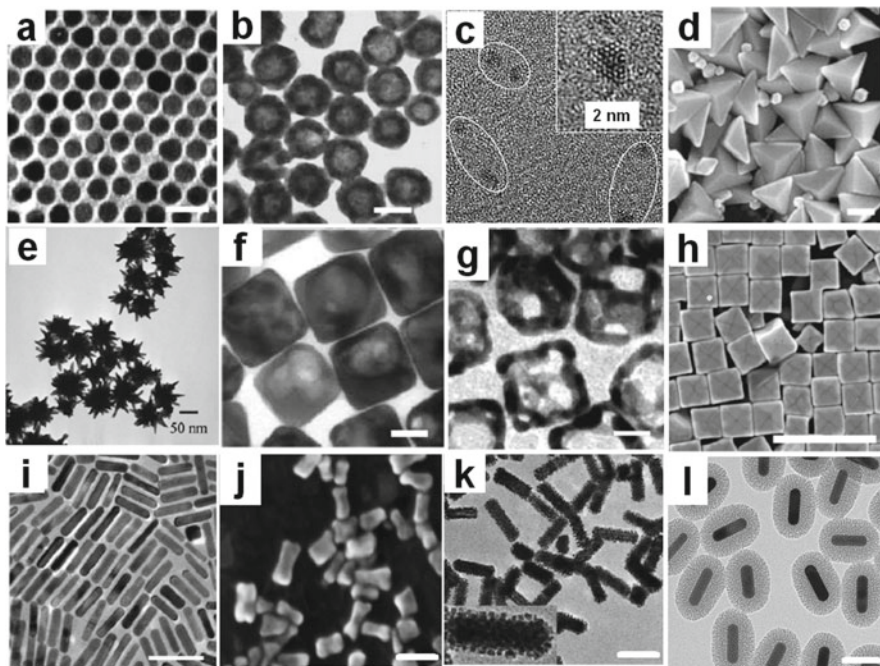


Fig. 1.1 Au nanomaterials of different shapes with potential biomedical use. (a) Au nanospheres (Reprinted with permission from ref. [6]. Copyright 2003, American Chemical Society). (b) Hollow Au nanospheres (Reprinted with permission from ref. [7]. Copyright 2005, American Chemical Society). (c) Au nanoclusters (Reprinted with permission from ref. [12]. Copyright 2011, American Chemical Society). (d) Au obtuse triangular bipyramids (Reprinted with permission from ref. [15]. Copyright 2011, American Chemical Society). (e) Au stars (Reprinted with permission from ref. [16]. Copyright 2012, Royal Society of Chemistry). (f) Au nanoboxes and (g) Au nanocages (Reprinted with permission from ref. [9]. Copyright 2007, American Chemical Society). (h) Au nanocubes (Reprinted with permission from ref. [10]. Copyright 2010, American Chemical Society). (i) Au nanorods (Reprinted with permission from ref. [11]. Copyright 2010, Elsevier Ltd.) (j) Au dog bones (Reprinted with permission from ref. [8]. Copyright 2006, John Wiley & Sons, Inc.). (k) Au@Pt nanorods with Pt nanodots (Reprinted with permission from ref. [13]. Copyright 2011, Elsevier Ltd.). (l) Mesoporous silica-coated Au nanorods (Reprinted with permission from ref. [14]. Copyright 2014, John Wiley & Sons, Inc.) Except of Fig. 1.1c, scale bar in all figures indicates 50 nm

resonant wavelength, which is known as localized surface plasmon resonance (LSPR). This phenomenon has been used for hundreds of years to give a brilliant color to stained glass and decorative artworks. However, the systematic study only began until 1857, when Michael Faraday demonstrated the synthesis of Au colloids in an aqueous medium and attributed the bright colors of the solutions to colloidal Au [19]. Then in 1908, by solving Maxwell's electromagnetic equation, Mie et al. attributed the intense colors in Faraday's Au solution to the absorption and scattering of light by Au nanospheres present in the solution [20]. John Turkevich pioneered a robust and simple synthesis method in 1951 [21]. Based on these studies, researchers developed novel strategies to exploit the unique physicochemical

properties and application of Au nanostructures [22–24]. By utilizing their optical properties, Au nanostructures have been extensively investigated for biomedical applications including biosensing, imaging, and cancer theranostics in recent years [25–28].

The frequency and cross section of LSPR absorption depend greatly on the size, shape, morphology, and dielectric environment of the Au nanostructures [29, 30]. For Au spherical nanoparticles (AuNSs), the LSPR absorption is at about 520 nm, and the peak wavelength varies slightly depending on the size and the embedding medium [29]. However, Au nanostructures such as nanoshells, nanorods, hollow nanospheres, and nanocages exhibit well-defined LSPR absorption features from the visible to the NIR region [31]. The optical properties of Au nanostructures enable their application as novel imaging and sensing probes. Due to the sensitivity of a nanostructure's LSPR to its surrounding environment, Au nanostructures have been developed as biosensors based on the shift of the LSPR for the detection of the local refractive index/dielectric constant of the environment surrounding the Au nanostructures [32].

Besides as biosensors, Au nanostructures with LSPR in the NIR region are also developed as novel imaging probes due to their interesting optical properties [33, 34]. Au nanostructures are especially attractive for their highly efficient absorption in the NIR region, a spectral window minimally absorbed by skin and tissue, which permits photons to penetrate biological tissues with relatively high transitivity. Au nanostructures have been employed as contrast agents for cancer imaging by using several imaging tools including dark-field microscope, two-photon luminescence (TPL), photoacoustic tomography (PAT), X-ray computed tomography (CT), optical coherence tomography (OCT), and surface-enhanced Raman scattering (SERS).

1.2.1 Dark-Field Microscopy

Au nanostructures exhibit enhanced Rayleigh scattering originating from their LSPR, which is heavily dependent on the nanostructure size and shape [35, 36]. Dark-field microscopic imaging is based on the intense light scattering ability of Au nanostructures [37]. The transmitted light is blocked, and scattered light is collected, showing bright scattering particles against a dark background. Compared to fluorescent dye molecules, the scattering cross sections of Au nanostructures give stronger photon intensity by more than four to five orders of magnitude [38]. Therefore, high-contrast images are attainable if the Au nanostructures accumulate within cancer cells by passive or active targeting.

Sokolov et al. functionalized AuNPs with the anti-epidermal growth factor receptor (EGFR) antibodies and observed bright light emission under dark-field monochromatic light illumination inside cervical cancer cell line SiHa, which over-expressed EGFR on the cell membrane. However, AuNPs functionalized with bovine serum albumin were not observed in the cell, which illustrated the necessity of EGFR-mediated targeting for cancer cell imaging [39]. El-Sayed et al. compared

the cellular binding and uptake of anti-EGFR conjugated AuNPs in nonmalignant malignant epithelial cell lines by dark-field imaging [40]. After incubation with anti-EGFR conjugated AuNPs, cancerous cells exhibited stronger light scattering than healthy cells when imaged using a dark-field microscopy, which demonstrated the great sensitivity of using dark-field light scattering to identify cancerous cells. Scattering from AuNPs has also been used for tracking dynamics of cancer cell mitosis and cell division [41].

Dark-field imaging has also enabled visualization of Au nanorods (AuNRs)-mediated cancer cell targeting and cellular localization [42, 43]. Huang et al. also observed strong light scattering from AuNRs in the NIR region [44]. They conjugated AuNRs with anti-EGFR antibodies to target two malignant epithelial cell lines, human oral squamous carcinomas HSC and HOC. The conjugate selectively accumulated in the malignant cell lines but not in a benign cell line HaCat (Fig. 1.2a, b). Oyelere et al. used the enhanced light scattering in a dark-field arrangement to identify nuclear localization of AuNRs after conjugation with nuclear localizing sequence (NLS) peptides [45]. Although the peptide-conjugated AuNRs were distributed into both nucleus and cytoplasm in either normal or cancer cells, the AuNRs were more concentrated in the nucleus of the cancer cells (Fig. 1.2c, d). By using

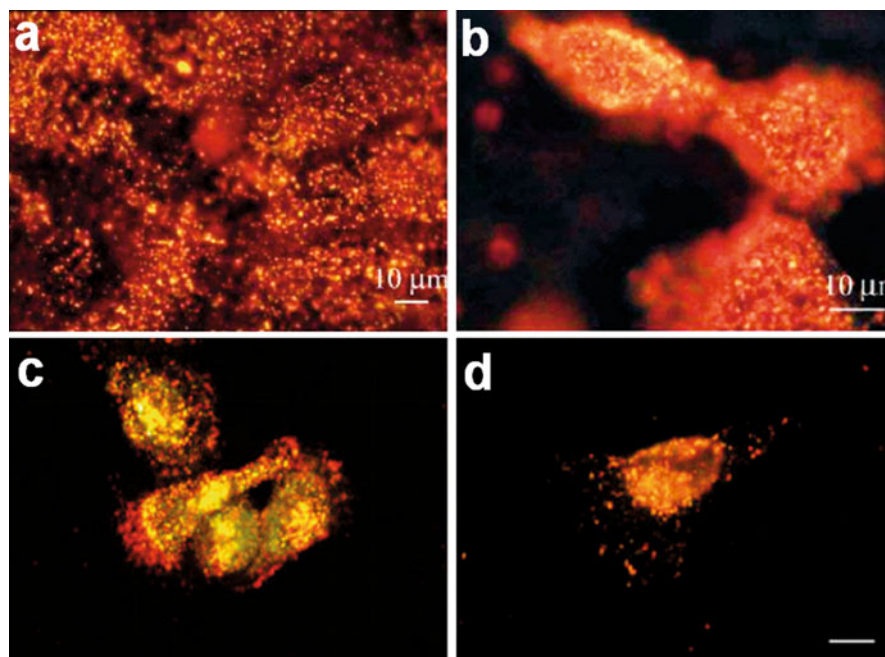


Fig. 1.2 Images of intracellular AuNRs. (a, b) Light scattering images of anti-EGFR-conjugated AuNRs after incubation with HaCaT nonmalignant cells (a) and HSC malignant cells for 30 min at room temperature (Reprinted with permission from ref. [44]. Copyright 2006, American Chemical Society). (c, d) HaCat normal cells (c) and HSC cancer cells (d) treated with nuclear localizing sequence (NLS) peptide-conjugated AuNRs. Scale bar: 10 μm (Reprinted with permission from ref. [45]. Copyright 2007, American Chemical Society)

dark-field microscopy and electron microscopy, Ding et al. studied the uptake and distribution of transferrin (Tf)-conjugated AuNRs in HeLa cells, which overexpressed the transferrin receptor (TfR) [46]. Minimal cellular uptake was observed with untargeted AuNRs compared to the conjugated AuNRs, which demonstrated receptor-mediated uptake of AuNRs into HeLa cells. Dark-field imaging has also been used for real-time tracking of AuNRs-induced DNA damage, causing cytokinesis arrest and apoptosis in cancer cells [47].

1.2.2 Two-Photon Luminescence (TPL)

Photoluminescence from Au nanostructures has drawn extensive interest in the past decade due to their bright, non-blinking, and stable emission. TPL of Au nanostructures exhibit increased light-penetration depth, submicron spatial resolution, low background fluorescence, and reduced photodamage to living tissues [48, 49]. Two-photon absorption occurs when Au nanostructures are excited with a femtosecond pulsed-NIR laser resonant with the surface plasmon energy. TPL is able to produce very strong signals under NIR laser excitation, even allowing single nanoparticle to be detected [50].

AuNRs, AuNSs, AuNCs, Au nanostars, and other nanostructures have been extensively exploited as TPL contrast agents. For instance, Durr et al. studied the capability of TPL imaging in a 3D tissue model using anti-EGFR antibody-conjugated AuNRs to target cancer cells embedded in the collagen matrices. The TPL signals of AuNRs are three orders of magnitude stronger than the autofluorescence from the surrounding tissues. These results demonstrated that AuNRs have strong signal, resistance to photobleaching, and good chemical stability and can serve as attractive contrast agent for TPL imaging of cancers [51]. Anti-EGFR antibody-conjugated AuNRs were also investigated for their effective binding both in A431, human squamous carcinoma cell line cells, in vitro and subcutaneous xenografts of A431 from Swiss nu/nu mice in vivo by using TPL imaging [52]. Tong et al. studied the targeting of folate-conjugated AuNRs and photo-induced injury to KB cancer cells and NIH-3T3 normal fibroblasts using TPL imaging. The localization of AuNRs after different incubation time was visualized, illustrating ligand-receptor binding-mediated endocytosis [53] (Fig. 1.3a–c). Selective targeting and internalization of chitosan oligosaccharide-modified AuNRs were visualized via TPL imaging in human oral adenosquamous carcinoma cell line CAL 27.

Further in vivo studies performed via NIR laser irradiation revealed similar targeting of the AuNRs conjugates in CAL 27 xenograft tumors [54]. By using fluorescence lifetime imaging microscopy (FLIM), which provides images with better contrast and sensitivity than intensity imaging, Zhang et al. studied the imaging of AuNRs in Madin-Darby canine kidney (MDCK) cells. They demonstrated that the characteristic fluorescence lifetime of AuNRs was less than 100 ps and could be used to distinguish AuNRs from other fluorescent labels and endogenous fluorophores in lifetime imaging [55]. As shown in Fig. 1.4a–c, AuNRs have the maximal

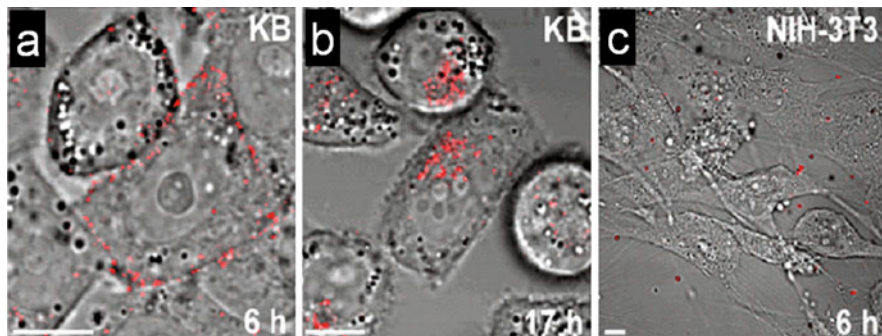


Fig. 1.3 (a–c) Targeted adsorption and uptake of folate-conjugated AuNRs (F-AuNRs, red) by KB cells overexpressing folate receptors. (a) A high density of F-AuNRs was observed on the surface of KB cells after 6 h incubation at 37 °C. (b) F-AuNRs were internalized into KB cells and delivered to the perinuclear region after 17 h incubation. (c) No binding was observed of F-AuNRs to NIH-3T3 cells, which express folate receptors at a low level. Scale bar = 10 μm (Reprinted with permission from ref. [53]. Copyright 2007, John Wiley & Sons, Inc.)

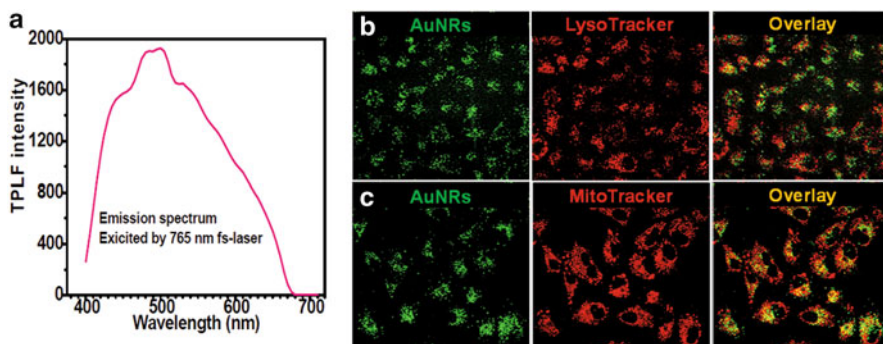


Fig. 1.4 Two-photon luminescence imaging of AuNRs and Au nanoshells in vitro and in vivo. (a) Luminescence emission spectrum of AuNRs when excited by two-photon laser at an optical wavelength of 765 nm, which is the LSPR maximum of these AuNRs (Reprinted with permission from ref. [14]. Copyright 2014, John Wiley & Sons, Inc.). (b, c) TPL images of serum protein-adsorbed CTAB-capped AuNRs with the organelles of human lung cancer cell line (A549). The green fluorescence indicates the AuNRs and the red color indicates the lysosomes (b) or the mitochondria (c). (Reprinted with permission from ref. [56]. Copyright 2011, American Chemical Society)

LSPR absorption, enabling TPL imaging of AuNRs inside cells. Based on TEM and TPL images, Wang et al. observed that CTAB-capped AuNRs can target the mitochondria of human lung cancer A549 cells and kill them efficiently. These AuNRs have a less storage at the lysosomes in normal human bronchiolar epithelial cell lines compared to cancer cells, which cause negligible effects on cell viability [56].

Besides AuNRs, Au nanostars have also been used as TPL contrast agents. Au nanostars functionalized with wheat-germ agglutinin have been utilized to image the cellular uptake in breast cancer cells, as well as the circulation in the vasculature in vivo in mouse models [57].

AuNSs [49, 58] and AuNCs [59] have also been extensively exploited as TPL contrast agents. The injected AuNS into a Balb/c mouse with subcutaneous tumors can clearly show the tumor and blood vessel structure based on in vivo TPL imaging [47]. AuNSs could be observed even as single nanoshell particles in blood vessels and generate optical contrast for blood vessel structure using TPL microscopy, which enable the tracking of AuNSs in vivo [60]. TPL of AuNCs has been used to examine the uptake of antibody-conjugated and PEGylated AuNCs by U87MGwtEGFR cells. Antibody-conjugated AuNCs could be attached to the surface of the cells and internalized into the cells via receptor-mediated endocytosis [61].

1.2.3 Photoacoustic Tomography (PAT)

PAT is a new combinational imaging method which detects the ultrasonic waves thermoelastically converted by photons in tissue through the photoacoustic effect. It requires a nanosecond-pulsed laser as an excitation source to stimulate thermal and acoustic responses. And acoustic waves are detected by an ultrasonic transducer to subsequently form a high-resolution tomographic image. The materials used for PAT imaging need to be able to absorb light and convert it into heat efficiently. Au nanostructures are ideal candidates for PAT imaging for their LSPR-based light absorption.

Au nanostructure-mediated PAT has been realized with AuNPs [62], AuNRs [63], and AuNSs [64]. Mallidi et al. performed multiwavelength PAT on gelatin implants in ex vivo mouse tissue containing anti-EGFR-labeled AuNPs targeted to epithelial carcinoma cells. High sensitivity and selectivity in the photoacoustic signal were achieved with the molecularly targeted AuNPs compared to nontargeted AuNPs and a NIR-absorbing dye [65]. Kim et al. investigated AuNCs conjugated with melanocyte-stimulating hormone for molecular PAT of melanomas in vivo. Compared to unconjugated AuNCs, a 300 % enhancement of contrast was achieved compared to the control PEGylated AuNCs [66]. AuNC-enhanced PAT was also used for sentinel lymph node mapping in a rat model, which provided valuable information for metastatic cancer staging [67]. Due to the tunable optical absorption property of AuNRs, multiple selective targeting on oral cancer cells both in vitro and in vivo can be observed according to PAT imaging [68]. The contour of the tumor region was sharply visualized in fusion images acquired from PAT signals with antibody-mediated targeting, while imaging was not obtained at the tumor sites of mice injected with AuNRs alone. Intracellular AuNRs imaging was reported by Yang et al. Using a homemade photoacoustic microscope, time-dependent cellular uptake and distribution of AuNRs in human breast adenocarcinoma cell line were

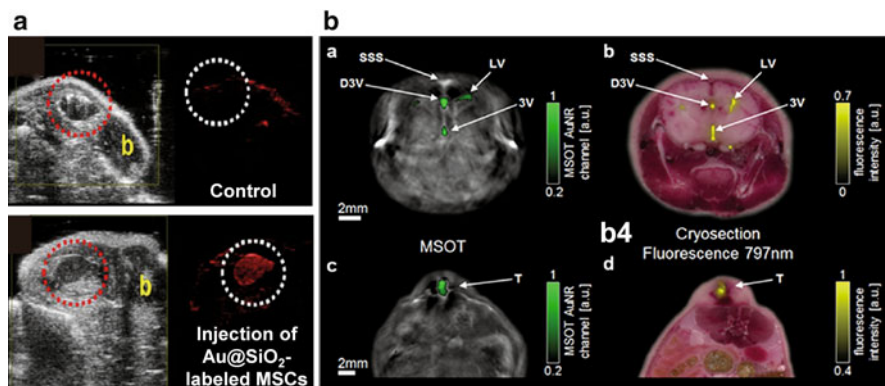


Fig. 1.5 (a) In vivo backscatter mode ultrasound (*gray scale*) and PAT (*red*) images of the intramuscular injection of a negative control (No Au@SiO₂, no cells) and Au@SiO₂-labeled mesenchymal stem cells in 50 % matrigel/PBS into hind limb muscle of an athymic mouse. “b” indicates bone and the *red-dashed circle* highlights the injection (Reprinted with permission from ref. [70]. Copyright 2012, American Chemical Society). (b) PAT and fluorescence imaging of NIR-liposome-AuNR hybrids in (b1, b2) the brain and (b3, b4) tumor tissue. (b1, b2) PAT image after injection of 5 μ L of the hybrid into the dorsal third ventricle (D3V) of the mouse brain. (b3, b4) Images are obtained 6 h after injection of the hybrid into an HT29 xenograft (T). (b2, b4) Corresponding images of cryosectioned brain tissue and tumor tissue. *Abbreviations*: SSS superior sagittal sinus, LV lateral ventricle, 3V third ventricle. The *green overlay* shows PAT signal from the AuNRs. The *grayscale* background is an optoacoustic image taken at 900 nm (Reprinted with permission from ref. [74]. Copyright 2012, American Chemical Society)

successfully monitored [69]. Recently, mesoporous silica-coated AuNRs (Au@SiO₂)-based PAT imaging has been investigated. Jokerst et al. reported PAT imaging of mesenchymal stem cells in living mice via Au@SiO₂ [70]. They monitored mesenchymal stem cells in living mice via Au@SiO₂ and found that the silica layer enhanced the photoacoustic signal of AuNRs (Fig. 1.5a). These studies demonstrate that Au nanostructures have great potential for contrast enhancement of PAT imaging. With the development in rational design and preparation of unique nanostructures with targeting capacity, the desired spatiotemporal resolution of PAT will be realized.

1.2.4 X-ray Computed Tomography (CT)

X-ray CT is an imaging technique based on the different absorption of X-ray by different compositions of the tissue. Small iodinated molecules are generally used as contrast agents in X-ray CT due to their high X-ray absorption coefficient. However, these contrast agents generally experience rapid renal excretion and allow very short time imaging.

Recently, Au nanostructures have attracted much attention as CT contrast agents for the detection of cells and tissues due to their strong X-ray absorption ability. von Maltzahn et al. developed a PEG-coated AuNRs which exhibited twofold higher X-ray absorption than a clinical iodine contrast agent [71]. By using X-ray CT, the biodistribution and accumulation of PEG-AuNRs were monitored. With four-dimensional biodistribution-based heat transfer simulations, they achieved complete tumor regression in mice treated with PEG-AuNRs following computationally tailored irradiation. Luo et al. reported Au@SiO₂ loading the cyanine dye indocyanine green (ICG) for the dual modality of X-ray CT and fluorescence imaging [72]. They demonstrated that Au@SiO₂ could enhance the CT contrast significantly and multiplexed images could be obtained by this dual-mode imaging. By conjugating Au@SiO₂ with the tumor-targeting molecule folic acid, the same group used X-ray CT to monitor the tumor-targeting ability of folic acid-conjugated Au@SiO₂ [73].

1.2.5 Optical Coherence Tomography (OCT)

OCT is a newly developed optical imaging technique which can capture three-dimensional cellular and subcellular tissue morphology using the coherence-gated detection of scattered light. OCT is based on low-coherence interferometry, in which tissue is illuminated with light of low coherence in NIR region, and the detection is based on coherence matching between the incident and reflected beams. Au nanostructures have been used as OCT contrast-enhancing agents due to their intense optical absorption or scattering ability (Fig. 1.5b) [70, 74].

Zagaynova et al. employed NIR-resonant AuNSs as OCT contrast agents for deep tissue (up to 2 mm depth) imaging of rabbit epidermal tissue. AuNSs enhanced the OCT signal of the different regions of the dermis with high spatiotemporal resolution [75]. AuNRs-mediated OCT contrast enhancement was also reported in human breast tissue samples [76]. AuNRs significantly enhance the tissue depth for the detection of OCT signals. In another work, AuNRs uptake in sentinel lymph node (SLN) of mice in situ was monitored by OCT imaging [77]. Improved resolution was obtained with AuNRs-mediated OCT system compared to conventional scattering OCT. Kim et al. employed AuNPs conjugated with anti-EGFR antibodies to enhance OCT contrast of oral dysplasia in a hamster model in vivo [78]. By using microneedles and ultrasound, the distribution and penetration depth of AuNPs into skin tissue were improved, and obvious differences could be observed between micro-morphologies of the carcinogen-treated and untreated epithelial tissues with OCT imaging. This study demonstrates an effective approach to improve the penetration and transportation of nanoparticles for OCT contrast enhancement for the early diagnosis of cancer.

1.2.6 *Surface-Enhanced Raman Scattering (SERS)*

SERS was first reported in the late 1970s. When a molecule is absorbed on rough metal surfaces or nanostructures, Raman signal enhancement occurs and results in up to 10^{14} enhancement compared to traditional Raman scattering [79]. Although the exact mechanism that results in surface enhancement has not been completely elucidated, there are two generally accepted mechanisms, electromagnetic (EM) and chemical enhancement (CE). The EM mechanism requires the excitation of the LSPR of a surface, which leads to an increase in the local EM field. The CE involves charge transfer interactions between the surface and the molecules adsorbed on it [80]. The EM is the dominant mode of enhancement between the two mechanisms.

Due to the strong LSPR, Au nanostructures can enhance the Raman signals of the molecules absorbed on their surface by many orders of magnitude. The Au nanostructure-based SERS enable ultrasensitive biomarkers detection, SERS-based imaging, and image-guided therapy [81–85]. Huang et al. reported label-free SERS for cancer identification using tumor-targeting AuNRs [86]. They recorded the SERS spectra in cancerous and healthy cell lines incubated with anti-EGFR antibody-conjugated AuNRs. The signals of SERS spectra obtained from cancerous cells were greatly enhanced. Kang et al. utilized AuNPs to obtain SERS spectra of living HSC-3 cells throughout the entire life cycle [87]. AuNPs were functionalized with nuclear localizing sequence (NLS) peptides to facilitate AuNPs nuclear localization. The different phases of cell cycle were simultaneously recorded by Rayleigh images and Raman spectra in real time, and the phase-specific SERS bands could be identified by the observed Raman DNA and protein peaks.

Dual modality imaging has been recently investigated with iron oxide-Au heteronanostructures functionalized with a Raman-active dye molecule, DTTC (AuMN-DTTC). The probe can be visualized both *in silico* and *in vivo* in deep tissue in live animals. After injecting the nanostructures deep into the gluteal muscle, MRI-SERS imaging was obtained, and Au nanostructure-mediated Raman enhancement was clearly observed [88] (Fig. 1.6). Wang et al. labeled AuNPs with epidermal growth factor (EGF) peptide for circulating tumor cells (CTCs) targeting. CTCs are cells circulating in the bloodstream which have been shed from a primary tumor. CTCs are responsible for the development of tumor metastasis. By using SERS, they successfully identified CTCs from blood samples of patients with different stages of squamous cell carcinoma of the head and neck, with a range of 1 to 720 CTCs per milliliter of whole blood [89]. These results demonstrate that Au nanostructure-based SERS imaging may provide a promising platform for multi-modal imaging and imaging-guided cancer therapy.

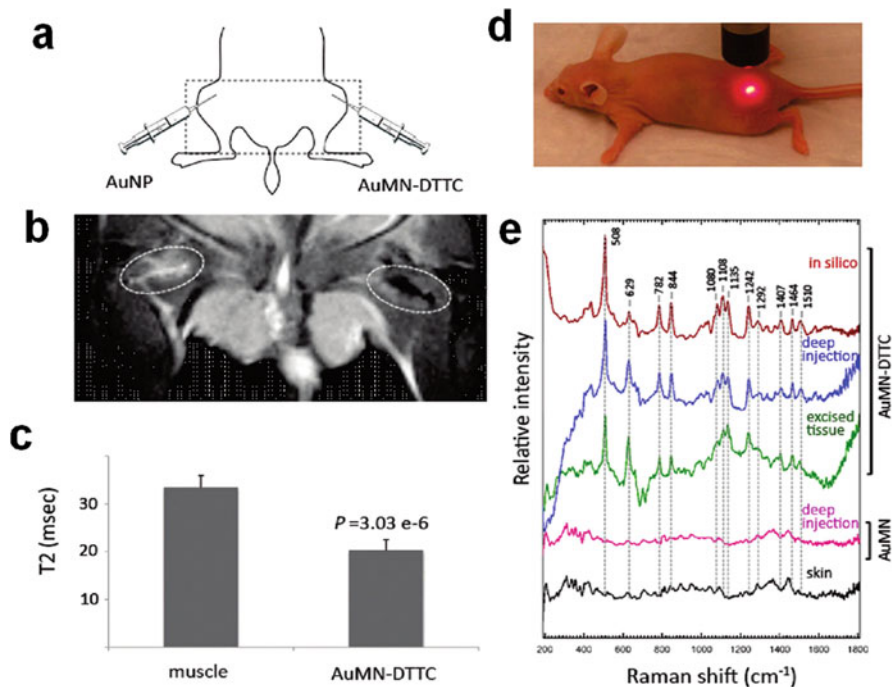


Fig. 1.6 MRI and Raman spectroscopy of AuNPs complexed with dextran-coated superparamagnetic iron oxide nanoparticles (AuMN-DTTC) in vivo. (a) A schematic of the probe injection setup. The experimental AuMN-DTTC probe was injected in the deep right gluteal muscle. A control probe was injected in the contralateral muscle. (b) In vivo T2-weighted MR image of a mouse injected intramuscularly (i.m.) with AuMN-DTTC and the control probe, AuNPs. Notable loss of signal intensity associated with the site of the AuMN-DTTC injection indicated the suitability of the probe as an in vivo MRI contrast agent. (c) Calculated T2 values based on multiecho T2-weighted MRI. The T2 relaxation time of AuMN-DTTC was significantly lower than both noninjected muscle and muscle injected with AuNPs ($n=3$; Student's t test; $p<0.05$). (d) A photograph demonstrating the Raman spectroscopy experimental setup. (e) In vivo Raman spectra of a mouse injected i.m. with AuMN-DTTC and the control probe, AuMN. The in vivo Raman spectrum of muscle injected with AuMN-DTTC has a clear SERS signature, which is indistinguishable from that obtained ex vivo and in silico and is absent in skin tissue and in muscle injected with the control probe (Reprinted with permission from ref. [88]. Copyright 2011, American Chemical Society)

1.3 Cancer Photothermal Therapy by Au Nanostructures

One of the major therapeutic applications of Au nanostructures is to treat cancers as photothermal therapy agents. Au nanostructures can efficiently absorb light followed by rapid heat conversion, which makes them suitable candidates for cancer photothermal therapy. Additionally, the absorption wavelength of Au nanostructures can be easily tuned to the NIR region by changing their size and shape, which allows high-depth cancer photothermal therapy in tissues.

The early research about Au nanostructure for photothermal therapy was spherical AuNPs reported by Lin and co-workers in 2003. They conjugated AuNPs with IgG to target the CD8 receptor on the peripheral blood lymphocyte cells. After irradiation with a nanosecond-pulsed visible laser, they found that 95 % of cells containing as few as ~500 nanoparticles per cell were killed (versus 5–8 % in a control treatment) [90]. After that, El-Sayed group reported selective cancer photothermal therapy using spherical AuNPs conjugated to anti-EGFR antibodies [91]. The tumor-targeting AuNPs could specifically accumulate in HSC and HOC human oral squamous cell lines while not in a benign cell line (HaCaT). Under the irradiation of a continuous wave argon ion laser at 514 nm, the two cancer cell lines were damaged by hyperthermia within 4 min at laser energy thresholds of 19 and 25 W/cm² respectively, which is much less than that of the benign cells (57 W/cm²). The results indicated a selective photothermal damage of cancer cells.

The absorption and scattering coefficients AuNRs are an order of magnitude higher than those of AuNPs and AuNSs. Therefore, the applications of AuNRs for cancer photothermal therapy have been extensively investigated in the past decade. Tong et al. studied the mechanism of hyperthermia-induced cell necrosis by folate-conjugated AuNRs [53]. They observed a rapid increase in intracellular calcium induced by photothermal therapy. Additionally, disruption of the actin-network and the formation of membrane blebs were observed. The authors found that the damage to the cells was more effective when AuNRs were adsorbed to the cell surface prior to uptake. They thus attributed the cell necrosis to the disruption of the plasma membrane. To avoid photothermal damage to the healthy cells, Rejiya et al. conjugated AuNRs with anti-EGFR antibody [92]. The targeting efficiency of anti-EGFR-AuNRs to tumor was evaluated by inductively coupled plasma-atomic emission spectroscopy (ICP-AES) and immunofluorescence studies, which showed much higher cellular uptake of anti-EGFR-AuNRs by A431 cells compared to unconjugated AuNRs. With laser irradiation, anti-EGFR-AuNRs treatment induced 92 % mortality of the carcinoma cells, while only 9 % cell death was induced by unconjugated AuNRs treatment. The author also demonstrated that anti-EGFR-AuNRs selectively induced cancer cell apoptosis through ROS-mediated mitochondrial pathway under low power laser exposure. By using PEG-conjugated AuNRs, Dickerson et al. studied the cancer photothermal therapy in vivo [93]. The nanoparticles were injected intravenously or directly to subcutaneous squamous cell carcinoma xenografts grown in nude (nu/nu) mice. Suppression of tumor growth was observed by NIR laser- induced hyperthermia after intravenous or direct injection. Li et al. investigated the cancer photothermal therapy of RGD-conjugated dendrimer-modified AuNRs (RGD-AuNRs) in vivo [94]. RGD-AuNRs could specifically target tumor cells overexpressing $\alpha_v\beta_3$ integrin both in vitro and in vivo. The selective destructive effects on solid tumors under NIR laser irradiation were therefore achieved. Our group has designed mesoporous silica-coated AuNRs (Au@SiO₂) loaded with doxorubicin (DOX) for simultaneous TPL imaging, photothermal therapy, and drug delivery in cancer cells [95]. NIR light-triggered drug release was realized for chemotherapy by low-intensity NIR laser irradiation, while higher irradiation intensity also induced obvious hyperthermia effects of the AuNRs for direct

cell killing. Synergistic effect was achieved for combined thermo-chemotherapy compared to hyperthermia or chemotherapy alone (Fig. 1.7).

Photothermal therapy of AuNSs has also been studied extensively to treat cancer, and the nanoshells are currently under FDA-trial. AuNSs exhibit similar optical properties to AuNPs, and the LSPR of AuNSs can be shifted to the NIR region, which is dependent on the relative thickness of Au shell to the core size [96]. Hirsh et al. first demonstrated that AuNSs as photothermal agents can be formulated with a dielectric silica core and an ultrathin Au shell [97]. Bernardi et al. conjugated AuNSs with antibodies against interleukin-13 receptor-alpha 2 (IL13R α 2) to target medulloblastoma and glioma human brain tumor cell lines [98]. The tumor-targeting AuNSs induced photothermal ablation in the two cell lines in vitro with high specificity and sensitivity. Day et al. reported in vivo photothermal therapy of glioma tumor models and demonstrated much longer survival rate of mice that were administered with nanoshells compared to that of mice with only laser treatment [99]. Combined cancer therapy has been reported by combining photothermal therapy and radiotherapy. AuNSs-mediated photothermal therapy can increase tumor vascular perfusion and reduces the resistance of the hypoxic region of tumors to radiotherapy [100].

These studies demonstrate the great potential of Au nanostructure-mediated hyperthermia in cancer therapy. Using the Au nanostructure-mediated photothermal therapy, multifunctional platforms could be constructed combining photothermal therapy with cancer imaging or other treatment strategies. In the past decade, Au nanostructures with unique geometrics have been explored for new diagnostic and therapeutic applications. The tunable geometric shapes endow Au nanostructures with unique LSPR effects, which make them highly potential both in cancer imaging and therapy. In addition, the easy functionalization of Au nanostructures endows them readily be adapted to various biomedical applications.

1.4 Functionalization of Au Nanostructures

One of the most advantageous properties of Au nanostructures in the biomedical field is their surface stability, which affords facile surface functionalization with various biological molecules. By noncovalent and covalent surface modification, specific biological targeting, imaging, and diagnostic molecules can be attached to Au nanostructures. Besides, the potentially toxic initial-stabilizing agents during the synthesis of Au nanostructures can be removed and replaced to improve their biocompatibility. For instance, AuNRs prepared by the wet chemical seed-mediated synthesis are coated with the surfactant of cetyltrimethylammonium bromide (CTAB), which makes the surface of AuNRs positively charged and prevents their aggregation. However, CTAB can cause cytotoxicity by disrupting the biomembrane integrity [11]. Noncovalent modifications include electrostatic interactions,

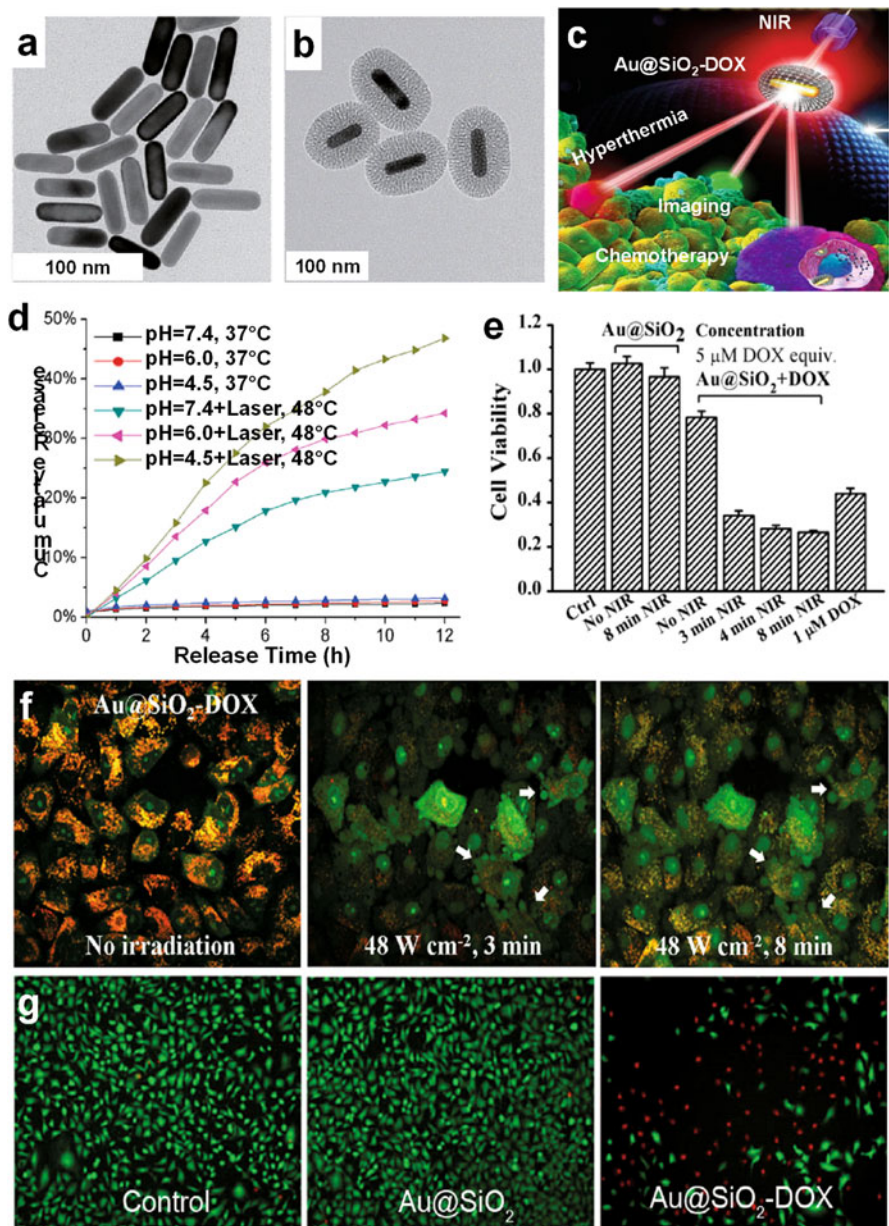


Fig. 1.7 TEM images of (a) AuNRs and (b) Au@SiO₂. (c) Schematic illustration of Au@SiO₂-DOX as a novel multifunctional theranostic platform to treat cancers. (d) DOX release profiles from Au@SiO₂-DOX at different pHs, with and without a 790 nm laser irradiation. (e) After 24 h uptake of Au@SiO₂ and Au@SiO₂-DOX, differences in viability of human lung cancer A549 cells irradiated by the laser for 3, 4, and 8 min, determined by CCK-8 assay. (f) Effects of NIR laser irradiation on the lysosomal membrane integrity determined by acridine orange (AO) staining. Au@SiO₂-DOX-treated cells are irradiated by a laser at 48 W/cm² for 0, 3, and 8 min. (g) Live-Dead staining of A549 cells 24 h postirradiation. A549 cells are treated with Au@SiO₂ or Au@SiO₂-DOX for 24 h and then radiated for 3 min using a laser at 20 W/cm² (Reprinted with permission from ref. [95]. Copyright 2012, John Wiley & Sons, Inc.)

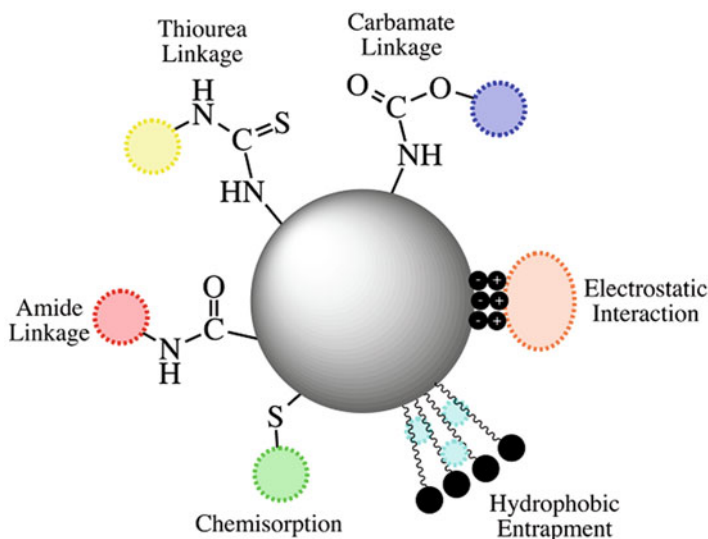


Fig. 1.8 Common surface functionalization strategies for Au nanostructures for use in biomedical applications (Reprinted with permission from ref. [33]. Copyright 2014, Springer-Verlag Berlin Heidelberg)

hydrophobic entrapment, and van der Waals force interactions, while covalent modifications utilize direct chemical attachment, linker molecules, or click chemistry (Fig. 1.8).

1.4.1 Noncovalent Functionalization

Noncovalent functionalization of Au nanostructures generally needs the assembly with a variety of superstructures and the inclusion of new functionalities, which can be realized by electrostatic attraction, antibody-antigen interaction, or DNA sequence recognition. Electrostatic interactions are common strategy to functionalize Au nanostructures to biomolecules, such as DNA, peptides, and antibodies. The interaction depends on the attraction between oppositely charged nanostructure and the biomolecule of interest. Since the biomolecule is not exposed to harsh chemical modifications, this functionalization could keep its native, active conformation. For instance, McIntosh et al. utilized electrostatic interaction to functionalize cationic Au clusters with DNA using the negatively charged phosphate backbone of DNA [101]. The stability of the DNA-functionalized Au clusters was verified by UV-Vis spectroscopy and dynamic light scattering (DLS). Huang et al. have also used this interaction to functionalize AuNPs and AuNRs with anti-EGFR antibodies to selectively target and photothermally ablate cancer cells [44, 86]. One widely used strategy for the surface modification of AuNRs is layer-by-layer electrostatic absorption,

which involves the sequential deposition of negatively and positively charged polyelectrolytes to the positively charged surface of AuNRs [102]. Negatively charged polyacrylic acid (PAA) and polystyrene sulfonate (PSS) are often used as a mild detergent and absorbent to remove CTAB, and then positively charged polyelectrolytes such as poly(diallyldimethyl-ammonium chloride) (PDDAC) or poly (allylamine hydrochloride) (PAH) will be absorbed on the surface of PAA/PSS-coated AuNRs. The deposition cycle can be repeated, and multilayered polyelectrolytes can be formed. Biological polyelectrolytes and proteins can also be deposited among the appropriate layer through electrostatic adsorption [103–105].

Hydrophobic entrapment is generally used for the loading of hydrophobic molecules. Kim et al. utilized the noncovalent interactions to load hydrophobic therapeutics tamoxifen and β -lapachone to AuNPs [106]. The AuNPs were functionalized with water-soluble zwitterionic ligands to form kinetically stable complexes with hydrophobic drugs and dyes. The complex mimicked micelle structures and facilitated the encapsulation of hydrophobic drugs in the hydrophobic pockets. Another noncovalent surface modification for AuNRs is to coat AuNRs with a mesoporous silica layer [107]. Mesoporous silica nanoparticles are ideal drug carriers with high surface area and large pore volume [108], which endow AuNRs excellent drug delivery system. Our group has developed Au@SiO₂ as a light-mediated multifunctional theranostic platform for cancer treatment [95, 109].

1.4.2 Covalent Functionalization

Covalent functionalization generally provides greater stability and reproducibility of the attached molecules compared to noncovalent functionalization. Au-thiol (Au-S) bonding chemistry is commonly utilized for the covalent surface modification of Au nanostructures. Thiolated biopolymers such as PEG have been extensively employed for the functionalization of Au nanostructures. Thiol-terminated PEG endows Au nanostructures high stabilities and improves their biocompatibilities. Additionally, PEG functionalization can avoid nonspecific binding of serum proteins when introduced into in vivo systems [110, 111].

Au-S bond formation has been used to attach oligonucleotides to the surfaces of Au nanostructures. Alivisatos and Mirkin have independently reported oligonucleotide functionalized AuNPs in 1996 [112, 113]. Then various biomedical applications have been explored by using this kind of functionalization, such as hepatitis C virus detection, intracellular gene regulation, and mercuric ion detection [114–116]. Tumor-targeting peptide RGD has also been conjugated to AuNPs and AuNRs surfaces through the Au-S bond [117, 118]. To promote nuclear localization, nuclear localizing sequence (NLS) peptide has also been conjugated to AuNPs and AuNRs via cysteine residues located within the peptides [45, 47]. Black et al. conjugated deltorphin, a high-affinity ligand for delta opioid receptor (deltaOR) to AuNRs through a thiolated PEG for specific targeting of cancer cells [119]. Some other

thiolated species have also been used for the surface functionalization of Au nanostructures, such as thiolated DNA for gene therapy. For instance, Yamashita et al. reported a controlled-release system of single-stranded DNA (ssDNA) triggered by the photothermal effect of AuNRs by modifying AuNRs with double-stranded DNA (dsDNA). When the dsDNA-modified AuNRs were irradiated by NIR light, the ssDNA could be released from AuNRs due to the photothermal effect [120].

Bifunctionalized linkers are generally used to covalently attach therapeutic drugs and biomolecules to nanostructures to reduce the possibility of structural changes, since it has been demonstrated that proteins that directly interact with the nanoparticle surface may undergo conformational changes and alter their biological activity [121]. By using a pH-sensitive hydrazone linker, Prabakaran et al. covalently attached DOX to the hydrophobic inner layer of the folic acid-conjugated amphiphilic AuNPs. The targeted DOX-conjugated AuNPs showed selective uptake and DOX release to breast cancer cells [122]. Qian et al. conjugated tumor-targeting antibodies, single-chain variable fragment (ScFv) antibodies, to AuNPs using heterobifunctional PEG linkers and EDC/NHS coupling [123]. Click chemistry has been utilized for Au nanostructures functionalization and related applications. By using click chemistry, Fischler et al. coupled azide-functionalized AuNPs to an alkyne-modified DNA duplex, to obtain a chain-like assembly of AuNPs on the DNA template [124]. Click chemistry-based assay has also been explored for quantitative detection of proteins. This assay has a broader linear range and good selectivity compared to conventional methods, which enables the analysis of total proteins in various sera and milk samples [125].

1.5 Au Nanoshells (AuNSs)

During the past decade, Au nanostructures have been extensively investigated for diagnostic agents and therapeutic actuators. Recently, researchers have begun to combine these two functionalities into a single nanoparticle to generate “theranostic” nanoplatform and realize simultaneous cancer diagnostics and therapy. Due to their unique optical properties and geometric structures, Au nanostructures can be used simultaneously as imaging probes, photothermal mediator, and drug delivery vehicles. Au nanostructure-based theranostic platforms have been extensively developed either by combining a single imaging modality and therapeutic modality or by integrating multimodality diagnostics with therapeutic functionalities.

As early as in a decade ago, the theranostic potential of AuNSs has been demonstrated with simultaneous dark-field imaging and photothermal therapy by Loo et al. [126, 127]. They first demonstrated the possibility of engineering AuNSs for combined imaging and therapy for cancer cells. Immunotargeted AuNSs nanoplatform for both detecting and thermally ablating human breast cancer cells that overexpress human epidermal growth factor receptor 2 (HER2) was designed. These theranostic AuNSs could provide scattering contrast for dark-field imaging and also sufficient absorption to enable effective photothermal therapy [127]. Dramatic contrast enhancement for optical coherence tomography (OCT) and effective photothermal

ablation of tumors *in vivo* have been reported by Gobin et al. [128]. PEG-modified AuNSs were injected intravenously in tumor-bearing mice, and significant accumulation of particles within the tumor tissue dramatically increased the NIR scattering and the OCT contrast. Meanwhile, photothermal ablation of the tumor significantly reduced the tumor size and prolonged the mice surviving rate. Lu et al. used PEG and $\alpha_v\beta_3$ integrin-targeted cyclic RGD peptide (c(KRGDf)-PEG)-modified hollow Au nanospheres (HAuNS) to track endothelial cells and glioma tumors in the mouse brains. With high target ability to tumor, the photothermal therapy is efficient to ablate the tumors and inhibit their growth (Fig. 1.9) [129].

Halas and Joshi synthesized theranostic immunotargeted AuNSs by encapsulating them in a thin silica epilayer doped with Fe_3O_4 nanocrystals and ICG molecules to target HER2 receptors in cancer cells [130, 131]. In this approach, the quantum yield of ICG increased from a mere $\sim 1\%$ to nearly $\sim 85\%$, and the porous silica layer enabled rapid water diffusion, which enhanced the MRI relaxivity of the Fe_3O_4 nanocrystals. In the *in vivo* mouse model with breast cancer xenografts, the MRI and fluorescence imaging revealed that the maximum AuNSs accumulation in tumors occurs within 4 h of injection [132]. This theranostic nanoplatform enabled simultaneous active targeting of HER2 expressing cancer cells, diagnosis via dual modal MRI and near-infrared fluorescence, and photothermal therapy. AuNSs with hollow interior have been developed to facilitate drug delivery for dual modal cancer thermo-chemotherapy. AuNSs consist of a mesoporous silica nanorattle core and a thin outer Au shell (SN@AuNSs) fabricated by Liu et al. [133]. Anticancer drug docetaxel was loaded in SN@AuNSs, and a synergistic effect of chemotherapy and photothermal therapy both *in vitro* and *in vivo* was observed [133, 134]. Additionally, FITC labeling of the SN@AuNSs enabled the fluorescent imaging for their intracellular localization. Lee et al. developed DOX-loaded poly(ethylene glycol)-poly(lactic-co-glycolic acid)-Au half-shell nanoparticles (DOX-loaded PEG-PLGA-Au H-S NPs) to facilitate combined NIR fluorescent imaging and thermo-chemotherapy treatment *in vivo* [135]. Both intravenously and intratumorally injected NPs could be accumulated in the tumor region in A431 tumor-bearing mice, which was revealed by time-lapse *in vivo* fluorescence imaging. DOX could be rapidly released in the tumor region upon NIR light irradiation, and the combined thermo-chemotherapy resulted in complete destruction of the tumors without weight loss or recurrence of tumors.

Other imaging modalities including PET and ultrasound imaging have also been integrated with photothermal therapy in AuNSs. Xie et al. demonstrated that integrin $\alpha_v\beta_3$ targeting using cyclo-(RGDfK) peptide-conjugated AuNSs improved the nanoshells' accumulation in tumors. Meanwhile, increased degree of tumor necrosis indicated biological effectiveness of targeted AuNSs in the photothermal therapy application [136]. Core-shell nanoparticles composed of a superparamagnetic iron oxide (SPIO) core and an Au shell (SPIO@AuNS) were fabricated by Melancon et al. to investigate their multifunctional imaging and therapeutic capabilities [137]. *In vivo*, significant temperature elevations were revealed by both MRI and magnetic resonance temperature imaging when intratumorally injected with SPIO@AuNSs and irradiated with NIR light. SPIO@AuNS-mediated simultaneous MRI and photothermal therapy demonstrated the potential use of SPIO@AuNS for real-time

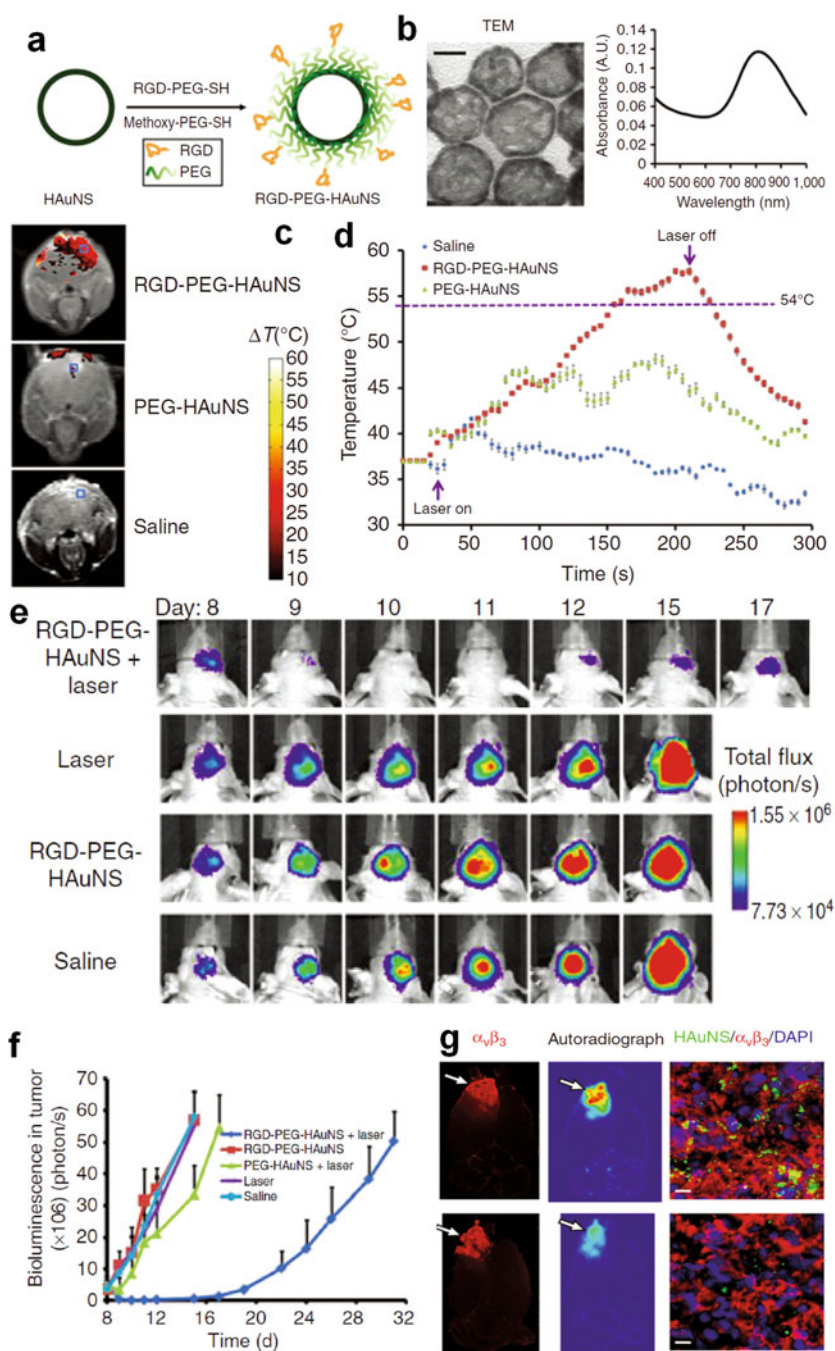


Fig. 1.9 (a) Scheme for c(KRGDf)-PEG-modified hollow AuNS (HAuNS). (b) TEM image and UV-visible spectrum of the nanoparticles. (c) Overlap of mouse brain T1-weighted magnetic resonance imaging (MRI) and MR temperature imaging at the end of laser irradiation. (d) Plots of tumor temperature change versus time in the region of interest (*blue rectangles in c*) during a laser (16 W/cm² at 808 nm) irradiation. (e, f) After different treatments, the bioluminescence images

imaging and cancer photothermal ablation. Ke et al. developed AuNSs microcapsule-based ultrasound contrast agents as a multifunctional theranostic agent for imaging-guided photothermal therapy. HeLa cells incubated with AuNSs microcapsules in vitro could be killed photothermally by exposure to NIR light, and the microcapsules maintained adequate acoustic properties that are required to act as an ultrasound contrast agent. The dual-functional theranostic composite holds great potential for ultrasound-guided photothermal cancer therapy [138]. Recently, Ma et al. constructed a multifunctional drug delivery platform based on cholesteryl succinyl silane (CSS) nanomicelles loaded with DOX, Fe_3O_4 magnetic nanoparticles and AuNSs (CDF-AuNSs nanomicelles) to combine MRI, magnetic-targeted drug delivery, light-triggered drug release, and photothermal therapy [139]. An enhancement for T2-weighted MRI is observed for the CDF-AuNSs nanomicelles. These nanomicelles exhibited LSPR absorbance in the NIR region, and a NIR light-triggered DOX release was realized. A synergistic effect of the photothermal therapy and the magnetic-field-guided drug delivery was observed in the presence of both NIR irradiation and magnetic field.

AuNSs provide great advantages for targeted cancer photothermal therapy for the light excitation-guided local heating. However, these nanoshells typically synthesized between 80 and 150 nm in diameter may be restricted for medical application for the quick clearance by the reticulum endothelial system (RES) and a limited diffusion within tissue. Therefore, it's necessary to overcome the challenge in the size of AuNSs and facilitate their biomedical applications [140].

1.6 Au Nanorods (AuNRs)

AuNRs are another kind of Au nanostructures which have been extensively investigated for cancer theranostics in the past few years. Due to their anisotropic shapes, AuNRs exhibit two LSPR absorbance peaks: the transverse mode at ~ 515 nm and the longitudinal mode whose position depends on the aspect ratio of the rod and can be finely tuned from visible to NIR region. AuNRs have been proved to be promising in a wide range of biomedical applications such as imaging, hyperthermia therapy, and drug delivery due to their unique LSPR and photothermal effects. Recently, AuNRs have been explored to combine imaging diagnosis and therapeutic treatment to function as NIR light-triggered theranostic platform.

Fig. 1.9 (continued) (e) and quantitative analysis (f) of nude mice bearing the luciferase gene-transfected U87-TGL human glioma tumors on day 8 after tumor inoculation. (g) Targeted delivery of ^{64}Cu -labeled c (KRGDf)-PEG-HAuNS to U87 cells in mouse brain. The *left* shows the photographs of mouse brains stained with hematoxylin and eosin (H&E) and $\alpha_v\beta_3$; the *middle* shows the location of HAuNS according to autoradiographs of mouse brains; the *right* shows immunofluorescence micrographs of tumor tissue at high magnification. The *red color* indicates the integrin $\alpha_v\beta_3$; the *green* indicates scattering signal of HAuNS under dark field; the *blue* indicates 40,6-diamidino-2-phenylindole (DAPI)-stained cell nuclei; the *arrows* indicate tumors with the bar of 10 μm (Reprinted with permission from ref. [129]. Copyright 2011, American Association for Cancer Research)

AuNRs were first reported as reagents for simultaneous molecular imaging and photothermal cancer therapy by El-Sayed et al. in 2006 [44]. They conjugated AuNRs with anti-EGFR antibodies and applied them to target and treat malignant oral epithelial cell lines. Using dark-field imaging and photothermal therapy, the malignant cells could be diagnosed and destroyed simultaneously. Due to the selective targeting, malignant cells required only half the laser energy to be photothermally destroyed than the nonmalignant cells. Later, imaging-guided hyperthermia therapy became the most investigated combination theranostic strategy. Many researchers reported the AuNRs-mediated cancer imaging and photothermal therapy, and targeting molecules are often conjugated to AuNRs for active targeting. For instance, Huff et al. found that both CTAB-AuNRs- and folate-AuNRs-mediated heating could produce severe blebbing in cell membranes and render them permeable to chemical reagents. The former was found to be internalized into KB cells within hours, while the latter was accumulated on the cell surface over the same time interval [141]. Black et al. conjugated AuNRs with deltorphin, a high-affinity ligand for delta opioid receptor (δ OR) which expressed on human colon carcinoma HCT-116 cell line. Selective imaging and photothermal ablation were observed in receptor-expressing cells while not in cells that did not express the receptor in a mixed population of cells [119]. By conjugation AuNRs with a NIR fluorescent dye through a peptide linker, which could be degraded by matrix metalloprotease (MMP), Yi et al. demonstrated the quenching effect of AuNRs and the recovery of quenched fluorescence when the substrate was degraded by MMP enzymes secreted by cancer cells [142]. The expression of MMP and cancer progress imaged by the recovery of quenched fluorescence and photothermal cancer therapy were realized simultaneously. Choi et al. attached epithelial cancer cells targeting molecules cetuximab (CET) to PEG-AuNRs (CET-AuNRs) and assessed their targeting, imaging, and photothermal therapy behavior [143]. In vivo NIR absorption imaging revealed that CET-AuNRs accumulated in the tumor region after intravenously injection, while CET-free AuNRs did not. Histological analysis of excised tumor tissue showed that CET-AuNRs-treated tumors exhibited severe cellular damage compared to the nontreated control after NIR laser irradiation.

Recently, imaging-guided dual modal cancer treatment has been developed to improve the therapy efficacy. For instance, Kuo et al. designed a fluorescent AuNRs conjugate to simultaneously serve as photodynamic therapy (PDT) and hyperthermia agents [144]. The conjugate was prepared by coating AuNRs with poly (styrene-alt-maleic acid) (PSMA) and ICG, a hydrophilic and anionic photosensitizer in sequence via electrostatic interaction. This theranostic nanoplatform combining fluorescence imaging of ICG, PDT, and hyperthermia could more efficiently extinguish cancer cells than PDT or hyperthermia treatment alone. Jang et al. constructed an AuNR-photosensitizer complex for noninvasive NIR fluorescence imaging and combined PDT and photothermal cancer therapy [145]. Fluorescence emission and singlet oxygen generation by photosensitizer AIPcS4 were quenched after conjugation with AuNRs. Increased cellular uptake and in vitro phototoxicity were observed in AuNR-AIPcS4-treated cells than in free AIPcS4-treated cells. In vivo, efficient NIR fluorescence imaging of tumor sites and improved therapeutic efficacy were

obtained by PDT and photothermal dual therapy. Huang et al. developed folic acid-conjugated silica-modified AuNRs for simultaneously targeting, X-ray/CT imaging, radiotherapy, and photothermal therapy [73]. The multifunctional theranostic nanoplatform exhibited excellent imaging and targeting ability for X-ray/CT imaging-guided dual-mode enhanced radio- and photothermal therapy. Recently, Zhang et al. have designed a triple-modal functional AuNRs for in vivo fluorescence imaging, SERS detection, and photodynamic therapy [146]. SERS and fluorescence agents are chemically doped in different layers of a silica/polymer-coated AuNR, thereby forming two individual imaging “channels.” These nanoparticles could accumulate inside the tumors by intravenously injection, thus allowing detection of the tumor by SERS and fluorescence measurements. Through the same doping method, a PDT photosensitizer, protoporphyrin IX (PpIX), was loaded into the multilayered shell, and PDT treatment could be conducted right after the detection of the tumor.

By using various surface modification or functionalization methods, AuNRs have been developed as NIR light-responsive drug delivery system. Combining photothermal therapy and drug delivery of AuNRs, thermo-chemotherapy was realized for dual treatment of cancer [147, 148]. Our group has designed mesoporous silica-coated AuNRs (Au@SiO₂) loaded with DOX for cancer theranostics [95]. Based on the simultaneous imaging, photothermal therapy, and drug delivery property of Au@SiO₂, we further developed a thermoresponsive nanocomposite by coating Au@SiO₂ with a thermo- and pH-responsive polymer shell, poly(N-isopropylacrylamide-co-acrylic acid), and explored them in vivo applications [109] (Fig. 1.10). The thermoresponsive polymer shell prolonged the blood circulation time of AuNRs, and both local water bath heating and NIR laser irradiation at the tumor site following intravenous administration could increase the nanocomposite accumulation in tumor. The nanocomposite served as targeted cancer thermo-chemotherapy platform which simultaneously delivers heat and anticancer drugs in a NIR laser-activation mechanism. There are also other reports on the application of AuNRs for NIR light-triggered thermo-chemotherapy and imaging. Guo et al. fabricated a chitosan/AuNR (CS-AuNR) hybrid nanosphere for the delivery of the anticancer drug cisplatin [149]. This hybrid nanosphere could serve as multifunctional theranostic platform for simultaneous dark-field imaging and NIR light-mediated thermo-chemotherapy. Xiao et al. conjugated AuNRs with DOX, cRGD, and ⁶⁴Cu-chelator for combined anticancer drug delivery, targeting, and PET imaging [118]. cRGD-conjugated nanocarriers exhibited improved cellular uptake and cytotoxicity compared to nontargeted ones in vitro.

1.7 Hollow Au Nanospheres (HAuNSs)

HAuNSs are novel Au nanostructures consisting of only a thin Au shell with a hollow interior. Different from solid Au nanoparticles, HAuNSs have LSPR absorption in the NIR region and display strong photothermal conducting properties.

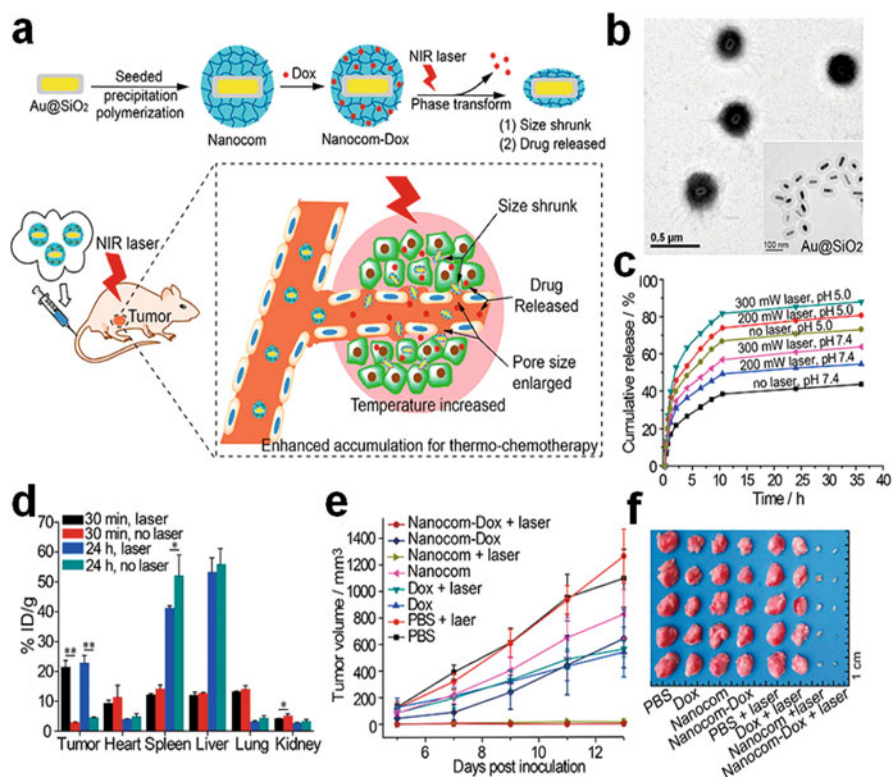


Fig. 1.10 (a) Nanocomposite formulation process and NIR laser-induced targeted thermo-chemotherapy using the nanocomposite. (b) TEM images of the nanocomposite and Au@SiO₂ (inset). (c) DOX release profiles from Nanocom-Dox with or without NIR laser irradiation at different pHs. (d) The biodistribution of the nanocomposite at 30 min and 24 h after systemic administration and NIR laser irradiation at the tumor based on ICP-MS analysis (data expressed as percentage of the injected dose per gram of tissue (% ID/g)). * $P < 0.05$ or ** $P < 0.01$, significant difference between irradiated and unirradiated groups. (e) The antitumor activity including PBS, DOX, Nanocom, and Nanocom-DOX groups (with or without laser irradiation) through tail vein by measuring the tumor volume. (f) Tumor dissection photographs through systematic administration (Reprinted with permission from ref. [109]. Copyright 2014, American Chemical Society)

Additionally, HAuNSs can act as drug delivery system due to their hollow interior. Combined with the strong and tunable absorption band in the NIR region, HAuNSs are ideal theranostic platform for simultaneous cancer imaging and thermo-chemotherapy. Additionally, the size of HAuNSs (30–50 nm in diameter) is much smaller than AuNSs (>120 nm) and therefore exhibits increased extravasation from tumor blood vessels and higher intracellular uptake by mammalian cells.

To achieve targeted delivery, Melancon et al. covalently conjugated HAuNSs with C225, a monoclonal antibody to EGFR (C225-HAuNSs). By using scattered imaging from the nanoshells, EGFR-mediated selective uptake of C225-HAuNSs but not IgG-HAuNS control in EGFR-positive A431 tumor cells was observed. Irradiation of A431 cells treated with C225-HAuNSs with NIR laser resulted in

selective destruction of these cells. The cells treated with C225-HAuNS alone, laser alone, or IgG-HAuNS plus NIR laser were not affected on cell viability [150]. Lu et al. conjugated HAuNSs with α -melanocyte-stimulating hormone (MSH) analog, [Nle⁴, D-Phe⁷] α -MSH (NDP-MSH), to develop melanoma-targeted HAuNSs, NDP-MSH-PEG-HAuNSs [151]. Enhanced extravasation and distribution of NDP-MSH-PEG-HAuNSs into tumor matrix were observed compared to nontargeting HAuNS. Furthermore, selective photothermal ablation of B16/F10 melanoma with NDP-MSH-PEG-HAuNSs was confirmed by histological and [¹⁸F] fluorodeoxyglucose positron emission tomography evaluation at 24 h post NIR laser irradiation. The same group also reported gene delivery by targeted HAuNSs-mediated photothermal transfection [152]. NF- κ B downregulation was achieved by NIR light and folate receptor-targeted HAuNSs carrying siRNA, recognizing NF- κ B p65 subunit. Using micro-PET/CT imaging, the targeted HAuNSs exhibited higher tumor uptake in nude mice bearing HeLa cervical cancer xenografts than nontargeted nanoparticles. Downregulation of NF- κ B p65 was observed only in tumors irradiated with NIR light but not in nonirradiated tumors grown in the same mice, which indicated the gene silence was mediated by controllable cytoplasmic delivery of siRNA through photothermal effect. Combined treatments with p65 siRNA photothermal transfection and chemotherapeutic agent irinotecan caused substantially enhanced tumor apoptosis and growth delay compared to other treatment regimens, which indicated photothermal transfection of NF- κ B p65 siRNA could enhance sensitivity to chemotherapeutic agents. Lu et al. also reported theranostic HAuNSs with multi-functions including tumor targeting, PAT imaging, and photothermal therapy [129]. By targeting brain tumor receptors via RGD peptides, the theranostic HAuNSs exhibited highly specific tumor diagnosis. Combined with the photothermal therapy, a decrease in tumor volume for up to 3-week post NIR laser treatment was observed in an orthotopic mouse xenograft model of glioma by targeting brain tumor receptors.

Li's group also did a series of excellent works on HAuNSs-mediated cancer theranostics [153–156]. They reported exceptionally high payload of DOX in HAuNSs for NIR light-triggered drug release, photothermal therapy, as well as dark-field imaging in vitro. As high as 63 % DOX by weight could be loaded to PEG-coated HAuNS since DOX was coated to both the outer and the inner surfaces of HAuNSs. Combined thermo-chemotherapy exhibited significantly greater cell killing when MDA-MB-231 cells were treated with DOX-loaded HAuNSs plus NIR light [154]. In another work, the thermo-chemotherapy efficacy of DOX-loaded PEG-coated HAuNSs with DOX:PEG:HAuNS weight ratio of 1:3:1 (NP3) was studied in vitro and in vivo using human MDA-MB-231 breast cancer and A2780 ovarian cancer cells [156]. In vitro, significantly greater cell killing was observed when cells were treated with both NP3 and NIR light irradiation, which is attributable to the combined photothermal therapy and the released DOX. In vivo, NP3 exhibited slower clearance in blood and greater accumulation in tumors than free DOX, which was demonstrated by μ PET images of mice bearing A2780 tumors after intravenous injection of ⁶⁴Cu-labeled NP3. NP3-mediated thermo-chemotherapy demonstrated greater antitumor activity than free DOX, NP3, or liposomal DOX, which represents a promising approach to effective anticancer therapy. DOX-loaded

HAuNSs can be further conjugated with a cyclic peptide targeting EphB4, a member of the Eph family of receptor tyrosine kinases that are overexpressed on the cell membrane of multiple tumors and angiogenic blood vessels.

Li et al. also observed an increased uptake of targeted nanoparticles (T-DOX@HAuNSs) in three EphB4-positive tumors both *in vitro* and *in vivo* [155]. By dual-radiotracer technique, *in vivo* release of DOX from DOX@HAuNS triggered by NIR laser was confirmed. Enhanced antitumor effect was obtained when mice were treated with T-DOX@HAuNSs plus NIR laser irradiation compared to nontargeted DOX@HAuNSs plus laser or HAuNSs plus laser. These results demonstrated that NIR light-guided thermo-chemotherapy with a single nanoplatform is capable of mediating simultaneous imaging, photothermal therapy, and local drug release which has great promise as a new cancer theranostic regime.

The authors also investigated the impact of nanoparticle-mediated localized hyperthermia on vascular permeability to enhance the efficacy of chemotherapy. By conjugating an anti-EGFR monoclonal antibody C225 to HAuNSs (C225-HAuNSs), they studied the vascular permeability and subsequent uptake of a water-soluble polymer using a combined approach with magnetic resonance temperature imaging (MRTI), ultrasound, and optical imaging [157]. MTRI showed a maximum temperature of 65.2 ± 0.10 °C and 47.0 ± 0.33 °C in A431 tumor xenograft of mice treated with C225-HAuNSs plus laser and saline plus laser, respectively. Dynamic contrast-enhanced magnetic resonance imaging (DCE MRI) demonstrated greater than twofold increase of DTPA-Gd in the initial area in mice injected with C225-HAuNS and exposed to NIR laser compared with control mice. Increased vascular perfusion was confirmed by Power Doppler ultrasound, which revealed a four- to sixfold increase in percentage vascularization in mice treated with C225-HAuNSs plus NIR laser compared to control mice. Based on NIR fluorescence imaging, intratumor accumulation of a model polymeric drug PG-Gd-NIR813 5 min post-laser therapy was significantly higher than those at 24 h-post laser therapy and the saline-treated ones. These results suggested photothermal effect of C225-HAuNSs in tumor site could increase the vascular perfusion and therefore enhance the permeability of chemotherapeutic agents to the tumors.

1.8 Au Nanocages (AuNCs)

AuNCs represent a novel class of Au nanostructures firstly synthesized by Xia's group in 2002 [158]. The LSPR peak position of the AuNCs is tunable from the visible to the NIR region, which makes them attractive for colorimetric sensing and biomedical applications. The extraordinarily large scattering and absorption cross sections of AuNCs endow them superb optical tracers or contrast agents for various imaging modalities such as dark-field microscopy, optical coherence tomography, photoacoustic tomography, and multiphoton luminescence imaging. Additionally, the hollow interiors of AuNCs can be used for drug encapsulation, and the porous walls can facilitate the drug release controlled by various stimuli such as hyperthermia. During the past decades, researchers have extensively explored the

applications of AuNCs in a variety of biomedical applications ranging from sensing to imaging, diagnosis, and cancer theranostics.

AuNCs have been conjugated with various ligands for selective tumor targeting and imaging. Xia et al. have quantitatively investigated the passive targeting of PEG-functionalized AuNCs in a tumor mouse model [159]. The amount of AuNCs distributed in tumor reached 3.4 ± 0.9 %ID/g at 24 h postinjection, while the distributions of AuNCs in normal tissues were low. The same group also compared the passive and active targeting efficiencies of AuNCs for melanomas based on in vivo photoacoustic imaging [66]. AuNCs were conjugated with [Nle⁴,D-Phe⁷] α -melanocyte-stimulating hormone (NDP-MSH), a peptide which selectively binds to the α -MSH receptors overexpressed on melanoma. The photoacoustic signal in the melanoma was much stronger for the NDP-MSH-conjugated AuNCs than that of nontargeted AuNCs, which demonstrated an enhanced uptake of AuNCs by the tumor due to active targeting.

The initial study on the ability to destroy cancer cells in vitro by AuNCs-mediated photothermal effect was also demonstrated by Xia's group [160, 161]. They also studied the efficacy of photothermal cancer treatment in a tumor mouse model in vivo [162]. PEGylated AuNCs were administrated intravenously to tumor-bearing mice, and the tumor on the right flank of each mouse was irradiated with NIR laser. The tumors treated with AuNCs were rapidly heated to temperatures over 55 °C, while no change was observed for the control. [¹⁸F] fluorodeoxyglucose (¹⁸F-FDG) positron emission tomography was applied to evaluate the response to the photothermal therapy. The normalized values suggest a decrease in metabolic activity by 70 % after AuNCs plus laser treatment compared to the untreated mice.

AuNCs have also been developed as drug delivery systems for cancer theranostics by integrating optical imaging and thermo-chemotherapy. Yavuz et al. coated the surface of AuNCs with a smart polymer, poly(N-isopropylacrylamide) (pNIPAAm) and its derivatives, which can change conformation in response to temperature variation at a point known as the low critical solution temperature (LCST) [163]. Under NIR laser irradiation, the temperature will increase due to the photothermal effect of AuNCs. The polymer chains collapse as the temperature increases beyond the LCST, which expose the pores of the nanocages and allow thus the preloaded drugs to be released. Moon et al. reported an AuNCs-based theranostic system, combining photoacoustic imaging and controlled drug by high-intensity-focused ultrasound (HIFU) [164]. The system was fabricated by filling the hollow interiors of AuNCs with a phase-change material (PCM) such as 1-tetradecanol that has a melting point of 38–39 °C. The PCM-loaded AuNCs simultaneously enhanced photoacoustic imaging contrast and demonstrated highly effective drug release ability triggered by HIFU or heat. PCM can reversibly change its physical state between solid and liquid according to the local temperature. When exposed to direct heating or HIFU, the PCM will melt and escape from the interiors of AuNCs through small pores on the surface, which allow the concurrent release of the encapsulated drugs. Since HIFU is a deeply penetrating energy source, the drug release profile could be controlled by adjusting the power of HIFU and/or the duration of exposure to HIFU. Shi et al. demonstrated the application of AuNCs in thermo-chemotherapy based on calcium phosphate-coated magnetic nanoparticles (Fe₃O₄@CaP)-capped

AuNCs [165]. This nanoplatform integrated magnetic targeting, photothermal therapy, and chemotherapy for killing cancer cells. The cell killing efficacy of DOX-loaded AuNCs under NIR irradiation was higher than the sum of chemotherapy of DOX-loaded AuNCs and AuNCs-induced photothermal therapy, which indicated the combined cancer thermo-chemotherapy resulted in a synergistic effect. Additionally, the magnetic component in the nanoplatform could potentially be used as an MRI contrast agent and targeted drug delivery.

1.9 Au Nanostars

Au nanostars contain multiple sharp branches with plasmons tunable in the NIR region, which have gained wide interest in biomedical areas including SERS spectroscopy, photoacoustic imaging, biosensing, photodynamic, and photothermal therapy. The extinction spectra of individual Au nanostars revealed that these nanoparticles have multiple plasmon resonances varying greatly due to shape polydispersity. Therefore, Au nanostar exhibits broad absorption peaks due to overlapping of many distinct spectra.

Yuan et al. functionalized Au nanostars with TAT-peptide, a cell-penetrating peptide encoded by human immunodeficiency virus type 1 (HIV-1), in order to increase the intracellular delivery of Au nanostars [166]. TAT-peptide-functionalized nanostars were found to enter cells more frequently than bare or PEGylated nanostars. The enhanced intracellular delivery in turn allows efficient photothermal therapy with lower irradiance. After incubation of TAT-nanostars on BT549 breast cancer cells, photothermal ablation was accomplished ultralow irradiance (0.2 W/cm^2), which is the lowest value ever reported for pulsed laser-induced photothermal therapy and below the maximal permissible exposure of skin. Both TPL and TEM imaging confirmed that the uptake mechanism of TAT-nanostars primarily relies on actin-driven lipid raft-mediated macropinocytosis. The same group also demonstrated the use of Au nanostars for particle tracking via TPL imaging and simultaneous Au photothermal therapy [167]. They demonstrated photothermal ablation of SKBR3 breast cancer cells incubated with bare nanostars within 5 min of irradiation in vitro. In vivo, PEGylated nanostars were injected intravenously into a mouse for 2 days, then extravasation of nanostars was observed, and localized photothermal ablation was demonstrated on a dorsal window chamber. Au nanostars interact intensely with incident light enabling highly sensitive in vivo tracking in the vasculature. Combined hyperthermia and photodynamic therapy (PDT) and upon single continuous wave (CW) laser using photosensitizer-functionalized Au nanostars were reported (Fig. 1.11) [168]. Chlorine 6 (Ce6), a commonly used photosensitizer,

Fig. 1.11 (continued) at 4 h postinjection of PBS, Ce6, GNS-PEG, and GNS-PEG-Ce6. (f) Tumor volume after laser irradiation treatment over time. (g) The ultrasound (*upper row*) and photoacoustic (*lower row*) imaging of tumor-bearing mice after laser irradiation with the same procedure as above. The *circles* indicate the region of interest in the tumors, and the *blue* shows the hypoxia state in the tumors. *Scale bars*: 1 mm (Reprinted with permission from ref. [168]. Copyright 2013, John Wiley & Sons, Inc.)

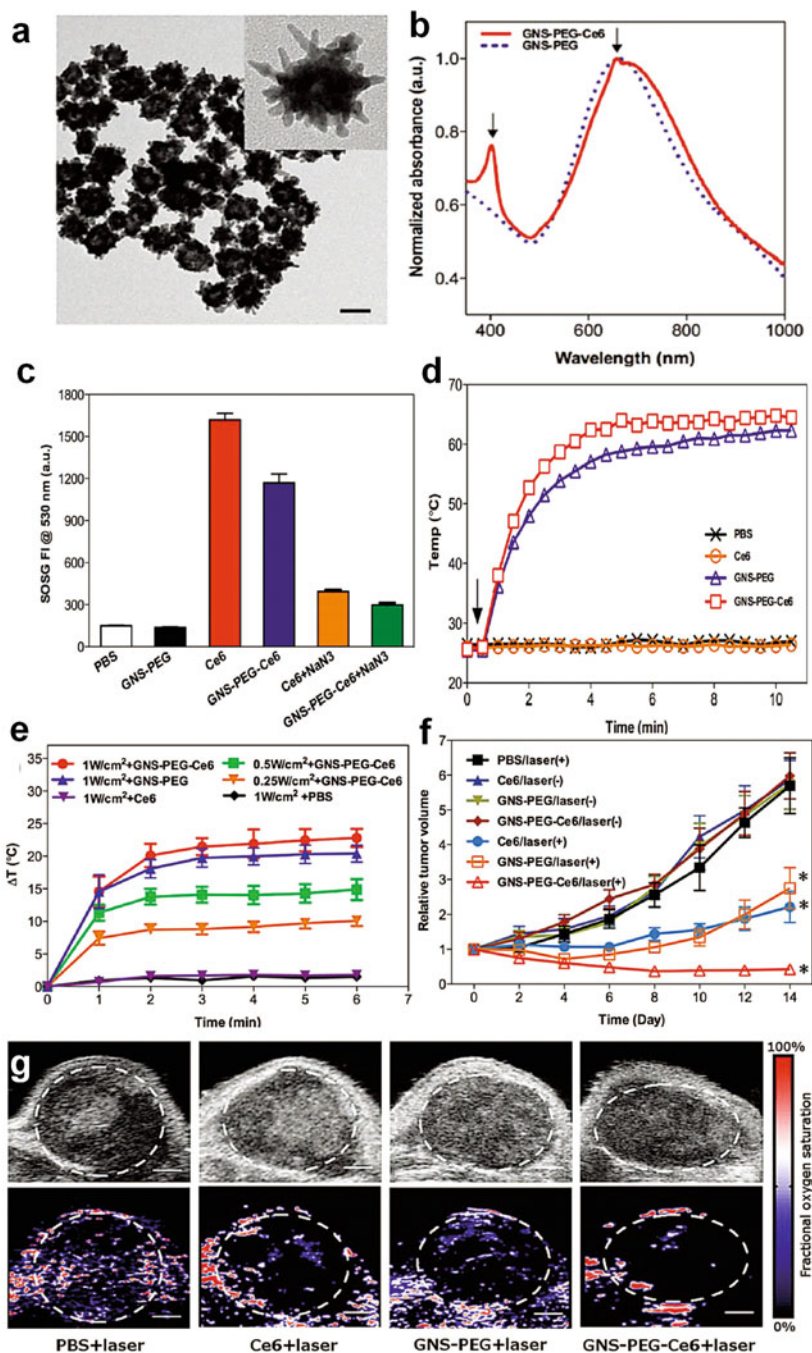


Fig. 1.11 (a) TEM images of Au nanostars (GNSs). (b) UV-vis-NIR spectra of GNSs. (c) The generation of free radicals under irradiation determined by the SOSG fluorescence intensity. (d, e) Temperature curves of different GNSs (d) and GNS-treated tumors (e) irradiated by laser over time. The MDA-MB-435 tumor-bearing mice are exposed to 671 nm laser (1.0 W/cm²) for 6 min

was covalently anchored on the surface of Au nanostars. To induce both hyperthermia and PDT effect by a single NIR CW laser, they adapted the LSPR of Au nanostars to fit that of Ce6. This strategy significantly improved the anticancer effect and simplified the treatment process. These results suggested Au nanostars as promising theranostic agents for cancer therapy.

1.10 Other Au Nanostructures

Other Au nanostructures including nanoroses, nanobubbles, and nanoparticles have also been investigated for their application in cancer theranostics. Lapotko et al. first reported laser-activated micro- and nanobubbles that were produced around plasmonic nanoparticles in cells [169]. These intracellular bubbles were found to be the universal phenomena that can be used for sensitive and noninvasive monitoring of individual cell. Systematic researches have been done to investigate the properties and biomedical applications of Au nanobubbles such as thermolysis of cancer cells, cell imaging, gene, and drug delivery [170–174]. Wagner et al. developed plasmonic nanobubbles (PNBs) as an *in vivo* tunable theranostic cellular agent in zebrafish hosting prostate cancer xenografts [170]. Plasmonic nanobubbles were selectively generated around Au nanoparticles in cancer cells in the zebrafish with short single-laser pulses. Two different-sized PNBs were produced by varying the energy of the laser pulse: an initial small PNB for detecting cancer cells by optical scattering, followed by a second bigger PNB for mechanically ablating cells. These results demonstrated that PNBs could be applied for the diagnosis and guided ablation of individual cancer cells in a living organism without damage to the host.

Recently, Hu et al. has reported a novel theranostic system based on Au cubic nano-aggregates as potential photoacoustic contrast and photothermal therapy [175]. The cubic Au nano-aggregates structure with edge-length of 80 nm (Au-80 CNAs) was synthesized with a simple and cost-effective method and exhibited strong NIR absorption, excellent water-solubility, and good photothermal stability. The temperature of the solution containing Au-80 CNAs (100 $\mu\text{g}/\text{mL}$) increased by about 38 °C under 808 nm laser irradiation for 5 min. Both *in vitro* and *in vivo* studies demonstrated that Au-80 CNAs were potent photothermal therapeutic agents and photoacoustic imaging contrast agents. Ma et al. reported a nanocluster of Au-coated iron oxide primary particles (nanoroses) for targeted cellular imaging and therapy [176]. The stable uniformly sized (ca. 30 nm) nanoclusters were NIR active, superparamagnetic formed by kinetically controlled self-assembly of Au-coated iron oxide nanoparticles. The nanoroses exhibited an order of magnitude larger than observed for typical iron oxide particles with thicker Au shells, because of the thin Au shells with an average thickness of only 2 nm. High uptake of the

nanoclusters by macrophages is facilitated by the small size of the nanoclusters and the dextran surface coating, which further provided intense NIR contrast in dark-field and hyperspectral microscopy, both *in vitro* and *in vivo*.

Solid Au nanoparticles (AuNPs) have been demonstrated as a novel CT contrast agent in blood pool imaging (angiography) and for diagnosis of hepatoma *in vivo*. Kim et al. reported multifunctional AuNPs for targeted molecular CT imaging and therapy of prostate cancer [177]. By functionalizing the surface of AuNPs with a prostate-specific membrane antigen (PSMA) RNA aptamer that binds to PSMA, they established a targeted CT imaging system for specifically imaging of prostate cancer cells that overexpressed the PSMA protein. Besides, the PSMA-specific aptamer formed a GC-rich duplex that acts as a loading site for the chemotherapeutic agent DOX, which enables combined prostate cancer imaging by CT and anti-cancer therapy. PSMA aptamer-conjugated AuNPs exhibited more than fourfold greater CT intensity for targeted LNCaP cells than that of nontargeted cells. Furthermore, DOX-loaded aptamer-conjugated AuNPs were more potent to kill targeted cancer cells than nontargeted cells, suggesting target-specific drug delivery [178].

A novel kind of nanoparticles has been explored by replacing the silica cores in traditional nanoshells with an Au-sulfide core structure. Zhou et al. first synthesized Au-Au sulfide nanoparticles (GGs NPs) that exhibited strong NIR-absorbing properties [179]. GGs NPs with a LSPR between 800 and 900 nm for therapeutic and imaging applications are generally synthesized in the range of 35–55 nm in diameter, much smaller than Au silica nanoshells which range from 120 to 140 nm for the same resonant wavelength [180]. Models have suggested that particles with diameter <100 nm could improve tumor extravasation [181], and experimental data also suggested that the greatest uptake of Au occurred in diameters between 30 and 50 nm [182]. Therefore, GGs NPs may prove advantageous in cancer therapeutic and imaging. Day et al. developed NIR-resonant GGs NPs as dual contrast and therapeutic agents for cancer theranostics [183]. After conjugation with anti-HER2 antibodies, GGs NPs could specifically bind SK-BR-3 breast carcinoma cells that overexpressed the HER2 receptor. TPL imaging of the cancer cells was obtained with irradiation by low energy pulsed-NIR laser (1 mW). Higher laser powers were applied for photothermal ablation of the cancerous cells (50 mW), which resulted in extensive membrane blebbing and cell death.

Gobin et al. investigated *in vivo* distribution of GGs NPs and found that these NPs remained in circulation longer than Au/silica nanoshells greater than 24 h [184]. Accumulation in the liver, spleen, and tumors showed that larger dose GGs NPs could avoid RES clearance and accumulate in tumors. Photothermal ablation of tumor cells with NIR irradiation of the GGs NPs resulted in increased survival of mice. With further optimization of laser power and NPs functionalization, GGs NPs may be an effective therapeutic agent to compliment the treatment of cancers.

1.11 Strategy for Combatting Cancer Drug Resistance and Inhibiting Cancer Stem Cells and Cancer Metastasis

The photothermal treatment using Au nanostructures can efficiently improve the therapy of cancer cells for drug resistance. Cancer cells develop drug resistance under evolutionary pressure from chemotherapy. They become less sensitive to chemotherapeutic drugs at a low dose compared to the sensitive cancer cells. It still lacks effective and successful approach to overcome drug resistance in clinic. Usually, the resistant cancer cells have little accumulation and low sensitivity of drugs. Wang et al. reported a simple strategy to combat cancer drug resistance using the photothermal properties of mesoporous silica-coated AuNRs. At a mild laser power density, the nanoparticle-mediated hyperthermia doesn't kill resistant cells, but successfully modulate the genes associated to drug resistance. In particular, this photothermal treatment triggers higher expression of heat shock factor (HSF-1) trimers and depresses the expression of P-glycoprotein (Pgp) and mutant p53. As a result, both drug accumulation in the resistant cells and their sensitivity to drugs can be greatly enhanced using NIR laser irradiation [14] (Fig. 1.12). Moreover, laser treatment of AuNRs can not only produce photothermal effects but also generate free radicals such as singlet oxygen [185, 186]. Resistant cells retain a low redox state, and the levels of reactive oxygen species are elevated due to laser irradiation on AuNPs [187]. To combine photothermia, the generation of free radicals, and chemotherapy, AuNR-based platform can successfully combat resistance due to the synergistic roles under laser treatment.

The photothermal treatment using Au nanostructures can also inhibit cancer stem cells (CSCs). These cells are found in a variety of cancers and resistant to chemotherapy and X-ray radiation therapy. Eradication of CSC cell population should provide a choice to cancer therapy. Our group reported that photothermal treatment of AuNRs can eliminate CSCs in breast cancer cells (MCF-7). As shown in Fig. 1.13, photothermal therapy significantly reduces the aldehyde dehydrogenase positive (ALDH⁺) cells subpopulation and the mammosphere formation ability of treated cells. The treatment also decreases the expression of stem cell markers and inhibits CSCs more significantly compared to non-CSCs because CSCs have a greater cell uptake of AuNRs to generate stronger heat stimulus. Furthermore, salinomycin (SA), a CSCs inhibitor, is loaded with polyelectrolyte-modified AuNRs to combine chemotherapy and thermal therapy. Due to triggered drug release and hyperthermia with laser irradiation, the synergistic effect can efficiently inhibit CSCs [188].

Our group also reported that CTAB-capped AuNRs with serum protein coating are capable of inhibiting tumor metastasis *in vitro* and *in vivo*. The major source of cancer-related deaths is not from the primary tumor itself but from metastasis to

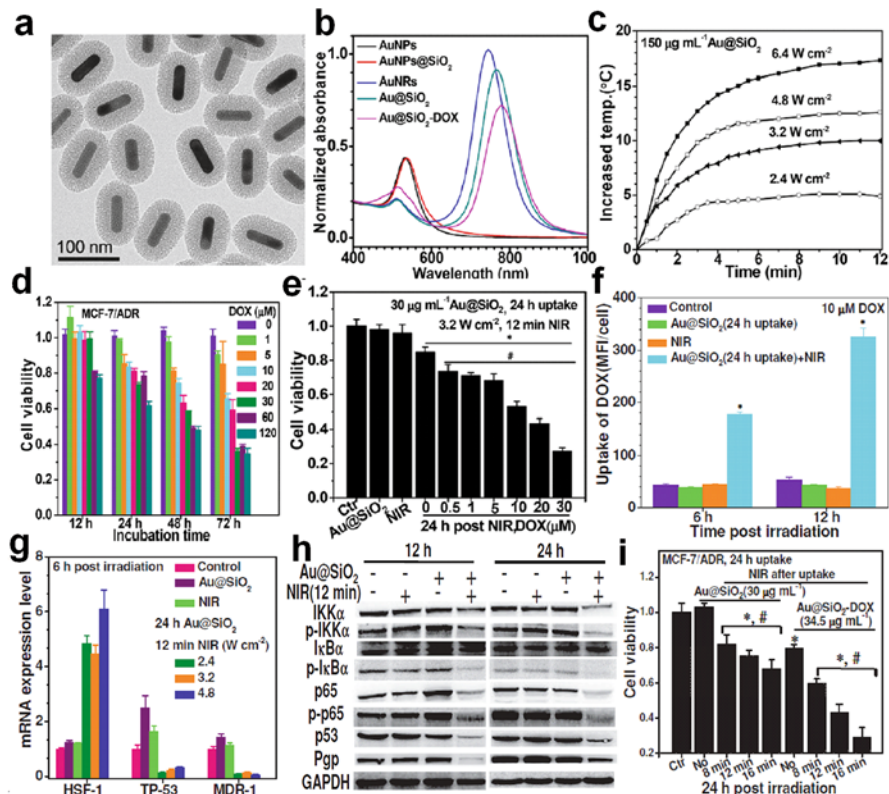


Fig. 1.12 Mesoporous silica-coated AuNRs (Au@SiO₂) as a platform to overcome chemotherapeutic resistance with a laser irradiation. (a) TEM image of Au@SiO₂ nanocarrier. (b) Optical absorption properties of AuNRs, Au@SiO₂, and DOX-loaded Au@SiO₂(Au@SiO₂-DOX). (c) Temperature curves of Au@SiO₂ under 780 nm fs-laser irradiation. (d) Dose-dependent cytotoxicity of DOX to the DOX-resistant human breast cancer cell (MCF-7/ADR). (e) Photothermal effects of Au@SiO₂ on cellular sensitivity to DOX when MCF-7/ADR cells internalize Au@SiO₂, and are irradiated by laser, and then are exposed to DOX. (f) The influences of laser irradiation on the ability of Au@SiO₂-engulfed cells to accumulate DOX. (g, h) The changes in the expression of resistance-associated genes at mRNA level (g) and at protein level (h) when MCF-7/ADR cells internalize Au@SiO₂ and then are exposed by 780 nm laser irradiation. (i) The synergistic effects of photothermia and chemotherapy from Au@SiO₂-DOX under laser irradiation to circumvent DOX resistance (Reprinted with permission from ref. [14] Copyright 2014, John Wiley & Sons, Inc.)

other organs in the body. Cancer cells need to invade host tissue, migrate from the primary tumor to blood or lymphatic vessels, translocate to distant sites, extravasate and adapt to new microenvironments, seed there, and form secondary tumors. We reported that serum protein-coated AuNRs exhibit negligible effects on the viability and proliferation metastatic cancer cell lines, but effectively inhibit their migration

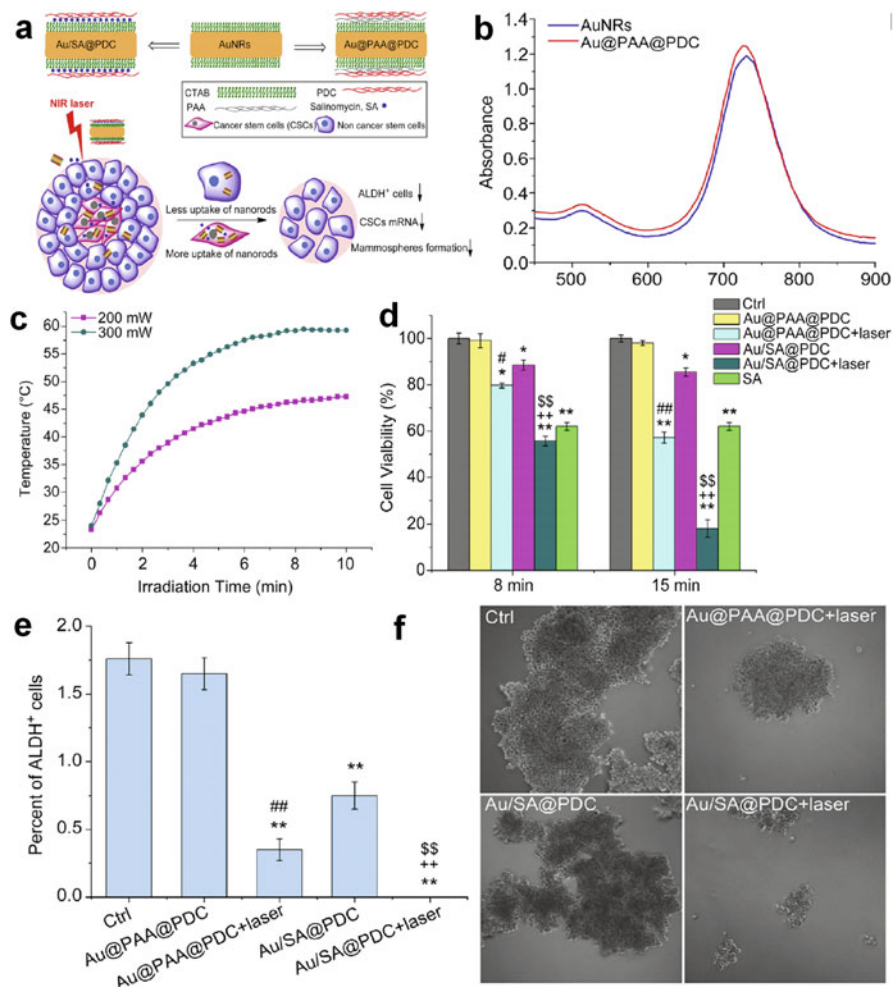


Fig. 1.13 Thermo-chemotherapy strategy to inhibition of breast cancer stem cells (CSCs) using polymer-modified and drug-loaded AuNRs. (a) A scheme to demonstrate that AuNRs serve as a combinatorial platform with thermo-chemotherapeutic capability of inhibiting cancer stem cells under laser irradiation. (b) UV-vis-NIR spectra of the pristine AuNRs and polyelectrolyte (PAA and PDDAC)-conjugated AuNRs. (c) Temperature curves of AuNRs after laser treatment. (d) Cell viability of human breast cancer cells (MCF-7) treated with Au@PAA@PDC, Au/SA@PDC, and SA (salinomycin) followed by NIR laser treatment, which triggers hyperthermia and SA release. (e) Synergistic inhibition of aldehyde dehydrogenase positive (ALDH⁺) cells (CSCs) in MCF-7 population by Au/SA@PDC with NIR laser-triggered hyperthermia and SA release. (f) Images of mammosphere formation ability of treated cells indicating the characteristic growth and proliferative properties of CSCs (Reprinted with permission from ref. [188]. Copyright 2014, Elsevier, Ltd.)

and invasion *in vitro* and *in vivo* (Fig. 1.14). For breast cancer cells (MDA-MB-231) treated with AuNRs or not, both stable isotope labeling by amino acids in cell culture (SILAC)-based proteomics analysis and real-time PCR array have been used to study the protein and mRNA expression. They found that exposure of cells to AuNRs can downregulate the expression of diverse energy generation-related genes, which is due to the inhibitory effects of AuNRs on mitochondrial oxidative phosphorylation (OXPHOS) and glycolysis. The impairment of mitochondrial functions results in a reduction of ATP production and an inhibition of F-actin cytoskeletal assembly, which is crucial for the migration and invasion of cancer cells [189].

1.12 Conclusions and Perspectives

In this chapter, we reviewed the recent progress on NIR light-mediated Au nanostructures for cancer theranostics (Fig. 1.15). During the past decade, Au nanostructures with different geometry and morphology have been synthesized, which possess unique optical and thermophysical properties, enabling multiple imaging and treatment strategies. Great theranostic potential has been revealed for Au nanostructures in serving as imaging contrast agents, photothermal therapy agents, and drug/gene delivery vehicles. More recently, simultaneous realization of imaging, hyperthermia, and chemotherapy in a single theranostic nanoplatfom has been developed to optimize the efficacy of cancer treatments. Au nanostructures-mediated cancer theranostics has great advantages including site-specific hyperthermia, NIR light-controllable drug release, and imaging-guided therapy. The multifunctional nanoplatfom can generally result in a synergistic effect for optimal treatment efficacy. For the construction of multifunctional theranostic platform, the ease surface modification of Au nanostructures plays a critical role. By noncovalent and covalent functionalization, targeting molecules, imaging contrasts, and chemotherapeutics can be conjugated or encapsulated into a single nanoparticle.

Although a few Au nanostructures have been approved by FDA due to the high biocompatibility, low cytotoxicity, and success in clinical trials [190], there are still challenges in the engineering and *in vivo* behavior of Au nanostructure-based theranostic platform. The first consideration in the use of Au nanostructures is their toxicity and stability in biological buffers. Au nanostructures are typically synthesized in aqueous media with surface ligands to facilitate their stability. To reduce the toxicity of these non-biocompatible surfactants such as CTAB, native ligands are replaced with neutral polymers, for example, PEG. However, removal of native-stabilizing agent often results in agglomeration of Au nanostructures. Therefore, long-term stability *in vivo* remains a challenge.

The second challenge is the fundamental understanding of the interaction between Au nanostructures and cells. Recently, our group demonstrated that intracellular localization, not uptake pathway, determines the fate of AuNRs in cancer and normal cells. AuNRs are toxic to cancer cells but not to normal and mesenchymal stem cells. Due to enhanced permeation of the lysosomal membrane of cancer

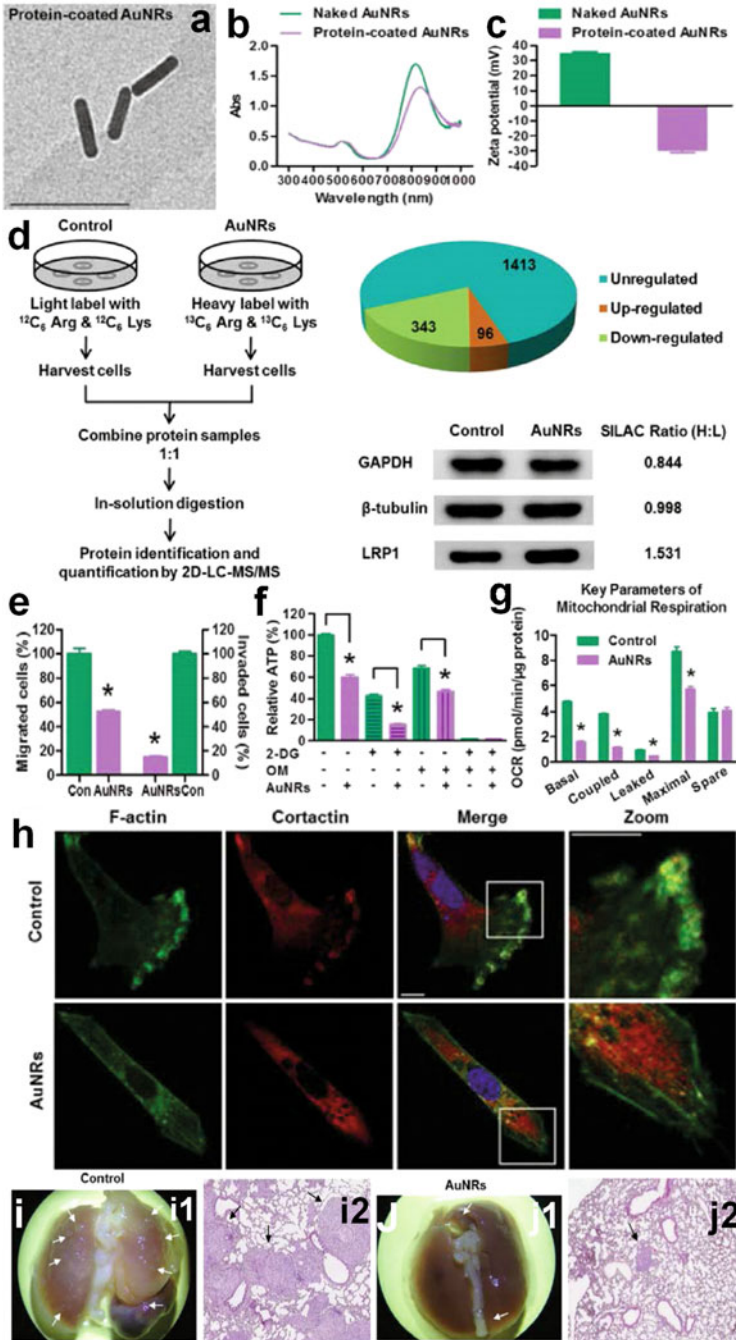


Fig. 1.14 Inhibitory effects of AuNRs on human breast cancer cell migration by disrupting energy metabolism and migration-associated pathway. **(a)** TEM image of protein-coated AuNRs. **(b, c)** UV-vis-NIR spectra and zeta potential of two kinds of AuNRs. **(d)** Stable isotope labeling by amino acids in cell culture (SILAC)-based proteomics analysis of the protein expression related to

cells, nanorods are released into the cytoplasm and transferred from the lysosomes to mitochondria and induce decreased mitochondrial membrane potentials, increasing oxidative stress and finally cell death. However, negligible toxicity was observed in normal cells and mesenchymal stem cells since the lysosomal membrane kept intact. This study provides a detailed understanding of the mechanism of cell-specific cytotoxicity and will guide the design of organelle-targeted Au nanostructures for cancer therapy. The photothermal treatment of Au nanostructures on the cancer-resistant cells and cancer stem cells are also reported, and significant differences exist compared to normal cancer cells [56, 188]. These results suggest the importance of the understanding on the direct interaction between Au nanostructures and different kinds of cells.

The third challenge is to understand the *in vivo* behavior of Au nanostructure-based theranostic agents including pharmacodynamics, pharmacokinetics, and their toxicity potential in animals and humans. For the past decades, several publications have reported the biodistribution and toxicity of Au nanoparticles [193]. However, systematic studies still lack about how the physicochemical properties of nanoparticles, the types of animals, even their physiological conditions of animals, etc., influence the biodistribution, circulation, translocation, metabolism, degradation, and secretion. Zhang et al. studied the biodistribution of GNRs, Au nanospheres (GNSs) of different sizes, and Au nanoclusters (GNCs) *in vivo*. They found that the administrated Au nanoparticles into mouse tail vein have a short term of blood circulation (<2 min) and except of hydrolyzed GNCs, most of these nanoparticles distribute in the liver for 28 days. Due to a small size distribution of GNCs, these hydrolyzed GNCs mainly reside in the kidney with high contents even 7 days postinjection. Except of 50 nm GNSs, most nanoparticles can be removed by secreting into urine [194]. For a long-term study, the liver and spleen are the major organs to accumulate these Au nanoparticles, which were consistent with our previous report [195]. Using X-ray absorption spectroscopy, we revealed that AuNRs in the liver and spleen remain stable chemical forms as elemental Au rather than ionic Au that is much toxic than NPs. To study the biocompatibility of Au nanoparticles of a larger size (>20 nm), we can exclude the possible degradation into ions *in vivo* but consider the effects from the properties such as surface chemistry, shape, size, etc.



Fig. 1.14 (continued) energy generation after MDA-MB-231 cells are treated with AuNRs. The *left* scheme represents SILAC strategy coupled with 2D-LC-MS/MS. The *right* indicates number of modulated proteins by AuNRs and the representative protein quantitative confirmation using western blot analyses. (e) The effects of AuNRs on the migration and invasion abilities of cancer cells, using transwell migration and invasion assays. (f) Effects of AuNRs on the intracellular ATP level, using a luciferase-based luminescence assay that is normalized to protein concentrations. Before ATP measurement, the cells are pretreated with or without 100 mM 2-deoxyglucose (2-DG), 1 μ M oligomycin (OM), or 50 μ M AuNRs for 24 h. (g) Effects of AuNRs on the oxygen consumption rate (OCR) in the presence or absence of AuNRs that is monitored using the Seahorse XF24 Extracellular Flux Analyzer in real time. (h) Impairment of F-actin cytoskeletal assembly by AuNRs in cancer cells. (i) The bright images (*i1*) and the section images (*i2*) after H&E staining for metastatic nodules of tumor on the lung surface of mice. (j) The corresponding images of metastatic nodules of tumor after the mice are administrated by tail-vein injection with AuNRs (Reprinted with permission from ref. [189]. Copyright 2014, John Wiley & Sons, Inc.)

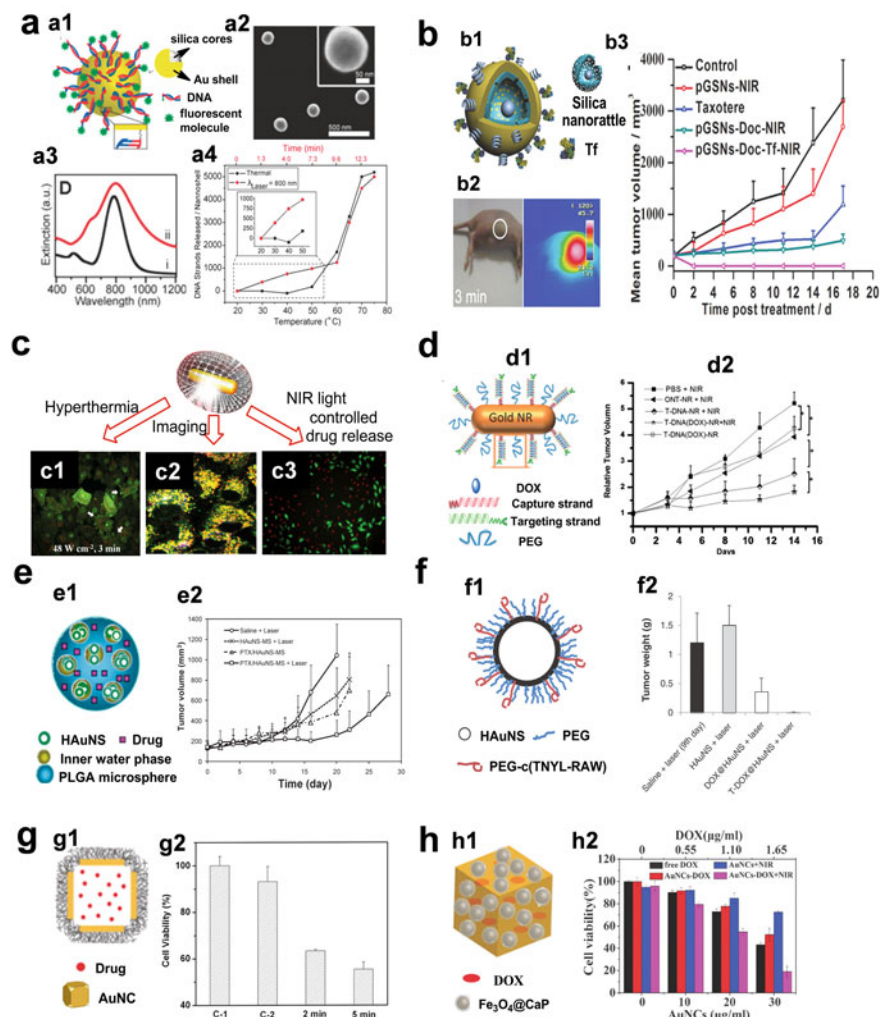


Fig. 1.15 Brief summary for applications of Au nanostructures as NIR light-mediated platforms for cancer theranostics. **(a)** Thermal- and light-triggered release of ssDNA from Au nanoshells (AuNSs). **(a1)** A scheme of single-stranded DNA-modified AuNSs containing a spherical silica core. **(a2)** Scanning electron microscope image of AuNSs. **(a3)** Extinction spectra of AuNSs (ii). **(a4)** The release profile of DNA strands from AuNSs after thermal treatment (black squares) and laser irradiation (red dots) (Reprinted with permission from ref. [191]. Copyright 2011, American Chemical Society). **(b)** GNSs as a drug cocktail to fight against cancers through NIR light irradiation. **(b1)** A scheme of GNSs with a silica nanorattle core (GNSs) and a targeting ligand-modified surface. **(b2)** Temperature imaging of a tumor-bearing nude mouse after injection with pGNSs-Tf during photothermal therapy (2 W/cm², 3 min). **(b3)** UV-vis-NIR spectra of GNSs and PEG- and transferrin-modified GNSs (pGNSs-Tf) that indicate NPs within the inset. **(b4)** In vivo antitumor activities on MCF-7 bearing nude BALB/c mice (Reprinted with permission from ref. [134]. Copyright 2012, John Wiley & Sons, Inc.) **(c)** Au@SiO₂ as a light-mediated multifunctional theranostic platform. **(c1)** Photothermal effect of NIR irradiation (790 nm, 48 W/cm²) on the lysosomal membrane integrity. **(c2)** Intracellular localization of DOX (red) and Au@SiO₂ (blue) with Lyso-Tracker (green) supported by TPL images. **(c3)** Photothermal stimulus triggering DOX release for chemotherapy and the efficiency evaluated by Live-Dead assay (Reprinted with permission from

However, GNCs of several nm diameters consist of both elemental and ionic Au, but their potential toxicity or compatibility for long-term *in vivo* needs more attention in the future.

To study the biodistribution of Au nanoparticles *in vivo*, ICP-MS has been widely used to qualify the contents of Au in various organs, tissues, biological fluids, and cells. For ICP-MS determination, animals must be sacrificed to obtain a given organ to digest samples in acidic solution and to measure the Au content. To capture the nanoparticles in blood, a short half-life for clearance is a challenge using ICP-MS procedure. The optoacoustic imaging is a novel noninvasive imaging technique which provides convenience for studying real-time and semiquantitative pharmacokinetic and biodistribution profiles of Au nanoparticles. With a maximal absorption of NIR light, the AuNRs and Au nanostars can produce heat to ultrasound wave signals, which can be quickly visualized by multispectral optoacoustic tomography (MSOT). This technique has a high spatial resolution (150 μm for whole body; 20–50 μm for local imaging) and good contrast and provides a real-time monitoring method to collect the signals from photothermal-responsive Au nanomaterials. The contents of AuNSs and AuNRs in the blood vessels, liver, spleen, and kidneys can be sensitively detected in real time to provide the blood clearance, the accumulation, and removal process of NPs in an interested tissue or the body (Fig. 1.16). Combination of MSOT and ICP-MS is thus an appropriate approach for short- and long-term monitoring of Au nanoparticles *in vivo* [196].

Cells lines are widely used to study the potential toxicity and to understand mechanism. The various factors including physicochemical properties of Au nanoparticles [11], the cell culture environment [50], and cell types [56] play important roles in mediating their cellular effects. Due to the diversity of these factors, it is difficult to reveal the underlying mechanism of cytotoxicity caused by

Fig. 1.15 (continued) ref. [95]. Copyright 2012, John Wiley & Sons, Inc.) **(d)** DNA self-assembly on AuNRs as cancer cell-targeted and NIR light-responsive nanoparticles for thermo-chemotherapy. *(d1)* Scheme of DNA assembly and DOX loading on the AuNRs. *(d2)* Antitumor effects of various treatments on tumor-bearing mice (Reprinted with permission from ref. [192]. Copyright 2012, John Wiley & Sons, Inc.). **(e)** HAuNS-loaded microspheres (HAuNS-MSs) for thermo-chemotherapy. *(e1)* Hypothetical structures of PTX/HAuNS-MSs. *(e2)* Inhibition of U87 human gliomas growth in tumor-bearing nude mice when treated with various modes (Reprinted with permission from ref. [153]. Copyright 2010, John Wiley & Sons, Inc.). **(f)** Targeted photothermal chemotherapy using DOX-loaded HAuNSs. *(f1)* Scheme of SH-PEG-c(TNYL-RAW)-conjugated HAuNSs. *(f2)* Impact of NIR laser treatment on the growth of the bearing tumors in mice (Reprinted with permission from ref. [155]. Copyright 2012, American Association for Cancer Research). **(g)** Polymer-coated AuNCs with capability of releasing chemotherapeutic drugs controllably under NIR light irradiation. *(g1)* Scheme of polymer-coated AuNCs for drug delivery. *(g2)* Effects of nanocarriers on cell viability after treatments: (C-1) 2 min irradiation in absence of AuNCs; (C-2) 2 min irradiation in the presence of Dox-free AuNCs; and (2/5 min) 2 min or 5 min irradiation by NIR laser in presence of Dox-loaded AuNCs (Reprinted with permission from ref. [163]. Copyright 2009, Nature Publishing Group). **(h)** Enhanced release of drug from AuNCs under NIR irradiation. *(h1)* Schematic illustration of Fe_3O_4 @CaP-capped AuNCs. *(h2)* Effects of dose and triggered photothermia of Fe_3O_4 @CaP-capped AuNCs on viabilities of cancer cells (Reprinted with permission from ref. [165]. Copyright 2012, Royal Society of Chemistry)

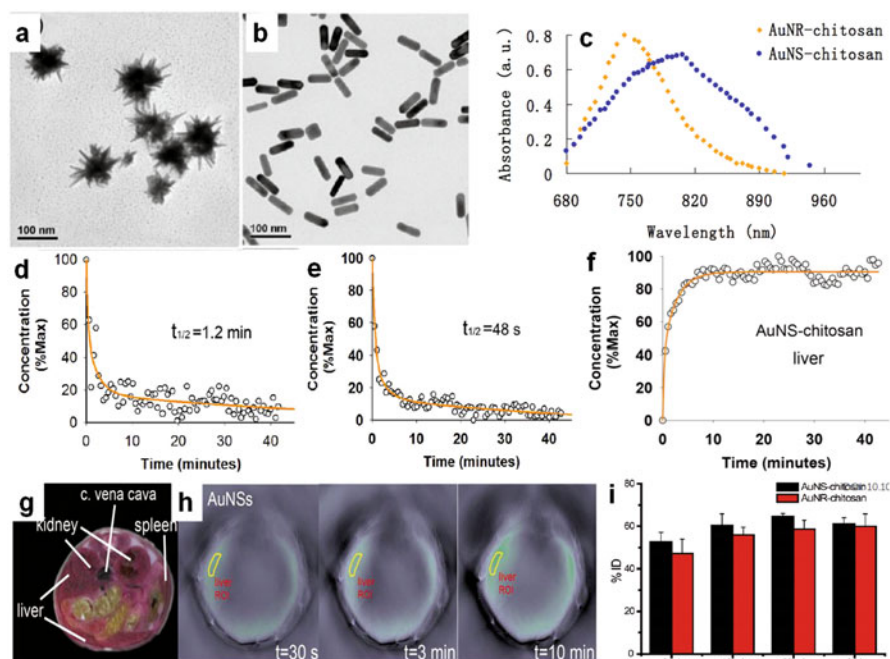


Fig. 1.16 In vivo pharmacokinetic features and biodistribution of Au nanorods and nanostars (AuNSs). (a, b) TEM images of AuNRs and AuNSs. (c) The vis-NIR light absorption spectra of AuNSs and AuNRs using multispectral optoacoustic tomography (MSOT). (d, e) Real-time pharmacokinetic studies of AuNSs (d) and AuNRs (e) by MSOT after injection of these Au nanoparticles into tail veins of mice. (f) Biodistribution and accumulation study of injected AuNSs in the liver measured by the optoacoustic signals using MSOT. (g) Images of a given section in the liver based on the distribution of AuNSs in a frozen section. (h) The real-time photoacoustic images of AuNSs at the region of interest (ROI, highlighted in yellow circle) in the liver slice. (i) Biodistribution of AuNSs and AuNRs in the liver, determined by ICP-MS (Reprinted with permission from ref. [196]. Copyright 2015, Royal Society of Chemistry)

Au nanoparticles. The -omics-related techniques have provided opportunity to study the induced toxicity. We thus used ^1H NMR spectroscopy-based metabolomics to study the pathway and to screen biomarkers of selective toxicity to cancer cells caused by CTAB-capped AuNRs. According to the results in molecular levels, normal cell lines and cancer cells show distinct changes in the metabolites that relate to oxidative stress and energy generation, the metabolism of amino acids, and nucleotides. The cellular responses are also time dependent that can illustrate how the molecular pathways contribute to distinct effects of two cell lines. The metabolomics results showed that AuNRs induce oxidative stress in both cell lines, but normal cells are more easily to offset the oxidative stress than cancer cells. Thus, the severe oxidative stress induces damage to cancer cells and to result in cell death [197]. We also employed SILAC-based proteomics to screen the signal network to inhibit the migration of cancer cells treated by AuNRs. The exposure of breast

cancer cells to AuNRs suppresses energy generation-related pathway like the mitochondrial oxidative phosphorylation (OXPHOS) and glycolysis [189]. The modulation in molecular levels helps us understand the underlying major mechanism of the cellular effects and predicts the potential risk of nanomaterials for biomedical applications.

In the end, most animal models were highly specific; thus the replicative results of biological effects and biomedical applications are sometimes hard to achieve. Predicting and evaluating toxicity of the designed Au nanostructures in vitro should base on systematic studies about how the varied factors regulate cellular effects, by combining conventional techniques for molecular and cell biology, multi-omics-based techniques, and some novel techniques in nanotoxicology. Evaluating in vivo behavior of Au nanostructures in multiple xenograft models is also necessary for clinical translation. More efforts are needed to acquire detailed information to pave the way of developing Au nanostructures for clinical applications.

Acknowledgment This work was supported by grants from the National Basic Research Program of China (973 Programs 2011CB933401 and 2012CB934003), National Major Scientific Instruments Development Project (2011YQ03013406), the National Natural Science Foundation of China (21320102003, 11205166) International Science & Technology Cooperation Program of MOST (2013DFG32340), and the National Science Fund for Distinguished Young Scholars (11425520).

References

1. Kintzel PE, Dorr RT (1995) Anticancer drug renal toxicity and elimination: dosing guidelines for altered renal function. *Cancer Treat Rev* 21:33–64
2. Jaracz S, Chen J, Kuznetsova LV, Ojima I (2005) Recent advances in tumor-targeting anticancer drug conjugates. *Bioorg Med Chem* 13:5043–5054
3. Schimmel KJ, Richel DJ, van den Brink RB, Guchelaar HJ (2004) Cardiotoxicity of cytotoxic drugs. *Cancer Treat Rev* 30:181–191
4. Moses MA, Brem H, Langer R (2003) Advancing the field of drug delivery: taking aim at cancer. *Cancer Cell* 4:337–341
5. Holohan C, Van Schaeybroeck S, Longley DB, Johnston PG (2013) Cancer drug resistance: an evolving paradigm. *Nat Rev Cancer* 13:714–726
6. Shimizu T, Teranishi T, Hasegawa S, Miyake M (2003) Size evolution of alkanethiol-protected gold nanoparticles by heat treatment in the solid state. *J Phys Chem B* 107:2719–2724
7. Liang HP, Wan LJ, Bai CL, Jiang L (2005) Gold hollow nanospheres: tunable surface plasmon resonance controlled by interior-cavity sizes. *J Phys Chem B* 109:7795–7800
8. Xu XD, Cortie MB (2006) Shape change and color gamut in gold nanorods, dumbbells, and dog bones. *Adv Funct Mater* 16:2170–2176
9. Lu XM, Au L, McLellan J, Li ZY, Marquez M, Xia YN (2007) Fabrication of cubic nanocages and nanoframes by dealloying au/ag alloy nanoboxes with an aqueous etchant based on $\text{Fe}(\text{NO}_3)_3$ or NH_4OH . *Nano Lett* 7:1764–1769
10. Zhang JA, Langille MR, Personick ML, Zhang K, Li SY, Mirkin CA (2010) Concave cubic gold nanocrystals with high-index facets. *J Am Chem Soc* 132:14012–14014

11. Qiu Y, Liu Y, Wang LM et al (2010) Surface chemistry and aspect ratio mediated cellular uptake of Au nanorods. *Biomaterials* 31:7606–7619
12. Sun CJ, Yang H, Yuan Y et al (2011) Controlling assembly of paired gold clusters within apoferritin nanoreactor for *in vivo* kidney targeting and biomedical imaging. *J Am Chem Soc* 133:8617–8624
13. He WW, Liu Y, Yuan JS et al (2011) Au@Pt nanostructures as oxidase and peroxidase mimetics for use in immunoassays. *Biomaterials* 32:1139–1147
14. Wang LM, Lin XY, Wang J et al (2014) Novel insights into combating cancer chemotherapy resistance using a plasmonic nanocarrier: enhancing drug sensitiveness and accumulation simultaneously with localized mild photothermal stimulus of femtosecond pulsed laser. *Adv Funct Mater* 24:4229–4239
15. Personick ML, Langille MR, Zhang J, Harris N, Schatz GC, Mirkin CA (2011) Synthesis and isolation of {110}-faceted gold bipyramids and rhombic dodecahedra. *J Am Chem Soc* 133:6170–6173
16. Cheng LC, Huang JH, Chen HM et al (2012) Seedless, silver-induced synthesis of star-shaped gold/silver bimetallic nanoparticles as high efficiency photothermal therapy reagent. *J Mater Chem* 22:2244–2253
17. Jiang XM, Wang LM, Wang J, Chen CY (2012) Gold nanomaterials: preparation, chemical modification, biomedical applications and potential risk assessment. *Appl Biochem Biotechnol* 166:1533–1551
18. Cheng LC, Jiang XM, Wang J, Chen CY, Liu RS (2013) Nano-bio effects: interaction of nanomaterials with cells. *Nanoscale* 5:3547–3569
19. Faraday M (1857) The bakerian lecture: experimental relations of gold (and other metals) to light. *Philos Trans R Soc Lond* 147:145–181
20. Mie G (1908) Beitrage zur optik truber medien speziell kolloidaler metallosungen. *Ann Phys* 25:377–445
21. Turkevich J, Stevenson PC, Hillier J (1951) A study of the nucleation and growth processes in the synthesis of colloidal gold. *Discuss Faraday Soc* 11:55–75
22. Xia Y, Xiong Y, Lim B, Skrabalak SE (2009) Shape-controlled synthesis of metal nanocrystals: simple chemistry meets complex physics? *Angew Chem Int Ed* 48:60–103
23. Grzelczak M, Perez-Juste J, Mulvaney P, Liz-Marzan LM (2008) Shape control in gold nanoparticle synthesis. *Chem Soc Rev* 37:1783–1791
24. Burda C, Chen X, Narayanan R, El-Sayed MA (2005) Chemistry and properties of nanocrystals of different shapes. *Chem Rev* 105:1025–1102
25. Skrabalak SE, Chen J, Au L, Lu X, Li X, Xia YN (2007) Gold nanocages for biomedical applications. *Adv Mater* 19:3177–3184
26. Lal S, Clare SE, Halas NJ (2008) Nanoshell-enabled photothermal cancer therapy: impending clinical impact. *Acc Chem Res* 41:1842–1851
27. Murphy CJ, Gole AM, Stone JW et al (2008) Gold nanoparticles in biology: beyond toxicity to cellular imaging. *Acc Chem Res* 41:1721–1730
28. Rosi NL, Mirkin CA (2005) Nanostructures in biodiagnostics. *Chem Rev* 105:1547–1562
29. Lee KS, El-Sayed MA (2006) Gold and silver nanoparticles in sensing and imaging: sensitivity of plasmon response to size, shape, and metal composition. *J Phys Chem B* 110:19220–19225
30. Link S, El-Sayed MA (2000) Shape and size dependence of radiative, non-radiative and photothermal properties of gold nanocrystals. *Int Rev Phys Chem* 19:409–453
31. Hu M, Chen J, Li ZY et al (2006) Gold nanostructures: engineering their plasmonic properties for biomedical applications. *Chem Soc Rev* 35:1084–1094
32. Haes AJ, Stuart DA, Nie S, Van Duyne RP (2004) Using solution-phase nanoparticles, surface-confined nanoparticle arrays and single nanoparticles as biological sensing platforms. *J Fluoresc* 14:355–367
33. Austin LA, Mackey MA, Dreaden EC, El-Sayed MA (2014) The optical, photothermal, and facile surface chemical properties of gold and silver nanoparticles in biodiagnostics, therapy, and drug delivery. *Arch Toxicol* 88:1391–1417

34. Nie X, Chen CY (2012) Au nanostructures: an emerging prospect in cancer theranostics. *Sci China Life Sci* 55:872–883
35. Jain PK, Huang X, El-Sayed IH, El-Sayed MA (2008) Noble metals on the nanoscale: optical and photothermal properties and some applications in imaging, sensing, biology, and medicine. *Acc Chem Res* 41:1578–1586
36. Jain PK, Huang X, El-Sayed IH, El-Sayad MA (2007) Review of some interesting surface plasmon resonance-enhanced properties of noble metal nanoparticles and their applications to biosystems. *Plasmonics* 2:107–118
37. Yguerabide J, Yguerabide EE (1998) Light-scattering submicroscopic particles as highly fluorescent analogs and their use as tracer labels in clinical and biological applications: I. Theory. *Anal Biochem* 262:137–156
38. Jain PK, Lee KS, El-Sayed IH, El-Sayed MA (2006) Calculated absorption and scattering properties of gold nanoparticles of different size, shape, and composition: applications in biological imaging and biomedicine. *J Phys Chem B* 110:7238–7248
39. Sokolov K, Follen M, Aaron J et al (2003) Real-time vital optical imaging of precancer using anti-epidermal growth factor receptor antibodies conjugated to gold nanoparticles. *Cancer Res* 63:1999–2004
40. El-Sayed IH, Huang XH, El-Sayed MA (2005) Surface plasmon resonance scattering and absorption of anti-EGFR antibody conjugated gold nanoparticles in cancer diagnostics: applications in oral cancer. *Nano Lett* 5:829–834
41. Qian W, Huang XH, Kang B, El-Sayed MA (2010) Dark-field light scattering imaging of living cancer cell component from birth through division using bioconjugated gold nanoprobcs. *J Biomed Opt* 15:046025-1-9
42. Eghtedari M, Liopo AV, Copland JA, Oraevsly AA, Motamedi M (2009) Engineering of hetero-functional gold nanorods for the *in vivo* molecular targeting of breast cancer cells. *Nano Lett* 9:287–291
43. Hu R, Yong KT, Roy I, Ding H, He S, Prasad PN (2009) Metallic nanostructures as localized plasmon resonance enhanced scattering probes for multiplex dark-field targeted imaging of cancer cells. *J Phys Chem C* 113:2676–2684
44. Huang XH, El-Sayed IH, Qian W, El-Sayed MA (2006) Cancer cell imaging and photothermal therapy in the near-infrared region by using gold nanorods. *J Am Chem Soc* 128:2115–2120
45. Oyelere AK, Chen PC, Huang XH, El-Sayed IH, El-Sayed MA (2007) Peptide-conjugated gold nanorods for nuclear targeting. *Bioconjug Chem* 18:1490–1497
46. Ding H, Yong KT, Roy I et al (2007) Gold nanorods coated with multilayer polyelectrolyte as contrast agents for multimodal imaging. *J Phys Chem C* 111:12552–12557
47. Kang B, Mackey MA, El-Sayed MA (2010) Nuclear targeting of gold nanoparticles in cancer cells induces DNA damage, causing cytokinesis arrest and apoptosis. *J Am Chem Soc* 132:1517–1519
48. Tong L, Wei QS, Wei A, Cheng JX (2009) Gold nanorods as contrast agents for biological imaging: optical properties, surface conjugation and photothermal effects. *Photochem Photobiol* 85:21–32
49. Park J, Estrada A, Sharp K et al (2008) Two-photon-induced photoluminescence imaging of tumors using near-infrared excited gold nanoshells. *Opt Express* 16:1590–1599
50. Maiorano G, Sabella S, Sorce B et al (2010) Effects of cell culture media on the dynamic formation of protein-nanoparticle complexes and influence on the cellular response. *ACS Nano* 4:7481–7491
51. Durr NJ, Larson T, Smith DK, Korgel BA, Sokolov K, Ben-Yakar A (2007) Two-photon luminescence imaging of cancer cells using molecularly targeted gold nanorods. *Nano Lett* 7:941–945
52. Puvanakrishnan P, Diagaradjane P, Kazmi SMS, Dunn AK, Krishnan S, Tunnell JW (2012) Narrow band imaging of squamous cell carcinoma tumors using topically delivered anti-EGFR antibody conjugated gold nanorods. *Lasers Surg Med* 44:310–317

53. Tong L, Zhao Y, Huff TB, Hansen MN, Wei A, Cheng JX (2007) Gold nanorods mediate tumor cell death by compromising membrane integrity. *Adv Mater* 19:3136–3141
54. Charan S, Sanjiv K, Singh N et al (2012) Development of chitosan oligosaccharide-modified gold nanorods for *in vivo* targeted delivery and noninvasive imaging by NIR irradiation. *Bioconjug Chem* 23:2173–2182
55. Zhang YA, Yu J, Birch DJS, Chen Y (2010) Gold nanorods for fluorescence lifetime imaging in biology. *J Biomed Opt* 15:020504
56. Wang LM, Liu Y, Li W et al (2011) Selective targeting of gold nanorods at the mitochondria of cancer cells: implications for cancer therapy. *Nano Lett* 11:772–780
57. Yuan HK, Khoury CG, Hwang H, Wilson CM, Grant GA, Vo-Dinh T (2012) Gold nanostars: surfactant-free synthesis, 3D modelling, and two-photon photoluminescence imaging. *Nanotechnology* 23:075102
58. Park J, Estrada A, Schwartz JA et al (2010) Intra-organ biodistribution of gold nanoparticles using intrinsic two-photon-induced photoluminescence. *Lasers Surg Med* 42:630–639
59. Wang YC, Xu JB, Xia XH et al (2012) Sv119-gold nanocage conjugates: a new platform for targeting cancer cells *via* sigma-2 receptors. *Nanoscale* 4:421–424
60. Gao L, Vadakkan TJ, Nammalvar V (2011) Nanoshells for *in vivo* imaging using two-photon excitation microscopy. *Nanotechnology* 22:365102
61. Au L, Zhang Q, Cobley CM et al (2010) Quantifying the cellular uptake of antibody-conjugated Au nanocages by two-photon microscopy and inductively coupled plasma mass spectrometry. *ACS Nano* 4:35–42
62. Yuan Z, Wu CF, Zhao HZ, Jiang HB (2005) Imaging of small nanoparticle-containing objects by finite-element-based photoacoustic tomography. *Opt Lett* 30:3054–3056
63. Li PC, Huang SW, Wei CW, Chiou YC, Chen CD, Wang CRC (2005) Photoacoustic flow measurements by use of laser-induced shape transitions of gold nanorods. *Opt Lett* 30:3341–3343
64. Wang YW, Xie XY, Wang XD et al (2004) Photoacoustic tomography of a nanoshell contrast agent in the *in vivo* rat brain. *Nano Lett* 4:1689–1692
65. Mallidi S, Larson T, Tam J et al (2009) Multiwavelength photoacoustic imaging and plasmon resonance coupling of gold nanoparticles for selective detection of cancer. *Nano Lett* 9:2825–2831
66. Kim C, Cho EC, Chen JY et al (2010) *In vivo* molecular photoacoustic tomography of melanomas targeted by bioconjugated gold nanocages. *ACS Nano* 4:4559–4564
67. Cai X, Li WY, Kim CH, Yuan YC, Wang LHV, Xia YN (2011) *In vivo* quantitative evaluation of the transport kinetics of gold nanocages in a lymphatic system by noninvasive photoacoustic tomography. *ACS Nano* 5:9658–9667
68. Li PC, Wang CRC, Shieh DB et al (2008) *In vivo* photoacoustic molecular imaging with simultaneous multiple selective targeting using antibody-conjugated gold nanorods. *Opt Express* 16:18605–18615
69. Yang SH, Ye F, Xing D (2012) Intracellular label-free gold nanorods imaging with photoacoustic microscopy. *Opt Express* 20:10370–10375
70. Jokerst JV, Thangaraj M, Kempen PJ, Sinclair R, Gambhir SS (2012) Photoacoustic imaging of mesenchymal stem cells in living mice via silica-coated gold nanorods. *ACS Nano* 6:5920–5930
71. von Maltzahn G, Park JH, Agrawal A et al (2009) Computationally guided photothermal tumor therapy using long-circulating gold nanorod antennas. *Cancer Res* 69:3892–3900
72. Luo T, Huang P, Gao G et al (2011) Mesoporous silica-coated gold nanorods with embedded indocyanine green for dual mode X-ray CT and NIR fluorescence imaging. *Opt Express* 19:17030–17039
73. Huang P, Bao L, Zhang CL et al (2011) Folic acid-conjugated silica-modified gold nanorods for x-ray/ct imaging-guided dual-mode radiation and photo-thermal therapy. *Biomaterials* 32:9796–9809
74. Lozano N, Al-Jamal WT, Taruttis A et al (2012) Liposome-gold nanorod hybrids for high-resolution visualization deep in tissues. *J Am Chem Soc* 134:13256–13258

75. Zagaynova EV, Shirmanova MV, Kirillin MY et al (2008) Contrasting properties of gold nanoparticles for optical coherence tomography: phantom, *in vivo* studies and Monte Carlo simulation. *Phys Med Biol* 53:4995–5009
76. Oldenburg AL, Hansen MN, Ralston TS, Wei A, Boppart SA (2009) Imaging gold nanorods in excised human breast carcinoma by spectroscopic optical coherence tomography. *J Mater Chem* 19:6407–6411
77. Jung Y, Reif R, Zeng YG, Wang RK (2011) Three-dimensional high-resolution imaging of gold nanorods uptake in sentinel lymph nodes. *Nano Lett* 11:2938–2943
78. Kim CS, Wilder-Smith P, Ahn YC, Liaw LHL, Chen ZP, Kwon YJ (2009) Enhanced detection of early-stage oral cancer *in vivo* by optical coherence tomography using multimodal delivery of gold nanoparticles. *J Biomed Opt* 14:034008
79. Nie SM, Emery SR (1997) Probing single molecules and single nanoparticles by surface-enhanced Raman scattering. *Science* 275:1102–1106
80. Moskovits M (2006) Surface-enhanced Raman spectroscopy: a brief perspective. In: Kneipp K, Moskovits M, Kneipp H (eds) *Surface-enhanced Raman scattering: physics and applications*. Springer, Berlin/Heidelberg, pp 1–17
81. Chon H, Lee S, Son SW, Oh CH, Choo J (2009) Highly sensitive immunoassay of lung cancer marker carcinoembryonic antigen using surface-enhanced Raman scattering of hollow gold nanospheres. *Anal Chem* 81:3029–3034
82. Bishnoi SW, Lin YJ, Tibudan M et al (2011) SERS biodetection using gold-silica nanoshells and nitrocellulose membranes. *Anal Chem* 83:4053–4060
83. Wu L, Wang ZY, Zong SF et al (2013) Simultaneous evaluation of p53 and p21 expression level for early cancer diagnosis using sers technique. *Analyst* 138:3450–3456
84. Wang GF, Lipert RJ, Jain M et al (2011) Detection of the potential pancreatic cancer marker muc4 in serum using surface-enhanced Raman scattering. *Anal Chem* 83:2554–2561
85. Li M, Cushing SK, Zhang JM et al (2013) Three-dimensional hierarchical plasmonic nano-architecture enhanced surface-enhanced Raman scattering immunosensor for cancer biomarker detection in blood plasma. *ACS Nano* 7:4967–4976
86. Huang XH, El-Sayed IH, Qian W, El-Sayed MA (2007) Cancer cells assemble and align gold nanorods conjugated to antibodies to produce highly enhanced, sharp, and polarized surface Raman spectra: a potential cancer diagnostic marker. *Nano Lett* 7:1591–1597
87. Kang B, Austin LA, El-Sayed MA (2012) Real-time molecular imaging throughout the entire cell cycle by targeted plasmonic-enhanced Rayleigh/Raman spectroscopy. *Nano Lett* 12:5369–5375
88. Yigit MV, Zhu LY, Ifediba MA et al (2011) Noninvasive MRI-SERS imaging in living mice using an innately bimodal nanomaterial. *ACS Nano* 5:1056–1066
89. Wang X, Qian XM, Beitler JJ et al (2011) Detection of circulating tumor cells in human peripheral blood using surface-enhanced Raman scattering nanoparticles. *Cancer Res* 71:1526–1532
90. Pitsillides CM, Joe EK, Wei XB, Anderson RR, Lin CP (2003) Selective cell targeting with light-absorbing microparticles and nanoparticles. *Biophys J* 84:4023–4032
91. El-Sayed IH, Huang XH, El-Sayed MA (2006) Selective laser photo-thermal therapy of epithelial carcinoma using anti-egfr antibody conjugated gold nanoparticles. *Cancer Lett* 239:129–135
92. Rejjiya CS, Kumar J, Raji V, Vibin M, Abraham A (2012) Laser immunotherapy with gold nanorods causes selective killing of tumour cells. *Pharmacol Res* 65:261–269
93. Dickerson EB, Dreaden EC, Huang XH et al (2008) Gold nanorod assisted near-infrared plasmonic photothermal therapy (pptt) of squamous cell carcinoma in mice. *Cancer Lett* 269:57–66
94. Li ZM, Huang P, Zhang XJ et al (2010) RGD-conjugated dendrimer-modified gold nanorods for *in vivo* tumor targeting and photothermal therapy. *Mol Pharm* 7:94–104
95. Zhang ZJ, Wang LM, Wang J et al (2012) Mesoporous silica-coated gold nanorods as a light-mediated multifunctional theranostic platform for cancer treatment. *Adv Mater* 24:1418–1423

96. Guo LH, Xu Y, Ferhan AR, Chen GN, Kim DH (2013) Oriented gold nanoparticle aggregation for colorimetric sensors with surprisingly high analytical figures of merit. *J Am Chem Soc* 135:12338–12345
97. Hirsch LR, Stafford RJ, Bankson JA et al (2003) Nanoshell-mediated near-infrared thermal therapy of tumors under magnetic resonance guidance. *Proc Natl Acad Sci U S A* 100:13549–13554
98. Bernardi RJ, Lowery AR, Thompson PA, Blaney SM, West JL (2008) Immunonanoshells for targeted photothermal ablation in medulloblastoma and glioma: an *in vitro* evaluation using human cell lines. *J Neurooncol* 86:165–172
99. Day ES, Thompson PA, Zhang LN et al (2011) Nanoshell-mediated photothermal therapy improves survival in a murine glioma model. *J Neurooncol* 104:55–63
100. Diagaradjane P, Shetty A, Wang JC et al (2008) Modulation of *in vivo* tumor radiation response via gold nanoshell-mediated vascular-focused hyperthermia: characterizing an integrated antihypoxic and localized vascular disrupting targeting strategy. *Nano Lett* 8:1492–1500
101. McIntosh CM, Esposito EA, Boal AK, Simard JM, Martin CT, Rotello VM (2001) Inhibition of DNA transcription using cationic mixed monolayer protected gold clusters. *J Am Chem Soc* 123:7626–7629
102. Alkilany AM, Thompson LB, Boulos SP, Sisco PN, Murphy CJ (2012) Gold nanorods: their potential for photothermal therapeutics and drug delivery, tempered by the complexity of their biological interactions. *Adv Drug Deliv Rev* 64:190–199
103. Park H, Lee S, Chen L et al (2009) SERS imaging of Her2-overexpressed MCF-7 cells using antibody-conjugated gold nanorods. *Phys Chem Chem Phys* 11:7444–7449
104. Wang LM, Li JY, Pan J et al (2013) Revealing the binding structure of the protein corona on gold nanorods using synchrotron radiation-based techniques: understanding the reduced damage in cell membranes. *J Am Chem Soc* 135:17359–17368
105. Wang L, Jiang X, Ji Y et al (2013) Surface chemistry of gold nanorods: origin of cell membrane damage and cytotoxicity. *Nanoscale* 5:8384–8391
106. Kim CK, Ghosh P, Pagliuca C, Zhu ZJ, Menichetti S, Rotello VM (2009) Entrapment of hydrophobic drugs in nanoparticle monolayers with efficient release into cancer cells. *J Am Chem Soc* 131:1360–1361
107. Gorelikov I, Matsuura N (2008) Single-step coating of mesoporous silica on cetyltrimethyl ammonium bromide-capped nanoparticles. *Nano Lett* 8:369–373
108. Slowing II, Vivero-Escoto JL, Wu CW, Lin VSY (2008) Mesoporous silica nanoparticles as controlled release drug delivery and gene transfection carriers. *Adv Drug Deliv Rev* 60:1278–1288
109. Zhang ZJ, Wang J, Nie X et al (2014) Near infrared laser-induced targeted cancer therapy using thermoresponsive polymer encapsulated gold nanorods. *J Am Chem Soc* 136:7317–7326
110. Amoozgar Z, Yeo Y (2012) Recent advances in stealth coating of nanoparticle drug delivery systems. *WIREs Nanomed Nanobiotechnol* 4:219–233
111. Wang J, Byrne JD, Napier ME, DeSimone JM (2011) More effective nanomedicines through particle design. *Small* 7:1919–1931
112. Alivisatos AP, Johnsson KP, Peng XG et al (1996) Organization of ‘nanocrystal molecules’ using DNA. *Nature* 382:609–611
113. Mirkin CA, Letsinger RL, Mucic RC, Storhoff JJ (1996) A DNA-based method for rationally assembling nanoparticles into macroscopic materials. *Nature* 382:607–609
114. Glynou K, Ioannou PC, Christopoulos TK, Syriopoulou V (2003) Oligonucleotide-functionalized gold nanoparticles as probes in a dry-reagent strip biosensor for DNA analysis by hybridization. *Anal Chem* 75:4155–4160
115. Lee JS, Han MS, Mirkin CA (2007) Colorimetric detection of mercuric ion (Hg^{2+}) in aqueous media using DNA-functionalized gold nanoparticles. *Angew Chem Int Ed* 46:4093–4096

116. Rosi NL, Giljohann DA, Thaxton CS, Lytton-Jean AK, Han MS, Mirkin CA (2006) Oligonucleotide-modified gold nanoparticles for intracellular gene regulation. *Science* 312:1027–1030
117. Austin LA, Kang B, Yen CW, El-Sayed MA (2011) Nuclear targeted silver nanospheres perturb the cancer cell cycle differently than those of nanogold. *Bioconjug Chem* 22:2324–2331
118. Xiao YL, Hong H, Matson VZ et al (2012) Gold nanorods conjugated with doxorubicin and crgd for combined anticancer drug delivery and pet imaging. *Theranostics* 2:757–768
119. Black KC, Kirkpatrick ND, Troutman TS et al (2008) Gold nanorods targeted to delta opioid receptor: plasmon-resonant contrast and photothermal agents. *Mol Imaging* 7:50–57
120. Yamashita S, Fukushima H, Akiyama Y et al (2011) Controlled-release system of single-stranded DNA triggered by the photothermal effect of gold nanorods and its *in vivo* application. *Bioorg Med Chem* 19:2130–2135
121. Lundqvist M, Stigler J, Elia G, Lynch I, Cedervall T, Dawson KA (2008) Nanoparticle size and surface properties determine the protein corona with possible implications for biological impacts. *Proc Natl Acad Sci U S A* 105:14265–14270
122. Prabakaran M, Grailer JJ, Pilla S, Steeber DA, Gong SQ (2009) Gold nanoparticles with a monolayer of doxorubicin-conjugated amphiphilic block copolymer for tumor-targeted drug delivery. *Biomaterials* 30:6065–6075
123. Qian XM, Peng XH, Ansari DO et al (2008) *In vivo* tumor targeting and spectroscopic detection with surface-enhanced Raman nanoparticle tags. *Nat Biotechnol* 26:83–90
124. Fischler M, Sologubenko A, Mayer J et al (2008) Chain-like assembly of gold nanoparticles on artificial DNA templates *via* ‘click chemistry’. *Chem Commun* 2:169–171
125. Zhu K, Zhang Y, He S et al (2012) Quantification of proteins by functionalized gold nanoparticles using click chemistry. *Anal Chem* 84:4267–4270
126. Loo C, Lin A, Hirsch L et al (2004) Nanoshell-enabled photonics-based imaging and therapy of cancer. *Technol Cancer Res Treat* 3:33–40
127. Loo C, Lowery A, Halas NJ, West J, Drezek R (2005) Immunotargeted nanoshells for integrated cancer imaging and therapy. *Nano Lett* 5:709–711
128. Gobin AM, Lee MH, Halas NJ, James WD, Drezek RA, West JL (2007) Near-infrared resonant nanoshells for combined optical imaging and photothermal cancer therapy. *Nano Lett* 7:1929–1934
129. Lu W, Melancon MP, Xiong CY et al (2011) Effects of photoacoustic imaging and photothermal ablation therapy mediated by targeted hollow gold nanospheres in an orthotopic mouse xenograft model of glioma. *Cancer Res* 71:6116–6121
130. Bardhan R, Chen WX, Perez-Torres C et al (2009) Nanoshells with targeted simultaneous enhancement of magnetic and optical imaging and photothermal therapeutic response. *Adv Funct Mater* 19:3901–3909
131. Chen WX, Bardhan R, Bartels M et al (2010) A molecularly targeted theranostic probe for ovarian cancer. *Mol Cancer Ther* 9:1028–1038
132. Bardhan R, Chen WX, Bartels M et al (2010) Tracking of multimodal therapeutic nanocomplexes targeting breast cancer *in vivo*. *Nano Lett* 10:4920–4928
133. Liu HY, Chen D, Li LL et al (2011) Multifunctional gold nanoshells on silica nanorattles: a platform for the combination of photothermal therapy and chemotherapy with low systemic toxicity. *Angew Chem Int Ed* 50:891–895
134. Liu HY, Liu TL, Wu XL et al (2012) Targeting gold nanoshells on silica nanorattles: a drug cocktail to fight breast tumors via a single irradiation with near-infrared laser light. *Adv Mater* 24:755–761
135. Lee SM, Park H, Yoo KH (2010) Synergistic cancer therapeutic effects of locally delivered drug and heat using multifunctional nanoparticles. *Adv Mater* 22:4049–4053
136. Xie HA, Diagaradjane P, Deorukhkar AA et al (2011) Integrin alpha(v) beta(3)-targeted gold nanoshells augment tumor vasculature-specific imaging and therapy. *Int J Nanomedicine* 6:259–269

137. Melancon MP, Elliott A, Ji XJ et al (2011) Theranostics with multifunctional magnetic gold nanoshells photothermal therapy and T2 magnetic resonance imaging. *Invest Radiol* 46:132–140
138. Ke HT, Wang JR, Dai ZF et al (2011) Gold-nanoshelled microcapsules: a theranostic agent for ultrasound contrast imaging and photothermal therapy. *Angew Chem Int Ed* 50:3017–3021
139. Ma Y, Liang XL, Tong S, Bao G, Ren QS, Dai ZF (2013) Gold nanoshell nanomicelles for potential magnetic resonance imaging, light-triggered drug release, and photothermal therapy. *Adv Funct Mater* 23:815–822
140. Choi J, Yang J, Jang E et al (2011) Gold nanostructures as photothermal therapy agent for cancer. *Anti Cancer Agents Med* 11:953–964
141. Huff TB, Tong L, Zhao Y, Hansen MN, Cheng JX, Wei A (2007) Hyperthermic effects of gold nanorods on tumor cells. *Nanomedicine* 2:125–132
142. Yi DK, Sun IC, Ryu JH et al (2010) Matrix metalloproteinase sensitive gold nanorod for simultaneous bioimaging and photothermal therapy of cancer. *Bioconjug Chem* 21:2173–2177
143. Choi J, Yang J, Bang D et al (2012) Targetable gold nanorods for epithelial cancer therapy guided by near-IR absorption imaging. *Small* 8:746–753
144. Kuo WS, Chang CN, Chang YT et al (2010) Gold nanorods in photodynamic therapy, as hyperthermia agents, and in near-infrared optical imaging. *Angew Chem Int Ed* 49:2711–2715
145. Jang B, Park JY, Tung CH, Kim IH, Choi Y (2011) Gold nanorod-photosensitizer complex for near-infrared fluorescence imaging and photodynamic/photothermal therapy *in vivo*. *ACS Nano* 5:1086–1094
146. Zhang Y, Qian J, Wang D, Wang YL, He SL (2013) Multifunctional gold nanorods with ultra-high stability and tunability for *in vivo* fluorescence imaging, sers detection, and photodynamic therapy. *Angew Chem Int Ed* 52:1148–1151
147. Zhang ZJ, Wang J, Chen CY (2013) Near-infrared light-mediated nanoplatfoms for cancer thermo-chemotherapy and optical imaging. *Adv Mater* 25:3869–3880
148. Zhang ZJ, Wang J, Chen CY (2013) Gold nanorods based platforms for light-mediated theranostics. *Theranostics* 3:223–238
149. Guo R, Zhang L, Qian H, Li R, Jiang X, Liu B (2010) Multifunctional nanocarriers for cell imaging, drug delivery, and near-IR photothermal therapy. *Langmuir* 26:5428–5434
150. Melancon MP, Lu W, Yang Z et al (2008) *In vitro* and *in vivo* targeting of hollow gold nanoshells directed at epidermal growth factor receptor for photothermal ablation therapy. *Mol Cancer Ther* 7:1730–1739
151. Lu W, Xiong CY, Zhang GD et al (2009) Targeted photothermal ablation of murine melanomas with melanocyte-stimulating hormone analog-conjugated hollow gold nanospheres. *Clin Cancer Res* 15:876–886
152. Lu W, Zhang GD, Zhang R et al (2010) Tumor site-specific silencing of NF-kappa b p65 by targeted hollow gold nanosphere-mediated photothermal transfection. *Cancer Res* 70:3177–3188
153. You J, Shao RP, Wei X, Gupta S, Li C (2010) Near-infrared light triggers release of paclitaxel from biodegradable microspheres: photothermal effect and enhanced antitumor activity. *Small* 6:1022–1031
154. You J, Zhang GD, Li C (2010) Exceptionally high payload of doxorubicin in hollow gold nanospheres for near-infrared light-triggered drug release. *ACS Nano* 4:1033–1041
155. You J, Zhang R, Xiong CY et al (2012) Effective photothermal chemotherapy using doxorubicin-loaded gold nanospheres that target Ephb4 receptors in tumors. *Cancer Res* 72:4777–4786
156. You J, Zhang R, Zhang GD et al (2012) Photothermal-chemotherapy with doxorubicin-loaded hollow gold nanospheres: a platform for near-infrared light-triggered drug release. *J Control Release* 158:319–328

157. Melancon MP, Elliott AM, Shetty A, Huang Q, Stafford RJ, Li C (2011) Near-infrared light modulated photothermal effect increases vascular perfusion and enhances polymeric drug delivery. *J Control Release* 156:265–272
158. Sun YG, Mayers BT, Xia YN (2002) Template-engaged replacement reaction: a one-step approach to the large-scale synthesis of metal nanostructures with hollow interiors. *Nano Lett* 2:481–485
159. Chen JY, Yang MX, Zhang QA et al (2010) Gold nanocages: a novel class of multifunctional nanomaterials for theranostic applications. *Adv Funct Mater* 20:3684–3694
160. Chen JY, Wang DL, Xi JF et al (2007) Immuno gold nanocages with tailored optical properties for targeted photothermal destruction of cancer cells. *Nano Lett* 7:1318–1322
161. Au L, Zheng DS, Zhou F, Li ZY, Li XD, Xia YN (2008) A quantitative study on the photothermal effect of immuno gold nanocages targeted to breast cancer cells. *ACS Nano* 2:1645–1652
162. Chen JY, Glaus C, Laforest R et al (2010) Gold nanocages as photothermal transducers for cancer treatment. *Small* 6:811–817
163. Yavuz MS, Cheng YY, Chen JY et al (2009) Gold nanocages covered by smart polymers for controlled release with near-infrared light. *Nat Mater* 8:935–939
164. Moon GD, Choi SW, Cai X et al (2011) A new theranostic system based on gold nanocages and phase-change materials with unique features for photoacoustic imaging and controlled release. *J Am Chem Soc* 133:4762–4765
165. Shi P, Qu KG, Wang JS, Li M, Ren JS, Qu XG (2012) Ph-responsive nir enhanced drug release from gold nanocages possesses high potency against cancer cells. *Chem Commun* 48:7640–7642
166. Yuan H, Fales AM, Vo-Dinh T (2012) Tat peptide-functionalized gold nanostars: enhanced intracellular delivery and efficient nir photothermal therapy using ultralow irradiance. *J Am Chem Soc* 134:11358–11361
167. Yuan HK, Khoury CG, Wilson CM, Grant GA, Bennett AJ, Vo-Dinh T (2012) *In vivo* particle tracking and photothermal ablation using plasmon-resonant gold nanostars. *Nanomedicine Nanotechnol* 8:1355–1363
168. Wang SJ, Huang P, Nie LM et al (2013) Single continuous wave laser induced photodynamic/plasmonic photothermal therapy using photosensitizer-functionalized gold nanostars. *Adv Mater* 25:3055–3061
169. Lapotko DO (2006) Laser-induced bubbles in living cells. *Lasers Surg Med* 38:240–248
170. Wagner DS, Delk NA, Lukianova-Hleb EY, Hafner JH, Farach-Carson MC, Lapotko DO (2010) The *in vivo* performance of plasmonic nanobubbles as cell theranostic agents in zebrafish hosting prostate cancer xenografts. *Biomaterials* 31:7567–7574
171. Lukianova-Hleb EY, Lapotko DO (2014) Nano-theranostics with plasmonic nanobubbles. *IEEE J Sel Top Quantum* 20:163–174
172. Lukianova-Hleb EY, Oginsky AO, Samaniego AP et al (2011) Tunable plasmonic nanoprobe for theranostics of prostate cancer. *Theranostics* 1:3–17
173. Lukianova-Hleb EY, Ren XY, Zasadzinski JA, Wu XW, Lapotko DO (2012) Plasmonic nanobubbles enhance efficacy and selectivity of chemotherapy against drug-resistant cancer cells. *Adv Mater* 24:3831–3837
174. Lukianova-Hleb EY, Samaniego AP, Wen JG, Metelitsa LS, Chang CC, Lapotko DO (2011) Selective gene transfection of individual cells *in vitro* with plasmonic nanobubbles. *J Control Release* 152:286–293
175. Hu J, Zhu XL, Li H et al (2014) Theranostic au cubic nano-aggregates as potential photoacoustic contrast and photothermal therapeutic agents. *Theranostics* 4:534–545
176. Ma LL, Feldman MD, Tam JM et al (2009) Small multifunctional nanoclusters (nanoroses) for targeted cellular imaging and therapy. *ACS Nano* 3:2686–2696
177. Kim D, Park S, Lee JH, Jeong YY, Jon S (2007) Antibiofouling polymer-coated gold nanoparticles as a contrast agent for *in vivo* X-ray computed tomography imaging. *J Am Chem Soc* 129:7661–7665

178. Kim D, Jeong YY, Jon S (2010) A drug-loaded aptamer-gold nanoparticle bioconjugate for combined ct imaging and therapy of prostate cancer. *ACS Nano* 4:3689–3696
179. Zhou HS, Honma I, Komiyama H, Haus JW (1994) Controlled synthesis and quantum-size effect in gold-coated nanoparticles. *Phys Rev B* 50:12052–12056
180. Averitt RD, Sarkar D, Halas NJ (1997) Plasmon resonance shifts of au-coated au₂s nanoshells: insight into multicomponent nanoparticle growth. *Phys Rev Lett* 78:4217–4220
181. Decuzzi P, Lee S, Bhushan B, Ferrari M (2005) A theoretical model for the margination of particles within blood vessels. *Ann Biomed Eng* 33:179–190
182. Chithrani BD, Ghazani AA, Chan WCW (2006) Determining the size and shape dependence of gold nanoparticle uptake into mammalian cells. *Nano Lett* 6:662–668
183. Day ES, Bickford LR, Slater JH, Riggall NS, Drezek RA, West JL (2010) Antibody-conjugated gold-gold sulfide nanoparticles as multifunctional agents for imaging and therapy of breast cancer. *Int J Nanomedicine* 5:445–454
184. Gobin AM, Watkins EM, Quevedo E, Colvin VL, West JL (2010) Near-infrared-resonant gold/gold sulfide nanoparticles as a photothermal cancer therapeutic agent. *Small* 6:745–752
185. Gao L, Liu R, Gao FP, Wang YL, Jiang XL, Gao XY (2014) Plasmon-mediated generation of reactive oxygen species from near-infrared light excited gold nanocages for photodynamic therapy *in vitro*. *ACS Nano* 8:7260–7271
186. Yy L, Wen T, Zhao RF et al (2014) Localized electric field of plasmonic nanoplatform enhanced photodynamic tumor therapy. *ACS Nano* 8:11529–11542
187. Trachootham D, Alexandre J, Huang P (2009) Targeting cancer cells by ros-mediated mechanisms: a radical therapeutic approach? *Nat Rev Drug Discov* 8:579–591
188. Xu YY, Wang J, Li XF et al (2014) Selective inhibition of breast cancer stem cells by gold nanorods mediated plasmonic hyperthermia. *Biomaterials* 35:4667–4677
189. Zhou T, Yu M, Zhang B et al (2014) Inhibition of cancer cell migration by gold nanorods: molecular mechanisms and implications for cancer therapy. *Adv Funct Mater* 24:6922–6932
190. Weintraub K (2013) Biomedicine: the new gold standard. *Nature* 495:S14–S16
191. Huschka R, Zuloaga J, Knight MW, Brown LV, Nordlander P, Halas NJ (2011) Light-induced release of DNA from gold nanoparticles: nanoshells and nanorods. *J Am Chem Soc* 133:12247–12255
192. Xiao ZY, Ji CW, Shi JJ et al (2012) DNA self-assembly of targeted near-infrared-responsive gold nanoparticles for cancer thermo-chemotherapy. *Angew Chem Int Ed* 51:11853–11857
193. Khlebtsov N, Dykman L (2011) Biodistribution and toxicity of engineered gold nanoparticles: a review of *in vitro* and *in vivo* studies. *Chem Soc Rev* 40:1647–1671
194. Zhang JJ, Nie X, Ji YL et al (2013) Quantitative biokinetics and systemic translocation of various gold nanostructures are highly dependent on their size and shape. *J Nanosci Nanotechnol* 13:1–15
195. Wang LM, Li YF, Zhou LJ et al (2010) Characterization of gold nanorods *in vivo* by integrated analytical techniques: their uptake, retention, and chemical forms. *Anal Bioanal Chem* 396:1105–1114
196. Wang J, Xie YD, Wang LM et al (2015) *In vivo* pharmacokinetic features and biodistribution of star and rod shaped gold nanoparticles by multispectral optoacoustic tomography. *RSC Adv* 5:7529–7538
197. Zhang LM, Wang LM, Hu YL et al (2013) Selective metabolic effects of gold nanorods on normal and cancer cells and their application in anticancer drug screening. *Biomaterials* 34:7117–7126

Chapter 2

Gold Nanostructures for Cancer Imaging and Therapy

Yongping Gao and Yongsheng Li

Abstract Gold nanostructures can manipulate light at the nanoscale based on the optical phenomenon widely known as localized surface plasmon resonance (LSPR). Upon light excitation, specific gold nanostructures are supposed to preferentially absorb or scatter light in the near-infrared (NIR) region, which enable them applicable as imaging and therapeutic agents. Furthermore, facile surface functionalization via Au-S bonding makes gold nanostructures as universal substrates to attach functional molecules, drug cargo, and targeting ligands. Together with their easy synthesis and non-toxicity, gold nanostructures have emerged as a greatly promising platform in cancer diagnostics and treatment. This chapter summarizes the progress made in cancer imaging and therapy with gold nanostructures (1) as therapeutic components for photothermal therapy, photodynamic therapy, chemotherapy, and their combination; (2) as probes for various imaging techniques including dark-field, optical coherence tomography, two-photon luminescence, photoacoustic imaging, computed tomography, and surface-enhanced Raman scattering based imaging; and (3) as a theranostic platform for imaging-guided therapy.

Keywords Gold nanostructures • Nanoshell • Nanorod • Nanocage • Photothermal therapy • Contrast agents • Imaging-guided therapy

2.1 Introduction

Gold nanostructures have emerged as a promising new platform in biomedical diagnostics and targeted therapeutics due to their unprecedented capability to manipulate light at the nanoscale and to integrate into biological systems [1, 2]. Most of these applications based on gold nanostructures come from an optical phenomenon known as localized surface plasmon resonance (LSPR), which is determined and highly tunable by the size and shape of the nanoparticle [3]. It can be tuned to

Y. Gao • Y. Li (✉)
East China University of Science and Technology,
130 Meilong Road, Shanghai 200237, China
e-mail: ysli@ecust.edu.cn

preferentially absorb or scatter light at specific wavelengths in the visible and near-infrared (NIR) regions of the spectrum. In the NIR “tissue window,” light penetration into tissue is optimal. Compared with conventional chemotherapy drugs or small-molecule imaging agents, gold nanostructures offer several advantages for biomedical applications, including high biocompatibility and noncytotoxicity [4], passive accumulation at tumor sites due to the enhanced permeability and retention (EPR) effect [5], and ease of bioconjugation via Au-S bonding to provide increased stability and active tumor targeting [6, 7].

Following excitation of LSPR by NIR laser, gold nanostructures tuned to absorb NIR irradiation are particularly useful as mediators for photothermal cancer therapy [8], to enhance contrasting effects in photoacoustic tomography [9] or to trigger thermosensitive release in drug-delivery systems [10–13]. Furthermore, the NIR light scattering of gold nanostructures has been applied for biomedical imaging such as dark-field microscopy and optical coherence tomography [14]. Other imaging modalities have also been integrated into gold nanostructures for imaging-guided therapy [15]. Over the past two decades, the pace of research in this field has advanced significantly and rapidly. It has been the present authors’ best attempt to follow new developments in the field, but, given the pace of progress, this chapter will be partially outdated by the time it hits the press. This chapter is designed for researchers already in the field to use it as a quick reference or “early-stage” researchers to gain a broader understanding of this field. The first section of this chapter will highlight the unique optical and material properties of gold nanostructures. Then, it will focus on the photothermal therapy based on various types of gold nanostructures. Also, the combination with other therapeutic approaches such as chemotherapy will be discussed. In the third section, gold nanostructures for diagnostics will be comprehensively described. Finally, gold nanostructures developed for imaging-guided therapy of cancer will be discussed.

2.2 Plasmonic Properties and Surface Functionalization of Gold Nanostructures

2.2.1 Radiative Properties

When light interacts with gold nanostructures, conduction electrons can be driven by the incident electric field in collective oscillations known as localized surface plasmon resonance (LSPR) [16]. Figure 2.1 illustrates this phenomenon for a gold nanosphere – the simplest type of LSPR (dipolar LSPR). This gives rise to a drastic alteration of electromagnetic fields on the gold surface with local field intensities which can be orders of magnitude greater than those of the incident field. The enhanced electromagnetic fields affect both radiative and nonradiative properties of gold nanostructures, resulting in absorption and light scattering following light incidence (Fig. 2.2). By adjusting the size and shape of gold nanostructures, the relative absorption and scattering behaviors can be controlled [3]. Small nanoparticles

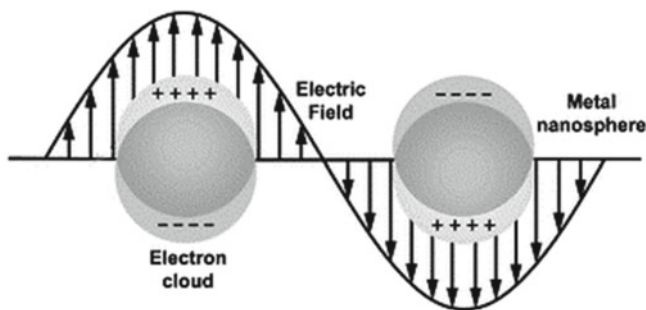
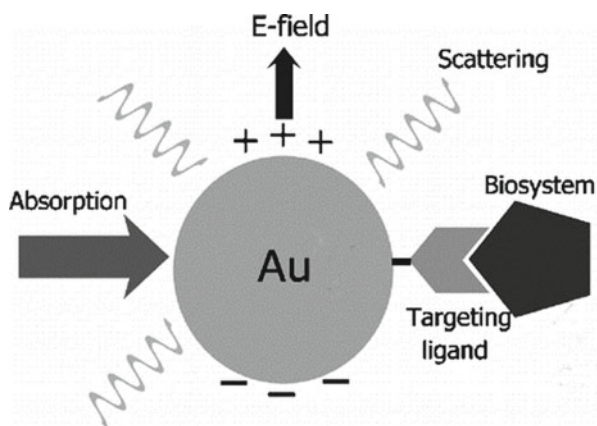


Fig. 2.1 Schematic illustration of LSPR of an individual gold nanosphere showing the collective oscillation of delocalized electrons in response to an external electric field

Fig. 2.2 Optical processes (radiative or nonradiative) resulting from the interaction of light with a gold nanoparticle



predominantly absorb light, while larger nanoparticles are largely scattering incident light. But for gold nanostructures with complex geometry, e.g., nanorods and nanostars, the absorption and scattering properties are dependent on their unique geometry greatly and their size on a small way [17]. Highly scattering gold nanostructures are particularly utilized as contrast agents for dark-field imaging [18, 19] and for computed tomographic (CT) imaging [20]. Moreover, the greatly intensified local field of gold nanostructures enhances the Raman signal of molecules in the vicinity of gold surface, enabling surface-enhanced Raman scattering (SERS)-based imaging [21].

Besides, by engineering the size, shape, and morphology of the nanostructure and the interparticle distance and dielectric environment, their LSPRs can be tuned from visible to the NIR region (700–1,400 nm) [22–24]. The NIR region is the so-called biological window defined as the spectral ranges where tissues become partially transparent due to the simultaneous reduction in both absorption and scattering [25, 26]. This is of particular interest for deep-tissue imaging and treatment.

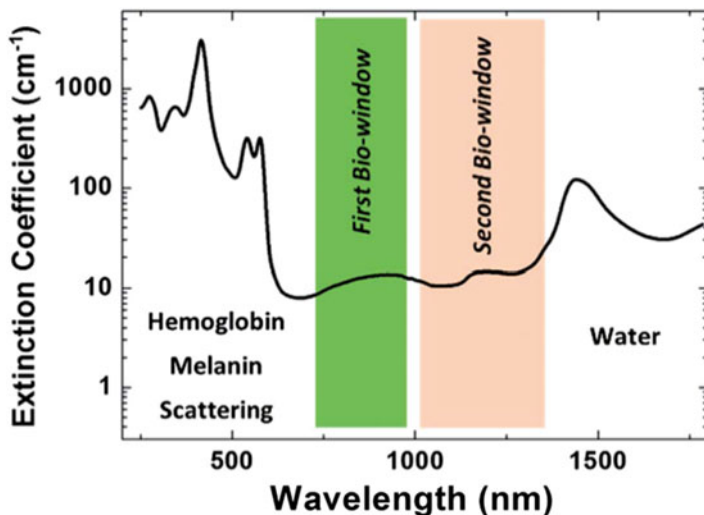


Fig. 2.3 Extinction coefficient of a representative tissue. The different effects leading to light attenuation (such as the presence of hemoglobin, water, and optical scattering) and the spectral extensions of the two biological windows are indicated (Reproduced from Ref. [17] by permission of The Royal Society of Chemistry)

Figure 2.3 shows the extinction spectrum of a typical human tissue [17]. The presence of several absorption bands is used to define two main biological windows. The first biological window extends from 700 to 980 nm, which was firstly proposed in 2001 [25] and has been extensively applied since then. In this spectral region, light absorption strongly vanishes but residual scattering still exists. The second biological window ranges from 1,000 to 1,400 nm, where optical absorption does not vanish completely; on the other hand, optical scattering is minimized. A range of gold nanostructures with variable shapes and sizes are shown in Fig. 2.4, and their tunable optical resonances are shown in Fig. 2.5. Since size-dependent LSPR tunability of gold nanospheres is quite limited (only in the visible region), the effective ways to achieve NIR plasmon resonance is usually by using nanoshells and anisotropic nanostructures. As seen from Fig. 2.5a, the plasmon peak shifts to the NIR region as branch aspect ratio of gold nanostars increases [27]. The long-axis LSPR peak redshifts from the visible to the NIR as the nanorod aspect ratio increases (Fig. 2.5b) [28]. Au nanocages (Fig. 2.5c) and nanoshells (Fig. 2.5d) show similar visible-NIR tunability of LSPR by facile control of the wall thickness and void size [29] and of the shell thickness (or thickness-to-core radius ratio) of the nanoshell [30], respectively.

Additionally, interparticle plasmonic coupling occurs when nanoparticles are brought in close proximity to one another as dimers, trimmers, and other higher-order clusters, leading to redshifts in LSPR and enhanced local electric field.

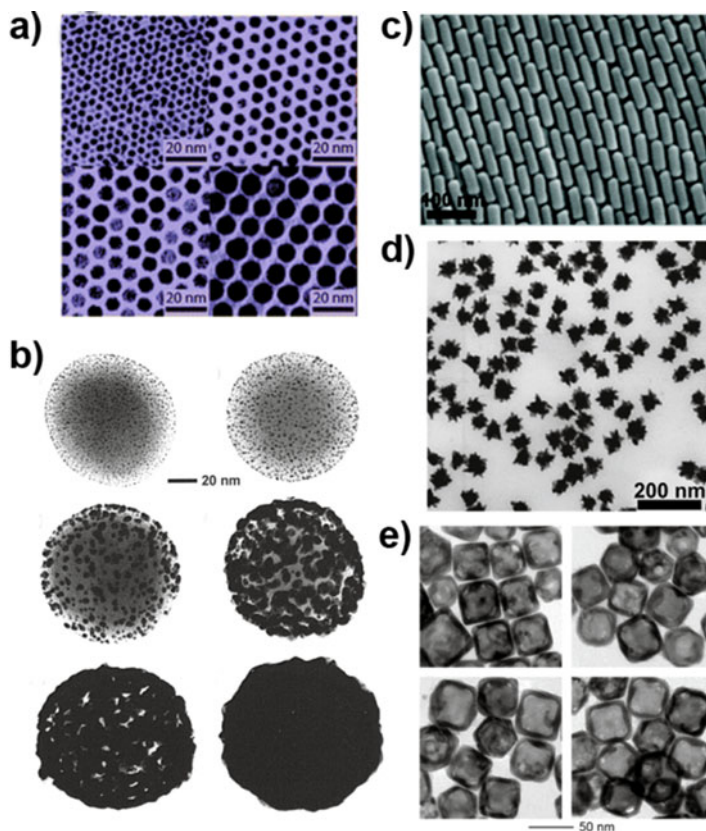


Fig. 2.4 TEM and SEM micrographs of gold nanostructures with various shapes and sizes: (a) nanospheres, (b) nanoshells, (c) nanorods, (d) nanostars, and (e) nanocages ((a) Reprinted with the permission from Ref. [31]. Copyright 2003 American Chemical Society. (b) Reprinted from Ref. [30], Copyright 1998, with permission from Elsevier. (c) Reprinted with the permission from Ref. [32]. Copyright 2012 American Chemical Society. (d) Reproduced from Ref. [33] by permission of IOP Publishing. (e) Reprinted with the permission from Ref. [34]. Copyright 2007 American Chemical Society)

Generally, the coupling does not occur until the interparticle separation is less than 2.5 times the particle diameter [35]. El-Sayed et al. proposed a universal relationship between the exponential decay of the spectral shift with respect to the interparticle separation [36]. Formation of gold nanostructure assemblies is not only distinguishable by clear redshift in the plasmon resonance but also by a dramatic change in solution color. These spectral and colorimetric changes have been harnessed in LSPR sensing of DNA, proteins, and biomolecules [37–40]. On the other hand, the significantly intensified local electric fields, also known as “hot spots” within the junctions of closely clusters, give rise to substantial enhancement in SERS enabling the detection of cancer cells [41–43].

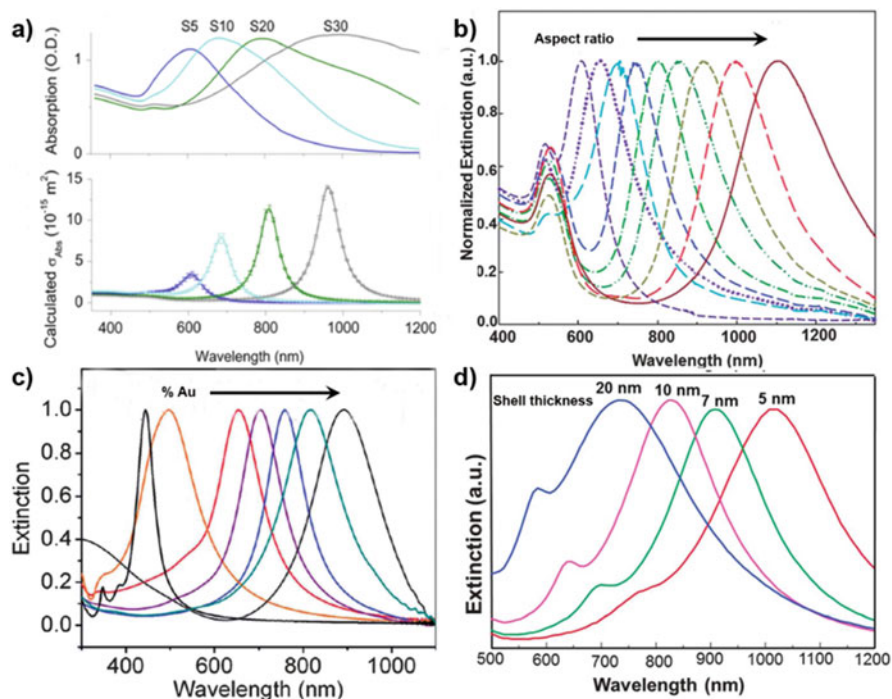


Fig. 2.5 Tunability of plasmon resonances achieved by varying the geometry of (a) nanostars, (b) nanorods, (c) nanocages, and (d) nanoshells [30] ((a) Reproduced from Ref. [27] by permission of IOP Publishing. (b) Reproduced from Ref. [28] by permission of IOP Publishing. (c) Reprinted by permission from Macmillan Publishers Ltd: Ref. [29], copyright 2007. (d) Reprinted from Ref. [30], Copyright 1998, with permission from Elsevier

2.2.2 Nonradiative Photothermal Effects

In addition to radiative decay, plasmons also relax nonradiatively through electron-electron collision or electron-lattice which generates light absorption by the nanoparticle [44]. Light to heat conversion has been extensively employed for photothermal therapy [45–48] and photothermal drug release in cancer cells [13, 49–52], as well as for two-photon luminescence imaging [27, 53]. The underlying mechanism of photothermal process has been extensively studied with ultrafast laser spectroscopy [22, 54]. Figure 2.6 illustrates the photothermal characteristics of gold nanostructures [15]. Upon excitation with the resonant photons, the photoexcitation of the electron gas results in rapid nonequilibrium heating. The initial electronic excitation is followed by relaxation at subpicosecond timescale (~ 30 ps) by means of electron-electron scattering which results in the surface temperature increase of the metal [55, 56], leading to the ablation of the nanoparticle, desorption of surface capping, or melting and reshaping. Then, cooling to equilibrium by energy exchange happens between the electrons and the lattice phonons. At slower

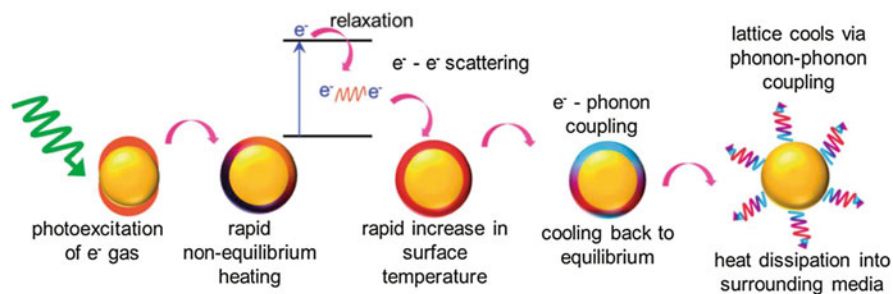


Fig. 2.6 Schematic illustration describing the principle of incident light to heat conversion by gold nanostructures (Reproduced from Ref. [15] by permission of The Royal Society of Chemistry)

rates, the lattice cools via phonon-phonon process (~ 100 ps) leading to heating of the local environment (surrounding medium). Thus, when gold nanostructures after incubation with cancer cells are illuminated, a large temperature difference between the hot nanoparticle surface and the much cooler surrounding biological medium occurs, resulting in an abrupt local temperature increment and the corresponding cell death.

The nonradiative properties of gold nanostructures also manifest themselves in the form of two-photon photoluminescence (TPL) of gold. An electron in the sp -conduction band is excited by the first photon from below the Fermi energy to above it via an intraband transition. This gives rise to a charge-separated state within the conduction band. An electronic transition from the d -band to sp -band occurs with a second-photon excitation, generating an electron-hole pair followed by recombination of separated charges resulting in TPL emission [57]. TPL based on variable gold nanostructures has been considerably investigated and applied for cancer imaging [58–62].

2.2.3 Surface Functionalization

The surface chemistry of gold is closely related to a number of critical attributes that make gold nanostructures a promising platform for biomedical applications. The nonreactive and relatively bio-inert nature of gold makes this metal a good candidate for both *in vitro* and *in vivo* applications. The low cytotoxicity of gold nanostructures, along with favorable clinical biocompatibility, has been demonstrated in a number of studies [63, 64]. Nevertheless, the synthetic reagent CTAB, for example, which is so crucial in a number of preparations of gold nanorods and other shapes, is highly toxic to cells at micromolar concentrations on its own [7]. The binding of toxic CTAB to a nanoparticle surface makes it far less bioavailable than it would be if it were free in solution. Thus, chemical tuning of the nanoparticle surface is still necessary to impart biological compatibility and specificity to gold nanoparticles.

Functional binding onto the surface of gold nanostructures for biomedical applications follows largely on work of self-assembled monolayers (SAMs), where molecules generate highly ordered monolayers once they adsorb onto a gold surface [65]. A rich variety of functional molecular linkers are currently employed in the conjugation of gold nanoparticles, and the anchoring groups utilized for attachment of these molecules to the gold surface generally include thiolate [66–68], dithiolate [69], dithiocarbamate [70], amine [71], carboxylate [71], selenide [72], isothiocyanate [68, 71], or phosphine [67, 73] moieties. Among these groups, thiolate and dithiolate are most well known for forming strong, stable gold-thiolate bonds (Au-S, ~50 kcal/mol) to molecules with thiol (-SH) or disulfide groups (S-S) [65]. By carefully choosing the functional groups at the distal end of the molecule, it is possible to design and generate a well-defined interface for better stability and interaction with cells and biomolecules in specific ways (Fig. 2.7). Apart from that, gold nanostructures can also adsorb biological molecules in a nonspecific manner. A variety of proteins will adsorb to a non-protected gold surface when it is transferred into a biological medium. The adsorbed proteins can affect the surface properties of gold nanostructures and thus their cellular uptake [7].

Thiolated poly(ethylene glycol), PEG-SH, is by far the most commonly employed surface ligand for gold nanostructures. It is a biocompatible polymer that helps prevent particle aggregation, nonspecific protein adsorption, and the uptake of circulating gold nanoparticles by the reticuloendothelial system (RES), allowing for longer circulation of gold nanoparticles in the bloodstream and consequently their greater accumulation in tumors through the enhanced permeability and retention (EPR) effect [74]. When the surface ligands for nanoparticle synthesis bind less strongly than gold thiolate interactions, their replacement with a thiol-terminated PEG is relatively straightforward [75].

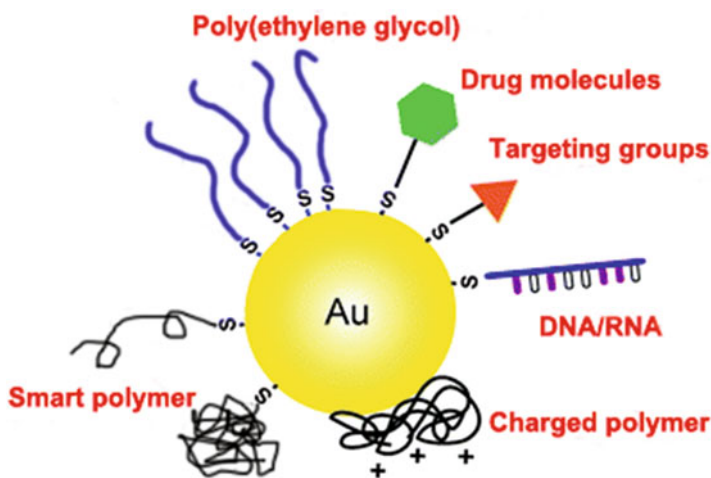


Fig. 2.7 Gold nanostructures can be conjugated with a wide variety of functional moieties

Gold nanostructures can be endowed with active targeting capabilities via careful surface modification. If nanoparticles are conjugated with a complimentary moiety (e.g., antibodies, peptides, and folate, among others), they will bind to cancer cells as they circulate, increasing their concentration in the desired region. Furthermore, the binding of the targeting moiety can either occur directly to the surface of the nanoparticle or to the terminal end of an attached PEG chain with an appropriate tail group [74, 75].

It is also possible to attach a number of other functional groups to the surface of gold nanostructures through thiolate binding, as shown in Fig. 2.7. For example, by adsorbing specific polymers to the surface, the charge of gold nanoparticle is supposed to be controlled, which is important as surface charges have a significant effect on both the cellular uptake and biodistribution of nanoparticles [76–78]. Inorganic complexes such as cisplatin or its prodrug forms can be bound to gold nanoparticle by way of appropriate ligands, which facilitate intracellular transport and subsequent activation of prodrug [79]. It is also simple to use the thiol group to attach for sensing applications, smart polymers for stealth delivery, as well as a wide variety of other types of molecules [13, 51, 71, 80–82].

Besides, gold nanoparticles could be fully encapsulated by silica (glass) shells by vitreophobic surface conjugation and facile silane chemistry [83–85]. This is of particular interest for use with gold nanorods, where CTAB molecules binding on the surface could be completely removed or displaced. Furthermore, Raman reporter molecules could be entrapped onto gold nanostructures followed by silica encapsulation, forming SERS probes with great potential in SERS detection [86].

2.3 Gold Nanostructures for Photothermal Therapy

Thermal treatments are based on driving a part of the body above its normal temperature for a defined period of time. Temperature plays an extremely important role in the dynamics and viability of biological system ranging from the simplest (cells) to the most sophisticated ones (tissues and organisms) [87]. In the case of human, any temperature increment above the normal body temperature (*circa* 37 °C) is usually regarded as a negative sign as it could indicate the presence of disease (fever) and even irreversible damage and fatal organ failure [88]. Nevertheless, controlled temperature increments could have positive effects in patients with an ongoing disease, such as cancer. In the last few years, great efforts have been put into the development of novel techniques for controlled and localized heating, along with understanding of the mechanisms on the basis of temperature-induced cell killing and modification [89, 90]. It is believed that the temperature-induced changes caused at the cellular level are unequivocally determined by the intensity and duration of the increment [91]. Depending on the magnitude of the induced temperature increment, thermal treatments and related effects on tumors would be classified into several periods, as depicted in Fig. 2.8 [92]. By increasing the tumor temperature above 48 °C during a period of time (a few minutes), irreversible injury treatments

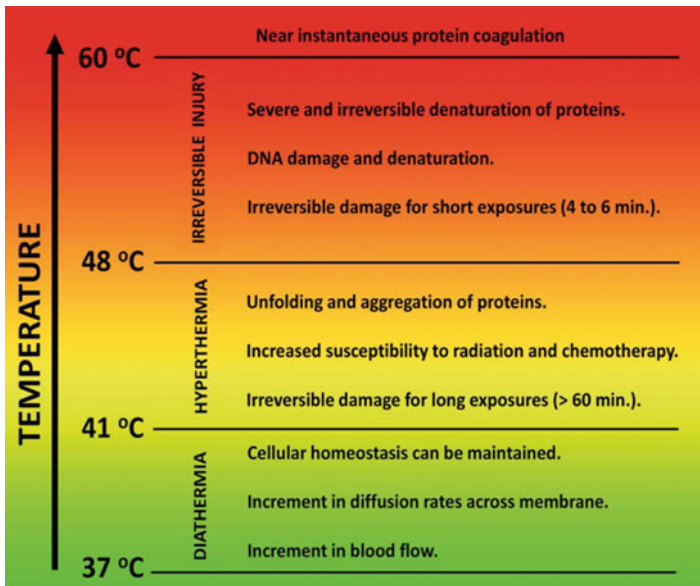


Fig. 2.8 Schematic diagram of the variety of effects caused by the different thermal treatment as classified by the corresponding operating temperature (Reproduced from Ref. [17] by permission of The Royal Society of Chemistry)

would occur. In this case, a drastic activation of cell death is achieved as a consequence of coagulative necrosis processes. As it is increased above 60 °C, an almost instantaneous and irreversible protein denaturation will be caused. These treatments are considered highly efficient but lack selectivity accompanied by relevant collateral damage to adjacent tissue. Within 41–48 °C temperature, tumor would experience hyperthermia treatments. Several processes of relevance at the cellular level are supposed to be simultaneously activated, including protein denaturation, transient thermo-tolerance, and cell inactivation. Temperature up to 41 °C does not induce relevant modifications at the cellular level, which is mainly applied in physiotherapy favoring muscle relaxation and pain relief.

Recently, the development of nanoparticles capable of efficient heat generation with laser irradiation has attracted much attention [93]. In particular, gold nanostructures with plasmonic properties tailored into NIR region have shown great promise for cancer photothermal therapy through nonradiative photothermal effect, demonstrating the ability to destroy cancerous lesion *in vivo* [94]. A diverse range of gold nanoparticles have been explored for use in photothermal therapy [95, 96]. Key features to consider when selecting a nanostructure for photothermal therapy are the plasmon resonance wavelength, the absorption cross section, and the size of the nanoparticle. In this section, the development of gold nanostructures including nanoshells, nanorods, nanocages, and other anisotropic gold nanoparticles for photothermal therapy will be discussed. Besides, as single photothermal therapy is not as effective as we expected, for example, caused by thermo-tolerance of cancer

cells [97], the combination of photothermal therapy with other therapeutic strategies, mainly photodynamic therapy and chemotherapy, has received tremendous interest in recent years [98–102], which will be covered in the second section.

2.3.1 Gold Nanoshells

Gold nanoshells are usually core/shell nanoparticles comprising a dielectric silica core surrounding by a gold shell and can be easily synthesized through the seed-mediated growth process [30, 103, 104]. As their LSPR can be easily tuned to NIR region by simply modifying the core-to-shell ratio, gold nanoshells were the first sample used to demonstrate photothermal cancer therapy, and now the transition of this approach to clinical trials is currently underway [105]. In 2003, Hirsch et al. [45] studied the temperature distribution in tumors during thermal therapy and highlighted the merits of injecting nanoshells directly into the tumor interstitium rather than administering them intravenously. The mean change in temperature for the nanoshell group (37.4 ± 6.6 °C) was high enough to cause irreversible thermal damage, whereas the more modest temperature increase in the nanoshell-free control group (9.1 ± 4.7 °C) was insufficient to cause any permanent damage. Interestingly, the heating profile was approximately homogeneous, which indicated that the tumor volume contained a near-uniform distribution of nanoshells. The maximum high temperature was measured approximately 1 mm below the surface and not at the site of injection. In another study in 2004, O'Neal et al. [106] have successfully treated mice inoculated with tumors after injection with PEGylated nanoshell solution via tail vein. A complete resorption of tumors was observed within 10 days, and all mice were healthy and free of tumors at 90 days. By contrast, in the control groups, the tumors continue to grow after treatment, with a mean survival time of 10.1 days.

Except for silica, different materials have been used as cores of nanoshells. Liu and coworkers reported a new approach toward the design of nanoshells on carboxylated polystyrene [107]. The tumor volumes of the treatment group by the nanoshells injected intraperitoneally were significantly lower than those of the control groups, with an average inhibition rate over 55 %. Recently, lipid vesicles, mesoporous silica, and other functional nanoparticles have also been used as the template to prepare nanoshells as photothermal therapy agents [108–111]. Furthermore, because of the ease of surface functionalization, gold nanoshells are often conjugated with targeting ligands for targeted photothermal therapy [98]. In 2009, Li and coworkers investigated in vivo tumor targeting by PEGylated nanoshells conjugated with a melanocyte-stimulating hormone (MSH) analogue for selective photothermal ablation of melanoma tumors [112]. In the meantime, it is found that intravenous injection of RGD peptide-conjugated nanoshells could target glioma tumors for photothermal treatment which significantly prolonged the survival of tumor-bearing mice [113].

Gold nanoshells have a significantly larger photothermal transduction cross section, compared to gold nanorods on a per particle basis [114]. However, the lower

absorption efficiency of gold nanoshells, usually below 60 % (much lower than that of gold nanorods, above 90 %) [114, 115], greatly limits their applications in photo-thermal therapies. By encapsulating gold cores into gold nanoshells, a gold-silica-gold multilayered nanoshell structure, known as a simple “nanomatryoshka” [24], has been created to provide a higher plasmonic tunability. Theoretically, the relative absorption and scattering efficiencies can be tuned in a wider range by controlling the geometry [116]. In a recent work, Halas and coworkers [117] calculated that the absorption efficiency for a nanomatryoshka with plasmon resonance at about 800 nm is 4.26, which corresponds to 77 % of the total extinction efficiency of 5.53 (Fig. 2.9). These nanomatryoshkas show a scattering efficiency of 1.26, 23 % of their extinction efficiency. For nanoshells exhibiting the similar plasmon resonance, the major contribution to the total extinction comes from a scattering efficiency of 7.25, which represents 85 % of the extinction efficiency, with a minor contribution from the absorption efficiency of 1.24, only 15 % of the total extinction efficiency.

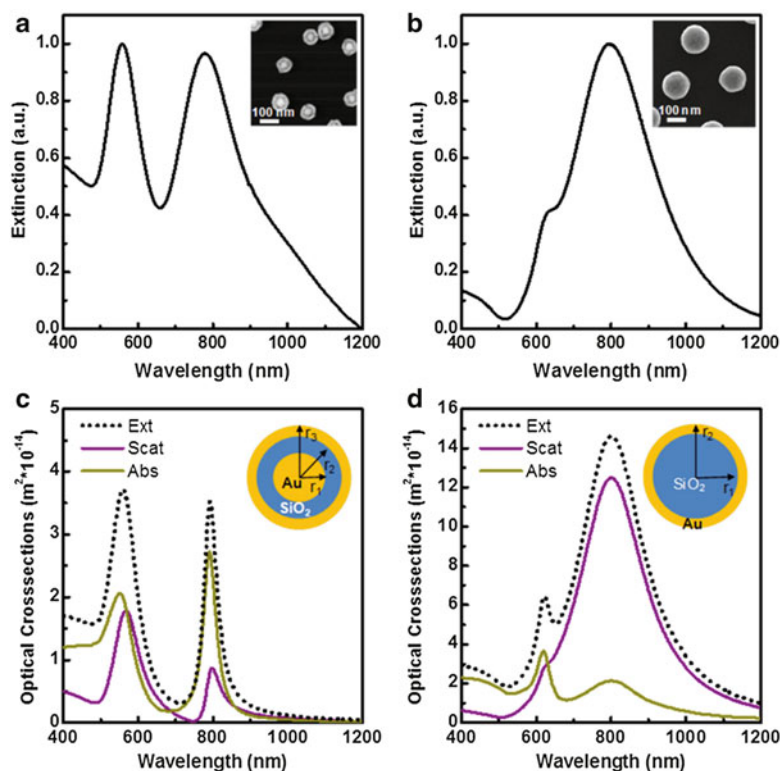


Fig. 2.9 Optical and structural properties of nanomatryoshka and nanoshells. Experimental ensemble extinction spectra of nanomatryoshkas (a) and nanoshells (b). Calculated extinction, scattering, and absorption cross-section spectra (Mie theory) of the $[r_1, r_2, r_3] = [21, 31, 44]$ nm nanomatryoshka (c) and the $[r_1, r_2] = [62, 76]$ nanoshell (d) (Reprinted with the permission from Ref. [117]. Copyright 2014 American Chemical Society)

The larger absorption efficiency and smaller scattering efficiency of nanomatryoshkas will result in higher photothermal transduction efficiency than that of the gold nanoshells. Furthermore, after an intravenous injection of Au nanomatryoshkas followed by a single NIR laser dose of 2 W/cm^2 for 5 min, 83 % of the TNBC tumor-bearing mice appeared healthy and tumor-free >60 days later, while only 33 % of mice treated with nanoshells survived the same period. The combination of smaller size and larger absorption cross section of Au nanomatryoshkas makes this nanoparticle more effective than gold nanoshells for photothermal cancer therapy. In another study, sub 100 nm gold nanomatryoshkas comprising concentric gold-silica-gold layers were demonstrated to accumulate into tumor with four- to fivefold the amount of gold nanoshells following equal dose of injected gold [118]. The survival time of mice-bearing large (>1,000 mm³) and highly aggressive triple-negative breast tumors is doubled for the nanomatryoshka treatment group under identical photothermal therapy conditions. Li and coworkers [119] have successfully developed a facile but controllable approach for the fabrication of the simple nanomatryoshka, in which organosilica layer was chosen as the dielectric spacer layer. Upon near-infrared (NIR) laser irradiation, nanomatryoshka performed much better than conventional gold nanoshells at the same extinction intensity and could kill cancer cells efficiently both in vitro and in vivo.

More excitingly, it is reported that gold nanoshells, as an effective class of photothermal agents, have entered clinic trials. Recently, Cancer Treatment Centers of America (CTCA) and Nanospectra Biosciences have carried out the first clinical trial for the treatment of primary and/or metastatic lung tumor by Aurolase therapy that uses Aurolase (Fig. 2.10) based on gold nanoshells invented by Halas's group at Rice University. The therapy begins with an intravenous deliver of Aurolase, and



Fig. 2.10 Individual auroshell particle (*left*) and IV bag of auroshell (*right*)

after 12–24 h, for the tumor accumulation, a NIR laser is used to illuminate and destroy tumors in the patient. It is known that this clinical trial is in phase II stage right now [120].

2.3.2 Gold Nanorods

Gold nanorods, which were developed during the same period as gold nanoshells, are generally smaller than nanoshells. They have been extensively explored in photothermal therapy due to their strong optical extinction in the visible and NIR region [121]. By simple manipulation of the aspect ratio of nanorods, the strong longitudinal plasmon resonance band of gold nanorods can be tuned into NIR region. Recent studies have investigated the photothermal heating efficiencies of NIR-absorbing gold nanostructures, and both theoretical and experimental results have shown that nanorods could offer a superior absorption cross section versus gold nanoshells when normalizing for particle size differences as well as heating per gram of gold that is at least six times faster than gold nanoshells [114, 122, 123].

There have been numerous examples of gold nanorods used for in vivo photothermal cancer therapy. Van Maltzahn et al. reported that PEG-coated gold nanorods could be used as an efficient photothermal nanoheater [123]. In their work, PEGylated nanorods exhibited a long blood half-life of ~17 h after intravenous injection into tumor-bearing mice and could accumulate in tumor at ~7 % ID/g at 72 h postinjection. It was found that the tumors of the treatment group were rapidly heated to over 70 °C by laser irradiation (810 nm, 2 W/cm², 5 min), whereas the control mice showed the maximum surface temperature at ~40 °C (Fig. 2.11). Thus, tumors on mice that received PEGylated nanorods through intravenous injection completely disappeared within 10 days after NIR laser irradiation, in marked contrast to the control groups with uninhibited tumor growth. Moreover, the survival time of mice of treatment groups was over 50 days as compared to ~33 days for control groups. Similar results of PEGylated gold nanorods for photothermal cancer treatment have also been reported by Dickerson et al. [124].

Similar to gold nanoshells, active tumor targeting with gold-nanorod bioconjugates for effective in vivo photothermal therapy has also been achieved by a number of groups. Choi et al. loaded gold nanorods into chitosan-conjugated pluronic-based nanocarriers that could selectively target the tumor [125]. The nanorods showed a rather high tumor uptake at over 20 % ID/g as compared with ~7 % ID/g for PEG modified nanorods. After intravenous injection and the followed NIR laser irradiation, tumor thermolysis was achieved, without showing any apparent damage to the surrounding healthy tissues (Fig. 2.11). In another work, Li et al. demonstrated tumor targeting and photothermal treatment using dendrimer-modified gold nanorods conjugated with arginine-glycine-aspartic acid (RGD) peptide [126]. The biodistribution study revealed the gradually increased tumor uptake of RGD

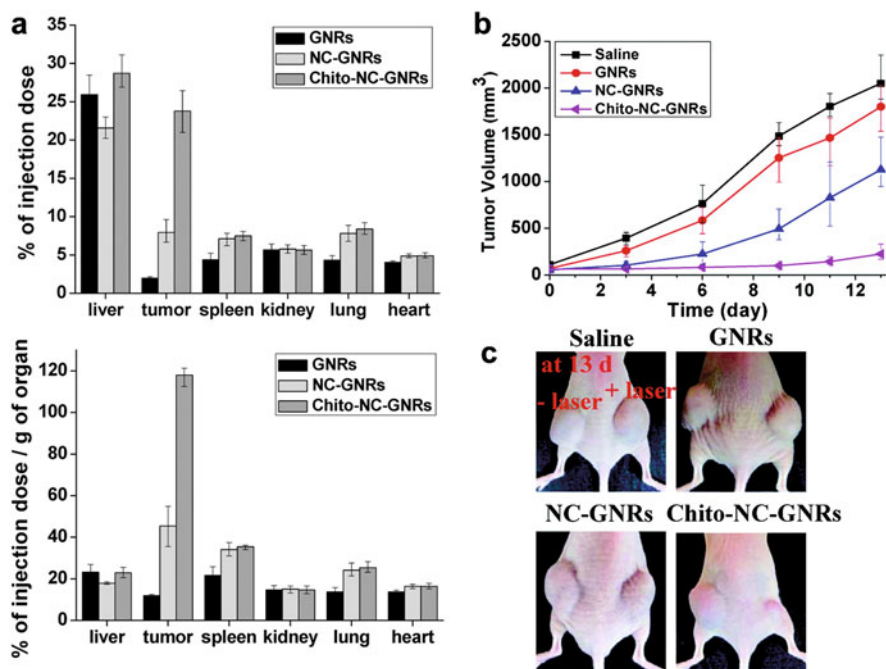


Fig. 2.11 (a) Biodistribution of GNRs or GNR-loaded nanocarriers in nude mice at 24 h after intravenous (tail vein) injection. (b) Changes in tumor volumes and (c) the tumor images after onetime NIR laser irradiation (808 nm, 4 W/cm²) for 4 min at 24 h after the i.v. injection of the nanomaterials (Reprinted with the permission from Ref. [125]. Copyright 2011 American Chemical Society)

nanorods over time, and disappearance of tumors was observed after the intravenous injection and NIR laser irradiation.

On the other hand, a major challenge to the use of gold nanorods for photothermal therapy is their susceptibility to reshaping into gold nanospheres under intense laser illumination, resulting in a loss of the longitudinal NIR resonance. Horiguchi et al. reported that CTAB could enhance heat isolation and cause the nanorods to reshape [127]. Photothermal reshaping also strongly depends on the surface conditions of the particle [128, 129, 130]. Chon et al. implemented a simple heat-diffusion model to estimate the heat relaxation time of gold nanorods encased in silica shells [129, 130]. They found that heat dissipation in the silica shell was much faster than the gold-nanorod-reshaping process, resulting in the shell inhibiting nanorod reshaping. Thus, silica coating could render gold-nanorod higher photothermal stability, as well as the biocompatibility resulting from the elimination of CTAB by the coating of silica layer. This is anticipated to have wide biomedical applications in cancer therapy [11, 131].

2.3.3 Gold Nanocages

Gold nanocages represent another novel class of nanostructures firstly developed by Xia and coworkers [132–134]. Gold nanocages are created by hollowing out the interior of a sacrificial template of silver nanocubes (as well as silver nanocrystals with other shapes). When silver nanocubes are titrated with a gold salt (typically HAuCl_4), a galvanic replacement reaction occurs, causing gold atoms to be deposited on the surface of the nanocube and silver atoms to be dissolved from a small pit in the surface. By increasing gold replacement, the LSPR peak position of gold nanocages is tunable through the visible and into the NIR region.

In 2007, Xia's group demonstrated the selective photothermal destruction of SK-BR-3 breast cancer cells *in vitro* with gold nanocages functionalized by the anti-HER-2 antibody [47]. After incubation with the immune nanocages, SK-BR-3 breast cells were irradiated with a femtosecond laser at various power densities for 5 min. A well-defined area of cellular death corresponding to the laser spot was observed. Later in 2010, they examined the efficacy of gold nanocages for photothermal cancer treatment in mice (Fig. 2.12) [135]. After intravenous injection of PEGylated gold nanocages for 3 days, the tumor on each mouse was irradiated with an 808 nm continuous-wave laser at a power density of 0.7 W/cm^2 for 10 min. It is measured that the temperature of the tumors containing nanocages was rapidly heated to over $55 \text{ }^\circ\text{C}$, leading to effective ablation of the tumors. In another study, they demonstrated that breast cancer stem cells (CSC) were targeted and eradicated through photothermal treatment with gold nanocages by functionalizing their surface with SV 119, a synthetic small molecule capable of binding to the sigma-2 receptor with high specificity [136].

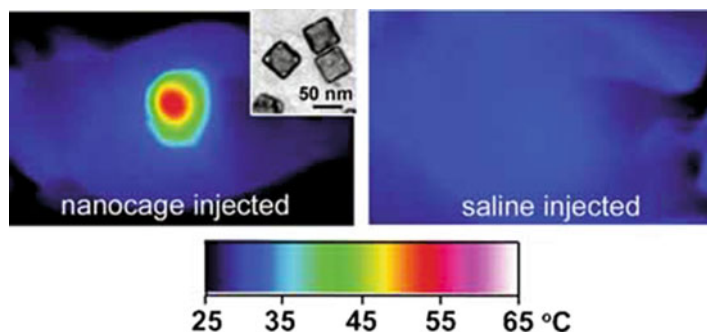


Fig. 2.12 IR thermal images of nanocage-injected (*left*) and saline-injected (*right*) tumor-bearing mice. The *inset* shows a TEM image of the as-made gold nanocages (Reproduced from Ref. [135] by permission of John Wiley & Sons Ltd)

2.3.4 Other Gold Nanostructures

Another type of gold nanostructures with NIR absorption for photothermal therapy is gold nanostars, which were spherical nanoparticles with multiple sharp edges and a high absorption-to-scattering ratio in the NIR region, favorable for photothermal heat generation [137, 138]. Lu et al. reported a multifunctional nanostars-based SERS assay for targeting sensing, photothermal treatment, and in situ monitoring of the photothermal response during the therapy process [138]. When nanostars were attached to cancerous cells, the localized heating that occurred during NIR irradiation was able to cause irreparable cellular damage. In another study, TAT-peptide functionalized nanostars were demonstrated to enter cells significantly more than bare or PEGylated gold nanostars [58]. After 4 h incubation of TAT-nanostars with BT549 breast cancer cells, efficient photothermal lysis was accomplished using 850 nm pulsed laser under 0.2 W/cm² irradiation, which was among the lowest power densities ever reported for pulsed lasers and below the maximal permissible exposure of skin. The photothermal ablation in vivo was further demonstrated using PEGylated gold nanostars [59]. On a mouse injected systemically with PEGylated nanostars for 2 days, extravasation of nanostars was observed, and localized photothermal ablation was demonstrated on a dorsal window chamber with 10 min of irradiation (785 nm, 1.1 W/cm²).

In addition, there are some other types of gold nanostructures with NIR absorption useful for photothermal therapy. Xia et al. synthesized gold hexapods and compared them with gold nanorods and nanocages [48]. They found that gold nanohexapods exhibited the highest cellular uptake and the lowest cytotoxicity in vitro for both the as-prepared and PEGylated samples. The PEGylated nanohexapods also showed significant blood circulation and tumor accumulation after intravenous injection. More importantly, the nanohexapods could significantly decrease the tumor metabolic activity following photothermal treatment after systemic administration. Another nanostructure, gold/gold sulfide NIR-absorbing nanoparticles (35–55 nm), was exploited to provide higher absorption (98 % absorption and 2 % scattering) as well as potentially better tumor penetration [139]. The ability to ablate tumor cells in vitro and efficacy for photothermal cancer therapy is demonstrated, and an in vivo model shows enhanced circulation and biodistribution and significantly increased long-term, tumor-free survival after photothermal treatment.

Though intensive effort has focused on shifting the absorbance of nanoparticles to the first biological window (650–900 nm) region for photoinduced therapy, gold nanostructures with plasmon absorption in the second biological window are also of great interest. Pelaz et al. described a novel and straightforward wet-chemical synthetic route to produce biocompatible single-crystalline gold nanoprisms [140], which could effectively ablate Vero cells after 2 min of 1,064 nm NIR illumination at 30 W/cm², which however was a rather high power density. Recently, Min-Fong Tsai et al. reported that a Au nanorod can be designed with a rod-in-shell (rattle-like) structure (Fig. 2.13a) smaller than 100 nm that is tailored to be responsive to

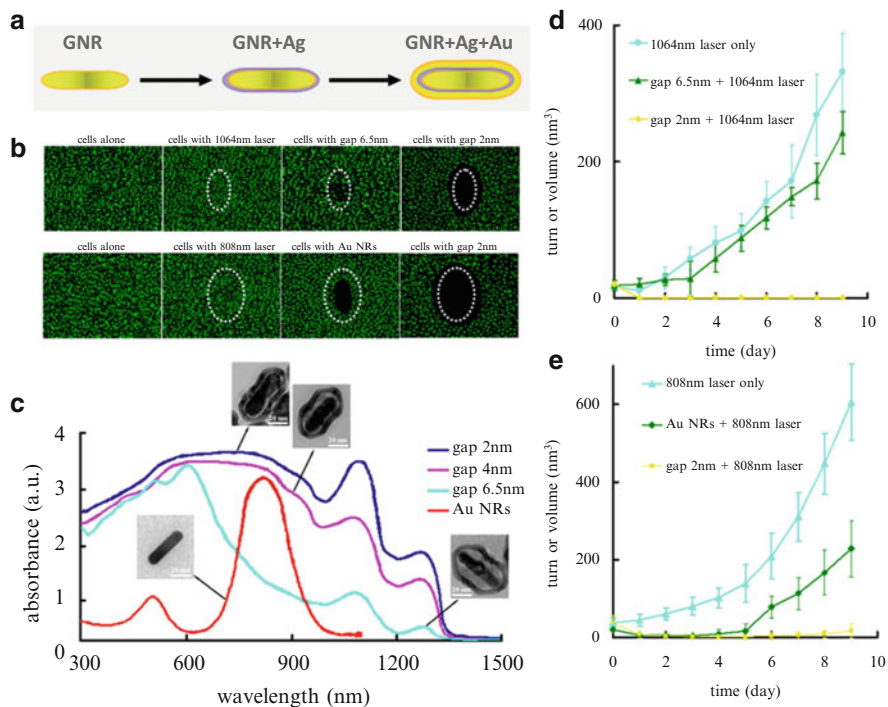


Fig. 2.13 (a) A schematic representation of the approach for the development of the rod-in-shell structure. (b) LLC/LL2 lung cancer cells treated with gap 6.5 nm and gap 2 nm rod in shells were irradiated using a 1,064 nm laser at 3 W/cm^2 for 5 min of exposure (*top*), and LLC/LL2 lung cancer cells treated with Au NRs and gap 2 nm rod-in-shells were irradiated using a diode 808 nm (*bottom*). The group of “cells with laser” was performed without treatment of rod in shell and exposed to laser. (c) The UV-vis-NIR spectra of Au rod in shells with different gaps and Au nanorods, and their corresponding TEM images. (d, e) Time-dependent tumor growth as a function of postirradiation days (Reprinted with the permission from Ref. [141]. Copyright 2013 American Chemical Society)

the first and second NIR windows [141]. In vitro performance clearly displays high efficacy in the NIR photothermal destruction of cancer cells, showing large cell-damaged area beyond the laser-irradiated area (Fig. 2.13b). Then, they tailored the plasmon resonances of the rod-in-shell structure by changing the gap distance between the nanorod core and the Au/Ag nanoshell, to evaluate the therapeutic effect of using a 1,064 nm diode laser (Fig. 2.13c). It was found that the mice injected with the 2 nm gap showed effective suppression of tumor growth under irradiation of 1,064 nm laser for 7 min (Fig. 2.13d). Furthermore, regarding the first NIR window with the use of an 808 nm laser, the photothermal ablation of solid tumors demonstrates that the rod in shell exhibits a more effective anticancer efficacy compared to Au nanorods (Fig. 2.13e).

2.4 Combination of Photothermal Therapy with Other Therapeutic Approaches

Numerous preclinical and clinical studies have proved that monotherapy (e.g., hyperthermia, chemotherapy, radiotherapy, surgery, and some other therapeutics) is not as effective as we expected [142, 143], due to incomplete tumor eradication, metastasis of cancer, development of drug resistance, individual differences in cancer patients, and so on [144–146]. Combination therapy, which uses more than one therapeutic approach, has shown great potential for the treatment of cancer and some other serious diseases [143, 147]. Combination of photothermal therapy with other therapeutic strategies based on gold nanostructures, such as photodynamic therapy and chemotherapy, has thus received tremendous interest in recent years.

2.4.1 *Combination of Photothermal Therapy with Photodynamic Therapy*

Photodynamic therapy generally falls into phototherapy, along with photothermal therapy. Both of them are deemed as minimal invasive and effective approaches for cancer treatment. Photodynamic therapy relies on the photosensitizer to transfer photo energy to the surrounding oxygen molecules, generating reactive oxygen species, such as singlet oxygen (SO), to kill tumor cells [148]. Owing to the tumor targeting ability of appropriately designed photosensitizers or photothermal agents based on gold nanostructures, as well as the selective light irradiation of the lesion region, combination of photothermal therapy and photodynamic therapy exhibits remarkably reduced side effects and improved selectivity compared with traditional remedies.

Jang and coworkers demonstrated that Al(III) phthalocyanine chloride tetrasulfonic acid (AlPcS4)-loaded gold nanorods could contribute to a strong reduced tumor growth effect (95 % inhibition) after combination of photothermal treatment and photodynamic treatment upon their intravenous injection, while the tumor growth inhibition effect was 79 % for those only receiving photodynamic therapy [149]. In another work by Wang and coworkers, an aptamer switch probe (ASP) linking chlorin e6 (Ce6), a photosensitizer molecule, to the surface of nanorods was constructed [150]. In the presence of target cancer cells, the ASP changes conformation to drive Ce6 away from the gold surface, thereby producing singlet oxygen for photodynamic upon light irradiation. Combined with destruction by the photothermal effect of gold nanorods, a remarkable and synergistic therapeutic effect compared to photothermal and photodynamic alone was observed for cancer cells.

In the abovementioned studies, two different lasers are independently used to trigger photothermal and photodynamic, separately. To simplify the treatment process, it would be helpful to find new strategies to accomplish photothermal and photodynamic treatment under a single laser irradiation. Chen et al. fabricated gold vesicles

composed of Ce6-loaded plasmonic vesicular assemblies of gold nanoparticles with strong NIR light absorbance in the NIR region of 650–850 nm [151]. Upon their intratumoral injection, effective combined photothermal and photodynamic treatment under a 671 nm laser irradiation was achieved. Furthermore, they constructed gold nanostars-PEG-Ce6 for coordinated photothermal/photodynamic therapy upon single CW laser irradiation both in vitro and in vivo [152]. It was demonstrated that the difference in photostability between photosensitizers and gold nanostructures could be used to modulate photothermal and photodynamic by adjusting irradiation time (Fig. 2.14), and the strategy significantly improved the anticancer effect and greatly simplified the treatment process. More recently, Kuo Chu Hwang and coworkers developed a unique morphology of a gold nanostructure, called nanoechinus (Fig. 2.15), [153] which sensitized the formation of singlet oxygen as well as exerted in vivo photodynamic and photothermal therapeutic effects in both the first and the second NIR biological windows for complete destruction of tumors in mice. The gold nanoechinus exhibits exceptionally high extinction coefficients at NIR biological window, seven to nine orders higher than conventional organic dyes and photosensitizers and three to four orders higher than that of gold nanoparticles, which are especially useful in deep-tissue-buried tumor treatment with a much lower amount of nanomaterials or lower incident light intensities/irradiation time.

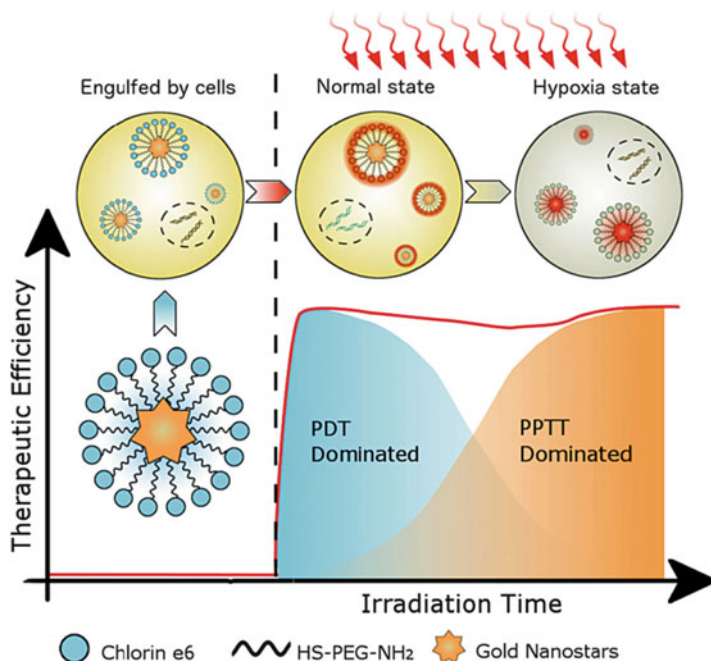


Fig. 2.14 Schematic illustration for explaining coordinated photothermal and photodynamic treatment upon single laser irradiation (Reproduced from Ref. [152] by permission of John Wiley & Sons Ltd)

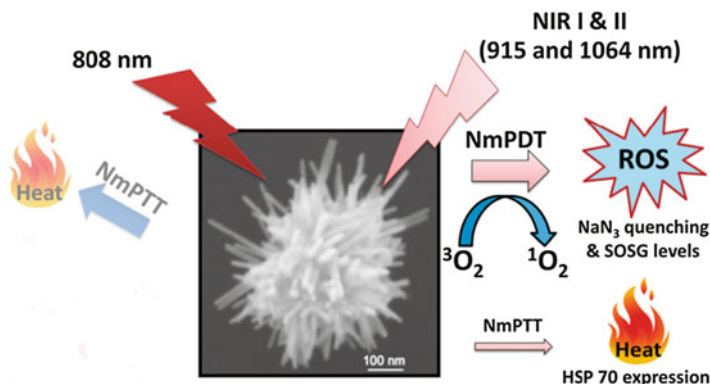


Fig. 2.15 Schematic representation of the working mechanisms of NIR light-induced phototherapeutic effects exerted by gold nanoechinus (Reproduced from Ref. [153] by permission of John Wiley & Sons Ltd)

The LSPR of gold nanostructures could be fine-tuned to overlap with the absorption of photodynamic dye with poor photostability and low quantum yield. Such overlap greatly increases the singlet oxygen yield by maximizing the local field enhancement and protecting photodynamic dye against photodegradation, thus enhancing the efficacy of photodynamic therapy. Very recently, Li et al. designed and validated a novel plasmon-enhanced photodynamic therapy for breast tumor by fabricating a nanoplatform composed of mesoporous silica-coated gold nanorods incorporating indocyanine green (ICG) [154]. The LSPR peak of the nanorod core has been regulated to overlap with the excitation band of ICG, thus increasing the absorption coefficient of incorporated ICG by virtue of the local enhanced field effect. The Au NR@SiO₂-ICG formulation dramatically increases the singlet oxygen generation under laser excitation, relative to free ICG, and demonstrates enhanced photodynamic destruction of human breast carcinoma MDA-MB-231. With mild laser irradiation, the growth of orthotopic breast tumors in mice was greatly inhibited through a synergistic effect of photodynamic and photothermal treatment.

2.4.2 *Combination of Photothermal Therapy with Chemotherapy*

Chemotherapy, one of the most commonly used cancer treatments, often causes systemic side effects due to unspecific drug delivery to all tissues including healthy ones. As a result, overall treatment efficacy is lowered by dose-limiting drug toxicity, and safe dosages may not completely eradicate tumors. In addition, half of all

chemotherapy patients develop drug resistance, a situation that also leads to treatment failure [155]. Temperature rise, induced by photothermal therapy, is sufficient to increase vascular permeability within tumors that have inefficient blood flow through their newly formed immature blood vessels, leading to selective drug delivery and enhanced cytotoxicity [156]. The combination of photothermal therapy and chemotherapy has proved to be effective on optimizing the efficacy of cancer treatment [157]. In recent years, various gold nanostructures with suitable surface modification have been extensively explored for the combined photothermal therapy and chemotherapy [100].

Gold nanoparticles have found various applications in the field of nanomedicine, which can be easily prepared in a size-controllable manner [95, 158]. You and coworkers prepared drug-delivery vehicles that encapsulate doxorubicin (DOX) with a pH-sensitive matrix embedded with gold nanoparticles. Such a nanostructure exhibited a high absorption in the NIR region. After being conjugated with a targeting moiety (Herceptin), the obtained drug carrier could be selectively engulfed by cancer cells, resulting in a combined therapeutic effect under the NIR laser irradiation [159]. In another study, Nam et al. designed a pH-responsive gold nanoparticle-based drug carrier, which could form aggregates in tumor regions by responding to micro acidic environment of the tumors [160]. Highly spatiotemporally concerted drug release and dramatically increased NIR light absorption were then observed, contributing to an effective synergistic tumor suppression effect in mouse xenografts.

Gold nanoshells prepared via various methods with strong NIR light absorptions are a useful nanoplatform for photothermal combination therapy. In 2010, Lee and coworkers fabricated an interesting half-nanoshell on the template of DOX-loaded PEG-PLGA nanomicelle, with plasmon absorption at 790 nm [161]. Under NIR laser irradiation upon intravenous injection, the intratumoral temperature was increased to 50–70 °C and DOX was rapidly released. Such a combination could result in the complete destruction of tumors without weight loss or tumor recurrence. Neither chemotherapy with a slightly higher dose of DOX nor the photothermal therapy alone without DOX could achieve the similar result. Recently, gold nanoshells consisting of a mesoporous silica nanorattle core and a thin outer gold nanoshell (SN@AuNSs) have been designed and synthesized by Tang et al. [108]. The amount of docetaxel (DOC) loaded in SN@AuNSs could reach up to 52 %. Both in vitro and in vivo results showed that the synergistic efficacy was much better than that of chemotherapy or photothermal therapy alone. By decorating SN@AuNSs with transferrin (SN@AuNSs-Tf), they further tested the efficacy of targeted thermo-chemotherapy for breast carcinoma [10]. Under NIR laser exposure, MCF-7 breast tumors in mice presented complete regression with the combination of selective targeting, photothermal therapy, and chemotherapy. It is worth noting that both SN@AuNSs and SN@AuNSs-Tf could be excreted from the body with a slow clearance rate via feces and urine, though the diameter of SN@AuNSs was around 130 nm. Additionally, hollow gold nanoshells have been intensively explored for drug delivery and photothermal ablation of tumors by Li's group [12, 19, 52, 162, 163]. In 2012, they demonstrated that hollow nanoshells could be used for

in vivo anticancer drug delivery, which exhibited effective synergistic tumor suppression capability when combined with the NIR light irradiation. Further studies indicated that hollow nanoshells, after being conjugated with a peptide targeting EphB4 overexpressed on the membrane of multiple types of cancer cells, exhibited an improved cellular uptake for three EphB4-positive tumors both in vitro and in vivo. The improved tumor accumulation of peptide-conjugated hollow nanoshells and NIR-triggered release of DOX ultimately contributed to an effective synergistic therapeutic effect on EphB4-positive tumors.

Gold nanorods with strong NIR absorbance and suitable surface modifications have also been widely explored for the combined photothermal and chemotherapy of cancer. One commonly used nanoplatform is mesoporous silica-coated gold nanorods, which have been widely studied for drug delivery and exhibit high drug loading capacity attributed to their mesoporous silica shell. In 2012, Chen's group fabricated mesoporous silica-coated gold nanorods for DOX delivery, observing a precisely NIR light-controllable drug release profile. It was demonstrated that the DOX-loaded mesoporous silica nanorods could offer a synergistic therapeutic effect on A549 cancer cells by utilizing a 790 nm laser irradiation [11]. In another work, Qu's group demonstrated that folic acid-conjugated mesoporous silica-coated gold nanorods with PEGylation after being loaded with an anticancer drug could realize a greatly enhanced treatment effect by combining photothermal therapy with chemotherapy [164]. Almost at the same time, a similar treatment effect in mice was observed, in which RGD peptide was introduced as the targeting moiety to realize a targeted synergistic therapeutic effect in a mouse tumor model [165].

In addition to the mesoporous silica layer incorporation method, a number of different NIR-responsive drug-delivery systems by coating gold nanoparticles with other thermal-responsive materials such as DNA or polymers have been developed. Among them, the most well known is based on gold nanocages, which was constructed by coating nanocages with thermosensitive polymers poly(*N*-isopropylacrylamide-*co*-acrylamide) (pNIPAAm-*co*-pAAm) as pore blockers [13]. As the temperature was increased above a certain threshold through NIR laser irradiation, the polymer coating would collapse due to a conformational change, and the pores of the nanocages were exposed, which allowed effectors preloaded in the interior to be released (Fig. 2.16). In 2012, Xiao and coworkers assembled DNA duplex strands, which consisted of sequential CG base pairs providing loading sites for DOX, onto gold nanorods [166]. Upon NIR laser illumination, DOX molecules were released at the target site for chemotherapy. The in vivo results showed that the DNA-based platform effectively inhibited tumor through thermo-chemotherapy upon NIR laser irradiation after intratumoral injection. Very recently, Chen et al. successfully coupled photothermal properties and thermoresponsive properties in a single nanocomposite by coating nanorods with a thermoresponsive polymer shell consisting mainly of poly(*N*-isopropylacrylamide-*co*-acrylic acid) [167]. Then, DOX was loaded into the nanocomposite through electrostatic interactions with high loading content up to 24 %. The activation mechanism was thus transformed from heat to NIR laser, which can be used to control the size as well as drug release. A synergistic efficacy of photothermal therapy and chemotherapy was

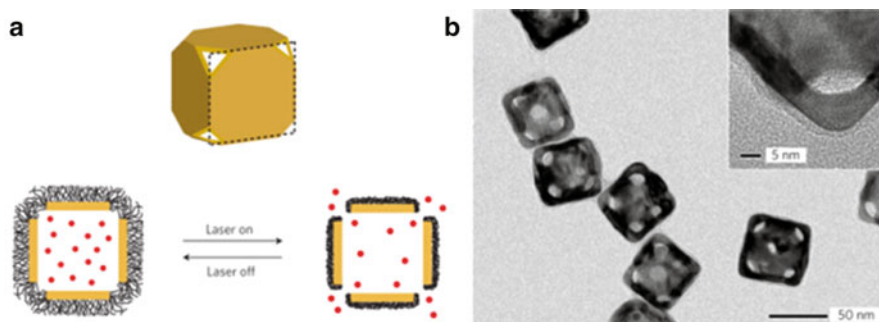


Fig. 2.16 (a) Schematic illustration of the controlled-release system. (b) TEM images of gold nanocages covered by a pNIPAAm-co-pAAm copolymer. The inset shows a magnified TEM image of the corner of such a nanocage (Reprinted by permission from Macmillan Publishers Ltd: Ref. [13], copyright 2009)

observed with complete tumor inhibiting by NIR laser irradiation-induced temperature increase and the released drug, showing very promising potentials for cancer treatments.

2.5 Gold Nanostructures for Diagnostics

As described above, plasmonic gold nanostructures exhibit significantly enhanced radiative properties compared with bulk gold (i.e., light absorption, scattering, and fluorescence). While electromagnetic field enhancement has been widely used in SERS, absorption, and scattering endow gold nanostructures with potentials as multimodal imaging agents [95]. Here we will outline several main modalities for bioimaging based on the intrinsic properties of gold nanostructures, including dark-field imaging, optical coherence tomography, fluorescence imaging, photoacoustic imaging, computed tomography, and SERS-based imaging.

2.5.1 Dark-Field Imaging (DFI)

Gold nanoparticles can strongly scatter light at their plasmon wavelengths, with the scattering cross sections 10^5 – 10^6 times stronger than that of the emission from a fluorescent dye molecule [122]. Using a simple optical microscope with high-resolution objective lens, light scattered from gold nanostructures can be detected as bright spots even when the size is smaller than the diffraction limit of the microscope. In addition, the light-scattering gold nanoparticles are indefinitely photostable and do not blink, in contrast to conventional fluorophores. These features make gold-based nanoparticle probes very powerful for bioimaging. Sokolov et al. showed

that when gold nanoparticles were conjugated to anti-epidermal growth factor receptor (anti-EGFR) antibodies, they specifically bound to EGFR proteins that are overexpressed on the surfaces of cervical cancer cells [168]. Illumination of the nanoparticle-labeled cells with laser light from either a laser pointer or a confocal microscope lit up the gold nanoparticles and, thus, their associated cancer cells. Later, El-sayed et al. used dark-field optical microscopy to detect gold nanoparticle-labeled cancer cells [169]. The key advantages of DFI are that nanoparticles are imaged in high contrast with true color, making the technique amenable to multiplexed detection schemes by using gold nanoparticles of different sizes and shapes. Furthermore, as demonstrated in 2006 by Huang et al. [46], gold nanorods scatter strongly in the near-infrared region, capable of detecting head and neck cancer cells under excitation at spectral wavelengths where biological tissues exhibit little attenuation. Currently, DFI based on gold nanostructures (spheres, rods, nanocages, and nanoshells) is widely used for cancer imaging through functionalized nanoparticle-receptor binding onto cell surface biomarkers [170–173].

Though highly scattering cross sections of gold nanostructures have been exploited extensively for contrast enhancement in DFI, this diagnostic technique has been limited to in vitro studies. Highly scattering nanostructures of sizes over 100 nm are needed in order to achieve good contrast, which is unsuitable for in vivo blood circulation and accumulation in tumor. Alternatively, a high density of smaller gold nanoparticles can be incubated with cells which upon agglomeration in the cellular environment will increase the effective size and provide enhanced contrast. However, this is also infeasible because of potential toxicity by high-density nanoparticles and its impracticability in vivo. Gold nanostructures with extremely high scattering cross section and small size have not yet been reported. These limitations have prohibited the application of DFI in animal models.

2.5.2 *Optical Coherence Tomography*

Another imaging modality based on scattering properties is optical coherence tomography (OCT). In OCT, tissue is illuminated with light of coherence, and back-scattering light is detected based on coherence matching between the incident and reflected beams. It can produce three-dimensional images of a subject with micrometer resolution. Since coherence is essential for the detection process, OCT is predominantly sensitive to scattering from tissues rather than absorption. Gold nanostructures resonant at the OCT excitation wavelength have been used as contrast agents due to their ability to produce distinctive backscattered light detectable in highly scattering tissue [174]. In 2007, Halas and coworkers used NIR resonant nanoshells as OCT contrast agents for tumor tissues after their systematical injection [14]. As shown in Fig. 2.17, a significant increase in image contrast from tumor tissue is observed compared with normal tissue or tumor tissue injected with PBS. In another study, gold nanoshells were employed for deep-tissue imaging of rabbit epidermal tissue with high spatial-temporal resolution [175]. Nanoshells enhanced

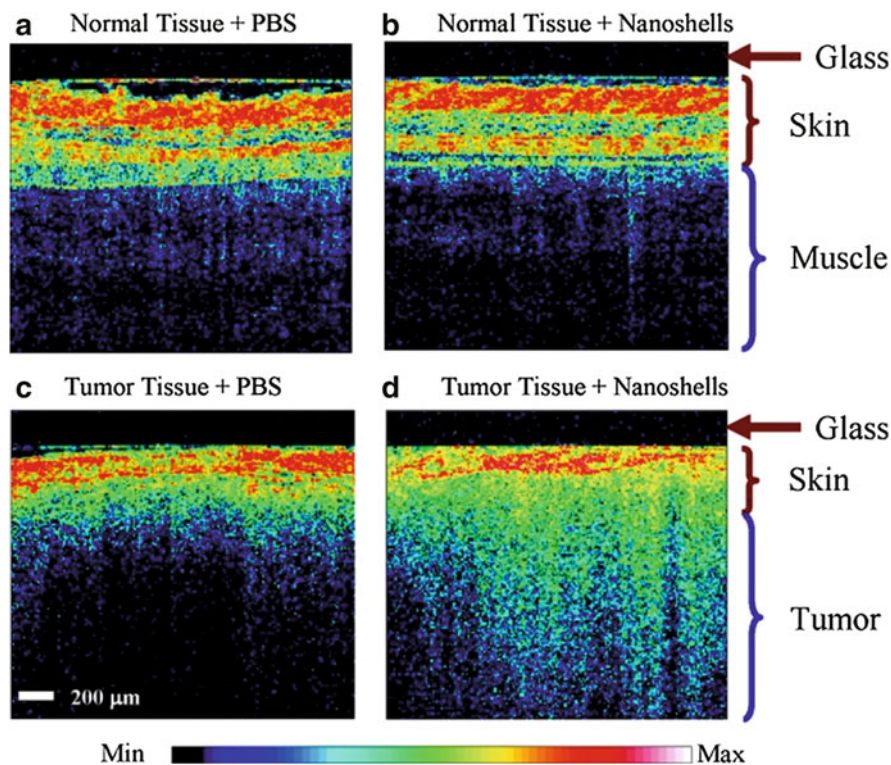


Fig. 2.17 Representative OCT images from normal skin and muscle tissue areas of mice systemically injected with nanoshells (a) or with PBS (b) and from tumors of mice injected with nanoshells (c) or with PBS (d) (Reprinted with the permission from Ref. [14]. Copyright 2007 American Chemical Society)

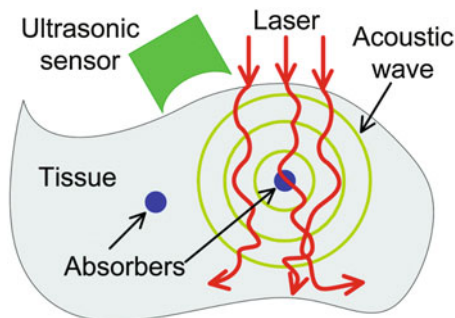
the OCT signal of the different regions of the dermis as well as augmented the contrast of hair follicles and glands in OCT images of skin tissue. In terms of gold nanorods, Oldenburg et al. reported strong OCT contrast at 2 mm depth of human breast tissue with only 10–20 nM of nanorods [176]. OCT signal could only be detected within a few hundred micrometer tissue depth in the control group. In the same year, gold nanoparticles conjugated with anti-EGFR were used to enhance OCT contrast of oral dysplasia in a hamster model *in vivo* [177]. By using microneedles, the delivery and penetration depth of gold nanoparticles into skin tissue were improved, and clear differences were observed in OCT images between micromorphologies of the carcinogen-treated and untreated epithelial tissues. As a powerful three-dimensional diagnostic tool for real-time imaging without the need to remove specimens, OCT has developed tremendously since its invention [178]. However, due to intense scattering from optically dense tissue, resolutions have remained low, and extensive applications for *in vivo* cancer imaging, especially deep cancer imaging, merit further investigations.

2.5.3 *Two-Photon Luminescence*

In comparison to confocal fluorescence microscopy, two-photon luminescence (TPL) has emerged as a powerful tool in the past two decades for cellular imaging and diagnostics, with the advantages of non-bleaching and stable signal, higher spatial resolution, and reduced background signal [179]. Gold nanostructures present enhanced TPL, whose efficiencies can now be improved by simply modifying the geometry [180], making them detectable at single particle levels under femtosecond NIR laser excitation [181, 182]. Durr et al. utilized gold nanorods for TPL imaging of cancer cells embedded in collagen matrix with 75 μm spatial resolution [183]. The TPL intensity enabled by nanorods was three orders of magnitude brighter than that of two-photon autofluorescence. By using TPL, single-particle tracking of targeted gold nanorods was reported to investigate the mechanisms of cellular uptake [184]. In 2007, He et al. reported the novel detection of circulating tumor cells in vivo using the TPL technique [185]. CTC-mimetic leukemia cells were firstly injected into the blood stream of live mice followed by injection of folate-conjugated gold nanorods to target the CTC in vivo. TPL imaging with an intravital flow cytometer detected single-circulating cells in the vasculature of the mouse ear. Apart from nanorods, other gold nanostructures have also been extensively exploited as TPL contrast agents. The TPL contrast of nanostars functionalized with wheat germ agglutinin was utilized to image their uptake in breast cancer cells as well as nanostars circulating in the vasculature in vivo in mouse models [27]. With nanostars, tissue vasculature was visible under 5 % transmission with minimal background fluorescence, while it required 20 % transmission to observe the vessels without nanostars injected. The feasibility of using nanoshells for single-particle-based in vivo imaging has been validated by Gao et al. [186]. They developed gold nanoshells with plasmon resonance at 800 nm and used them for in vivo blood vessel imaging using two-photon excitation microscopy at an excitation wavelength of 750 nm. They successfully imaged single nanoshell particle in blood vessels and generate optical contrast for blood vessel structure using luminescent signals. Nanocages, nontargeted or targeted, have also been utilized for TPL imaging to probe the dynamical processes of cellular uptake [62, 75].

In particular, due to their large multiphoton absorption capabilities, nanocages have been demonstrated to generate three-photon luminescence (3PL) when excited at 1,290 nm with a femtosecond laser at 4 mW [187]. 3PL exhibited the detection of the distribution of intravenously injected nanocages in the liver of a mouse with minimal autofluorescence from the background and negligible photothermal toxicity. While 3PL contrast agents based on gold nanostructures have not been substantially investigated, these initial results demonstrate the efficacy of this imaging modality and provide a great potential in in vivo diagnostics.

Fig. 2.18 Schematic illustration of laser-induced photoacoustic effect in biological tissue (Reproduced from Ref. [9] by permission of The Royal Society of Chemistry)



2.5.4 Photoacoustic Imaging

Optical imaging, as described previously including DFI, OCT, and TPL, provides rich contrast in biological tissues based on their distinct chemical components. However, the incident photons in tissue, after optical transport mean free path (~ 1 mm), severely suffer from strong diffusion and thus lose optical coherence and focusing properties. Consequently, the shallow penetration depth of optical imaging in scattering medium fundamentally hampers their application in biomedicine. Nonetheless, photons in tissues can be thermoelastically converted to ultrasonic pressure waves through the photoacoustic (PA) effect, and photoacoustic tomography (PAT) generates images by detecting these ultrasonic waves in tissues. The principle is illustrated in Fig. 2.18 [9]. When a pulsed (or intensity-modulated) laser beam irradiates a biological tissue, a small temperature rise ΔT in the tissue leads to a pressure rise p_0 due to thermoelastic expansion that will produce ultrasonic waves. This pressure is given by $p_0 = \beta \Delta T / \kappa$, where β is the thermal expansion coefficient and κ is the isothermal compressibility. Theoretically, only 1 mK temperature leap can generate about 800 Pa pressure rise that is far beyond the noise level of a typical ultrasonic transducer [188]. The acoustic pressure, after propagating in the tissue and coupling medium, can be received by an ultrasonic transducer to reconstruct a PA image. By converting the incident photon into ultrasonic emission, PAT can break through the optical diffusion limit in biological tissue, which hybridizes both the merits of rich optical contrast and high ultrasonic resolution, but alleviates their shortcomings in a single modality, permitting anatomical, functional, molecular, and genetic imaging.

Since PA effect is dependent on temperature rise in the tissues, gold nanostructures capable of photothermal heating have great potential as PAT contrast agents in cancer diagnosis. Nearly a decade ago, gold nanostructure-mediated PAT was first realized by gold nanoshells [189]. Three successive injections of nanoshells were administered to the rat through intravenous injection. The PAT image acquired 20 min after the third administration of contrast agent showed the brain vasculature with enhanced contrast. With the exogenous contrast agent, the optical absorption of blood was increased and the contrast between the vessels and the background tissues was also enhanced. The differential PAT image mapped the exogenous

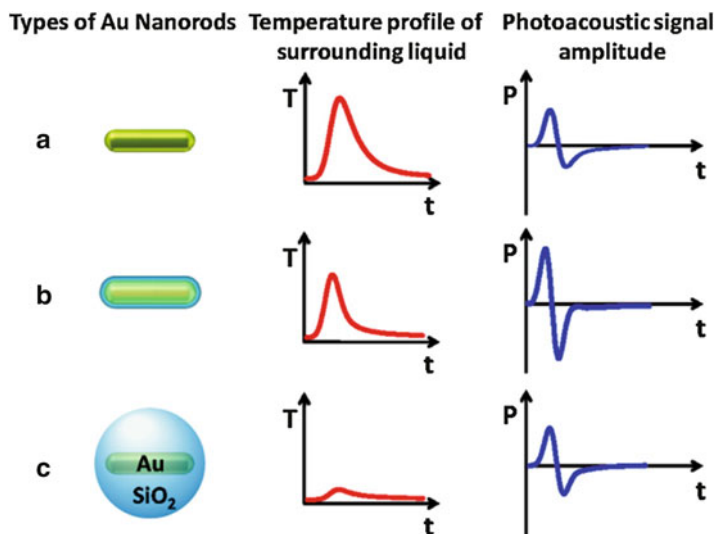


Fig. 2.19 Schematic mechanism of the proposed thermal transport processed from the nanoparticle to the environment and the resulting temporal profiles of the temperature (T) near the surface and the amplitude of the photoacoustic signal (P) far from the surface of the nanoparticle for (a) a bare nanorod, (b) a thin silica shell coating nanorod, and (c) very thick shell coating nanorod (Reprinted with the permission from Ref. [191]. Copyright 2011 American Chemical Society)

nanoshell distribution in the rat brain. With photothermal conversion efficiency higher than nanoshells, gold nanorods enabled PA signal increasing on a wide variety of ovarian tumor types including 2008, HEY, and SKOV3 cell lines after their intravenous injection [190]. In addition, silica coating of gold nanorods provides a simple method to enhance their performance as contrast agents, producing about threefold higher PA signals than bare nanorods [191, 192]. As shown in Fig. 2.19, silica coating endows nanorods with reduced interfacial resistance and a sharper profile peak and, thus, increased PA signal amplitude. However, silica at a further larger thickness leads to a decrease in the PA signal. Therefore, silica-coated gold nanorods are very promising as a multifunctional platform for enhanced PAT imaging and photothermal therapy of cancer with good photothermal stability, as discussed in the previous section.

Gold nanocages are also excellent contrast agents for PAT, due to the large absorption cross sections [193]. Xia's group demonstrated PAT of cerebral cortex in a rat brain by using nanocages as intravascular contrast agents [194]. A maximum of 80 % PA signal enhancement in the brain cortex was observed after 4 h injection of nanocage solution. In an animal model, sentinel lymph nodes (SLN) containing gold nanocages were identified as deep as 33 mm below the skin surface with good contrast [195]. Nanocage-mediated PAT may potentially eliminate the invasive axillary staging procedures for SLN identification and imaging. In a further study, they investigated nanocages bioconjugated with melanocyte-stimulating hormone in vivo

for molecular PAT of melanomas, and 300 % enhancement was achieved relative to non-conjugated nanocages [196]. Like nanocages, gold nanostars also have great absorption-to-scattering ratio, favorable for photoacoustic imaging. Wang et al. demonstrated that plasmon-resonant gold nanostars could be used with volumetric spectroscopic PAT for noninvasive in vivo mapping of lymphatic systems [197]. In another study, RGD-conjugated gold nanostars targeted the tumor for tumor angiogenesis mapping and monitoring the response of photothermal treatment [198]. Meanwhile, other gold nanostructures with NIR absorption like nanotripods [199] and nanovesicles [151] have also been reported as PAT contrast agents in vivo. All these studies demonstrate the potential of gold nanostructures for contrast enhancement of PAT, and with development of new nanostructures and molecular targeting strategies, the spatiotemporal resolution of PAT can be improved even further.

2.5.5 *Computed Tomography*

Computed tomography (CT) is one of the most commonly used noninvasive clinical imaging modalities due to its wide availability, high efficiency, and low cost. Owing to the high atomic number ($Z=79$) and k-edge value (80.7 keV), gold nanoparticles generally provide greater contrast than widely used iodinated contrast agents. In addition, X-ray attenuation of gold nanoparticles was not significantly reduced in water or water containing calcium phosphate, in contrast to iodine with contrast effect sensitive to the environment [200]. In 2006, gold nanoparticles with an average size of 1.9 nm from Nanoprobes Inc. were initially studied as X-ray contrast agents [201]. After intravenous injection, in vivo X-ray imaging revealed detailed anatomic structures such as tumors and blood vessels less than 100 μm in diameter. Later, PEGylated gold nanoparticles with diameter of 30 nm were demonstrated to show a high contrast (~ 2 -fold) between hepatoma and normal liver tissue after their intravenous injection into rats [202]. In other studies, gold nanoparticles prepared within the phytochemical gum-arabic (GA) matrix were used as CT contrast agents in pigs, which have physiological and anatomical characteristic similar to those of humans [203, 204]. The GA-gold nanoparticles showed excellent biocompatibility, and significant CT contrast effects were observed at the liver and spleen. The dendrimer-entrapped gold nanoparticles with properties controlled via modification of terminal groups of dendrimers were also successfully used for in vivo blood pool and tumor CT imaging after intravenous injection [205]. With the larger gold nanoparticles entrapped in the dendrimer, greater CT contrast effects could be achieved [206]. In addition to spherical gold nanoparticles, various gold nanostructures can be used as CT contrast agents because the CT contrast effect is not affected by the shape nanoparticles [20, 123, 131].

To acquire information on cellular and molecular processes using CT, contrast agents with targeting ability are required. Tobi Reuveni et al. intravenously injected anti-EGFR-conjugated gold nanoparticles (30 nm) into nude mice implanted with

human squamous cell carcinoma head and neck cancer [207]. The results clearly demonstrated that a small tumor, which was undetectable through anatomical CT, was clearly visible by the molecularly targeted gold nanoparticles. It was further shown that active tumor targeting was more efficient and specific than passive targeting. In another work, gold nanoparticles were modified with glycol chitosan (GC) polymers (GC-Au NPs), which exhibited excellent stability and tumor-targeting ability [208]. Tumor tissue was able to be delineated from the surrounding tissues after 2 h postinjection at high concentration (200 μL , 300 mgkg^{-1}). In particular, after 24 h postinjection, the HU value in the tumor tissue increase about fivefold (HU=254) relative to normal tissue. Furthermore, detailed anatomical information could be acquired from the three-dimensional reconstructed images in which the exact shape of the tumor tissue was clearly visualized. In addition to tumor, gold nanoparticles conjugated with anti-CD4 antibodies were used for in vivo CT studies of peripheral lymph nodes [209]. Larger and targeted nanoparticles showed the highest contrast enhancement compared to nontargeted nanoparticles and smaller nanoparticles because they could deliver more gold atoms.

2.5.6 Surface-Enhanced Raman Scattering (SERS) Based Imaging

Surface-enhanced Raman scattering (SERS) is an ultrasensitive vibrational spectroscopic technique to detect molecules on or near the surface of plasmonic nanostructures, greatly extending the role of standard Raman spectroscopy. Since its discovery in the late 1970s, SERS has been applied to many analyses, especially in biochemistry and life sciences. Particularly, by designing novel nanoprobe named “SERS tags,” the past decade has witnessed a plethora of clinical SERS-based studies demonstrating the efficacy of gold nanostructures conjugated with Raman active molecules for molecular imaging in cells and animal model [86]. Raman scattering enhancement of vicinal molecules based on gold nanostructures is primarily attributed to two mechanisms: electromagnetic (EM) and chemical enhancement (CE). EM arises from intense EM fields generated on surface of gold nanoparticles when illuminated at the plasmon resonance. CE is based on dynamical charge transfer where photoexcitation of the metal creates a hot-electron-hole pair which can transfer into the lowest unoccupied molecular orbital of the nearby molecule. The electron subsequently transfers back to the metal with some changed internal molecular vibrations, which gives rise to CE [210, 211]. Together, the two primary mechanisms contribute to the total enhancement. Though eminent progress has been made on SERS-based in vitro bioanalysis [86, 212–216], SERS-based imaging in vivo has yet to reach the status of its counterpart, fluorescence imaging, mainly due to the expensive instrumentation and weak signal of Raman scattering. However, compared with fluorescence imaging as a clinical diagnostic tool, SERS has many advantages including high signal-to-noise ratio, non-photobleaching feature,

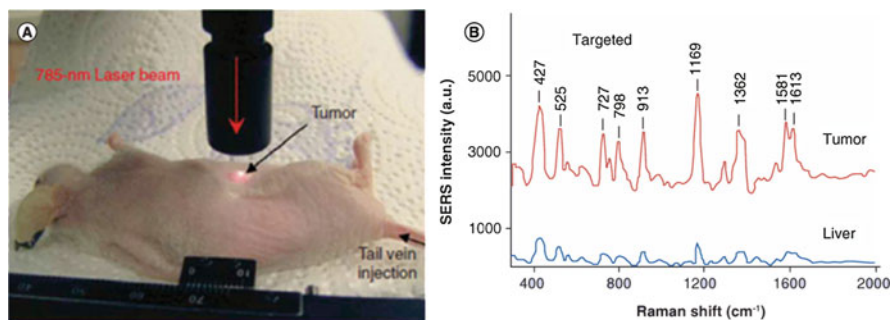


Fig. 2.20 (a) Photographs showing a laser beam focusing on the tumor site or on the anatomical location of liver. (b) SERS spectra obtained from the tumor and the liver locations by using targeted nanoparticles (Reprinted by permission from Macmillan Publishers Ltd: Ref. [217], copyright 2008)

subpicomolar level sensitivity, excellent multiplexing capability, and single photoexcitation. Owing to these advantages, SERS-based imaging *in vivo* has aroused increasing attention with some remarkable achievements over the past several years.

Early in 2008, Nie's group investigated SERS-based *in vivo* tumor targeting using functionalized gold nanoparticles (GNPs) [217]. In this study, diethylthiatri-carbocyanine (DTTC), a commercial NIR Raman reporter, was adsorbed onto the surface of 60 nm colloidal GNPs. Then, mixed PEG was applied to conjugate single-chain variable fragment (ScFv) antibodies, which thereby formed targeted SERS nanoprobes. After 5 h of their injection into tumor-bearing mice, clearly distinguished signal intensities were observed on the Raman spectra from targeted nanotags in the tumor region (Fig. 2.20), confirming successful delivery of targeted nanotags to a specific tumor and the capability of noninvasive spectroscopic detection. This highly sensitive technique opens up a new opportunity for the detection of targeting tumors. Then, Park et al. investigated PEGylated Cy7-tagged gold nanorods for SERS detection by a passive mechanistic pathway, indicating the clear differentiation between the tumorigenic area and normal skin after their intravenous injection [218]. In 2011, Young-Tae Chang et al. prepared a lipoic acid-containing NIR-active CyNAMLA-381 as a highly sensitive NIR SERS reporter molecule and further applied it to the preparation of ultrasensitive SERS probes for *in vivo* cancer imaging by conjugating CyNAMLA-381-Au NPs to ScFv anti-HER2 antibodies [219]. Furthermore, Gambhir and coworkers fabricated a unique triple-modality MR-photoacoustic-SERS imaging nanocomposite (termed MPR nanoparticles) to accurately help delineate the margins of brain tumors in living mice both preoperatively and intraoperatively [220]. Specifically, Raman imaging was used for guidance of intraoperative tumor resection. Cancerous foci, not visible to the naked eye, were successfully detected after the tumor resection seems to be completed (Fig. 2.21). Later, they employed SERS probes based on gold nanorods to visualize the margin of ovarian cancer tumors, followed by tumor debulking under guidance of SERS imaging. These two studies highlight the extremely high sensitivity of Raman

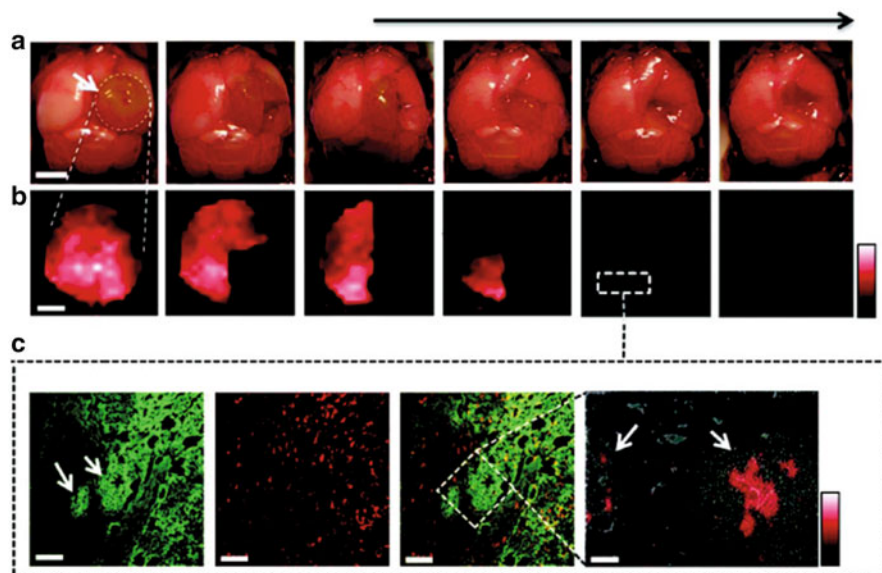


Fig. 2.21 Living tumor-bearing mice underwent craniotomy under general anesthesia. Quarters of the tumor were then sequentially removed as illustrated in the photographs (a), and intraoperative Raman imaging was performed after each resection step (b) until the entire tumor had been removed, as assessed by visual inspection. After the gross removal of the tumor, several small foci of Raman signal were found in the resection bed. (c) A subsequent histological analysis of sections from these foci showed an infiltrative pattern of the tumor in this location, forming finger-like protrusions extending into the surrounding brain tissue. As shown in the Raman microscopy image (*right*), a Raman signal was observed within these protrusions, indicating the selective presence of MPRs. The Raman signal is shown in a linear *red* color scale (Reprinted by permission from Macmillan Publishers Ltd: Ref. [220], copyright 2012)

imaging and open up a new avenue of SERS-tagged gold nanoparticles for clinical translation. More recently, gold-silica SERS nanoparticles combined with a handheld Raman scanner, which is easy to handle in the operating room and allows real-time scanning, to provide SERS image-guided surgical resection of brain tumor was demonstrated, a bigger stride into clinical translation [221].

Specially, multiplexing is the distinctive feature of SERS due to the narrow bandwidths of the vibrational Raman spectra of the reporter molecules. The recent high demand for a sensitive and simultaneous detection of multiple targets *in vivo* has made SERS technique highly favorable. Gambhir et al. demonstrated multiplexing *in vivo* with ten different SERS nanotags with distinct spectral characteristics [222, 223]. A mixture of multiple SERS nanotags were administered intravenously, and their uptake in the liver was imaged 24 h postinjection. Clear distinguishable spectral characteristics were observed *in vivo* for each individual SERS nanotag at picomolar sensitivity. In another study, molecule-coded gold nanorods as a platform for multiplexed NIR detection were synthesized [224]. It was found that under a NIR excitation source, three unique Raman-coded nanorods might be

distinguished efficiently within ~ 6 nm of spectral bandwidth, in contrast to ~ 30 nm of semiconductor quantum dots. Highly sensitive novel NIR Raman reporters, such as Cy7LA, Cy7.5LA, and CyNAMLA-381, were also used to construct SERS nanotags for *in vivo* multiplexed targeted detection [225]. In addition, Homan Kang et al. developed novel NIR SERS dots consisting of Au/Ag hollow shell assemblies on the surface of silica nanospheres [226]. The signals were detected effectively from deep tissue of up to 8 mm depth and three kinds of NIR SERS dots produce strong SERS signals from deep tissues without spectral overlap after their injection into live animal tissues, demonstrating their potential for *in vivo* multiplexed detection of specific target molecules. More recently in 2014, “schizophotonic” all-in-one gold nanoparticles were designed by integrating various SERS reporters into biocompatible polymeric surface coating [227]. This technique allows the synthesis of very small (<20 nm) SERS probes, which is crucial for the design of excretable and thus highly translatable imaging agents, and the all-in-one nanoparticles were demonstrated to be capable for multiplexed lymph-node imaging.

SERS imaging has tremendous potentials to deliver accurate diagnosis from the single cell level to subcutaneous tumors. When coupled with other imaging techniques, multimodal SERS can simultaneously achieve high sensitivity and spatial resolution. Gold nanostructures enabled SERS imaging probes from a promising platform for combining SERS imaging with a therapeutic response to generate plasmonic theranostic agents.

2.6 Gold Nanostructures for Imaging-Guided Therapy

To improve the treatment efficiency, combining imaging ability or introducing imaging modalities during therapy within single nanoscale platform, namely, imaging-guided therapy or theranostics, has been proposed. In terms of photothermal theranostics, the exact tumor location, size, and shape should be visualized by imaging initially to ensure that the whole tumor is effectively exposed to the laser during the treatment. Advanced imaging techniques would then allow real-time monitoring of therapeutic responses to achieve optimized efficiency. Nearly a decade ago, before the term theranostics or imaging-guided therapy was coined, the theranostic potential of nanoshells was demonstrated with simultaneous dark-field imaging and photothermal therapy [14, 170, 174]. This was soon followed by the use of nanorods and other core-shell nanostructures for the imaging and therapy of malignant cells *in vitro* [46, 228, 229]. The past several years have witnessed a tremendous increase in theranostic agents based on gold nanostructures either by combining a single imaging and therapeutic technique or by integrating dual-modality diagnostics with multiple therapeutic functionalities.

Intrinsically, NIR resonant gold nanostructures are theranostic agents without introducing other imaging or therapeutic modalities. As discussed in the previous sections, gold nanoparticles like nanoshells, nanorods, and nanostars with NIR absorption have been widely used in cancer photothermal therapy. Meanwhile,

imaging capabilities based on these gold nanoparticles have also been demonstrated, such as PAT and CT. For example, hollow gold nanoshells have been shown to generate intense photoacoustic signals and induce efficient photothermal treatment. Li et al. used PAT to assess the intravenous delivery of hollow nanoshells targeted to integrins that are overexpressed in both glioma and angiogenic blood vessels in a mouse model of glioma [113]. Mice were then treated with NIR laser, which elevated tumor temperature by 20.7 °C. It was found that photothermal therapy under PAT guidance significantly prolonged the survival of tumor-bearing mice. Recently, cyclic RGD peptide-conjugated plasmonic gold nanostars (RGD-GNS) were designed to specifically target overexpressed integrin $\alpha_v\beta_3$ on tumor neovasculature [198]. By using RGD-GNS, PA signal was significantly boosted for neovasculature visualization, offering high imaging specificity and nanomolar sensitivity. Furthermore, the high absorption-to-scattering ratio of RGD-GNS in the NIR region allows photothermal ablation to neovessels in tumor by laser irradiation, whose therapeutic effect can be noninvasively monitored by PAT. Thus, combining PAT with RGD-GNS makes it possible to image and inhibit tumor angiogenesis and monitor the tumor response in one “on-spot” theranostic platform.

Though gold nanostructures with NIR absorption are greatly promising as theranostic agents, introducing other imaging and therapeutic modalities is nevertheless necessary because of intrinsic drawbacks of these optical imaging methods and single photothermal treatment, as described in Sect. 2.4. Ballistic imaging methods such as OCT, TPL, and SERS suffer from shallow penetration and low spatial resolution, undermining their application in *in vivo* diagnosis, while for clinical CT, radiation risk is rather a serious concern. As a hybrid imaging modality, PAT manages to break through the optical diffusion limit in biological tissue, but its imaging sensitivity is mainly hampered by surrounding thermal noise and acoustic inherence of the medium itself in the form of black body. Thus, integrating other imaging and therapeutic modalities with advantages compensating for the existing weak points can provide comprehensive information and enable more accurate cancer imaging. In the clinic, magnetic resonance imaging (MRI) is one of the most powerful and noninvasive diagnostic techniques based on the interaction of protons with the surrounding molecules of tissues. MRI can offer high spatial resolution and the capacity to simultaneously obtain physiological and anatomical information. By combining MRI and the above imaging modalities, it is possible to obtain multiple imaging data using the advantages of both methods. Together with therapeutic approaches, gold nanostructures are supposed to find wide applications in imaging-guided therapy.

Recently, Halas group synthesized theranostic nanoshells by encapsulating them in a thin silica epilayer doped with Fe_3O_4 nanoparticles and ICG molecules and targeted HER-2 receptors in breast cancer cells via antibodies [109, 230, 231]. In this design, nanoshells enabled enhancement of ICG quantum yield from ~1 % to nearly ~85 %, and simultaneously, the porous silica layer enabled rapid water diffusion enhancing the MRI relaxivity of the Fe_3O_4 nanoparticles. These theranostic nanoshells provided dual modal MRI and NIR fluorescence imaging capabilities in breast cancer cells *in vitro* and simultaneous photothermal therapy when excited

with a 200 mW NIR laser overlapping the nanoshell plasmon resonance. The efficacy was also extended *in vivo* to mouse models with breast cancer xenografts. Nanoshells were administered intravenously, and the animals were imaged between 4 and 72 h postinjection. MRI and fluorescence imaging *in vivo* revealed that the maximum nanoshell accumulation in tumors occurs within 4 h of injection, and within 72 h, nanoshells clear from the tumors to the liver. By using gold-shelled iron oxide nanoclusters, Liu et al. designed a multimodal imaging-guided, magnetic targeting-enhanced photothermal ablation cancer treatment strategy [232]. Such nanocomposites after intravenous injection could be effectively attracted to the tumor, nearby which an external magnetic field was applied. Under the guidance of MRI and PAT, photothermal ablation with excellent therapeutic outcomes (100 % of tumor elimination after NIR laser treatment) was achieved in our animal experiments. In another study, ultrasmall superparamagnetic Fe₃O₄ nanoparticles were adsorbed on the surface of NaYF₄-based upconversion nanoparticles, on top of which thin gold shells were formed by seed-mediated reduction growth [233]. The multifunctional nanoparticles were successfully used for *in vivo* MR and upconversion luminescence imaging-guided and magnetically targeted photothermal therapy. Very recently, West et al. tethered gadolinium to NIR resonant nanoshells, imparting high r_1 relaxivity [234]. MRI- and CT-based modalities with gadolinium-nanoshell enhancement could be used to initially identify suspicious lesions within tissue. Afterwards, optical imaging including OCT and TPL with low-power NIR light could then be performed within appropriate fields of view to obtain molecular information regarding disease state. Finally, under the guidance of the multimodal imaging, NIR laser could be applied site specifically to locally ablate tumor. This class of core-shell nanoparticles is expected to be an attractive theranostic agent for imaging-guided tumor ablation.

Apart from nanoshells, nanorod-mediated theranostics have also rapidly increased within the past few years. Recently, Chen et al. designed theranostic nanorods coated by a mesoporous silica layer loaded with DOX for simultaneous TPL imaging with dual chemo-photothermal therapy in human lung cancer cells [11]. Maximum DOX release was observed with NIR laser treatment at a low pH (4.5) and solution temperature of 48 °C. A cell viability assay clearly indicated that enhanced therapeutic capability was achieved with dual treatment mechanisms rather than hyperthermia or chemotherapy. In another work, He's group developed silica-coated gold nanorods with an additional layer of PEG and loaded the two layers with 3,3'-diethylthiatricarbocyanine iodide (DTTC) and protoporphyrin IX (PpIX), a photosensitizer molecule [235]. The multifunctional nanorods successfully demonstrated diagnosis via SERS and fluorescence imaging *in vivo* in mice-bearing Hela tumors and treatment via photodynamic treatment mediated by PpIX. In 2011, Cui et al. synthesized folic acid-conjugated silica-modified gold nanorods with highly selective targeting, enhanced radiation therapy effects and excellent photothermal treatment effects on the gastric cancer cells, and strong X-ray attenuation for *in vivo* X-ray/CT imaging. The nanoprobe is claimed to be a promising candidate with excellent imaging and targeting ability for X-ray/CT imaging-guided targeting dual-mode-enhanced radiation and photothermal therapy.

2.7 Concluding Remarks

Because of their unique features and great potential for a variety of biomedical applications, gold nanostructures represent a major achievement in nanotechnology. The synergy of ideal chemical, physical, and optical properties in a single particle is a resounding affirmation of the promise of nanotechnology in general.

Gold nanostructures have opened new frontiers in medicine. As they are biocompatible, optically tunable, and bind to antibodies, nanogold have a great potential as agents for photothermal cancer therapy, as confirmed by their success in multiple animal studies. Clinical trials, spearheaded by gold nanoshells and currently under way, will most likely establish their efficacy for the treatment of human forms of cancer. Gold nanoparticles are also highly suitable for *in vivo* imaging studies based on their intrinsic optical and physical properties or through introducing other imaging modalities, with the added benefit of serving as agents for cancer therapy. Likewise, because they accumulate within tumors due to passive and active mechanisms, they hold great promise for revolutionizing cancer detection and therapy.

However, there are several problems, which are yet to be investigated. One of the most important issues is the potential long-term safety concerns of the gold nanoparticles since they are not biodegradable and would retain inside the body for long periods after administration. Another major challenge both in phototherapy and optical imaging is the limited light (even NIR light) penetration depth of no deeper than 1 cm, a great obstacle for tumors located deeply inside the body. Other basic mechanism questions like the response of immune system to photothermal treatment and tumor residues after photothermal ablation merit further investigation. It is hoped that, in the near future, these problems will be addressed and the novel properties of gold nanostructures will continue to be exploited in a growing number of applications. Clearly, it will be very exciting to see many existing applications make the successful transition from the laboratory bench to the clinic.

References

1. Dreaden EC, Alkilany AM, Huang X, Murphy CJ, El-Sayed MA (2012) The golden age: gold nanoparticles for biomedicine. *Chem Soc Rev* 41(7):2740–2779
2. Schuller JA, Barnard ES, Cai W, Jun YC, White JS, Brongersma ML (2010) Plasmonics for extreme light concentration and manipulation. *Nat Mater* 9(3):193–204
3. Grzelczak M, Perez-Juste J, Mulvaney P, Liz-Marzan LM (2008) Shape control in gold nanoparticle synthesis. *Chem Soc Rev* 37(9):1783–1791
4. Boisselier E, Astruc D (2009) Gold nanoparticles in nanomedicine: preparations, imaging, diagnostics, therapies and toxicity. *Chem Soc Rev* 38(6):1759–1782
5. Torchilin VP (2006) Multifunctional nanocarriers. *Adv Drug Deliv Rev* 58(14):1532–1555
6. Schneider GF, Subr V, Ulbrich K, Decher G (2009) Multifunctional cytotoxic stealth nanoparticles. A model approach with potential for cancer therapy. *Nano Lett* 9(2):636–642
7. Alkilany AM, Nagaria PK, Hexel CR, Shaw TJ, Murphy CJ, Wyatt MD (2009) Cellular uptake and cytotoxicity of gold nanorods: molecular origin of cytotoxicity and surface effects. *Small* 5(6):701–708

8. Qin Z, Bischof JC (2012) Thermophysical and biological responses of gold nanoparticle laser heating. *Chem Soc Rev* 41(3):1191–1217
9. Nie L, Chen X (2014) Structural and functional photoacoustic molecular tomography aided by emerging contrast agents. *Chem Soc Rev* 43(20):7132–7170
10. Liu H, Liu T, Wu X, Li L, Tan L, Chen D, Tang F (2012) Targeting gold nanoshells on silica nanorattles: a drug cocktail to fight breast tumors via a single irradiation with near-infrared laser light. *Adv Mater* 24(6):755–761
11. Zhang Z, Wang L, Wang J, Jiang X, Li X, Hu Z, Ji Y, Wu X, Chen C (2012) Mesoporous silica-coated gold nanorods as a light-mediated multifunctional theranostic platform for cancer treatment. *Adv Mater* 24(11):1418–1423
12. You J, Zhang R, Xiong C, Zhong M, Melancon M, Gupta S, Nick AM, Sood AK, Li C (2012) Effective photothermal chemotherapy using doxorubicin-loaded gold nanospheres that target EphB4 receptors in tumors. *Cancer Res* 72(18):4777–4786
13. Yavuz MS, Cheng Y, Chen J, Cobley CM, Zhang Q, Rycenga M, Xie J, Kim C, Song KH, Schwartz AG, Wang LV, Xia Y (2009) Gold nanocages covered by smart polymers for controlled release with near-infrared light. *Nat Mater* 8(12):935–939
14. Gobin AM, Lee MH, Halas NJ, James WD, Drezek RA, West JL (2007) Near-infrared resonant nanoshells for combined optical imaging and photothermal cancer therapy. *Nano Lett* 7(7):1929–1934
15. Webb JA, Bardhan R (2014) Emerging advances in nanomedicine with engineered gold nanostructures. *Nanoscale* 6(5):2502–2530
16. Giannini V, Fernández-Domínguez AI, Heck SC, Maier SA (2011) Plasmonic nanoantennas: fundamentals and their use in controlling the radiative properties of nanoemitters. *Chem Rev* 111(6):3888–3912
17. Jaque D, Martínez Maestro L, del Rosal B, Haro-Gonzalez P, Benayas A, Plaza JL, Martín Rodríguez E, García Sole J (2014) Nanoparticles for photothermal therapies. *Nanoscale* 6(16):9494–9530
18. Dong W, Li Y, Niu D, Ma Z, Liu X, Gu J, Zhao W, Zheng Y, Shi J (2013) A simple route to prepare monodisperse Au NP-decorated, dye-doped, superparamagnetic nanocomposites for optical, MR, and CT trimodal imaging. *Small* 9(15):2500–2508
19. Melancon MP, Lu W, Yang Z, Zhang R, Cheng Z, Elliot AM, Stafford J, Olson T, Zhang JZ, Li C (2008) In vitro and in vivo targeting of hollow gold nanoshells directed at epidermal growth factor receptor for photothermal ablation therapy. *Mol Cancer Ther* 7(6):1730–1739
20. Popovtzer R, Agrawal A, Kotov NA, Popovtzer A, Balter J, Carey TE, Kopelman R (2008) Targeted gold nanoparticles enable molecular CT imaging of cancer. *Nano Lett* 8(12):4593–4596
21. Samanta A, Jana S, Das RK, Chang YT (2014) Biocompatible surface-enhanced Raman scattering nanotags for in vivo cancer detection. *Nanomedicine (Lond)* 9(3):523–535
22. Jain PK, Huang X, El-Sayed IH, El-Sayed MA (2008) Noble metals on the nanoscale: optical and photothermal properties and some applications in imaging, sensing, biology, and medicine. *Acc Chem Res* 41(12):1578–1586
23. Huang X, Neretina S, El-Sayed MA (2009) Gold nanorods: from synthesis and properties to biological and biomedical applications. *Adv Mater* 21(48):4880–4910
24. Halas NJ, Lal S, Chang W-S, Link S, Nordlander P (2011) Plasmons in strongly coupled metallic nanostructures. *Chem Rev* 111(6):3913–3961
25. Weissleder R (2001) A clearer vision for in vivo imaging. *Nat Biotechnol* 19(4):316–317
26. Smith AM, Mancini MC, Nie S (2009) Bioimaging: second window for in vivo imaging. *Nat Nanotechnol* 4(11):710–711
27. Hsiangkuo Y, Christopher GK, Hanjun H, Christy MW, Gerald AG, Tuan V-D (2012) Gold nanostars: surfactant-free synthesis, 3D modelling, and two-photon photoluminescence imaging. *Nanotechnology* 23(7):075102
28. Zhu J, Yong KT, Roy I, Hu R, Ding H, Zhao LL, Swihart MT, He GS, Cui YP, Prasad PN (2010) Additive controlled synthesis of gold nanorods (GNRs) for two-photon luminescence imaging of cancer cells. *Nanotechnology* 21(28):8

29. Skrabalak SE, Au L, Li X, Xia Y (2007) Facile synthesis of Ag nanocubes and Au nanocages. *Nat Protoc* 2(9):2182–2190
30. Oldenburg SJ, Averitt RD, Westcott SL, Halas NJ (1998) Nanoengineering of optical resonances. *Chem Phys Lett* 288(2–4):243–247
31. Shimizu T, Teranishi T, Hasegawa S, Miyake M (2003) Size evolution of alkanethiol-protected gold nanoparticles by heat treatment in the solid state. *J Phys Chem B* 107(12):2719–2724
32. Ye X, Jin L, Caglayan H, Chen J, Xing G, Zheng C, Doan-Nguyen V, Kang Y, Engheta N, Kagan CR, Murray CB (2012) Improved size-tunable synthesis of monodisperse gold nanorods through the use of aromatic additives. *ACS Nano* 6(3):2804–2817
33. Pandian Senthil K, Isabel P-S, Benito R-G, JGd Abajo F, Luis ML-M (2008) High-yield synthesis and optical response of gold nanostars. *Nanotechnology* 19(1):015606
34. Lu X, Au L, McLellan J, Li Z-Y, Marquez M, Xia Y (2007) Fabrication of cubic nanocages and nanoframes by dealloying Au/Ag alloy nanoboxes with an aqueous etchant based on Fe(NO₃)₃ or NH₄OH. *Nano Lett* 7(6):1764–1769
35. Sonnichsen C, Reinhard BM, Liphardt J, Alivisatos AP (2005) A molecular ruler based on plasmon coupling of single gold and silver nanoparticles. *Nat Biotechnol* 23(6):741–745
36. Jain PK, Huang W, El-Sayed MA (2007) On the universal scaling behavior of the distance decay of plasmon coupling in metal nanoparticle pairs: a plasmon ruler equation. *Nano Lett* 7(7):2080–2088
37. Guo L, Xu Y, Ferhan AR, Chen G, Kim D-H (2013) Oriented gold nanoparticle aggregation for colorimetric sensors with surprisingly high analytical figures of merit. *J Am Chem Soc* 135(33):12338–12345
38. Xia F, Zuo X, Yang R, Xiao Y, Kang D, Vallee-Belisle A, Gong X, Yuen JD, Hsu BB, Heeger AJ, Plaxco KW (2010) Colorimetric detection of DNA, small molecules, proteins, and ions using unmodified gold nanoparticles and conjugated polyelectrolytes. *Proc Natl Acad Sci U S A* 107(24):10837–10841
39. Chen JIL, Chen Y, Ginger DS (2010) Plasmonic nanoparticle dimers for optical sensing of DNA in complex media. *J Am Chem Soc* 132(28):9600–9601
40. Anker JN, Hall WP, Lyandres O, Shah NC, Zhao J, Van Duyne RP (2008) Biosensing with plasmonic nanosensors. *Nat Mater* 7(6):442–453
41. Lim D-K, Jeon K-S, Kim HM, Nam J-M, Suh YD (2010) Nanogap-engineerable Raman-active nanodumbbells for single-molecule detection. *Nat Mater* 9(1):60–67
42. Nam J, Won N, Jin H, Chung H, Kim S (2009) pH-induced aggregation of gold nanoparticles for photothermal cancer therapy. *J Am Chem Soc* 131(38):13639–13645
43. Indrasekara AS, Paladini BJ, Naczynski DJ, Starovoytov V, Moghe PV, Fabris L (2013) Dimeric gold nanoparticle assemblies as tags for SERS-based cancer detection. *Adv Healthc Mater* 2(10):1370–1376
44. Lukianova-Hleb EY, Anderson LJE, Lee S, Hafner JH, Lapotko DO (2010) Hot plasmonic interactions: a new look at the photothermal efficacy of gold nanoparticles. *Phys Chem Chem Phys* 12(38):12237–12244
45. Hirsch LR, Stafford RJ, Bankson JA, Sershen SR, Rivera B, Price RE, Hazle JD, Halas NJ, West JL (2003) Nanoshell-mediated near-infrared thermal therapy of tumors under magnetic resonance guidance. *Proc Natl Acad Sci U S A* 100(23):13549–13554
46. Huang X, El-Sayed IH, Qian W, El-Sayed MA (2006) Cancer cell imaging and photothermal therapy in the near-infrared region by using gold nanorods. *J Am Chem Soc* 128(6):2115–2120
47. Chen J, Wang D, Xi J, Au L, Siekkinen A, Warsen A, Li Z-Y, Zhang H, Xia Y, Li X (2007) Immuno gold nanocages with tailored optical properties for targeted photothermal destruction of cancer cells. *Nano Lett* 7(5):1318–1322
48. Wang Y, Black KC, Luehmann H, Li W, Zhang Y, Cai X, Wan D, Liu SY, Li M, Kim P, Li ZY, Wang LV, Liu Y, Xia Y (2013) Comparison study of gold nanohexapods, nanorods, and nanocages for photothermal cancer treatment. *ACS Nano* 7(3):2068–2077

49. Chen C-C, Lin Y-P, Wang C-W, Tzeng H-C, Wu C-H, Chen Y-C, Chen C-P, Chen L-C, Wu Y-C (2006) DNA-gold nanorod conjugates for remote control of localized gene expression by near infrared irradiation. *J Am Chem Soc* 128(11):3709–3715
50. Jin Y, Gao X (2009) Spectrally tunable leakage-free gold nanocontainers. *J Am Chem Soc* 131(49):17774–17776
51. Huschka R, Barhoumi A, Liu Q, Roth JA, Ji L, Halas NJ (2012) Gene silencing by gold nanoshell-mediated delivery and laser-triggered release of antisense oligonucleotide and siRNA. *ACS Nano* 6(9):7681–7691
52. You J, Zhang G, Li C (2010) Exceptionally high payload of doxorubicin in hollow gold nanospheres for near-infrared light-triggered drug release. *ACS Nano* 4(2):1033–1041
53. Liu Y, Chang Z, Yuan H, Fales AM, Vo-Dinh T (2013) Quintuple-modality (SERS-MRI-CT-TPL-PTT) plasmonic nanoprobe for theranostics. *Nanoscale* 5(24):12126–12131
54. Link S, El-Sayed MA (2003) Optical properties and ultrafast dynamics of metallic nanocrystals. *Annu Rev Phys Chem* 54:331–366
55. Link S, El-Sayed MA (2000) Shape and size dependence of radiative, non-radiative and photothermal properties of gold nanocrystals. *Int Rev Phys Chem* 19(3):409–453
56. Link S, Burda C, Mohamed MB, Nikoobakht B, El-Sayed MA (1999) Laser photothermal melting and fragmentation of gold nanorods: energy and laser pulse-width dependence. *J Phys Chem A* 103(9):1165–1170
57. Tong L, Wei Q, Wei A, Cheng J-X (2009) Gold nanorods as contrast agents for biological imaging: optical properties, surface conjugation and photothermal effects†. *Photochem Photobiol* 85(1):21–32
58. Yuan H, Fales AM, Vo-Dinh T (2012) TAT peptide-functionalized gold nanostars: enhanced intracellular delivery and efficient NIR photothermal therapy using ultralow irradiance. *J Am Chem Soc* 134(28):11358–11361
59. Yuan H, Khoury CG, Wilson CM, Grant GA, Bennett AJ, Vo-Dinh T (2012) In vivo particle tracking and photothermal ablation using plasmon-resonant gold nanostars. *Nanomedicine* 8(8):1355–1363
60. Zhang Y, Yu J, Birch DJS, Chen Y (2010) Gold nanorods for fluorescence lifetime imaging in biology. *J Biomed Opt* 15(2):020504, 020504-020503
61. Park J, Estrada A, Schwartz JA, Diagaradjane P, Krishnan S, Dunn AK, Tunnell JW (2010) Intra-organ biodistribution of gold nanoparticles using intrinsic two-photon-induced photoluminescence. *Lasers Surg Med* 42(7):630–639
62. Wang Y, Xu J, Xia X, Yang M, Vangveravong S, Chen J, Mach RH, Xia Y (2012) SV119-gold nanocage conjugates: a new platform for targeting cancer cells via sigma-2 receptors. *Nanoscale* 4(2):421–424
63. Lewinski N, Colvin V, Drezek R (2008) Cytotoxicity of nanoparticles. *Small* 4(1):26–49
64. Paciotti GF, Myer L, Weinreich D, Goia D, Pavel N, McLaughlin RE, Tamarkin L (2004) Colloidal gold: a novel nanoparticle vector for tumor directed drug delivery. *Drug Deliv* 11(3):169–183
65. Love JC, Estroff LA, Kriebel JK, Nuzzo RG, Whitesides GM (2005) Self-assembled monolayers of thiolates on metals as a form of nanotechnology. *Chem Rev* 105(4):1103–1170
66. Brust M, Walker M, Bethell D, Schiffrin DJ, Whyman R (1994) Synthesis of thiol-derivatised gold nanoparticles in a two-phase liquid-liquid system. *J Chem Soc Chem Commun* 7:801–802
67. Walter M, Akola J, Lopez-Acevedo O, Jadzinsky PD, Calero G, Ackerson CJ, Whetten RL, Gronbeck H, Hakkinen H (2008) A unified view of ligand-protected gold clusters as superatom complexes. *Proc Natl Acad Sci U S A* 105(27):9157–9162
68. Martin BR, Dermody DJ, Reiss BD, Fang M, Lyon LA, Natan MJ, Mallouk TE (1999) Orthogonal self-assembly on colloidal gold-platinum nanorods. *Adv Mater* 11(12):1021–1025
69. Hou W, Dasog M, Scott RWJ (2009) Probing the relative stability of thiolate- and dithiolate-protected Au monolayer-protected clusters. *Langmuir* 25(22):12954–12961

70. Zhao Y, Pérez-Segarra W, Shi Q, Wei A (2005) Dithiocarbamate assembly on gold. *J Am Chem Soc* 127(20):7328–7329
71. Daniel M-C, Astruc D (2003) Gold nanoparticles: assembly, supramolecular chemistry, quantum-size-related properties, and applications toward biology, catalysis, and nanotechnology. *Chem Rev* 104(1):293–346
72. Yee CK, Ulman A, Ruiz JD, Parikh A, White H, Rafailovich M (2003) Alkyl selenide- and alkyl thiolate-functionalized gold nanoparticles: chain packing and bond nature. *Langmuir* 19(22):9450–9458
73. Schmid G, Pfeil R, Boese R, Bandermann F, Meyer S, Calis GHM, van der Velden JWA (1981) Au₅₅[P(C₆H₅)₃]₁₂Cl₆ – ein Goldcluster ungewöhnlicher Größe. *Chem Ber* 114(11):3634–3642
74. Peer D, Karp JM, Hong S, Farokhzad OC, Margalit R, Langer R (2007) Nanocarriers as an emerging platform for cancer therapy. *Nat Nanotechnol* 2(12):751–760
75. Au L, Zhang Q, Cobley CM, Gidding M, Schwartz AG, Chen J, Xia Y (2009) Quantifying the cellular uptake of antibody-conjugated Au nanocages by two-photon microscopy and inductively coupled plasma mass spectrometry. *ACS Nano* 4(1):35–42
76. Gittins DI, Caruso F (2001) Tailoring the polyelectrolyte coating of metal nanoparticles. *J Phys Chem B* 105(29):6846–6852
77. Gole A, Murphy CJ (2005) Polyelectrolyte-coated gold nanorods: synthesis, characterization and immobilization. *Chem Mater* 17(6):1325–1330
78. Murphy CJ, Thompson LB, Alkilany AM, Sisco PN, Boulos SP, Sivapalan ST, Yang JA, Chernak DJ, Huang J (2010) The many faces of gold nanorods. *J Phys Chem Lett* 1(19):2867–2875
79. Brown SD, Nativo P, Smith J-A, Stirling D, Edwards PR, Venugopal B, Flint DJ, Plumb JA, Graham D, Wheate NJ (2010) Gold nanoparticles for the improved anticancer drug delivery of the active component of oxaliplatin. *J Am Chem Soc* 132(13):4678–4684
80. Wong JK, Yip SP, Lee TM (2012) Silica-modified oligonucleotide-gold nanoparticle conjugate enables closed-tube colorimetric polymerase chain reaction. *Small* 8(2):214–219
81. Wu P, Gao Y, Zhang H, Cai C (2012) Aptamer-guided silver-gold bimetallic nanostructures with highly active surface-enhanced Raman scattering for specific detection and near-infrared photothermal therapy of human breast cancer cells. *Anal Chem* 84(18):7692–7699
82. Huh YS, Chung AJ, Erickson D (2009) Surface enhanced Raman spectroscopy and its application to molecular and cellular analysis. *Microfluid Nanofluid* 6(3):285–297
83. Liz-Marzán LM, Giersig M, Mulvaney P (1996) Synthesis of nanosized gold–silica core-shell particles. *Langmuir* 12(18):4329–4335
84. Jana NR, Earhart C, Ying JY (2007) Synthesis of water-soluble and functionalized nanoparticles by silica coating. *Chem Mater* 19(21):5074–5082
85. Banholzer MJ, Harris N, Millstone JE, Schatz GC, Mirkin CA (2010) Abnormally large plasmonic shifts in silica-protected gold triangular nanoprisms†. *J Phys Chem C* 114(16):7521–7526
86. Wang Y, Yan B, Chen L (2013) SERS tags: novel optical nanoprobe for bioanalysis. *Chem Rev* 113(3):1391–1428
87. Roti Roti JL (2008) Cellular responses to hyperthermia (40–46°C): cell killing and molecular events. *Int J Hyperther* 24(1):3–15
88. O’Grady NP, Barie PS, Bartlett JG, Bleck T, Garvey G, Jacobi J, Linden P, Maki DG, Nam M, Pasculle W, Pasquale MD, Tribett DL, Masur H (1998) Practice guidelines for evaluating new fever in critically ill adult patients. *Clin Infect Dis* 26(5):1042–1059
89. Fisher JW, Sarkar S, Buchanan CF, Szot CS, Whitney J, Hatcher HC, Torti SV, Rylander CG, Rylander MN (2010) Photothermal response of human and murine cancer cells to multi-walled carbon nanotubes after laser irradiation. *Cancer Res* 70(23):9855–9864
90. Hildebrandt B, Wust P, Ahlers O, Dieing A, Sreenivasa G, Kerner T, Felix R, Riess H (2002) The cellular and molecular basis of hyperthermia. *Crit Rev Oncol Hematol* 43(1):33–56

91. Habash RW, Bansal R, Krewski D, Alhafid HT (2007) Thermal therapy, part IV: electromagnetic and thermal dosimetry. *Crit Rev Biomed Eng* 35(1–2):123–182
92. Chicheł A, Skowronek J, Kubaszewska M, Kanikowski M (2007) Hyperthermia – description of a method and a review of clinical applications. *Rep Pract Oncol Radiother* 12(5):267–275
93. Pissuwan D, Valenzuela SM, Cortie MB (2006) Therapeutic possibilities of plasmonically heated gold nanoparticles. *Trends Biotechnol* 24(2):62–67
94. Kennedy LC, Bickford LR, Lewinski NA, Coughlin AJ, Hu Y, Day ES, West JL, Drezek RA (2011) A New Era for cancer treatment: gold-nanoparticle-mediated thermal therapies. *Small* 7(2):169–183
95. Dreaden EC, Mackey MA, Huang X, Kang B, El-Sayed MA (2011) Beating cancer in multiple ways using nanogold. *Chem Soc Rev* 40(7):3391–3404
96. Cheng L, Wang C, Feng L, Yang K, Liu Z (2014) Functional nanomaterials for phototherapies of cancer. *Chem Rev* 114(21):10869–10939
97. Caccamo AE, Desenzani S, Belloni L, Borghetti AF, Bettuzzi S (2006) Nuclear clusterin accumulation during heat shock response: implications for cell survival and thermo-tolerance induction in immortalized and prostate cancer cells. *J Cell Physiol* 207(1):208–219
98. Bardhan R, Lal S, Joshi A, Halas NJ (2011) Theranostic nanoshells: from probe design to imaging and treatment of cancer. *Acc Chem Res* 44(10):936–946
99. Melancon MP, Zhou M, Li C (2011) Cancer theranostics with near-infrared light-activatable multimodal nanoparticles. *Acc Chem Res* 44(10):947–956
100. Zhang Z, Wang J, Chen C (2013) Near-infrared light-mediated nanoplatfoms for cancer thermo-chemotherapy and optical imaging. *Adv Mater* 25(28):3869–3880
101. Matsushita-Ishiodori Y, Ohtsuki T (2012) Photoinduced RNA interference. *Acc Chem Res* 45(7):1039–1047
102. Chen W, Carubelli R, Liu H, Nordquist R (2003) Laser immunotherapy. *Mol Biotechnol* 25(1):37–43
103. Phonthammachai N, Kah JCY, Jun G, Sheppard CJR, Olivo MC, Mhaisalkar SG, White TJ (2008) Synthesis of contiguous silica–gold core–shell structures: critical parameters and processes. *Langmuir* 24(9):5109–5112
104. Brinson BE, Lassiter JB, Levin CS, Bardhan R, Mirin N, Halas NJ (2008) Nanoshells made easy: improving Au layer growth on nanoparticle surfaces. *Langmuir* 24(24):14166–14171
105. Lal S, Clare SE, Halas NJ (2008) Nanoshell-enabled photothermal cancer therapy: impending clinical impact. *Acc Chem Res* 41(12):1842–1851
106. O’Neal DP, Hirsch LR, Halas NJ, Payne JD, West JL (2004) Photo-thermal tumor ablation in mice using near infrared-absorbing nanoparticles. *Cancer Lett* 209(2):171–176
107. Huiyu L, Dong C, Fangqiong T, Gangjun D, Linlin L, Xianwei M, Wei L, Yangde Z, Xu T, Yi L (2008) Photothermal therapy of Lewis lung carcinoma in mice using gold nanoshells on carboxylated polystyrene spheres. *Nanotechnology* 19(45):455101
108. Liu H, Chen D, Li L, Liu T, Tan L, Wu X, Tang F (2011) Multifunctional gold nanoshells on silica nanorattles: a platform for the combination of photothermal therapy and chemotherapy with low systemic toxicity. *Angew Chem Int Ed* 50(4):891–895
109. Bardhan R, Chen W, Bartels M, Perez-Torres C, Botero MF, McAninch RW, Contreras A, Schiff R, Pautler RG, Halas NJ, Joshi A (2010) Tracking of multimodal therapeutic nanocomplexes targeting breast cancer in vivo. *Nano Lett* 10(12):4920–4928
110. Ma Y, Liang X, Tong S, Bao G, Ren Q, Dai Z (2013) Gold nanoshell nanomicelles for potential magnetic resonance imaging, light-triggered drug release, and photothermal therapy. *Adv Funct Mater* 23(7):815–822
111. Dong W, Li Y, Niu D, Ma Z, Gu J, Chen Y, Zhao W, Liu X, Liu C, Shi J (2011) Facile synthesis of monodisperse superparamagnetic Fe₃O₄ Core@hybrid@Au shell nanocomposite for bimodal imaging and photothermal therapy. *Adv Mater* 23(45):5392–5397
112. Lu W, Xiong C, Zhang G, Huang Q, Zhang R, Zhang JZ, Li C (2009) Targeted photothermal ablation of murine melanomas with melanocyte-stimulating hormone analog–conjugated hollow gold nanospheres. *Clin Cancer Res* 15(3):876–886

113. Lu W, Melancon MP, Xiong C, Huang Q, Elliott A, Song S, Zhang R, Flores LG, Gelovani JG, Wang LV, Ku G, Stafford RJ, Li C (2011) Effects of photoacoustic imaging and photothermal ablation therapy mediated by targeted hollow gold nanospheres in an orthotopic mouse xenograft model of glioma. *Cancer Res* 71(19):6116–6121
114. Cole JR, Mirin NA, Knight MW, Goodrich GP, Halas NJ (2009) Photothermal efficiencies of nanoshells and nanorods for clinical therapeutic applications. *J Phys Chem C* 113(28):12090–12094
115. Jain PK, El-Sayed IH, El-Sayed MA (2007) Au nanoparticles target cancer. *Nano Today* 2(1):18–29
116. Bardhan R, Mukherjee S, Mirin NA, Levit SD, Nordlander P, Halas NJ (2010) Nanosphere-in-a-nanoshell: a simple nanomatryushka†. *J Phys Chem C* 114(16):7378–7383
117. Ayala-Orozco C, Urban C, Knight MW, Urban AS, Neumann O, Bishnoi SW, Mukherjee S, Goodman AM, Charron H, Mitchell T, Shea M, Roy R, Nanda S, Schiff R, Halas NJ, Joshi A (2014) Au nanomatryoshkas as efficient near-infrared photothermal transducers for cancer treatment: benchmarking against nanoshells. *ACS Nano* 8(6):6372–6381
118. Ayala-Orozco C, Urban C, Bishnoi S, Urban A, Charron H, Mitchell T, Shea M, Nanda S, Schiff R, Halas N, Joshi A (2014) Sub-100nm gold nanomatryoshkas improve photo-thermal therapy efficacy in large and highly aggressive triple negative breast tumors. *J Control Release* 191:90–97
119. Gao Y, Li Y, Wang Y, Chen Y, Gu J, Zhao W, Ding J, Shi J (2014) Controlled synthesis of multilayered gold nanoshells for enhanced photothermal therapy and SERS detection. *Small* 11(1):77–83
120. Jorden D, Goodrich GP, Schwartz J, Halas NJ, West J (2012) Nanospectra biosciences. <http://www.nanospectra.com/index.html>
121. Nikoobakht B, El-Sayed MA (2003) Preparation and growth mechanism of gold nanorods (NRs) using seed-mediated growth method. *Chem Mater* 15(10):1957–1962
122. Jain PK, Lee KS, El-Sayed IH, El-Sayed MA (2006) Calculated absorption and scattering properties of gold nanoparticles of different size, shape, and composition: applications in biological imaging and biomedicine. *J Phys Chem B* 110(14):7238–7248
123. von Maltzahn G, Park J-H, Agrawal A, Bandaru NK, Das SK, Sailor MJ, Bhatia SN (2009) Computationally guided photothermal tumor therapy using long-circulating gold nanorod antennas. *Cancer Res* 69(9):3892–3900
124. Dickerson EB, Dreaden EC, Huang X, El-Sayed IH, Chu H, Pushpanketh S, McDonald JF, El-Sayed MA (2008) Gold nanorod assisted near-infrared plasmonic photothermal therapy (PPTT) of squamous cell carcinoma in mice. *Cancer Lett* 269(1):57–66
125. Choi WI, Kim J-Y, Kang C, Byeon CC, Kim YH, Tae G (2011) Tumor regression in vivo by photothermal therapy based on gold-nanorod-loaded, functional nanocarriers. *ACS Nano* 5(3):1995–2003
126. Li Z, Huang P, Zhang X, Lin J, Yang S, Liu B, Gao F, Xi P, Ren Q, Cui D (2009) RGD-conjugated dendrimer-modified gold nanorods for in vivo tumor targeting and photothermal therapy†. *Mol Pharm* 7(1):94–104
127. Horiguchi Y, Honda K, Kato Y, Nakashima N, Niidome Y (2008) Photothermal reshaping of gold nanorods depends on the passivating layers of the nanorod surfaces. *Langmuir* 24(20):12026–12031
128. Candice LD, Pinhas E, Astrid C-R, Steven LJ, Jeffrey JLC (2009) Depth of photothermal conversion of gold nanorods embedded in a tissue-like phantom. *Nanotechnology* 20(19):195102
129. Chon JWM, Bullen C, Zijlstra P, Gu M (2007) Spectral encoding on gold nanorods doped in a silica sol-gel matrix and its application to high-density optical data storage. *Adv Funct Mater* 17(6):875–880
130. Zijlstra P, Chon JWM, Gu M (2007) Effect of heat accumulation on the dynamic range of a gold nanorod doped polymer nanocomposite for optical laser writing and patterning. *Opt Express* 15(19):12151–12160

131. Huang P, Bao L, Zhang C, Lin J, Luo T, Yang D, He M, Li Z, Gao G, Gao B, Fu S, Cui D (2011) Folic acid-conjugated silica-modified gold nanorods for X-ray/CT imaging-guided dual-mode radiation and photo-thermal therapy. *Biomaterials* 32(36):9796–9809
132. Sun Y, Xia Y (2004) Mechanistic study on the replacement reaction between silver nanostructures and chloroauric acid in aqueous medium. *J Am Chem Soc* 126(12):3892–3901
133. Chen J, McLellan JM, Siekkinen A, Xiong Y, Li Z-Y, Xia Y (2006) Facile synthesis of gold–silver nanocages with controllable pores on the surface. *J Am Chem Soc* 128(46):14776–14777
134. Skrabalak SE, Chen J, Sun Y, Lu X, Au L, Copley CM, Xia Y (2008) Gold nanocages: synthesis, properties, and applications. *Acc Chem Res* 41(12):1587–1595
135. Chen J, Glaus C, Laforest R, Zhang Q, Yang M, Gidding M, Welch MJ, Xia Y (2010) Gold nanocages as photothermal transducers for cancer treatment. *Small* 6(7):811–817
136. Sun T, Wang Y, Wang Y, Xu J, Zhao X, Vangveravong S, Mach RH, Xia Y (2014) Using SV119-gold nanocage conjugates to eradicate cancer stem cells through a combination of photothermal and chemo therapies. *Adv Healthc Mater* 3(8):1283–1291
137. Julien RGN, Delphine M, Frederic L, Nicholas PB, Sophie M, Yann L, Jacqueline M, Frederic C, Guillaume M, Ana-Maria G, Alexis M, Emmanuel C, Patrice LB, Kenji K, Stephane P (2012) Synthesis of PEGylated gold nanostars and bipyramids for intracellular uptake. *Nanotechnology* 23(46):465602
138. Lu W, Singh AK, Khan SA, Senapati D, Yu H, Ray PC (2010) Gold nano-popcorn-based targeted diagnosis, nanotherapy treatment, and in situ monitoring of photothermal therapy response of prostate cancer cells using surface-enhanced Raman spectroscopy. *J Am Chem Soc* 132(51):18103–18114
139. Gobin AM, Watkins EM, Quevedo E, Colvin VL, West JL (2010) Near-infrared-resonant gold/gold sulfide nanoparticles as a photothermal cancer therapeutic agent. *Small* 6(6):745–752
140. Pelaz B, Grazu V, Ibarra A, Magen C, del Pino P, de la Fuente JM (2012) Tailoring the synthesis and heating ability of gold nanoprisms for bioapplications. *Langmuir* 28(24):8965–8970
141. Tsai MF, Chang SH, Cheng FY, Shanmugam V, Cheng YS, Su CH, Yeh CS (2013) Au nanorod design as light-absorber in the first and second biological near-infrared windows for in vivo photothermal therapy. *ACS Nano* 7(6):5330–5342
142. Rosenberg SA, Lotze MT, Yang JC, Linehan WM, Seipp C, Calabro S, Karp SE, Sherry RM, Steinberg S, White DE (1989) Combination therapy with interleukin-2 and alpha-interferon for the treatment of patients with advanced cancer. *J Clin Oncol* 7(12):1863–1874
143. O’Shaughnessy J, Miles D, Vukelja S, Moiseyenko V, Ayoub J-P, Cervantes G, Fumoleau P, Jones S, Lui W-Y, Mauriac L, Twelves C, Van Hazel G, Verma S, Leonard R (2002) Superior survival with capecitabine plus docetaxel combination therapy in anthracycline-pretreated patients with advanced breast cancer: phase III trial results. *J Clin Oncol* 20(12):2812–2823
144. Coley HM (2008) Mechanisms and strategies to overcome chemotherapy resistance in metastatic breast cancer. *Cancer Treat Rev* 34(4):378–390
145. Fidler IJ (2003) The pathogenesis of cancer metastasis: the ‘seed and soil’ hypothesis revisited. *Nat Rev Cancer* 3(6):453–458
146. Sargent DJ, Wieand HS, Haller DG, Gray R, Benedetti JK, Buyse M, Labianca R, Seitz JF, O’Callaghan CJ, Francis G, Grothey A, O’Connell M, Catalano PJ, Blanke CD, Kerr D, Green E, Wolmark N, Andre T, Goldberg RM, De Gramont A (2005) Disease-free survival versus overall survival as a primary end point for adjuvant colon cancer studies: individual patient data from 20,898 patients on 18 randomized trials. *J Clin Oncol* 23(34):8664–8670
147. Lee S-M, Kim HJ, Ha Y-J, Park YN, Lee S-K, Park Y-B, Yoo K-H (2012) Targeted chemophotothermal treatments of rheumatoid arthritis using gold half-shell multifunctional nanoparticles. *ACS Nano* 7(1):50–57
148. Dougherty TJ, Gomer CJ, Henderson BW, Jori G, Kessel D, Korbek M, Moan J, Peng Q (1998) Photodynamic therapy. *J Natl Cancer Inst* 90(12):889–905

149. Jang B, Park J-Y, Tung C-H, Kim I-H, Choi Y (2011) Gold nanorod–photosensitizer complex for near-infrared fluorescence imaging and photodynamic/photothermal therapy in vivo. *ACS Nano* 5(2):1086–1094
150. Wang J, Zhu G, You M, Song E, Shukoor MI, Zhang K, Altman MB, Chen Y, Zhu Z, Huang CZ, Tan W (2012) Assembly of aptamer switch probes and photosensitizer on gold nanorods for targeted photothermal and photodynamic cancer therapy. *ACS Nano* 6(6):5070–5077
151. Lin J, Wang S, Huang P, Wang Z, Chen S, Niu G, Li W, He J, Cui D, Lu G, Chen X, Nie Z (2013) Photosensitizer-loaded gold vesicles with strong plasmonic coupling effect for imaging-guided photothermal/photodynamic therapy. *ACS Nano* 7(6):5320–5329
152. Wang S, Huang P, Nie L, Xing R, Liu D, Wang Z, Lin J, Chen S, Niu G, Lu G, Chen X (2013) Single continuous wave laser induced photodynamic/plasmonic photothermal therapy using photosensitizer-functionalized gold nanostars. *Adv Mater* 25(22):3055–3061
153. Vijayaraghavan P, Liu CH, Vankayala R, Chiang CS, Hwang KC (2014) Designing multi-branched gold nanoechinus for NIR light activated dual modal photodynamic and photothermal therapy in the second biological window. *Adv Mater* 26(39):6689–6695
154. Li Y, Wen T, Zhao R, Liu X, Ji T, Wang H, Shi X, Shi J, Wei J, Zhao Y, Wu X, Nie G (2014) Localized electric field of plasmonic nanoplatform enhanced photodynamic tumor therapy. *ACS Nano* 8(11):11529–11542
155. Min Y, Mao C-Q, Chen S, Ma G, Wang J, Liu Y (2012) Combating the drug resistance of cisplatin using a platinum prodrug based delivery system. *Angew Chem Int Ed* 51(27):6742–6747
156. May JP, Li S-D (2013) Hyperthermia-induced drug targeting. *Expert Opin Drug Deliv* 10(4):511–527
157. Hauck TS, Jennings TL, Yatsenko T, Kumaradas JC, Chan WCW (2008) Enhancing the toxicity of cancer chemotherapeutics with gold nanorod hyperthermia. *Adv Mater* 20(20):3832–3838
158. Ghosh P, Han G, De M, Kim CK, Rotello VM (2008) Gold nanoparticles in delivery applications. *Adv Drug Deliv Rev* 60(11):1307–1315
159. You J-O, Guo P, Auguste DT (2013) A drug-delivery vehicle combining the targeting and thermal ablation of HER2+ breast-cancer cells with triggered drug release. *Angew Chem Int Ed* 52(15):4141–4146
160. Nam J, La W-G, Hwang S, Ha YS, Park N, Won N, Jung S, Bhang SH, Ma Y-J, Cho Y-M, Jin M, Han J, Shin J-Y, Wang EK, Kim SG, Cho S-H, Yoo J, Kim B-S, Kim S (2013) pH-responsive assembly of gold nanoparticles and “Spatiotemporally Concerted” drug release for synergistic cancer therapy. *ACS Nano* 7(4):3388–3402
161. Lee S-M, Park H, Yoo K-H (2010) Synergistic cancer therapeutic effects of locally delivered drug and heat using multifunctional nanoparticles. *Adv Mater* 22(36):4049–4053
162. You J, Shao R, Wei X, Gupta S, Li C (2010) Near-infrared light triggers release of paclitaxel from biodegradable microspheres: photothermal effect and enhanced antitumor activity. *Small* 6(9):1022–1031
163. You J, Zhang R, Zhang G, Zhong M, Liu Y, Van Pelt CS, Liang D, Wei W, Sood AK, Li C (2012) Photothermal-chemotherapy with doxorubicin-loaded hollow gold nanospheres: a platform for near-infrared light-triggered drug release. *J Control Release* 158(2):319–328
164. Yang X, Liu Z, Li Z, Pu F, Ren J, Qu X (2013) Near-infrared-controlled, targeted hydrophobic drug-delivery system for synergistic cancer therapy. *Chem Eur J* 19(31):10388–10394
165. Shen S, Tang H, Zhang X, Ren J, Pang Z, Wang D, Gao H, Qian Y, Jiang X, Yang W (2013) Targeting mesoporous silica-encapsulated gold nanorods for chemo-photothermal therapy with near-infrared radiation. *Biomaterials* 34(12):3150–3158
166. Xiao Z, Ji C, Shi J, Pridgen EM, Frieder J, Wu J, Farokhzad OC (2012) DNA self-assembly of targeted near-infrared-responsive gold nanoparticles for cancer thermo-chemotherapy. *Angew Chem Int Ed* 51(47):11853–11857
167. Zhang Z, Wang J, Nie X, Wen T, Ji Y, Wu X, Zhao Y, Chen C (2014) Near infrared laser-induced targeted cancer therapy using thermoresponsive polymer encapsulated gold nanorods. *J Am Chem Soc* 136(20):7317–7326

168. Sokolov K, Follen M, Aaron J, Pavlova I, Malpica A, Lotan R, Richards-Kortum R (2003) Real-time vital optical imaging of precancer using anti-epidermal growth factor receptor antibodies conjugated to gold nanoparticles. *Cancer Res* 63(9):1999–2004
169. El-Sayed IH, Huang X, El-Sayed MA (2005) Surface plasmon resonance scattering and absorption of anti-EGFR antibody conjugated gold nanoparticles in cancer diagnostics: applications in oral cancer. *Nano Lett* 5(5):829–834
170. Loo C, Lowery A, Halas N, West J, Drezek R (2005) Immunotargeted nanoshells for integrated cancer imaging and therapy. *Nano Lett* 5(4):709–711
171. Loo C, Hirsch L, Lee M-H, Chang E, West J, Halas N, Drezek R (2005) Gold nanoshell bioconjugates for molecular imaging in living cells. *Opt Lett* 30(9):1012–1014
172. Ding H, Yong K-T, Roy I, Pudavar HE, Law WC, Bergey EJ, Prasad PN (2007) Gold nanorods coated with multilayer polyelectrolyte as contrast agents for multimodal imaging. *J Phys Chem C* 111(34):12552–12557
173. Chanda N, Shukla R, Katti KV, Kannan R (2009) Gastrin releasing protein receptor specific gold nanorods: breast and prostate tumor avid nanovectors for molecular imaging. *Nano Lett* 9(5):1798–1805
174. Loo C, Lin A, Hirsch L, Lee MH, Barton J, Halas NJ, West J, Drezek R (2004) Nanoshell-enabled photonics-based imaging and therapy of cancer. *Technol Cancer Res Treat* 3(1):33–40
175. Zagaynova EV, Shirmanova MV, Kirillin MY, Khlebtsov BN, Orlova AG, Balalaeva IV, Sirotkina MA, Bugrova ML, Agrba PD, Kamensky VA (2008) Contrasting properties of gold nanoparticles for optical coherence tomography: phantom, in vivo studies and Monte Carlo simulation. *Phys Med Biol* 53(18):4995
176. Oldenburg AL, Hansen MN, Ralston TS, Wei A, Boppart SA (2009) Imaging gold nanorods in excised human breast carcinoma by spectroscopic optical coherence tomography. *J Mater Chem* 19(35):6407–6411
177. Kim CS, Wilder-Smith P, Ahn Y-C, Liaw L-HL, Chen Z, Kwon YJ (2009) Enhanced detection of early-stage oral cancer in vivo by optical coherence tomography using multimodal delivery of gold nanoparticles. *J Biomed Opt* 14(3):034008, 034008-034008
178. Huang D, Swanson E, Lin C, Schuman J, Stinson W, Chang W, Hee M, Flotte T, Gregory K, Puliafito C et al (1991) Optical coherence tomography. *Science* 254(5035):1178–1181
179. Zhou Y, Wu X, Wang T, Ming T, Wang PN, Zhou LW, Chen JY (2010) A comparison study of detecting gold nanorods in living cells with confocal reflectance microscopy and two-photon fluorescence microscopy. *J Microsc* 237(2):200–207
180. Jiang Y, Horimoto NN, Imura K, Okamoto H, Matsui K, Shigemoto R (2009) Bioimaging with two-photon-induced luminescence from triangular nanoplates and nanoparticle aggregates of gold. *Adv Mater* 21(22):2309–2313
181. Wang H, Huff TB, Zweifel DA, He W, Low PS, Wei A, Cheng JX (2005) In vitro and in vivo two-photon luminescence imaging of single gold nanorods. *Proc Natl Acad Sci U S A* 102(44):15752–15756
182. Loumagne M, Richard A, Laverdant J, Nutarelli D, Débarre A (2010) Ligand-induced anisotropy of the two-photon luminescence of spherical gold particles in solution unraveled at the single particle level. *Nano Lett* 10(8):2817–2824
183. Durr NJ, Larson T, Smith DK, Korgel BA, Sokolov K, Ben-Yakar A (2007) Two-photon luminescence imaging of cancer cells using molecularly targeted gold nanorods. *Nano Lett* 7(4):941–945
184. Huff TB, Hansen MN, Zhao Y, Cheng J-X, Wei A (2007) Controlling the cellular uptake of gold nanorods. *Langmuir* 23(4):1596–1599
185. He W, Wang H, Hartmann LC, Cheng JX, Low PS (2007) In vivo quantitation of rare circulating tumor cells by multiphoton intravital flow cytometry. *Proc Natl Acad Sci U S A* 104(28):11760–11765
186. Liang G, Tegy JV, Vengadesan N (2011) Nanoshells for in vivo imaging using two-photon excitation microscopy. *Nanotechnology* 22(36):365102

187. Tong L, Cobley CM, Chen J, Xia Y, Cheng J-X (2010) Bright three-photon luminescence from gold/silver alloyed nanostructures for bioimaging with negligible photothermal toxicity. *Angew Chem Int Ed* 49(20):3485–3488
188. Wang LV (2008) Tutorial on photoacoustic microscopy and computed tomography. *IEEE J Sel Top Quantum Electron* 14(1):171–179
189. Wang Y, Xie X, Wang X, Ku G, Gill KL, O'Neal DP, Stoica G, Wang LV (2004) Photoacoustic tomography of a nanoshell contrast agent in the in vivo rat brain. *Nano Lett* 4(9):1689–1692
190. Jokerst JV, Cole AJ, Van de Sompel D, Gambhir SS (2012) Gold nanorods for ovarian cancer detection with photoacoustic imaging and resection guidance via Raman imaging in living mice. *ACS Nano* 6(11):10366–10377
191. Chen Y-S, Frey W, Kim S, Kruizinga P, Homan K, Emelianov S (2011) Silica-coated gold nanorods as photoacoustic signal nanoamplifiers. *Nano Lett* 11(2):348–354
192. Jokerst JV, Thangaraj M, Kempen PJ, Sinclair R, Gambhir SS (2012) Photoacoustic imaging of mesenchymal stem cells in living mice via silica-coated gold nanorods. *ACS Nano* 6(7):5920–5930
193. Li W, Brown PK, Wang LV, Xia Y (2011) Gold nanocages as contrast agents for photoacoustic imaging. *Contrast Media Mol Imaging* 6(5):370–377
194. Yang X, Skrabalak SE, Li Z-Y, Xia Y, Wang LV (2007) Photoacoustic tomography of a rat cerebral cortex in vivo with Au nanocages as an optical contrast agent. *Nano Lett* 7(12):3798–3802
195. Song KH, Kim C, Cobley CM, Xia Y, Wang LV (2008) Near-infrared gold nanocages as a new class of tracers for photoacoustic sentinel lymph node mapping on a rat model. *Nano Lett* 9(1):183–188
196. Kim C, Cho EC, Chen J, Song KH, Au L, Favazza C, Zhang Q, Cobley CM, Gao F, Xia Y, Wang LV (2010) In vivo molecular photoacoustic tomography of melanomas targeted by bioconjugated gold nanocages. *ACS Nano* 4(8):4559–4564
197. Kim C, Song H-M, Cai X, Yao J, Wei A, Wang LV (2011) In vivo photoacoustic mapping of lymphatic systems with plasmon-resonant nanostars. *J Mater Chem* 21(9):2841–2844
198. Nie L, Wang S, Wang X, Rong P, Ma Y, Liu G, Huang P, Lu G, Chen X (2014) In vivo volumetric photoacoustic molecular angiography and therapeutic monitoring with targeted plasmonic nanostars. *Small* 10(8):1585–1593
199. Cheng K, Kothapalli S-R, Liu H, Koh AL, Jokerst JV, Jiang H, Yang M, Li J, Levi J, Wu JC, Gambhir SS, Cheng Z (2014) Construction and validation of nano gold tripods for molecular imaging of living subjects. *J Am Chem Soc* 136(9):3560–3571
200. Galper MW, Saung MT, Fuster V, Roessl E, Thran A, Proksa R, Fayad ZA, Cormode DP (2012) Effect of computed tomography scanning parameters on gold nanoparticle and iodine contrast. *Invest Radiol* 47(8):475–481
201. Hainfeld JF, Slatkin DN, Focella TM, Smilowitz HM (2006) Gold nanoparticles: a new x-ray contrast agent. *Br J Radiol* 79(939):248–253
202. Kim D, Park S, Lee JH, Jeong YY, Jon S (2007) Antibiofouling polymer-coated gold nanoparticles as a contrast agent for in vivo x-ray computed tomography imaging. *J Am Chem Soc* 129(24):7661–7665
203. Boote E, Fent G, Kattumuri V, Casteel S, Katti K, Chanda N, Kannan R, Katti K, Churchill R (2010) Gold nanoparticle contrast in a phantom and juvenile swine: models for molecular imaging of human organs using x-ray computed tomography. *Acad Radiol* 17(4):410–417
204. Kattumuri V, Katti K, Bhaskaran S, Boote EJ, Casteel SW, Fent GM, Robertson DJ, Chandrasekhar M, Kannan R, Katti KV (2007) Gum Arabic as a phytochemical construct for the stabilization of gold nanoparticles: in vivo pharmacokinetics and x-ray-contrast-imaging studies. *Small* 3(2):333–341
205. Peng C, Zheng L, Chen Q, Shen M, Guo R, Wang H, Cao X, Zhang G, Shi X (2012) PEGylated dendrimer-entrapped gold nanoparticles for in vivo blood pool and tumor imaging by computed tomography. *Biomaterials* 33(4):1107–1119

206. Chie K, Yasuhito U, Mikako O, Atsushi H, Yasuhiro M, Kenji K (2010) X-ray computed tomography contrast agents prepared by seeded growth of gold nanoparticles in PEGylated dendrimer. *Nanotechnology* 21(24):245104
207. Reuveni T, Motiei M, Romman Z, Popovtzer A, Popovtzer R (2011) Targeted gold nanoparticles enable molecular CT imaging of cancer: an in vivo study. *Int J Nanomedicine* 6:2859–2864
208. Sun I-C, Eun D-K, Koo H, Ko C-Y, Kim H-S, Yi DK, Choi K, Kwon IC, Kim K, Ahn C-H (2011) Tumor-targeting gold particles for dual computed tomography/optical cancer imaging. *Angew Chem Int Ed* 50(40):9348–9351
209. Eck W, Nicholson AI, Zentgraf H, Semmler W, Bartling S (2010) Anti-CD4-targeted gold nanoparticles induce specific contrast enhancement of peripheral lymph nodes in x-ray computed tomography of live mice. *Nano Lett* 10(7):2318–2322
210. Campion A, Kambhampati P (1998) Surface-enhanced Raman scattering. *Chem Soc Rev* 27(4):241–250
211. Moskovits M (2005) Surface-enhanced Raman spectroscopy: a brief retrospective. *J Raman Spectrosc* 36(6–7):485–496
212. Alvarez-Puebla RA, Liz-Marzan LM (2012) Traps and cages for universal SERS detection. *Chem Soc Rev* 41(1):43–51
213. Vo-Dinh T, Wang HN, Scaffidi J (2010) Plasmonic nanoprobe for SERS biosensing and bioimaging. *J Biophotonics* 3(1–2):89–102
214. Wachsmann-Hogiu S, Weeks T, Huser T (2009) Chemical analysis in vivo and in vitro by Raman spectroscopy—from single cells to humans. *Curr Opin Biotechnol* 20(1):63–73
215. Levin CS, Kundu J, Barhoumi A, Halas NJ (2009) Nanoshell-based substrates for surface enhanced spectroscopic detection of biomolecules. *Analyst* 134(9):1745–1750
216. Larmour IA, Graham D (2011) Surface enhanced optical spectroscopies for bioanalysis. *Analyst* 136(19):3831–3853
217. Qian X, Peng XH, Ansari DO, Yin-Goen Q, Chen GZ, Shin DM, Yang L, Young AN, Wang MD, Nie S (2008) In vivo tumor targeting and spectroscopic detection with surface-enhanced Raman nanoparticle tags. *Nat Biotechnol* 26(1):83–90
218. Park J-H, von Maltzahn G, Ong LL, Centrone A, Hatton TA, Ruoslahti E, Bhatia SN, Sailor MJ (2010) Cooperative nanoparticles for tumor detection and photothermally triggered drug delivery. *Adv Mater* 22(8):880–885
219. Samanta A, Maiti KK, Soh K-S, Liao X, Vendrell M, Dinis US, Yun S-W, Bhuvaneshwari R, Kim H, Rautela S, Chung J, Olivo M, Chang Y-T (2011) Ultrasensitive near-infrared Raman reporters for SERS-based in vivo cancer detection. *Angew Chem Int Ed* 50(27):6089–6092
220. Kircher MF, de la Zerda A, Jokerst JV, Zavaleta CL, Kempen PJ, Mittra E, Pitter K, Huang RM, Campos C, Habte F, Sinclair R, Brennan CW, Mellinghoff IK, Holland EC, Gambhir SS (2012) A brain tumor molecular imaging strategy using a new triple-modality MRI-photoacoustic-Raman nanoparticle. *Nat Med* 18(5):829–835
221. Karabeber H, Huang R, Iacono P, Samii JM, Pitter K, Holland EC, Kircher MF (2014) Guiding brain tumor resection using surface-enhanced Raman scattering nanoparticles and a hand-held Raman scanner. *ACS Nano* 8(10):9755–9766
222. Keren S, Zavaleta C, Cheng Z, de la Zerda A, Gheysens O, Gambhir SS (2008) Noninvasive molecular imaging of small living subjects using Raman spectroscopy. *Proc Natl Acad Sci U S A* 105(15):5844–5849
223. Zavaleta CL, Smith BR, Walton I, Doering W, Davis G, Shojaei B, Natan MJ, Gambhir SS (2009) Multiplexed imaging of surface enhanced Raman scattering nanotags in living mice using noninvasive Raman spectroscopy. *Proc Natl Acad Sci U S A* 106(32):13511–13516
224. von Maltzahn G, Centrone A, Park JH, Ramanathan R, Sailor MJ, Hatton TA, Bhatia SN (2009) SERS-coded gold nanorods as a multifunctional platform for densely multiplexed near-infrared imaging and photothermal heating. *Adv Mater* 21(31):3175–3180

225. Maiti KK, Dinish US, Samanta A, Vendrell M, Soh KS, Park SJ, Olivo M, Chang YT (2012) Multiplex targeted in vivo cancer detection using sensitive near-infrared SERS nanotags. *Nano Today* 7(2):85–93
226. Kang H, Jeong S, Park Y, Yim J, Jun BH, Kyeong S, Yang JK, Kim G, Hong S, Lee LP, Kim JH, Lee HY, Jeong DH, Lee YS (2013) Near-infrared SERS nanoprobe with plasmonic Au/Ag hollow-shell assemblies for in vivo multiplex detection. *Adv Funct Mater* 23(30):3719–3727
227. Iacono P, Karabeber H, Kircher MF (2014) A “Schizophonic” all-in-one nanoparticle coating for multiplexed SE(R)RS biomedical imaging. *Angew Chem Int Ed* 126(44):11950–11955
228. Kim J, Park S, Lee JE, Jin SM, Lee JH, Lee IS, Yang I, Kim JS, Kim SK, Cho MH, Hyeon T (2006) Designed fabrication of multifunctional magnetic gold nanoshells and their application to magnetic resonance imaging and photothermal therapy. *Angew Chem Int Ed* 45(46):7754–7758
229. Ji X, Shao R, Elliott AM, Stafford RJ, Esparza-Coss E, Bankson JA, Liang G, Luo Z-P, Park K, Markert JT, Li C (2007) Bifunctional gold nanoshells with a superparamagnetic iron oxide–silica core suitable for both MR imaging and photothermal therapy. *J Phys Chem C* 111(17):6245–6251
230. Chen W, Bardhan R, Bartels M, Perez-Torres C, Pautler RG, Halas NJ, Joshi A (2010) A molecularly targeted theranostic probe for ovarian cancer. *Mol Cancer Ther* 9(4):1028–1038
231. Bardhan R, Chen WX, Perez-Torres C, Bartels M, Huschka RM, Zhao LL, Morosan E, Pautler RG, Joshi A, Halas NJ (2009) Nanoshells with targeted simultaneous enhancement of magnetic and optical imaging and photothermal therapeutic response. *Adv Funct Mater* 19(24):3901–3909
232. Li Z, Yin S, Cheng L, Yang K, Li Y, Liu Z (2014) Magnetic targeting enhanced theranostic strategy based on multimodal imaging for selective ablation of cancer. *Adv Funct Mater* 24(16):2312–2321
233. Cheng L, Yang K, Li Y, Chen J, Wang C, Shao M, Lee ST, Liu Z (2011) Facile preparation of multifunctional upconversion nanoprobe for multimodal imaging and dual-targeted photothermal therapy. *Angew Chem Int Ed Engl* 50(32):7385–7390
234. Coughlin AJ, Ananta JS, Deng N, Larina IV, Decuzzi P, West JL (2014) Gadolinium-conjugated gold nanoshells for multimodal diagnostic imaging and photothermal cancer therapy. *Small* 10(3):556–565
235. Zhang Y, Qian J, Wang D, Wang Y, He S (2013) Multifunctional gold nanorods with ultrahigh stability and tunability for in vivo fluorescence imaging, SERS detection, and photodynamic therapy. *Angew Chem Int Ed Engl* 52(4):1148–1151

Chapter 3

Gold Nanorods for Biomedical Imaging and Therapy in Cancer

Zhenzhi Shi, Yu Xu, and Aiguo Wu

Abstract Gold nanorods (AuNRs) are an important type of noble metal nanoparticles with some superior performances, such as easy synthesis, easy modification, excellent biocompatibility, tunable surface plasmon effect, and photothermal and photodynamic effects. They have been proved to be promising in a wide range of biomedical applications such as biomedical imaging, photothermal therapy, photodynamic therapy, and drug or gene delivery. Because the longitudinally localized surface plasmon resonance absorption of AuNRs can be easily adjusted to the range of near-infrared (NIR) light which can penetrate deeply into human tissues with minimal invasion, AuNRs as great nanocarriers and imaging agents reveal a great application prospect for photoacoustic tomography, photothermal therapy, or NIR light-mediated theranostic platform. Herein, we begin this chapter of AuNRs by summarizing their synthesis methods, surface modification, and functionalization, then we describe their optical properties. Besides, we focus on the recent progress in diagnostic, therapeutic, and theranostic applications of AuNRs in cancer.

Keywords Gold nanorods • Theranostics • Cancer therapy • Biomedical imaging • Photothermal therapy • Photodynamic therapy • Photoacoustic imaging

3.1 Introduction

In 1957, physicist Richard Feynman at an American Physical Society meeting gave a famous lecture “There’s Plenty of Room at the Bottom” which is considered to be a seminal event in the history of nanotechnology. Nowadays, nanotechnology is becoming more and more popular. With its rapid development in recent decades, nanotechnology has been integrated into various disciplines and fields, including nanomedicine. Nanomaterials as an important part of nanotechnology have been

Z. Shi • Y. Xu • A. Wu (✉)

Division of Functional Materials and Nano Devices, Key Laboratory of Magnetic Materials and Devices, Ningbo Institute of Materials Technology and Engineering (NIMTE), Chinese Academy of Sciences (CAS), Ningbo 315201, People’s Republic of China
e-mail: aiguo@nimte.ac.cn

extensively developed. In this chapter, we only focus on the gold-based nanomaterials (gold nanorods) and their applications in biomedicine, which have perhaps attracted the most attention among all noble metal nanoparticles.

Chinese people are full of wisdom. In the classical Chinese epic novel *Journey to the West*, Golden-Bound Cudgel of Monkey King as a “macroscopic magic weapon” had been created to fight demons, which could change its size and length [1]. However, if ancient Chinese people added the localized surface plasmon resonance (LSPR) effect and color-changed effect to the Golden-Bound Cudgel, the weapon of Monkey King would become much more magic and powerful. Today, Golden-Bound Cudgel comes true. Scientists in the field of nanotechnology have developed the realistic method to make gold rods at nanoscale which have been proven to be a “microscopic magic weapon” to image the lesion location and fight human diseases. Due to their remarkable capacity to absorb near-infrared region light, enhance Rayleigh scattering, and convert the light into heat, AuNRs are of great interest for biomedical imaging and disease therapy. For gold nanospheres, the surface plasmon resonance (SPR) absorption peak is at ~ 520 nm, which shows red color [2]. Because the SPR absorption peak of gold nanospheres does not fit for bio-optical imaging and light propagation in biological tissue due to the large absorption of biological tissue and water, gold nanospheres are still not widely used in the field of biomedical imaging and disease therapy. AuNRs with their anisotropic shapes exhibit two distinct SPR bands, a weak transverse SPR peak at ~ 510 nm, similar to that of gold nanospheres, and an intense longitudinal SPR band (with larger extinction coefficients and higher photothermal conversion efficiency) which can be tuned from visible to near-infrared (NIR, 650–1400 nm) regions by increasing their aspect ratios, shown in Fig. 3.1. The intense longitudinal SPR band becomes the key factor for biomedical applications, as NIR light specifically at 650–950 nm only has minimal light absorption of water and tissue, leading to minimal tissue invasion and deeper light penetration depth. The interaction between electromagnetic radiation and AuNRs produces local electromagnetic field enhancement at the surface of AuNRs, resulting in some special features, such as the surface plasmon resonance (SPR) absorption, surface-enhanced Raman scattering, surface-enhanced fluorescence, photothermal conversion, and light emission [3]. These features quickly

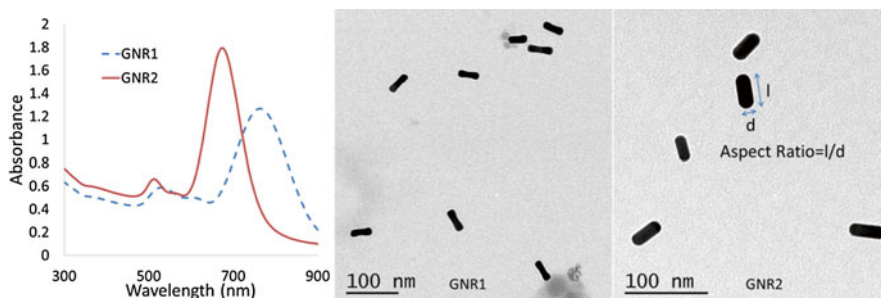


Fig. 3.1 UV-vis-NIR extinction spectra and TEM images of gold nanorods determined by their different aspect ratios

make AuNRs become a hot platform in the fields of *in vitro* diagnostics and prognostics, *in vivo* molecular imaging, molecular therapeutics, image-guided therapy, biosensors, DNA/RNA/drug carriers, or other areas to realize theranostics for optimizing accuracy, efficacy, and safety of therapeutic regimes [1, 4, 5].

In this chapter, we will discuss the synthesis methods, surface modification, functionalization, and optical properties of AuNRs. And then, we will describe recent progress in diagnostic, therapeutic, and theranostic applications of AuNRs for accurate, efficient, and safe therapy.

3.2 Gold Nanorod Synthesis

The synthesis of spherical gold colloids has a long history which can date back to the Roman Empire and early Chinese dynasties [3, 6–12]. However, it is only within the past two decades that chemists gained a controlled and reproducible way to synthesize anisotropic metals, such as AuNRs [3, 6–12]. Until now, scientists have created a variety process for the preparation of AuNRs. There are “hard-template” synthesis method [13], photochemical synthesis method [14], electrochemical synthesis [15], seed-mediated growth method [9, 16–19], microwave synthesis method [20], seedless growth technique [21–23], etc. Over the past decade, the seed-mediated growth approaches have become the most popular method for the synthesis of AuNRs due to their convenience, high quality and yield of nanorods, easy control of particle size and shape, and flexibility for structural modifications. Now, this effective seeded growth method enables researchers to easily synthesize a wide variety of AuNRs applicable for different areas. However, the development and maturation of this method is still experiencing some difficulties.

The basic principle of the seed growth method is adding a certain amount of the gold seeds into the growth liquid under the action of surfactant. The growth orientation of the seed crystal becomes a constant aspect ratio of AuNRs. In 2001, a three-step non-silver-assisted seeded growth approach was introduced by C. Murphy’s group (Fig. 3.2) [17]. Firstly, 3.5 nm citrate-stabilized gold seeds were synthesized by using NaBH_4 , HAuCl_4 , and sodium citrate. Secondly, the previous synthesized gold seeds were added to a growth solution containing HAuCl_4 , CTAB, and ascorbic acid. After a short time, a certain amount of growth solution was added to a new growth solution. This procedure was repeated three times. Finally, this three-step seeded growth approach obtained penta-twinned AuNRs with long aspect ratios between 6 and 20 in low yield (only about 4 %) [17]. Later, the problem of low rod yield was solved by making minor adjustments of the pH condition (from 2.8 to 3.5) to improve the rod yield to near 90 % [16]. This approach remains the preferred one to synthesize AuNRs with aspect ratios of more than 10.

In 2003, M. El-Sayed’s group developed a silver-assisted one-step AuNR seeded growth approach, which obtains a higher rod yield of single-crystalline AuNRs with short aspect ratios between 2 and 5 (Fig. 3.2) [18]. The approach contains two main improvements. One was that the new seeded growth procedure utilized smaller

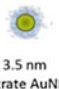




Year	Seed	Growth Solution	AuNR Properties/Structure	Notes	
2001	 3.5 nm Citrate AuNP	HAuCl ₄ , CTAB, Ascorbic Acid	 Dimensions: ~400 x 25 nm	<ul style="list-style-type: none"> • 5% rod yield (by shape) • AR 6-20 • Penta-twinned crystals 	
2003	 1.5 nm CTAB AuNP		HAuCl ₄ , CTAB, AgNO ₃ , Ascorbic Acid	 Dimensions: ~60 x 12 nm	<ul style="list-style-type: none"> • 95% rod yield (by shape) • 15% rod yield (total gold) • AR 1.5-5.0 • Single crystals
2005	-- No Seed BH ₄ ⁻ addition		HAuCl ₄ , CTAB, AgNO ₃ , Ascorbic Acid	 Dimensions: ~20 x 6 nm	<ul style="list-style-type: none"> • Undetermined yield • AR 1.5-5.0 • Single crystals

Fig. 3.2 Three primary seeded growth synthesis methods for gold nanorods (Reprinted with the permission from ref. [9]. Copyright 2013 American Chemical Society)

single-crystalline gold seeds (1.5 nm) stabilized by CTAB, instead of citrate-stabilized polycrystalline gold seeds. The other was that a small amount of silver nitrate was added to the growth solution to control the aspect ratios of AuNRs. These improvements simplified the synthetic procedure and greatly increased the rod yield. However, the effect and precise location of silver is still a matter of some controversy, and the overall yield of the synthesis is relatively low compared to the total amount of gold ions used in the synthesis (near 15 %) [24–26]. The precise aspect ratio control and the ease of use of the silver-assisted one-step seeded growth synthesis have become the standard methods for the synthesis of AuNRs with short aspect ratios. Following this silver-assisted one-step seeded growth synthesis method which has become the most popular synthetic route, the interest of AuNRs has skyrocketed since 2003. Until now, more than 6500 research articles about AuNRs have been published [27].

In 2005, this synthetic approach was modified using a one-step non-seeding aqueous surfactant-based colloidal chemical method to synthesize anisotropic noble metal nanoparticles (AuNRs) on the milligram to multigram scale. In this non-seeding synthesis method, two kinds of strong and weak reducing agents are introduced into the growth medium at the same time. Strong reducing agent (NaBH₄) leads to nucleation. Weak reducing agent (ascorbic acid) helps the particles grow up. Fine control of the nucleation-growth kinetics and growth rate at the stage of nanorod growth is the key to producing high-quality and high-yield anisotropic nanoparticles [21]. This “seedless” silver-assisted AuNR growth provided single-crystalline AuNRs with aspect ratios between 1.5 and 5, and the dimensions of AuNRs are smaller than those of the traditional silver-assisted seeded growth approach. These small AuNRs have less scattering than big ones which can transport through biological systems more easily.

Over the past decade, a number of additional modifications have been made to the seeded synthesis approach and the seedless synthesis approach to improve the yield, dimension, reproducibility, and aspect ratio control. The size and the concentration of the seeds influence the growth of AuNRs. In the non-silver-assisted seeded

growth approach, large seeds resulted in the decline of aspect ratio of AuNRs [28]. The aging time influenced the size of seeds and further affected the rod yield. The growth of the seeds aged for 2 h (about 3.5 nm) obtained 90 % yield of AuNRs. With increasing the aging time and seed size, the irregular-shape rod appeared and the rod yield decreased [29]. The proposed mechanism explains the symmetry breaking results in producing anisotropic nanoparticle as the final product. The size of seeds is an important factor for the symmetry breaking. Starting with a 1.5 nm seed, the symmetry breaking can occur at the 1–3 nm range, which leads to predominately one-dimensional growth and then growth in two dimensions (nanosheets) or three dimensions (spheroids) in the later stages. Using 3.5 nm seeds, the symmetry breaking starts at a range above 3.5 nm and leads to inefficient one-dimensional and two-dimensional growth to produce spheroids (10–30 nm short axis and 15–100 nm length). If the seed size is greater than 5 nm, the nanoparticles grow mainly in symmetric nanoparticles or fractals, as the template mechanism does not work [21]. The concentration of seeds in the non-silver-assisted or silver-assisted seeded growth approach shows different effects in the change of aspect ratios. In the non-silver-assisted seeded growth approach, an increase of seed concentration leads to a blueshift of LSPR peak. However, in the silver-assisted seeded growth approach, the LSPR peak is redshifted [19, 30].

In addition, the purity of CTAB is also an important factor. Part-per-million impurities in CTAB were either preventing or facilitating the growth of AuNRs, which affected the reproducibility from lab to lab [31, 32].

Improving the performance of AuNR syntheses will ultimately require in-depth knowledge of the mechanisms of the growth of AuNRs, which has remained a challenge for clear mechanism [9]. In 2012, M. Cortie's group studied the early stages of the growth of AuNRs and proposed a new growth mechanism ("popcorn"-like mechanism of growth), using a combination of techniques including the low-temperature TEM, the monitoring of the growth process, and theoretical simulation [33]. Through the experiments, they found that at different stages of AuNR growth, the growth of the seeds could be seen, that is, the dormant gold seeds could quickly grow as AuNRs at different stages just like "popcorn," shown in Fig. 3.3 [33].

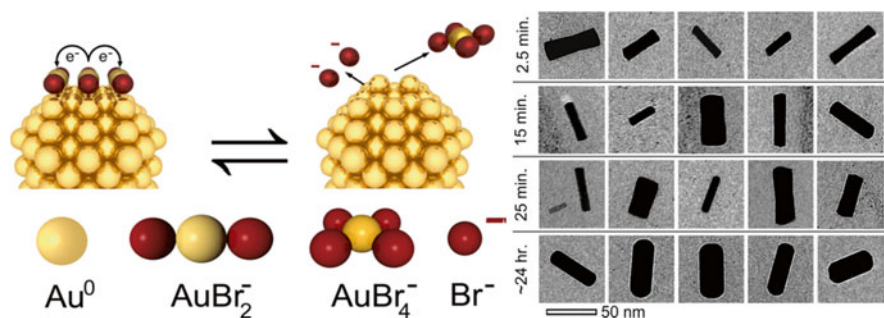


Fig. 3.3 Disproportionation of AuBr₂ according to the reaction leading to growth of the particle "popcorn"-like mechanism of growth through disproportionation reaction (Reprinted with the permission from ref. [33]. Copyright 2012 American Chemical Society)

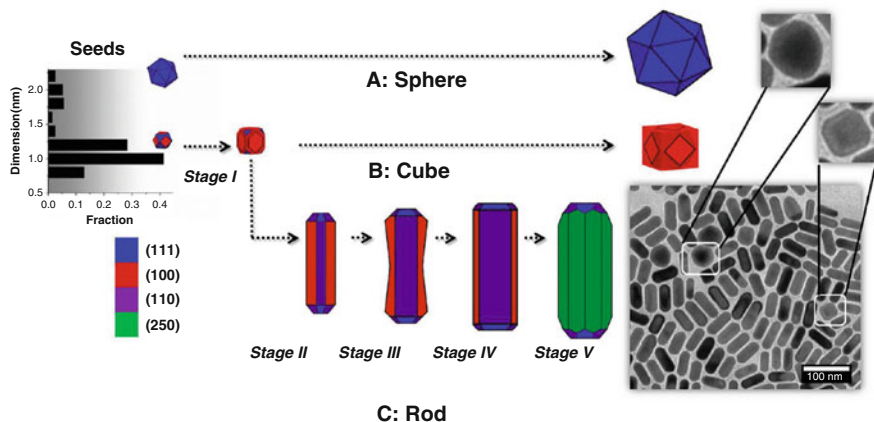


Fig. 3.4 The five main stages of the growth of CTAB-coated AuNRs from different crystal structure seed upon the formation of a surfactant bilayer on different crystal facets due to a fine balance between kinetic and thermodynamic factors. The *scale bar* in the TEM image is 100 nm (Reprinted with the permission from ref. [34]. Copyright 2013 American Chemical Society)

In 2013, R. Vaia's group used thiolated-polystyrene microspheres through ligand exchange and solvent transfer to capture AuNRs in different growth periods, showing the evolution of the entire AuNRs and proposing the five key stages of growth in Fig. 3.4. In the first stage, the seed crystal formed about 6 nm gold particles through fast isotropic growth. Then, the seed crystal rapidly grew to one dimension as the anisotropic growth manner, forming elongated round-cylindrical AuNRs during the second stage. In the third stage, the length of the rod growth gradually slowed down, and the diameter growth gradually accelerated. The both ends of AuNRs grew faster than the middle part of them to obtain the dumbbell-shaped AuNRs. The fourth stage was that the end and side face of AuNRs flattened with the reconstruction of the surface crystal of dumbbell-shaped AuNRs. The fifth stage was the relaxation of the surface structure, eventually forming eight prism AuNRs [34].

In 2014, Núria López's group studied the formation of AuNRs with the density functional theory simulations, providing an atomistic description of the role of different compounds in the synthesis of AuNRs, shown in Fig. 3.5. Results have shown that the anisotropy is caused by the formation of a complex consisting of the surfactant, bromine, and silver that preferentially adsorbs on some facets of the seeds to prevent its further growth. Nanorod structure is driven by the adsorbed surfactant to induce the {520} lateral facets [35].

In order to get a larger optical tunable range, higher yield, and better uniformity, the researchers proposed some improved synthesis methods on the basis of seed growth method. In 2012, an improved synthesis method of colloidal AuNRs using aromatic additives was reported by C. Murray's group [36]. This method reduced the concentration of CTAB to ~ 0.05 M as opposed to 0.1 M in well-established protocols and optimized the synthesis for each of the 11 aromatic additives used,

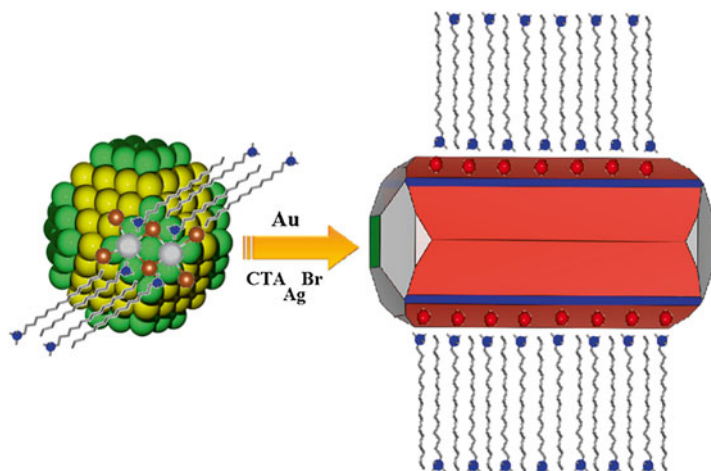


Fig. 3.5 The growth mechanism with the adsorption of a complex between the surfactant, bromine, and silver (Reprinted with the permission from ref. [35]. Copyright 2014 American Chemical Society)

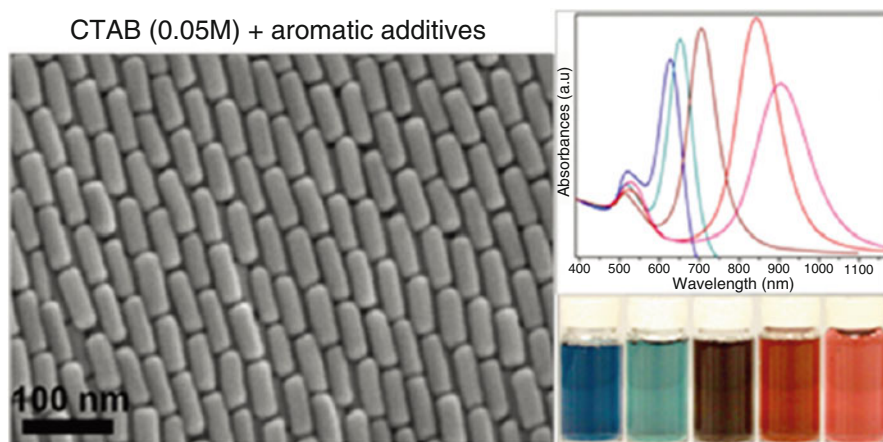


Fig. 3.6 An improved synthesis of colloidal AuNRs by using aromatic additives and CTAB (Reprinted with the permission from ref. [36]. Copyright 2012 American Chemical Society)

generating a rich array of monodisperse AuNRs of high rod yield with LSPR tunable from 627 to 1246 nm (Fig. 3.6).

In 2013, C. Murray's group used a binary surfactant mixture composed of CTAB and sodium oleate (NaOL) to improve synthesis of colloidal gold nanorods (NRs). Both thin and thick AuNRs with exceptional monodispersity and broadly tunable LSPR can be synthesized at reduced CTAB concentrations (as low as 0.037 M). This binary surfactant system overcomes the difficulty of growing uniform thickness and greatly expands the dimensions of AuNRs [37]. Soon after, they

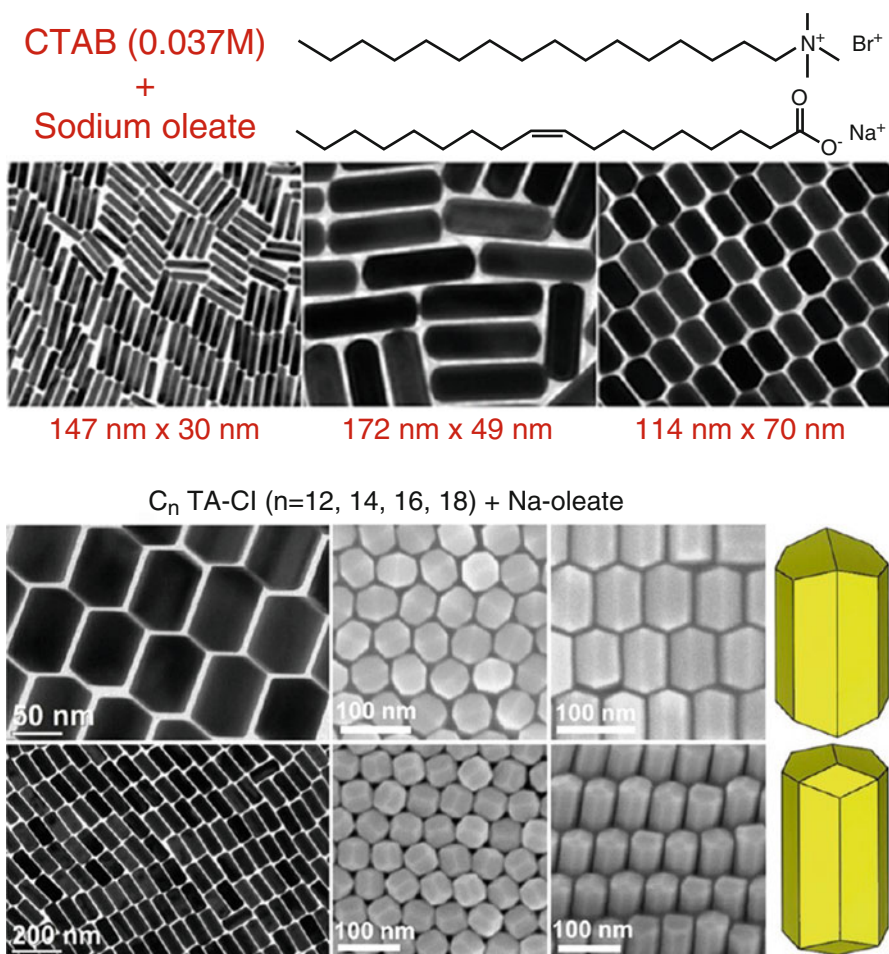


Fig. 3.7 A binary surfactant system (CTAB-NaOL and CTAC-NaOL) for the synthesis of AuNRs (Reprinted with the permission from ref. [37, 38]. Copyright 2013 American Chemical Society)

demonstrated for the first time that monodisperse AuNRs with broadly tunable dimensions and LSPR can be synthesized using a bromide-free surfactant mixture composed of CTAC and sodium oleate. It demonstrated that neither bromide as the surfactant counterion nor a high concentration of bromide ions in the growth solution was essential for AuNR formation [38] (Fig. 3.7).

In 2012, E. Zubarev's group successfully used hydroquinone as a reducing agent to synthesize broadly tunable LSPR of AuNRs from 770 to 1230 nm, overcoming the sensitivity problem of nanorod synthesis to the amount of ascorbic acid. The efficiency of chloroauric acid to synthesize AuNRs was nearly 100 %, in Fig. 3.8 [39].

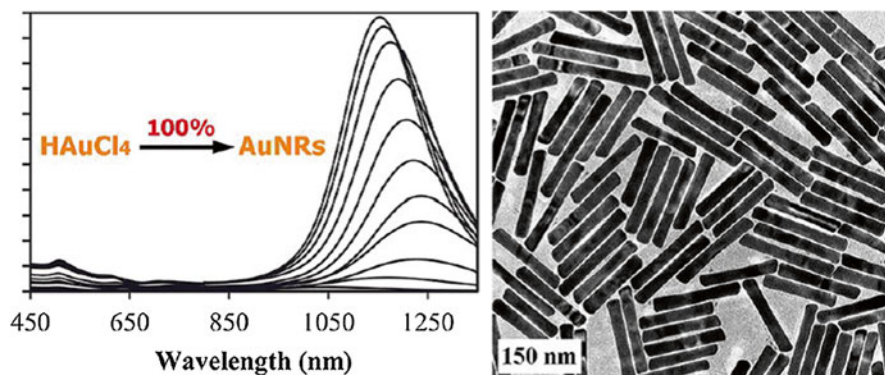


Fig. 3.8 Hydroquinone as a reducing agent for 100 % efficiency to synthesize AuNRs (Reprinted with the permission from ref. [39]. Copyright 2013 American Chemical Society)

About the development of seedless growth method, there were some improvements. M. El-Sayed's group developed a one-pot seedless synthetic technique to prepare relatively small monodisperse AuNRs. With the control of the pH, NaBH₄, and silver concentrations, smaller and different aspect ratio of AuNRs were produced by adjusting the CTAB concentration in the growth solution [23]. Recently, Liang et al. developed a seedless method for the synthesis of high aspect ratio AuNRs with an LSPR peak of larger than 1400 nm in one step. The yield of this method was high with a broader size tunability and better reproducibility [22].

Secondary growth method is the process of the secondary control of AuNRs' shape and size, wherein continuous addition of growth solution or other reagents to single crystalline AuNRs, synthesized via common seed-mediated growth. Xiang et al. successfully obtained thermodynamically more stable morphologies (arrow-headed AuNRs and gold nano-octahedra) with a high quality and yield using secondary growth procedure by switching the growth of the high-energy {110} facet [40] (Fig. 3.9).

In 2013, J. Tracy's group proposed a large-scale synthesis method of AuNRs through continuous secondary growth to control the aspect ratio and size of AuNRs. In this method, the ascorbic acid (AA) was continuously added to a stirred solution of CTAB-coated AuNRs, which deposited the remaining (~70 %) of the Au precursor onto the AuNRs. Stirring made it possible to synthesize high yield of rod-shaped nanoparticles. Stirring coupled with continuous addition of AA to previously prepared AuNRs (the LSPR is ~820 nm) could tune the LSPR of AuNRs between ~700 and 880 nm during secondary growth by adjusting the rate of AA addition or adding benzyldimethylhexadecylammonium chloride hydrate (BDAC) [41] (Fig. 3.10).

Overall, the above synthesis methods are all contributed to improving the rod yield and uniformity, also to tuning the size, shape, LSPR, and aspect ratio precisely. All these are the important prerequisites for AuNRs to better playing their roles in biomedical applications.

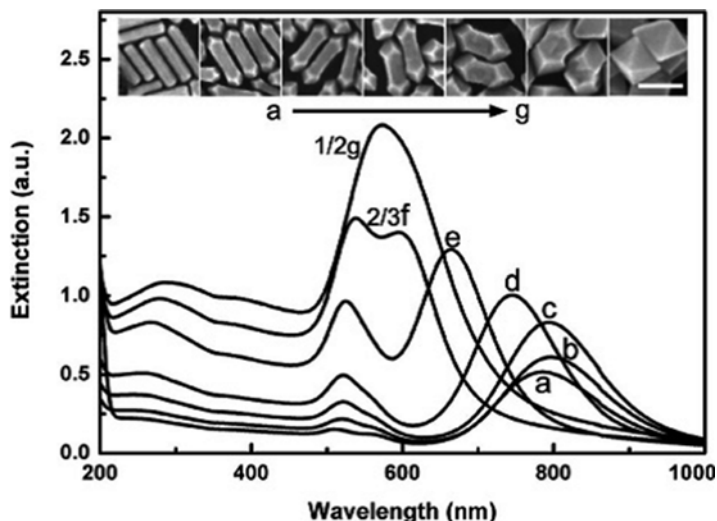


Fig. 3.9 Secondary growth for arrow-headed AuNRs and gold nano-octahedra (Reprinted with the permission from ref. [40]. Copyright 2008 American Chemical Society)

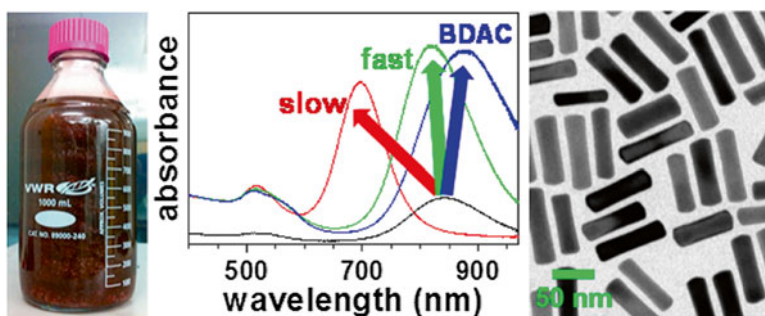


Fig. 3.10 A large-scale synthesis method of AuNRs through continuous secondary growth (Reprinted with the permission from ref. [41]. Copyright 2013 American Chemical Society)

3.3 Surface Modification and Functionalization

Low toxicity, functionality, and stability of AuNRs are essential to their biomedical applications. Seed-mediated synthesis of AuNRs generally uses cetyl trimethyl ammonium bromide (CTAB) as the surfactant. Thus, the surface of AuNRs is coated with the structure-directing surfactant of CTAB which makes the surface of AuNRs positively charged and thus prevents their aggregation in certain aqueous media via electrostatic repulsion. Due to the presence of high concentrations of salts and buffers in biological systems, the bilayer of CTAB on the surface can easily detach from the AuNRs to reduce the zeta potential of AuNRs, leading to aggregation of AuNRs. In addition, as CTAB with strong cytotoxicity can degrade the biofilm and

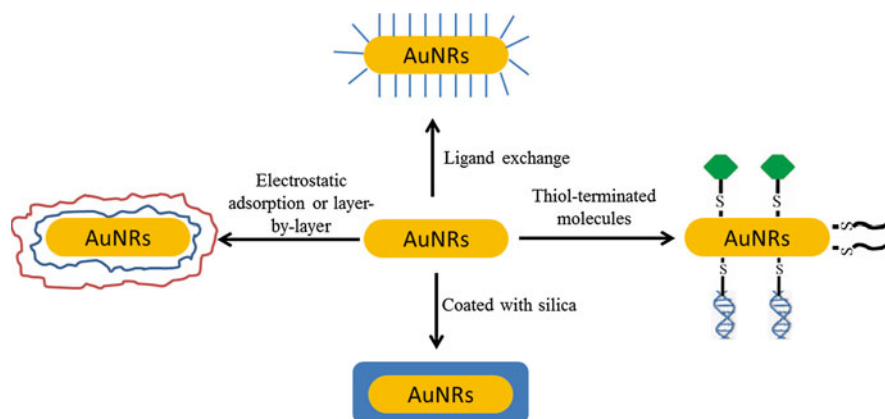


Fig. 3.11 Four most widely used methods for surface modification and functionalization of AuNRs

peptides, it has great challenge for the use of biological applications. Therefore, applying the chemical or physical modification and functionalization to change the surface properties of AuNRs and increase the stability, biocompatibility, and desirable functionalities such as specific targeting, additional imaging modalities, and incorporation of an outer layer for drug delivery will significantly improve the performance of AuNRs in biological applications [1] (Fig. 3.11).

There are four most widely used methods for surface modification and functionalization of AuNRs. Due to the strong affinity between thiol and Au, the surface modification of AuNRs covalently modified by thiolated compounds via unstable CTAB displacement with thiolated species, such as thiol-terminated polyethylene glycol (PEG-SH), thiol-terminated peptide, thiol-terminated oligonucleotide, etc., is conducive to enhance the stability and functionalization of AuNRs [5, 42, 43]. The displacement of CTAB reduces the cytotoxicity and is relatively simple, just requiring a few hours incubation of AuNRs with an excessive amount of thiolated species under stirring, such as PEG-SH [44, 45]. As a common strategy for preparing biocompatible nanomaterials, the coating of PEG helps prevent particle aggregation and nonspecific protein adsorption from having longer circulation time in bloodstream for greater accumulation in tumors. For active targeting function, targeting ligands such as RGD peptide [46], folic acids (FA), and deltorphin [47] can be conjugated at the end of PEG-SH for specific interaction with cells to minimize nonspecific cellular uptake which may cause adverse effects to healthy cells. This is a good way to realize the safe and efficient therapy. Some other thiolated species have also been used for surface modification and functionalization of AuNRs, such as thiolated DNA for gene therapy [48], thiolated peptides to build AuNR-AIPcS4 complexes for near-infrared fluorescence imaging, photothermal therapy, and photodynamic therapy [49] (Fig. 3.12).

Electrostatic adsorption or layer-by-layer polyelectrolyte self-assembly method is another widely used method for surface modification of AuNRs [50–52].

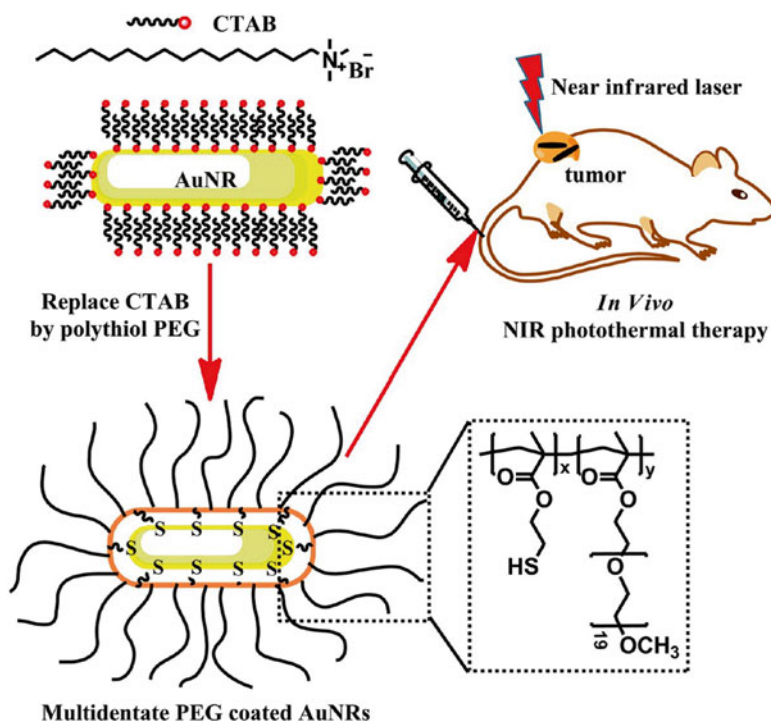


Fig. 3.12 Schematic representation of surface modification of CTAB-capped AuNRs with polythiol PEG-based copolymer with good stabilities in high saline condition and wide pH range for biomedical application (Reprinted with the permission from ref. [43]. Copyright 2014 American Chemical Society)

C. Murphy's group has shown lots of work [50, 53, 54]. Electrostatic adsorption between anionic and cationic polyelectrolytes makes this method very straightforward. In this method, negatively charged polystyrene sulfonate (PSS) is often used as a mild absorbent to coat CTAB. Then, cationic polyelectrolytes such as poly(diallyldimethylammonium chloride) (PDDAC or PDADMAC) or polyethyleneimine (PEI) will be absorbed on the surface of PSS-coated AuNRs to change the surface charge. This process can be repeated many times to obtain several layers [50]. This method allows for attachment of drugs, genes, antibodies, proteins, or other targeting molecules to realize multifunctional applications. In addition, surface charges also have a significant effect on cellular uptake and biodistribution. PDDAC-coated AuNRs exhibit negligible cytotoxicity and a much greater ability to be internalized by the cells than CTAB-coated AuNRs and PSS-coated AuNRs [55] (Figs. 3.13 and 3.14).

Ligand exchange method is another effective method for the surface modification of AuNRs. In this method, AuNRs replaced the CTAB bilayer on the surface with more stable and more biocompatible amphiphilic molecules such as phospholipids (POPC, Phosphatidylserine) or cationic transfection reagent (Oligofectamine,

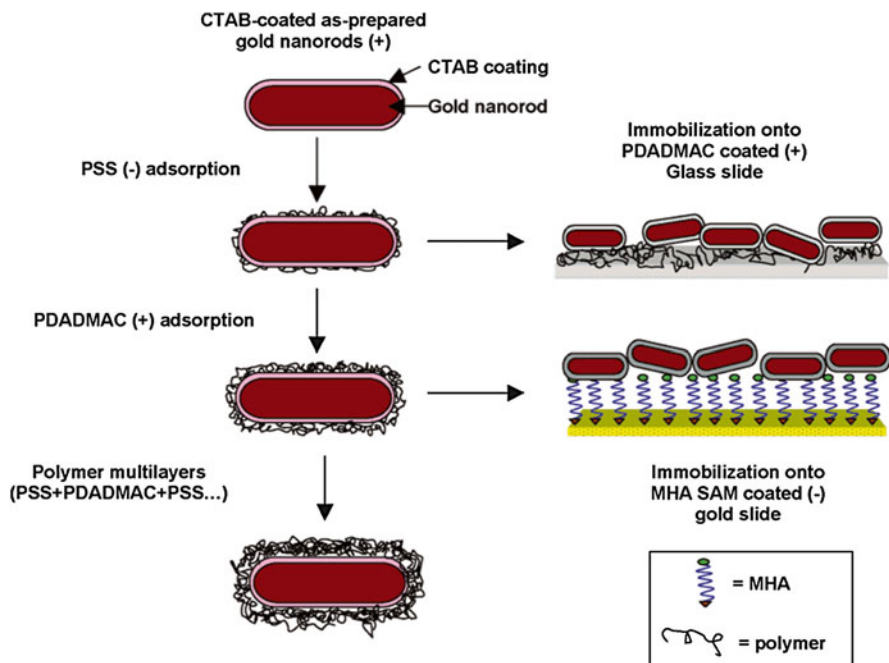


Fig. 3.13 Layer-by-layer polyelectrolyte self-assembly method for surface modification of AuNRs (Reprinted with the permission from ref. [50]. Copyright 2005 American Chemical Society)

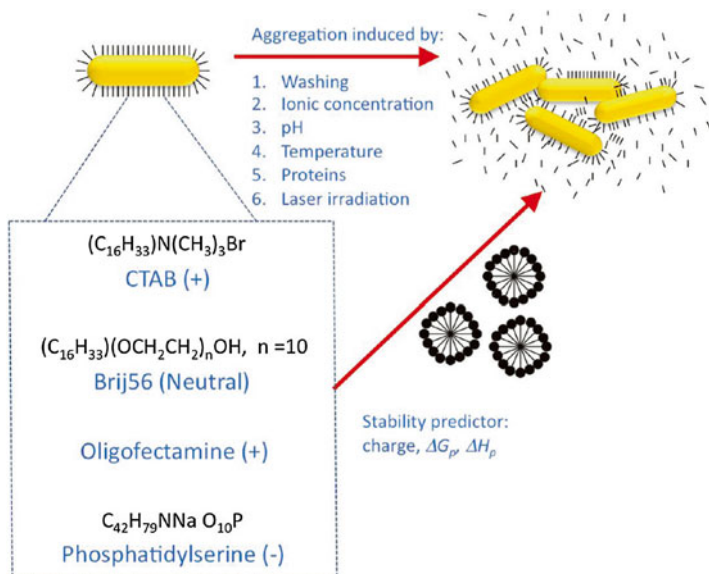


Fig. 3.14 Ligand exchange method for surface modification of AuNRs to enhance the stability (Reprinted with the permission from ref. [58]. Copyright 2012 American Chemical Society)

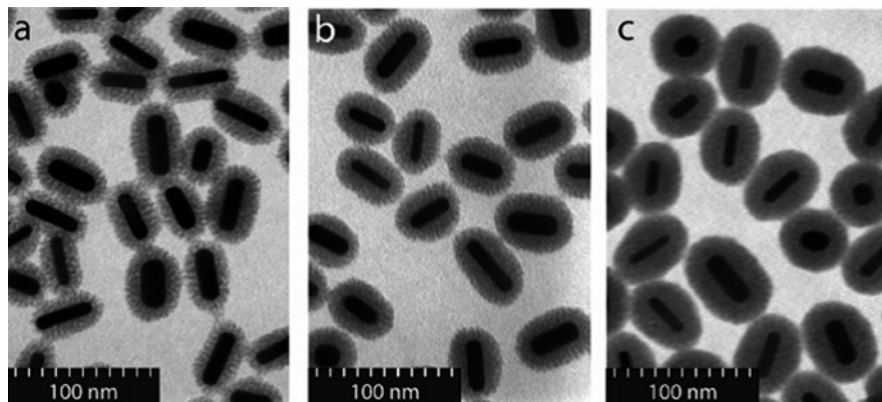


Fig. 3.15 Mesoporous silica-coated AuNRs with different thickness (Reprinted with the permission from ref. [60]. Copyright 2008 American Chemical Society)

Sc29528, Lipofectamine2000) to enhance the stability and biocompatibility [56–58]. Another strategy to improve the material stability is the coating of a layer of inorganic materials, such as Fe_3O_4 , TiO_2 , and SiO_2 . The most commonly used method is the coating of silica layer around AuNRs to form dense silica [59], mesoporous silica [60], or hollow mesoporous silica [61]. In 2008, Gorelikov et al. reported a general and single-step synthesis method to coat CTAB-coated AuNRs with a thin layer of mesoporous silica, shown in Fig. 3.15 [60]. The CTAB molecules on the surface of AuNRs functioned as the template for the three-dimensional polymerization of tetraethyl orthosilicate and thus help to form the mesoporous silica layer. It is well known that mesoporous silica-coated AuNRs are ideal multifunctional drug carriers with high surface area, large pore volume, excellent biocompatibility, and good chemical and thermal stability to solve the CTAB toxicity and dispersion issues of AuNRs [62, 63]. Hollow mesoporous silica can further improve the drug-carrying ability [61]. Until now, lots of applications of silica-coated AuNRs in imaging [59], photothermal therapy [64], photodynamic therapy [65], drug delivery [61], and multifunctional theranostic platform [63] have been reported, respectively, by different groups.

3.4 Properties

The main optical properties of AuNRs are closely related to their localized surface plasmon resonance (LSPR) effect, such as surface plasmon absorption and scattering, surface-enhanced Raman scattering properties (SERS), fluorescence effect, photothermal effect, and photosensitizing effect.

3.4.1 Localized Surface Plasmon Resonance Effect

Localized surface plasmon resonance (LSPR) is a collective excitation mode which is collective electron charge oscillations in metallic nanoparticles that are excited by light. When the frequency of the electromagnetic wave and the whole vibration frequency of metallic material are consistent, resonance enhancement effect occurs. For gold nanospheres, the surface plasmon resonance (SPR) absorption peak is at ~ 520 nm, which shows red color [2]. For anisotropic AuNRs, there are two horizontal and vertical SPR bands. One is the collective movement of the free electron along the long axis of nanorods, generally referred as longitudinal SPR band. The other one shows the collective movement of the free electron along the short axis of nanorods, generally referred as transverse SPR band. Longitudinal SPR band is closely related to the aspect ratio of AuNRs, which has strong oscillator strength and forms a characteristic absorption peak of AuNRs. By adjusting the aspect ratio of AuNRs, longitudinal SPR absorption peak can change from the visible region to the near-infrared region. Transverse SPR absorption peak is not related to the aspect ratio of AuNRs with a relatively fixed position (about 510 nm). The oscillator strength is not strong [24, 66] (Fig. 3.16).

When the light is applied to the gold nanoparticles, the light corresponding to the plasmon oscillation frequency will generate surface plasmon absorption (SPRA) and scattering (SPRS). The sum of them is called as extinction. Gans modified Mie theory is generally used to calculate the surface plasmon absorption and scattering of anisotropy AuNRs [67, 68]. SPRA effect can lead to many properties, such as photoacoustic effect and photothermal effect. The photoacoustic effect is, in essence, the formation of sound waves following light absorption in a material sample, which can be used for ultrasonic imaging. AuNRs have a sufficiently large optical absorption cross section to maximize the agent's photoacoustic signal. Photothermal effect is a phenomenon associated with electromagnetic radiation which is produced by the photoexcitation of material, resulting in the production of thermal energy (heat). Large optical absorption cross and high photothermal conversion efficiency are the main factors affecting the photothermal effect. SPRS effect can be used for light scattering imaging.

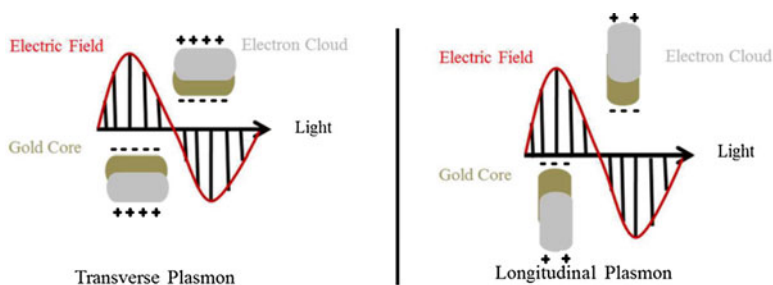


Fig. 3.16 Schematic representation of AuNR transverse and longitudinal plasmon absorbances in AuNRs (Reprinted with the permission from ref. [9]. Copyright 2013 American Chemical Society)

3.4.2 *Surface-Enhanced Raman Scattering*

Surface-enhanced Raman scattering (SERS) is a surface-sensitive technique that enhances Raman scattering by Raman reporter molecules adsorbed on rough metal surfaces or nanostructures such as gold, silver, platinum, and other precious metal nanoparticles, which will produce electromagnetic field enhancement effect [69]. The enhancement factor can be as high as 10¹⁰–10¹¹, [70] which means the technique may detect single molecules [71]. AuNRs are a kind of excellent materials for SERS enhancement. Because SERS enhancement is closely related to SPR absorption peak and intensity, AuNRs with a strong LSPR absorption peak exhibit superior properties. It has been shown that when the LSPR peak of AuNRs coincides with the excitation wavelength of SERS, SERS enhancement factor would be improved 10–100 times [72].

3.4.3 *Single-/Two-Photon Fluorescence*

Molecules adsorbed on rough metal surfaces produce sharp SERS signal, and meanwhile, the SERS spectrum usually accompanies fluorescence background, which arousing the interest in the precious metal fluorescence. This phenomenon was first discovered in 1969 by A. Mooradia et al. [73]. In 2000, it was first reported that AuNRs had the property of significantly enhanced single-photon fluorescence [74]. The essence of single-photon fluorescence is that the ground state atom absorbs a photon, leading to the transition of excited electrons from d band to sp band and resulting in electron-hole pairs. Relaxation of these electronic motions to new electronic ground state followed by the recombination of the sp-electrons with holes in the d band leads to the fluorescence emission. Two-photon fluorescence excitation of AuNRs is the process of sequence two-photon excitation. The first photon excites an electron in the sp conduction band below the Fermi surface to the band above the Fermi surface via an intraband transition. Simultaneously, a hole is produced in the sp conduction band below the Fermi level. Then, the second photon excites an electron in the d band to the hole in the sp conduction band produced by the first photon. The second photon also generates a hole in the d band. As a consequence, the recombination of the electron-hole pair radiates fluorescence later [75]. AuNRs showed significantly enhanced single-/two-photon fluorescence, mainly due to the overlap of the excitation spectra and LSPR peak of AuNRs, causing the fluorescence enhancement of SPR effect [76, 77].

3.4.4 *Near-Field Plasmon Coupling*

LSPR of AuNRs is the result of the collective oscillation of conduction electrons within the particle upon interaction with light. The resonance energy of the LSPR is highly sensitive to the distance between two nanoparticles. The close approach

(the distance between two nanoparticles from 2 nm to 2.5 times the particle diameter) of two nanoparticles leads to interaction of their localized surface plasmon resonances, named as near-field plasmon coupling. The near-field plasmon coupling is a special property, and it has been exploited in a number of applications, including the change of LSPR peak of AuNRs [78, 79], SERS [80], near-field enhanced fluorescence [81], measuring the distance between two metal nanoparticles using the universal plasmon ruler in biological systems, [82], and in optoelectronics where the near-field plasmon coupling of nanoparticles (distances less than 2 diameters) results in the transmission of light energy through a nanoparticle chain [83].

3.4.5 Photosensitive Effect

Singlet oxygen ($^1\text{O}_2$) is known to play an essential role in photodynamic therapy (PDT). It is conventionally formed by sensitization of organic photosensitizers (such as AlPcS_4), photocatalytic materials (such as ZnO and TiO_2), and quantum dot (such as graphene quantum dots [84]). However, these nanomaterials have their own drawbacks (photoinduced degradation of organic photosensitizers, cytotoxicity of QDs, and poor absorption in the near-IR region of ZnO and TiO_2), which limit their clinical applications in PDT. In 2011, metal nanoparticles (such as Au, Ag, and Pt) were found to sensitize the formation of singlet oxygen [85]. In two-photon photodynamic therapy (TP-PDT), photosensitizers are excited by simultaneously absorbing two long-wavelength photons to generate $^1\text{O}_2$. The key advantage of TP-PDT is deep penetration into biological tissues by using the near-infrared excitation wavelength, resulting in a 10- to 100-fold increase in the light penetration depth. However, spherical metal nanoparticles generally have small two-photon absorption cross sections, and it may limit their singlet oxygen generation. AuNRs have emerged as promising materials with a high TPA action cross section by LSPR enhancement for TP-PDT. In 2012, TP-PDT of AuNRs has been first demonstrated to produce the $^1\text{O}_2$ which is dependent on LSPR peak [86]. The TPA cross sections [87] and different crystal faces [88] are also important factors to impact the singlet oxygen generation. More recently, in single-photon photodynamic therapy (SP-PDT), it was demonstrated for the first time that AuNRs alone can sensitize formation of $^1\text{O}_2$ and exert dramatic PDT effects on destruction of solid tumors under very low laser doses of single-photon NIR light excitation (915 nm, $<130 \text{ mW/cm}^2$) [89].

3.5 Biomedical Applications

Because of their exceptional properties based on the LSPR effects, such as their remarkable capacity to absorb and scatter light, near-field plasmon coupling, photosensitive effect, excellent photothermal conversion properties, and single-/two-photon fluorescence, AuNRs have emerged as a promising platform for various biomedical applications, particularly in cancer diagnosis and therapy.

3.5.1 AuNRs as Biomedical Imaging Agents

Compared with conventional organic dyes for NIR light-mediated biomedical imaging, AuNRs have several significant advantages such as large absorption/scattering cross sections and chemical and photophysical stabilities. During the last 10 years, the applications of AuNRs in various imaging techniques have been intensively investigated, such as light scattering imaging, two-photon fluorescence imaging, photoacoustic imaging (PAT), SERS [90], and optical coherent tomography (OCT) [91]. These imaging techniques have been widely recognized and applied. Thus, in this part, we only give a brief introduction.

3.5.1.1 Light Scattering Imaging

Light scattering imaging is a simple imaging way. Based on SPR-enhanced Rayleigh scattering in the near-infrared region and the weak scattering background of the organism, AuNRs became biological imaging contrast agents because of strong light scattering. M. El-Sayed's group made a representative work in the application of AuNRs for cell scattering imaging. The use of anti-EGFR antibody-modified gold nanoparticles and AuNRs as contrast agents achieved light scattering imaging of tumor cells, shown in Fig. 3.17. The light scattering imaging contrast of AuNRs was significantly better than gold nanoparticles due to SPR-enhanced Rayleigh scattering [92]. Taking advantages of the photothermal therapeutic or drug delivery property of AuNRs or by combining targeting molecules, it is easy to design the integrated multifunction imaging and therapy.

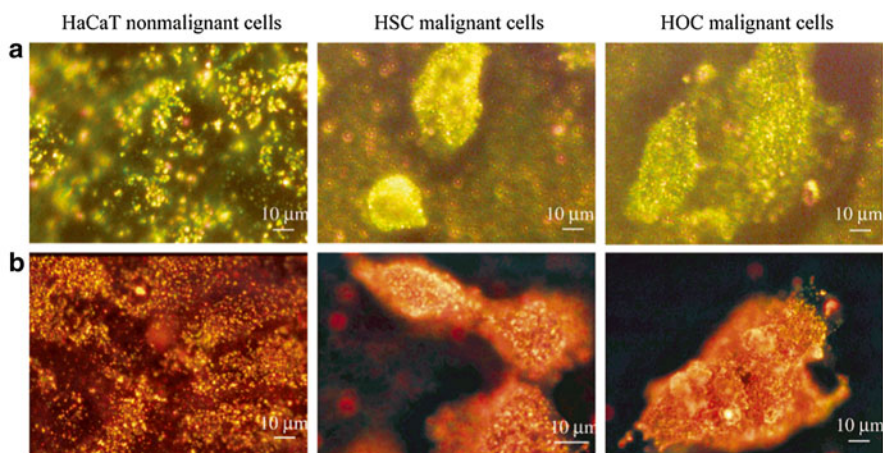


Fig. 3.17 (a) Light scattering images of anti-EGFR/Au nanospheres after incubation with nonmalignant and malignant cells for 30 min. (b) Light scattering images of anti-EGFR/Au nanorods after incubation with nonmalignant and malignant cells for 30 min (Reprinted with the permission from ref. [92]. Copyright 2006 American Chemical Society)

3.5.1.2 Two-Photon Fluorescence Imaging

Two-photon fluorescence is a powerful technique for the early diagnosis of superficial tumor and tissue because it is a way of noninvasive imaging of subcellular features potentially hundreds of micrometers deep into tissue. TPL has been identified as a serial process involving sequential absorption of photons which requires near-simultaneous absorption of two coherent photons and emission from the recombination of electrons in the sp conduction band and holes in the d band. The LSPR effect of AuNRs increases the probability of transitions between the radiation belts, which makes two-photon fluorescence or multiphoton fluorescence of AuNRs possible. The SPR-enhanced quantum yield is more than a million times higher compared with single-photon fluorescence. One of typical applications has been demonstrated in the use of anti-EGFR antibody-modified AuNRs as bright contrast agents for two-photon fluorescence imaging of cancer cells in a three-dimensional tissue phantom. The imaging deep using AuNRs was down to 75 μm and deeper than 40 μm from two-photon imaging of endogenous fluorophores which could be used to distinguish cancerous and precancerous from normal tissue. The two-photon fluorescence intensity of AuNR-labeled cancer cells was 4000 times brighter than the two-photon autofluorescence emission intensity from intrinsic fluorophores of unlabeled cancer cells at 760 nm excitation light. Their strong signal, high contrast, resistance to photobleaching, chemical stability, ease of synthesis and modification, and biocompatibility make AuNRs become an attractive contrast agent for two-photon fluorescence imaging [93] (Fig. 3.18).

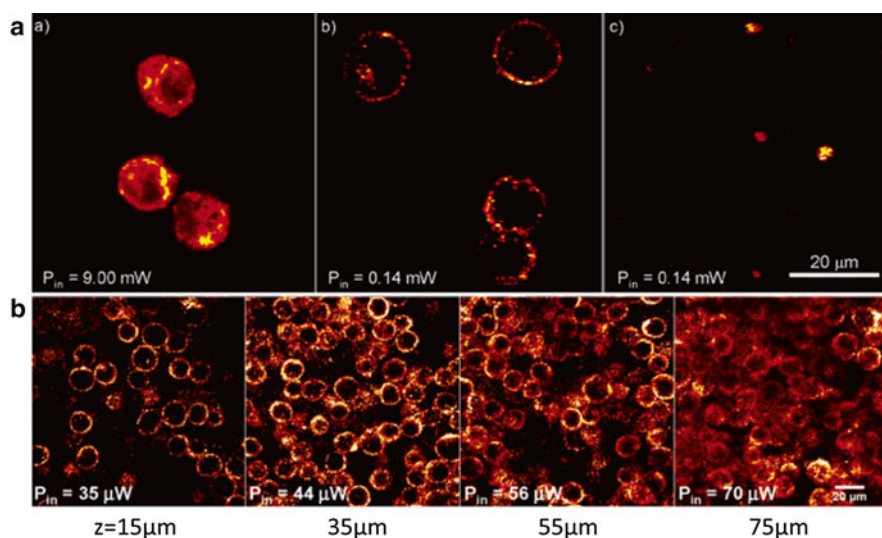


Fig. 3.18 (a) Two-photon fluorescence images of cancer cells: *a* two-photon autofluorescence of unlabeled cells using 9 mW of excitation power. *b* Two-photon fluorescence image of AuNR-labeled cells using 140 μW of excitation power. *c* Two-photon autofluorescence of unlabeled cells using 140 μW of excitation power. (b) Two-photon fluorescence images AuNR-labeled cells at different depths (Reprinted with the permission from ref. [93]. Copyright 2007 American Chemical Society)

3.5.1.3 Photoacoustic Imaging

Photoacoustic imaging can greatly enhance the contrast for visualization of structures and biomarkers in biological tissues which overcome the high light scattering in biological tissue by making use of the photoacoustic effect. Light absorption by tissue or materials creates a thermally induced pressure jump that launches ultrasonic waves, which can be received by acoustic detectors to form images [94]. AuNRs are of particular interest for in vivo photoacoustic imaging because of their compacted sizes, strong and highly wavelength-tunable optical absorption in the NIR optical window of soft tissues, excellent photothermal conversion efficiency, and good biocompatibility. As a photoacoustic imaging agent, AuNRs improve the photoacoustic imaging contrast and resolution. Sanjiv S. Gambhir's group showed one of the typical applications using silica-coated AuNRs to achieve ovarian cancer detection [95] and mesenchymal stem cell detection [96] with photoacoustic imaging in living mice. AuNRs with an aspect ratio of 3.5 were selected for their highest ex vivo and in vivo photoacoustic signal and used to image subcutaneous tumors of the 2008, HEY, and SKOV3 ovarian cancer cell lines in living mice [95]. As can be seen from Fig. 3.19, photoacoustic imaging of AuNR-labeled ovarian cancer had the characteristics of weak background signal, high contrast, high spatial resolution, and clear outline. In fact, any nanomaterials with strong and highly wavelength-tunable optical absorption in the NIR optical window and excellent photothermal conversion efficiency can be used as photoacoustic contrast agents, such as gold nanocages characterized by hollow interiors, ultrathin and porous walls (better than AuNRs) [97], and nano-reduced graphene oxide [98].

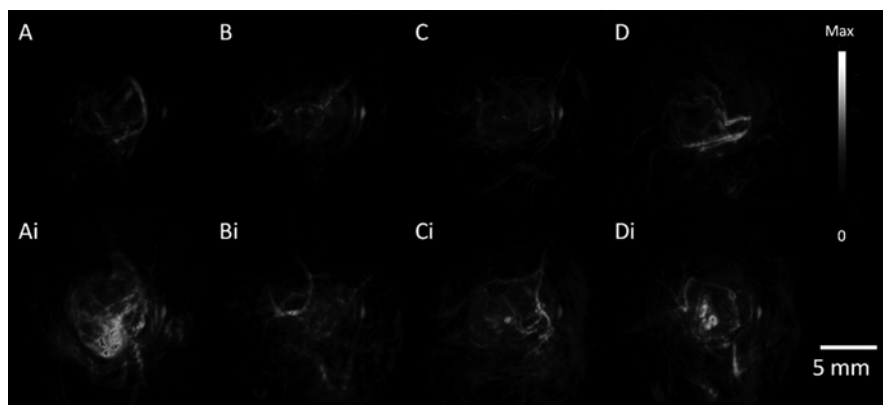


Fig. 3.19 Photoacoustic tumor imaging with AuNRs. (a) MDA-435S tumors serve as a positive control. (Ai) MDA-435S tumors with AuNRs. Panels (b–d), are 2008, HEY, SKOV3 tumors, respectively (Reprinted with the permission from ref. [95]. Copyright 2012 American Chemical Society)

3.5.2 *AuNRs for Cancer Therapy*

AuNRs as biocompatible nanocarriers with high specific surface area, tunable localized surface plasmon resonance, photothermal effect, photosensitive effect, and photothermally controlled release property are widely used for photothermal therapy, drug/gene/photosensitizer delivery to realize drug/gene therapy, and photodynamic therapy [1, 99].

3.5.2.1 Drug/Gene Therapy

Chemotherapy is a common way of cancer therapy. However, due to the disadvantages of large doses, side effect, nontargeting, and easily leading to multidrug resistance, the efficacy of chemotherapy is greatly limited. Gene therapy through the correction of the defective gene achieves a new way of therapy. But in the physiological environment, exogenous gene or siRNA is easily degraded by nuclease, leading to short half-life and low transfection efficiency, thereby limiting its application in the treatment of disease. AuNRs as drug (doxorubicin, paclitaxel, cisplatin) and gene (DNA, siRNA) nanocarriers can increase drug/gene loading and the intake of the body, to promote controlled release of the drug/gene and improve the stability of the gene and transfection efficiency. And it also can be modified to improve targeting, prolong circulation time in vivo, and promote tumor cell uptake and retention.

C. Y. Chen's group from the National Center for Nanoscience and Technology, China, used PDDAC- or PEI-modified AuNRs with HIV-1 Env plasmid DNA to transfect HEK293 cells and found that the carrier has greatly enhanced the efficiency of gene transfection and promoted humoral immunity as well as the maturation of dendritic cells and T cell proliferation through activating antigen-presenting cells compared to naked Env plasmid DNA treatment in vivo. The possible mechanism of AuNRs as vaccine adjuvants is shown in Fig. 3.20 [51]. Luke P. Lee's group developed cationic phospholipid-modified AuNRs as a gene delivery carrier to enhance biocompatibility and colloidal stability, reduce nuclease degradation, and improve transfection and gene therapy [56].

For drug delivery, the main objective of the study is to improve the biocompatibility of the carrier, drug-carrying rate, and the intake of the body and the controlled release properties of the drug and reverse drug resistance. C. Y. Chen's group fabricated polymer-encapsulated AuNRs to couple the photothermal properties of AuNRs and the thermo- and pH-responsive properties of polymers in a single nanocomposite to develop a novel targeted anticancer strategy with facile control and practical efficacy without using targeting ligands. The loading content into the nanocomposite through electrostatic interactions could be up to 24 %. The accumulation of nanocomposite in tumor post systematic administration could be signifi-

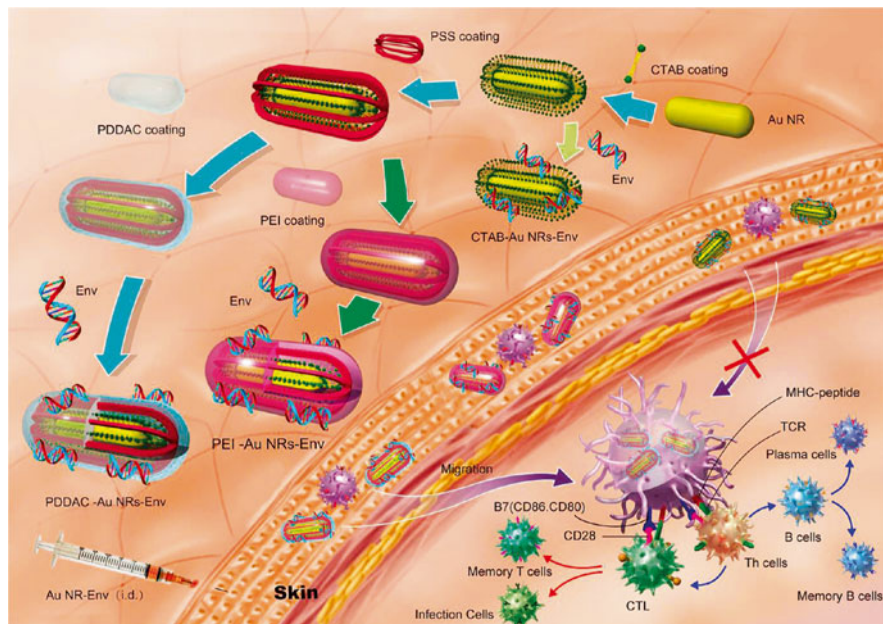


Fig. 3.20 The possible mechanism of different surface-coated AuNRs as vaccine adjuvants to enhance the efficiency of gene transfection and promote the maturation of dendritic cells and T cell proliferation through activating antigen-presenting cells (Reprinted with the permission from ref. [51]. Copyright 2012 American Chemical Society)

cantly enhanced by NIR laser irradiation due to the shrunk of the nanocomposite's size. Simultaneously, the laser was easily transformed to heat to accelerate drug release. Compared to simple drug delivery, this work has great novelty [100] (Fig. 3.21).

3.5.2.2 Photothermal Therapy

Photothermal therapy is the most common treatment modality of AuNRs due to the LSPR effect in the near-infrared region with better tissue penetration depth. AuNRs induced by higher-power near-infrared light generate heat to cause tumor cell membrane blebbing and enhance cell membrane permeability significantly. In addition, heat will result in intracellular protein denaturation and the loss of mitochondrial function, leading to cell necrosis. Mostafa A. El-Sayed's group used anti-EGFR-modified AuNRs for photothermal therapy of cancer cells at different power. Malignant cells required about half the laser energy to be photothermally destroyed compared with the nonmalignant cells after exposure to 800 nm laser [92]. Recently, other structures of gold nanoparticles have been studied in comparison with AuNRs. Au nanohexapods exhibited the highest cellular uptake, the lowest cytotoxicity, and the most efficient of photothermal therapy compared with AuNRs and Au

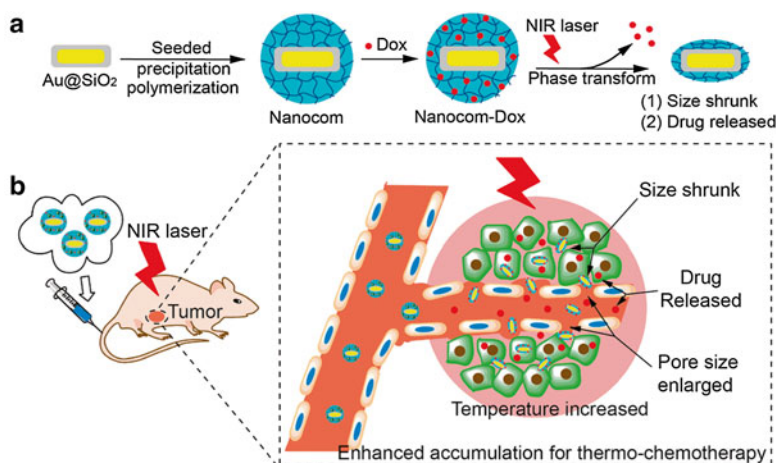


Fig. 3.21 (a) The process of nanocomposite formulation. (b) NIR laser-induced targeted thermo-chemotherapy (Reprinted with the permission from ref. [100]. Copyright 2014 American Chemical Society)

nanocages [101]. AuNRs could also be designed with a rod-in-shell (rattle-like) structure to be responsive to the first (650–950 nm) and second (1000–1350 nm) NIR windows. The UV-vis-NIR spectrum of the rod-in-shell structure could be controlled by changing the gap distance between the AuNR core and the AuAg nanoshell. Regarding the first NIR window, rod-in-shell particles exhibited a more effective treatment in the laser ablation of solid tumors compared to AuNRs only with 808 nm laser [102] (Fig. 3.22).

3.5.2.3 Photodynamic Therapy

AuNRs as a nanocarrier to deliver photosensitizers to realize photodynamic therapy is the commonly used method [103]. For more advanced applications, intelligent control or multimode treatment was used for efficient and safe therapy. W. Tan's group designed an aptamer switch probe (ASP) linking photosensitizer Ce6 to the surface of AuNRs to target cancer cells for PDT and PTT, as shown in Fig. 3.23. In the region of target cancer cells, the ASP changed conformation to drive Ce6 away from the gold surface to activate photosensitive effect for PDT upon light irradiation. If not, Ce6 would remain on the gold surface resulting in quenching the photosensitive effect. The AuNR-ASP-Ce6 complex also had the added ability to carry many photosensitizers, which enhanced its therapeutic efficiency. Induced by high-power laser, this complex enabled further cell destruction by the photothermal effect. Consequently, this multimodal complex offered a light controlled and remarkably improved therapeutic method, providing high specificity and therapeutic efficiency [104].

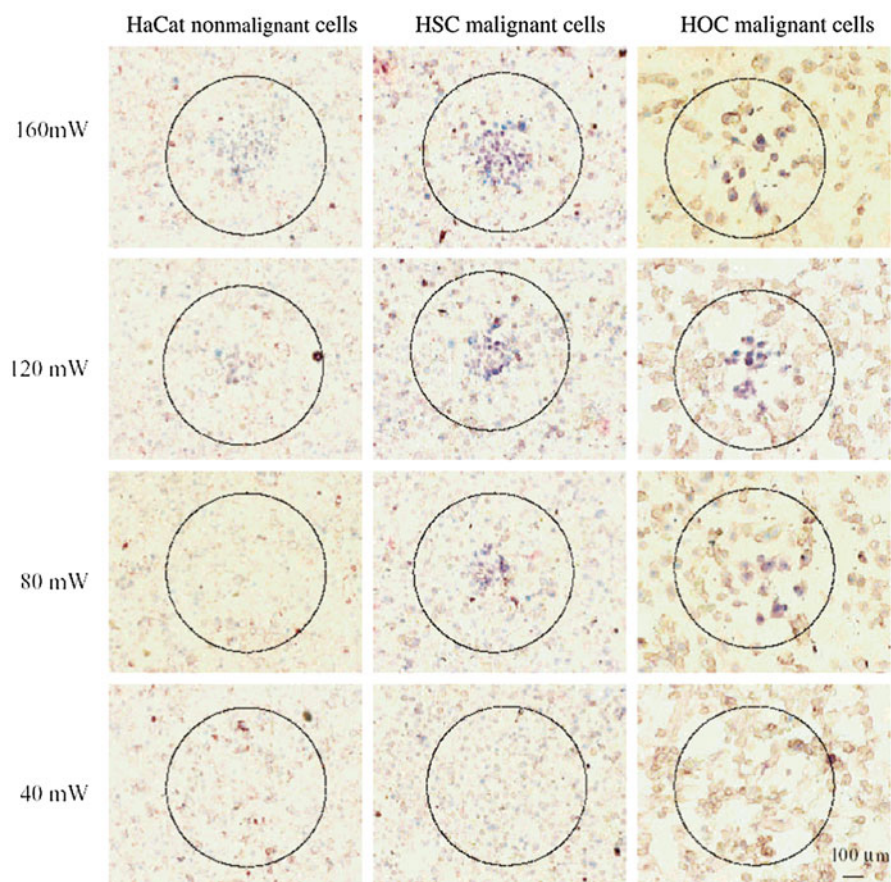
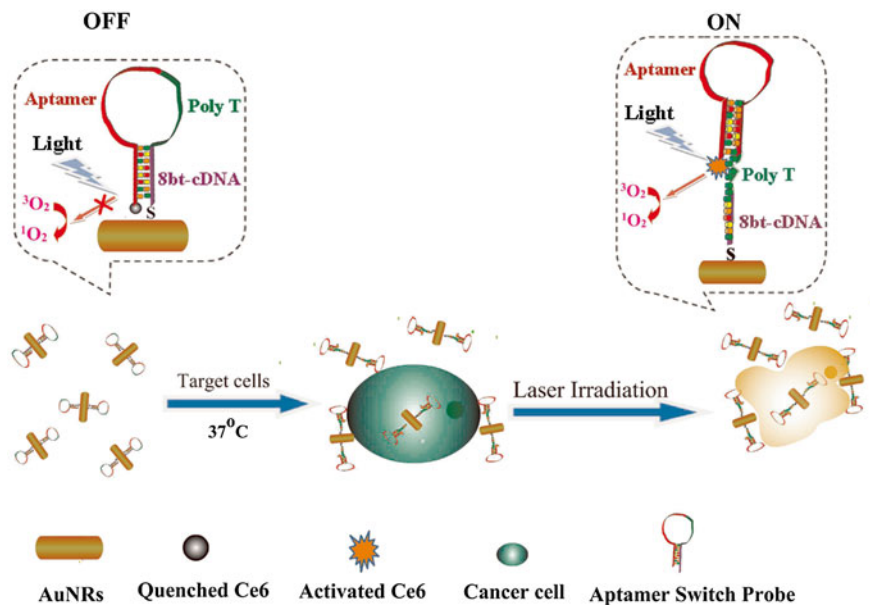


Fig. 3.22 Selective photothermal therapy of cancer cells with anti-EGFR-modified AuNRs at different power (Reprinted with the permission from ref. [92]. Copyright 2006 American Chemical Society)

3.5.2.4 Combined Applications

Nanomaterials have great potential to integrate imaging diagnosis and therapeutic treatment into a single nanoplatform for combined applications such as imaging-guided therapy, multimode therapy, and therapeutic monitoring following treatments for optimizing therapeutic efficacy and safety of therapeutic regimes, compared with single-function application. AuNRs modified with fluorescence agents, targeted molecules, or photosensitizers, combining the inherently capable of various types of imaging and therapeutic functionalities, have provided great opportunities for the combination application of AuNRs in biomedicine [1, 105]. Y. Choi's group [49] from Korean National Cancer Center synthesized positively charged short peptide RRLAC and thiol-terminated monomethoxy poly(ethylene glycol)-modified AuNR-AIPcS4 composite to achieve near-infrared fluorescence imaging, light-activated



Sequence: 5'-SH-CTA ACC GTT TTT TTT TTT TTT TTT TTT TTT TTT TTT TTT TAT CTA
ACT GCT GCG CCG CCG GGA AAA TAC TGT ACG GTT AGA-Ce6-3'

Fig. 3.23 Schematic representation of AuNR-ASP-Ce6 for light-controlled PTT and PDT [104] (Reprinted with the permission from ref. [104]. Copyright 2012 American Chemical Society)

photodynamic therapy, and photothermal therapy (Fig. 3.24). This composite has four advantages: (1) Safety and intelligent control. Fluorescence emission and singlet oxygen generated by AlPcS4 were quenched on the surface of AuNRs. If there was no light to release and activate the photosensitizers, there was no phototoxicity to normal cells or tissues. (2) Near-infrared fluorescence imaging. Tumor sites were clearly identified on near-infrared fluorescence images after injection with AuNR-AlPcS4 complex. (3) Great intracellular uptake. Fourfold greater intracellular uptake was observed in GNR-AlPcS4-injected cells than free AlPcS4. (4) High treatment efficiency with synergistic therapeutic. Tumor growth was reduced by 79 % with PDT alone and by 95 % with dual PTT and PDT. All of these advantages were based on this multifunctional nanomaterial. However, only the combination of multiple functions without innovation has been extensively studied. The study of new applications, new features, and new functionalities is the direction of future development.

3.5.3 AuNRs for New Applications

After more than 10 years of extensive research, the applications of AuNRs based on traditional ideas are difficult to be further developed. Recently, some typically new applications of AuNRs provide a new way of thinking.

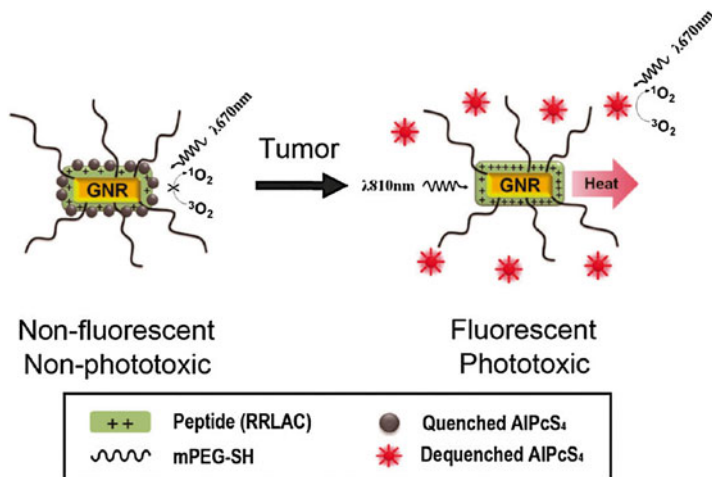


Fig. 3.24 AuNR-AIPcS₄ complex for near-infrared fluorescence imaging and PTT/PDT [49] (Reprinted with the permission from ref. [49]. Copyright 2011 American Chemical Society)

3.5.3.1 New Unique Way to Challenge Drug Resistance

Drug resistance is a common phenomenon in chemotherapy. Generally, resistant cells develop a high expression of drug transporters such as P-glycoprotein (Pgp) to effuse a wide variety of natural drugs. Nanomaterials are widely used to overcome drug resistance through intracellular endocytosis to improve drug accumulation. Is there any new unique way to challenge drug resistance? Recently, C. Chen's group has reported a novel yet simple strategy to overcome cancer drug resistance using the plasmonic feature-based photothermal properties. The use of localized plasmonic heating of AuNRs at a mild laser power density of femtosecond pulsed laser could modulate the drug-resistance-related genes to overcome drug resistance, rather than directly killing cancer cells using AuNR-mediated photothermal therapy. This photothermal effect could trigger higher expression of heat shock factor (HSF-1) trimmers and depress the expression of Pgp and mutant p53 to accumulate drugs in the breast cancer-resistant cells (MCF-7/ADR) and improve their sensitivity to drugs to develop chemotherapy efficiency. Not only the intracellular endocytosis, but also the plasmonic feature-based photothermal properties of AuNRs were innovatively applied to modulate the drug-resistance-related genes. Considering the universality and feasibility of this strategy, it indicated the direction of new applications and greatly broadened the applications of AuNRs [106].

3.5.3.2 Localized Electric Field of Plasmonic AuNR-Enhanced Photodynamic Therapy

Generally, it was known that fluorescence emission and singlet oxygen generation of the photosensitizers on the surface of AuNRs would be quenched by virtue of the effective energy transfer from the photosensitizer to the GNR [49]. Recently,

the mechanism of plasmonic AuNRs has been explored to control $^1\text{O}_2$ generation of photosensitizers. When the LSPR band is in resonance with the absorption band of the photosensitizer on the surface of AuNRs, the absorption of the photosensitizer is greatly enhanced by localized electric field to remarkably enhance the production of $^1\text{O}_2$ [107]. G. Nie's group tailor designed a nanoplatform, composed of mesoporous silica-coated AuNRs with loading near-infrared photodynamic dye (ICG) to optimize the photodynamic therapy (PDT) for tumor based on the electromagnetic near-field enhancement. ICG was one of photosensitizers with poor photostability and low quantum yield. The overlap of LSPR peak of AuNRs and the exciton absorption of ICG increased the $^1\text{O}_2$ yield of incorporated ICG by maximizing the electromagnetic near-field enhancement and protected the ICG molecules against photodegradation due to the high-absorption cross section of the AuNRs. The silica shell on the AuNRs also greatly increased the payload of ICG with the additional benefit of improving the photosensitive efficiency with the high-concentration ICG and enhancing ICG photostability by facilitating the formation of ICG aggregates. The integrated strategy was a novel and important way to significantly improve the photodynamic destruction of tumors with mild laser irradiation through the effect of the electromagnetic near-field enhancement [108] (Fig. 3.25).

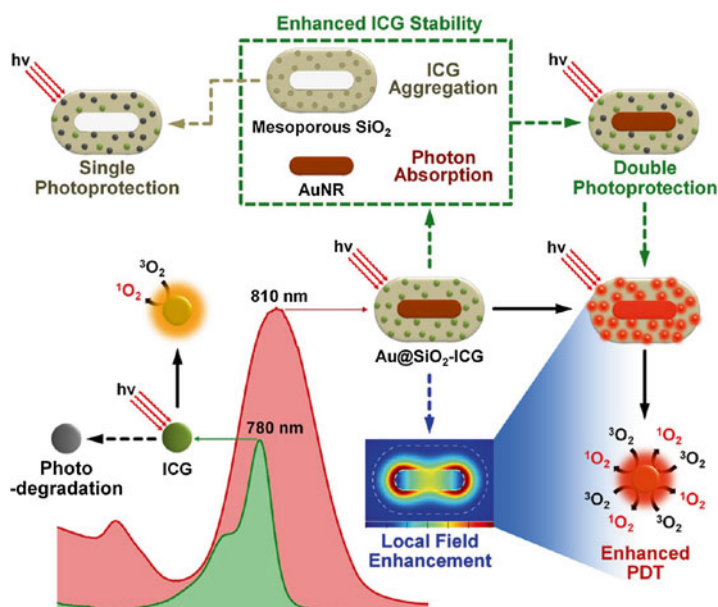


Fig. 3.25 Design of enhanced PDT by utilizing the electromagnetic near-field enhancement of AuNRs [108] (Reprinted with the permission from ref. [108]. Copyright 2014 American Chemical Society)

3.5.3.3 Highly Efficient and Safe Photodynamic Therapy

With the development of nanotechnology, the delivery of photosensitizers by nanomaterials has been widely used to improve the treatment efficacy in PDT based on the passive/active targeting and accumulation of tumors. However, photosensitizers that are electrostatically adsorbed onto the surface of AuNRs can easily release when transporting throughout the body, resulting in uncontrollable damage to normal cells by light irradiation. Recently, our group investigated a highly efficient and safe photodynamic therapy mode by developing a high-/low-power density photodynamic therapy mode (high/low PDT mode) induced by single continuous wave laser using mPEG-SH and polyelectrolyte-modified AuNR-AIPcS4 photosensitizer complexes. mPEG-SH contacted with the gold surface to form Au-S bond through the gap of the polyelectrolyte layer acted as a “brush” to enhance the spatial stability of the nanoparticles and help the small AIPcS4 molecules to adsorb onto polyelectrolyte and reduce the chances of escaping from the surface of AuNRs to improve encapsulation and loading efficiency. Based on the high loading efficiency of AuNR-AIPcS4 complexes, high-power density light (short duration) was firstly used to accelerate the release of AIPcS4 from the surface of AuNRs through the plasmonic photothermal effect of AuNRs. Simultaneously, the PDT was activated by the same laser. Next, low-power density light (long duration) was used to attain prolonged PDT efficacy through AIPcS4 release over a relatively long time frame. Overall, this high/low PDT mode realized high PDT efficacy (about 90 % tumor cell killing) with high light dose = 80 mW/cm² for 0.5 min and low light dose = 25 mW/cm² for 1.5 min. However, applying the same condition in the control group (free AIPcS4 equiv.), there was no significant cytotoxicity due to lower cellular concentrations of AIPcS4 and insufficient irradiation doses. Consequently, free AIPcS4 released from AuNRs prior to cellular entry did not contribute to cytotoxicity of normal cells. This high/low PDT mode also reduced the use of high-power density laser to decrease the treatment risk. Combined with the special properties of AuNRs, this high/low PDT mode could effectively reduce the treatment risk and the cytotoxicity to normal cells and may effectively lead to a safer and more efficient photodynamic therapy for superficial tumors [109].

3.6 Perspectives

As described in the previous sections, we have reviewed the synthesis methods, surface modification and functionalization, optical properties, and the research-level biomedical applications of AuNRs with some representative work and some new applications in diagnostic, therapeutic, and theranostic applications for accurate, efficient, and safe therapy. An in-depth understanding on how to optimize the properties of AuNRs for designing and preparing new AuNR-based nanoplatfoms is needed. Collaboration between chemists, biologists, optical scientists, materials scientists, and clinicians would further help to promote the innovative biomedical

applications of AuNRs. On one hand, we need more *in vivo* studies on the therapeutic efficacy, biocompatibility, and biodistribution which are required to make these techniques more clinically relevant. On the other hand, more studies on new applications, new features, and new functionalities are also needed to make AuNRs shine in the scientific world.

Acknowledgments This work was supported by the National Nature Science Foundation of China (81401452 and U1432114), Hundred Talents Program of the Chinese Academy of Sciences (2010-735), and by Key Breakthrough Program of Chinese Academy of Sciences (KGZD-EW-T06), and Ningbo Natural Science Foundation (2014A610158).

References

1. Zhang ZJ, Wang J, Chen CY (2013) Gold nanorods based platforms for light-mediated theranostics. *Theranostics* 3:223–238
2. Huang X, Jain PK, El-Sayed IH et al (2007) Gold nanoparticles: interesting optical properties and recent applications in cancer diagnostics and therapy. *Nanomedicine* 2:681–693
3. Vigderman L, Khanal BP, Zubarev ER (2012) Functional gold nanorods: synthesis, self-assembly, and sensing applications. *Adv Mater* 24:4811–4841
4. Kelkar SS, Reineke TM (2011) Theranostics: combining imaging and therapy. *Bioconjug Chem* 22:1879–1903
5. Xie J, Lee S, Chen XY (2010) Nanoparticle-based theranostic agents. *Adv Drug Deliv Rev* 62:1064–1079
6. Jain PK, Huang XH, El-Sayed IH et al (2008) Noble metals on the nanoscale: optical and photothermal properties and some applications in imaging, sensing, biology, and medicine. *Acc Chem Res* 41:1578–1586
7. Dreaden EC, Alkilany AM, Huang XH et al (2012) The golden age: gold nanoparticles for biomedicine. *Chem Soc Rev* 41:2740–2779
8. Eustis S, El-Sayed MA (2006) Why gold nanoparticles are more precious than pretty gold: noble metal surface plasmon resonance and its enhancement of the radiative and nonradiative properties of nanocrystals of different shapes. *Chem Soc Rev* 35:209–217
9. Lohse SE, Murphy CJ (2013) The quest for shape control: a history of gold nanorod synthesis. *Chem Mater* 25:1250–1261
10. Grzelczak M, Perez-Juste J, Mulvaney P et al (2008) Shape control in gold nanoparticle synthesis. *Chem Soc Rev* 37:1783–1791
11. Langille MR, Personick ML, Zhang J et al (2012) Defining rules for the shape evolution of gold nanoparticles. *J Am Chem Soc* 134:14542–14554
12. Burda C, Chen XB, Narayanan R et al (2005) Chemistry and properties of nanocrystals of different shapes. *Chem Rev* 105:1025–1102
13. Martin CR (1994) Nanomaterials: a membrane-based synthetic approach. *Science* 266:1961–1966
14. Kim F, Song JH, Yang PD (2002) Photochemical synthesis of gold nanorods. *J Am Chem Soc* 124:14316–14317
15. Yu YY, Chang SS, Lee CL et al (1997) Gold nanorods: electrochemical synthesis and optical properties. *J Phys Chem B* 101:6661–6664
16. Busbee BD, Obare SO, Murphy CJ (2003) An improved synthesis of high-aspect-ratio gold nanorods. *Adv Mater* 15:414–416
17. Jana NR, Gearheart L, Murphy CJ (2001) Wet chemical synthesis of high aspect ratio cylindrical gold nanorods. *J Phys Chem B* 105:4065–4067

18. Nikoobakht B, El-Sayed MA (2003) Preparation and growth mechanism of gold nanorods (NRs) using seed-mediated growth method. *Chem Mater* 15:1957–1962
19. Sau TK, Murphy CJ (2004) Seeded high yield synthesis of short Au nanorods in aqueous solution. *Langmuir* 20:6414–6420
20. Liu FK, Chang YC, Ko FH et al (2004) Microwave rapid heating for the synthesis of gold nanorods. *Mater Lett* 58:373–377
21. Jana NR (2005) Gram-scale synthesis of soluble, near-monodisperse gold nanorods and other anisotropic nanoparticles. *Small* 1:875–882
22. Xu X, Zhao Y, Xue X et al (2014) Seedless synthesis of high aspect ratio gold nanorods with high yield. *J Mater Chem A* 2:3528–3535
23. Ali M, Snyder B, El-Sayed MA (2012) Synthesis and optical properties of small Au nanorods using a seedless growth technique. *Langmuir* 28:9807–9815
24. Murphy CJ, Sau TK, Gole AM et al (2005) Anisotropic metal nanoparticles: synthesis, assembly, and optical applications. *J Phys Chem B* 109:13857–13870
25. Murphy CJ, Thompson LB, Alkilany AM et al (2010) The many faces of gold nanorods. *J Phys Chem Lett* 1:2867–2875
26. Orendorff CJ, Murphy CJ (2006) Quantitation of metal content in the silver-assisted growth of gold nanorods. *J Phys Chem B* 110:3990–3994
27. Gold* AND nanorod*. Web of Science, Thomson Reuters: Philadelphia. Accessed 11 Nov 2014
28. Gole A, Murphy CJ (2004) Seed-mediated synthesis of gold nanorods: role of the size and nature of the seed. *Chem Mater* 16:3633–3640
29. Jiang XC, Pileni MP (2007) Gold nanorods: influence of various parameters as seeds, solvent, surfactant on shape control. *Colloid Surf A* 295:228–232
30. Perez-Juste J, Liz-Marzan LM, Carnie S et al (2004) Electric-field-directed growth of gold nanorods in aqueous surfactant solutions. *Adv Funct Mater* 14:571–579
31. Smith DK, Miller NR, Korgel BA (2009) Iodide in CTAB prevents gold nanorod formation. *Langmuir* 25:9518–9524
32. Rayavarapu RG, Ungureanu C, Krystek P et al (2010) Iodide impurities in hexadecyltrimethyl ammonium bromide (CTAB) products: lot-lot variations and influence on gold nanorod synthesis. *Langmuir* 26:5050–5055
33. Edgar JA, McDonagh AM, Cortie MB (2012) Formation of gold nanorods by a stochastic “popcorn” mechanism. *ACS Nano* 6:1116–1125
34. Park K, Drummy LF, Wadams RC et al (2013) Growth mechanism of gold nanorods. *Chem Mater* 25:555–563
35. Almora-Barrios N, Novell-Leruth G, Whiting P et al (2014) Theoretical description of the role of halides, silver, and surfactants on the structure of gold nanorods. *Nano Lett* 14:871–875
36. Ye X, Jin L, Caglayan H et al (2012) Improved size-tunable synthesis of monodisperse gold nanorods through the use of aromatic additives. *ACS Nano* 6:2804–2817
37. Ye XC, Zheng C, Chen J et al (2013) Using binary surfactant mixtures to simultaneously improve the dimensional tunability and monodispersity in the seeded growth of gold nanorods. *Nano Lett* 13:765–771
38. Ye XC, Gao YZ, Chen J et al (2013) Seeded growth of monodisperse gold nanorods using bromide-free surfactant mixtures. *Nano Lett* 13:2163–2171
39. Vigdeman L, Zubarev ER (2013) High-yield synthesis of gold nanorods with longitudinal SPR peak greater than 1200 nm using hydroquinone as a reducing agent. *Chem Mater* 25:1450–1457
40. Xiang YJ, Wu XC, Liu DF et al (2008) Tuning the morphology of gold nanocrystals by switching the growth of {110} facets from restriction to preference. *J Phys Chem C* 112:3203–3208
41. Kozek KA, Kozek KM, Wu WC et al (2013) Large-scale synthesis of gold nanorods through continuous secondary growth. *Chem Mater* 25:4537–4544

42. Cobley CM, Chen JY, Cho EC et al (2011) Gold nanostructures: a class of multifunctional materials for biomedical applications. *Chem Soc Rev* 40:44–56
43. Liu X, Huang N, Li H et al (2014) Multidentate polyethylene glycol modified gold nanorods for in vivo near-infrared photothermal cancer therapy. *ACS Appl Mater Interfaces* 6:5657–5668
44. Alkilany AM, Shatanawi A, Kurtz T et al (2012) Toxicity and cellular uptake of gold nanorods in vascular endothelium and smooth muscles of isolated rat blood vessel: importance of surface modification. *Small* 8:1270–1278
45. Boca SC, Astilean S (2010) Detoxification of gold nanorods by conjugation with thiolated poly(ethylene glycol) and their assessment as SERS-active carriers of Raman tags. *Nanotechnology* 21:235601
46. Xiao Y, Hong H, Matson VZ et al (2012) Gold nanorods conjugated with doxorubicin and cRGD for combined anticancer drug delivery and PET imaging. *Theranostics* 2:757–768
47. Black KC, Kirkpatrick ND, Troutman TS et al (2008) Gold nanorods targeted to delta opioid receptor: plasmon-resonant contrast and photothermal agents. *Mol Imaging* 7:50–57
48. Yamashita S, Fukushima H, Akiyama Y et al (2011) Controlled-release system of single-stranded DNA triggered by the photothermal effect of gold nanorods and its in vivo application. *Bioorg Med Chem* 19:2130–2135
49. Jang B, Park JY, Tung CH et al (2011) Gold nanorod-photosensitizer complex for near-infrared fluorescence imaging and photodynamic/photothermal therapy in vivo. *ACS Nano* 5:1086–1094
50. Gole A, Murphy CJ (2005) Polyelectrolyte-coated gold nanorods: synthesis, characterization and immobilization. *Chem Mater* 17:1325–1330
51. Xu L, Liu Y, Chen Z et al (2012) Surface-engineered gold nanorods: promising DNA vaccine adjuvant for HIV-1 treatment. *Nano Lett* 12:2003–2012
52. Alkilany AM, Thompson LB, Boulos SP et al (2012) Gold nanorods: their potential for photothermal therapeutics and drug delivery, tempered by the complexity of their biological interactions. *Adv Drug Deliv Rev* 64:190–199
53. Alkilany AM, Nagaria PK, Wyatt MD et al (2010) Cation exchange on the surface of gold nanorods with a polymerizable surfactant: polymerization, stability, and toxicity evaluation. *Langmuir* 26:9328–9333
54. Huang J, Jackson KS, Murphy CJ (2012) Polyelectrolyte wrapping layers control rates of photothermal molecular release from gold nanorods. *Nano Lett* 12:2982–2987
55. Qiu Y, Liu Y, Wang L et al (2010) Surface chemistry and aspect ratio mediated cellular uptake of Au nanorods. *Biomaterials* 31:7606–7619
56. Lee SE, Sasaki DY, Perroud TD et al (2009) Biologically functional cationic phospholipid-gold nanoplasmonic carriers of RNA. *J Am Chem Soc* 131:14066–14074
57. Orendorff CJ, Alam TM, Sasaki DY et al (2009) Phospholipid-gold nanorod composites. *ACS Nano* 3:971–983
58. Kah JC, Zubieta A, Saavedra RA et al (2012) Stability of gold nanorods passivated with amphiphilic ligands. *Langmuir* 28:8834–8844
59. Chen YS, Frey W, Kim S et al (2011) Silica-coated gold nanorods as photoacoustic signal nanoamplifiers. *Nano Lett* 11:348–354
60. Gorelikov I, Matsuura N (2008) Single-step coating of mesoporous silica on cetyltrimethyl ammonium bromide-capped nanoparticles. *Nano Lett* 8:369–373
61. Choi E, Kwak M, Jang B et al (2013) Highly monodisperse rattle-structured nanomaterials with gold nanorod core-mesoporous silica shell as drug delivery vehicles and nanoreactors. *Nanoscale* 5:151–154
62. Slowing II, Vivero-Escoto JL, Wu CW et al (2008) Mesoporous silica nanoparticles as controlled release drug delivery and gene transfection carriers. *Adv Drug Deliv Rev* 60:1278–1288
63. Zhang ZJ, Wang LM, Wang J et al (2012) Mesoporous silica-coated gold nanorods as a light-mediated multifunctional theranostic platform for cancer treatment. *Adv Mater* 24:1418–1423

64. Huang P, Bao L, Zhang C et al (2011) Folic acid-conjugated silica-modified gold nanorods for X-ray/CT imaging-guided dual-mode radiation and photo-thermal therapy. *Biomaterials* 32:9796–9809
65. Zhang Y, Qian J, Wang D et al (2013) Multifunctional gold nanorods with ultrahigh stability and tunability for in vivo fluorescence imaging, SERS detection, and photodynamic therapy. *Angew Chem Int Ed* 52:1148–1151
66. Liz-Marzan LM (2006) Tailoring surface plasmons through the morphology and assembly of metal nanoparticles. *Langmuir* 22:32–41
67. Link S, El-Sayed MA, Mohamed MB (2005) Simulation of the optical absorption spectra of gold nanorods as a function of their aspect ratio and the effect of the medium dielectric constant. *J Phys Chem B* 109:10531–10532
68. Sprunken DP, Omi H, Furukawa K et al (2007) Influence of the local environment on determining aspect-ratio distributions of gold nanorods in solution using Gans theory. *J Phys Chem C* 111:14299–14306
69. Xu XB, Li HF, Hasan D et al (2013) Near-field enhanced plasmonic-magnetic bifunctional nanotubes for single cell bioanalysis. *Adv Funct Mater* 23:4332–4338
70. Blackie EJ, Le Ru EC, Etchegoin PG (2009) Single-molecule surface-enhanced raman spectroscopy of nonresonant molecules. *J Am Chem Soc* 131:14466–14472
71. Nie SM, Emery SR (1997) Probing single molecules and single nanoparticles by surface-enhanced Raman scattering. *Science* 275:1102–1106
72. Orendorff CJ, Gearheart L, Jana NR et al (2006) Aspect ratio dependence on surface enhanced Raman scattering using silver and gold nanorod substrates. *Phys Chem Chem Phys* 8:165–170
73. Mooradia A (1969) Photoluminescence of metals. *Phys Rev Lett* 22:185–187
74. Mohamed MB, Volkov V, Link S et al (2000) The ‘lightning’ gold nanorods: fluorescence enhancement of over a million compared to the gold metal. *Chem Phys Lett* 317:517–523
75. Imura K, Nagahara T, Okamoto H (2005) Near-field two-photon-induced photoluminescence from single gold nanorods and imaging of plasmon modes. *J Phys Chem B* 109:13214–13220
76. Varnavski OP, Mohamed MB, El-Sayed MA et al (2003) Relative enhancement of ultrafast emission in gold nanorods. *J Phys Chem B* 107:3101–3104
77. Wang HF, Huff TB, Zweifel DA et al (2005) In vitro and in vivo two-photon luminescence imaging of single gold nanorods. *Proc Natl Acad Sci U S A* 102:15752–15756
78. Song J, Pu L, Zhou J et al (2013) Biodegradable theranostic plasmonic vesicles of amphiphilic gold nanorods. *ACS Nano* 7:9947–9960
79. Funston AM, Novo C, Davis TJ et al (2009) Plasmon coupling of gold nanorods at short distances and in different geometries. *Nano Lett* 9:1651–1658
80. Huang H, Wang JH, Jin W et al (2014) Competitive reaction pathway for site-selective conjugation of Raman dyes to hotspots on gold nanorods for greatly enhanced SERS performance. *Small* 10:4012–4019
81. Bardhan R, Grady NK, Cole JR et al (2009) Fluorescence enhancement by Au nanostructures: nanoshells and nanorods. *ACS Nano* 3:744–752
82. Jain PK, Huang WY, El-Sayed MA (2007) On the universal scaling behavior of the distance decay of plasmon coupling in metal nanoparticle pairs: a plasmon ruler equation. *Nano Lett* 7:2080–2088
83. Maier SA, Kik PG, Atwater HA et al (2003) Local detection of electromagnetic energy transport below the diffraction limit in metal nanoparticle plasmon waveguides. *Nat Mater* 2:229–232
84. Ge JC, Lan MH, Zhou BJ et al (2014) A graphene quantum dot photodynamic therapy agent with high singlet oxygen generation. *Nat Commun* 5:1–8
85. Vankayala R, Sagadevan A, Vijayaraghavan P et al (2011) Metal nanoparticles sensitize the formation of singlet oxygen. *Angew Chem Int Ed* 50:10640–10644

86. Zhao T, Shen X, Li L et al (2012) Gold nanorods as dual photo-sensitizing and imaging agents for two-photon photodynamic therapy. *Nanoscale* 4:7712–7719
87. Jiang CF, Zhao TT, Yuan PY et al (2013) Two-photon induced photoluminescence and singlet oxygen generation from aggregated gold nanoparticles. *ACS Appl Mater Interfaces* 5:4972–4977
88. Vankayala R, Kuo CL, Sagadevan A et al (2013) Morphology dependent photosensitization and formation of singlet oxygen ($(^1\Delta_g)$) by gold and silver nanoparticles and its application in cancer treatment. *J Mater Chem B* 1:4379–4387
89. Vankayala R, Huang YK, Kalluru P et al (2014) First demonstration of gold nanorods-mediated photodynamic therapeutic destruction of tumors via near infra-red light activation. *Small* 10:1612–1622
90. Yang JP, Shen DK, Zhou L et al (2014) Mesoporous silica-coated plasmonic nanostructures for surface-enhanced Raman scattering detection and photothermal therapy. *Adv Healthc Mater* 3:1620–1628
91. Jung Y, Reif R, Zeng YG et al (2011) Three-dimensional high-resolution imaging of gold nanorods uptake in sentinel lymph nodes. *Nano Lett* 11:2938–2943
92. Huang X, El-Sayed IH, Qian W et al (2006) Cancer cell imaging and photothermal therapy in the near-infrared region by using gold nanorods. *J Am Chem Soc* 128:2115–2120
93. Durr NJ, Larson T, Smith DK et al (2007) Two-photon luminescence imaging of cancer cells using molecularly targeted gold nanorods. *Nano Lett* 7:941–945
94. Wang L, Hu S (2012) Photoacoustic tomography: in vivo imaging from organelles to organs. *Science* 335:1458–1462
95. Jokerst JV, Cole AJ, Van de Sompel D et al (2012) Gold nanorods for ovarian cancer detection with photoacoustic imaging and resection guidance via Raman imaging in living mice. *ACS Nano* 6:10366–10377
96. Jokerst JV, Thangaraj M, Kempen PJ et al (2012) Photoacoustic imaging of mesenchymal stem cells in living mice via silica-coated gold nanorods. *ACS Nano* 6:5920–5930
97. Li WY, Brown PK, Wang L et al (2011) Gold nanocages as contrast agents for photoacoustic imaging. *Contrast Media Mol Imaging* 6:370–377
98. Sheng ZH, Song L, Zheng JX et al (2013) Protein-assisted fabrication of nano-reduced graphene oxide for combined in vivo photoacoustic imaging and photothermal therapy. *Biomaterials* 34:5236–5243
99. Huang XH, Neretina S, El-Sayed MA (2009) Gold nanorods: from synthesis and properties to biological and biomedical applications. *Adv Mater* 21:4880–4910
100. Zhang Z, Wang J, Nie X et al (2014) Near infrared laser-induced targeted cancer therapy using thermoresponsive polymer encapsulated gold nanorods. *J Am Chem Soc* 136:7317–7326
101. Wang YC, Black K, Luehmann H et al (2013) Comparison study of gold nanohexapods, nanorods, and nanocages for photothermal cancer treatment. *ACS Nano* 7:2068–2077
102. Tsai MF, Chang SH, Cheng FY et al (2013) Au nanorod design as light-absorber in the first and second biological near-infrared windows for in vivo photothermal therapy. *ACS Nano* 7:5330–5342
103. Huang X, Tian XJ, Yang WL et al (2013) The conjugates of gold nanorods and chlorin e6 for enhancing the fluorescence detection and photodynamic therapy of cancers. *Phys Chem Chem Phys* 15:15727–15733
104. Wang J, Zhu GZ, You MX et al (2012) Assembly of aptamer switch probes and photosensitizer on gold nanorods for targeted photothermal and photodynamic cancer therapy. *ACS Nano* 6:5070–5077
105. Srivatsan A, Jenkins SV, Jeon M et al (2014) Gold nanocage-photosensitizer conjugates for dual-modal image-guided enhanced photodynamic therapy. *Theranostics* 4:163–174
106. Wang L, Lin X, Wang J et al (2014) Novel insights into combating cancer chemotherapy resistance using a plasmonic nanocarrier: enhancing drug sensitiveness and accumulation simultaneously with localized mild photothermal stimulus of femtosecond pulsed laser. *Adv Funct Mater* 24:4229–4239

107. Kochuveedu ST, Kim DH (2014) Surface plasmon resonance mediated photoluminescence properties of nanostructured multicomponent fluorophore systems. *Nanoscale* 6:4966–4984
108. Li Y, Wen T, Zhao R et al (2014) Localized electric field of plasmonic nanoplatform enhanced photodynamic tumor therapy. *ACS Nano* 8:11529–11542
109. Shi Z, Ren W, Gong A et al (2014) Stability enhanced polyelectrolyte-coated gold nanorod-photosensitizer complexes for high/low power density photodynamic therapy. *Biomaterials* 35:7058–7067

Part II
Theranostic Luminescent Nanoparticles

Chapter 4

Lanthanide-Doped Upconversion Nanoparticles for Imaging-Guided Drug Delivery and Therapy

Zhanjun Li, Yuanwei Zhang, and Gang Han

Abstract Lanthanide-doped upconversion nanoparticles (UCNPs) possess unique anti-Stokes optical properties, in which low-energy near-infrared (NIR) excitation can be converted into high-energy UV and/or visible emission with pronounced luminescence and chemical stability. Due to the rapid development of synthesis chemistry, lanthanide-doped UCNPs can be fabricated with narrow distribution and modulated physical behaviors. These unique characters endow them unique NIR-driven imaging/delivery/therapeutic applications, especially in the cases of the deep tissue environments. Herein, we introduce both the basic concepts and the up-to-date progresses of UCNPs in material engineering, toxicology, and bio-applications in imaging, molecular delivery, and tumor therapeutics.

Keywords Upconversion nanoparticles • Optical imaging • Drug delivery • Optical therapy

4.1 Introduction

Upconversion is a nonlinear optical process in which long wavelength (usually near-infrared) photons are absorbed by upconversion materials followed by emitting photons with shorter wavelength (typically visible) [1]. Lanthanide-doped UCNPs can be excited with deep tissue-penetrating NIR light (800 nm, 925 nm, 980 nm) and emitting light in a broad range from ultraviolet (UV) to near-infrared (NIR) with various distinctive characteristics, like narrow emission band, large anti-Stokes shift, and less light scattering. These attributes make them unique optical tools for biological studies [2]. In addition, these nanoparticles are non-blinking, non-photobleaching, and extremely stable and dodged the endogenous cellular

Z. Li • Y. Zhang • G. Han (✉)

Department of Biochemistry and Molecular Pharmacology, University of Massachusetts-Medical School, 364 Plantation Street, LRB 806, Worcester, MA 01605, USA
e-mail: gang.han@umassmed.edu

fluorophore spectral window [3, 4]. Thus, low autofluorescent background can be obtained, and therapeutic trackings can be conducted both *in vitro* and *in vivo*.

The working window at both NIR excitation and NIR emission (NIR-to-NIR), which are both within the biological NIR optical transmission window (700–1,000 nm), is particularly important for *in vivo* imaging of small animals, because it permits deep tissue penetration beyond 3 cm and less absorption and scattering of biotissues and organs [5]. The unique advantages of UCNPs make them ideal nano-platform for diverse applications in both imaging and therapy. (1) They can serve as background-free optical probes for targeted imaging [6]. (2) They can be adapted as nanocarriers to precisely deliver therapeutic cargoes, in which way the side effects are minimized in nearby tissues and organs [7]. (3) UCNPs can be used as remote control photoswitches to precisely control the therapeutic procedures in deep tissue [8].

4.2 Engineering of UCNPs for Biomedical Applications

4.2.1 Basic Mechanism of UCNPs

In general, lanthanide-doped UCNPs contain three essential components, (1) sensitizer (usually Yb^{3+}), (2) emitter (usually Tm^{3+} , Er^{3+} , Ho^{3+}), and (3) host matrix. Because of the requirements in the matching of energy levels, the most effective sensitizer/emitter pairs are found to be Yb/Er, Yb/Tm, and Yb/Ho (Fig. 4.1). The upconversion host matrix must have low phonon energies; thus, lattice stress and nonradiative pathways can be minimized. In general, hexagonal AReF_4 (e.g., A: Li/Na/K, Re: Y/Lu/Gd) is broadly considered as the best host matrix for UCNPs [9–11]. Recently, we found that Nd^{3+} , which has a strong absorption at ~ 800 nm, can be used as a novel sensitizer (Fig. 4.2) [12]. By the fabrication of a tri-doped $\text{NaYF}_4:\text{Nd}, \text{Yb}, \text{Er}/\text{Tm}$, the excitation wavelength of lanthanide-based UCNPs can be transferred to 800 nm. This design not only offers a new excitation choice but also can decrease the thermal effect obviously because the absorption coefficient of

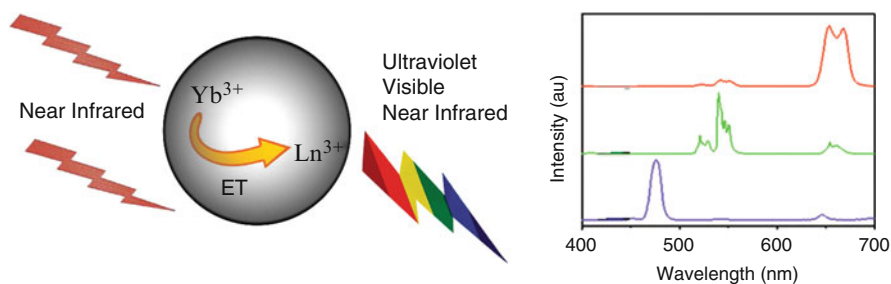


Fig. 4.1 Schematic representation of the excitation/emission and interatomic energy transfer profiles of UCNPs and examples of upconversion emission spectra upon 980 nm excitation

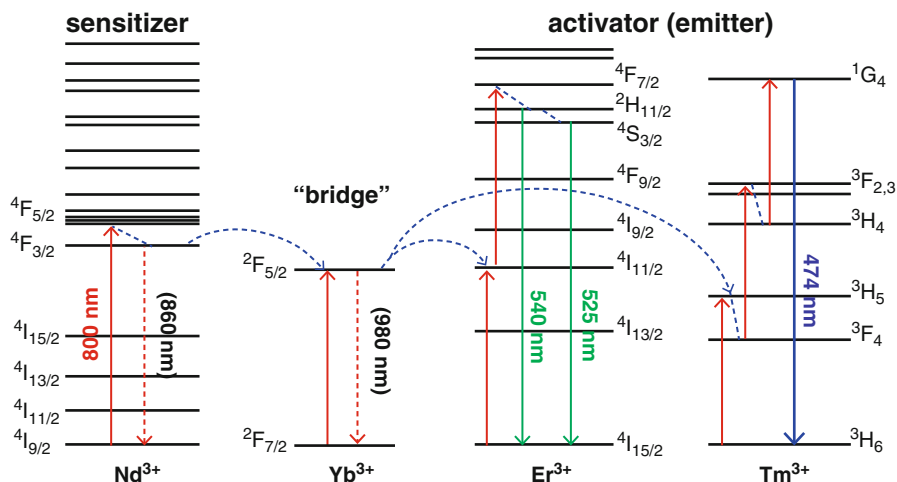


Fig. 4.2 Upconversion process of Nd/Yb/Er(Tm) tri-dopants system with 800 nm excitation (Reproduced from Ref. [12] by permission of John Wiley & Sons Ltd.)

water at 800 nm is several magnitudes lower than that at 980 nm. Thus, we can minimize the thermal side effect during upconversion imaging or therapy by using these tri-doped UCNPs. It should be noted that the upconversion efficiency of these simple tri-doped system is low because of the reverse energy transfer from Er/Tm to Nd. Soon after our report, this problem was solved by fabrication of a core@shell structure which will be discussed later.

4.2.2 Synthesis of UCNPs

Due to the requirement of narrow size distribution and high dispersibility for biological studies, thermal decomposition and solvothermal synthesis techniques are the most widely employed strategies. In addition, with nicely controlled conditions, like temperature, materials ratio, and selected component, the UCNPs can be fabricated with diverse sizes and shapes [13]. In order to generate solvent dispersible UCNPs, Yan et al. developed a high-temperature decomposition strategy, and a variety of monodispersed cubic and hexagonal NaYF₄-based nanocrystals were fabricated with high quality [14]. Generally, the size and morphology of UCNPs can be well controlled by decomposing metal trifluoroacetate precursors at high temperature in mixed solvents of oleic acid, oleicamine, and octadecene. This strategy has become a most typical method to fabricate UCNPs, and the critical synthesis parameters have been thoroughly investigated, such as coordinating solvent compositions [15], decomposition temperature [16], starting material species and ratio [17], and core/shell structures [18]. For example, to synthesize high luminescent and

ultrasmall upconversion nanoparticles with biomolecules of comparable size, Chow et al. fabricated ca. 11 nm β - $\text{NaYF}_4\text{:Yb,Er}$ and β - $\text{NaYF}_4\text{:Yb,Tm}$ UCNPs in pure oleylamine solutions, and further upconversion efficiency was improved by coating inert shell structure [15].

Using hydrothermal synthesis strategy, UCNPs with uniform sizes and shapes can also be achieved. Generally, UCNPs are obtained by mixing fluoride salts (e.g., NH_4F) with lanthanide compounds in solvent with high boiling point such as ethylene glycol and reacted under high temperature and pressure. For example, using this method, β -phased NaYF_4 UCNPs were fabricated with corresponding oleate precursor [19]. More sophisticated strategy was developed using a liquid-solid-solution phase-transfer method in water/alcohol/oleic acid mixture to fulfill predictable size, shapes, and phase UCNPs [20, 21].

4.2.3 UCNPs with Core@shell Structures

As optical bio-probes, high fluorescent efficiency will be required in water solutions. However, the OH and NH_2 groups surrounding the surface of UCNPs could quench the excited states through nonradiative relaxation processes. Nevertheless, when the nanoparticle sizes go smaller, those quenching effects become more severe. In order to conquer this problem, an inert shell (undoped NaYF_4 , NaGaF_4 , NaLuF_4 , etc.) is usually needed to protect the upconverting active core (namely, a core@shell nanostructure) from the outside quenching reagents. Thus, the possibility of energy loss from the active core is highly reduced and consequently enhancing upconversion efficiency. For example, Kong and Zhang carefully studies β - $\text{NaYF}_4\text{:Yb}^{3+},\text{Er}^{3+}$ @ β - NaYF_4 core-shell structure; from the kinetics analysis, they discovered the quenching effect of luminescent centers can be effectively reduced by homogeneous coating with NaYF_4 shell and conduct luminescence enhancing [22]. Later on, Liu et al. showed direct evidence for the surface quenching effect related to the nanoparticle sizes in $\text{NaGaF}_4\text{:Yb,Tm}$. They also intensified the optical integrity, and surface quenching effects of the nanoparticles can be greatly preserved after an inert thin shell coating ($\text{NaGdF}_4\text{:Yb,Tm}@$ NaGdF_4) (Fig. 4.3) [23].

Usually, β - NaY/Gd/LuF_4 is considered to be the best upconversion matrix. And the same host matrix will be used in the active core@inert shell design. Quite interestingly, we find that an epitaxial CaF_2 heteroshell can increase the upconversion efficiency of α - NaYF_4 for hundreds of times (Fig. 4.4). The UV upconversion in α - $\text{NaYbF}_4\text{:Tm}@$ CaF_2 (362 nm) is even higher than β - $\text{NaYF}_4\text{:30 %Yb, 0.5 %Tm}@$ β - NaYF_4 and larger β -phase counterparts [24]. In addition, the CaF_2 coating is found to be more effective in resisting quenching in aqueous medium to preserve the upconverting UV emissions. In the same material, we also find that CaF_2 heteroshell could increase the NIR emission of α - $\text{NaYbF}_4\text{:0.5 %Tm}$ for 35 times with a relative high NIR-to-NIR quantum yield of 0.6 % under low-energy excitation of 0.3 W/cm^2 [5].

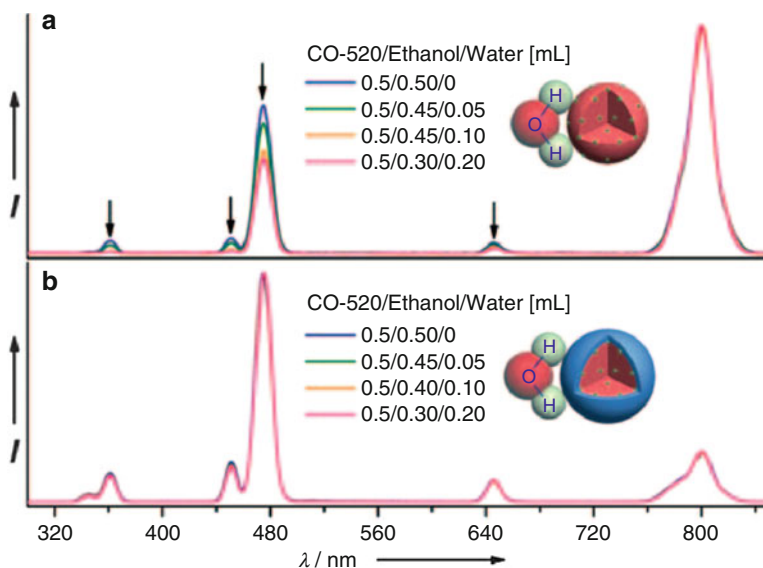


Fig. 4.3 Upconversion emission spectra of (a) NaGdF₄:25 %Yb/0.3 %Tm (15 nm) and (b) corresponding core/shell nanoparticles (20 nm) in nonylphenylether/ethanol/water solutions with different water ratio (Reproduced from Ref. [23] by permission of John Wiley & Sons Ltd.)

For the Nd³⁺-sensitized UCNPs, the upconversion efficiency using 800 nm excitation is relatively low than the traditional 980 nm-excited counterparts. In order to address this issue, Zhao and Yao fabricated quenching-shielded sandwich-structured rare-earth nanoparticles that have high upconversion emissions with excitation at wavelength of 800 nm, as shown in Fig. 4.5 [25]. In this system, the nanostructure has been well defined to eliminate the potential cross-relaxation pathways between the activator and sensitizer by introducing an interlayer of NaYF₄:Yb³⁺. The emission intensity of the nanoparticles reached maximum when the interlayer thickness was ~1.45 nm (NaYF₄:Yb³⁺). This well-defined unique nanostructure is essential to eliminate the deleterious cross-relaxation pathways between the activator and sensitizer by means of a precisely controlled transition layer. The as-synthesized UCNPs are even brighter than conventional 980 nm-excited nanoparticles at low excitation power density of 0.5 W/cm². Further, the use of 800 nm laser source instead of 980 nm one is able to increase the penetration depth in biotissue and suppress overheating.

By simultaneously harnessing the sensitizer Yb³⁺ and Nd³⁺ together into different shell layers of one single nanoparticle, Feng Wang et al. designed a kind of core@multishell nanostructure named NaGdF₄:Yb,Tm @NaGdF₄ @NaYbF₄:Nd @Na(Yb,Gd)F₄:Ho @NaGdF₄, in which different emission can be realized by altering excitation light source (976 nm/blue, 808 nm/green, Fig. 4.6) [26]. Under 976 nm laser excitation, the excitation light will be absorbed by Yb³⁺ in both the core and the shell of the UCNPs. But the energy back transfer from Ho³⁺ to Nd³⁺ will inhibit

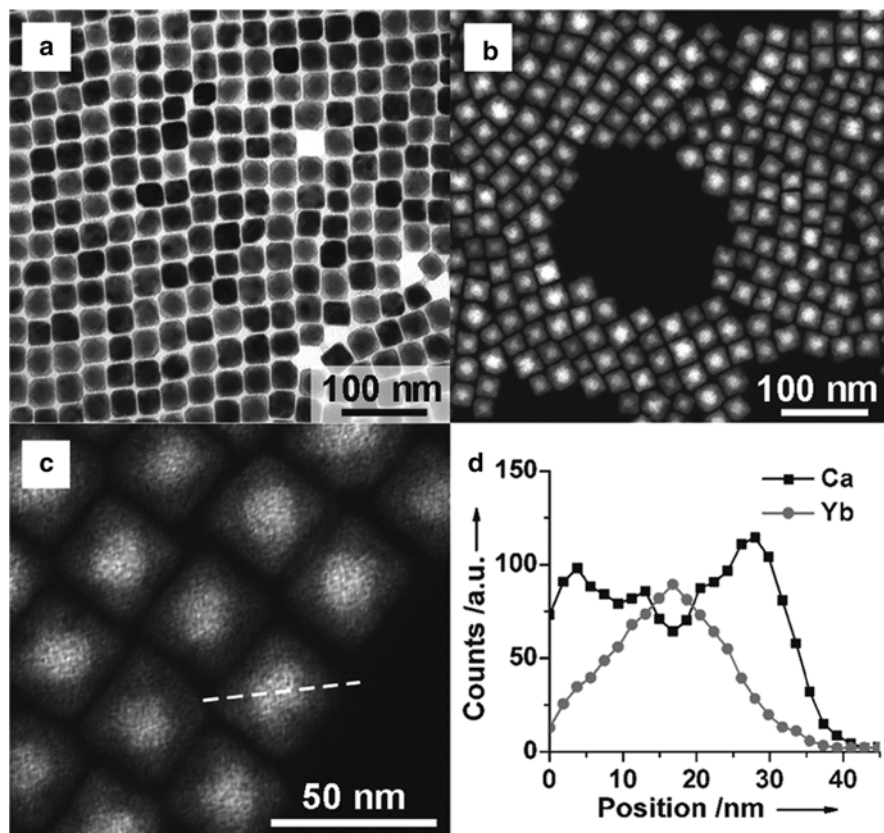


Fig. 4.4 Heteroshell structure of α -NaYbF₄:Tm@CaF₂. (a) TEM, (b) high-angle annular dark-field STEM, (c) linear EDX scanning of a single UCNP, and (d) corresponding elemental ratio analysis (Reproduced from Ref. [24] by permission of John Wiley & Sons Ltd.)

the emission of Ho³⁺ (green). The general emission color will be dominated by transition from Yb to Tm in the core. But, under 808 nm excitation, Nd³⁺ will be sensitized and then transfer the absorbed energy to Ho³⁺ to generate green emission. The energy transfer to the inner core is blocked by the inert NaGdF₄ layer between the Tm³⁺ activated core and the Ho activated shell. Thus, the 808 nm-excited emission will be dominated by Ho³⁺ (green). This kind of excitation-regulated upconversion emission properties will have great potential in the field of multichannel photoactive processes.

Lee's group synthesized a similar dual-channel upconversion system, and more importantly, they demonstrated the two-way photoswitching applications of this novel UCNPs (Fig. 4.7) [27]. The photoisomerization between spiropyran and merocyanine can be regulated by UV and visible light. The maximum absorption peaks of spiropyran and merocyanine that locate at 342 nm and 560 nm overlap well with the UV emission from the Tm³⁺ and Er³⁺, respectively. Thus, under excitation

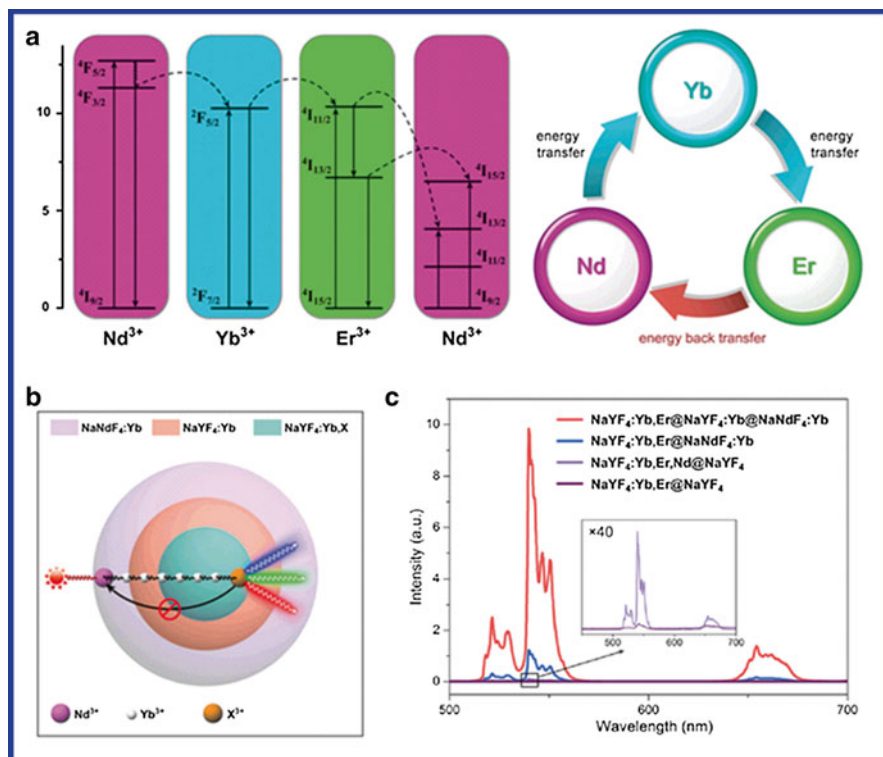


Fig. 4.5 Bright upconversion under 800 nm excitation by engineering core@shell@shell structure. (a) Simplified energy-level diagrams depicting the energy transfer between Nd, Yb, and Er ions upon 800 nm excitation. (b) Schematic illustration of the proposed energy transfer mechanisms in the quenching-shield sandwich-structured UCNPs; c upconversion emission spectra of the as-synthesized UCNPs (Reproduced from Ref. [25] by permission of John Wiley & Sons Ltd.)

of 808 nm, UV emission will be activated by energy transfer from Nd^{3+} to Tm^{3+} , leading to the photoisomerization of spiropyran to merocyanine (pink solution). Thereafter, under the excitation of 980 nm laser, green emission from Er^{3+} can be generated, leading to the photoisomerization of merocyanine back to spiropyran (colorless).

4.2.4 Surface Modification for Upconversion Enhancing and Bio-conjugation

Post-modification of the surface of UCNPs by charged or polar groups can offer them aqueous solubilities and biocompatibilities. In this regard, several strategies have been developed to transfer the as-synthesized hydrophobic nanoparticles into

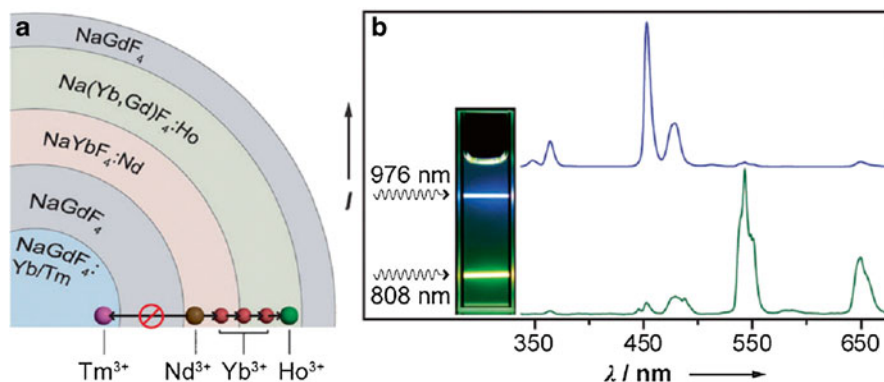


Fig. 4.6 (a) Schematic design of tuning the Nd-sensitized upconversion process through nanostructural engineering. (b) Emission spectra of the multishelled nanoparticles under excitation at 808 and 976 nm, respectively. Inset: digital camera photograph of corresponding solution sample (Reproduced from Ref. [26] by permission of John Wiley & Sons Ltd.)

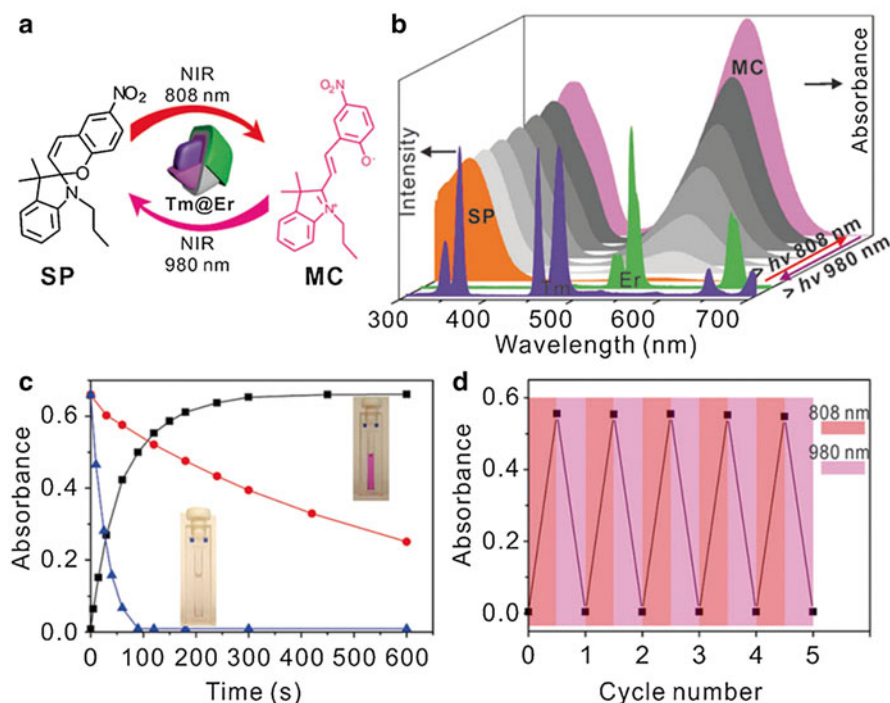


Fig. 4.7 (a) Illustration of two-way photoswitching of spirocyanine by using UCNP with dual NIR excitations. (b) Tm^{3+} and Er^{3+} emissions from the UCNP under 808 nm and 980 nm excitations and the evolution of the UV/vis absorption spectrum of the photoisomerization. (c) Kinetic monitoring of the photoswitching reaction. The red dotted line shows the kinetics of the reaction of merocyanine to spirocyanine. (d) Dual NIR-driven photoswitching of spirocyanine over many cycles in THF/methanol (9/1, v/v) solution by monitoring the absorbance of merocyanine at 560 nm (Reproduced from Ref. [27] by permission of John Wiley & Sons Ltd)

water solution using amphiphilic polymer [28] and ligand oxidation [29]. Firstly, Yadong Li's group developed a polyol solvent ligand exchange method to transfer hydrophobic inorganic nanocrystals from organic solvent to aqueous solution by modifying polyelectrolytes, such as poly(acrylic acid), poly(allylamine), and poly(sodium styrenesulfonate) [30]. In this method, a toluene solution containing hydrophobic nanocrystals is rapidly injected into a heated mixture of polyol (diethylene glycol) and exchanging ligands. The solution becomes turbid immediately because of the insolubility of hydrophobic nanocrystals in the polar solvent. Upon continued heating at a higher temperature close to the boiling point of the solvent, the solution slowly turns clear, indicating the occurrence of ligand exchange and dissolution of nanocrystals in DEG. The nanocrystals can then be precipitated, for example, by adding excess amount of diluted aqueous solution of hydrochloric acid and finally redispersed in water by transforming remaining uncoordinated groups into ionized form. This method is found also effective in the case of UCNPs.

Another effective phase transition method was developed by Angang Dong et al., characterized by using NOBF_4 (Fig. 4.8) [31]. In this method, nitrosonium tetrafluoroborate (NOBF_4) is used to replace the original organic ligands attached to the nanoparticle surface, stabilizing the nanoparticles in various polar, hydrophilic media such as *N,N*-dimethylformamide for years of storage. The hydrophilic nanoparticles obtained can subsequently be further functionalized by using a variety of capping reagents. Furthermore, the phase transition and ligand exchange reaction is so fast that it can be finished in several minutes. And more significantly, the hydrophilic nanoparticles obtained by NOBF_4 treatment can readily undergo secondary surface modification due to the weak binding affinity of BF_4^- anions to the particle surface, allowing reversible phase transition.

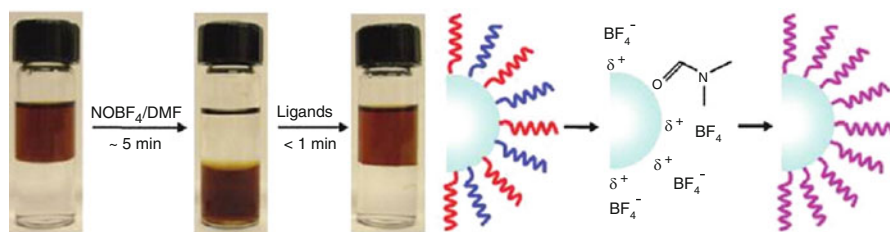


Fig. 4.8 Scheme of the phase transition and ligand exchange procedure by using NOBF_4 (Reprinted with the permission from Ref. [31]. Copyright 2011 American Chemical Society)

4.3 Biosafety of UCNPs

4.3.1 *Internalization of UCNPs into Cells*

The toxic effects of UCNPs in cells and animals are determined by the cell internalization and their distribution sites. Thus, the study of the internalization and distribution sites of UCNPs in cells is important in the assessment of their biosafety. Different from small molecules, it is difficult for UCNPs to cross the plasma membrane on their own. Generally, UCNPs are internalized from endocytosis process of cells. According to previous researches [32], the internalization of nanoparticles is usually regulated through a process termed pinocytosis which involves at least four basic mechanisms: (1) micropinocytosis ($>1\ \mu\text{m}$), (2) clathrin-mediated endocytosis ($\sim 120\ \text{nm}$), (3) caveolae-mediated endocytosis ($\sim 60\ \text{nm}$), and (4) clathrin- and caveolae-independent endocytosis. The real mechanism might vary depending on many factors, such as particle sizes, surface ligands, and incubation conditions. The most common interactions are electrostatic interactions between the UCNPs and the plasma membrane of UCNPs (negatively charged). According to current report, the surface charge of UCNPs severely affects their cellular uptake efficiency. Generally, positive charge can greatly enhance cellular uptake of UCNPs, which is significantly higher than their neutral and negative counterparts. For example, Wong et al. [33] found that positively charged UCNPs modified with polyetherimide (PEI) (50 nm, 51 mV) had five times of cellular uptake than that of neutral UCNPs modified with polyvinylpyrrolidone (PVP). And negatively charged UCNPs modified with poly(acrylic acid) (PAA) (50 nm, $-23\ \text{mV}$) showed the lowest cellular uptake efficiency. Although positive charges can facilitate the internalization of UCNPs, several studies also reported the uptake of negatively charged nanoparticles into cells. For example, Li's group found that citrate-modified UCNPs (20 nm, $-18\ \text{mV}$) could be internalized by KB cells after 1 h incubation [34]. Similar results were also found in sodium glutamate and diethylene triamine pentaacetic acid-modified UCNPs [35]. In addition, it should be noted that the absorption of serum protein *in vitro* or *in vivo* might change the hydrodynamic size and surface charges significantly. On the other hand, there is still no detailed investigation on the internalization process and the intracellular distribution sites of UCNPs.

4.3.2 *Biodistributions of Injected UCNPs in Mice Models*

The *in vivo* imaging study usually applies mice model via intravenous (*i.v.*) injection. Except for some ultrasmall nanoparticles, the final deposition site was mainly the liver and spleen, which is usually attributed to the capture by the reticuloendothelial system (RES). To increase the systemic circulation time of injected UCNPs, a well-designed surface modification will be needed to avoid the capture by the RES. In this regard, polyethylene glycol (PEG) is usually the most effective surface

ligand, and it is approved by the US Food and Drug Administration because of its low immunogenicity and antigenicity. The highly flexible chains of PEG can provide a “conformational cloud” around the particles, which prevents the surface absorption of blood components and the subsequent recognition of the RES. Li’s group found that the half-life circulation time of PEG-UCNPs was about ten times (4.3 h vs. 0.4 h) as high as nude UCNPs [36]. Targeting moieties are required to increase the concentration of UCNPs in specific sites of diseases, namely, targeted delivery/imaging. In this regard, folic acid was frequently applied to modify UCNPs to fabricate targeted imaging nanoprobes, on the basis of the high affinity of folic acid and its receptor (usually highly expressed in tumor) [37]. To date, there is a series of targeting moieties developed to decrease the nonspecific distributions of UCNPs, such as tripeptide [38], chlorotoxin [39], heparin [40], and antibodies [41].

4.3.3 Excretion of UCNPs

The FDA requires that injected agents, especially the diagnosis agents, should be completely cleared in a reasonable time period. It is known that most injected agents can be excreted from the hepatobiliary or renal route. Hepatocytes serve as an important site for the elimination of injected nanoparticles through phagocytosis. In a previous report by Li’s group [42], PAA-modified UCNPs could be found in the intestinal tract after 7 days postinjection, indicating the clearance via hepatobiliary transport. After 21 days postinjection, the UCNPs could only be detected in the intestinal tract and remained unchanged up to 90 days. After 115 days, almost no UCNPs could be found in the mouse. These results indicated that the internalized UCNPs can be excreted out of the body, although for a long time. Moreover, no significant change could be observed in size, size distribution, and morphology using transmission electron microscopy in the excreted UCNPs comparing with the initial nanoparticles before injection.

Renal excretion is the other vital important way for the clearance of nanoparticles. It is generally accepted that the size of nanoparticle is one of the most important determinants of the excretion pathway. Although the smallest nanostructural dimensions are *ca.* 43 nm in the glomerular capillary wall, the functional or physiologic pore size is considered to be only 4.5–5 nm in diameter, considering the combined effects of several layers of glomerular capillary [43]. Li’s group studied the *in vivo* metabolism of sub-10 nm PEG-UCNPs labeled by radioactive ^{153}Sm , which could be observed in the bladder from 0.5 to 6 h at a concentration of $5.28 \pm 0.2 \% \text{ID g}^{-1}$ [36]. It should be noted that the particle size is the precondition of renal excretion but not the only one. $\text{Gd}_2\text{O}_3@ \text{SiO}_2$ nanoparticles without PEG modification with 3.3 nm hydrodynamic diameter were found not to be excreted from the body, but deposited in the liver and lung. Only the PEG-modified ones could be found in the bladder 1 h after *i.v.* injection, indicating fast elimination by renal excretion [44]. Regarding the time that is needed for the excretion, generally, smaller particles excrete from the kidney faster, from hours to days, while bigger

particles take longer time from weeks to months or even years. Gao et al. found that it needed 1.4 days for PEG-coated UCNPs (~5 nm) to be half excreted. Yet, most of the bigger counterparts (~19 nm) needed 7 days to be half excreted [45].

4.3.4 Cellular and In Vivo Toxicity of UCNPs

Quite a lot of studies have been performed to investigate the potential toxicity of UCNPs in cells. Mitochondrial metabolic activity has been generally taken to evaluate the influence of UCNPs on cell viability of normal or tumor cells. The most adopted method is the well-known MTT method. To date, many studies have been conducted with concentrations up to tens of 20 mg/mL and incubation time up to hundreds of hours and the particle sizes ranging from several nanometers to hundreds of nanometers. Nearly all the results reported more than 75 % of cell viability, indicating the weak toxic effects of UCNPs on cellular level *in vitro*, which is usually considered one of the advantages of UCNPs comparing with other luminescent nanoparticles such as quantum dots. On the other hand, some of the researches were also done on the influence of UCNPs on cell behavior. Han's group studied the influence of UCNPs (α -NaYF₄:0.5 %Tm@CaF₂) on the proliferation and differentiation of mesenchymal stem cells. They found that PEI covalently conjugated UCNPs had no short-term influence on the cell proliferation ability. The labeled stem cells were able to undergo osteogenic and adipogenic differentiation under *in vitro* induction. However, the osteogenesis of the labeled stem cells seemed to have less potency comparing with the unlabeled cells [28].

For *in vivo* toxicology studies, related reports are relatively rare comparing with the cytotoxicity studies. However, till now, the available published data have indicated the safety of UCNPs at the dosage used for imaging and drug delivery. Zhang et al. reported that mice treated with a dose of 10 mg/kg body weight of silica-coated NaYF₄:Yb,Er (~30 nm) did not show any significant difference in body weight with the control group. And the health status and behavior of all the mice were observed normal through the entire experiment. Moreover, all organ weights were consistent among all the mice at all the time points ranging from 10 min to 7 days [46]. In a longer time range up to 115 days, Li's group systematically studied the long-term toxicity of PAA-coated UCNPs after *i.v.* injection. No abnormal indicators, including eating and drinking behavior, fur color, exploratory behavior, activity, and neurological status, were observed except a weak weight difference compared with the control group [42]. Although there were no reports of abnormal behavior and death after *i.v.* injection, the current evidence is still far from enough to draw the conclusion that the UCNPs are safe for biology and medicine.

4.4 UCNPs as Imaging Contrast Reagents

The upconversion property of UCNPs makes them very appealing for bio-imaging studies due to their dark background for autofluorescence derived from biological samples. The near-infrared excitation wavelength also permits deep tissue penetrations. In addition to the non-blinking and stable properties, UCNPs can conduct improved detection limits with large signal-to-noise ratio compared with classical imaging probes, like organic dyes and quantum dots. For example, β -NaYF₄:Er,Yb nanocrystals were fabricated for luminescence imaging studies, and the nanoparticles with size around 30 nm were found to have improved signal-to-noise ratio and to be non-photobleaching and non-blinking (Fig. 4.9) [3]. After encapsulating with amphiphilic polymer, the UCNPs can be dispersed in water solutions and further incubated with murine fibroblasts and inoculated by endocytosis. In another example, NaYbF₄-based UCNPs have been synthesized with CaF₂ shell coating. Both in vitro and in vivo imaging were performed with high contrast imaging properties after tail vein injection to mouse, demonstrating the efficiency for practical imaging researches [5] (Fig. 4.10).

Because many tumor cells overexpress corresponding transmembrane receptors, UCNPs with small peptide labeling are particularly interesting for tumor-targeting drug delivery tracking within complex biological systems. For example, peptide motif of c(RGD) with high binding affinity to $\alpha_v\beta_3$ integrin receptor was used to functionalize UCNPs for ex vivo and in vivo imaging studies. Intense luminescence from the tumor could be observed 24 h after injection, while the luminescence from liver was reduced significantly (Fig. 4.11). Also, due to the specific peptide labeling, the afforded nano-system was found to have more affinity to U87MG tumor cell line compared with MCF-7 tumor, suggesting the potential application as cancer detection technique [38]. Another peptide, polypeptide neurotoxins, was shown to effectively bind with many types of cancer cells of high specificity and affinity. For instance, a typical neurotoxin peptide of recombinant chlorotoxin was used to conjugate with hexagonal-phase NaYF₄:Yb,Er/Ce nanoparticles, which were later injected into Balb/c nude mice [39]. The sensitivity and specificity of neurotoxin-mediated UCNPs tumor targeting was readily imaged using 980 nm excitation.

UCNPs with folic acid modification were also developed for tumor-targeting studies. In one case, folic acid-coupled NaYF₄:Yb,Er UCNPs were fabricated and exhibit effectiveness in targeting folate-receptor overexpressing HeLa cells in vitro and HeLa tumors in vivo [37]. Therein, NaYF₄:Yb,Er nanocrystals were fabricated by a modified hydrothermal microemulsion strategy using 6-aminohexanoic acid. The outside amine functional group of the resulting UCNPs not only conferred excellent water solubilities but also enabled further modification by carboxylic acid-activated folic acid. After the folic acid-modified UCNPs were injected into HeLa tumor-bearing nude mice for 24 h, an upconverting luminescence signal (around 650 nm) was observed in the tumor regions, while no significant luminescence signal was detected for controlled mice injected with UCNPs without FA modification.

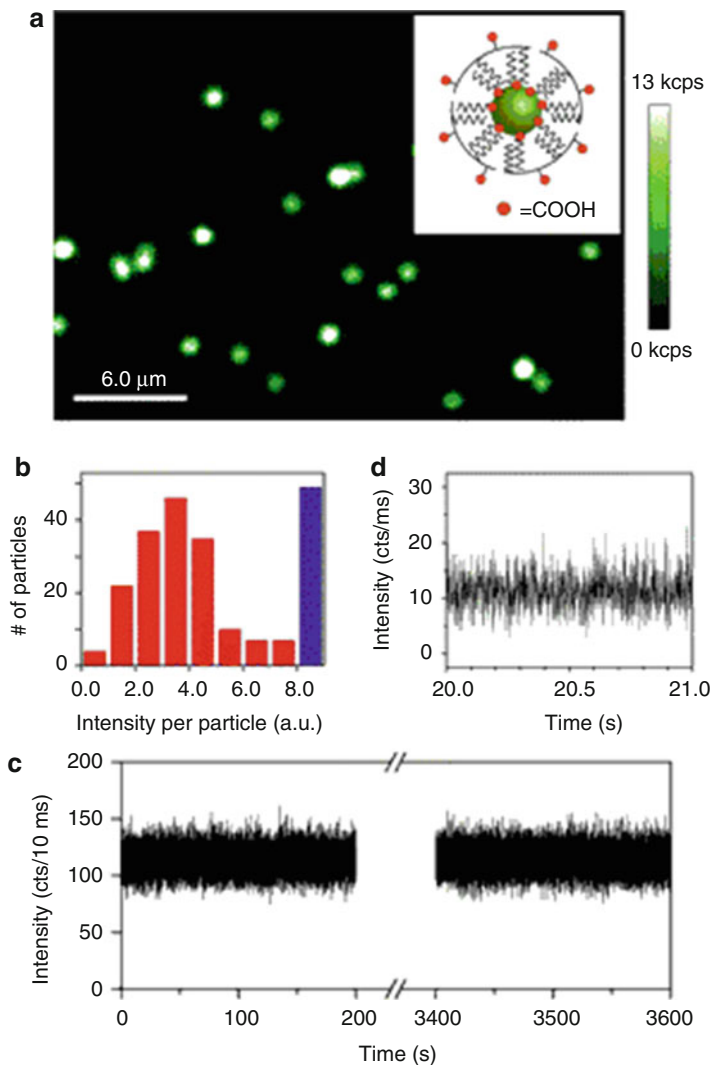


Fig. 4.9 Upconverted luminescence of individual water-soluble UCNPs. (a) Confocal upconverted luminescent image of individual amphiphilic polymer-coated UCNPs (schematically shown in the *inset*) sparsely dispersed on a clean cover glass. The laser power is approximately 10 mW, equivalent to approximately 5×10^6 W/cm². Some of the bright luminescent spots represent multiple UCNPs within the diffraction-limited area, generating saturated “white” spots in the image. (b) A histogram of integrated emission intensity from over 200 upconverted luminescent spots, suggesting that most of the luminescent spots are from single polymer-coated UCNPs. The data were analyzed from confocal upconverted luminescent images over a 75×75 μ m area, and the number of saturated “white” spots was shown in the histogram as a blue bar. Such single water-soluble UCNPs also exhibit exceptional photostability (c) and non-blinking behavior (d) (Reprinted with permission from Ref. [3]. Copyright 2009 Highwire press PNAS)

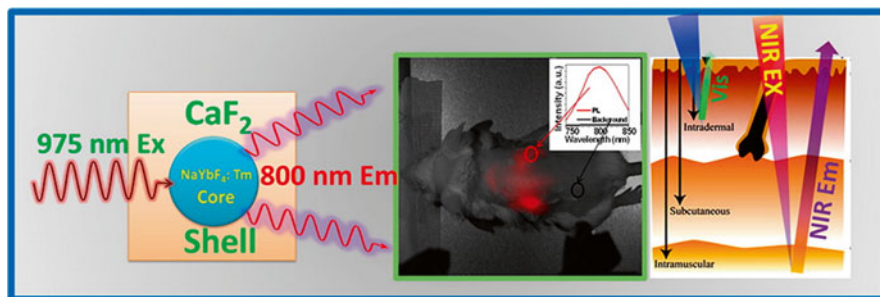


Fig. 4.10 Example of lanthanide-doped UCNPs of core/shell structures with NIR-to-NIR optical transitions and their application for small animal imaging studies plus illustration showing the better penetration of NIR light in contrast with visible light (Reprinted with the permission from Ref. [5]. Copyright 2012 American Chemical Society)

4.5 UCNPs as Drug Delivery Nanoplatform

4.5.1 UCNPs as Traditional Drug Delivery Tools

Using drug delivery carriers can greatly enhance the efficacy of pharmaceutical payloads for the improved solubility, stability, and pharmacokinetics of drugs. A wide variety of materials have been used as drug carriers, and more recently, fluorescent quantum dots have been used as platforms of optical imaging-guided carriers in real time in live organisms. However, the high toxic components in quantum dots limited its further applications for studies in cells and small animals. UCNP systems with unique optical and biocompatible components have emerged as promising candidates for traceable drug delivery.

Two of the most important UCNP-based drug delivery systems are hydrophobic pockets and porous silica shell. In the first method, drugs are encapsulated into “hydrophobic pockets” on the surface of UCNPs through hydrophobic interactions (Fig. 4.12) [47]. For example, by functionalizing the nanoparticle surface with polyethylene glycol-grafted amphiphilic polymer, hydrophobic pockets can form between the hydrophobic side chains of the polymers and the oleic acid on UCNPs’ surface, thus enabling encapsulation of anticancer drug molecules (e.g., doxorubicin). The releasing of doxorubicin can be controlled by pH, with increased dissociation rate in acid conditions, which is favorable for drug releasing in tumor cells. The intracellular delivery process of doxorubicin can be monitored by a laser scanning confocal microscope. In another way, drugs can be deposited in the pores of mesoporous silica shell coated onto UCNPs. For example, ibuprofen was studied as a model drug and loaded onto mesoporous silica-coated -NaYF₄:Yb,Er UCNP fibers by electro-spinning process [48]. Large ibuprofen loading amount can be performed because of the high specific surface area and large pore volume of silica shell. After loading ibuprofen, significant upconverting luminescence quenching will occur; thus, the loading quantity can be determined by measuring the quenching extent,

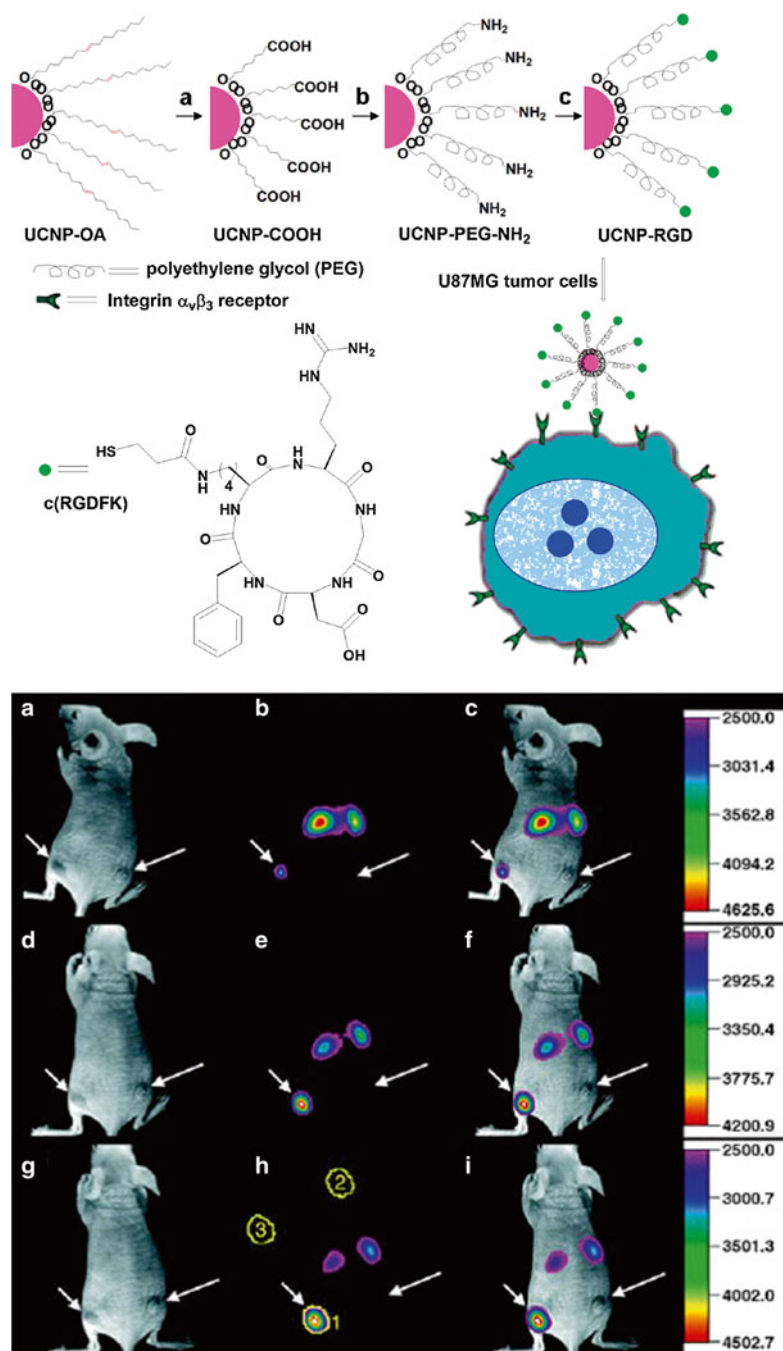


Fig. 4.11 Illustration scheme for UCNPs and in vivo upconversion luminescence imaging of subcutaneous U87MG tumor (*left* hind leg) and MCF-7 tumor (*right* hind leg) after intravenous injection of UCNPs-RGD conjugate over 24-h period (Reprinted with the permission from Ref. [38]. Copyright 2009 American Chemical Society)

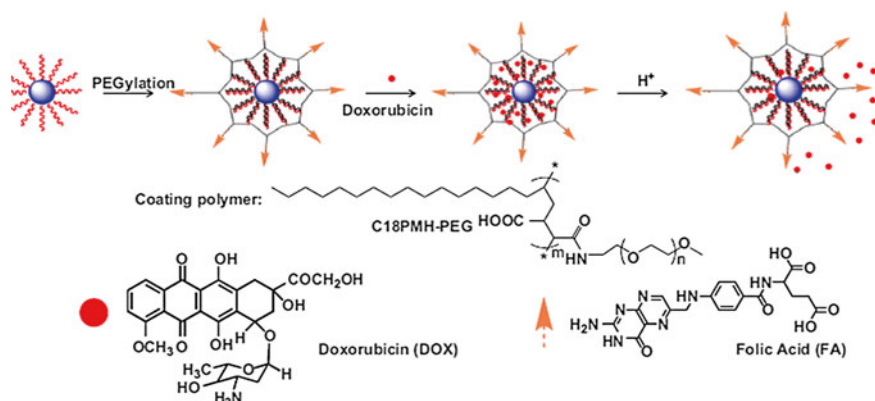


Fig. 4.12 Schematic illustration of the UCNP-based drug delivery system. (a) As-synthesized oleic acid capped UCNPs, (b) C18PMH-PEG-FA functionalized UCNPs, and (c) DOX loading on UCNPs. DOX molecules are physically adsorbed into the oleic acid layer on the nanoparticle surface by hydrophobic interactions. (d) Release of DOX from UCNPs triggered by decreasing pH (Reprinted from Ref. [47], Copyright 2011, with permission from Elsevier)

and more importantly, the subsequent drug releasing can be monitored by the recovering of luminescence intensity.

4.5.2 Light-Controllable Drug Release Based on UCNPs

Releasing bioactive molecules or drugs at desired time and location is of great interest for delivery systems development, in which way determinative therapeutic and diagnostic consequence can be greatly enhanced with minimized side effects during treatment. In addition, studies at directing cellular processes and disease regulation would benefit from the delivery of multi-payloads in varied doses at different time intervals [49, 50]. Among the release controlling methods, light-triggered molecular cleavage has received growing interest, due to the well-defined time and spatial drug releasing, thus offering unique precisely compared with other classical stimuli. Using the upconversion properties of UCNPs, remote control of photo-release of imaging probes and drug payloads has been demonstrated. For example, NIR light-responsive cross-linked mesoporous silica-coated UCNP drug delivery conjugate has been designed as photocaged nanocarriers (Fig. 4.13) [50]. The lanthanide-doped UCNPs were first coated with silica shell and followed by polymerization of 1-(2-nitrophenyl)ethyl photocaged oligo(ethylene) glycol vinyl monomers. Antitumor drug (doxorubicin) was able to be encapsulated in the hydrophobic pockets within the aforementioned polymer. Under NIR light irradiation, the cleavage of the cross-linked photocaged linker can be triggered by the upconverting emissions from UCNPs, and precisely release of targeted drug can be performed at controlled position and regulated time.

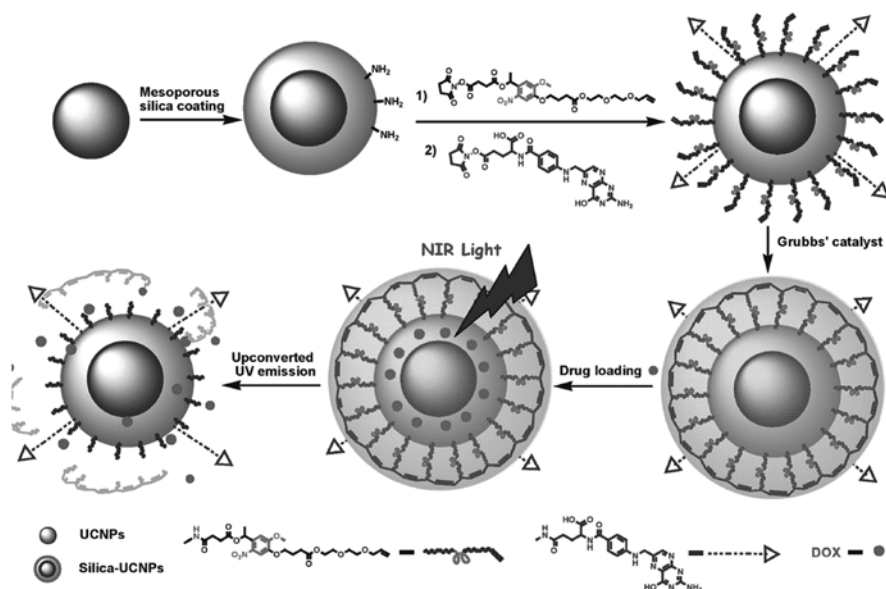


Fig. 4.13 Illustration for photocontrolled DOX delivery through photocage mesoporous silica-coated UCNP (Reproduced from Ref. [50] by permission of John Wiley & Sons Ltd.)

4.5.3 UCNP for Gene Delivery

The limitation for gene therapy is designing effective gene delivery vectors for specific and controllable delivering gene cargoes into living cells and tissues. There is a growing interest for developing nonviral synthetic nanocarriers for gene delivery [51]. Such carriers require four important factors, namely, (1) biocompatible, (2) traceable by long-term and real-time imaging, (3) controllable release, and (4) targeting. UCNP have been employed to deliver nucleic acids in gene therapy and exhibit promising benefits. For example, silica-coated $\text{-NaYF}_4\text{:Yb, Er}$ UCNP were used to track the delivery of siRNA into cells using luminescence resonance energy transfer system for studying the intracellular uptake, release, and biostability of UCNP-bound siRNA in live cells [52]. In this system, cationic silica-coated $\text{-NaYF}_4\text{:Yb, Er}$ acts as the donor and the siRNA-intercalating dye BOBO-3 as the corresponding acceptor. Under 980 nm excitation, the nanoparticles emit upconverted fluorescence at the wavelength of 543 nm, which was consequently absorbed by BOBO-3-stained siRNA (siRNA-BOBO3) acceptor via overlapped absorption band. These UCNP were shown to bind and protect siRNA from RNase cleavage and to effectively deliver siRNA into cells. Under excitation at 980 nm, when the amino-modified UCNP were bound with BOBO-3-stained siRNA, energy was allowed to transfer from UCNP to BOBO-3 and consequently generate characteristic BOBO emissions at 602 nm (Fig. 4.14). Once the siRNA was separated from UCNP, the energy transfer process was inhibited. The results showed that siRNA

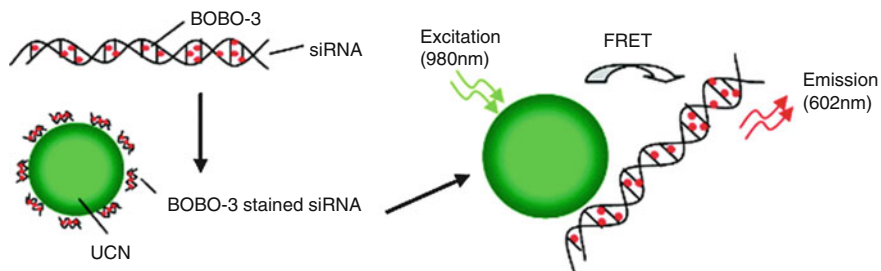


Fig. 4.14 Schematic drawing of FRET-based UCN/siRNA-BOBO3 complex system. siRNA is stained with BOBO-3 dyes, and the stained siRNA is attached to the surface of $\text{NaYF}_4:\text{Yb,Er}$ nanoparticles. Upon excitation of the nanoparticles at 980 nm, energy is transferred from the donor (UCN) to the acceptor (BOBO-3) (Reprinted with the permission from Ref. [52]. Copyright 2010 American Chemical Society)

could gradually release from the UCNPs' surface into the cytoplasm over 24 h. Subsequently, similar strategy was used to monitor green fluorescent protein (GFP)-encoded plasmid DNA delivery and release in live cells [53].

4.6 UCNPs as Phototherapeutic Reagents

4.6.1 Photodynamic Therapy

Typical photosensitizer is capable of excitation under visible light and generates cytotoxic reactive oxygen species (ROS) which can be used to kill tumor cells. Only light, neither toxic nor invasive, is used as the therapeutic reagents in such process, namely, photodynamic therapy (PDT) [54]. Yet, such wavelength of light has rather limited tissue penetration depth (<1 cm). A promising nanocarrier and energy donor for these sensitizers is NIR-excitable UCNPs [55]. The design of UCNP-based PDT system includes the aforementioned UCNPs, surface coating, and the hereafter photosensitizers. Ideally, a photosensitizer should have good ROS production efficiency, a high absorption coefficient at longer wavelengths for better tissue penetration, amphiphilicity, low dark toxicity, ease of synthesis, and ease of formulation in aqueous solvents for in vivo delivery. Several different kinds of photosensitizers have been developed for PDT, and they can be broadly classified into chemical groups such as porphyrins, phthalocyanines, chlorins, 5-aminolevulinic acid (ALA), and naphthalocyanines; photosensitizers like porfimer sodium, temoporfin, 5-aminolevulinic acid, methyl aminolevulinic acid, hexyl aminolevulinic acid, talaporfin sodium, aluminum phthalocyanine disulfonate, tin ethyl etiopurpurin, and verteporfin have been approved for clinical use [8].

For example, tris(bipyridine)ruthenium(II) ($\text{Ru}(\text{bpy})_3^{2+}$)-doped SiO_2 shell was used to encapsulate $\text{NaYF}_4:\text{Yb,Tm}$ core [56]. Under 980 nm excitation, the blue emission from Tm^{3+} could be absorbed by $^1\text{O}_2$ generator $\text{Ru}(\text{bpy})_3^{2+}$, and the

consequently generated $^1\text{O}_2$ could be detected by chemical method. For the purpose of increase loading amount of photosensitizer, $\text{NaYF}_4:\text{Yb},\text{Er}$ nanoparticles were fabricated with 100 nm size, and 10 wt.% photosensitizer loading ratio was achieved by coating meso-tetraphenylporphine in poly(ethylene glycol-block-(DL)lactic acid) [57]. Using this system, efficient cancer cell killing activity was observed on NIR excitation, with low cytotoxicity in the absence of NIR light. Moreover, in vivo UCNP-based PDT system was introduced by non-covalently incorporating photosensitizing porphyrin derivative into amphiphilic polymer-coated $\text{NaYF}_4:\text{Yb},\text{Er}$ nanoparticles. Excellent tumor regression was observed under 980 nm CW laser excitation, plus low toxicity and gradual clearout from mouse organs (Fig. 4.15) [58].

Recently, we developed high Yb-doped UCNPs with a biocompatible CaF_2 shell with an optimal 15-fold increase in red emissions compared to their hexagonal phased counterparts. The absolute quantum yield of R- $\text{NaYF}_4:80\% \text{Yb}, 2\% \text{Er}$ @

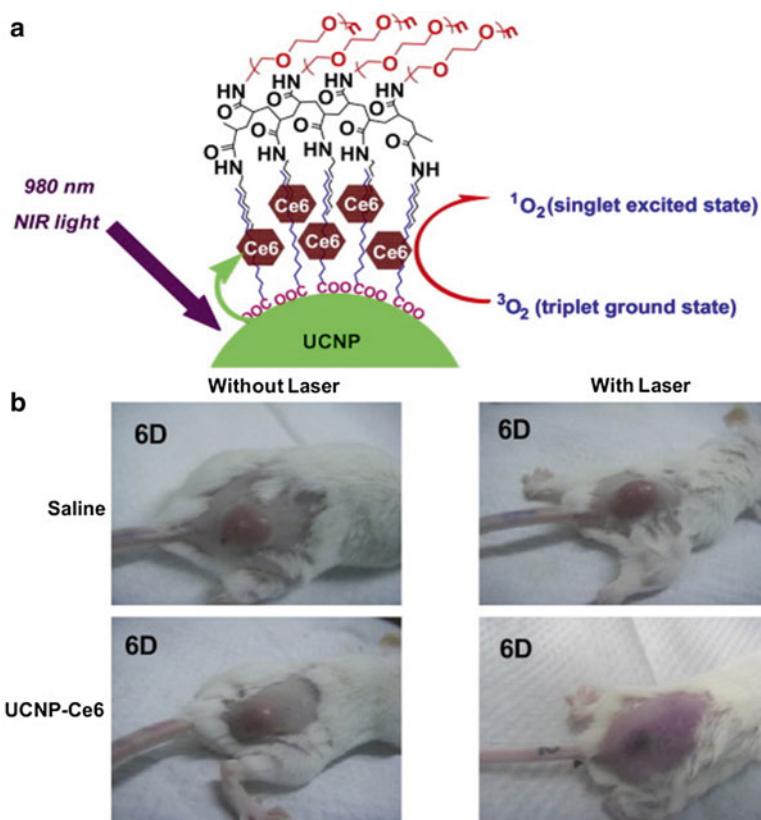


Fig. 4.15 (a) A schematic drawing showing NIR-induced PDT using UCNP-Ce6. (b) Representative photos of mice after various treatments indicated at the sixth day (Reprinted from ref. [58], Copyright 2011, with permission from Elsevier)

CaF₂ is measured to be 3.2 ± 0.1 %, the highest reported value for red emissions. Furthermore, we demonstrate conjugating ALA (aminolevulinic acid), a clinically used prodrug for the red absorbing photosensitizer PpIX, to the UCNP surface via a hydrazone linkage, giving us exquisite control over their PDT effect in the cell. This photodynamic therapy system was tested for its therapeutic potential: it exhibited strong singlet oxygen generation and ~ 70 % cell death after 20 min of NIR irradiation. Furthermore, significant cell death (~ 30 %) was produced in simulated deep tumor conditions with as much as 12 mm of pork tissue and a biocompatible low power density of 0.5 W/cm^2 , while ALA-UCNPs based on the known optimal red-emitting UCNP cannot. Finally, in vivo mice models of tumors when treated with these ALA-UCNPs demonstrated size reduction significant from the controls even under 12 mm of pork tissue (the greatest depth at which UCNP PDT has been achieved), while clinically used red light could not (Fig. 4.16) [59]. This study marks an important step forward in biocompatible photodynamic therapy utilizing UCNPs to effectively access deep-set tumors at a low irradiation power density. It may also provide new opportunities for a variety of applications using upconverting red radiation in photonics and biophotonics.

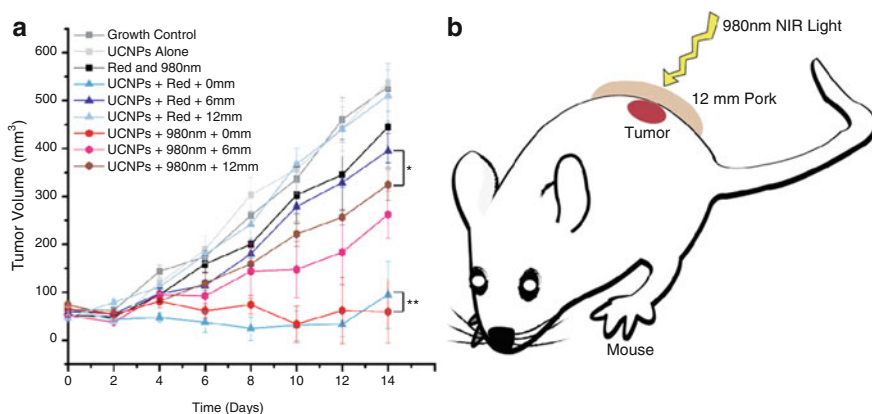


Fig. 4.16 In vivo volume of tumors exposed to various controls and ALA-UCNPs with red and near-infrared irradiation (0.5 w/cm^2) in simulated deep tumors. Growth control, untreated tumors; UCNPs alone, tumors exposed to ALA-UCNPs without irradiation; red and 980 nm, tumors simultaneously exposed to red and NIR light both at 0.5 w/cm^2 but no ALA-UCNPs; UCNPs+red+0 mm, tumors exposed to ALA-UCNPs and clinically used red light; UCNPs+red+6 mm, tumors 6 mm deep exposed to ALA-UCNPs and clinically used red light; UCNPs+red+12 mm, tumors 12 mm deep exposed to ALA-UCNPs and clinically red light; UCNPs+980 nm+0 mm, tumors exposed to ALA-UCNPs and NIR light; UCNPs+980 nm+6 mm, tumors 6 mm deep exposed to ALA-UCNPs and NIR light; UCNPs+980 nm+12 mm, tumors 12 mm deep exposed to ALA-UCNPs and NIR light. Statistical significance was determined from one-way t-tests; significance (8) was based on $p < 0.05$ and $P > 0.05$ for not significant (**) pairs (Reprinted with the permission from Ref. [59]. Copyright 2014 American Chemical Society)

4.6.2 Photothermal Therapy

The basic model for photothermal therapy (PTT) is in part similar with PDT, in which vibrational energy (heat) is generated from photosensitizer for cell killings [60]. -NaYF₄:Yb,Er nanoparticles were coated with silver shell with stronger plasmonic resonance performance, and PTT was applied in vitro on HepG2 and BCap-37 cells from human hepatic cancer and human breast cancer separately [61].

In order to achieve a multimodal cancer therapy, multifunctional core/satellite nanotheranostic was developed by attaching ultrasmall CuS nanoparticles onto the surface of silica-coated UCNPs (Fig. 4.17). These nanocomposites exhibit many advantages as multifunctional nanotheranostics, such as (1) NIR light can be transferred to local thermal energy for photothermal therapy agents; (2) Z elements (Yb, Gd, and Er) can cause large local radiation dose enhancement around nanoparticles as radiosensitizers; and (3) UCL/MR/CT trimodal imaging could be simultaneously performed with this multifunctional nanotheranostic. This development laid the groundwork for the image-guided therapy in the future [62].

4.6.3 Combined PDT/PTT

A surface functionalization strategy was developed for UCNPs by coating those nanoparticles with BSA protein [63]. In such a UCNP@BSA system, the Gd-based UCNPs, which are useful contrast agents for dual modal optical/MR imaging, in the mean time are able to trigger photodynamic therapy under NIR light by resonance energy transfer if coupled with photosensitizers. On the other hand, the BSA coating not only improves the physiological stability of UCNPs but also could serve as a delivery platform to load various molecules with therapeutic functions. RB, a photodynamic agent, together with IR825, a photothermal agent, is simultaneously

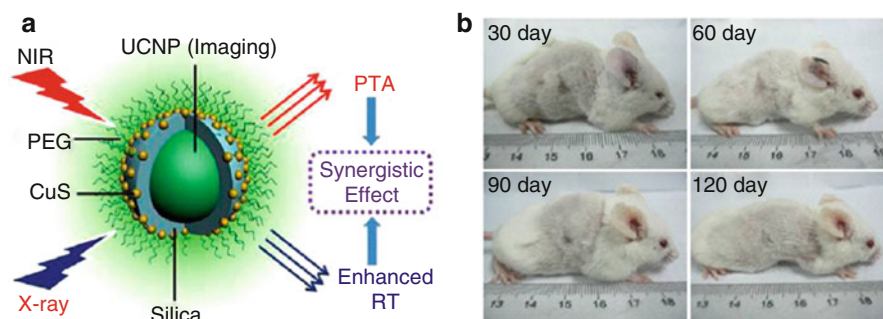


Fig. 4.17 (a) Illustration of nanocarriers for enhanced photothermal ablation and radiotherapy synergistic therapy; (b) photographs of mice in 30, 60, 90, and 120 days of treatment, showing complete eradication of the tumor and no visible recurrences of the tumors in at least 120 days (Reprinted with the permission from Ref. [62]. Copyright 2013 American Chemical Society)

loaded on UCNP@BSA for combined phototherapy of cancer, demonstrating outstanding synergistic antitumor effect in our animal experiments. Although further studies are still ongoing in our laboratory aiming at achieving combination therapy of cancer upon systemic administration (e.g., intravenous injection) of such UCNP-based theranostic agent, our work presents a new design of a simple nanoplatform, in which multiple imaging and therapy functions can be integrated together for imaging-guided cancer combination therapy (Fig. 4.18).

4.7 Conclusion and Prospects

In the past decade, we have witnessed the rapid development of UCNPs both in synthesis and applications. The unique optical properties and outperformed chemical and physical behaviors of UCNPs make them attractive candidates for bio-related applications, especially bio-imaging, drug delivery, and photodynamic therapy. Their UV/vis emission can be excited by biotissue-penetrable NIR light, which endows them deep tissue applications such as remote switchable smart bio-devices and NIR-driven PDT process. However, the upconversion efficiency of lanthanide-based UCNPs is still very low, especially under low power density excitation. Moreover, it is still challenging to generate small UCNPs, especially sub-10 nm, without sacrificing the upconversion efficiency. In addition, the development of commercially available systems of more versatile UCNPs with unique excitation and emission wavelength is critical to expand the applications of UCNPs. Meanwhile, further work is needed for better understanding the uptake, release rate, and toxicity of UCNPs for harnessing these nanoplatforms for applications in photonics and biophotonics.

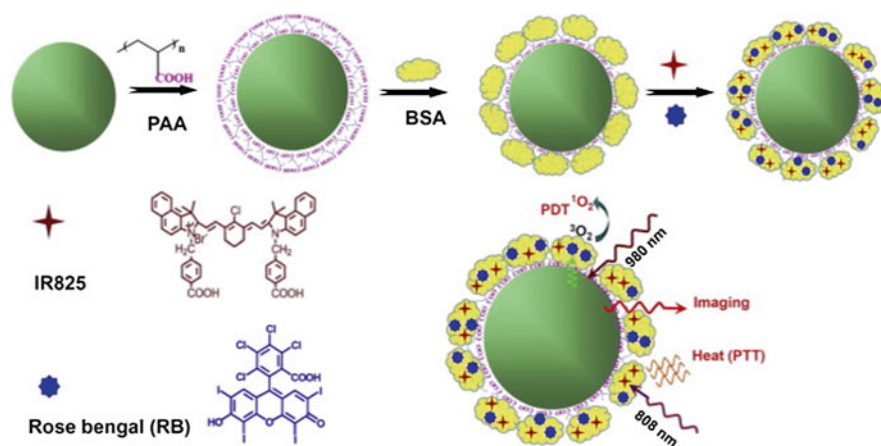


Fig. 4.18 A schematic illustration to show the synthesis of UCNP@BSA-RB&IR825 nanocomplex and the mechanism of both PDT and PTT therapies based on this system (Reprinted from Ref. [63], Copyright 2014, with permission from Elsevier)

References

1. Auzel F (2004) Upconversion and anti-stokes processes with f and d ions in solids. *Chem Rev* 104(1):139–173
2. Wu X, Chen G, Shen J et al (2015) Upconversion nanoparticles: a versatile solution to multi-scale biological imaging. *Bioconjug Chem* 28(2):166–175
3. Wu SW, Han G, Milliron DJ et al (2009) Non-blinking and photostable upconverted luminescence from single lanthanide-doped nanocrystals. *Proc Natl Acad Sci U S A* 106(27):10917–10921
4. Liu Q, Feng W, Yang TS et al (2013) Upconversion luminescence imaging of cells and small animals. *Nat Protoc* 8(10):2033–2044
5. Chen GY, Shen J, Ohulchanskyy TY et al (2012) (α -NaYbF₄:Tm³⁺)/CaF₂ core/shell nanoparticles with efficient near-infrared to near-infrared upconversion for high-contrast deep tissue bioimaging. *ACS Nano* 6(9):8280–8287
6. Yang TS, Liu Q, Li JC et al (2014) Photoswitchable upconversion nanophosphors for small animal imaging in vivo. *R Soc Chem Adv* 4(30):15613–15619
7. Shen J, Zhao L, Han G (2013) Lanthanide-doped upconverting luminescent nanoparticle platforms for optical imaging-guided drug delivery and therapy. *Adv Drug Deliv Rev* 65(5):744–755
8. Idris NM, Jayakumar MKG, Bansal A et al (2015) Upconversion nanoparticles as versatile light nanotransducers for photoactivation applications. *Chem Soc Rev* 44(6):1449–1478
9. Wang J, Deng RR, MacDonald MA et al (2014) Enhancing multiphoton upconversion through energy clustering at sublattice level. *Nat Mater* 13(2):157–162
10. Liu Q, Sun Y, Yang TS et al (2011) Sub-10 nm hexagonal lanthanide-doped NaLuF₄ upconversion nanocrystals for sensitive bioimaging in vivo. *J Am Chem Soc* 133(43):17122–17125
11. Ryu J, Park HY, Kim K et al (2010) Facile synthesis of ultrasmall and hexagonal NaGdF₄:Yb³⁺, Er³⁺ nanoparticles with magnetic and upconversion imaging properties. *J Phys Chem C* 114(49):21077–21082
12. Shen J, Chen GY, Vu AM et al (2013) Engineering the upconversion nanoparticle excitation wavelength: cascade sensitization of tri-doped upconversion colloidal nanoparticles at 800 nm. *Adv Opt Mater* 1(9):644–650
13. Qiu PY, Zhou N, Chen HY et al (2013) Recent advances in lanthanide-doped upconversion nanomaterials: synthesis, nanostructures and surface modification. *Nanoscale* 5(23):11512–11525
14. Mai HX, Zhang YW, Si R et al (2006) High-quality sodium rare-earth fluoride nanocrystals: controlled synthesis and optical properties. *J Am Chem Soc* 128(19):6426–6436
15. Yi GS, Chow GM (2006) Synthesis of hexagonal-phase NaYF₄: Yb, Er and NaYF₄: Yb, Tm nanocrystals with efficient up-conversion fluorescence. *Adv Funct Mater* 16(18):2324–2329
16. Boyer JC, Vetrone F, Cuccia LA et al (2006) Synthesis of colloidal upconverting NaYF₄ nanocrystals doped with Er³⁺, Yb³⁺ and Tm³⁺, Yb³⁺ via thermal decomposition of lanthanide trifluoroacetate precursors. *J Am Chem Soc* 128(23):7444–7445
17. Boyer JC, Cuccia LA, Capobianco JA (2007) Synthesis of colloidal upconverting NaYF₄: Er³⁺/Yb³⁺ and Tm³⁺/Yb³⁺ monodisperse nanocrystals. *Nano Lett* 7(3):847–852
18. Yi GS, Chow GM (2007) Water-soluble NaYF₄: Yb, Er(Tm)/NaYF₄/polymer core/shell/shell nanoparticles with significant enhancement of upconversion fluorescence. *Chem Mater* 19(3):341–343
19. Zeng JH, Su J, Li ZH et al (2005) Synthesis and upconversion luminescence of hexagonal-phase NaYF₄: Yb, Er, phosphors of controlled size and morphology. *Adv Mater* 17(17):2119–2123
20. Wang X, Zhuang J, Peng Q et al (2005) A general strategy for nanocrystal synthesis. *Nature* 437(7055):121–124
21. Liang X, Wang X, Zhuang J et al (2007) Synthesis of NaYF₄ nanocrystals with predictable phase and shape. *Adv Funct Mater* 17(15):2757–2765

22. Wang Y, Tu LP, Zhao JW et al (2009) Upconversion luminescence of beta-NaYF₄: Yb³⁺, Er³⁺@β-NaYF₄ core/shell nanoparticles: excitation power, density and surface dependence. *J Phys Chem C* 113(17):7164–7169
23. Wang F, Wang JA, Liu XG (2010) Direct evidence of a surface quenching effect on size-dependent luminescence of upconversion nanoparticles. *Angew Chem Int Ed* 49(41):7456–7460
24. Shen J, Chen GY, Ohulchanskyy TY et al (2013) Tunable near infrared to ultraviolet upconversion luminescence enhancement in (α-NaYF₄:Yb, Tm)/CaF₂ core/shell nanoparticles for in situ real-time recorded biocompatible photoactivation. *Small* 9(19):3213–3217
25. Zhong YT, Tian G, Gu ZJ et al (2014) Elimination of photon quenching by a transition layer to fabricate a quenching-shield sandwich structure for 800 nm excited upconversion luminescence of Nd³⁺ sensitized nanoparticles. *Adv Mater* 26(18):2831–2837
26. Wen HL, Zhu H, Chen X et al (2013) Upconverting near-infrared light through energy management in core-shell-shell nanoparticles. *Angew Chem Int Ed* 52(50):13419–13423
27. Lai J, Zhang Y, Pasquale N et al (2014) An upconversion nanoparticle with orthogonal emissions using dual NIR excitations for controlled two-way photoswitching. *Angew Chem Int Ed* 126(52):14647–14651
28. Zhao L, Kutikov A, Shen J et al (2013) Stem cell labeling using polyethylenimine conjugated (α-NaYbF₄:Tm³⁺)/CaF₂ upconversion nanoparticles. *Theranostics* 3(4):249–257
29. Chen ZG, Chen HL, Hu H et al (2008) Versatile synthesis strategy for carboxylic acid-functionalized upconverting nanophosphors as biological labels. *J Am Chem Soc* 130(10):3023–3029
30. Zhang TR, Ge JP, Hu YX et al (2007) A general approach for transferring hydrophobic nanocrystals into water. *Nano Lett* 7(10):3203–3207
31. Dong AG, Ye XC, Chen J et al (2011) A generalized ligand-exchange strategy enabling sequential surface functionalization of colloidal nanocrystals. *J Am Chem Soc* 133(4):998–1006
32. Conner SD, Schmid SL (2003) Regulated portals of entry into the cell. *Nature* 422(6927):37–44
33. Jin JF, Gu YJ, Man CWY et al (2011) Polymer-coated NaYF₄:Yb³⁺, Er³⁺ upconversion nanoparticles for charge-dependent cellular imaging. *ACS Nano* 5(10):7838–7847
34. Cao TY, Yang Y, Gao YA et al (2011) High-quality water-soluble and surface-functionalized upconversion nanocrystals as luminescent probes for bioimaging. *Biomaterials* 32(11):2959–2968
35. Zhou J, Zhu XJ, Chen M et al (2012) Water-stable NaLuF₄-based upconversion nanophosphors with long-term validity for multimodal lymphatic imaging. *Biomaterials* 33(26):6201–6210
36. Peng JJ, Sun Y, Zhao LZ et al (2013) Polyphosphoric acid capping radioactive/upconverting NaLuF₄:Yb, Tm, Sm-153 nanoparticles for blood pool imaging in vivo. *Biomaterials* 34(37):9535–9544
37. Xiong LQ, Chen ZG, Yu MX et al (2009) Synthesis, characterization, and in vivo targeted imaging of amine-functionalized rare-earth up-converting nanophosphors. *Biomaterials* 30(29):5592–5600
38. Xiong LQ, Chen ZG, Tian QW et al (2009) High contrast upconversion luminescence targeted imaging in vivo using peptide-labeled nanophosphors. *Anal Chem* 81(21):8687–8694
39. Yu XF, Sun ZB, Li M et al (2010) Neurotoxin-conjugated upconversion nanoprobe for direct visualization of tumors under near-infrared irradiation. *Biomaterials* 31(33):8724–8731
40. Bogdan N, Rodriguez EM, Sanz-Rodriguez F et al (2012) Bio-functionalization of ligand-free upconverting lanthanide doped nanoparticles for bio-imaging and cell targeting. *Nanoscale* 4(12):3647–3650
41. Wang M, Mi CC, Wang WX et al (2009) Immunolabeling and NIR-excited fluorescent imaging of HeLa cells by using NaYF₄:Yb, Er upconversion nanoparticles. *ACS Nano* 3(6):1580–1586

42. Xiong LQ, Yang TS, Yang Y et al (2010) Long-term in vivo biodistribution imaging and toxicity of polyacrylic acid-coated upconversion nanophosphors. *Biomaterials* 31(27):7078–7085
43. Cheng L, Yang K, Shao MW et al (2011) In vivo pharmacokinetics, long-term biodistribution and toxicology study of functionalized upconversion nanoparticles in mice. *Nanomedicine* 6(8):1327–1340
44. Bridot JL, Faure AC, Laurent S et al (2007) Hybrid gadolinium oxide nanoparticles: multi-modal contrast agents for in vivo imaging. *J Am Chem Soc* 129(16):5076–5084
45. Liu CY, Gao ZY, Zeng JF et al (2013) Magnetic/upconversion fluorescent NaGdF₄:Yb, Er nanoparticle-based dual-modal molecular probes for imaging tiny tumors in vivo. *ACS Nano* 7(8):7227–7240
46. Jalil RA, Zhang Y (2008) Biocompatibility of silica coated NaYF₄ upconversion fluorescent nanocrystals. *Biomaterials* 29(30):4122–4128
47. Wang C, Cheng LA, Liu ZA (2011) Drug delivery with upconversion nanoparticles for multi-functional targeted cancer cell imaging and therapy. *Biomaterials* 32(4):1110–1120
48. Hou ZY, Li CX, Ma PA et al (2011) Electrospinning preparation and drug-delivery properties of an up-conversion luminescent porous NaYF₄:Yb³⁺, Er³⁺@silica fiber nanocomposite. *Adv Funct Mater* 21(12):2356–2365
49. Min YZ, Li JM, Liu F et al (2014) Near-infrared light-mediated photoactivation of a platinum antitumor prodrug and simultaneous cellular apoptosis imaging by upconversion-luminescent nanoparticles. *Angew Chem Int Ed* 53(4):1012–1016
50. Yang YM, Velmurugan B, Liu XG et al (2013) NIR photoresponsive crosslinked upconverting nanocarriers toward selective intracellular drug release. *Small* 9(17):2937–2944
51. Thomas M, Klivanov AM (2003) Non-viral gene therapy: polycation-mediated DNA delivery. *Appl Microbiol Biotechnol* 62(1):27–34
52. Jiang S, Zhang Y (2010) Upconversion nanoparticle-based FRET system for study of siRNA in live cells. *Langmuir* 26(9):6689–6694
53. Guo HC, Idris NM, Zhang Y (2011) LRET-based biodetection of DNA release in live cells using surface-modified upconverting fluorescent nanoparticles. *Langmuir* 27(6):2854–2860
54. Fisher AMR, Murphree AL, Gomer CJ (1995) Clinical and preclinical photodynamic therapy. *Laser Surg Med* 17(1):2–31
55. Shan GB, Weissleder R, Hilderbrand SA (2013) Upconverting organic dye doped core-shell nano-composites for dual-modality NIR imaging and photo-thermal therapy. *Theranostics* 3(4):267–274
56. Guo YY, Kumar M, Zhang P (2007) Nanoparticle-based photosensitizers under CW infrared excitation. *Chem Mater* 19(25):6071–6072
57. Shan JN, Budijono SJ, Hu GH et al (2011) Pegylated composite nanoparticles containing upconverting phosphors and meso-tetraphenyl porphine (TPP) for photodynamic therapy. *Adv Funct Mater* 21(13):2488–2495
58. Wang C, Tao HQ, Cheng L et al (2011) Near-infrared light induced in vivo photodynamic therapy of cancer based on upconversion nanoparticles. *Biomaterials* 32(26):6145–6154
59. Punjabi A, Wu X, Tokatli-Apollon A et al (2014) Amplifying the red-emission of upconverting nanoparticles for biocompatible clinically used prodrug-induced photodynamic therapy. *ACS Nano* 8(10):10621–10630
60. Saxton RE, Paiva MB, Lufkin RB, Castro DJ (1995) Laser photochemotherapy – a less invasive approach for treatment of cancer. *Semin Surg Oncol* 11(4):283–289
61. Dong BA, Xu S, Sun JA et al (2011) Multifunctional NaYF₄: Yb³⁺, Er³⁺@Agcore/shell nanocomposites: integration of upconversion imaging and photothermal therapy. *J Mater Chem* 21(17):6193–6200
62. Xiao QF, Zheng XP, Bu WB et al (2013) A core/satellite multifunctional nanotheranostic for in vivo imaging and tumor eradication by radiation/photothermal synergistic therapy. *J Am Chem Soc* 135(35):13041–13048
63. Chen Q, Wang C, Cheng L et al (2014) Protein modified upconversion nanoparticles for imaging-guided combined photothermal and photodynamic therapy. *Biomaterials* 35(9):2915–2923

Chapter 5

Engineering Upconversion Nanoparticles for Multimodal Biomedical Imaging-Guided Therapeutic Applications

Wenpei Fan, Jianlin Shi, and Wenbo Bu

Abstract As one of the most important branches of nanotechnology, nanotheranostic medicine that aims at integrating diagnostic/therapeutic functions in one system is expected to provide novel strategies for accurate imaging-guided therapy of human major diseases like cancer. Among various inorganic or organic theranostic probes, lanthanide-doped upconversion nanoparticles (UCNPs) demonstrate superior advantages in upconversion luminescent imaging by contrast with traditional luminescent probes as well as great potential in the development as multimodal imaging (e.g., magnetic resonance imaging, computed tomography imaging, etc.) probes by the selective doping of various functional ions (e.g., Gd^{3+} , Yb^{3+} , Ho^{3+} , etc.). Furthermore, by suitable surface engineering (e.g., mesoporous silica coating, biological molecule conjugation etc.), UCNPs can simultaneously serve as delivery vehicles of drugs/photosensitizers for multimodal therapeutic applications (e.g., chemotherapy, photodynamic therapy, etc.) under the above significant multimodal imaging guidance. Herein, we summarize and discuss the very recent progresses in the engineering of UCNPs for multimodal imaging-guided therapeutic applications.

Keywords Upconversion nanoparticles • Nanotheranostic medicine • Hydrophilic modification • Multimodal imaging • Synergetic therapy • Imaging-guided therapy

5.1 Introduction

As a new generation of luminescent probes, lanthanide-doped upconversion nanoparticles can convert low-energy/long-wavelength near-infrared (NIR) light into high-energy/short-wavelength visible or ultraviolet (UV) light [1, 2]. Unlike

W. Fan • J. Shi • W. Bu (✉)

State Key Laboratory of High Performance Ceramics and Superfine Microstructures,
Shanghai Institute of Ceramics, Chinese Academy of Sciences,

1295 Ding-xi Road, Shanghai 200050, People's Republic of China

e-mail: wbbu@mail.sic.ac.cn

the traditional organic dyes or quantum dots that need ultrashort-pulsed laser excitation due to their nonlinear multiphoton absorption, UCNPs can be excited by low-cost continuous-wave diode laser for upconversion luminescence emission [3]. More importantly, UCNPs demonstrate unique advantages in upconversion luminescent (UCL) imaging that could not be achieved by other luminescent probes, such as high sensitivity, superior photostability, large anti-Stokes shift, sharp emission bandwidths, extremely weak autofluorescence, deep penetration of NIR light excitation, and so on [4–7]. Besides, by doping various rare earth ions (e.g., Er^{3+} , Tm^{3+} , Eu^{3+} , Tb^{3+} , etc.) into the UCNPs lattice, diverse wavelengths of UV/vis light can be simultaneously emitted for multicolor luminescent imaging upon a single NIR source excitation [8–10].

Another unique feature of UCNPs in bio-imaging is the realization of multimodal imaging by incorporating special functional ions into the crystal lattice. For example, Gd^{3+} -doped UCNPs can be used as contrast agents for magnetic resonance imaging (MRI) [11, 12]. The doping of some high-Z heavy metal ions (e.g., Yb^{3+} , Ba^{3+} , Bi^{3+} , Lu^{3+} , etc.) can realize enhanced computed tomography (CT) imaging [13–15]. The introduction of some radionuclides like $^{18}\text{F}/^{153}\text{Sm}$ can offer UCNPs with positron emission tomography (PET) and even single-photon positron emission tomography (SPECT) imaging capabilities [16–19]. Therefore, by the selective co-doping of the above functional ions, multimodal imaging probes based on UCNPs can be successfully designed by integrating MRI/UCL/CT/PET modalities in a single system, which may contribute to future accurate diagnosis of big diseases.

By suitable surface engineering, UCNPs can even be used for multimodal imaging-guided therapeutic applications. For example, mesoporous silica-coated UCNPs serve as drug vehicles for enhanced chemotherapy [20–23]. Moreover, based on the fluorescence resonance energy transfer (FRET) from UCNPs to some photosensitizers, photodynamic therapy (PDT) [24–28] can be achieved on deep-seated tumors upon NIR irradiation. By the co-delivery of drugs/photosensitizers/radiosensitizers, the three major treatments of chemo-/radio-/photodynamic therapy can be integrated in a single UCNP-based system. Therefore, UCNPs can be developed into the next generation of theranostic medicine for multimodal imaging-guided therapy, which may substantially enhance the diagnostic/therapeutic efficacy.

Herein, we will summarize the latest studies regarding the engineering of UCNPs for multimodal imaging-guided therapeutic applications. The useful strategies for hydrophilic surface modifications of UCNPs are introduced. Particularly, the recent progress of UCNPs in multimodal biomedical imaging (e.g., MR/UCL, MR/UCL/CT, etc.) as well as imaging-guided therapeutic applications (photodynamic therapy, radiotherapy, etc.) are emphasized and highlighted. Finally, the current challenges and future research directions of UCNPs are also outlooked. We hope that this chapter can offer researchers in this field a timely and comprehensive figure of the recent developments in UCNP-based nanotheranostics and attract increasing attentions among researchers in other related fields and even nonspecialists as well.

5.2 Hydrophilic Surface Modification of UCNPs

So far, among the various synthetic approaches for UCNPs, the hydrothermal method and thermal decomposition method are the two widely used strategies for the fabrication of high-quality, single-crystal, monodispersed UCNPs. However, the synthesized UCNPs are usually not soluble in water due to their hydrophobic surface capped by oleic acid (OA) or oleylamine (OM), so the suitable surface modification may be a key step to make UCNPs water dispersible and suitable for the following biomedical functionalization and applications. A variety of surface modification strategies [2, 6, 8] have been successfully adopted to transfer hydrophobic UCNPs into water, and the most frequently used three modification methods (polymer coating, ligand-free synthesis, silica coating) will be briefly discussed in the following sections.

5.2.1 Polymer Coating Modification

Some biocompatible polymers can be capped onto the surface of UCNPs by replacing the OA/OM ligands, which can not only make UCNPs well dispersible in water but also functionalize UCNPs for biomedical use. For example, Yin et al. [29] described a general ligand-exchange method to replace hydrophobic OA ligands at an elevated temperature (~240 °C) in a glycol solvent. Those short-chain hydrophilic polyelectrolyte molecules (such as poly(acrylic acid) (PAA), poly(allylamine) (PAAm), and poly(sodium styrene sulfonate) (PSS)) could be coated on UCNPs based on the strong coordination of their functional groups to the UCNP surface. Van Veggel et al. [30] reported an efficient technique to use the PEG–phosphate ligand for the replacement of OA ligands, thus producing water-dispersible UCNPs that can be further conjugated with various functional biomolecules. Then, they further developed a facile ligand-exchange strategy to use polyvinylpyrrolidone (PVP) to replace OA ligands and transfer UCNPs into water without aggregation by refluxing in 1:1 DMF–DCM at 100 °C for 6 h [31]. More interestingly, Li et al. [32] reported a simple yet versatile method for using the Lemieux–von Rudloff reagent to directly oxidize the oleic acid ligands on the UCNP surface, thus yielding water-soluble and carboxylic acid-functionalized UCNPs capable of conjugating with other proteins. Lin et al. [33] also modified hydrophilic sodium dodecyl sulfate (SDS) on the surface of OA-UCNPs by heating at 60 °C to evaporate the chloroform solution. In addition, other biocompatible polymers, such as PAH [34], PEI [35], HAD [36], 3MA [37], MSA [38], and PAMAM [39], have also been successfully used to replace the OA ligands to render modified UCNP excellent water dispersity/stability, which may also improve the biocompatibility of UCNPs for the following biomedical applications.

5.2.2 *Ligand-Free Synthesis Modification*

In order to render the original hydrophobic UCNPs water soluble by completely removing the OA ligand, the ligand-free synthesis method has been developed to make the modified hydrophilic UCNPs capable of directly conjugating with those biocompatible molecules with electronegative groups (-COOH, NH₂, etc.) for further biomedical applications. The OA ligand on the surface of UCNPs can be thoroughly removed by acidic treatment or longtime sonication in excess ethanol. For example, Xu et al. [40] found that the OA ligand on the surface of UCNP nanocrystals could be washed away by excess ethanol under ultrasonic for four times. In addition, after being treated with a HCl solution (pH=4), Capobianco et al. [41] reported that the OA ligand could be removed, thus yielding positively charged ligand-free UCNPs with high stability and dispersity. These synthesized ligand-free UCNPs could be used for further conjugation with biological molecules like heparin [42], TAT [43], etc., which will make UCNPs target the specific tumors or the cell nucleus.

5.2.3 *Silica Coating Modification*

Due to the high biocompatibility and easy surface modification, inorganic silica was usually coated on the surface of hydrophobic nanocrystals to endow them with high water stability as well as easy conjugation with other functional biomolecules. There are two chemical strategies for the dense silica coating on UCNPs. One is the Stöber method, which can be used to coat uniform silica on the surface hydrophilic UCNPs by the addition of TEOS into mixed solution of water/ethanol/ammonia. For example, van Veggel et al. utilized this method to coat thickness controllable on LaF₃:Yb³⁺/Er³⁺ nanoparticles [44]. The other is the reverse emulsion method [45–49] that is extensively adopted to coat dense silica on hydrophobic UCNPs. Zhang et al. [50] successfully coated a very thin and uniform dense silica shell on hydrophobic NaYF₄:Yb/Er/Tm nanocrystals by using a reverse emulsion method to produce monodisperse NaYF₄:Yb/Er/Tm@SiO₂ nanoparticles. Our group [51] also employed this method to coat a thickness-controllable silica shell on NaYF₄:Yb/Er nanoparticles by changing the adding amount of TEOS, which was then functionalized with APTES to attach small Au nanoparticles.

In addition to dense silica, mesoporous silica was also frequently coated on UCNPs to fabricate UCNPs@mSiO₂ nanoparticles, which could serve as delivery vehicles of drugs, photosensitizers, etc. As expected, the integration of UCNPs with mesoporous silica can achieve the combination of fluorescent imaging and drug-delivered chemotherapy, which may be developed as a new generation of imaging-guided nanotheranostics. Zhang et al. [25] reported the successful coating of mesoporous silica on UCNPs to encapsulate photosensitizer ZnPc for photodynamic therapy under NIR excitation. Our group [52] coated a thickness-dependent

mesoporous silica shell on UCNPs by simply adjusting the TEOS addition amount. Lin et al. [53] also coated mesoporous silica on CTAB-modified UCNPs to load anticancer drug DOX for targeted imaging and chemotherapy. In a word, the silica coating method may provide an extremely useful platform for fabricating multifunctional UCNP-based nanostructures in addition to the hydrophobic–hydrophilic transition. However, the remaining excess surfactants may cause low colloidal stability and potential toxicity over time. Therefore, the development of more advanced/efficient surface modification strategies that ensure long dispersity/stability of UCNPs in physiological environment will be the next topic of research.

5.3 Engineering UCNPs for Multimodal Biomedical Imaging

After hydrophilic modification, UCNPs can serve as an excellent luminescent probe for *in vitro* and *in vivo* UCL imaging due to their incomparable superiorities (e.g., low autofluorescence interference, high photostability, etc.) over quantum dots/organic dyes [54]. Moreover, by the co-incorporating of multiple functional ions (e.g., Gd^{3+} , Ba^{2+} , Mn^{2+} , etc.), UCNPs can be developed into a promising multimodal imaging probe based on the integration of other molecular imaging techniques (MRI/CT/PET/SPECT) with UCL into one single system [8]. Since no single imaging modality is perfect because of its intrinsic drawbacks, the design of multimodal imaging probes by engineering UCNPs may integrate all the advantages of different imaging modalities as well as provide multi-aspect imaging information necessary for the accurate diagnosis in the future.

5.3.1 UCNPs for Single-Modality UCL Imaging

5.3.1.1 UCNPs for Multicolor UCL Imaging

A unique feature lies in UCNPs that their upconversion luminescent (UCL) emission spectra can be well turned by selectively doping various rare earth ions to realize multicolor UCL imaging [55]. For example, by only changing the luminescent ions and adjusting their doping concentrations, Liu's group [56] synthesized a series of PEGylated UCNPs with different UCL emission colors: UCNP1 ($\text{NaY}_{0.78}\text{Yb}_{0.2}\text{Er}_{0.02}\text{F}_4$), UCNP2 ($\text{NaY}_{0.69}\text{Yb}_{0.3}\text{Er}_{0.01}\text{F}_4$), and UCNP3 ($\text{NaY}_{0.78}\text{Yb}_{0.2}\text{Tm}_{0.02}\text{F}_4$). When subcutaneously injected into a rat, multicolor UCL imaging was demonstrated *in vivo* upon 980 nm laser excitation (Fig. 5.1a). Based on the same method, Hao et al. [57] also realized the tunable multicolor (from blue to white to yellow) fluorescence emission in hexagonal phase NaGdF_4 : Yb/Tm/Ho nanorods by simply adjusting the Ho^{3+} concentrations.

Another approach for realizing multicolor UCL imaging is to modulate the luminescence emission spectra of UCNP-QD (organic dyes) complex based on lumines-

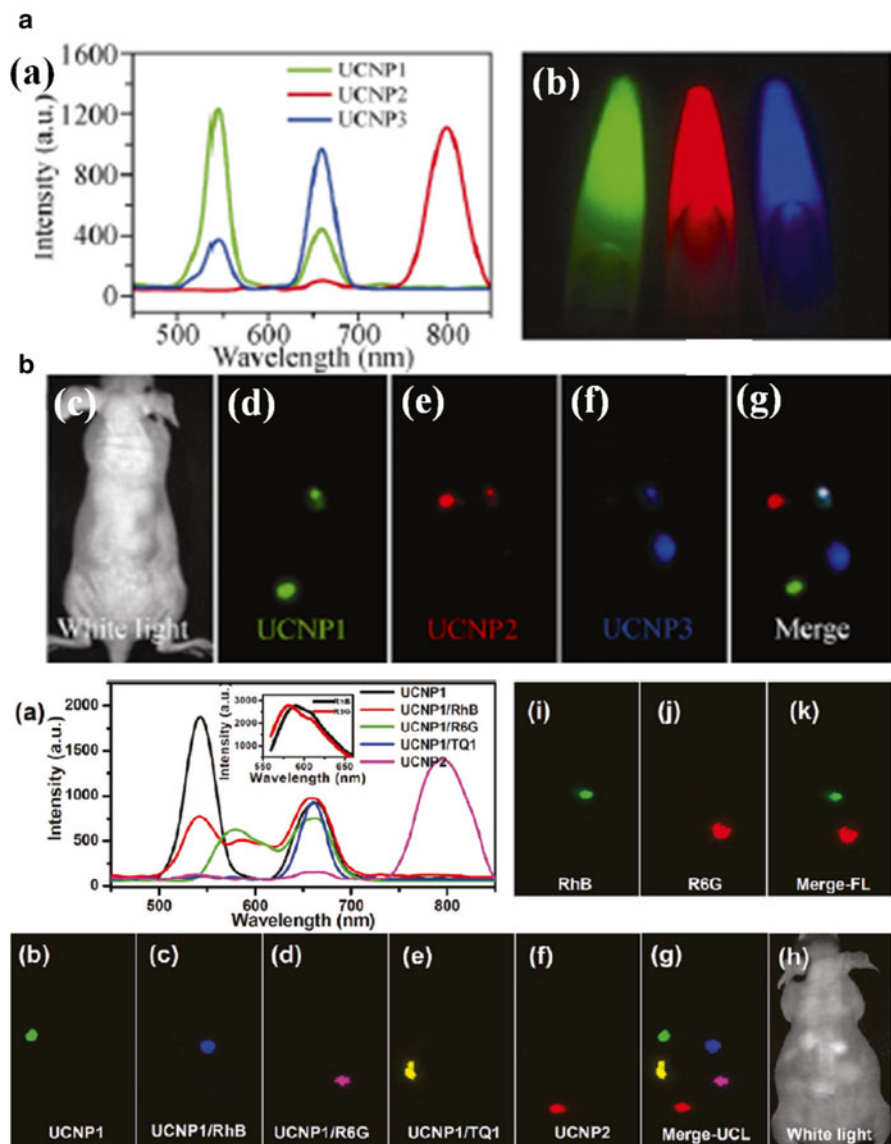


Fig. 5.1 (a) Multicolor UCL imaging: (a) UCL emission spectra of three UCNPs solutions under 980 nm NIR laser excitation; (b) a multicolor fluorescence image of three UCNPs solutions obtained by the Maestro in vivo imaging system (CRI, Inc.); (c) a *white light* image of a mouse subcutaneously injected with UCNPs; (d–f) in vivo multicolor images of a nude mouse subcutaneously injected with different UCNPs solutions; (g) three colors of UCNPs were clearly differentiated after spectral unmixing. (b) Multicolor in vivo UCL imaging of LRET-tuned UCNPs in mice: (a) UCL emission spectra of solutions of *UCNP1*, *UCNP2*, *UCNP1/RhB*, *UCNP1/R6G*, and *UCNP1/TQ1*. Inset: down-conversion fluorescence spectra of *RhB* and *R6G* under *green light* excitation. (b–g) In vivo multicolor UCL images of a nude mouse subcutaneously injected with five colors of UCNPs solutions after spectral unmixing. (h) A *white light* image of the imaged mouse. (i–k) In vivo multicolor down-conversion fluorescence images of the mouse under *green light* excitation ((a) Reprinted from Ref. [56], with kind permission from Springer Science+Business Media. (b) Reprinted with the permission from Ref. [9]. Copyright 2011 American Chemical Society)

cence resonance energy transfer (LRET) from UCNP core to QDs (or organic dyes). In the work by Liu et al. [9], organic dyes (RhB/R6G/TQ1) were integrated with UCNPs by hydrophobic force to make a multicolor UCL imaging probe with tunable luminescence emission based on the LRET under NIR excitation. As shown in Fig. 5.1b, by subcutaneously injecting five different UCNP solutions (UCNP1, UCNP1/RhB, UCNP1/R6G, UCNP1/TQ1, and UCNP2) into the back of nude mice, five different colors were obtained after spectral deconvolution, which clearly demonstrated the UCL imaging of different colors at their corresponding injection sites without noticeable interference (parts b–h of Fig. 5.1b). Based on the same LRET strategy, Kim's group designed the UCNP-QD complex system for multi-color imaging upon different wavelengths of light excitation [58].

5.3.1.2 UCNPs for Tracking UCL Imaging

Thanks to the extremely low autofluorescence of UCL imaging, UCNPs can be used for *in vitro* cell labeling as well as *in vivo* tracking. For example, Zhang et al. [59] used silica-coated UCNPs to dynamically track live myoblast cells *in vitro* and transplanted cells in a living mouse model *in vivo*. Then Li et al. [60] fabricated strong luminescent UCNPs (β -NaLuF₄: Gd/Yb/Tm) to label KB cells *in vivo* with high tracking sensitivity. The corresponding detection limits are 50 and 1,000 UCNP-labeled KB cells for subcutaneous and intravenous injection, respectively (Fig. 5.2a, b). Moreover, high-contrast deep-seated UCL imaging of a whole-body black mouse was also achieved with a large penetration depth of ~ 2 cm.

Besides cancerous cells, mesenchymal stem cells (MSCs) can be also labeled by UCNPs. In a recent study by Liu's group [61], oligoarginine-conjugated UCNPs were used for highly efficient MSC labeling and *in vivo* long-term tracking with ultrahigh sensitivity at nearly the single-cell level, which can hardly be achieved by other exogenous fluorescent or magnetic labeling probes. More importantly, the UCNP-based MSC labeling/tracking approach would not affect the proliferation and differentiation of MSCs over a course of 2 weeks, and as few as ten UCNP-labeled cells were successfully detected *in vivo*, thus demonstrating the super advantages over other stem cell labeling techniques. On this basis, they further designed multifunctional UCNPs@IONPs@Au composite (MFNPs) for *in vitro* labeling and *in vivo* tracking of MSCs by both UCL optical and MR imaging techniques, which also achieves a ultrahigh tracking sensitivity with as few as ≈ 10 cells detectable in a mouse (Fig. 5.2c, d) [62]. Under a magnetic field, MFNP-labeled MSCs after being injected into mice can be remotely controlled and magnetically targeted and delivered to the wound site for enhancing the tissue-repairing efficacy (Fig. 5.2e, f), which demonstrates a promising prospect for future magnetic/luminescent imaging-guided MSC therapy applications.

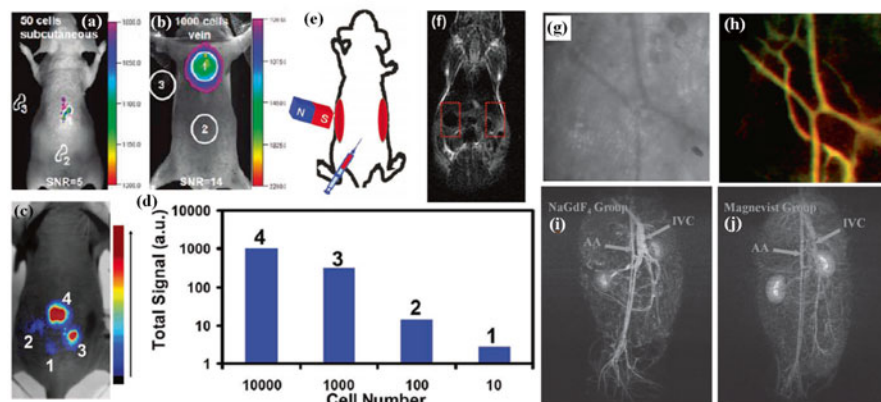


Fig. 5.2 (a, b) In vivo UCL imaging of athymic nude mice after (a) subcutaneous injection of 50 KB cells and (b) vein injection of 1,000 cells. The KB cells were incubated with 200 $\mu\text{g/mL}$ $\beta\text{-NaLuF}_4\text{:Gd/Yb/Tm}$ nanoparticles for 2 h. (c–f) In vivo tracking of MFNP-labeled mMSCs: (c) A UCL image of a mouse subcutaneously injected with various numbers of mMSCs ($\approx 10\text{--}10^4$) labeled with MFNP-PEG. (d) Quantification of UCL signals. (e) A scheme showing that the wound-bearing mouse was anesthetized by isoflurane inhalation and i.p. injected with MFNP-labeled mMSCs. A magnet was attached to the left-side wound for 6 h before imaging. (f) In vivo MR image of the wound-bearing mouse. (g, h) UCL imaging of blood vessels in the mouse ear following tail vein injection of PEG-coated $\text{Y}_2\text{O}_3\text{:Yb/Er}$ nanoparticles; (g) blood vessels imaged with a blue light filter. (h) UCL image with excitation at 980 nm. (i, j) MR angiography of rabbits within 3 min after injected with the i) NaGdF_4 nanodots or j) Magnevist: abdominal aorta (AA) and inferior vena cava (IVC) ((a, b) Reprinted with the permission from Ref. [60]. Copyright 2011 American Chemical Society. (c–f) Reprinted with the permission from Ref. [62]. Copyright 2013 Wiley-VCH Verlag GmbH & Co. KGaA. (g, h) Reprinted with the permission from Ref. [66]. Copyright 2009 Royal Society of Chemistry. (i, j) Reprinted with the permission from Ref. [67]. Copyright 2014 Wiley-VCH Verlag GmbH & Co. KGaA)

5.3.1.3 UCNPs for Tumor-Targeted UCL Imaging

Tumor-targeted imaging plays a very important role in cancer diagnosis and the following imaging-guided positioned therapy. By the attachment of some special targeting ligands, UCNPs can be efficiently accumulated in tumors for high-contrast UCL imaging upon NIR light excitation. In 2009, Li's group firstly realized the in vivo tumor-targeting UCL imaging by using folic acid (FA)-modified UCNPs [63]. As a widely used targeting agent, FA has a high affinity for folate receptors (FR) that are overexpressed in many human cancerous cells like HeLa. Therefore, after intravenous injection of FA-modified UCNPs into HeLa tumor-bearing nude mice for 24 h, strong UCL signal appeared in the HeLa tumor region, while no UCL signal was observed in the control group (mice intravenously injected with amine-modified UCNPs), thus demonstrating excellent tumor-targeted UCL imaging. Besides FA, RGD (arginine–glycine–aspartic acid) peptide can target $\alpha_v\beta_3$ -integrin receptor overexpressed tumors. In about 4 h postinjection of RGD-modified UCNPs, Li et al. observed obvious UCL signal in the U87MG tumor (expressing high levels

of integrin $\alpha_v\beta_3$) as compared to invisible signal in MCF-7 tumor (expressing low levels of integrin $\alpha_v\beta_3$) [64]. Our group also successfully used RGD-conjugated BaYbF₅:Tm nanoparticles for targeted UCL imaging of U87MG tumor [15]. Besides subcutaneously xenotransplanted U87MG tumors, the UCL imaging intracranial glioblastomas have been also realized by attaching a dual-targeting ligand ANG to UCNPs [65], which can efficiently cross the blood–brain barrier (BBB) and target the glioblastoma for UCL imaging diagnosis. Therefore, in order to realize highly efficient tumor-targeting UCL imaging, superior targeting ligands with strong binding affinity should be designed for the rich accumulation of UCNPs in tumors, which will be a research hotspot in the future.

5.3.1.4 UCNPs for Vascular UCL Imaging

Up to date, the early diagnosis of vascular permeability and vessel functional abnormality can help efficiently prevent the vascular diseases which have been another major threat to human health. Due to the high sensitivity and photostability without autoluminescence, UCNPs may serve as an advanced imaging tool for visualizing blood vessels *in vivo*. The first report of using UCNPs for vascular UCL imaging is Hilderbrand's group [66], who synthesized PEG-coated Y₂O₃:Yb/Er nanoparticles with UCL emissions centered at 660 nm for strong red luminescent blood pool imaging *in vivo* upon NIR irradiation. The ear blood vessel could be clearly visualized by intravenous injection of UCNPs under a whole-field-illumination upconversion microscope (Fig. 5.2g, h). Then Zhang et al. also used silica-coated UCNPs (NaYF₄:Yb/Er@SiO₂ nanoparticles) for the live myoblast cell tracking as well as ear blood vessel UCL imaging via tail vein injection [59]. However, as limited by the relatively low spatial resolution, luminescent imaging fails to distinguish the whole blood vessels more clearly, which can be improved by magnetic resonance (MR) imaging or other high-resolution imaging tools. For example, our group synthesized ultrasmall NaGdF₄ nanoparticles (with a high r_1 value of 8.93 mM⁻¹s⁻¹) for high-resolution blood pool MR imaging with the abdominal aorta (AA) and inferior vena cava (IVC) distinctly delineated (Fig. 5.2i, j) [67]. More importantly, the subvascular details and micrangium can be also clearly distinguished, which can contribute to the accurate diagnosis of vascular pathema or other vascular diseases.

5.3.1.5 UCNPs for Lymphatic UCL Imaging

As most cancerous cells frequently metastasize to the local lymph nodes, the identification of sentinel lymph nodes based on the lymphatic imaging is of essential importance for monitoring the tumor metastasis and guiding the surgical operation. As an excellent luminescent probe, UCNPs have been used by many researchers for high-contrast UCL imaging of lymph nodes without autofluorescence. The first use of UCNPs for lymphatic UCL imaging is Kobayashi's group [68], who directly captured the lymph node pictures without post-processing. Then Li et al. [69] and

Liu et al. [56] also successfully realized the lymphatic capillary UCL imaging of small animals with high signal to noise ratio upon relatively low power density of NIR irradiation (Fig. 5.3a, b). More interestingly, by intracutaneous injection of three different kinds of UCNP with multicolor emission, strong multicolor UCL imaging signals appeared in the three primary lymph nodes where each color of UCNP migrated via lymphatic drainage (Fig. 5.3a), thus demonstrating the advantages of UCNP in multicolor lymphatic UCL imaging. However, due to the limited penetration depth of NIR irradiation, deep-seated lymph nodes can't be achieved by UCL imaging, which needs the exploration of more advanced imaging modalities, such as PET imaging with high sensitivity and unlimited penetration.

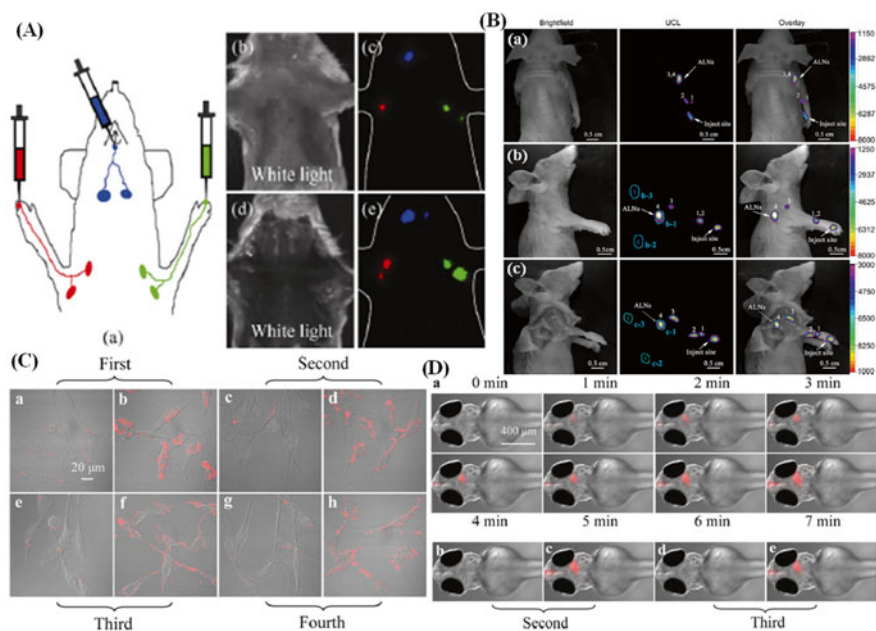


Fig. 5.3 (a) In vivo multiplexed lymphangiography with UCNP: (a) a schematic illustration of UCNPs-based lymph node mapping; (b) a *white light* image of a mouse injected with UCNP; (c) a three-color spectrally resolved in vivo UCL image showing different UCNPs colors from the corresponding lymph nodes under the skin; (d) a *white light* image of the same mouse after dissection; (e) a UCL image of the dissected mouse. (b) In vivo lymphatic drainage UCL imaging at 800 nm was clearly detected at four different draining lymph basins (1, 2, 3, 4) along the right antebrachium of the nude mouse. Detection of upconversion luminescence in (a) prostrate or (b) lateral position. (c) The lymphatic drainage UCL imaging after removal of skin and fatty tissues. (c) CLSM images of U87MG cells loaded with nanosensors and exposed to cycles of normoxia (a, c, e, g) and hypoxia (b, d, f, h) conditions for 6 h. (d) CLSM images of living zebrafish embryos after injection of nanosensors followed by adding BDM. UCL images were obtained under the excitation at 980 nm and emission at 550–650 nm. After adding freshwater, red emission in the brain was quenched under NIR exposure ((a) Reprinted from Ref. [56], with kind permission from Springer Science+Business Media. (b) Reprinted with the permission from Ref. [69]. Copyright 2011 Elsevier B. V. (c, d) Reprinted with the permission from Ref. [71]. Copyright 2014 American Chemical Society)

5.3.1.6 UCNPs for Hypoxic UCL Imaging

As a principal signature of solid tumors, tumor hypoxia, arising from the inadequate supply of oxygen in blood vessels, has been a major cause for the treatment failure of solid tumors and the induction of tumor invasion/metastasis [70]. Luminescent imaging has been used for the accurate diagnosis of tumor hypoxia and quantitative estimation of hypoxic degree. Considering the intrinsic drawbacks (e.g., low photostability in bioreductive microenvironment, low penetration depth, etc.) of traditional oxygen probes, our group developed an ultrasensitive nanosensor by engineering UCNPs for selective hypoxic UCL imaging based on the LRET from UCNPs to oxygen indicator $[\text{Ru}(\text{dpp})_3]^{2+}\text{Cl}_2$ under NIR irradiation [71]. Compared with free $[\text{Ru}(\text{dpp})_3]^{2+}\text{Cl}_2$, our designed nanosensor can reversibly detect the level of hypoxia both in vitro (hypoxic U87 cells, Fig. 5.3c) and in vivo (zebrafish, Fig. 5.3d) based on the corresponding luminescence emission intensity with high sensitivity and large penetration depth. The ultrasensitive nanosensor is expected to be used for hypoxic UCL imaging of solid tumors to provide significant guidance for the subsequent therapeutic decisions.

In summary, thanks to the superior advantages over traditional luminescent probes, UCNPs can serve as an excellent UCL imaging probe for the accurate diagnosis of big diseases as well as quantitative sensing of some biological matters and tumor microenvironment (e.g., hypoxia, pH, temperature, etc.). However, in order to promote the future clinical applications of UCNPs, many aspects need to be further improved, such as the enhancement of UCNPs' quantum yield, the lowering of UCNPs' potential toxicity, and so on.

5.3.2 UCNPs for Multimodal Imaging

As the saying goes, there exists no perfect single imaging probe because each imaging modality has its intrinsic drawbacks and thus fails to reflect all the necessary imaging information. Therefore, the development of multimodal imaging probe by the combination of multiple imaging modalities into one system is of essential importance for acquiring all the imaging data and enhancing the diagnostic accuracy. By suitable doping strategy, UCNPs can be engineered as an excellent multimodal imaging probe to realize the cellular scale to whole-body level imaging with extremely high sensitivity and spatial resolution.

5.3.2.1 UCNPs for MR/UCL Bimodal Imaging

The most common UCNP-based multimodal imaging probe is the simple combination of MR/UCL by doping Gd^{3+} into the host lattice. This bimodal imaging probe possesses all the advantages of MR/UCL and provides high sensitivity for in vitro imaging as well as and high spatial resolution for in vivo imaging [8]. For example,

Li et al. synthesized PAA-coated Yb/Er/Tm/Gd co-doped UCNPs (NaGdF₄:Yb/Er/Tm–PAA) for simultaneous T₁-MR imaging and NIR-NIR UCL imaging of the whole-body animals in vivo (Fig. 5.4a, b) [72]. Zhao et al. synthesized Yb/Er/Tm-doped Gd₂O₃ nanoparticles for simultaneous T₁-MR and strong multicolor UCL imaging [73]. The corresponding emission colors could be tuned by simply changing either the doping Ln³⁺ or co-dopant concentrations. Furthermore, by doping Mn²⁺ instead of Gd³⁺ into UCNPs, strong red UCL emission plus MR imaging capacities can be realized [74].

Besides incorporating Gd³⁺ into the host, the epitaxial growth of a NaGdF₄ layer on the surface of the NaYF₄ host to fabricate core/shell (multi-shell) structured UCNPs can not only improve the MR imaging contrast by significantly increasing the r₁ value but also greatly enhance the UCL imaging intensity by suppressing non-radiative decay and passivating surface defects. In order to evidence this point, our group conducted a series of comparative studies [11, 75] by fabricating various kinds of core/shell structured UCNPs or dense/mesoporous silica-coated UCNPs and comparing their r₁ value/UCL emission intensity, which provides a deep perspective for magnetic resonance (MR) sensitivity, and UCL emission intensity optimization of Gd³⁺-doped UCNPs. Liu et al. [76] and Zhang et al. [77] have performed similar systemic studies, which all shed light on the design of optimized Gd³⁺-doped UCNPs and speeding up the future clinical translation of the promising MR/UCL bimodal molecule imaging probes.

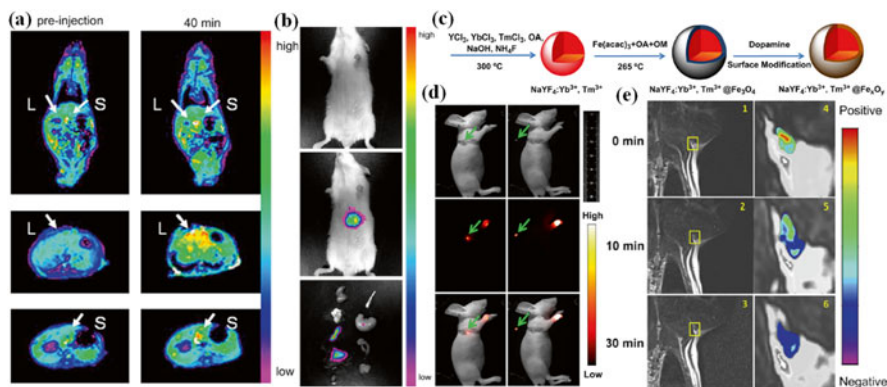


Fig. 5.4 (a) Color-mapped MR coronal images of the whole body and transversal cross-sectional images of the (L) liver and (S) spleen of mice at preinjection and at 40 min after intravenous injection of NaGdF₄:Yb/Er/Tm–PAA. (b) In vivo and ex vivo UCL imaging of mouse after intravenous injection of NaGdF₄:Yb/Er/Tm–PAA. (c) Schematic representation of the synthetic routine of the water-soluble NaYF₄:Yb³⁺, Tm³⁺@Fe_xO_y nanocrystals. (d) Ex vivo UCL images of the lymphatic system of a nude mouse sacrificed after injection with NaYF₄:Yb³⁺, Tm³⁺@Fe_xO_y nanocrystals for 40 min. Green arrow marked the lymphatic nodes. (e) MR images of the armpit region after injection with NaYF₄:Yb³⁺, Tm³⁺@Fe_xO_y nanocrystals and color-mapped coronal images of lymph node at various times ((a, b) Reprinted with the permission from Ref. [72]. Copyright 2010 Elsevier B. V. (c–e) Reprinted with the permission from Ref. [79]. Copyright 2011 Elsevier B. V.)

It is well known that T_1 -weighted MRI contrast agents (as called positive MRI contrast agents) can change the spin–lattice/the protons of coordinated/nearby water molecules to brighten the image signals, while T_2 -weighted MRI contrast agents (as called negative MRI contrast agents) can alter the spin–spin relaxation time to darken the image signals. As a representative T_2 -MRI probe, Fe_3O_4 nanoparticles (SPIONs) have been widely used for darken MR imaging of human organs due to their good biocompatibility and special superparamagnetic properties. Unfortunately, black Fe_3O_4 nanoparticles could largely absorb the UCL emission and thus quench the luminescence of UCNPs, which adds to the difficulty in preparing excellent T_2 -MR/UCL bimodal imaging probes.

Some groups have tried to prevent the UCL emission quenching by SPIONs through the smart design of UCNP/SPION nanocomposite. For example, in the year 2010, our group firstly developed a “neck-formation” strategy [78] to fabricate silica-shielded magnetic upconversion fluorescent oligomers (SMUFOS) by connecting SPION@ SiO_2 and UCNPs@ SiO_2 nanoparticles through the Si–O–Si bridges between them. Due to the high magnetic/photostability and quenchless UCL properties, the designed SUMFOs were successfully used for T_2 -weighted MR and UCL bimodal imaging of Walker 256 tumor in a SD mouse. By coating a 5 nm Fe_xO_y shell on the $NaYF_4:Yb/Tm$ core, Li et al. synthesized silica-free $NaYF_4:Yb/Tm@Fe_xO_y$ nanocomposites which could be applied for T_2 -MR/UCL bimodal imaging of the lymphatic systems in vivo (Fig. 5.4c–e) [79]. Besides, Liu et al. developed a layer-by-layer assembly approach to synthesize core/shell/shell structured nanocomposites (MFNPs) with UCNPs as the core, a thin gold layer as the outer shell, and a layer of ultrasmall SPIONs in between [80]. Thanks to the smart integration of UCNPs/SPIONs and strong NIR absorption of gold, the designed MFNPs could be used for T_2 -MR/UCL bimodal imaging as well as magnetically targeted photothermal therapy in vitro and in vivo. Zhang et al. also used a facile ion exchange route to fabricate a hydrophilic rattle-structured $Fe_3O_4@SiO_2@NaYF_4:Yb/Er$ nanoprobes for T_2 -MR/UCL bimodal imaging as well as the antitumor drug doxorubicin (DOX)-delivered chemotherapy against H22 tumors under the enhanced magnetic targeting [81].

In order to completely eliminate the UCL quenching by SPIONs in the design of excellent T_2 -MR/UCL bimodal imaging probes, the exploration of other functional ions for T_2 -MR imaging is urgently needed. Fortunately, van Veggel et al. found that the paramagnetic dysprosium (Dy^{3+}) ion-doped UCNP was one of the best choices for T_2 -weighted MR imaging because of its high magnetic moment (10.6 μ_B) and short electronic relaxation time (~ 0.5 ps) [82]. Moreover, these Dy^{3+} -doped UCNPs (e.g., $NaDyF_4$, $NaHoF_4$, etc.) have been found especially suitable for T_2 -MR imaging in ultrahigh field (9.4 T) MRI because their corresponding r_2 relaxivity value was greatly enhanced with the increasing magnetic field, which should be explained by the Curie spin relaxation mechanism. Therefore, the van Veggel’s exciting finding provides a new perspective for the design of ultrahigh field T_2 -MR/UCL bimodal imaging probe with much higher spatial resolution in ultrahigh field MRI and negligible luminescence quenching.

5.3.2.2 UCNPs for UCL/MRI/CT (PET/SPECT) Trimodal Imaging

Besides MR/UCL bimodal imaging probes, recently more attentions have been paid to the construction of MRI/UCL/CT or MRI/UCL/PET trimodal imaging probes, which can greatly improve the imaging quality and enhance the diagnostic accuracy. Different from MR and UCL imaging with high sensitivity and spatial resolution, X-ray computed tomography (CT) imaging can provide high-resolution three-dimensional (3D) structure details of tissues based on their differential X-ray absorption. Therefore, the combination of MR, UCL, and CT into one system to generate a trimodal imaging probe may not only achieve high-sensitivity cellular imaging but also provide clear 3D soft tissue details. Instead of small iodinated molecules, several high-Z atom (e.g., Yb, Lu, Au, etc.)-doped/contained nanoparticles can serve as better CT contrast agents because of their stronger X-ray attenuation [83]. By the smart assembly of these CT contrast agents with the above MR/UCL bimodal imaging probes, MR/UCL/CT trimodal imaging probes are produced for concurrent trimodal imaging of malignant tumors.

The first trimodal imaging probe was designed by our group [51], who synthesized PEGylated $\text{NaYF}_4:\text{Yb/Er/Tm/Gd@SiO}_2\text{-Au@PEG5000}$ nanoparticles (UCS-Balls) by attaching ultrasmall Au nanoparticles to the surface of silica-coated Gd-UCNPs. These UCS-Balls can serve as an excellent trimodal probe for simultaneous T_1 -weighted MR/NIR-vis UCL/enhanced CT imaging of Walker 256 tumors after intratumoral injection (Fig. 5.5a). In order to avoid the potential UCL signal blocking by the outer Au nanoparticles, our group further synthesized radiopaque fluorescence-transparent TaOx nanoparticles decorated upconversion nanophosphors (UCNLs) for high-intensity/contrast CT/MRI/UCL trimodal imaging in vitro and in vivo without detectable mutual imaging interference among the three modalities [12]. Besides, with the help of the strong X-ray attenuation characteristics of Gd/Yb elements and good biocompatibility of PEG, the long-circulating trimodal imaging probe PEGylated $\text{Gd}_2\text{O}_3:\text{Yb}^{3+}/\text{Er}^{3+}$ nanorods were synthesized by Qu's group through a facile and large-scale hydrothermal approach, which could provide detailed and complementary information from T_1 -MR/UCL/CT trimodal imaging [84]. Thanks to the high atomic number of Lu, Li et al. [85] even developed Gd^{3+} complex-modified NaLuF_4 -based UCNPs for efficient trimodal imaging of the whole body of mice with high T_1 -MRI enhancement, bright NIR-to-NIR UCL emissions, and excellent X-ray absorption.

Besides T_1 -MR/UCL/CT trimodal imaging probes, T_2 -MR/UCL/CT probes were also designed by Li et al. [86], who synthesized core/shell structured $\text{Fe}_3\text{O}_4@\text{NaLuF}_4:\text{Yb/Er/Tm}$ nanoparticles (MUCNP) [86] by a stepwise method to realize T_2 -MRI/UCL/CT trimodal imaging of cancerous cells in vitro and tumor tissues in vivo (Fig. 5.5b). Very recently, our group developed a novel T_2 -MR/UCL/CT trimodal imaging probe by exploring the T_2 -weighted contrast properties of Ho^{3+} to replace black Fe_3O_4 , which can completely solve the luminescent emission quenching problem and even enhance the UCL intensity [87]. Unlike other composite nanostructures, the single Ho^{3+} -doped UCNPs ($\text{NaYbF}_4:\text{Ho}$) were synthesized by a simple one-pot thermal decomposition method for win-win multimodal T_2 -MRI/

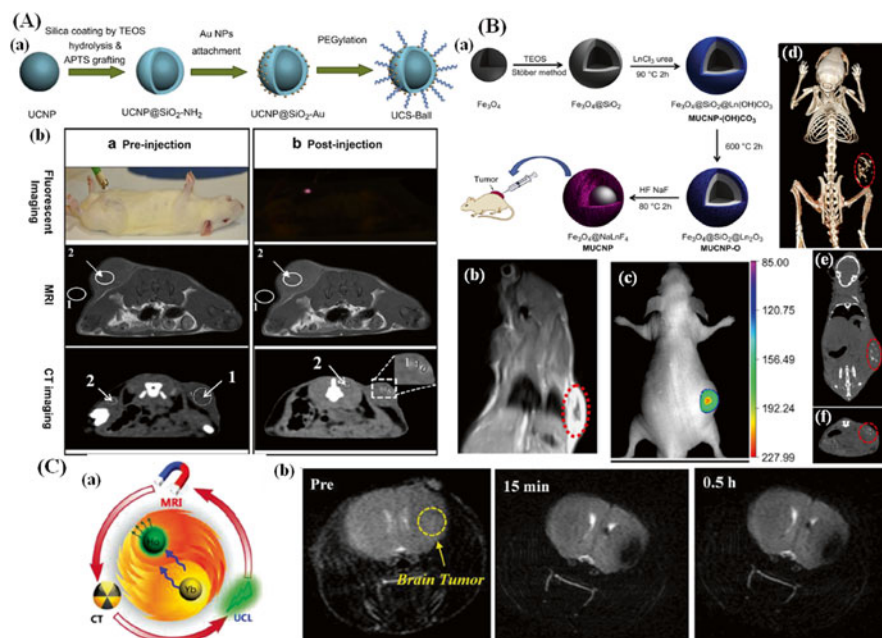


Fig. 5.5 (a) Schematic illustration for the synthesis of UCS-Balls. (b) Trimodal images of mice bearing a Walker 256 tumor using UCS-Balls: preinjection (left), postinjection (right). (b) (a) Schematic representation of the synthetic routine of the multifunctional $\text{Fe}_3\text{O}_4@/\text{NaLuF}_4:\text{Yb}/\text{Er}/\text{Tm}$ nanoparticle (MUCNP). (b) T_2 -weighted coronal images of the nude mice bearing a tumor after intratumoral injection of MUCNP. (c) In vivo UCL images of the tumor-bearing nude mice. (d-f) In vivo (d) CT volume-rendered and maximum intensity projection of (e) coronal, (f) transversal images of the tumor-bearing mouse. (e) (a) Schematic diagram of Ho^{3+} -doped UCNPs as the T_2 -MR/UCL/CT multimodal imaging. (b) In vivo T_2 -MR imaging of glioblastoma-bearing mice before and at various time points after intravenous injection of Ho^{3+} -doped UCNPs ((a) Reprinted with the permission from Ref. [51]. Copyright 2012 Elsevier B. V. (b) Reprinted with the permission from Ref. [86]. Copyright 2012 Elsevier B. V. (c) Reprinted with the permission from Ref. [87]. Copyright 2014 Wiley-VCH Verlag GmbH & Co. KGaA)

UCL/CT imaging of the whole mouse body without luminescence quenching. More importantly, the Ho^{3+} -doped UCNPs could be also used for the efficient T_2 -weighted MR imaging of glioblastoma by overcoming the difficulty in the clinical diagnosis of brain tumors (Fig. 5.5c).

As another noninvasive radioactive imaging modality, PET/SPECT has been used for the whole-body imaging and quantitative biodistribution estimation due to its extremely high detection intensity. Especially, PET imaging is very suitable for the lymphatic imaging and accurate localization of lymph node by overcoming the drawbacks of traditional luminescent imaging, such as autofluorescence from biological sample, low signal to noise ratio (SNR), and so on. Recently, some radionuclides have been used for PET imaging. For example, by incorporating ^{18}F into the UCNPs lattice, Li's group [16] developed ^{18}F -labeled $\text{NaYF}_4:\text{Yb}/\text{Tm}$ nanoparticles

with an average yield of more than 90 % for the high-sensitivity PET imaging of whole-body small animals and lymphatic monitoring (Fig. 5.6a, b). Meanwhile, the ^{18}F -doped UCNPs could be also real-time tracked in vivo for biodistribution analysis. However, due to the extremely short half-life ($t_{1/2}$, 1.829 h) of ^{18}F that may seriously limit its biological applications in long-term imaging, the same group embedded ^{153}Sm into $\text{NaLuF}_4:\text{Yb/Tm}$ nanoparticles to replace ^{18}F by a one-pot hydrothermal synthetic method [19]. Thanks to the much longer half-life (46.3 h) of ^{153}Sm and emission of medium-energy beta rays, the synthesized $\text{NaLuF}_4:^{153}\text{Sm}/\text{Yb/Tm}$ nanoparticles could be used for long-term SPECT imaging (Fig. 5.6c–g) for in vivo quantitative distribution monitoring of the nanomaterials. Certainly, there are other long-term radionuclides that remain to be explored/applied for PET/SPECT imaging, such as ^{64}Cu ($t_{1/2}$, 12.7 h), ^{86}Y ($t_{1/2}$, 14.7 h), ^{124}I ($t_{1/2}$, 4.2d), and so on.

By the co-doping of $\text{Gd}^{3+}/\text{Yb}^{3+}/\text{Er}^{3+}$ into ^{18}F -labeled UCNPs (^{18}F -labeled $\text{NaYF}_4:\text{Gd}/\text{Yb}/\text{Er}$ nanoparticles), Li et al. successfully fabricate a novel MR/UCL/PET trimodal imaging probe for high-sensitivity/solution imaging from the cellular scale to whole-body evaluation by integrating the advantages of these three imaging modalities [88]. Specially, PET imaging can realize the whole-body imaging with high detection sensitivity as well as reach below the picomolar range for functional imaging. The in vivo MR and ex vivo UCL imaging can provide the complementary information including the cellular-level observation. So the combination of MR/UCL/PET imaging modalities within the trimodal probe is of great value for the future accurate diagnostic applications in clinic.

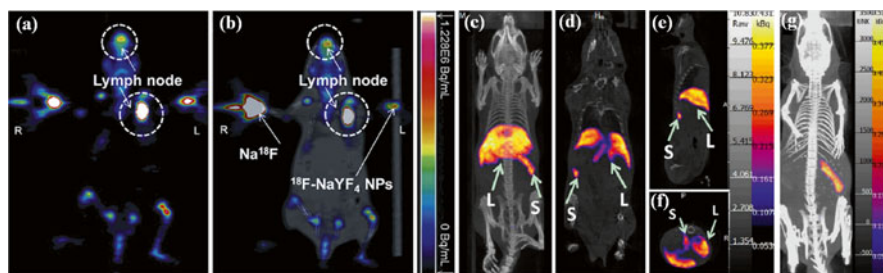


Fig. 5.6 (a) PET imaging and (b) PET/CT imaging of lymph node 30 min after subcutaneous injection of ^{18}F -UCNPs. ^{18}F -UCNPs into the left paw footpad, signal in lymph node reached the peak intensity and maintained it to 60 min postinjection. While as control-free ^{18}F ions injected into the right paw showed no lymphatic imaging ability. (c–g) In vivo SPECT images after intravenous injection of Sm-UCNPs. (c) Whole-body three-dimensional projection, (d) coronal, (e) sagittal, and (f) transversal images acquired at 1 h and (g) whole-body three-dimensional projection images acquired at 24 h are shown, respectively. The arrows inset point to the liver (L) and spleen (S) ((a, b) Reprinted with the permission from Ref. [16]. Copyright 2011 Elsevier B. V. (c–g) Reprinted with the permission from Ref. [19]. Copyright 2013 Elsevier B. V)

5.3.2.3 UCNPs for UCL/MRI/CT/SPECT Four-Modal Imaging

In order to further enhance the diagnostic accuracy, the integration of all the above four imaging modalities (MR/UCL/CT/SPECT) into one system for generating a four-modal imaging probe may be an ideal strategy. Very recently, Li's group [18] synthesized core/shell structured $\text{NaLuF}_4:\text{Yb,Tm}@ \text{NaGdF}_4-(^{153}\text{Sm})$ nanoparticles by the epitaxial growth of a 4 nm $^{153}\text{Sm}^{3+}$ -doped NaGdF_4 shell on the $\text{NaLuF}_4:\text{Yb/Tm}$ core (Fig. 5.7a, b), which resulted in a novel excellent MR/UCL/CT/SPECT four-modal probe for high-quality tumor angiogenesis imaging. Due to the multiple functional ions (Lu^{3+} , Yb^{3+} , Tm^{3+} , Gd^{3+} , $^{153}\text{Sm}^{3+}$) co-doping, the $\text{NaLuF}_4:\text{Yb,Tm}@ \text{NaGdF}_4-(^{153}\text{Sm})$ nanoparticles possess the multifunctional properties of enhanced UCL emission, excellent X-ray attenuation, relatively high r_1 value, and gamma photon emissive radioactivity. Meanwhile, the corresponding imaging results (Fig. 5.7c–h) confirmed that the designed four-modal probe could be effectively applicable for simultaneously enhanced UCL imaging, X-ray computed tomography (CT), magnetic resonance imaging, and single-photon emission computed tomography (SPECT) *in vivo*. It is worth mentioning that such a four-modal imaging probe may be expected to shed light on the fabrication of multifunctional nanoprobes for future bio-imaging applications by acquiring more comprehensive and accurate imaging information.

Despite the rapid progress in the development of UCNP-based multimodal imaging probes, there is still a long way to go to apply these bioprobes for clinical diagnostic applications. Firstly, more potential toxicity and biosafety of these probes should be thoroughly evaluated to ensure their biocompatibility. Secondly, suitable surface engineering should be adopted to prevent their uptake by the RES system. Thirdly, the exploitation of multimodal imaging equipment should also be speeded up to realize the concurrent multimodal in one machine. In all, we hope the UCNP-based multimodal probes will be actually applied for the early accurate diagnosis of human diseases in the near future.

5.4 Engineering UCNPs for Imaging-Guided Synergetic Therapy

Beyond applications in multimodal biomedical imaging, UCNPs can be further expanded to be used for imaging-guided therapy. By mesoporous silica coating, UCNPs can serve as delivery vehicles of anticancer drugs/radiosensitizers/photosensitizers for chemotherapy, radiotherapy, and photodynamic therapy (PDT). In clinic, only single treatment can't eradicate malignant tumors due to its intrinsic drawbacks, so the integration of different therapeutic modalities into UCNP-based theranostic system may help lead to the optimal treatment efficacy as well as realize our dream of thorough tumor elimination.

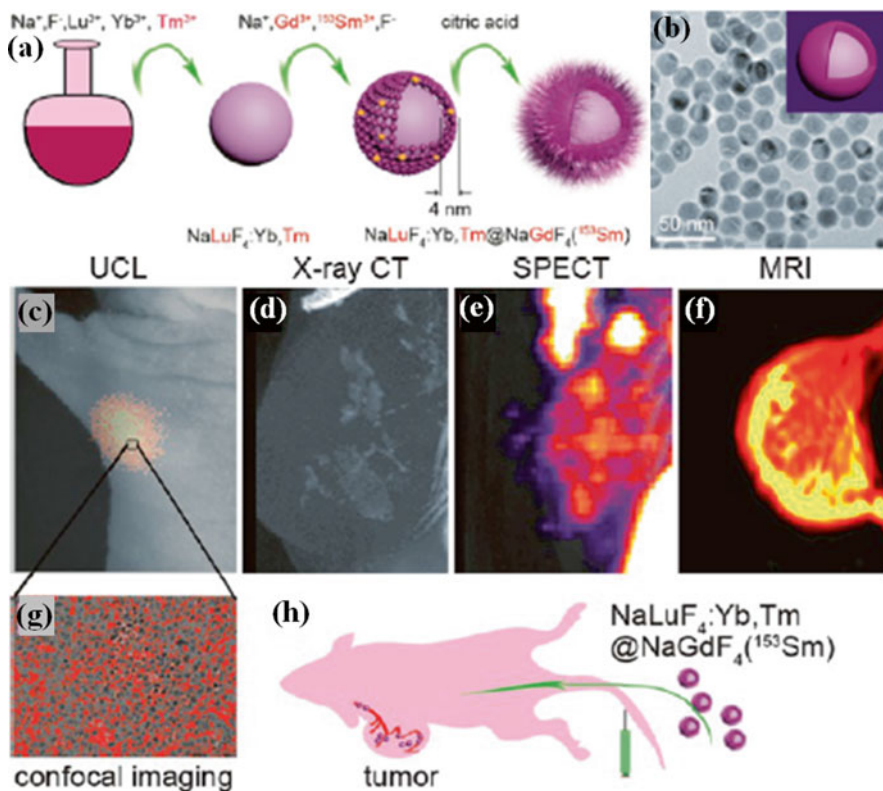


Fig. 5.7 (a) Schematic illustration of synthetic routine of the core/shell nanocomposite $\text{NaLuF}_4:\text{Yb/Tm}@ \text{NaGdF}_4(^{153}\text{Sm})$. (b) TEM image $\text{NaLuF}_4:\text{Yb/Tm}@ \text{NaGdF}_4(^{153}\text{Sm})$. (c–f) Four-modal imaging of the focused tumor from the tumor-bearing nude mouse 1 h after intravenous injection of $\text{NaLuF}_4:\text{Yb/Tm}@ \text{NaGdF}_4(^{153}\text{Sm})$. (c) In vivo UCL image, (d) X-ray CT image, e SPECT image, (f) MR imaging of tumor. (g) UCL confocal image of the paraffin section of tumor tissue. (h) Schematic illustration of tumor angiogenesis imaging using $\text{NaLuF}_4:\text{Yb/Tm}@ \text{NaGdF}_4(^{153}\text{Sm})$ as the probe (Reprinted with the permission from Ref. [18]. Copyright 2013 American Chemical Society)

5.4.1 UCNPs for PDT

As a noninvasive light-triggered treatment tool, PDT has been widely used for cancer therapy by producing cytotoxic reactive oxygen species (ROS) to kill cancerous cells. However, traditional PDT strategy of using UV or visible light to excite photosensitizers fails to treat those deep-seated tumors due to the limited penetration depth, which remains a big challenge to be overcome. Thanks to the unique feature of UCNPs in the conversion of NIR light to UV/vis light, a great deal of singlet oxygen ($^1\text{O}_2$) can be generated upon NIR irradiation based on the fluorescence resonance energy transfer (FRET) from UCNPs to photosensitizers. More importantly, by the targeted delivery of UCNPs, photosensitizers, especially those hydrophobic

ones, can be transported to tumor tissues for the further improved NIR-triggered PDT effects.

The first realization of NIR-triggered PDT is by Zhang's group [89], who coated a merocyanine-540-doped silica shell on UCNPs. Upon NIR light irradiation, merocyanine-540 could efficiently absorb the visible light emission from UCNPs to generate $^1\text{O}_2$ on killing MCF-7/AZ bladder cancerous cells. By aid of a water-in-oil reverse microemulsion strategy, Zheng's group [90] successfully synthesized UCNPs@SiO₂ nanoparticles with photosensitizer AlC₄Pc covalently incorporated into the dense silica shells, which could improve the PDT effects by enhancing the loading efficacy and avoiding the leakage of photosensitizers. Based on the same method, our group [91] prepared a new kind of sub-50 nm UCNPs@SiO₂(MB) PDT drug. In this study, we firstly focused on the control of various parameters (e.g., MB concentration, reaction time, silica shell thickness, etc.) for the inhibition of MB dimerization as well as the excellent spectral overlap between UCNP emission and MB absorption for the realization of ever higher FRET efficiency. Although the above photosensitizers loaded into the nonporous dense silica could be protected from the surrounding intricate environment, the diffusion of oxygen molecules and release of ROS are extremely limited, thus resulting in the lowering PDT efficacy to some extent. To overcome this drawback, the following effective loading strategies have been adopted for combining photosensitizer with UCNPs.

By loading photosensitizers into the mesoporous silica instead of dense silica, more oxygen molecules are diffused to "contact" UCNPs/photosensitizers and thus involved in the PDT reaction for generating much more $^1\text{O}_2$. Zhang et al. [25] firstly incorporated photosensitizers ZnPc into the mesoporous silica-coated UCNPs, which led to the continuous production of $^1\text{O}_2$ for causing significant cancerous cell death upon NIR irradiation. Unlike the above physical encapsulation of hydrophilic photosensitizers, the covalent grafting method was used for the loading of hydrophobic ones by avoiding premature leakage. For example, in a recent report by Yan et al. [92], hydrophobic photosensitizers (SPCD/HP) were covalently bonded to mesoporous silica channels to improve their solubility/stability in cell microenvironment. Meanwhile, the mesoporous silica also created the conditions for faster release of $^1\text{O}_2$ into the surrounding tumor regions. Upon NIR irradiation, the photosensitizers could absorb green/red luminescence emission from UCNPs to generate a great deal of $^1\text{O}_2$ to efficiently killing many tumor cells. Instead of covalently incorporating photosensitizers into the mesoporous silica by Si-O-Si bonds, Zhang et al. [93] developed another covalent bonding strategy to directly link rose bengal (RB) onto the surface of UCNPs. They found this covalent linking strategy could improve both the loading capacity of RB and FRET efficiency from UCNPs to RB, thus leading to the greatly elevated PDT effects. Moreover, by the attachment of targeting ligand FA (folic acid), the FA-conjugated UCNPs/RB could realize the targeted PDT by killing much more FR (folate receptor) positive JAR carcinoma cells than FR negative NIJ 3T3 cells upon 980 nm irradiation (Fig. 5.8a). Certainly, with the development of nanochemistry and nanotechnology, more effective targeted UCNP-photosensitizer drugs will be designed and applied for PDT in the near future.

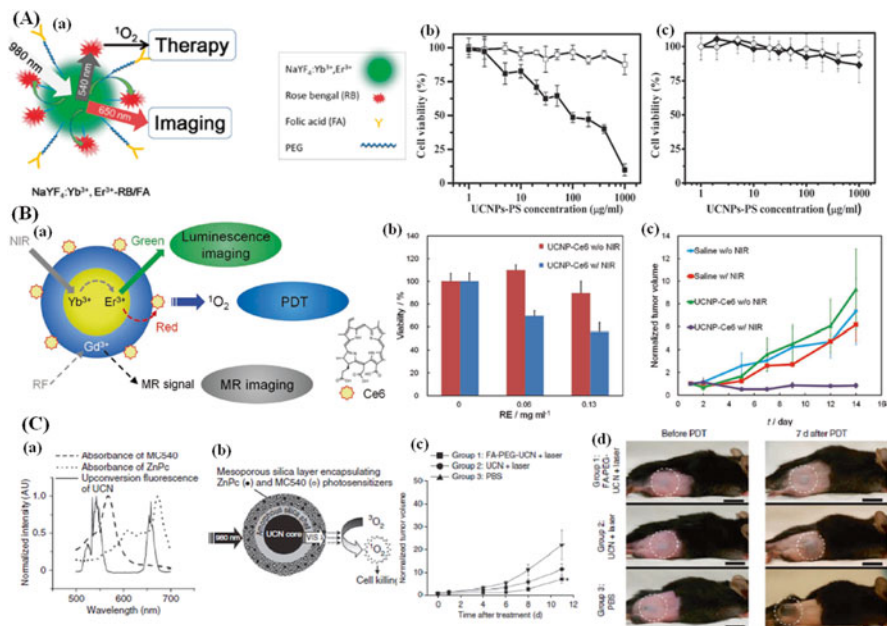


Fig. 5.8 (a) (a) Covalent conjugation of NaYF₄:Yb₃t,Er₃t UCNPs, photosensitizer RB, and target molecule FA. (b, c) Viability of JAR cells (b) and NIH 3T3 fibroblasts (c) treated with FA-UCNPs/RB of different concentrations with (solid) or without (open) 980 nm exposure. (b) (a) Schematic illustration of dual-modal imaging and PDT using UCNPs-Ce6. (b) Cell viability of U87MG cells incubated with UCNPs-Ce6, with or without exposure to 980 nm laser. (c) Growth of tumors after treatment to assess the effectiveness of UCN-based mediated targeted PDT in tumor-bearing mice intravenously injected with FA-PEG-UCNs. (d) Representative gross photos of a mouse from groups 1–3 intravenously injected with FA-PEG-UCNs, unmodified UCNs, or PBS showing the change in tumor size (highlighted by dashed white circles) before (0 d) and 7 d after PDT treatment ((a) Reprinted with the permission from Ref. [93]. Copyright 2012 American Chemical Society. (b) Reprinted with the permission from Ref. [94]. Copyright 2012 Wiley-VCH Verlag GmbH & Co. KGaA. (c) Reprinted with the permission from Ref. [95]. Copyright 2012 Nature Publishing Group)

Unlike the above PDT-related researches that mainly focus on the in vitro PDT, the following in vivo PDT studies may be more exciting and closer to future clinical cancer therapy. In 2011, Liu et al. [26] firstly performed UCNPs-based PDT on tumor-bearing mice. In his study, the photosensitizer Ce6 was adsorbed onto PEGylated UCNP to form a new UCNP-Ce6 PDT agent, which could induce significant cancerous cell death by producing ¹O₂ upon NIR irradiation. After injecting the UCNP-Ce6 agent into 4T₁ tumors grown on balb/c mice, about 70 % of tumors were completely eradicated for even without regrowth within the next 2 months by exposure to NIR light. So the mice after PDT treatment had much longer survival lifetime than the non-treated mice. Furthermore, they also evaluated the potential use of UCNPs-based PDT on treating deep-seated tumors. By comparison

with the direct excitation of Ce6 using visible light, the NIR-triggered PDT using UCNPs-Ce6 demonstrated a much deeper tissue penetration depth and thus exhibited great potential in the future therapy of large or internal tumors. By the appropriate structural optimization, Hyeon et al. [94] synthesized UCNPs-Ce6 nanocomplex via both physical adsorption and covalent conjugation for in vivo MR/UCL bimodal imaging-guided PDT via intravenous injection. On the one hand, there appeared strong MR/UCL imaging signal in tumors, which evidenced that UCNPs-Ce6 nanocomplex was successfully accumulated in tumors owing to the enhanced permeability and retention (EPR) effect. On the other hand, the tumor growth was remarkably inhibited upon NIR irradiation due to the improved PDT effects (Fig. 5.8b). This study may shed on the design of high-performance UCNP-based PDT agents by accurate imaging-guided photodynamic therapy.

In order to further enhance the PDT efficacy, the excitation of two or more kinds of photosensitizers using a single-wavelength light may be a desirable strategy. In a recent report by Zhang's group [95], two photosensitizers (ZnPc and M540) whose absorption peaks overlapped with the two emission (red and green) peaks of UCNPs were simultaneously loaded into the mesoporous silica-coated UCNPs. Compared with single photosensitizer-loaded UCNPs, the ZnPc/M540 co-loaded UCNPs demonstrated substantially enhanced PDT efficacy by the greatly elevated generation of $^1\text{O}_2$ for significantly reduced tumor cell viability upon NIR irradiation. More interestingly, by the conjugation of targeting ligand FA to ZnPc/M540 co-loaded UCNPs, the in vivo targeted PDT was firstly realized in animal experiments, which showed remarkable tumor growth delay (Fig. 5.8c). In all, this study is the first example of using UCNPs for in vivo targeted PDT, which may greatly promote the exploration of other targeted UCNP-based PDT agents for future NIR-triggered therapeutic applications.

5.4.2 UCNPs for Radiotherapy

As another noninvasive treatment tool, radiotherapy has achieved great success in relieving tumor patients of pain by applying high-energy X-rays or γ -rays radiation to damage the DNA of cancerous cells [96]. Besides, by focusing all radiation precisely on tumors, radiotherapy has been used for site-specific cancer therapy with relatively low adverse effects on surrounding normal tissues. Unfortunately, most hypoxic solid tumors often develop resistance to radiation and cause the treatment failure of radiotherapy [97]. Therefore, in order to eradicate solid tumors, some radiosensitizers (radiation sensitizers) should be used to enhance the radiotherapy efficacy on killing hypoxic tumors. Based on the Compton scattering effects, some high-Z metallic nanoparticles (e.g., Au, Pt, etc.) can decompose a beam of X-rays into several beams of X-rays [98], thus greatly enlarging the X-ray radiation doses on malignant tumors and causing large-scale localized DNA damage/cell apoptosis. Therefore, by doping high-Z metal ions into the UCNP lattice, both CT contrast imaging and radiation enhancement can be realized, which will lead to the CT imaging-guided radiosensitization for enhanced diagnostic/therapeutic efficacy.

Our group is the first one to introduce high-Z ion-doped UCNP into the fields of CT imaging-guided radiotherapy. In our study [15], BaYbF₅:Er nanocubes (UCA) were synthesized by a hydrothermal method with high dispersity and stability. Due to the co-doping of high-Z ions Ba²⁺ and Yb³⁺, CT contrast imaging and radiosensitization were simultaneously realized. Finally, by the conjugation of active tumor-targeting ligand RGD, UCA-RGD nanocubes were efficiently accumulated in U87 tumors for CT imaging and enhanced radiotherapy by amplifying X-ray radiation doses due to the Compton scattering effects (Fig. 5.9). The corresponding in vivo therapy results (Fig. 5.9c) clearly showed that the combination of UCA-RGD and radiotherapy led to more significantly tumor growth delay than radiotherapy alone due to the radiosensitizing effects of high-Z ions Ba²⁺ and Yb³⁺. Therefore, the designed UCA-RGD may be potentially developed into the next generation of targeted imaging-guided radiosensitive drugs.

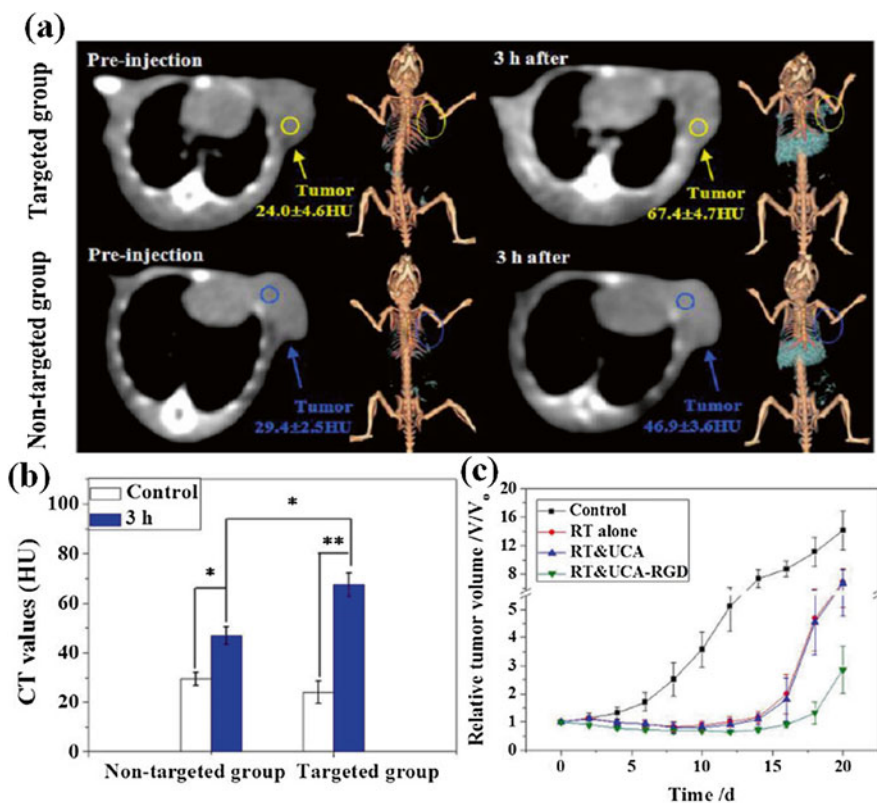


Fig. 5.9 (a) In vivo transverse slices and 3D volume rendering CT images of U87MG tumor-bearing mice at preinjection and 3 h after intravenous injection of UCA-RGD (targeted group) or UCA (nontargeted group). (b) The corresponding CT value changes in the tumor. (c) Growth of U87MG tumors from different groups after various treatments ($n=6$) (Reprinted with the permission from Ref. [15]. Copyright 2013 Nature Publishing Group)

5.4.3 UCNPs for Synergetic Therapy

So far, chemotherapy, radiotherapy, and PDT have become the major treatments for clinical cancer therapy, but they all have intrinsic drawbacks. For example, chemotherapy may cause systemic toxic side effects by using large amounts of free anti-cancer drugs. Radiotherapy and PDT are too dependent on oxygen to eradicate most hypoxic solid tumors. Therefore, in order to achieve the optimal treatment efficacy, the combinational use of the three treatments by integrating their respective superiorities may be a desirable strategy. Fortunately, by means of smart structural design, two or three therapeutic modalities can be integrated in one system to cooperate with each other to produce superadditive therapeutic effects that are greater than the theoretically projected sum. Recently, our group and other researchers have tried to engineer UCNPs for multimodal synergetic therapy.

In 2013, Zhao's group [99] co-encapsulated drugs (DOX) and photosensitizers (Ce6) onto the surface of UCNPs for synergetic chemo-/photodynamic therapy upon NIR irradiation (Fig. 5.10a). It was found that Ce6 showed negligible leakage in acidic environment and enhanced PDT efficacy based on the high FRET efficiency, while DOX was rapidly released in low pH for enhanced chemotherapy efficacy. Therefore, the *in vitro* therapy results (Fig. 5.10b) showed that Ce6/DOX co-loaded UCNPs killed much more cancerous cells upon NIR irradiation than any single treatment due to the cooperative interactions between chemotherapy and PDT.

Besides high-Z metallic nanoparticles, some anticancer drugs (e.g., CDDP, Dtxl, 5-Fu, etc.) could be also used as radiosensitizers for radiation enhancement effects. Recently, our group firstly designed rattle-structured UCNPs/silica nanotheranostics (UCSNs) for synergetic chemo-/radiotherapy by the encapsulation radiosensitive drugs CDDP upon X-ray irradiation (Fig. 5.10c) [100]. The corresponding *in vitro* and *in vivo* therapy results showed that CDDP-loaded UCSNs demonstrated much stronger radiation enhancement effects than free CDDP upon X-ray irradiation by killing more cancerous cells as well as causing more remarkable tumor growth delay (Fig. 5.10d). By the conjugation of targeting ligand FA to UCSNs, *in vivo* tumor-targeted imaging-guided synergetic chemo-/radiotherapy could be realized, which demonstrated much strong radiation enhancement effects than free CDDP (Fig. 5.10e).

In order to realize the goal of thorough tumor elimination, the above three therapeutic modalities should be simultaneously used in combination. More importantly, there exist cooperative interactions among the three treatments. For example, X-ray radiation could not only directly break down the DNA but also improve the sensitivity of cancerous cells to drugs and ROS, which thus resulted in the permanent DNA damage and cell death by imposing chemo-/photodynamic therapy. In our latest report [101], radiosensitive drugs Dtxl and radio-/photosensitizer HP (hematoporphyrin) were simultaneously loaded into the cavity and mesoporous shells of rattle-structured UCNP core/mesoporous silica nanotheranostics for synergetic chemo-/radio-/photodynamic therapy upon NIR/X-ray irradiation. It was found that the

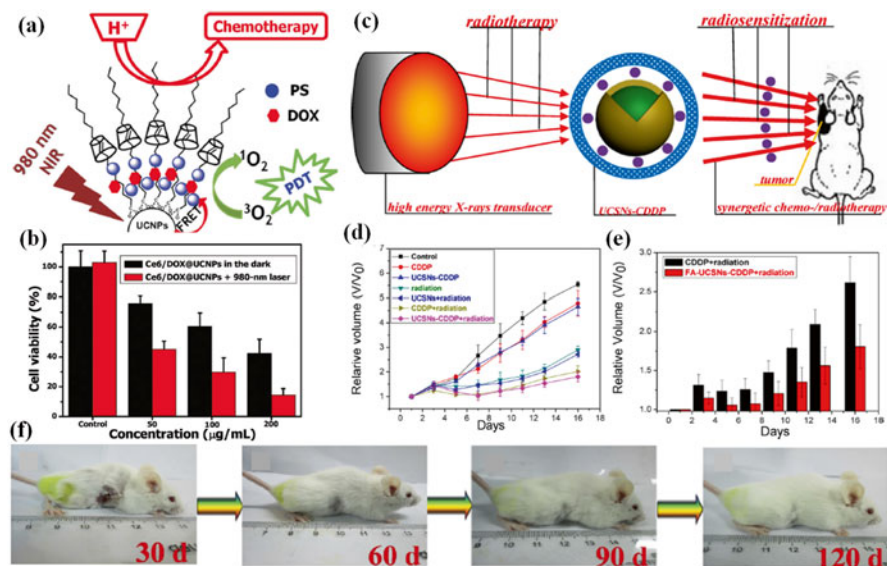


Fig. 5.10 (a) Scheme illustration of the combined therapeutic system for chemotherapy and PDT treatment by co-loading Ce6/DOX onto UCNPs. (b) Cell viabilities of A-549 cells treated with Ce6/DOX@UCNP complex (980 nm laser density, 1 W/cm²; irradiation time, 5 min). (c) Schematic illustration of radiosensitization by UCSNs-CDDP. (d) Tumor growth curves of HeLa tumor xenografts following the different treatment in different modes; (e) comparison between relative volumes of HeLa tumor xenografts treated with FA-UCSNs-CDDP + radiation and CDDP + radiation. Mice were intravenously injected with FA-UCSNs-CDDP and free CDDP, respectively. (f) Digital photos of mice at 30, 60, 90, and 120 days after the treatment of synergistic chemo-/radio-/photodynamic therapy ((a, b) Reprinted with the permission from Ref. [99]. Copyright 2013 Wiley-VCH Verlag GmbH & Co. KGaA. (c–e) Reprinted with the permission from Ref. [100]. Copyright 2013 American Chemical Society. (f) Reprinted with the permission from Ref. [101]. Copyright 2014 Elsevier B. V)

tumors treated by the synergistic trimodal therapy were completely eliminated without regrowth during the next 120 days (Fig. 5.10f). We hope this study will provide a simple and useful strategy for future highly efficient oncotherapy by thorough tumor eradication. Certainly, many improvements are needed to put this technique into practice.

5.5 Summary and Outlook

In conclusion, we have summarized the latest developments in the engineering of UCNPs for multimodal biomedical imaging-guided synergistic therapy. Several effective surface modification methods have been introduced to transfer hydrophobic UCNPs into water phase for future biomedical applications. By the selective doping of different functional ions (e.g., Yb³⁺, Gd³⁺, Er³⁺, ¹⁵³Sm³⁺, etc.), multimodal

biomedical imaging (MR/UCL/CT/PET) can be realized to provide superior advantages in accurate/comprehensive cancer diagnosis. As well, multimodal synergetic therapy can be achieved for highly efficient cancer treatment by the co-encapsulation of various drugs/photosensitizers/radiosensitizers into UCNP-based nanotheranostics. Therefore, UCNPs are expected to be developed into the novel intelligent nanotheranostic medicine for multimodal biomedical imaging and synergetic therapy. However, many aspects about UCNPs need to be greatly improved before going into future clinical applications.

Firstly, the quantum yield of UCNPs is very low (about 0.35 %), which inevitably results in the quite low UCL emission intensity and PDT efficacy. Therefore, more attentions should be paid to the enhancement of QY by exploring other better host matrix to fabricate much brighter UCNPs.

Secondly, similar to other inorganic materials, the potential long-term toxicity of UCNPs is a serious problem. Although the current *in vitro/in vivo* studies demonstrate negligible toxicity and good biocompatibility of UCNPs, the long-term *in vivo* chronic toxicity remains unknown and should be systemically observed. In addition, more effective surface modification strategies should be explored to further improve the biocompatibility of UCNPs.

Thirdly, in order to promote the future use of UCNPs for the *in vitro/in vivo* tracking and whole-body UCL imaging, the exploration of commercial imaging instruments for UCNPs with 980 nm laser module is extremely in need and should be accelerated.

Fourthly, the relative low tumor-targeting efficiency has become a big obstacle in the further improvement of the theranostic effects of UCNPs. Consequently, more effective strategies (e.g., structural optimization, surface modification, attachment of tumor-specific targeting ligands, etc.) should be developed to enhance the accumulation of UCNPs in tumors by passive/active targeting.

Last but not the least, for the realization of real-time monitoring of the therapeutic progress as well as the optimized theranostic efficacy, it is of significant importance to develop “intelligent” multifunctional nanotheranostics by the smart engineering of UCNPs. Certainly, there is still a long way to go for the true translational applications of UCNPs.

References

1. Shen J, Zhao L, Han G (2012) Lanthanide-doped upconverting luminescent nanoparticle platforms for optical imaging-guided drug delivery and therapy. *Adv Drug Deliv Rev* 66(5):744–755. doi:[10.1016/j.addr.2012.05.007](https://doi.org/10.1016/j.addr.2012.05.007)
2. Chen G, Qiu H, Prasad PN, Chen X (2014) Upconversion nanoparticles: design, nanochemistry, and applications in theranostics. *Chem Rev* 114(10):5161–5214. doi:[10.1021/cr400425h](https://doi.org/10.1021/cr400425h)
3. He GS, Markowicz PP, Tzu-Chau Lin, Prasad PN (2002) Observation of stimulated emission by direct three-photon excitation. *Nature* 415:767–770
4. Gu Z, Yan L, Tian G, Li S, Chai Z, Zhao Y (2013) Recent advances in design and fabrication of upconversion nanoparticles and their safe theranostic applications. *Adv Mater* 25(28):3758–3779. doi:[10.1002/adma.201301197](https://doi.org/10.1002/adma.201301197)

5. Feng W, Han C, Li F (2013) Upconversion-nanophosphor-based functional nanocomposites. *Adv Mater* 25(37):5287–5303. doi:[10.1002/adma.201301946](https://doi.org/10.1002/adma.201301946)
6. Liu Y, Tu D, Zhu H, Chen X (2013) Lanthanide-doped luminescent nanoprobe: controlled synthesis, optical spectroscopy, and bioapplications. *Chem Soc Rev* 42(16):6924–6958. doi:[10.1039/c3cs60060b](https://doi.org/10.1039/c3cs60060b)
7. Chen G, Yang C, Prasad PN (2013) Nanophotonics and nanochemistry: controlling the excitation dynamics for frequency up- and down-conversion in lanthanide-doped nanoparticles. *Acc Chem Res* 46(7):1474–1486
8. Zhou J, Liu Z, Li F (2012) Upconversion nanophosphors for small-animal imaging. *Chem Soc Rev* 41(3):1323–1349. doi:[10.1039/c1cs15187h](https://doi.org/10.1039/c1cs15187h)
9. Cheng L, Yang K, Shao M, Lee S-T, Liu Z (2011) Multicolor in vivo imaging of upconversion nanoparticles with emissions tuned by luminescence resonance energy transfer. *J Phys Chem C* 115(6):2686–2692. doi:[10.1021/jp111006z](https://doi.org/10.1021/jp111006z)
10. Wang F, Liu X (2008) Upconversion multicolor fine-tuning: visible to near-infrared emission from lanthanide-doped NaYF₄ nanoparticles. *J Am Chem Soc* 130:5642–5643
11. Chen F, Bu W, Zhang S, Liu J, Fan W, Zhou L, Peng W, Shi J (2013) Gd³⁺-ion-doped upconversion nanoprobe: relaxivity mechanism probing and sensitivity optimization. *Adv Funct Mater* 23(3):298–307. doi:[10.1002/adfm.201201469](https://doi.org/10.1002/adfm.201201469)
12. Xiao Q, Bu W, Ren Q, Zhang S, Xing H, Chen F, Li M, Zheng X, Hua Y, Zhou L, Peng W, Qu H, Wang Z, Zhao K, Shi J (2012) Radiopaque fluorescence-transparent TaOx decorated upconversion nanophosphors for in vivo CT/MR/UCL trimodal imaging. *Biomaterials* 33(30):7530–7539. doi:[10.1016/j.biomaterials.2012.06.028](https://doi.org/10.1016/j.biomaterials.2012.06.028)
13. Xing H, Bu W, Ren Q, Zheng X, Li M, Zhang S, Qu H, Wang Z, Hua Y, Zhao K, Zhou L, Peng W, Shi J (2012) A NaYbF₄: Tm³⁺ nanoprobe for CT and NIR-to-NIR fluorescent bimodal imaging. *Biomaterials* 33(21):5384–5393. doi:[10.1016/j.biomaterials.2012.04.002](https://doi.org/10.1016/j.biomaterials.2012.04.002)
14. Sun Y (2013) Upconversion nanophosphors NaLuF₄:Yb, Tm for lymphatic imaging in vivo by real-time upconversion luminescence imaging under ambient light and high-resolution x-ray CT. *Theranostics* 3(5):346–353. doi:[10.7150/thno.5137](https://doi.org/10.7150/thno.5137)
15. Xing H, Zheng X, Ren Q, Bu W, Ge W, Xiao Q, Zhang S, Wei C, Qu H, Wang Z, Hua Y, Zhou L, Peng W, Zhao K, Shi J (2013) Computed tomography imaging-guided radiotherapy by targeting upconversion nanocubes with significant imaging and radiosensitization enhancements. *Sci Rep*:3:1751. doi:[10.1038/srep01751](https://doi.org/10.1038/srep01751)
16. Sun Y, Yu M, Liang S, Zhang Y, Li C, Mou T, Yang W, Zhang X, Li B, Huang C, Li F (2011) Fluorine-18 labeled rare-earth nanoparticles for positron emission tomography (PET) imaging of sentinel lymph node. *Biomaterials* 32(11):2999–3007. doi:[10.1016/j.biomaterials.2011.01.011](https://doi.org/10.1016/j.biomaterials.2011.01.011)
17. Liu Q, Sun Y, Li C, Zhou J, Li C, Yang T, Zhang X, Yi T, Wu D, Li F (2011) ¹⁸F-labeled magnetic-upconversion nanophosphors via rare-earth cation-assisted ligand assembly. *ACS Nano* 5(4):3146–3157
18. Sun Y, Zhu X, Peng J, Li F (2013) Core-shell lanthanide upconversion nanophosphors as four-modal probes for tumor angiogenesis imaging. *ACS Nano* 7(12):11290–11300
19. Yang Y, Sun Y, Cao T, Peng J, Liu Y, Wu Y, Feng W, Zhang Y, Li F (2013) Hydrothermal synthesis of NaLuF₄:153Sm, Yb, Tm nanoparticles and their application in dual-modality upconversion luminescence and SPECT bioimaging. *Biomaterials* 34(3):774–783. doi:[10.1016/j.biomaterials.2012.10.022](https://doi.org/10.1016/j.biomaterials.2012.10.022)
20. Wang C, Cheng L, Liu Z (2011) Drug delivery with upconversion nanoparticles for multi-functional targeted cancer cell imaging and therapy. *Biomaterials* 32(4):1110–1120. doi:[10.1016/j.biomaterials.2010.09.069](https://doi.org/10.1016/j.biomaterials.2010.09.069)
21. Hou Z, Li C, Ma PA, Cheng Z, Li X, Zhang X, Dai Y, Yang D, Lian H, Lin J (2012) Up-conversion luminescent and porous NaYF₄:Yb³⁺, Er³⁺@SiO₂ nanocomposite fibers for anti-cancer drug delivery and cell imaging. *Adv Funct Mater* 22(13):2713–2722. doi:[10.1002/adfm.201200082](https://doi.org/10.1002/adfm.201200082)
22. Yunlu Dai, Ping'an Ma, Ziyong Cheng, Xiaojiao Kang, Xiao Zhang, Zhiyao Hou, Chunxia Li, Dongmei Yang, Xuefeng Zhai, Lin J (2012) Up-conversion cell imaging and pH induced

- thermally controlled drug release from NaYF₄:Yb³⁺/Er³⁺@Hydrogel core/shell hybrid microspheres. *ACS Nano* 6(4):3327–3338
23. Xiao Q, Ji Y, Xiao Z, Zhang Y, Lin H, Wang Q (2013) Novel multifunctional NaYF₄:Er³⁺, Yb³⁺/PEGDA hybrid microspheres: NIR-light-activated photopolymerization and drug delivery. *Chem Commun* 49(15):1527. doi:[10.1039/c2cc37620b](https://doi.org/10.1039/c2cc37620b)
 24. Ungun B, Prud'homme RK, Budijono SJ, Shan J, Lim SF, Yiguang J, Austin R (2009) Nanofabricated upconversion nanoparticles for photodynamic therapy. *Opt Express* 17(1):80–86
 25. Qian HS, Guo HC, Ho PC-L, Mahendran R, Zhang Y (2009) Mesoporous-silica-coated upconversion fluorescent nanoparticles for photodynamic therapy. *Small* 5(20):2285–2290. doi:[10.1002/sml.200900692](https://doi.org/10.1002/sml.200900692)
 26. Wang C, Tao H, Cheng L, Liu Z (2011) Near-infrared light induced in vivo photodynamic therapy of cancer based on upconversion nanoparticles. *Biomaterials* 32:6145–6154. doi:[10.1016/j.biomaterials.2011.05.007](https://doi.org/10.1016/j.biomaterials.2011.05.007)
 27. Shan J, Budijono SJ, Hu G, Yao N, Kang Y, Ju Y, Prud'homme RK (2011) Pegylated composite nanoparticles containing upconverting phosphors and meso-tetraphenyl porphine (TPP) for photodynamic therapy. *Adv Funct Mater* 21(13):2488–2495. doi:[10.1002/adfm.201002516](https://doi.org/10.1002/adfm.201002516)
 28. Liu X, Zheng M, Kong X, Zhang Y, Zeng Q, Sun Z, Buma WJ, Zhang H (2013) Separately doped upconversion-C60 nanopatform for NIR imaging-guided photodynamic therapy of cancer cells. *Chem Commun* 49(31):3224. doi:[10.1039/c3cc41013g](https://doi.org/10.1039/c3cc41013g)
 29. Zhang T, Ge J, Hu Y, Yin Y (2007) A general approach for transferring hydrophobic nanocrystals into water. *Nano Lett* 7(10):3203–3207
 30. Boyer J-C, Manseau M-P, Murray JI, van Veggel FCJM (2010) Surface modification of upconverting NaYF₄Nanoparticles with PEG–phosphate ligands for NIR (800 nm) biolabeling within the biological window. *Langmuir* 26(2):1157–1164. doi:[10.1021/la902260j](https://doi.org/10.1021/la902260j)
 31. Johnson NJJ, Sangeetha NM, Boyer J-C, van Veggel FCJM (2010) Facile ligand-exchange with polyvinylpyrrolidone and subsequent silica coating of hydrophobic upconverting β-NaYF₄:Yb³⁺/Er³⁺ nanoparticles. *Nanoscale* 2(5):771. doi:[10.1039/b9nr00379g](https://doi.org/10.1039/b9nr00379g)
 32. Chen Z, Chen H, Hu H, Yu M, Li F, Zhang Q, Zhou Z, Yi T, Huang C (2008) Versatile synthesis strategy for carboxylic acid-functionalized upconverting nanophosphors as biological labels. *J Am Chem Soc* 130:3023–3029
 33. Yang D, Dai Y, Ma P, Kang X, Shang M, Cheng Z, Li C, Lin J (2012) Synthesis of Li_{1-x}Na_xYF₄:Yb³⁺/Ln³⁺ (0 ≤ x ≤ 0.3, Ln = Er, Tm, Ho) nanocrystals with multicolor upconversion luminescence properties for in vitro cell imaging. *J Mater Chem* 22(38):20618. doi:[10.1039/c2jm33910b](https://doi.org/10.1039/c2jm33910b)
 34. Wang L, Yan R, Huo Z, Wang L, Zeng J, Bao J, Wang X, Peng Q, Li Y (2005) Fluorescence resonant energy transfer biosensor based on upconversion-luminescent nanoparticles. *Angew Chem Int Ed* 44(37):6054–6057. doi:[10.1002/anie.200501907](https://doi.org/10.1002/anie.200501907)
 35. Yi G, Peng Y, Gao Z (2011) Strong red-emitting near-infrared-to-visible upconversion fluorescent nanoparticles. *Chem Mater* 23(11):2729–2734. doi:[10.1021/cm103175s](https://doi.org/10.1021/cm103175s)
 36. Zhang Q, Song K, Zhao J, Kong X, Sun Y, Liu X, Zhang Y, Zeng Q, Zhang H (2009) Hexanedioic acid mediated surface–ligand-exchange process for transferring NaYF₄:Yb/Er (or Yb/Tm) up-converting nanoparticles from hydrophobic to hydrophilic. *J Colloid Interface Sci* 336(1):171–175. doi:[10.1016/j.jcis.2009.04.024](https://doi.org/10.1016/j.jcis.2009.04.024)
 37. Kumar R, Nyk M, Ohulchanskyy TY, Flask CA, Prasad PN (2009) Combined optical and MR bioimaging using rare earth ion doped NaYF₄Nanocrystals. *Adv Funct Mater* 19(6):853–859. doi:[10.1002/adfm.200800765](https://doi.org/10.1002/adfm.200800765)
 38. Zhan Q, Qian J, Liang H, Somesfalean G, Wang D, He S, Zhang Z, Andersson-Engels S (2011) Using 915 nm laser excited Tm³⁺/Er³⁺/Ho³⁺-Doped NaYbF₄ upconversion nanoparticles for in vitro and deeper in vivo bioimaging without overheating irradiation. *ACS Nano* 5(5):3744–3757
 39. Bogdan N, Vetrone F, Roy R, Capobianco JA (2010) Carbohydrate-coated lanthanide-doped upconverting nanoparticles for lectin recognition. *J Mater Chem* 20(35):7543. doi:[10.1039/c0jm01617a](https://doi.org/10.1039/c0jm01617a)

40. Wang M, Liu J-L, Zhang Y-X, Hou W, Wu X-L, Xu S-K (2009) Two-phase solvothermal synthesis of rare-earth doped NaYF₄ upconversion fluorescent nanocrystals. *Mater Lett* 63(2):325–327. doi:[10.1016/j.matlet.2008.10.028](https://doi.org/10.1016/j.matlet.2008.10.028)
41. Bogdan N, Vetrone F, Ozin GA, Capobianco JA (2011) Synthesis of ligand-free colloiddally stable water dispersible brightly luminescent lanthanide-doped upconverting nanoparticles. *Nano Lett* 11(2):835–840. doi:[10.1021/nl1041929](https://doi.org/10.1021/nl1041929)
42. Bogdan N, Rodríguez EM, Sanz-Rodríguez F, Iglesias de la Cruz MC, Juarranz Á, Jaque D, Solé JG, Capobianco JA (2012) Bio-functionalization of ligand-free upconverting lanthanide doped nanoparticles for bio-imaging and cell targeting. *Nanoscale* 4(12):3647. doi:[10.1039/c2nr30982c](https://doi.org/10.1039/c2nr30982c)
43. Liu J-n, Bu W, Pan L-m, Zhang S, Chen F, Zhou L, Zhao K-L, Peng W, Shi J (2012) Simultaneous nuclear imaging and intranuclear drug delivery by nuclear-targeted multifunctional upconversion nanoprobcs. *Biomaterials* 33(29):7282–7290. doi:[10.1016/j.biomaterials.2012.06.035](https://doi.org/10.1016/j.biomaterials.2012.06.035)
44. Sivakumar S, Diamente PR, van Veggel FCJM (2006) Silica-coated Ln³⁺-doped LaF₃ nanoparticles as robust down- and upconverting biolabels. *Chem Eur J* 12(22):5878–5884. doi:[10.1002/chem.200600224](https://doi.org/10.1002/chem.200600224)
45. Das GK, Heng BC, Ng S-C, White T, Loo JSC, D'Silva L, Padmanabhan P, Bhakoo KK, Selvan ST, Tan TTY (2010) Gadolinium oxide ultranarrow nanorods as multimodal contrast agents for optical and magnetic resonance imaging. *Langmuir* 26(11):8959–8965. doi:[10.1021/la903512m](https://doi.org/10.1021/la903512m), [10.1021/la904751q](https://doi.org/10.1021/la904751q), [10.1002/jbm.a.32533](https://doi.org/10.1002/jbm.a.32533)
46. Hu H, Xiong L, Zhou J, Li F, Cao T, Huang C (2009) Multimodal-luminescence core-shell nanocomposites for targeted imaging of tumor cells. *Chem Eur J* 15(14):3577–3584. doi:[10.1002/chem.200802261](https://doi.org/10.1002/chem.200802261)
47. Abdul Jalil R, Zhang Y (2008) Biocompatibility of silica coated NaYF₄ upconversion fluorescent nanocrystals. *Biomaterials* 29(30):4122–4128. doi:[10.1016/j.biomaterials.2008.07.012](https://doi.org/10.1016/j.biomaterials.2008.07.012)
48. Li Z, Wang L, Wang Z, Liu X, Xiong Y (2011) Modification of NaYF₄:Yb, Er@SiO₂Nanoparticles with gold nanocrystals for tunable green-to-red upconversion emissions. *J Phys Chem C* 115(8):3291–3296. doi:[10.1021/jp110603r](https://doi.org/10.1021/jp110603r)
49. Liu Z, Yi G, Zhang H, Ding J, Zhang Y, Xue J (2008) Monodisperse silica nanoparticles encapsulating upconversion fluorescent and superparamagnetic nanocrystals. *Chem Commun* 6:694. doi:[10.1039/b715402j](https://doi.org/10.1039/b715402j)
50. Li Z, Zhang Y, Jiang S (2008) Multicolor core/shell-structured upconversion fluorescent nanoparticles. *Adv Mater* 20(24):4765–4769. doi:[10.1002/adma.200801056](https://doi.org/10.1002/adma.200801056)
51. Xing H, Bu W, Zhang S, Zheng X, Li M, Chen F, He Q, Zhou L, Peng W, Hua Y, Shi J (2012) Multifunctional nanoprobcs for upconversion fluorescence, MR and CT trimodal imaging. *Biomaterials* 33(4):1079–1089. doi:[10.1016/j.biomaterials.2011.10.039](https://doi.org/10.1016/j.biomaterials.2011.10.039)
52. Liu J, Bu W, Zhang S, Chen F, Xing H, Pan L, Zhou L, Peng W, Shi J (2012) Controlled synthesis of uniform and monodisperse upconversion core/mesoporous silica shell nanocomposites for bimodal imaging. *Chem Eur J* 18(8):2335–2341. doi:[10.1002/chem.201102599](https://doi.org/10.1002/chem.201102599)
53. Li C, Hou Z, Dai Y, Yang D, Cheng Z, Ma P, Lin J (2013) A facile fabrication of upconversion luminescent and mesoporous core-shell structured β-NaYF₄:Yb³⁺, Er³⁺@mSiO₂ nanocomposite spheres for anti-cancer drug delivery and cell imaging. *Biomater Sci* 1:213–223. doi:[10.1039/c2bm00087c](https://doi.org/10.1039/c2bm00087c)
54. Wang F, Liu X (2009) Recent advances in the chemistry of lanthanide-doped upconversion nanocrystals. *Chem Soc Rev* 38(4):976. doi:[10.1039/b809132n](https://doi.org/10.1039/b809132n)
55. Yu X, Li M, Xie M, Chen L, Li Y, Wang Q (2010) Dopant-controlled synthesis of water-soluble hexagonal NaYF₄ nanorods with efficient upconversion fluorescence for multicolor bioimaging. *Nano Res* 3(1):51–60. doi:[10.1007/s12274-010-1008-2](https://doi.org/10.1007/s12274-010-1008-2)
56. Cheng L, Yang K, Zhang S, Shao M, Lee S, Liu Z (2010) Highly-sensitive multiplexed in vivo imaging using pegylated upconversion nanoparticles. *Nano Res* 3(10):722–732. doi:[10.1007/s12274-010-0036-2](https://doi.org/10.1007/s12274-010-0036-2)

57. Ren G, Zeng S, Hao J (2011) Tunable multicolor upconversion emissions and paramagnetic property of monodispersed bifunctional lanthanide-doped NaGdF₄Nanorods. *J Phys Chem C* 115(41):20141–20147. doi:[10.1021/jp2064529](https://doi.org/10.1021/jp2064529)
58. Jeong S, Won N, Lee J, Bang J, Yoo J, Kim SG, Chang JA, Kim J, Kim S (2011) Multiplexed near-infrared in vivo imaging complementarily using quantum dots and upconverting NaYF₄:Yb³⁺, Tm³⁺ nanoparticles. *Chem Commun* 47(28):8022. doi:[10.1039/c1cc12746b](https://doi.org/10.1039/c1cc12746b)
59. Idris NM, Li Z, Ye L, Wei Sim EK, Mahendran R, Ho PC-L, Zhang Y (2009) Tracking transplanted cells in live animal using upconversion fluorescent nanoparticles. *Biomaterials* 30(28):5104–5113. doi:[10.1016/j.biomaterials.2009.05.062](https://doi.org/10.1016/j.biomaterials.2009.05.062)
60. Liu Q, Sun Y, Yang T, Feng W, Li C, Li F (2011) Sub-10 nm hexagonal lanthanide-doped NaLuF₄ Upconversion nanocrystals for sensitive bioimaging in vivo. *J Am Chem Soc* 133(43):17122–17125. doi:[10.1021/ja207078s](https://doi.org/10.1021/ja207078s)
61. Wang C, Cheng L, Xu H, Liu Z (2012) Towards whole-body imaging at the single cell level using ultra-sensitive stem cell labeling with oligo-arginine modified upconversion nanoparticles. *Biomaterials* 33(19):4872–4881. doi:[10.1016/j.biomaterials.2012.03.047](https://doi.org/10.1016/j.biomaterials.2012.03.047)
62. Cheng L, Wang C, Ma X, Wang Q, Cheng Y, Wang H, Li Y, Liu Z (2013) Multifunctional upconversion nanoparticles for dual-modal imaging-guided stem cell therapy under remote magnetic control. *Adv Funct Mater* 23(3):272–280. doi:[10.1002/adfm.201201733](https://doi.org/10.1002/adfm.201201733)
63. Xiong L-Q, Chen Z-G, Yu M-X, Li F-Y, Liu C, Huang C-H (2009) Synthesis, characterization, and in vivo targeted imaging of amine-functionalized rare-earth up-converting nanophosphors. *Biomaterials* 30(29):5592–5600. doi:[10.1016/j.biomaterials.2009.06.015](https://doi.org/10.1016/j.biomaterials.2009.06.015)
64. Xiong L, Chen Z, Tian Q, Cao T, Xu C, Li F (2009) High contrast upconversion luminescence targeted imaging in vivo using peptide-labeled nanophosphors. *Anal Chem* 81(21):8687–8694. doi:[10.1021/ac901960d](https://doi.org/10.1021/ac901960d)
65. Ni D, Zhang J, Bu W, Xing H, Han F, Xiao Q, Yao Z, Chen F, He Q, Liu J, Zhang S, Fan W, Zhou L, Peng W, Shi J (2014) Dual-targeting upconversion nanoprobe across the blood-brain barrier for magnetic resonance/fluorescence imaging of intracranial glioblastoma. *ACS Nano* 8(2):1231–1242
66. Hilderbrand SA, Shao F, Salthouse C, Mahmood U, Weissleder R (2009) Upconverting luminescent nanomaterials: application to in vivo bioimaging. *Chem Commun* 28:4188. doi:[10.1039/b905927j](https://doi.org/10.1039/b905927j)
67. Xing H, Zhang S, Bu W, Zheng X, Wang L, Xiao Q, Ni D, Zhang J, Zhou L, Peng W, Zhao K, Hua Y, Shi J (2014) Ultrasmall NaGdF₄Nanodots for efficient MR angiography and atherosclerotic plaque imaging. *Adv Mater* 26(23):3867–3872. doi:[10.1002/adma.201305222](https://doi.org/10.1002/adma.201305222)
68. Kobayashi H, Kosaka N, Ogawa M, Morgan NY, Smith PD, Murray CB, Ye X, Collins J, Kumar GA, Bell H, Choyke PL (2009) In vivo multiple color lymphatic imaging using upconverting nanocrystals. *J Mater Chem* 19(36):6481. doi:[10.1039/b910512c](https://doi.org/10.1039/b910512c)
69. Cao T, Yang Y, Gao Y, Zhou J, Li Z, Li F (2011) High-quality water-soluble and surface-functionalized upconversion nanocrystals as luminescent probes for bioimaging. *Biomaterials* 32(11):2959–2968
70. Moulder JE, Rockwell S (1987) Tumor hypoxia: its impact on cancer therapy. *Cancer Metastasis Rev* 5(4):313–341
71. Liu J, Liu Y, Bu W, Bu J, Sun Y, Du J, Shi J (2014) Ultrasensitive nanosensors based on upconversion nanoparticles for selective hypoxia imaging in vivo upon near-infrared excitation. *J Am Chem Soc* 136(27):9701–9709. doi:[10.1021/ja5042989](https://doi.org/10.1021/ja5042989)
72. Zhou J, Sun Y, Du X, Xiong L, Hu H, Li F (2010) Dual-modality in vivo imaging using rare-earth nanocrystals with near-infrared to near-infrared (NIR-to-NIR) upconversion luminescence and magnetic resonance properties. *Biomaterials* 31(12):3287–3295. doi:[10.1016/j.biomaterials.2010.01.040](https://doi.org/10.1016/j.biomaterials.2010.01.040)
73. Zhou L, Gu Z, Liu X, Yin W, Tian G, Yan L, Jin S, Ren W, Xing G, Li W, Chang X, Hu Z, Zhao Y (2012) Size-tunable synthesis of lanthanide-doped Gd₂O₃ nanoparticles and their applications for optical and magnetic resonance imaging. *J Mater Chem* 22(3):966. doi:[10.1039/c1jm13758a](https://doi.org/10.1039/c1jm13758a)

74. Tian G, Gu Z, Zhou L, Yin W, Liu X, Yan L, Jin S, Ren W, Xing G, Li S, Zhao Y (2012) Mn²⁺ dopant-controlled synthesis of NaYF₄:Yb/Er upconversion nanoparticles for in vivo imaging and drug delivery. *Adv Mater* 24(9):1226–1231. doi:[10.1002/adma.201104741](https://doi.org/10.1002/adma.201104741)
75. Chen F, Bu W, Zhang S, Liu X, Liu J, Xing H, Xiao Q, Zhou L, Peng W, Wang L, Shi J (2011) Positive and negative lattice shielding effects co-existing in Gd (III) ion doped bifunctional upconversion nanoprobes. *Adv Funct Mater* 21(22):4285–4294. doi:[10.1002/adfm.201101663](https://doi.org/10.1002/adfm.201101663)
76. Wang F, Wang J, Liu X (2010) Direct evidence of a surface quenching effect on size-dependent luminescence of upconversion nanoparticles. *Angew Chem Int Ed* 49(41):7456–7460. doi:[10.1002/anie.201003959](https://doi.org/10.1002/anie.201003959)
77. Zhang F, Che R, Li X, Yao C, Yang J, Shen D, Hu P, Li W, Zhao D (2012) Direct imaging the upconversion nanocrystal core/shell structure at the subnanometer level: shell thickness dependence in upconverting optical properties. *Nano Lett* 12(6):2852–2858. doi:[10.1021/nl300421n](https://doi.org/10.1021/nl300421n)
78. Chen F, Zhang S, Bu W, Liu X, Chen Y, He Q, Zhu M, Zhang L, Zhou L, Peng W, Shi J (2010) A “neck-formation” strategy for an anti-quenching magnetic/upconversion fluorescent bimodal cancer probe. *Chem Eur J* 16(37):11254–11260. doi:[10.1002/chem.201000525](https://doi.org/10.1002/chem.201000525)
79. Xia A, Gao Y, Zhou J, Li C, Yang T, Wu D, Wu L, Li F (2011) Core-shell NaYF₄:Yb³⁺, Tm³⁺@FexOy nanocrystals for dual-modality T₂-enhanced magnetic resonance and NIR-to-NIR upconversion luminescent imaging of small-animal lymphatic node. *Biomaterials* 32(29):7200–7208. doi:[10.1016/j.biomaterials.2011.05.094](https://doi.org/10.1016/j.biomaterials.2011.05.094)
80. Cheng L, Yang K, Li Y, Zeng X, Shao M, Lee S-T, Liu Z (2012) Multifunctional nanoparticles for upconversion luminescence/MR multimodal imaging and magnetically targeted photothermal therapy. *Biomaterials* 33(7):2215–2222. doi:[10.1016/j.biomaterials.2011.11.069](https://doi.org/10.1016/j.biomaterials.2011.11.069)
81. Zhang F, Braun GB, Pallaoro A, Zhang Y, Shi Y, Cui D, Moskovits M, Zhao D, Stucky GD (2012) Mesoporous multifunctional upconversion luminescent and magnetic “Nanorattle” materials for targeted chemotherapy. *Nano Lett* 12(1):61–67. doi:[10.1021/nl202949y](https://doi.org/10.1021/nl202949y)
82. Das GK, Johnson NJJ, Cramen J, Blasiak B, Latta P, Tomanek B, van Veggel FCJM (2012) NaDyF₄Nanoparticles as T₂Contrast agents for ultrahigh field magnetic resonance imaging. *J Phys Chem Lett* 3(4):524–529. doi:[10.1021/jz201664h](https://doi.org/10.1021/jz201664h)
83. Lee N, Choi SH, Hyeon T (2013) Nano-sized CT contrast agents. *Adv Mater*. doi:[10.1002/adma.201300081](https://doi.org/10.1002/adma.201300081)
84. Liu Z, Pu F, Huang S, Yuan Q, Ren J, Qu X (2013) Long-circulating Gd₂O₃:Yb³⁺, Er³⁺ up-conversion nanoprobes as high-performance contrast agents for multi-modality imaging. *Biomaterials* 34(6):1712–1721. doi:[10.1016/j.biomaterials.2012.11.009](https://doi.org/10.1016/j.biomaterials.2012.11.009)
85. Xia A, Chen M, Gao Y, Wu D, Feng W, Li F (2012) Gd³⁺ complex-modified NaLuF₄-based upconversion nanophosphors for trimodality imaging of NIR-to-NIR upconversion luminescence, X-Ray computed tomography and magnetic resonance. *Biomaterials* 33(21):5394–5405. doi:[10.1016/j.biomaterials.2012.04.025](https://doi.org/10.1016/j.biomaterials.2012.04.025)
86. Zhu X, Zhou J, Chen M, Shi M, Feng W, Li F (2012) Core-shell Fe₃O₄@NaLuF₄:Yb, Er/Tm nanostructure for MRI, CT and upconversion luminescence tri-modality imaging. *Biomaterials* 33(18):4618–4627. doi:[10.1016/j.biomaterials.2012.03.007](https://doi.org/10.1016/j.biomaterials.2012.03.007)
87. Ni D, Bu W, Zhang S, Zheng X, Li M, Xing H, Xiao Q, Liu Y, Hua Y, Zhou L, Peng W, Zhao K, Shi J (2014) Single Ho³⁺-doped upconversion nanoparticles for high-performance T₂-weighted brain tumor diagnosis and MR/UCL/CT multimodal imaging. *Adv Funct Mater* 24(42):6613–6620. doi:[10.1002/adfm.201401609](https://doi.org/10.1002/adfm.201401609)
88. Zhou J, Yu M, Sun Y, Zhang X, Zhu X, Wu Z, Wu D, Li F (2011) Fluorine-18-labeled Gd³⁺/Yb³⁺/Er³⁺ co-doped NaYF₄ nanophosphors for multimodality PET/MR/UCL imaging. *Biomaterials* 32(4):1148–1156. doi:[10.1016/j.biomaterials.2010.09.071](https://doi.org/10.1016/j.biomaterials.2010.09.071)
89. Zhang P, Steelant W, Kumar M, Scholfield M (2007) Versatile photosensitizers for photodynamic therapy at infrared excitation. *J Am Chem Soc* 129:4526–4527
90. Zhao Z, Han Y, Lin C, Hu D, Wang F, Chen X, Chen Z, Zheng N (2012) Multifunctional core-shell upconverting nanoparticles for imaging and photodynamic therapy of liver cancer cells. *Chem Asian J* 7(4):830–837. doi:[10.1002/asia.201100879](https://doi.org/10.1002/asia.201100879)

91. Chen F, Zhang S, Bu W, Chen Y, Xiao Q, Liu J, Xing H, Zhou L, Peng W, Shi J (2012) A uniform sub-50 nm-sized magnetic/upconversion fluorescent bimodal imaging agent capable of generating singlet oxygen by using a 980 nm laser. *Chem Eur J* 18:7082–7090. doi:[10.1002/chem.201103611](https://doi.org/10.1002/chem.201103611)
92. Qiao X-F, Zhou J-C, Xiao J-W, Wang Y-F, Sun L-D, Yan C-H (2012) Triple-functional core-shell structured upconversion luminescent nanoparticles covalently grafted with photosensitizer for luminescent, magnetic resonance imaging and photodynamic therapy in vitro. *Nanoscale* 4(15):4611–4623. doi:[10.1039/c2nr30938f](https://doi.org/10.1039/c2nr30938f)
93. Liu K, Liu X, Zeng Q, Zhang Y, Tu L, Liu T, Kong X, Wang Y, Cao F, Lambrechts SAG, Aalders MCG, Zhang H (2012) Covalently assembled NIR nanoplatform for simultaneous fluorescence imaging and photodynamic therapy of cancer cells. *ACS Nano* 6(5):4054–4062
94. Park YI, Kim HM, Kim JH, Moon KC, Yoo B, Lee KT, Lee N, Choi Y, Park W, Ling D, Na K, Moon WK, Choi SH, Park HS, Yoon S-Y, Suh YD, Lee SH, Hyeon T (2012) Theranostic probe based on lanthanide-doped nanoparticles for simultaneous in vivo dual-modal imaging and photodynamic therapy. *Adv Mater* 24(42):5755–5761. doi:[10.1002/adma.201202433](https://doi.org/10.1002/adma.201202433)
95. Idris NM, Gnanasammandhan MK, Zhang J, Ho PC, Mahendran R, Zhang Y (2012) In vivo photodynamic therapy using upconversion nanoparticles as remote-controlled nanotransducers. *Nat Med* 18(10):1580–1585. doi:[10.1038/nm.2933](https://doi.org/10.1038/nm.2933)
96. Juzenas P, Chen W, Sun Y-P, Coelho MAN, Generalov R, Generalova N, Christensen IL (2008) Quantum dots and nanoparticles for photodynamic and radiation therapies of cancer. *Adv Drug Deliv Rev* 60(15):1600–1614. doi:[10.1016/j.addr.2008.08.004](https://doi.org/10.1016/j.addr.2008.08.004)
97. Ridder MD, Esch GV, Engels B, Verovskl V, Storme G (2008) Hypoxic tumor cell radiosensitization: role of the iNOS/NO pathway. *Bull Cancer* 95(3):282–291. doi:[10.1684/bdc.2008.0592](https://doi.org/10.1684/bdc.2008.0592)
98. Hainfeld JF, Dilmanian FA, Slatkin DN, Smilowitz HM (2008) Radiotherapy enhancement with gold nanoparticles. *J Pharm Pharmacol* 60(8):977–985. doi:[10.1211/jpp.60.8.0005](https://doi.org/10.1211/jpp.60.8.0005)
99. Tian G, Ren W, Yan L, Jian S, Gu Z, Zhou L, Jin S, Yin W, Li S, Zhao Y (2013) Red-emitting upconverting nanoparticles for photodynamic therapy in cancer cells under near-infrared excitation. *Small* 9(11):1929–1938. doi:[10.1002/smll.201201437](https://doi.org/10.1002/smll.201201437)
100. Fan W, Shen B, Bu W, Chen F, Zhao K, Zhang S, Zhou L, Peng W, Xiao Q, Xing H, Liu J, Ni D, He Q, Shi J (2013) Rattle-structured multifunctional nanotheranostics for synergetic chemo-/radiotherapy and simultaneous magnetic/luminescent dual-mode imaging. *J Am Chem Soc* 135(17):6494–6503. doi:[10.1021/ja312225b](https://doi.org/10.1021/ja312225b)
101. Fan W, Shen B, Bu W, Chen F, He Q, Zhao K, Zhang S, Zhou L, Peng W, Xiao Q, Ni D, Liu J, Shi J (2014) A smart upconversion-based mesoporous silica nanotheranostic system for synergetic chemo-/radio-/photodynamic therapy and simultaneous MR/UCL imaging. *Biomaterials* 35(32):8992–9002. doi:[10.1016/j.biomaterials.2014.07.024](https://doi.org/10.1016/j.biomaterials.2014.07.024)

Chapter 6

Multifunctional Quantum Dot-Based Nanoscale Modalities for Theranostic Applications

Bowen Tian

Abstract Quantum dots (QD) have shown unprecedented fluorescent properties that are capable of revolutionising the field of optical imaging. Due to its unique fluorescent properties, QD have been extensively explored as imaging reagents for the investigation of various biological behaviours in vitro and in vivo. The design and engineering of multifunctional, QD-based modalities have recently attracted enormous interest for simultaneous imaging and therapy. The presence of QD as imaging agent in the theranostic modalities allows for the visualisation of their behaviour in real time and, thus, allows the monitoring of biodistribution, the percentage of drugs in the target site and regional uptake of the drug, as well as clearance from the body in real time, after systematic administration. All this information obtained from QD-based theranostic modalities is believed to be greatly helpful for the better understanding of biological behaviours and further optimization of novel therapeutic modalities, in preclinical and clinical investigations. This chapter attempts to give a brief overview of QD ranging from fundamental knowledge to multifunctional QD-based theranostic modalities for gene therapy, chemotherapy and photodynamic therapy.

Keywords Multifunctional modality • QD • Theranostics • Cancer therapy and imaging • Nanomedicine • Optical imaging

B. Tian (✉)

Laboratory of Biophysics and Surface Analysis Division, School of Pharmacy,
University of Nottingham, Nottingham NG7 2RD, UK

e-mail: bowen.tian@nottingham.ac.uk

6.1 Quantum Dot

6.1.1 Optical Imaging

Optical imaging is a non-invasive, reliable and highly sensitive technique, with nanometre-scale resolution for exploring various biological activities in the life sciences [1–4]. Fluorescent imaging methods rely on the detection of emission light from fluorophores, when the fluorophores are excited by using a light source with specific wavelength. Therefore, the fluorescent properties of the fluorophores are of utmost importance in the successful application of such techniques. Ideal fluorophores require strong emission, high photostability, no toxicity and ease of chemical modification (e.g. conjugation with targeting ligands). Furthermore, for in vivo imaging, both excitation and emission light require efficient penetration through the tissues. NIR (near infrared, 700–1000 nm) imaging [5, 6] has recently attracted enormous interest, due to deep-tissue fluorescence imaging, compared to short light (<700 nm). NIR offers image-guided operation in the clinic [6–8]. The recent development of fluorescence molecular tomography [9] and photoacoustic tomography [10] will promote the applications of optical imaging in the life sciences.

The fluorophores are divided into inorganic (QD [11], graphene QD [12], gold nanoparticles [13]), carbon nanotube [14], hybrids (lanthanide chelates [15]) and organic dyes (cyanine [16]). One of the most promising fluorescent probes is the quantum dot, which can revolutionise the fluorescent detection techniques given QD's unprecedented superior fluorescent properties, compared to traditionally used fluorescent dyes.

6.1.2 Quantum Dot Fluorescence Characteristics

QD are fluorescent, semiconductor, nanocrystals with typical diameters ranging from 1 to 10 nm [17]. Due to their superior fluorescence characteristics in comparison with traditionally used organic dyes, QD have been extensively used for a variety of biological investigations in vitro and in vivo [18–23]. Their unique fluorescent properties are characterised by size-dependent colour, pronounced photostability and sharper emission spectra and much broader absorption spectra.

- First, QD are characterised by their unique size and/or composition-dependent colour. This allows the design and synthesis of QD with customised colour, such that it is visible to infrared for specific applications [24–27].
- Second, QD have shown pronounced photostability. The growth of a passivation shell (e.g. zinc sulphur) around it can further improve their photostability for long-term and stable fluorescent imaging [17, 28, 29]. These core/shell QD, for example, CdSe/ZnS, are excellent fluorescent probes for long-term fluorescence imaging applications.

- Third, QD possess sharper emission spectra and much broader absorption spectra, compared to organic dyes. This unique fluorescent characteristic enables simultaneous imaging of QD of different colours, using one single excitation light source [26, 30–32]. In practice, this has been used for multiplex imaging to track cancer cell metastasis [33, 34] and differentiate tumour tissue [35] *in vivo*.
- Fourth, QD are much brighter and robust against photobleaching [36, 37]. Under the exposure of excitation light, QD can maintain stable fluorescence for a much longer time than organic dyes.

All these fluorescent characteristics form the basis for QD-based imaging applications for various biological studies; for example, for cell tracking [38–40], tumour vessels [41, 42], lymph nodes [43, 44] and solid tumours [19, 45, 46] *in vivo*.

6.1.3 *Quantum Dot Synthesis and Composition*

High-quality monodisperse QD was first reported by Bawendi and co-workers in 1993 [47]. Their synthetic method controlled well the colloidal stability of QD to maintain its monodispersed status and, therefore, elucidated its unique fluorescent characteristics, including size-dependent fluorescence for the first time. CdSe QD are the mostly widely used in biological applications due to a well-established synthetic chemistry [21]. In a typical CdSe QD synthesis, selenium (commonly trioctylphosphine selenide or tributylphosphine selenide) and cadmium precursors (dimethylcadmium or cadmium oleate) are injected into a high-temperature (300 °C) organic solvent containing coordinating polymers (trioctylphosphine oxide or hexadecylamine) [28, 47, 48]. Selenium and cadmium precursors are fast reacting to form the CdSe nucleus, and, in the meantime, coordinating ligands are attached to the CdSe nucleus surface to maintain colloidal stability. Cadmium and selenium continuously grow on the existing CdSe core, until the growth of QD reaches a desired size as monitored by the absorption spectrum [49]. A ZnS shell can be grown on the CdSe surface to enhance QD photoluminescence efficiency [17], stability against oxidative photobleaching [17, 28, 29] and colloidal stability [50]. Due to coordinating polymer coating (e.g. trioctylphosphine oxide, TOPO), QD are extremely hydrophobic and require further engineering to be dispersible in water.

With the development of QD synthetic chemistry, QD have been synthesised in aqueous solutions, high-temperature organic solvents and solid substrates [21] using various materials, mainly from II–IV (e.g. ZnS and CdS) and III–V (e.g. InP and InAs) group semiconductor materials. Alloyed QD tunes emission wavelengths by manipulating compositions [24, 26]. Cadmium-free QD of CuInS₂ emits fluorescence in the NIR range and greatly minimises toxicity compared to traditionally used cadmium containing QD (e.g. CdSe) [51]. Many more novel types of QD, with different properties, are under development, including graphene QD [52, 53] and nitrogen-rich QD [54].

6.1.4 *Quantum Dot Solubilisation and Functionalisation*

Both Nie and Alivisatos groups first engineered water-soluble QD for biological applications. This was achieved by coating hydrophobic QD with mercaptoacetic acid [55] or silica [56]. For the engineering of water-soluble QD, two typical methods have been developed, namely, ligand exchange and amphiphilic polymer coating.

For ligand exchange, bifunctional ligands composed of a thiol group at one end are used. The thiol group is used to replace hydrophobic coordinating polymers (e.g. trioctylphosphine oxide (TOPO)), due to a stronger binding affinity to cadmium. The other end of the bifunctional ligand is normally composed of a hydrophilic group, which is exposed outside to interact with hydrophilic molecules (e.g. water) [36, 55, 56]. A variety of thiol-containing molecules have been used to make water-soluble QD following the ligand-exchange strategy, including (1) thiol-containing chemical molecules, such as mercaptoacetic acid (MAA), dihydrolipoic acid and mercaptopropyltris (methoxy) silane (MPS) [36, 55, 56], (2) peptides [57], (3) dendron [58], (4) oligomeric phosphine [59] and (5) silica [60]. It is notable that the replacement of TOPO coating successfully makes water-soluble QD, but it has been found to result in unfavourable effects on QD fluorescence and colloidal stability [55, 56, 61].

For amphiphilic polymer coating, their hydrophobic domain is used to interact with hydrophobic coordinating polymers, leading to the formation of an amphiphilic polymer coating around TOPO-capped QD. A variety of amphiphilic polymers have been used following this strategy, such as phospholipid micelles, triblock copolymer and amphiphilic diblock. Moreover, amphiphilic polymer coating has shown minimal effect on QD fluorescence and colloidal stability, compared to ligand exchange [19, 39, 62, 63] and, thus, has been the most commonly adopted approach for engineering stable, water-soluble QD. However, it is also notable that the formation of amphiphilic polymer coating around QD leads to a size increase [21].

For the functionalisation of QD, a variety of methods have been utilised, such as electrostatic absorption, covalent conjugation and streptavidin-biotin linking [21, 55, 64]. QD have been functionalised using various molecules for biological applications, such as antibodies [65–69], peptides [41, 42, 70], endosome-disruptive polymers [71], aptamers [72–75], radionuclides [76–78], magnetic resonance imaging (MRI) agents [79, 80] and therapeutic molecules [81–84]. Moreover, polyethylene glycol (PEG) has been successfully used to prolong QD blood circulation half-life in vivo and minimise immunogenicity and cytotoxicity [43, 85–87]. Figure 6.1 shows a schematic structure of functionalised QD for in vivo targeted imaging.

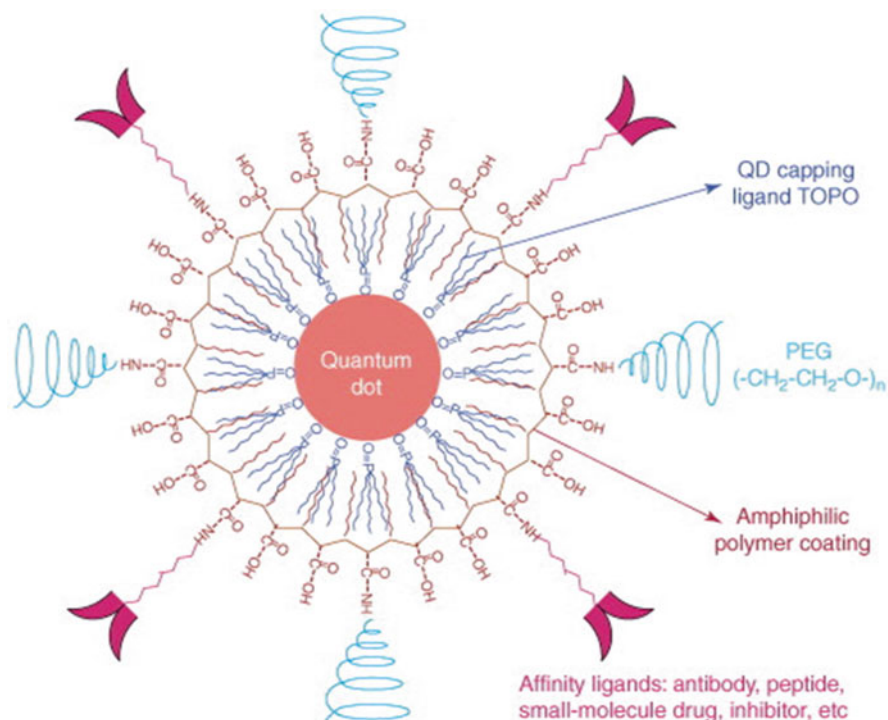


Fig. 6.1 The structure of a multifunctional QD. Schematic illustration showing the capping ligand TOPO, encapsulating copolymer layer, tumour-targeting ligands (such as peptides, antibodies or small-molecule inhibitors) and polyethylene glycol (PEG) (Reprinted from Ref. [87], copyright 2005, with the permission from Elsevier)

6.1.5 Quantum Dot in Biomedical Application

QD have been successfully used in fluorescent-based imaging and diagnostic applications *in vitro* and *in vivo*, for instance, (a) *in vitro* cell labelling [38, 39], fluorescent nanoprobe [88, 89] and biosensors based on the fluorescence resonance energy transfer (FRET) [90, 91] and (b) *in vivo* tumour vascular imaging [41, 92], tracking cells [40, 62, 93], lymph nodes [43, 44, 94] and solid tumours [95–97]. Due to the broad excitation spectra of QD, simultaneous detection using different coloured QD has enabled multiplex imaging to be used for tracking cancer cell metastasis [33, 34] and differentiating tumour tissue [35] *in vivo*.

Nowadays, fluorescent imaging using QD *in vivo* offers direct visualised evidence, but is mostly semi-quantitative. For accurate quantitative analysis, QD require the combination of fluorescence with other detection methods (e.g. radiolabelling). Recently, QD have been engineered such that they are equipped with magnetic [80, 98], paramagnetic [99] or radioactive properties [76, 78, 100], for more sensitive and quantitative diagnostic applications. Such dual-function nanoprobe

allow detection using multiple techniques, such as magnetic resonance imaging (MRI), positron emission tomography (PET) and single-photon emission computed tomography (SPET), along with fluorescence techniques such as IVIS camera [76, 99, 101]. For instance, tumour targeting of ^{64}Cu -labelled QD was directly visualised by NIR fluorescence imaging of QD. With radiolabelling of ^{64}Cu , the tumour-targeting efficiency of the QD was accurately quantified by the means of ultrahigh sensitivity of the radionuclide using PET [77]. Interestingly, Cai et al. (2007) further found that the tumour-to-muscle ratios obtained from NIR imaging were in agreement with PET analysis for certain organs, for example, the liver and spleen [77].

6.1.6 Quantum Dot Biodistribution and Pharmacokinetics In Vivo

Most studies have shown that QD are rapidly taken up by the reticuloendothelial system (RES), with high accumulation in the liver and spleen after systemic administration [100, 102–106]. Studies, so far, have shown that PEGylation, size and surface coating are the three critical factors which determine QD biodistribution and pharmacokinetics.

With respect to PEGylation, Ballou et al. have reported, by non-invasive fluorescent imaging, that the QD surface modified with PEG₅₀₀₀ (5,000 Da) greatly prolongs blood circulation half-life ($t_{1/2}$ = 140 min), compared to short PEG₇₅₀ and PEG₃₄₀₀ ($t_{1/2}$ < 12 min) [102]. However, high uptake by the liver, spleen, lymph nodes and bone marrow was observed up to 4 months [102]. Consistently, PEG₅₀₀₀-conjugated QD achieved long blood circulation half-life and, thus, facilitated targeting to the desired tissues in vivo [19, 45]. In 2009, Choi and co-workers reported that the biodistribution and pharmacokinetics of QD can be manipulated by surface modification using different lengths of PEG [103]. Choi et al. (2009) found that QD conjugated with PEG2 (two monomers) primarily accumulate in the liver; PEG8 accumulate in the pancreas; PEG3 and PEG4 are excreted via renal clearance and PEG22 circulate in the vasculature.

With respect to QD size, Fischer et al. (2006) have reported that QD linked to proteins (bovine serum albumin, BSA), 80 nm in diameter, were prominently accumulated in the liver compared to small QD (cross-linked with lysine, 25 nm in diameter) (99 % ID/g vs. 36 % ID/g, respectively) after 90 min postinjection [104]. This finding indicates that the interaction between QD and blood proteins leads to QD size increase and thus would result in rapid clearance by the RES system in vivo, similar to QD-BSA conjugates. In 2007, Choi et al. reported that zwitterionic QD showed biodistribution and clearance in a size-dependent manner. QD of 5.5 nm in hydrodynamic diameter can be efficiently excreted via urine, whereas larger QD (8.65 nm in diameter) showed high liver uptake but no urine clearance [105].

Moreover, it is evident that the extent of QD migration in the lymphatic system depends on QD size. QD with an average diameter of 15–20 nm migrate rapidly to

the sentinel lymph nodes (SLN), but primarily accumulate in the first lymph node, when administrated through subcutaneous, intradermal, intraperitoneal and intraparenchymal routes [20, 107–112]. In comparison, smaller QD with mean diameter of 9 nm migrate further into the lymphatic system up to five nodes [112].

Very recently, Schipper et al. (2009) attempted to investigate the effect of particle size, surface coating and PEGylation on QD biodistribution and pharmacokinetics in nude mice after intravenous administration [106]. Schipper et al. (2009) injected polymer- or peptide-coated ^{64}Cu -labelled QD, 2 and 12 nm in diameter, with or without surface-conjugated PEG₂₀₀₀, and did the analysis using both PET and ICP-MS (inductively coupled plasma mass spectrometry). It was found that PEG₂₀₀₀ conjugation to the large QD (12 nm) surface delayed accumulation in the liver and spleen, whereas such delayed uptake by the RES system was not observed from PEG₂₀₀₀-conjugated small QD (2 nm). Moreover, unlike polymer coating, peptide coating enhanced QD excretion, with higher accumulation in the bladder observed from small QD compared to large QD (7.6 % ID/g vs. 2.5 % ID/g, respectively).

Overall, it can be seen that QD biodistribution and pharmacokinetics in living animals are affected by many factors, such as hydrodynamic diameter, surface charge, PEG length and the route of administration. Furthermore, it has been shown that only very small neutral and zwitterionic QD (<5.5 nm in diameter) can be excreted efficiently via urine [103, 105], while larger QD have a tendency to accumulate in the body [104, 113], which will consequently raise the toxicity issue of QD.

6.1.7 Toxicity Profiles of Non-functionalised Quantum Dot

The concern over QD toxicity is mainly derived from their intrinsic core compositions, such as cadmium (e.g. CdSe and CdTe). The correlation between cytotoxicity and free Cd²⁺ ions has been established [60, 114, 115] with the occurrence of significant cell death in the range of 100–400 μM Cd²⁺ ions [43]. Derfus et al. reported that CdSe QD are toxic due to the release of cadmium ions (Cd²⁺) initiated upon photolysis and/or oxidation. This was evidenced by the blue shift in QD absorbance spectra due to size deduction and subsequent release of Cd²⁺ [114]. Furthermore, the process in the production of Cd²⁺ ions has been found to be accompanied by the formation of reactive oxygen species (ROS), such as singlet oxygen (O₂⁻), due to QD electron donation to oxygen [105, 116, 117]. Cho et al. observed significant lysosomal damage due to the presence of both Cd²⁺ ions and ROS after a 24-h cell incubation [118].

So far, studies have demonstrated that QD cytotoxicity is attributed to the use of core QD (e.g. CdTe), without ZnS coating, especially those solubilised by the ligand-exchange method, such as mercaptopropionic acid (MPA-QD) [77, 117, 119–121], mercaptoacetic acid (MAA-QD) [114], mercaptoundecanoic acid (MUA-QD) [121], cysteamine (QD-NH₂) [118, 119] and thioglycerol (QD-OH) [115]. These ligands have weak electrostatic interactions with QD and are found to

detach from the QD surface [122, 123]. Such ligand detachment may be worse in harsh conditions like endosomal compartment [56] leading to severe cell death [60, 105, 117, 119, 120].

In comparison, QD coated with ZnS shell (CdSe/ZnS [114] and CdTe/ZnS [118]) can protect the QD core from oxidation, thereby minimising Cd²⁺ leakage and subsequently reducing the QD-induced cytotoxicity [60, 118, 119]. Moreover, QD solubilised with a stable coating, such as silica, were shown to be non-toxic up to a high Cd²⁺ surface concentration [60] and highly resistant to chemical and metabolic degradation [124], as well as non-toxic even if translocated to the cell nucleus [125], or at the gene level [86].

Nowadays, most biological investigations have selected core/shell QD with stable amphiphilic polymer coating, used at relatively low concentrations (nmol to pmol). Therefore, no obvious toxicity has been observed from QD. For example, *Xenopus* embryos [62] and zebrafish embryos [126] microinjected with QD did not exhibit any sign of toxicity until a high concentration was used, leading to abnormalities in the embryos. Furthermore, QD injected systemically in mice and rats has shown no apparent toxicity in pmol-nmol range, even after 4 months [43, 104, 127, 128]. Moreover, large animals (e.g. Yorkshire pigs) injected with 200–400 pmol of QD for the sentinel lymph node (SLN) mapping showed no physiological changes in the heart rate, blood pressure and oxygen level even after several hours [20, 109–111].

Overall, cytotoxicity studies have shown that the toxicity of QD can be minimised by coating with ZnS shell and solubilising using amphiphilic polymer coating, especially when a low dose is used during the period of the experiment. However, heavy metal containing (e.g. cadmium) QD composition would be a major obstacle for clinical use.

6.2 Quantum Dot for Theranostic Applications

6.2.1 Quantum Dot-Based Gene Therapy Modalities

Gene therapy is one of the most promising solutions to various formidable diseases, including cancer. However, to achieve effective gene therapy requires the efficient and specific delivery of nucleic acid inside of cellular compartments (e.g. nucleus). Various biological barriers, therefore, need to be overcome to deliver nucleic acid inside of cells. Moreover, the release of nucleic acid from delivery vectors inside of the cells is guaranteed. This is a complicated process, which is currently not yet fully understood. QD offers excellent fluorescent properties in studying various processes associated with nucleic acid delivery, including complexation, and the release and intracellular trafficking of nucleic acid complexation. The fluorescence resonance energy transfer (FRET) phenomenon is used to construct the QD-FRET pair for the investigation of nucleic acid delivery.

The FRET effect is used to monitor fluorescent changes in a fluorescent molecule pair, including a donor and an acceptor. Fluorescent changes are due to the distance alteration in nanoscale (called the Forster radius, typically several nanometres) between the pair. For example, when a donor molecule and an acceptor molecule are approaching each other within Forster radius, the receptor starts to absorb energy from the donor, and as a result, the donor loses its fluorescence. When the two molecules are separating from each other (beyond Forster radius), the receptor cannot absorb energy from the donor, and as a result, the donor recovers fluorescence to a normal level.

The advantage of constructing the QD-FRET pairs is that QD stable fluorescent properties, against photobleaching, allows stable and long-term fluorescent imaging of nucleic acid delivery, release and related behaviours. In a typical example of QD-FRET pairs, QD-labelled pDNA forms complexation with fluorescently Cys5-labelled chitosan [129]. The FRET effect allows the monitoring of the integrity of the complexation inside of cells (by observing Cys5 fluorescence due to energy transfer from QD-labelled pDNA), whereas released pDNA only shows QD fluorescence. Moreover, intracellular trafficking was conducted in a highly sensitive and quantitative way. Following the same FRET strategy, similar studies have been carried out to investigate DNA condensation and stability [130], as well as DNA polymer complexation [131]. It is notable that photoactivation of QD is often accompanied with the production of reactive oxygen species (ROS), which leads to the breakage of DNA in QD-DNA conjugates [132]. This could offer a novel strategy to induce the release of DNA from QD upon light activation for controlled delivery of DNA inside of cells.

Apart from constructing QD-FRET pairs with DNA, QD is also explored as a delivery vector for DNA delivery. QD-loaded micelles carrying functional groups (e.g. maleimide) have been directly conjugated with pDNA molecules [133]. Such pDNA-QD micelle conjugates allow stable monitoring of pDNA intracellular trafficking, by QD fluorescence, for a long period of time. Moreover, pDNA-QD conjugates can successfully deliver pDNA inside of cells and result in the expression of reporter proteins, relevant to pDNA control. Positively charged QD have been used to complex with DNA due to electrostatic interactions [134]. Such a QD-DNA complex demonstrated a DNA release induced by glutathione in a concentration-dependent manner. This is probably due to the fact that glutathione has preferential interactions with the QD surface, leading to QD's surface charge change and, thus, release of DNA [134]. Near-infrared QD has been used to track the biodistribution of QD-DNA complexes in vivo [135]. The QD-DNA complex demonstrated a high accumulation in the lung, initially, followed by fast redistribution from the lung to the liver. QD control, however, showed a predominant accumulation in the liver straightaway. Furthermore, after weeks postinjection, QD fluorescent signals were still detectable due to QD's excellent photostability.

QD has been explored to investigate the process of small interference RNA (siRNA) delivery. The typical process for siRNA delivery, including delivery siRNA into cells, release siRNA and gene knockdown, normally takes longer than 24 h since post-administration. Over this period of time, traditionally used organic dye

could suffer from significant fluorescence loss due to photobleaching and is, thus, not suitable for long-term monitoring of siRNA delivery [136]. In comparison, QD offers significant improvement in terms of photostability and, thus, has been extensively used to explore various processes related to siRNA delivery.

Cationic liposomes have been used to co-complex both QD and siRNA by simple mixing [137]. This study demonstrates the monitoring of siRNA delivery inside of cells, as well as an improvement in gene silencing, but suffers from an adverse effect on the size increase of the complex in comparison to the liposome control. Both siRNA and a tumour-targeting peptide have been covalently conjugated to the surface of PEGylated QD [136]. Such targeted nanoconstructs can be internalised by cancer cells and achieve efficient gene silencing. Moreover, siRNA conjugation to QD, using a cleavable linker, was found to improve the gene silencing effect due to the enhanced release of siRNA inside of cells, compared to a non-cleavable linker. Antibody-targeted chitosan nanoparticles encapsulating QD inside was complex with siRNA on the surface [138]. By monitoring QD fluorescence, such a multifunctional delivery system demonstrated an enhanced cellular uptake in cancer cell lines that overexpressed certain receptors. The siRNA-QD conjugates have been engineered by two different linking strategies: (a) a disulphide bond, which allows cleavage to release siRNA inside of cells, and (b) a covalent bond, to form stable siRNA-QD conjugates for monitoring siRNA delivery [139]. Two targeting ligands are conjugated on the surface of siRNA-QD conjugates, to ensure efficient cellular uptake (e.g. RGD peptide targeting) and effective gene silencing through HIV-Tat peptide. By monitoring QD fluorescence, intracellular trafficking can be monitored in real time, and, more importantly, such targeted siRNA-QD conjugates achieved therapeutic knockdown of specific proteins in brain tumour cells.

Peptide-QD conjugates have been explored as delivery vectors for simultaneously monitoring intracellular transportation and delivery of siRNA into cells. Cell-penetrating peptide conjugated QD are used to complex with cy3-labelled siRNA [140]. This study demonstrated successful intracellular delivery and cellular distribution of siRNA in the cells. However, the complex was found to be entrapped in the endosome. To release siRNA from the endosome, acid neutralisation of the endosome as well as destabilisation of such peptide-QD-siRNA complexes were achieved by the addition of chloroquine to the cell culture environment. The addition of chloroquine was found to lead to a successful redistribution of siRNA to the cytoplasm from the endosome. The engineering of QD-based delivery systems for siRNA delivery can improve gene silencing by up to 20-fold, compared to traditionally used transfection agents [141]. It is also notable that such QD-siRNA complexes can achieve gene silencing in the presence of serum, whereas traditionally used gene transfection agents need to work in serum-free environments. Such dramatic improvement is owing to a proton sponge effect, which is achieved by grafting equal amounts of carboxylic and amine groups on the QD surface. Moreover, fluorescence microscopy study has revealed that QD-siRNA complexes fast stick to the cell membrane, followed by internalisation and accumulation in the area outside of the cell nucleus, by monitoring QD fluorescence. The same group reported that

amphiphilic polymer amphipol-coated QD (with both carboxylic and amine groups) can achieve efficient siRNA delivery, irrespective of the presence of serum [142].

6.2.2 *Quantum Dot-Based Chemotherapy Modalities*

The engineering of theranostic modalities integrated with imaging and therapy into one unit has attracted enormous interest for cancer [143–146]. The presence of QD as an imaging agent in the theranostic modalities allows for the visualisation of their behaviour in real time. QD could allow the monitoring of biodistribution, the percentage of drugs in the target site, the regional uptake of the drug as well as the clearance from the body in real time, after systematic administration. All this information is believed to be greatly helpful for better understanding biological behaviours and for the further optimization of novel therapeutic modalities, in preclinical and clinical investigations.

For the engineering of QD theranostic modalities, QD can be directly surface conjugated with therapeutic molecules and targeting ligands [143–145]. One of the most successful QD-based theranostic modalities is reported by Bagalkot et al. in 2007, who covalently conjugated PSMA-targeted aptamers to the surface of hydrophilic QD and allowed doxorubicin loading through intercalation with the aptamers [145]. In this QD-aptamer(Apt)-doxorubicin(Dox) conjugates, QD and Dox formed a FRET pair (donor-receptor) and the loading of Dox quenched the QD fluorescence. This multifunctional QD demonstrated enhanced therapeutic effect in the targeted cells (LNCAP), and the gradual recovery of QD fluorescence inside of the cells indicated Dox release. Such theranostic modality showed promise for cancer targeting, imaging, therapy and traceable drug delivery simultaneously *in vitro*.

Alternatively, nanoscaled delivery systems (e.g. liposomes [96, 147–150], micelles [62, 151] and carbon nanotubes [152, 153]) can be used as a platform for the construction of QD theranostic modalities [144, 146]. Liposomes are the most established nanoscaled delivery systems. By the use of liposomes as a platform, various targeting ligands, diagnostic and therapeutic agents of interests can be integrated into liposomes for cancer imaging and therapy. This is particularly the case when liposome-QD hybrid constructs are successfully engineered. For example, Weng et al. (2008) covalently conjugated both anti-HER2-targeted scFv and hydrophilic QD to the liposome surface and loaded doxorubicin into the aqueous core of the liposomes for cancer imaging and therapy [146]. By tracking QD fluorescence, high drug delivery into (MCF-7/HER2) tumour *in vivo* was evidenced by the visualisation of strong QD fluorescence (14 % of total body fluorescence) in the tumour site after systemic administration. However, the conjugation of QD directly to the liposome surface has an adverse effect on the size of the whole structure. This was evidenced by the fact that QD-conjugated liposomes showed a decrease in blood circulation half-life, compared to liposome control (without QD).

Both Vogel and Kostarelos have proposed the engineering of lipid-QD hybrid, by the incorporation of hydrophobic QD (2 nm in diameter) into the lipid bilayer of

liposomes [147, 148, 150]. This is a straightforward method to make water-soluble QD. The lipid-QD hybrid engineered using cationic lipids has been used to label cells effectively *in vitro* and *in vivo*. Moreover, the lipid-QD hybrid can be used as a modular platform to load anticancer drugs (e.g. doxorubicin) into the aqueous core, and their surface can be further functionalised with targeting ligands for targeted cancer theranostics. The successful engineering of lipid-QD hybrids represents a feasible way to engineer multimodal nanoconstructs, for the development of personalised medicine. Such hybrids not only combine the unique fluorescent properties of QD with the physicochemical and pharmacokinetics of liposomes into one single vesicle but also allow further surface modification with polyethylene glycol and various targeting ligands (e.g. antibody).

Alternative multifunctional modalities can be engineered by simultaneous encapsulation of Dox, QD and magnetic nanoparticles into PEG-lipid micelles, for combined MRI and fluorescent imaging as well as cancer therapy [154]. Tumour accumulation of such modalities was confirmed by both fluorescent and MRI imaging after 20-h administration. Recently, the anticancer drug daunorubicin was reported to complex with anionic QD (3-mercaptopropionic acid coated) inside of cells, which could overcome multidrug resistance and improve the therapeutic effect in leukaemia cell lines [155].

6.2.3 *Quantum Dot-Based Photodynamic Therapy Modalities*

Photodynamic therapy (PDT) is the use of a specific light to activate photosensitisers (PS), in order to produce a toxic effect on certain cells and organs (e.g. tumour). For quantum dot, the exposure of excitation light produces both QD fluorescences and, in the meanwhile, leads to the production of reactive oxygen intermediates (ROI) to cause cell toxicity for simultaneous photodynamic therapy and imaging [156–158]. Photoactivation of QD is often accompanied by the production of ROI, which could lead to the breakage of DNA in the QD-DNA conjugates [132]. In the presence of antioxidant scavengers (e.g. N-acetylcysteine), such ROI-induced cell toxicity can be suppressed significantly [120]. It is also notable that QD by itself as photosensitisers cannot produce ROI for efficient cell toxicity.

An alternative strategy has been explored to use QD to enhance the toxicity of conventional photosensitisers, by taking advantage of the fluorescence resonance energy transfer (FRET) effect. QD can be used as a delivery platform for photosensitisers due to large surface area, efficient energy transfer and photostability, for improved photodynamic therapy. For example, the complexation between QD and photosensitiser (e.g. chlorin e6) increases the photodynamic therapy by twofold compared to chlorin e6 alone [157]. This was thought to be due to enhanced energy transfer from QD to the photosensitiser through the FRET effect.

6.3 Conclusion

QD has been used for the engineering of multifunctional theranostic modalities, for the investigation of various biological behaviours, including gene therapy, chemotherapy and photodynamic therapy. For gene therapy, QD allows the monitoring of complexation stability, release and intracellular trafficking inside of cells. For chemotherapy, QD allows the monitoring of the release of the drug inside of the cells and tracing nanoscaled delivery vectors' (e.g. liposome) behaviours, in vivo, including biodistribution and tumour accumulation. For photodynamic therapy, QD can be successfully used as an energy donor to enhance the toxicity of conventional photosensitisers. All these successes are attributable to QD's superior fluorescent properties. Although the concerns regarding QD toxicity could delay their clinical applications, QD as imaging agents are very useful for various biological studies and in vitro sample analysis. With the development of novel water-soluble and cadmium-free QD, the applications of QD-based theranostic modalities could offer useful tools for the investigation and optimization of novel therapeutic agents in clinical applications.

References

1. Byrne WL, DeLille A, Kuo C et al (2013) Use of optical imaging to progress novel therapeutics to the clinic. *J Control Release* 172:523–534
2. Ntziachristos V (2010) Going deeper than microscopy: the optical imaging frontier in biology. *Nat Methods* 7:603–614
3. Pan D, Caruthers SD, Chen J et al (2010) Nanomedicine strategies for molecular targets with MRI and optical imaging. *Future Med Chem* 2:471–490
4. Stender AS, Marchuk K, Liu C et al (2013) Single cell optical imaging and spectroscopy. *Chem Rev* 113:2469–2527
5. Zhang ZJ, Wang J, Chen CH (2013) Near-infrared light-mediated nanoplatforms for cancer thermo-chemotherapy and optical imaging. *Adv Mater* 25:3869–3880
6. Vahrmeijer AL, Hutteman M, van der Vorst JR et al (2013) Image-guided cancer surgery using near-infrared fluorescence. *Nat Rev Clin Oncol* 10:507–518
7. Gioux S, Choi HS, Frangioni JV (2010) Image-guided surgery using invisible near-infrared light: fundamentals of clinical translation. *Mol Imaging* 9:237–255
8. Handgraaf HJ, Verbeek FP, Tummers QR et al (2014) Real-time near-infrared fluorescence guided surgery in gynecologic oncology: a review of the current state of the art. *Gynecol Oncol* 135:606–613
9. Mohajerani P, Adibi A, Kempner J, Yared W (2009) Compensation of optical heterogeneity-induced artifacts in fluorescence molecular tomography: theory and in vivo validation. *J Biomed Opt* 14:034021
10. Wang LHV, Hu S (2012) Photoacoustic tomography: in vivo imaging from organelles to organs. *Science* 335:1458–1462
11. Michalet X, Pinaud FF, Bentolila LA et al (2005) Quantum dots for live cells, in vivo imaging, and diagnostics. *Science* 307:538–544
12. Li LL, Wu GH, Yang GH et al (2013) Focusing on luminescent graphene quantum dots: current status and future perspectives. *Nanoscale* 5:4015–4039

13. Cao-Milan R, Liz-Marzan LM (2014) Gold nanoparticle conjugates: recent advances toward clinical applications. *Expert Opin Drugs Deliv* 11:741–752
14. Gong H, Peng R, Liu Z (2013) Carbon nanotubes for biomedical imaging: the recent advances. *Adv Drugs Deliv Rev* 65:1951–1963
15. Liu YS, Tu DT, Zhu HM, Chen XY (2013) Lanthanide-doped luminescent nanoprobe: controlled synthesis, optical spectroscopy, and bioapplications. *Chem Soc Rev* 42:6924–6958
16. Wang X, Lv JZ, Yao XY et al (2014) Screening and investigation of a cyanine fluorescent probe for simultaneous sensing of glutathione and cysteine under single excitation. *Chem Commun* 50:15439–15442
17. Alivisatos AP (1996) Semiconductor clusters, nanocrystals, and quantum dots. *Science* 271:933–937
18. Alivisatos P (2004) The use of nanocrystals in biological detection. *Nat Biotechnol* 22:47–52
19. Gao X, Cui Y, Levenson RM et al (2004) In vivo cancer targeting and imaging with semiconductor quantum dots. *Nat Biotechnol* 22:969–976
20. Kim S, Lim YT, Soltész EG et al (2004) Near-infrared fluorescent type II quantum dots for sentinel lymph node mapping. *Nat Biotechnol* 22:93–97
21. Smith AM, Duan H, Mohs AM, Nie S (2008) Bioconjugated quantum dots for in vivo molecular and cellular imaging. *Adv Drugs Deliv Rev* 60:1226–1240
22. Zrazhevskiy P, True LD, Gao XH (2013) Multicolor multicycle molecular profiling with quantum dots for single-cell analysis. *Nat Protoc* 8:1852–1869
23. Benito-Alifonso D, Tremel S, Hou B et al (2014) Lactose as a “Trojan Horse” for quantum dot cell transport. *Angew Chem Int Ed* 53:810–814
24. Bailey RE, Nie S (2003) Alloyed semiconductor quantum dots: tuning the optical properties without changing the particle size. *J Am Chem Soc* 125:7100–7106
25. Hines MA, Scholes GD (2003) Colloidal PbS nanocrystals with size-tunable near-infrared emission: observation of post-synthesis self-narrowing of the particle size distribution. *Adv Mater* 15:1844–1849
26. Zhong X, Feng Y, Knoll W, Han M (2003) Alloyed Zn(x)Cd(1-x)S nanocrystals with highly narrow luminescence spectral width. *J Am Chem Soc* 125:13559–13563
27. Nakane Y, Tsukasaki Y, Sakata T et al (2013) Aqueous synthesis of glutathione-coated PbS quantum dots with tunable emission for non-invasive fluorescence imaging in the second near-infrared biological window (1000–1400 nm). *Chem Commun* 49:7584–7586
28. Dabbousi BO, RodriguezViejo J, Mikulec FV et al (1997) (CdSe)ZnS core-shell quantum dots: synthesis and characterization of a size series of highly luminescent nanocrystallites. *J Phys Chem B* 101:9463–9475
29. Hines MA, Guyot-Sionnest P (1996) Synthesis and characterization of strongly luminescing ZnS-capped CdSe nanocrystals. *J Phys Chem-U S* 100:468–471
30. Kim S, Fisher B, Eisler HJ, Bawendi M (2003) Type-II quantum dots: CdTe/CdSe(core/shell) and CdSe/ZnTe(core/shell) heterostructures. *J Am Chem Soc* 125:11466–11467
31. Pietryga JM, Schaller RD, Werder D et al (2004) Pushing the band gap envelope: mid-infrared emitting colloidal PbSe quantum dots. *J Am Chem Soc* 126:11752–11753
32. Qu L, Peng X (2002) Control of photoluminescence properties of CdSe nanocrystals in growth. *J Am Chem Soc* 124:2049–2055
33. Voura EB, Jaiswal JK, Mattoussi H, Simon SM (2004) Tracking metastatic tumor cell extravasation with quantum dot nanocrystals and fluorescence emission-scanning microscopy. *Nat Med* 10:993–998
34. Walker KAD, Morgan C, Doak SH, Dunstan PR (2012) Quantum dots for multiplexed detection and characterisation of prostate cancer cells using a scanning near-field optical microscope. *PLoS One* 7:e31592
35. Stroh M, Zimmer JP, Duda DG et al (2005) Quantum dots spectrally distinguish multiple species within the tumor milieu in vivo. *Nat Med* 11:678–682

36. Jaiswal JK, Mattoussi H, Mauro JM, Simon SM (2003) Long-term multiple color imaging of live cells using quantum dot bioconjugates. *Nat Biotechnol* 21:47–51
37. Medintz IL, Uyeda HT, Goldman ER, Mattoussi H (2005) Quantum dot bioconjugates for imaging, labelling and sensing. *Nat Mater* 4:435–446
38. Alivisatos AP, Gu W, Larabell C (2005) Quantum dots as cellular probes. *Annu Rev Biomed Eng* 7:55–76
39. Wu X, Liu H, Liu J et al (2003) Immunofluorescent labeling of cancer marker Her2 and other cellular targets with semiconductor quantum dots. *Nat Biotechnol* 21:41–46
40. Herod MR, Pineda RG, Mautner V, Onion D (2014) Quantum dot labelling of adenovirus allows highly sensitive single cell flow and imaging cytometry. *Small*
41. Cai WB, Shin DW, Chen K et al (2006) Peptide-labeled near-infrared quantum dots for imaging tumor vasculature in living subjects. *Nano Lett* 6:669–676
42. Chen Y, Molnar M, Li L et al (2013) Characterization of VCAM-1-binding peptide-functionalized quantum dots for molecular imaging of inflamed endothelium. *PLoS One* 8:e83805
43. Ballou B, Ernst LA, Andreko S et al (2007) Sentinel lymph node imaging using quantum dots in mouse tumor models. *Bioconjug Chem* 18:389–396
44. Si C, Zhang Y, Lv X et al (2014) In vivo lymph node mapping by cadmium tellurium quantum dots in rats. *J Surg Res* 192:305–311
45. Akerman ME, Chan WC, Laakkonen P et al (2002) Nanocrystal targeting in vivo. *Proc Natl Acad Sci U S A* 99:12617–12621
46. Nurunnabi M, Cho KJ, Choi JS et al (2010) Targeted near-IR QDs-loaded micelles for cancer therapy and imaging. *Biomaterials* 31:5436–5444
47. Murray CB, Norris D, Bawendi MG (1993) Synthesis and characterization of nearly monodisperse CdE (E = S, Se, Te) semiconductor nanocrystallites. *J Am Chem Soc* 115:8706–8715
48. Talapin DV, Rogach AL, Kornowski A, Haase M, Weller H (2001) Highly luminescent monodisperse CdSe and CdSe/ZnS nanocrystals synthesized in a hexadecylamine-trioctylphosphine oxide-trioctylphosphine mixture. *Nano Lett* 1:207–211
49. Yu WW, Qu LH, Guo WZ, Peng XG (2003) Experimental determination of the extinction coefficient of CdTe, CdSe, and CdS nanocrystals. *Chem Mater* 15:2854–2860
50. Xie R, Kolb U, Li J et al (2005) Synthesis and characterization of highly luminescent CdSe-core CdS/Zn0.5Cd0.5S/ZnS multishell nanocrystals. *J Am Chem Soc* 127:7480–7488
51. Pons T, Pic E, Lequeux N et al (2010) Cadmium-free CuInS2/ZnS quantum dots for sentinel lymph node imaging with reduced toxicity. *ACS Nano* 4:2531–2538
52. Zheng XT, Ananthanarayanan A, Luo KQ, Chen P (2014) Glowing graphene quantum dots and carbon dots: properties, syntheses, and biological applications. *Small*
53. Wang L, Wang Y, Xu T et al (2014) Gram-scale synthesis of single-crystalline graphene quantum dots with superior optical properties. *Nat Commun* 5:5357
54. Chen XX, Jin QQ, Wu LZ et al (2014) Synthesis and unique photoluminescence properties of nitrogen-rich quantum dots and their applications. *Angew Chem Int Ed* 53:12542–12547
55. Chan WC, Nie S (1998) Quantum dot bioconjugates for ultrasensitive nonisotopic detection. *Science* 281:2016–2018
56. Bruchez M Jr, Moronne M, Gin P et al (1998) Semiconductor nanocrystals as fluorescent biological labels. *Science* 281:2013–2016
57. Pinaud F, King D, Moore HP, Weiss S (2004) Bioactivation and cell targeting of semiconductor CdSe/ZnS nanocrystals with phytochelatin-related peptides. *J Am Chem Soc* 126:6115–6123
58. Huang BH, Tomalia DA (2005) Dendronization of gold and CdSe/cdS (core-shell) quantum functionalized dendrons dots with tomalia type, thiol core, poly(amidoamine) (PAMAM) dendrons. *J Lumin* 111:215–223
59. Kim S, Bawendi MG (2003) Oligomeric ligands for luminescent and stable nanocrystal quantum dots. *J Am Chem Soc* 125:14652–14653

60. Kirchner C, Javier AM, Susha AS et al (2005) Cytotoxicity of nanoparticle-loaded polymer capsules. *Talanta* 67:486–491
61. Gerion D, Pinaud F, Williams SC et al (2001) Synthesis and properties of biocompatible water-soluble silica-coated CdSe/ZnS semiconductor quantum dots. *J Phys Chem B* 105:8861–8871
62. Dubertret B, Skourides P, Norris DJ et al (2002) In vivo imaging of quantum dots encapsulated in phospholipid micelles. *Science* 298:1759–1762
63. Larson DR, Zipfel WR, Williams RM et al (2003) Water-soluble quantum dots for multiphoton fluorescence imaging in vivo. *Science* 300:1434–1436
64. Mattoussi H, Mauro JM, Goldman ER et al (2000) Self-assembly of CdSe-ZnS quantum dot bioconjugates using an engineered recombinant protein. *J Am Chem Soc* 122:12142–12150
65. Liu TC, Zhang HL, Wang JH et al (2008) Study on molecular interactions between proteins on live cell membranes using quantum dot-based fluorescence resonance energy transfer. *Anal Bioanal Chem* 391:2819–2824
66. Xing Y, Chaudry Q, Shen C et al (2007) Bioconjugated quantum dots for multiplexed and quantitative immunohistochemistry. *Nat Protoc* 2:1152–1165
67. Lee J, Choi Y, Kim K et al (2010) Characterization and cancer cell specific binding properties of anti-EGFR antibody conjugated quantum dots. *Bioconjug Chem* 21:940–946
68. Hafian H, Sukhanova A, Turini M et al (2014) Multiphoton imaging of tumor biomarkers with conjugates of single-domain antibodies and quantum dots. *Nanomed Nanotechnol* 10:1701–1709
69. Rakovich TY, Mahfoud OK, Mohamed BM et al (2014) Highly sensitive single domain antibody-quantum dot conjugates for detection of HER2 biomarker in lung and breast cancer cells. *ACS Nano* 8:5682–5695
70. Anas A, Okuda T, Kawashima N et al (2009) Clathrin-mediated endocytosis of quantum dot-peptide conjugates in living cells. *ACS Nano* 3:2419–2429
71. Duan HW, Nie SM (2007) Cell-penetrating quantum dots based on multivalent and endosome-disrupting surface coatings. *J Am Chem Soc* 129:3333–3338
72. Bakalova R, Ohba H, Zhelev Z et al (2004) Quantum dot anti-CD conjugates: are they potential photosensitizers or potentiators of classical photosensitizing agents in photodynamic therapy of cancer? *Nano Lett* 4:1567–1573
73. Chen XC, Deng YL, Lin Y et al (2008) Quantum dot-labeled aptamer nanoprobe specifically targeting glioma cells. *Nanotechnology* 19:235105
74. Zhang J, Jia X, Lv XJ et al (2010) Fluorescent quantum dot-labeled aptamer bioprobes specifically targeting mouse liver cancer cells. *Talanta* 81:505–509
75. Zhang MZ, Yu RN, Chen J et al (2012) Targeted quantum dots fluorescence probes functionalized with aptamer and peptide for transferrin receptor on tumor cells. *Nanotechnology* 23:485104
76. Patt M, Schildan A, Habermann B et al (2010) F-18- and C-11-labelling of quantum dots with n.c.a. [F-18]fluoroethyltosylate and [C-11]methyl iodide: a feasibility study. *J Radioanal Nucl Chem* 283:487–491
77. Cai WB, Chen K, Li ZB et al (2007) Dual-function probe for PET and near-infrared fluorescence imaging of tumor vasculature. *J Nucl Med* 48:1862–1870
78. Sun X, Huang X, Guo J et al (2014) Self-illuminating 64Cu-doped CdSe/ZnS nanocrystals for in vivo tumor imaging. *J Am Chem Soc* 136:1706–1709
79. Fan HM, Olivo M, Shuter B et al (2010) Quantum dot capped magnetite nanorings as high performance nanoprobe for multiphoton fluorescence and magnetic resonance imaging. *J Am Chem Soc* 132:14803–14811
80. Jing LH, Ding K, Kershaw SV et al (2014) Magnetically engineered semiconductor quantum dots as multimodal imaging probes. *Adv Mater* 26:6367–6386
81. Chakravarthy KV, Davidson BA, Helinski JD et al (2010) Doxorubicin-conjugated quantum dots to target alveolar macrophages and inflammation. *Nanomedicine*

82. Jung J, Solanki A, Memoli KA et al (2010) Selective inhibition of human brain tumor cells through multifunctional quantum-dot-based siRNA delivery. *Angew Chem Int Ed Engl* 49:103–107
83. Ho YP, Leong KW (2010) Quantum dot-based theranostics. *Nanoscale* 2:60–68
84. Li JM, Wang YY, Zhao MX et al (2012) Multifunctional QD-based co-delivery of siRNA and doxorubicin to HeLa cells for reversal of multidrug resistance and real-time tracking. *Biomaterials* 33:2780–2790
85. Ryman-Rasmussen JP, Riviere JE, Monteiro-Riviere NA (2007) Surface coatings determine cytotoxicity and irritation potential of quantum dot nanoparticles in epidermal keratinocytes. *J Invest Dermatol* 127:143–153
86. Zhang TT, Stilwell JL, Gerion D et al (2006) Cellular effect of high doses of silica-coated quantum dot profiled with high throughput gene expression analysis and high content cello-mics measurements. *Nano Lett* 6:800–808
87. Gao X, Yang L, Petros JA et al (2005) In vivo molecular and cellular imaging with quantum dots. *Curr Opin Biotechnol* 16:63–72
88. Smith RA, Giorgio TD (2009) Quantitative measurement of multifunctional quantum dot binding to cellular targets using flow cytometry. *Cytom Part A* 75A:465–474
89. Mathur A, Kelso DM (2010) Multispectral image analysis of binary encoded microspheres for highly multiplexed suspension arrays. *Cytometry A* 77:356–365
90. Prasuhn DE, Feltz A, Blanco-Canosa JB et al (2010) Quantum dot peptide biosensors for monitoring caspase 3 proteolysis and calcium ions. *ACS Nano* 4:5487–5497
91. He X, Li Z, Chen M, Ma N (2014) DNA-programmed dynamic assembly of quantum dots for molecular computation. *Angew Chem* 53:14447–14450
92. Chen K, Li ZB, Wang H et al (2008) Dual-modality optical and positron emission tomography imaging of vascular endothelial growth factor receptor on tumor vasculature using quantum dots. *Eur J Nucl Med Mol Imaging* 35:2235–2244
93. Yoshioka T, Mishima H, Kaul Z et al (2010) Fate of bone marrow mesenchymal stem cells following the allogeneic transplantation of cartilaginous aggregates into osteochondral defects of rabbits. *J Tissue Eng Regen Med*
94. Liu J, Lau SK, Varma VA et al (2010) Multiplexed detection and characterization of rare tumor cells in Hodgkin's lymphoma with multicolor quantum dots. *Anal Chem* 82:6237–6243
95. Papagiannaros A, Upponi J, Hartner W et al (2010) Quantum dot-loaded immunomicelles for tumor imaging. *BMC Med Imaging* 10:22
96. Al-Jamal WT, Al-Jamal KT, Tian B et al (2009) Tumor targeting of functionalized quantum dot-liposome hybrids by intravenous administration. *Mol Pharm* 6:520–530
97. Lu Y, Zhong Y, Wang J et al (2013) Aqueous synthesized near-infrared-emitting quantum dots for RGD-based in vivo active tumour targeting. *Nanotechnology* 24:135101
98. Mulder WJM, Koole R, Brandwijk RJ et al (2006) Quantum dots with a paramagnetic coating as a bimodal molecular imaging probe. *Nano Lett* 6:1–6
99. van Tilborg GAF, Mulder WJM, Chin PTK et al (2006) Annexin A5-conjugated quantum dots with a paramagnetic lipidic coating for the multimodal detection of apoptotic cells. *Bioconjug Chem* 17:865–868
100. Schipper ML, Cheng Z, Lee SW et al (2007) MicroPET-based biodistribution of quantum dots in living mice. *J Nucl Med* 48:1511–1518
101. Cai WB, Chen XY (2007) Nanoplatforms for targeted molecular imaging in living subjects. *Small* 3:1840–1854
102. Ballou B, Lagerholm BC, Ernst LA et al (2004) Noninvasive imaging of quantum dots in mice. *Bioconjug Chem* 15:79–86
103. Choi HS, Ipe BI, Misra P et al (2009) Tissue- and organ-selective biodistribution of NIR fluorescent quantum dots. *Nano Lett* 9:2354–2359

104. Fischer HC, Liu LC, Pang KS, Chan WCW (2006) Pharmacokinetics of nanoscale quantum dots: in vivo distribution, sequestration, and clearance in the rat. *Adv Funct Mater* 16:1299–1305
105. Choi AO, Cho SJ, Desbarats J et al (2007) Quantum dot-induced cell death involves Fas upregulation and lipid peroxidation in human neuroblastoma cells. *J Nanobiotechnol* 5:1
106. Schipper ML, Iyer G, Koh AL et al (2009) Particle size, surface coating, and PEGylation influence the biodistribution of quantum dots in living mice. *Small* 5:126–134
107. Gopee NV, Roberts DW, Webb P et al (2007) Migration of intradermally injected quantum dots to sentinel organs in mice. *Toxicol Sci* 98:249–257
108. Parungo CP, Colson YL, Kim SW et al (2005) Sentinel lymph node mapping of the pleural space. *Chest* 127:1799–1804
109. Parungo CP, Ohnishi S, Kim SW et al (2005) Intraoperative identification of esophageal sentinel lymph nodes with near-infrared fluorescence imaging. *J Thorac Cardiovasc Surg* 129:844–850
110. Soltesz EG, Kim S, Kim SW et al (2006) Sentinel lymph node mapping of the gastrointestinal tract by using invisible light. *Ann Surg Oncol* 13:386–396
111. Soltesz EG, Kim S, Laurence RG et al (2005) Intraoperative sentinel lymph node mapping of the lung using near-infrared fluorescent quantum dots. *Ann Thorac Surg* 79:269–277
112. Zimmer JP, Kim SW, Ohnishi S et al (2006) Size series of small indium arsenide-zinc selenide core-shell nanocrystals and their application to in vivo imaging. *J Am Chem Soc* 128:2526–2527
113. Yang RS, Chang LW, Wu JP et al (2007) Persistent tissue kinetics and redistribution of nanoparticles, quantum dot 705, in mice: ICP-MS quantitative assessment. *Environ Health Perspect* 115:1339–1343
114. Derfus AM, Chan WC, Bhatia SN (2003) Probing the cytotoxicity of semiconductor quantum dots. *Nano Lett* 4:11–18
115. Kirchner C, Liedl T, Kudera S et al (2005) Cytotoxicity of colloidal CdSe and CdSe/ZnS nanoparticles. *Nano Lett* 5:331–338
116. Clarke SJ, Hollmann CA, Zhang Z et al (2006) Photophysics of dopamine-modified quantum dots and effects on biological systems. *Nat Mater* 5:409–417
117. Lovric J, Bazzi HS, Cuie Y et al (2005) Differences in subcellular distribution and toxicity of green and red emitting CdTe quantum dots. *J Mol Med* 83:377–385
118. Cho SJ, Maysinger D, Jain M et al (2007) Long-term exposure to CdTe quantum dots causes functional impairments in live cells. *Langmuir* 23:1974–1980
119. Hoshino A, Fujioka K, Oku T et al (2004) Physicochemical properties and cellular toxicity of nanocrystal quantum dots depend on their surface modification. *Nano Lett* 4:2163–2169
120. Lovric J, Cho SJ, Winnik FM, Maysinger D (2005) Unmodified cadmium telluride quantum dots induce reactive oxygen species formation leading to multiple organelle damage and cell death. *Chem Biol* 12:1227–1234
121. Shiohara A, Hoshino A, Hanaki K et al (2004) On the cyto-toxicity caused by quantum dots. *Microbiol Immunol* 48:669–675
122. Boldt K, Bruns OT, Gaponik N, Eychmuller A (2006) Comparative examination of the stability of semiconductor quantum dots in various biochemical buffers. *J Phys Chem B* 110:1959–1963
123. Dollefeld H, Hoppe K, Kolny J et al (2002) Investigations on the stability of thiol stabilized semiconductor nanoparticles. *Phys Chem Chem Phys* 4:4747–4753
124. Pellegrino T, Manna L, Kudera S et al (2004) Hydrophobic nanocrystals coated with an amphiphilic polymer shell: a general route to water soluble nanocrystals. *Nano Lett* 4:703–707
125. Chen FQ, Gerion D (2004) Fluorescent CdSe/ZnS nanocrystal-peptide conjugates for long-term, nontoxic imaging and nuclear targeting in living cells. *Nano Lett* 4:1827–1832
126. Rieger S, Kulkarni RP, Darcy D et al (2005) Quantum dots are powerful multipurpose vital labeling agents in zebrafish embryos. *Dev Dyn* 234:670–681

127. Manabe N, Hoshino A, Liang YQ et al (2006) Quantum dot as a drug tracer in vivo. *IEEE Trans Nanobiosci* 5:263–267
128. Stroh M, Zimmer JP, Duda DG et al (2005) Quantum dots spectrally distinguish multiple species within the tumor milieu in vivo. *Nat Mater* 11:678–682
129. Ho YP, Chen HH, Leong KW, Wang TH (2006) Evaluating the intracellular stability and unpacking of DNA nanocomplexes by quantum dots-FRET. *J Control Release* 116:83–89
130. Chen HH, Ho YP, Jiang X et al (2009) Simultaneous non-invasive analysis of DNA condensation and stability by two-step QD-FRET. *Nano Today* 4:125–134
131. Zhang BQ, Zhang YJ, Mallapragada SK, Clapp AR (2011) Sensing polymer/DNA polyplex dissociation using quantum dot fluorophores. *ACS Nano* 5:129–138
132. Anas A, Akita H, Harashima H et al (2008) Photosensitized breakage and damage of DNA by CdSe-ZnS quantum dots. *J Phys Chem B* 112:10005–10011
133. Srinivasan C, Lee J, Papadimitrakopoulos F et al (2006) Labeling and intracellular tracking of functionally active plasmid DNA with semiconductor quantum dots. *Mol Ther: J Am Soc Genet Ther* 14:192–201
134. Li D, Li G, Guo W et al (2008) Glutathione-mediated release of functional plasmid DNA from positively charged quantum dots. *Biomaterials* 29:2776–2782
135. Zintchenko A, Susha AS, Concia M et al (2009) Drug nanocarriers labeled with near-infrared-emitting quantum dots (quantoplexes): imaging fast dynamics of distribution in living animals. *Mol Ther: J Am Soc Genet Ther* 17:1849–1856
136. Derfus AM, Chen AA, Min DH et al (2007) Targeted quantum dot conjugates for siRNA delivery. *Bioconjug Chem* 18:1391–1396
137. Chen AA, Derfus AM, Khetani SR, Bhatia SN (2005) Quantum dots to monitor RNAi delivery and improve gene silencing. *Nucleic Acids Res* 33:e190
138. Tan WB, Jiang S, Zhang Y (2007) Quantum-dot based nanoparticles for targeted silencing of HER2/neu gene via RNA interference. *Biomaterials* 28:1565–1571
139. Jung JJ, Solanki A, Memoli KA et al (2010) Selective inhibition of human brain tumor cells through multifunctional quantum-dot-based siRNA delivery. *Angew Chem Int Ed* 49:103–107
140. Walther C, Meyer K, Rennert R, Neundorf I (2008) Quantum dot-carrier peptide conjugates suitable for imaging and delivery applications. *Bioconjug Chem* 19:2346–2356
141. Yezhelyev MV, Qi L, O'Regan RM et al (2008) Proton-sponge coated quantum dots for siRNA delivery and intracellular imaging. *J Am Chem Soc* 130:9006–9012
142. Qi L, Gao X (2008) Quantum dot-amphipol nanocomplex for intracellular delivery and real-time imaging of siRNA. *ACS Nano* 2:1403–1410
143. Rowe MD, Thamm DH, Kraft SL, Boyes SG (2009) Polymer-modified gadolinium metal-organic framework nanoparticles used as multifunctional nanomedicines for the targeted imaging and treatment of cancer. *Biomacromolecules* 10:983–993
144. Kim K, Kim JH, Park H et al (2010) Tumor-homing multifunctional nanoparticles for cancer theragnosis: simultaneous diagnosis, drug delivery, and therapeutic monitoring. *J Control Release* 146:219–227
145. Bagalkot V, Zhang L, Levy-Nissenbaum E et al (2007) Quantum dot – aptamer conjugates for synchronous cancer imaging, therapy, and sensing of drug delivery based on bi-fluorescence resonance energy transfer. *Nano Lett* 7:3065–3070
146. Weng KC, Noble CO, Papahadjopoulos-Sternberg B et al (2008) Targeted tumor cell internalization and imaging of multifunctional quantum dot-conjugated immunoliposomes in vitro and in vivo. *Nano Lett* 8:2851–2857
147. Tian B, Al-Jamal WT, Al-Jamal KT, Kostarelos K (2011) Doxorubicin-loaded lipid-quantum dot hybrids: surface topography and release properties. *Int J Pharm* 416:443–447
148. Al-Jamal WT, Al-Jamal KT, Tian B et al (2008) Lipid-quantum dot bilayer vesicles enhance tumor cell uptake and retention in vitro and in vivo. *ACS Nano* 2:408–418
149. Al-Jamal WT, Al-Jamal KT, Bomans PH et al (2008) Functionalized-quantum-dot-liposome hybrids as multimodal nanoparticles for cancer. *Small* 4:1406–1415

150. Gopalakrishnan G, Danelon C, Izewska P et al (2006) Multifunctional lipid/quantum dot hybrid nanocontainers for controlled targeting of live cells. *Angew Chem* 45:5478–5483
151. Erogbogbo F, Yong KT, Hu R et al (2010) Biocompatible magnetofluorescent probes: luminescent silicon quantum dots coupled with superparamagnetic iron (III) oxide. *ACS Nano* 4:5131–5138
152. Nair LV, Nagaoka Y, Maekawa T et al (2014) Quantum dot tailored to single wall carbon nanotubes: a multifunctional hybrid nanoconstruct for cellular imaging and targeted photothermal therapy. *Small* 10:2771–2775, 2740
153. Shi DL, Cho HS, Huth C et al (2009) Conjugation of quantum dots and Fe₃O₄ on carbon nanotubes for medical diagnosis and treatment. *Appl Phys Lett* 95:223702
154. Park JH, von Maltzahn G, Ruoslahti E et al (2008) Micellar hybrid nanoparticles for simultaneous magnetofluorescent imaging and drug delivery. *Angew Chem* 47:7284–7288
155. Zhou Y, Shi L, Li Q et al (2010) Imaging and inhibition of multi-drug resistance in cancer cells via specific association with negatively charged CdTe quantum dots. *Biomaterials* 31:4958–4963
156. Juzenas P, Chen W, Sun YP et al (2008) Quantum dots and nanoparticles for photodynamic and radiation therapies of cancer. *Adv Drug Deliv Rev* 60:1600–1614
157. Martynenko IV, Kuznetsova VA, Orlova AC et al (2015) Chlorin e6-ZnSe/ZnS quantum dots based system as reagent for photodynamic therapy. *Nanotechnology* 26:055102
158. Yaghini E, Seifalian AM, MacRobert AJ (2009) Quantum dots and their potential biomedical applications in photosensitization for photodynamic therapy. *Nanomedicine (Lond)* 4:353–363

Chapter 7

Organic Dye-Loaded Nanoparticles for Imaging-Guided Cancer Therapy

Zonghai Sheng and Lintao Cai

Abstract Recently, organic dye-based imaging-guided cancer therapy has attracted much attention in the field of cancer nanomedicine. As a small molecular compound, organic dye has an exact molecular weight and chemical structure. It can be not only used as fluorescence and photoacoustic imaging probes but also applied as therapeutic agents for photodynamic and photothermal therapy. Functionalized with the different delivery nanomaterials, organic dyes exhibit a long half-time and high tumor targeting and promoted stability. In this chapter, we review the development of organic dyes for cancer imaging and therapy applications in decades and illustrate the use of functional nanomaterials as organic dye delivery systems for enhancing their stability and tumor targeting, which show the bright prospects and challenges toward organic dye-based imaging-guided cancer therapy.

Keywords Organic dye • Imaging-guided therapy • Theranostics • Fluorescence imaging • Photoacoustic imaging • Photodynamic therapy • Photothermal therapy • Photoimmunotherapy

7.1 Introduction of Organic Dye

Organic molecular dye has attracted much attention as diagnostic and therapeutic agents in the field of tumor research [1]. They have demonstrated great successes in imaging the treatment of cancer [2]. As a small molecular compound, organic dye

Z. Sheng • L. Cai (✉)
Guangdong Key Laboratory of Nanomedicine, Institute of Biomedicine and Biotechnology,
Shenzhen Institutes of Advanced Technology, Chinese Academy of Sciences,
1068 Xueyuan Avenue, Shenzhen University Town, Shenzhen 518055,
People's Republic of China
e-mail: lt.cai@siat.ac.cn

has exact molecular weight and chemical structure. Moreover, it can be synthesized easily. As a diagnostic agent, organic dye can be used as fluorescent and photoacoustic contrast agents [3]. Compared with current clinical imaging modalities, such as computed tomography, ultrasound, MRI, single-photon emission computed tomography, and positron emission tomography, fluorescence imaging has the advantages of low cost, portability, no radiation exposure, and high-resolution and real-time image acquisition, demonstrating promise in intraoperative and endoscopic cancer diagnosis [4]. Photoacoustic (PA) imaging as a novel imaging modality has received increasing attention in recent years [5]. PA imaging is based on the PA effect, in which the absorbed short-pulsed electromagnetic (optical) energy is transformed into heat, leading to acoustic emission due to a transient thermoelastic expansion. In PA imaging, the detected acoustic signals are used to reconstruct the optical absorption distribution in tissue. Therefore, excellent optical absorption contrast with high ultrasonic resolution is achieved at large depths inaccessible to other high-resolution ballistic optical imaging modalities [6]. In addition, organic dye has been used as a therapeutic agent for phototherapy, including photodynamic therapy (PDT), photothermal therapy (PTT), and photoimmunotherapy (PIT). This type of light-triggered treatment modalities has remarkably improved selectivity and fewer side effects as compared to conventional radiotherapies and chemotherapies. In the section, we will introduce some organic dyes, including indocyanine green (ICG), IR700, IR780, IR825, chlorin e6 (Ce6), and fluorescein isothiocyanate (FITC) for imaging-guided surgical therapy and phototherapy, respectively. *The structures of these organic dyes are listed in Fig. 7.1.*

7.1.1 ICG

Indocyanine green (ICG, molecular weight 774.96 g/mol, CAS number 3599-32-4) is a tricyanobenzene dye [7]. It is composed of two polycyclic (benzoindodicarbocyanine) lipophilic moieties, linked with a polyene bridge. A sulfonate group, bound to the nitrogens of each polycyclic part, provides net negative charge and water solubility. Therefore, the entire molecular structure leads to amphiphilic characteristics of ICG. ICG exhibits NIR emission maxima around 800 nm that make it highly suitable for bio-imaging applications with high signal-to-background ratio. It also can convert the absorbed light energy to produce heat and toxic chemical species (such as singlet oxygen, superoxide anions, and hydroxyl radicals), forming the respective bases for PA imaging, PDT, and PTT, respectively. Therefore, ICG has been considered as a good imaging and therapy agent. However, the limitations of ICG are clearly understood along with going deep into research gradually. It is mainly manifested in the following aspects: (1) photo-degradation, degradation of ICG in aqueous solution followed first-order kinetics and was accelerated by light exposure; (2) thermal degradation, higher temperatures markedly accelerate the degradation of ICG in aqueous solutions; (3) aqueous instability, ICG undergoes degradation in aqueous media resulting in a simultaneous loss of absorption and

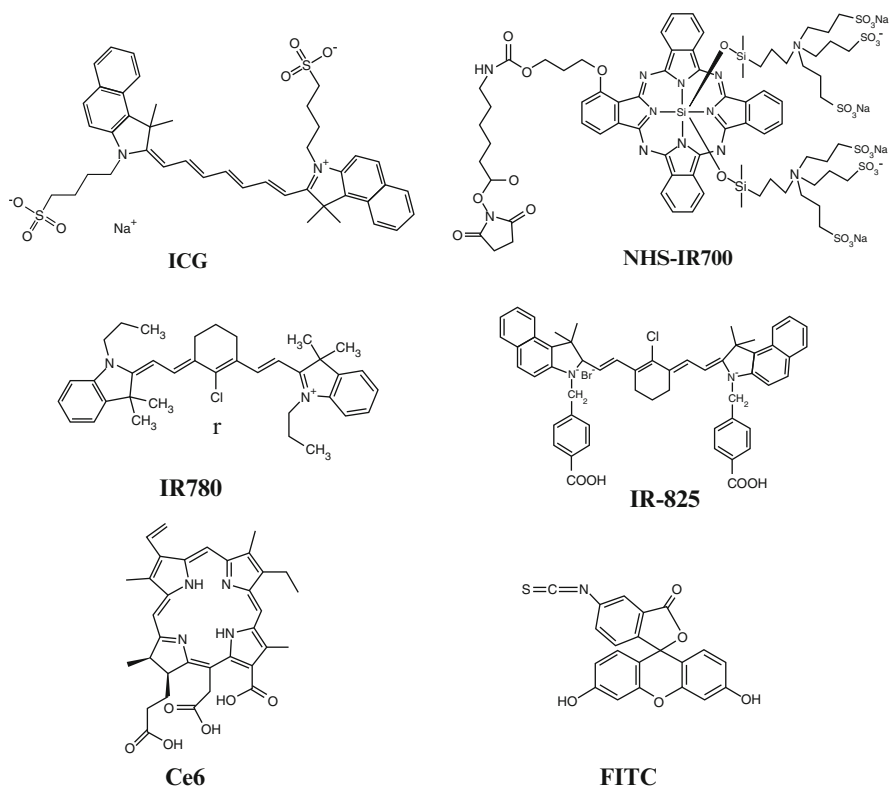


Fig. 7.1 The structural formulas of several organic dyes (ICG, NHS-IR700, IR780, IR825, Ce6 and FITC)

fluorescence; (4) short circulation time (half-life 2–4 min); (5) easy to bind nonspecifically to human serum albumin and result in its rapid clearance by the liver; and (6) low fluorescence quantum yield due to internal conversion and photobleaching. Therefore, to overcome these limitations, ICG molecular can be loaded, doped, and conjugated with different NPs with different modification strategies. The prepared ICG NPs have high photostability, thermal stability, long circulation time, and tumor-targeting ability.

7.1.2 IR 700

IR700 is a relatively hydrophilic NIR phthalocyanine dye (excitation wavelength, 689 nm; emission wavelength, 700 nm) [8]. It has excellent photochemical stability and water solubility. It is considerably less sensitive to photobleaching than many other organic fluorochromes. Therefore, IR700 is suitable for optical imaging when

conjugated to antibodies, receptor-binding ligands, small molecules, and more. In addition, as a photodynamic agent, IR700 has a more than fivefold higher extinction coefficient ($2.1 \times 10^5 \text{ M}^{-1} \text{ cm}^{-1}$ at the absorption maximum of 689 nm) than conventional photosensitizers such as the hematoporphyrin derivative Photofrin ($1.2 \times 10^3 \text{ M}^{-1} \text{ cm}^{-1}$ at 630 nm), the meta-tetrahydroxyphenylchlorin Foscan ($2.2 \times 10^4 \text{ M}^{-1} \text{ cm}^{-1}$ at 652 nm), and the mono-L-aspartylchlorin e6 NPe6/Laserphyrin ($4.0 \times 10^4 \text{ M}^{-1} \text{ cm}^{-1}$ at 654 nm). Therefore, it can be applied for NIR imaging-guided PDT.

7.1.3 IR 780

The IR-780 iodide (excitation wavelength, 740 nm; emission wavelength, 780–810 nm) is a lipophilic cation dye with peak absorption at 780 nm that can be conveniently detected by a NIR fluorescent detection system [9]. As a NIR dye, IR-780 provides a better sensitivity for in vivo detection due to significantly less background from tissue auto-fluorescence. IR-780 iodide has higher fluorescence intensity and is more stable than ICG. A rigid cyclohexenyl ring in the heptamethine chain with a central chlorine atom maintains photostability, increases quantum yield, decreases photobleaching, and reduces dye aggregation in solution. Therefore, IR-780 can be well utilized in PTT with laser irradiation. However, it is virtually insoluble in all pharmaceutically acceptable solvents. To overcome the solubility problem, IR-780 iodide usually needs to be delivered by micelles or nanoparticles for in vivo experiments and clinical uses. IR-780 is still an important theranostic agent although its lipophilicity limits its application.

7.1.4 IR825

IR825 is a heptamethine indocyanine dye which is a lipophilic cation with strong adsorption at 825 nm (in methanol) [10]. The molar absorption coefficient of IR825 at the peak of 825 nm in methanol is about to be $1.145 \times 10^5 \text{ M}^{-1} \text{ cm}^{-1}$. The fluorescence quantum yield (QY) of IR825 dye is <0.1 % in methanol, which is much lower than that of ICG. IR825 was not water soluble. It always needs to be modified by hydrophilic molecular amphiphilic polymer to become biocompatible. As IR825 shows a strong NIR absorption band and a rather low quantum yield, it can be used for in vivo PTT of cancer. Most of organic dyes have low photothermal efficiency because a part or even a majority of the absorbed optical energy is emitted from those dye molecules as fluorescence instead of heat. IR825, with high NIR absorption coefficients but low QYs, can offer the best photothermal efficiency, since the thermal effect would prevail in the energy dissipation process of those molecules after light excitation. Therefore, IR825 could serve as an effective photothermal agent to destruct cancer cells under NIR light.

7.1.5 *Ce6*

Chlorin e6 (*Ce6*, molecular weight, 596.68; CAS number, 19660-77-6), a second-generation PS, is an asymmetric molecule with three ionizable carboxylic groups and has lipophilic characteristics and exists in different ionic forms, dependent on pH [11]. *Ce6* is the reduced form of porphyrin whose core absorbs wavelengths of light too short for optimal penetration in tissue. The reduction of a pyrrole double bond on the porphyrin periphery gives the chlorin core a high absorption at longer wavelengths of 660–670 nm than those of porphyrins and is yet efficient in generating singlet oxygen. *Ce6* is a promising photosensitizer as it exhibits advantageous photophysical properties for PDT such as having long lifetimes in their photoexcited triplet states and high molar absorption in the red region of the visible spectrum. Moreover, a 664-nm laser light can penetrate tissue deeper than the 630-nm laser light used for Photofrin. In addition, *Ce6* has a shorter tumor accumulation time, more rapid clearance, and higher singlet oxygen generation efficiency, compared against first-generation PS photosensitizers such as hematoporphyrin derivatives, Photofrin, Photosens, Levulan, and Visudyne which have been used exclusively. Therefore, *Ce6* is a good second-generation photosensitizer to be applied for PDT with a high selective affinity for tumors.

7.1.6 *FITC*

Fluorescein isothiocyanate (*FITC*, molecular weight, 389.9; CAS number, 3326-32-7), as a xanthene dye, is a derivative of fluorescein used in wide-ranging applications including flow cytometry and immunofluorescence (IF) microscopy. *FITC* has excitation and emission spectrum peak wavelengths of approximately 488 nm/525 nm. It is the original fluorescein molecule functionalized with an isothiocyanate reactive group ($-N=C=S$), replacing a hydrogen atom on the bottom ring of the structure. This derivative is reactive toward nucleophiles including amine and sulfhydryl groups on proteins. Like most fluorochromes, it is prone to photobleaching. Because of the problem with photobleaching, derivatives of fluorescein have been improved for various chemical and biological applications where greater photostability, higher fluorescence intensity, or different attachment groups are needed. In addition, the intensity of fluorescence of *FITC* is also affected by the pH value, which must be taken into account during various applications. *FITC* has a good quantum yield. Almost half of the absorbed photons are emitted in the form of fluorescent light. So *FITC* is widely used in the area of flow cytometry. This fluorochrome can usually be measured with any standard commercial flow cytometer and sorter. Another application of *FITC* is *FITC*-conjugated antibodies, which are used very widely in laser scanning microscopy (LSM) and in immunofluorescence (IF) microscopy. However, the low photostability of the *FITC* becomes an imperfection in these applications.

7.2 Organic Dye for Imaging-Guided Surgical Therapy

Fluorescence imaging has been demonstrated to be feasible during cancer surgery using available imaging systems and contrast agents. As an important part of the imaging-guided surgery, fluorescent contrast agents are important to visualize tumor tissue [12]. At present, several fluorescent dyes have been applied for imaging-guided surgery, including FITC, ICG, methylene blue (MB), and 5-aminolevulinic acid (5-ALA)-induced protoporphyrin IX (PpIX). Among them, only ICG, MB, and 5-ALA have been approved by the US Food and Drug Administration (FDA) for clinical applications.

Tumor-specific fluorescence imaging-guided surgical treatments could assist the surgeon by providing real-time feedback on residual malignant tissue [13]. It may improve staging and debulking efforts in cytoreductive surgery and thereby improve prognosis. Clinical applicability has been described in sentinel lymph-node mapping, tumor imaging, visualization of vital structures, and imaging of vascularization and perfusion [14]. As novel contrast agents are developed and camera systems are optimized, the technique should prove its true clinical value. For example, Ntziachristos et al. developed a folate conjugated to FITC (folate-FITC) probe for targeting FR- α with a real-time multispectral intraoperative fluorescence imaging system (Fig. 7.2) [15]. They reported for the use of this tumor-targeting probe for real-time surgical visualization of tumor tissue in patients undergoing an exploratory laparotomy for suspected ovarian cancer. Real-time image-guided excision of fluorescent tumor deposits of size <1 mm was feasible, and all fluorescent tissue was confirmed to be malignant by histopathology. In the same patient, the tumor-specific fluorescent signal originating from disseminated tumor deposits could be detected up to 8 h after injection during a prolonged procedure. The real-time intraoperative fluorescence imaging modality has several advantages compared to the radiologic approaches such as X-ray, CT, MRI, and ultrasound. It offers a large field of view for inspection and staging, which may decrease the number of needless extensive surgical procedures. In addition, it may guide the surgeon in debulking efforts, which may improve the effect of adjuvant chemotherapy in patients with reduced tumor load. However, the emission wavelength of FITC dye is in the range of visible light, which limited its tissue penetration. Therefore, development of new fluorescent probe in the near-infrared spectrum will allow for identification of more deeply seated tumors, based on the stronger penetration properties of NIR dyes with an excitation wavelength >700 nm. Moreover, the miniaturization of the real-time fluorescence imaging system will be a tendency. Nie et al. constructed an integrated fiber-optic spectroscopic system (termed SpectroPen) that is stably aligned and calibrated and is thus well suited for robust surgical use [16]. The handheld spectroscopic pen device can be used to detect small tumors and other lesions in real time during surgery using ICG as NIR probe. The main advantage of the SpectroPen is that the observed ICG contrast between tumor and normal tissues is very clear and strong, even though no tumor-targeting ligands are used. NIR fluorescence imaging is a safe, low-energy (10^{-1} eV) approach to imaging and delivers 10^5 less energy

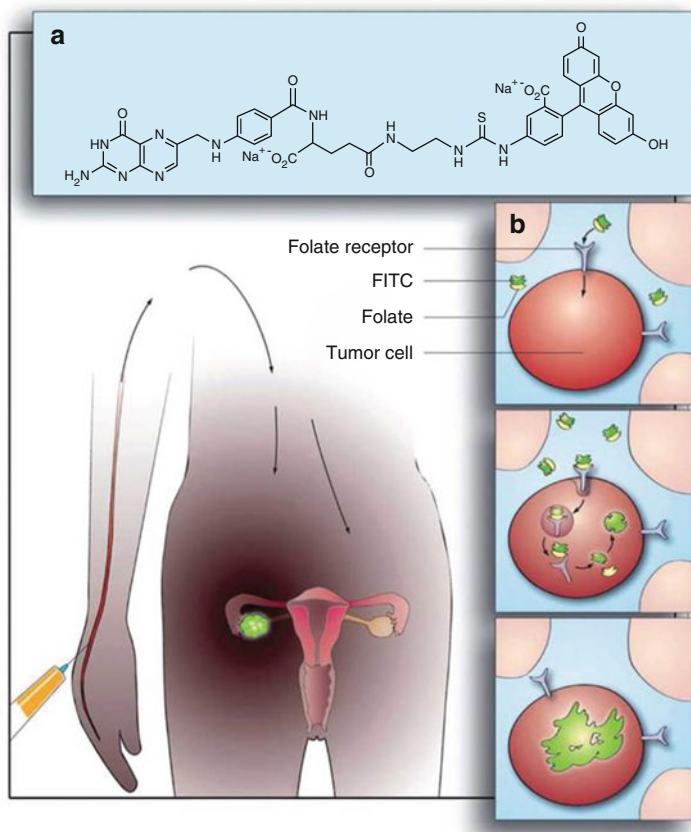


Fig. 7.2 A schematic presentation of the targeting of ovarian cancer using a tumor-specific fluorescent agent folate-FITC (Reprinted by permission from Macmillan Publishers Ltd: ref. [15], copyright 2011)

than a routine chest radiograph (10^4 eV) making it safe for the surgeon, patient, and surgical team. The *in vivo* studies by using mouse models bearing bioluminescent 4T1 breast tumors showed that the tumor borders could be precisely detected preoperatively and intraoperatively, resulting in real-time detection of both positive and negative tumor margins around the surgical cavity. Next, Nie et al. further used this method for detecting tumor margins and discovering residual tumor deposits during surgery [17]. They used a novel local recurrence model in small animals in this experiment. They found that residual tumor deposits could be detected with remarkable accuracy. There was no associated toxicity and surgical outcomes were remarkably improved by combining NIR imaging with standard-of-care surgical resection. Therefore, it may add to the surgeon's armamentarium in judging completeness of resection.

7.3 Organic Dye-Conjugated Antibody for Imaging-Guided Photoimmunotherapy

Photoimmunotherapy (PIT) is a novel PDT treatment method developed by Hisataka Kobayashi's group in 2011 [18]. The PIT utilizes a monoclonal antibody (mAb) conjugated with a dye, also known as photosensitizer. The mAb can specifically identify the targeted site, and the dye or photosensitizer can be applied for PDT. Therefore, the dye–mAb conjugation exhibits a good selectivity which derived from target-specific antibody binding to the cell membrane of target cells. In a xenograft tumor model, the A431 tumors (HER1 positive) were visualized with IR700 fluorescence 1 day after intravenous injection of 50 μg of mAb-IR700. The fluorescence intensity of mAb-IR700 in the A431 tumors decreased gradually over the 4 days after injection, whereas the tumor-to-background ratios (TBRs) increased during this period. However, the fluorescence intensity of the 3T3-HER2 tumor (HER1 negative) was the same as that of the background (nontumor lesions). The results showed the target-specific accumulation of mAb-IR700 *in vivo*. After that, the A431 tumors were treated with a single dose of light at 1 day after injection of mAb-IR700. Tumor volume was significantly reduced in A431 tumors treated with mAb-IR700-mediated PIT compared to untreated control mice, and survival was significantly prolonged in mice treated with mAb-IR700-mediated PIT compared to controls. This selective cell killing minimizes damage to normal cells [19]. Although single administration of the therapy was highly effective, recurrences were seen in treated mice, because inhomogeneous mAb-IR700 distribution in the targeted tumor could lead to not killing a small fraction of cancer cells, to which mAb-IR700 did not bind with NIR light. Therefore, to overcome the shortcomings, Makoto Mitsunaga et al. developed an optimized regimen of effective PIT method [20]. Under the guidance of IR700 fluorescence signal, the HER1-overexpressing tumors were irradiated by NIR laser for more times, and therapeutic effects were monitored. Eighty percent of the A431 tumors were eradicated with repeated PIT without apparent side effects and survived tumor-free for more than 120 days even after stopping therapy at day 30. The results showed that PIT was a promising highly selective and clinically feasible theranostic method for treatment of mAb-binding tumors with minimal offtarget effects. In addition, Takahito Nakajima et al. developed fluorescence lifetime imaging for real-time monitoring of *in vivo* acute necrotic cancer cell death induced by near-infrared PIT [21]. Moreover, Takahito Nakajima et al. further demonstrated that a cocktail injection of two different antibody-IR700 conjugates created a more homogeneous microdistribution of antibody conjugates resulting in enhanced therapeutic effects after PIT, compared to the use of either antibody-IR700 conjugate. Therefore, the tumor-targeting PIT shows a potential application in clinic (Fig. 7.3).

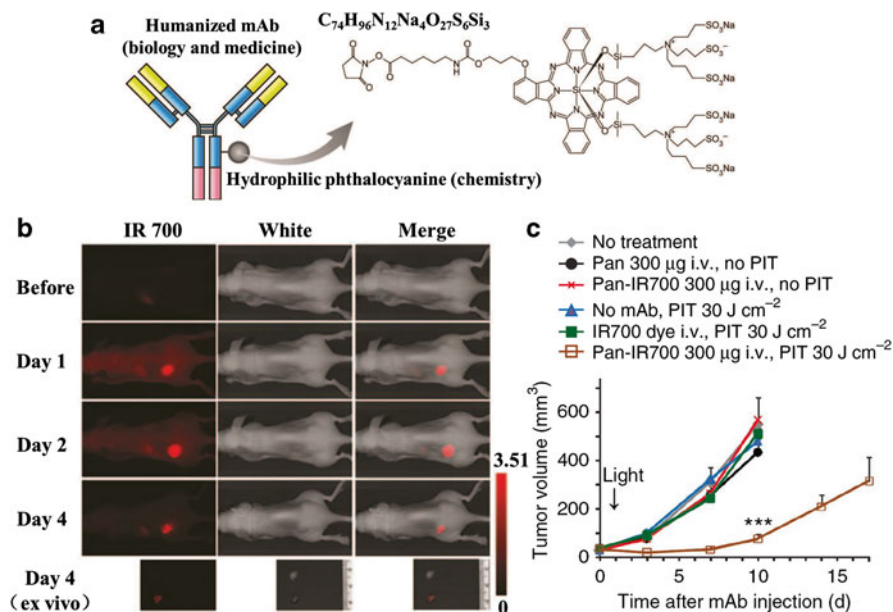


Fig. 7.3 IR-700 dye-conjugated monoclonal antibodies (mAbs) for fluorescence imaging and photoimmunotherapy (PIT). (a) A schematic for explaining the conjugated process of IR-700 dye and mAbs. (b) IR-700-mAb conjugations for fluorescence imaging of HER1-positive A431 tumors. (c) Target-specific tumor growth inhibition by IR-700-mAb conjugation-mediated PIT in A431 tumors (Reprinted by permission from Macmillan Publishers Ltd: ref. [18], copyright 1993)

7.4 Organic Dye-Loaded Inorganic Nanoparticles for Imaging-Guided Phototherapy

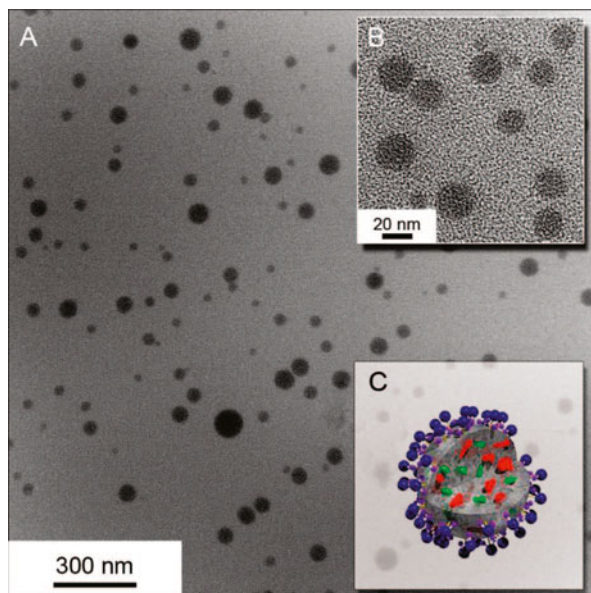
Dye-loaded inorganic nanoparticles for imaging-guided phototherapy have attracted much attention in recent years. Several inorganic nanoparticles have been used as dye delivery materials, including calcium phosphosilicate, poly(allylamine hydrochloride) assembled mesocapsules, and SiO_2 nanoparticles. In this part, we will introduce the three kinds of inorganic nanoparticles for imaging-guided phototherapy.

7.4.1 Calcium Phosphosilicate Nanoparticles

Calcium phosphate (CP) is a primary biomineral and exhibits an excellent compatibility and low immune response [22]. CP nanoparticles are nontoxic, colloidally stable, nanoscale vehicles that deliver chemotherapeutics and imaging agents. Adair et al. developed bioresorbable CP nanoparticles for loading ICG for In vivo imaging of human breast cancer, pancreatic cancers, and in vivo photodynamic therapy of

leukemia [23–25]. Spherical CP nanoparticles doped with ICG were synthesized using aqueous coprecipitation of calcium chloride and disodium hydrogen phosphate in the presence of disodium silicate within water-in-oil microemulsions. The mean particle diameter is 16 nm with a carboxylate or PEG surface termination that provides electrostatic dispersion in physiological conditions. The optical properties of ICG were further enhanced after ICG-encapsulated CP nanoparticles. PEGylated ICG–CP nanoparticles accumulate in tumors via enhanced retention and permeability (EPR) within 24 h after systemic tail vein injection in a nude mouse model. Ex situ tissue imaging further verifies the facility of the ICG–CP nanoparticles for deep-tissue imaging with NIR signals detectable from depths up to 3 cm in porcine muscle tissue. Based on the exciting results, Barth et al. further developed ICG–CP nanoparticles that can be systemically targeted to breast and pancreatic cancer lesions. The human holotransferrin, anti-CD71 antibody, and short gastrin peptides were conjugated with the ICG–CP NPs by a maleimide coupling strategy. The obtained ICG–CP nanoparticles permit targeting of transferrin receptors, which are highly expressed on breast cancer cells. Moreover, ICG–CP nanoparticles could cross the blood–brain-barrier, which may expand the utility of the CP nanoparticles to therapeutics targeted to glioblastoma or even to neurodegenerative or psychiatric disorders. In 2011, ICG–CP nanoparticles were further evaluated as photosensitizers for PDT of leukemia. The in vivo efficacy of PDT was dramatically enhanced in a murine leukemia model by utilizing CD117-targeted ICG–CP nanoparticles, resulting in 29 % disease-free survival. Altogether, this study demonstrates that leukemia-targeted ICG-loaded CP nanoparticles offer the promise to effectively treat relapsing and multidrug-resistant leukemia and to improve the life of leukemia patients (Fig. 7.4).

Fig. 7.4 The TEM image of ICG-loaded CP nanoparticles (Reprinted with permission from ref. [23]. Copyright 2008, American Chemical Society)



7.4.2 *Poly(allylamine hydrochloride)-Assembled Mesocapsules*

Poly(allylamine hydrochloride)-assembled mesocapsules were developed by Wong and coworkers in 2007 [26]. The self-assembly process is very simple and rapid. Aqueous solutions of polyallylamine hydrochloride (PAH) and dihydrogen phosphate salt are mixed together to form spherical aggregates. ICG was encapsulated into the NPs with electrostatic interactions. The reaction can be carried out under mild conditions, such as room temperature, aqueous solution, and neutral pH. In a typical synthesis, poly(allylamine hydrochloride) (PAH, 2 mg/mL, 20 μ L) was mixed with the Na₂HPO₄ solution (0.01 M, 120 μ L) and aged for 10 min at 4 °C. ICG solution with different concentrations was added to the polymer aggregate suspension. After that, the SiO₂ sol (diluted to 7 wt.%, 60 μ L) was added and aged for 2 h at 4 °C. The prepared ICG loading PAH capsules exhibited a spherical shape with particle size range of 0.6–1.0 μ m. The maximum loading efficiency of ICG was 23 wt.%. ICG molecule shows a negligible leakage from the PAH capsules after 24 h at room temperature in phosphate buffer saline solution. Under the NIR laser irradiation (808 nm, 155 W/cm²), the ICG-containing NACs showed a good photothermal response behavior and photothermal stability. The temperatures of ICG–NACs capsules reached >80 °C after 30 s of laser irradiation. After multiple photothermal heating cycles, the capsules were stable. Moreover, the ICG–NACs capsules were biocompatible in cell experiments. The results indicated the potential applications of ICG–NACs capsules in imaging-guided PTT [27]. However, the large particle size of ICG–NACs limited its in vivo application. Anvari et al. prepared three different ICG–NACs capsules: 100 nm diameter, coated with dextran; 500 nm diameter, coated with dextran; and 100 nm diameter, coated with 10 nm ferromagnetic iron oxide nanoparticles, themselves coated with polyethylene glycol. They investigated the effects of surface coating and size of the NACs capsules on the ICG's biodistribution in healthy Swiss Webster mice and evaluated the biodistribution kinetics of various formulations of MCs [28]. These coating materials were selected considering their excellent biocompatibility. The results suggested that the capsules' coating influenced their biodistribution to a greater extent than their size. The ICG–NACs capsules accumulated in the liver and spleen, as well as the lungs. It suggested that MCs were removed from the blood stream by hepatic filtration, phagocytosis by cells of the RES, and endocytosis by pulmonary endothelial cells. The NACs-based ICG delivery systems enabled the potential development of new optical imaging and therapeutic strategies. Based on this, Anvari et al. investigated fluorescence imaging of ICG–NACs coated with polylysine or magnetite/polyacrylic in living mice [29]. They indicated that the coating influenced the circulation time and tissue distribution of the capsules. For example, a coating of superparamagnetic magnetite NPs was readily taken up by the lungs. The positively charged polylysine capsules exhibited a prolonged circulation time in the blood stream. Therefore, the next works should be focused on the surface modification of ICG–NACs capsules. These results showed that ICG-nano-NACs-based had potential applications in fluorescence imaging-guided tumor-targeting PTT. However, the experiments needed to be further investigated in the future (Fig. 7.5).

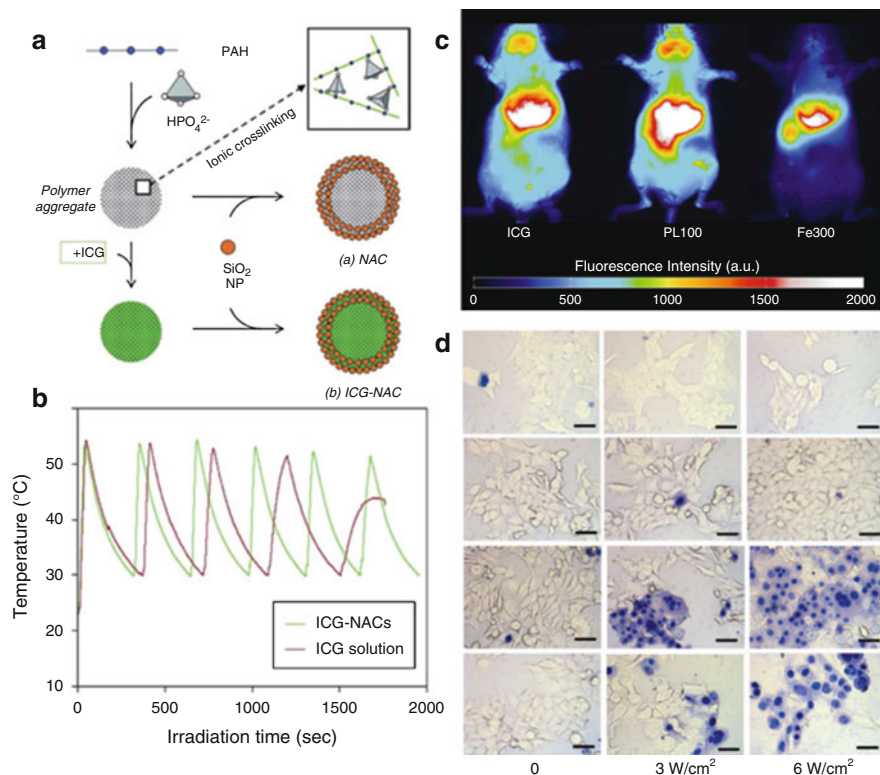


Fig. 7.5 Synthesis and application of ICG–NACs. **(a)** Schematic of ICG encapsulation in silica NP-assembled capsule (NAC). **(b)** Multiple laser irradiation/cooling cycles demonstrating increased stability of encapsulated ICG–NACs compared to free ICG. **(c)** ICG–NACs for in vivo fluorescence imaging. **(d)** In vitro PTT using ICG–NACs (Reprinted with permission from ref. [27]. Copyright 2010, American Chemical Society)

7.4.3 SiO_2 Nanoparticles

As an inorganic material, SiO_2 exhibits excellent stability and biocompatibility. The FDA listed silica as “generally recognized as safe.” ICG-doped SiO_2 NPs protect the ICG from photobleaching and photodegradation. The silica surface also enables easy and flexible surface treatments. Recently, Quan et al. successfully developed a method for preparation of ICG-doped silica NPs [30]. Cationic polymer polyethyl-imine (PEI) was interacted with anion ICG, and the ion pair was encapsulated by a silica layer using the Stöber method. The prepared ICG-doped SiO_2 NPs have diameters in the range 50–200 nm. The isolation of ICG molecules from the surroundings by the silica layer greatly enhanced the photostability of ICG-doped SiO_2 NPs. However, in vivo imaging and therapy ability of the ICG-doped SiO_2 NPs have not been investigated. Lee et al. reported ICG-doped mesoporous silica NPs for

optical imaging in living mice for the first time [31, 32]. The high dispersion of ICG molecules in the large surface areas of mesoporous silica could efficiently prevent them from aggregation and thus decrease the fluorescence self-quench. In addition, the nanochannels of mesoporous silica providing the confined space not only can protect ICG molecules from the irreversible degradation but also diminish the immune response. The studies of *in vivo* biodistribution of ICG-doped mesoporous silica revealed that the particles in the size of 50–100 nm possessing relatively positive surface charge were mainly targeting to the liver.

7.5 Organic Dye-Loaded Organic Nanoparticles for Imaging-Guided Phototherapy

Organic nanoparticles have been widely used as nanocarriers for cancer-targeted delivery [33]. As a clinically promising nanocarrier, organic nanoparticles have multiple advantages such as sustained release, prolonged circulation, and enhanced permeability and retention (EPR) effect [34–36]. In particular, the nanoparticles possess an excellent biocompatibility and biodegradability, which is important for clinical transformation applications. So far, several organic nanoparticles have been used to encapsulate or conjugate organic dye for improving their photostability, drug loading efficiency, as well as *in vivo* tumor-targeting accumulation, which could be prone to achieve imaging-guided tumor phototherapy [37, 38]. These dye-loaded organic nanoparticles mainly included polymeric nanomicelles, protein nanoparticles, and so on. In this part, we will focus on the introduction of the dye-loaded polymeric nanomicelles, PLGA nanoparticles, and protein nanoparticles for imaging-guided tumor phototherapy.

7.5.1 Dye-Loaded Polymeric Nanomicelles for Imaging-Guided Tumor Phototherapy

Polymeric nanomicelles with a unique core–shell structure have been successfully applied for organic dye delivery. Generally, the inner core served as a nanocontainer of organic dye, and the shell was surrounded by hydrophilic polymers, such as poly(ethylene glycol) (PEG). Therefore, the nanomicelles exhibited longevity in the blood stream and effective tumor accumulation after their systemic administration. In addition, nanomicelles have also several advantages, such as a simple preparation, efficient drug loading without chemical modification of the parent drug, and controlled dye release [39]. In this part, we will show nanomicelles as dye delivery for imaging-guided tumor phototherapy.

7.5.2 *Poly(ethylene glycol)–Distearoylphosphatidylethanolamine Block Copolymers (DSPE–PEG) Nanomicelles*

Poly(ethylene glycol)–distearoylphosphatidylethanolamine (PEG–DSPE) block copolymers are biocompatible and amphiphilic polymers, have been approved by the Food and Drug Administration (FDA) for medical applications, and can be widely utilized in the preparation of different nanomicelles [40]. The amphiphilic polymers are nanostructures composed of a hydrophobic core (DSPE) and a hydrophilic shell (PEG). The core–shell structure can encapsulate and carry poorly water-soluble dyes to congregate in the core of DSPE, and the terminal groups of PEG can be activated and linked to various targeting ligands, which can prolong the circulation time, improve the drug bioavailability, reduce undesirable side effects, and especially target specific cells, tissues, and even the intracellular localization in organelles. At present, the commonly used lipid derivative of PEG is methoxy–PEG–DSPE with a methoxy terminal. In order to link with different ligands, the terminal groups of methoxy–PEG–DSPE needed to be further modified. The common end-group forms of PEG–DSPE derivatives include carboxylation, amination, and maleylation. To improve treatment and efficacy and reduce drug toxicity, targeted moieties in the modification of the PEG–DSPE end groups have been recognized as a promising strategy. Folate acid (FA) [41], transferrin [42], peptide [43], and antibody [44] were used to graft to the end groups of PEG–DSPE. Previous reports have demonstrated that the DSPE–PEG could effectively encapsulate dye for imaging-guided tumor phototherapy. For example, Cai et al. reported a tumor-targeting ICG-loaded nanomicellar probe for in vitro and in vivo fluorescence imaging [45]. The nanomicelle was prepared by using a modified nanoprecipitation technique combined with self-assembly. All the raw materials, including PLGA, DSPE–PEG, lecithin, are approved by the FDA and showed a high biocompatibility. The prepared FA–ICG–PLGA–lipid NPs exhibited good monodispersity, excellent NIR penetration ability, significant stability against photobleaching, and long circulation time. The cancer cell targeting experiments showed the folic acid (FR)-targeting ICG nanomicelle could be effectively internalized by the MCF-7 cancer cells (known to overexpress FR). On the contrary, A549 cells (low FR expressing) did not take up the FA–ICG–PLGA–lipid NPs anymore. Moreover, the in vivo experiments showed the FA–ICG–PLGA–lipid NPs were specifically targeted to the tumor, and its circulation time was much longer than free ICG. The results demonstrated that nanomicelle as ICG delivery system showed a potential application in tumor diagnosis and targeted imaging. After that, Cai et al. further developed a single-step assembly strategy for sonication-assisted synthesis of ICG-/DOX-loaded lipid–polymer nanomicelle for NIR fluorescence imaging and chem-photothermal combination therapy [46]. PLGA polymer co-encapsulated ICG and DOX to form a core. Lecithin and DSPE–PEG self-assembled around the PLGA core to form a lipid monolayer covered by a PEG shell for the stabilization of the core. The ICG nanomicelle had a high temperature response under NIR laser irradiation. The temperature of ICG-/DOX-loaded lipid–polymer nanomicelle

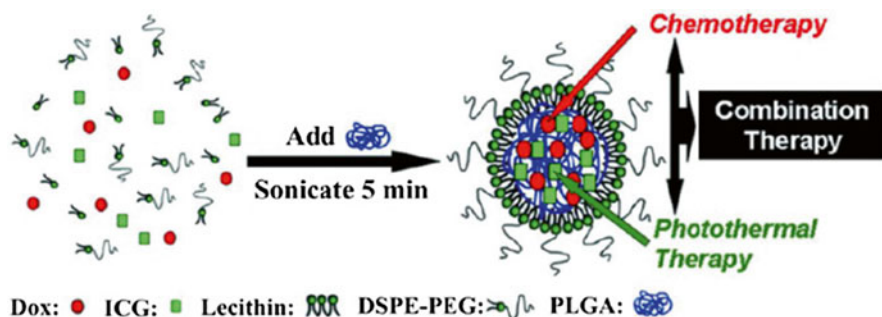


Fig. 7.6 ICG and DOX-loaded nanomicelles for fluorescence imaging-guided chem-photothermal combination therapy (Reprinted with permission from ref. [46]. Copyright 2013, American Chemical Society)

maximally reached 53.2 °C, which could lead to an irreversible damage to tumor cells. Moreover, the temperature increase could accelerate DOX released from the nanomicelle. The total release of DOX by 72 h was significantly enhanced to 97.00 %, indicating that the drug release of DINPs could be controlled by laser irradiation. Therefore, under the NIR fluorescence imaging, the combined treatment of ICG/DOX nanomicelle with laser irradiation synergistically induced the apoptosis and death of DOX-sensitive MCF-7 and DOX-resistant MCF-7/ADR cells and suppressed MCF-7 and MCF-7/ADR tumor growth *in vivo*. The prognosis could be evaluated by NIR fluorescence imaging (Fig. 7.6).

In addition, Cai et al. studied the effect of particle sizes of ICG nanomicelle on the ICG accumulation and photothermal efficacy in tumor. They prepared ICG nanomicelles with 39 nm, 68 nm, and 116 nm via single-step nanoprecipitation and demonstrated that 39-nm INPs were more easily absorbed by pancreatic carcinoma tumor cells (BxPC-3) and showed better photothermal damage than that of 68 nm and 116 nm size of nanomicelles [47]. Simultaneously, the fluorescence of INPs offered a real-time imaging monitor for subcellular locating and *in vivo* metabolic distribution. The NIR fluorescence imaging and photothermal therapy illustrated that 68-nm nanomicelles showed the strongest efficiency to suppress tumor growth due to abundant accumulation in BxPC-3 xenograft tumor model. The findings revealed that a nontoxic, size-dependent, theranostic nanomicellar model was built for *in vivo* NIR fluorescence imaging-guided photothermal therapy without adverse effect. Xing et al. prepared ICG-containing nanostructure, phospholipid–polyethylene glycol (PL-PEG) micelle conjugated with folic acid (FA), and integrin $\alpha\beta 3$ monoclonal antibody (mAb), for NIR fluorescence imaging and PTT, respectively [48]. The preparation process is very simple. ICG and PL-PEG were mixed with a mass ratio of 1:100. The solution was stirred at room temperature for 5 min and was filtrated using 2,000-Da filters (Millipore) to remove excess nonbinding ICG. The FA or mAb was conjugated with ICG–PL–PEG–COOH by EDC/NHS coupling chemistry. The self-assembled nanostructures of PEGylated phospholipids have

several advantages. For example, phospholipids and PEG are biocompatible and relatively nontoxic. Phospholipids are the major component of cell membranes, and PEG has been approved for human use; therefore, both of them are safe to use in biological systems. As hydrophobic materials, phospholipid (PL) provides additional stability, because the existence of two hydrocarbon chains contributes considerably to the increased hydrophobic interactions. The hydrophilic PEG surrounding the micelle surface renders the micelle sterically stable, protecting it from mononuclear phagocytic system (MPS) uptake and increasing drug circulation time. Both passive and active targeting can be realized, which will greatly increase drug accumulation in targeted tissues. When the ICG-PL-PEG micelles were exposed to an 808-nm NIR laser at a power density of 2 W/cm² for 10 min, a rapid increase of temperature was observed, and the maximum temperature increased up to 57.3 °C. The tumor cells could be effectively killed, exhibiting distinctive characteristics of cellular damage, including coagulative necrosis, abundant pyknosis, and considerable regions of karyolysis [49]. Irradiation of an 808-nm laser after intravenous administration of ICG-PL-PEG-mAb micelles resulted in tumor suppression in mice. Meanwhile, the ICG-PL-PEG-mAb could effectively target tumor cells and increase their accumulation in tumors. Therefore, the NPs could be applied for in vivo fluorescence imaging for cancer detection. Therefore, this unique ICG-PL-PEG-mAb nanomicelle, with integrated fluorescence imaging and photothermal therapeutic capabilities, can serve as theranostic nanoprobe for imaging-guided therapy.

7.5.3 PEG-b-poly(aspartate) (PEG-PAsp) Block Copolymer Nanomicelles

PEG-b-poly(aspartate) (PEG-PAsp) block copolymers were firstly developed as drug delivery system by Kataoka's group [50]. Compared with polymer micelles from amphiphilic block copolymers, PEG-PAsp micelles have some unique characteristics. For example, the size of PEG-PAsp micelles can be precisely controlled between 100 and 400 nm, by changing the concentration of the component polymers. Loading of antitumor drug can be achieved by simply vortex mixing in aqueous milieu without using any organic solvents. In addition, the PEG-PAsp micelles can be cross-linked in a controlled manner to tune the stability and the permeability, leading to a controlled release of antitumor drug in physiological environment [51]. The optimized PEG-PAsp nanomicelle is currently under phase II clinical trial in Japan [52]. As a dye delivery system, PEG-PAsp micelles have been also investigated in recent years. For example, Chen et al. prepared ICG-loaded micelles using monomethoxy poly(ethylene glycol) and alkylamine-grafted poly(L-aspartic acid) [53]. The polyaspartamide was chosen as the copolymer backbone in the consideration of biocompatibility requirements and versatile modification of hydrophobic segments. It had the smallest diameter of 41.4 nm with the polydispersity index of

0.09, which indicated the formation of the most compact micellar cores with a spherical morphology. The ICG loading efficiency was 20 %, which was higher than those of existing NPs. Compared with free ICG, the micelles had a good fluorescent stability during 48 h at 4 °C and 25 °C and exhibited a significant sustained release capability. Cell uptake experiments showed that the micelles could easily be internalized by cancer cells and mainly distributed into endosomes/lysosomes. The *in vivo* experiments showed that the micelles were effectively distributed into tumor at 24 h postinjection and also maintained a good retention of NIRF signals of tumor at 96 h postinjection, which was better than that of free ICG. For the mice bearing hypervascular A549 and hypovascular BxPC-3 tumors, the micelles exhibited a high tumor targeting and exhibited a significant accumulation of NIR fluorescence signals at tumor at 24 h postinjection. Therefore, the ICG–polyaspartamide could be applied for long-term NIR fluorescence tumor imaging. In addition, under the NIR laser irradiation (1.0 W/cm² for 5 min at 24 h postinjection), the tumor tissue temperature could rapidly increase to above 42 °C, which could efficiently kill the cancer cells. Therefore, the ICG–polyaspartamide micelles could be used as a powerful theranostic nanocarrier for simultaneous cancer imaging with high contrast and superior photothermal therapy (Fig. 7.7).

To further enhance the cancer treatment efficiency, Chen et al. prepared report a PS (Ce6)-loaded micelle system encapsulating cyanine dye for PTT and PDT synergistic phototherapy [54]. The micelles exhibited high loading capacity to encapsulate Ce6 (20 % (w/w)) and cypate (20 % (w/w)). The particle size is 55.0 nm. The micelles showed a stable micelles structure in aqueous solution and physiological environment. The binary micelles exhibited excellent photothermal effects. It exhibited a quick increase of temperature from 28 to 42 °C in 200 s at the concentration of 2.0 mg/mL upon 1.5 W/cm² photoirradiation. Meanwhile, the Cy/Ce6 micelles could also generate singlet oxygen via photodynamic effect. Both of the photothermal and photodynamic effects are Cy/Ce6 micelle concentration dependent. Moreover, under the laser irradiation, the Cy/Ce6 micelles showed a negligible

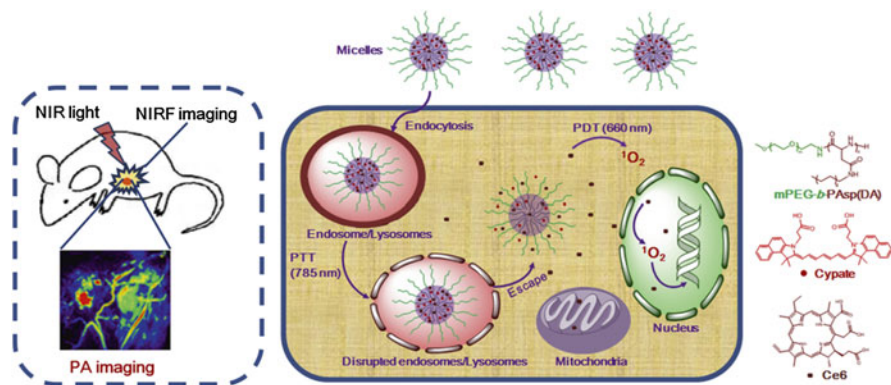


Fig. 7.7 Schematic illustration of PS-loaded nanomicelles for dual-modal imaging-guided PDT/PTT synergistic therapy (Reprinted from ref. [54]. Copyright 2014, with permission from Elsevier)

influence on the photostability, which are expected to improve PDT and PTT efficacy. In vitro experiments, the study showed that the micelles can easily improve the cellular uptakes of PS and cypate dye. The endocytotic pathways were focused on the clathrin-mediated endocytosis. Under the NIR laser irradiation, the photo-thermal and photodynamic effects from Cy/Ce6 micelles could effectively disrupt the lysosomal membranes. Therefore, the Cy/Ce6 micelles might escape from lysosomes into cytosol and enhance the treatment efficiency. In vivo experiments demonstrated that the Cy/Ce6 micelles could accumulate in tumor tissue and exhibited a relatively prolonged retention of NIRF signals in the tumor during the imaging period of 4 days. In addition, the PA imaging of Cy/Ce6 micelles exhibited a powerful capacity to visualize the tumor microstructure with high spatial resolution and imaging contrast. Therefore, after fluorescence and PA dual-modal imaging-guided therapy, the tumor growth could be efficiently inhibited, showing a synergistic efficacy on tumor via the enhanced cytoplasmic delivery of Ce6. The studies provided dual-modal imaging-guided synergistic cancer treatments and showed a great potential for clinical translation. After that, Chen et al. further developed ICG/DOX micelles for imaging-guided combined PTT and chemotherapy [55]. Upon photoirradiation, ICG/DOX micelles could induce NIR fluorescence imaging, acute photo-thermal therapy via hyperthermia, and simultaneous synergistic chemotherapy via singlet oxygen-triggered disruption of lysosomal membranes, eventually leading to enhanced NIR fluorescence imaging and superior tumor eradication without any regrowth.

7.5.4 Surfactant Micelles

Surfactant micelles, such as Tween 80, Pluronic F 68, Cremophor RH 40, and Solutol HS 15, two sugar-based surfactants (Ryoto sugar ester L 1695 and S 1170), and mixed micelles containing glycocholic acid and phosphatidylcholine have been investigated for parenteral use, because of their low toxicity, biodegradability, and excellent emulsifying properties. Additionally, they are nonionic and display lower temperature sensitivity in comparison to the PEG surfactants [56]. Therefore, these micelles have been used to encapsulate NIR dye ICG for overcoming their limitations, including concentration-dependent aggregation, poor aqueous stability in vitro, and low quantum yield. For example, Mäder et al. prepared a variety of ICG nanomicelle by direct dissolution method and carefully investigated the effects of different surfactants, such as Tween 80, Pluronic F 68, Cremophor RH 40, and Solutol HS 15 and two sugar-based surfactants (Ryoto sugar ester L 1695 and S 1170) on the size, morphology, zeta potential, stability, optical properties, and hemolytic activity [57]. The results showed clearly that surfactant micelles were useful tools with which to overcome the drawbacks of ICG. Moreover, after comparative studies, Solutol HS 15 micelles were used as potential nanocarriers for ICG that improve the optical properties of the dye and provide for high aqueous stability and low hemolytic activity. The micelles were monodisperse with an average

diameter of 12 nm and a zeta potential close to zero. ICG within Solutol HS 15 micelles was stable over a 4-week period when stored at 4 and 25 °C. The hemolytic activity of free ICG in water was significantly reduced by incorporation into the micelles. The studies provided some important results for the further application of ICG in NIR fluorescence imaging and PTT.

7.5.5 Polypeptide Micelles

Polypeptide micelles have been widely used in drug and gene delivery for their biocompatibility and biodegradability [58]. Compared with traditional polymers, the component and structure of synthetic polypeptides are more similar to natural proteins. Moreover, the synthetic polypeptides have stable secondary structures in physiological solutions, which would contribute to the high stability of delivery systems [59]. Moreover, the polypeptide micelles usually have a positive charge. In contrast with water-soluble cationic polymers, cationic micelles have a core-shell structure in aqueous medium with hydrophobic segments as the core and cationic hydrophilic segments as the shell. This special structure can improve the efficiency of cell uptake. Recently, Cai et al. also used a new type of amphiphilic PEG-polypeptide hybrid triblock copolymer of poly(ethylene glycol)-b-poly(L-lysine)-b-poly(L-leucine) (PEGPLL-PLLeu) nanomicelle-encapsulated ICG for tumor imaging and PTT [60]. Compared with free ICG, the hybrid polypeptide nanomicelles significantly improved quantum yield and fluorescent stability. The cellular uptake experiments showed that nanomicelles have a high cellular uptake rate. And the in vivo experiments demonstrated the excellent passive tumor targeting ability and long circulation time of the ICG nanomicelles. The above results indicated the broad prospects of hybrid polypeptide application in the fields of tumor diagnosis and imaging. In addition, temperature measurements under NIR laser irradiation and in vitro photothermal ablation studies proved the potential application of hybrid ICG nanomicelles in tumor photothermal therapy. Therefore, the ICG-loaded hybrid polypeptide nanomicelles could also be applied for imaging-guided PTT. In addition to polymer and polypeptide, the dextran could be used as an ICG delivery system for NIR fluorescence imaging and PTT in vivo.

7.5.6 Pluronic F-127 Micelles

Pluronic® triblock copolymers are a class of ABA triblock copolymers, which offer a pool of more than 50 amphiphilic, water-soluble, and polymorphic materials (A $\frac{1}{4}$ hydrophilic block poly(ethylene oxide) (PEO) and B $\frac{1}{4}$ hydrophobic block poly(propylene oxide) (PPO)). It has been used as drug delivery carriers in clinical use, clinical trials, or preclinical development [61]. Moreover, Pluronic F-127 has been approved by the FDA for parenteral use, demonstrating its excellent biosafety.

Additionally, the physical and chemical properties of Pluronic® copolymers can be tuned by modifying the molar mass ratio between the PEO and PPO blocks (from 1:9 to 8:2), which provides high potential for the design of innovative nanomedicines and new biomaterials. In addition, the thermosensitive micellization property of PF-127 is another advantage for efficient ICG stabilization and tumor localization in vivo. Pun et al. prepared Pluronic F-127 (PF-127, PEO100-PPO65-PEO100) polymeric micelles using solvent evaporation method for ICG delivery in vivo [62]. Pluronic F-127 has been approved by the FDA for parenteral use. The Pluronic F-127 exhibited a thermosensitive property. At room temperature, both the hydrophilic EO and hydrophobic PO blocks within a Pluronic molecule are hydrated and are relatively soluble in water, but when temperature is above the critical micelle temperature, the PO block dehydrates and becomes insoluble, resulting in the formation of compact micelles of 20–30 nm size. The ICG-Pluronic F-127 micelles have small particle size with narrow size distribution, excellent stabilizing ability at physiological temperature, and prolonged circulation time. The surface of the micelles can potentially be engineered for specific purposes such as incorporation of a targeting ligand for active tumor targeting. Solid tumors in mice were specifically visualized after intravenous administration of ICG-loaded micelles, which suggested that PF-127 micelle could be an efficient ICG delivery system for tumor targeting and also for potential tumor diagnosis for long-term follow-up. Moreover, clinical translation of the micelles may also be facilitated due to the raw materials, including PF-127 and ICG, already approved by the FDA.

7.5.7 Dye-Loaded PLGA for Imaging-Guided Tumor Phototherapy

Poly(lactic-co-glycolic acid) (PLGA) is biodegradable and biocompatible carriers, which have been approved by the FDA for therapeutic use in humans [63]. The PLGA nanoparticle exhibited enhanced permeation and retention (EPR) effect that allows passive targeting from the blood stream into the tumor site. Therefore, PLGA as ICT's carriers for imaging-guided PTT has attracted much attention in recent years. ICG encapsulation by PLGA nanoparticles effectively protects ICG from aggregation and protein interaction, thereby stabilizing the optical characteristics of ICG. It not only preserves the aqueous, thermal, and photostability of ICG but also increases the circulation half-life. In addition, targeting ligands can be conjugated to ICG-PLGA nanoparticles to make them cancer specific. Patel et al. reported a double-emulsion technique for the synthesis of ICG-loaded PLGA NPs. The TEM image showed PLGA NPs with the spherical shape and smooth surface and its particle size in 250–300 nm range [64]. The ICG loading efficiency was found to be 48.8 %. The optical properties of ICG were not changed after PLGA encapsulation. Moreover, PLGA improved the stability of ICG in aqueous conditions and also preserved the fluorescence property of ICG. The ICG-loaded PLGA NPs were

cytocompatible with the healthy cells for lower concentrations and showed no toxic effects. After conjugated with different ligands, such as RGD-4C peptides, folic acid, and R11 peptides, the ICG-loaded PLGA NPs showed a good cancer cell targeting. In phantom experiments, the ICG-loaded PLGA NPs exhibited the great absorbing and heating ability similar to that of ICG, leading to augmented thermal effects and possible tissue hyperthermia for future cancer treatments. Xu et al. developed novel dual-modal PLGA microbubbles for the structural and functional imaging of cancer. Three SEM images show that the microbubbles have a mean diameter of 3.4 μm , and the thickness is around 0.5 μm . The in vitro results demonstrated that the ICG-PLGA microbubbles have excellent fluorescence and ultrasonic contrast abilities. The changes of microbubble flow rate and concentration with high linearity and accuracy can be successfully captured, showing one potential application of the proposed ICG-encapsulated PLGA microbubbles for the identification and characterization of peritumoral neovasculature for enhanced coregistration between tumor structural and functional boundaries in ultrasound-guided near-infrared diffuse optical tomography.

7.5.8 Dye-Loaded Protein Nanoparticles for Imaging-Guided Tumor Phototherapy

Natural protein nanoparticles have attracted much attention as a novel class of drug delivery vehicles in recent years [65]. Compared with polymer nanomicelles, protein nanoparticles are native nanoscale structures with unique, defined three-dimensional structures, biological functions, excellent biocompatibility and nonimmunogenicity. The size of protein nanoparticles could be easily controlled and shows unique nanostructures. These good properties allowed protein nanoparticles to be applied in the clinic. For example, albumin-based drug delivery systems such as methotrexate-albumin conjugates, an albumin-binding prodrug of doxorubicin (DOX), and nanoparticle albumin-bound paclitaxel (Abraxane) have been evaluated in the clinic. Therefore, in this part, we will introduce the dye-loaded protein nanoparticles, mainly including ferritin and albumin nanoparticles, for imaging-guided tumor phototherapy.

7.5.9 Dye-Loaded Ferritin Nanocages

Ferritin (FRT) is a major iron storage protein found in humans and many living organisms [66]. In nature, the interiors of FRTs are filled with iron. When expressed artificially in iron-free conditions, the yielded apoferritins are hollow, comprising 24 subunits made up of heavy-chain ferritin (H-ferritin) and light-chain ferritin (L-ferritin). It can assemble above pH 5.0 into a robust hollow protein sphere with

outer and inner diameters of 12 and 8 nm, respectively. Between the junctions of each subunit are 14 channels, 0.3–0.4 nm in diameter, which can serve as the pathways between the exterior and interior. Therefore, the apoferritins can be loaded with different dyes for imaging-guided therapy [67]. There are several unique advantages using apoferritin as a dye delivery system: (1) Biosafety: apoferritin is a major iron storage protein in humans and therefore is biocompatible and nonimmunogenic. (2) Uniform size: The average particle size was 12 nm, which lead to a longer circulation half-life and a better tumor accumulation rate. (3) Unique nanostructure: the apoferritin nanocages can be broken down into subunits in an acidic environment (e.g., pH = 2). When the pH is tuned back to neutral, the apoferritin subunits will be reconstituted into a nanocage structure [68]. Zhen et al. reported RGD4C-modified ferritin (RFRT) as a safe and efficient zinc hexadecafluorophthalocyanine (ZnF16Pc) delivery system for imaging-guided photodynamic therapy [69]. ZnF16Pc is a potent photosensitizer with a high $^1\text{O}_2$ quantum yield but poor water solubility ($\lambda_{\text{max}}=671$ nm; $\Phi\Delta=0.85$ in tetrahydrofuran). It can be encapsulated into RFRTs with a loading rate as high as ~ 60 wt.% [70]. The particle size of ZnF16Pc-RFRT was 18.6 nm. The in vivo imaging experiments showed that the ZnF16Pc-RFRTs could efficiently home to tumors through interactions with integrin $\text{Rv}\beta 3$ overexpressed on tumor vasculatures and tumor cells (tumor-to-normal tissue ratio of 26.82 ± 4.07 at 24 h). Moreover, the in vivo treatment results showed a good tumor inhibition rate (83.64 % on day 12), as well as minimal toxicity to the skin and other major organs. Therefore, this imaging-guided therapy using ZnF16Pc-RFRTs holds great clinical translation potential. Huang et al. reported NIR dye (ICG and IR820)-loaded ferritin nanocages for multimodal imaging-guided photothermal therapy [71]. As hydrophilic dyes, ICG and IR820 were easily encapsulated into the cavity of ferritin. The obtained dye-loaded ferritin exhibited small particle size, good stability, and excellent tumor selectivity. When the mice were treated with an intravenous injection of IR820-loaded ferritin nanocages, the tumor could be easily differentiated from the surrounding normal tissue with good NIR fluorescence contrast 4–24 h postinjection. Meanwhile, the PA signal in the tumor regions was also increased with time. Under the NIR fluorescence and PA dual-modal imaging-guided photothermal treatments, the tumor cells could be killed, and no laser-treatment-induced toxicity and tumor recurrence were observed. Therefore, this concept of protein-based imaging-guided therapy has potential applications for clinical translation of personalized nanomedicine with targeted dye/drug delivery, diagnosis, and treatment (Fig. 7.8).

7.5.10 Dye-Loaded Albumin Nanoparticles

Albumin is the most abundant protein in blood plasma (35–50 g/L human serum), and its average half-life is 19 days [72]. As an important protein, albumin has several functions and binding properties [73]. For example, it can keep the colloid osmotic pressure of the blood. When albumin is broken down, the amino acids

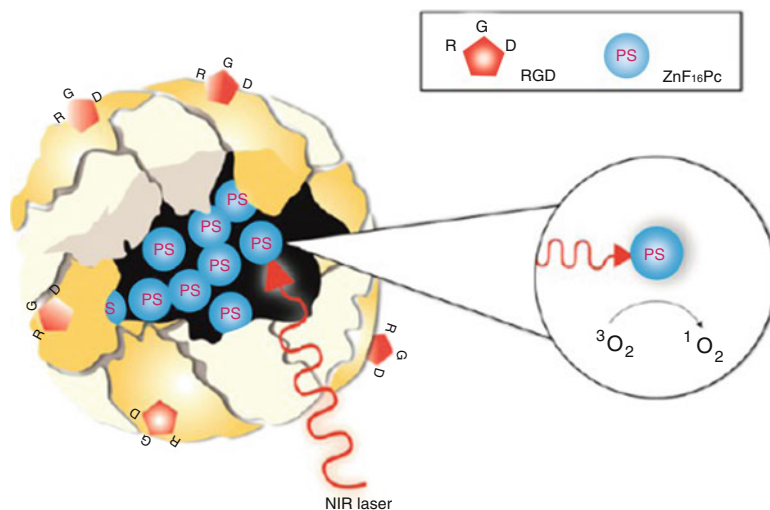


Fig. 7.8 Schematic illustration of PS-loaded ferritin nanoparticle for imaging-guided PDT (Reprinted with permission from ref. [69]. Copyright 2013, American Chemical Society)

provide nutrition to peripheral tissue. It can bind a great number of therapeutic drugs and metal ions and acts as a transport vehicle. In addition, albumin has excellent stability under different conditions (in the pH range of 4–9, soluble in 40 % ethanol, and heating at 60 °C for up to 10 h without deleterious effects.). These properties as well as its preferential uptake in tumor and inflamed tissue, its ready availability, its biodegradability, and its lack of toxicity and immunogenicity make it an ideal candidate for dye delivery [74]. Liu et al. prepared HSA–IR825 dye complex by bonding dye with human serum albumin (HSA). The simple method provided a strategy for developing a novel theranostic nanoprobe for imaging-guided photothermal therapy [75]. The HSA–IR825 complex exhibited strong fluorescence under the 600-nm excitation. The excellent fluorescence properties could enhance NIR fluorescence contrast. Moreover, under irradiation by an 808-nm laser, the nanoprobe could also convert the laser excitation energy into heat for photothermal therapy. Therefore, the nanoprobe not only could be used for the fluorescence imaging under the 600-nm excitation (high QY, low photothermal conversion efficiency) but also for photothermal therapy under the 808-nm irradiation (low QY, high photothermal conversion efficiency). The in vivo tumor treatment experiment demonstrated that 100 % of tumor ablation in mice using a rather low dose of HSA–IR825 nanoprobe. After that, Liu et al. further fabricated an IR825 dye–albumin theranostic nanoprobe for dual-modal imaging-guided tumor photothermal therapy [76]. The synthesis process was very simple, just complexing an IR825 dye with human serum albumin (HSA). The formed HSA–IR825 nanoprobe exhibited strong fluorescence and highly efficient photothermal effect. In addition, the clinically used MRI contrast agent, diethylenetriamine pentaacetic acid–Gd, was conjugated to HSA for MRI imaging. Therefore, the nanoprobe has three functions, including NIR fluorescence imaging, MRI dual-modal imaging, and photothermal therapy. They developed a lymphatic metastasis tumor model for evaluating the theranostic

nanoprobe. *In vivo* fluorescence imaging and MR dual-modal imaging indicated that HSA–Gd–IR825 could migrate into nearby sentinel lymph nodes (SLNs) after intratumoral injection. The combination therapy of surgery and photothermal therapy could remarkably reduce lymphatic tumor metastasis and greatly prolong animal survival. In addition, Cai et al. developed smart HSA–ICG nanoparticles for dual-modal imaging-guided tumor synergistic phototherapy [77]. The nanoparticles were prepared by a programmed assembly strategy, which used the intermolecular disulfide bonds as cross-linkers. The obtained nanoprobe exhibited excellent properties. For example, it could effectively maintain the biological activity of HSA without using exogenous cross-linkers and toxic chemicals. The encapsulation of dye in HSA NPs remarkably improved the stability of dye. HSA NPs enhanced delivery of ICG into cancer cells due to the active and passive tumor targeting. Therefore, when the ICG was used as NIR dye in this system, a dual-modal imaging and photodynamic–photothermal therapy system was developed. The HSA–ICG nanoprobe had a high accumulation and a long-term retention in tumor-bearing mice, where the tumor and its normal tissue margin were clearly identified via ICG-based *in vivo* near-infrared (NIR) fluorescence and photoacoustic dual-modal imaging and spectrum-resolved technology. Meanwhile, HSA–ICG NPs efficiently induced ROS and local hyperthermia simultaneously for synergetic PDT/PTT treatments under a single NIR laser irradiation. Therefore, HSA–ICG nanoprobe as smart theranostic nanoplatforms are highly potential for imaging-guided cancer phototherapy with PDT/PTT synergistic effects (Fig. 7.9).

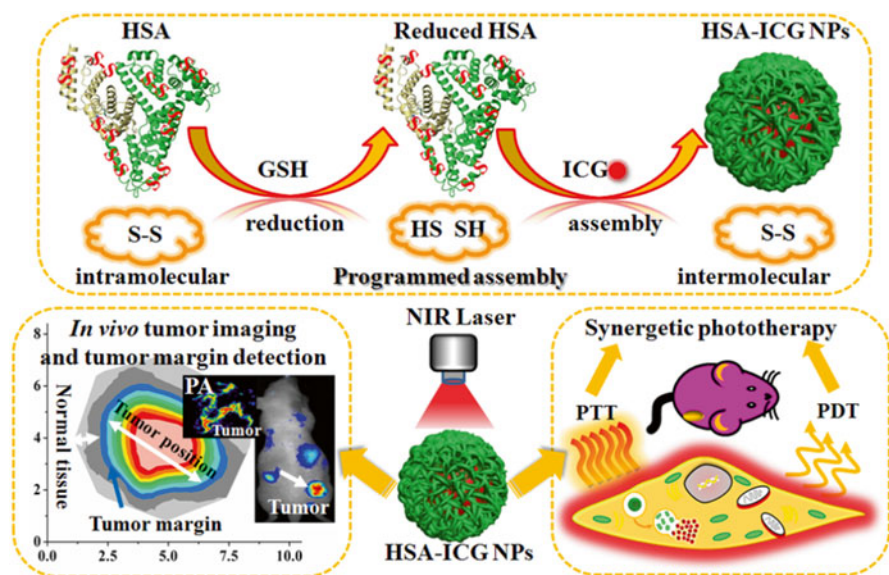


Fig. 7.9 Schematic illustration of HSA–ICG NPs for *in vivo* fluorescence and photoacoustic dual-modal imaging, tumor margin detection, and simultaneous PDT/PTT treatments (Reprinted with permission from ref. [77]. Copyright 2014, American Chemical Society)

7.6 Prospects and Outlook

In this section, we have systematically introduced the recent development of organic dye-based imaging-guided cancer therapy. The fluorescence and photoacoustic imaging and surgical therapy or phototherapies are summarized in detail. Different dye delivery systems are further discussed. Although the tremendous amount of exciting results are reported in the past few years in this field, there are still many challenges ahead toward further clinical applications of this technology: (1) The safety of dye delivery system. Although several reports have indicated that dye delivery systems, such as SiO₂ and CP nanoparticles, are not noticeably toxic in the tested dose ranges, it could still not be approved by the US FDA for clinical use. (2) The real-time monitoring of treatment process and therapeutic results. The current imaging technology is focused on the tumor diagnosis and paid little attention to monitoring the process, including treatment and prognosis processes. (3) Combination therapy. Single therapeutic approach has its own limitations. Therefore, the combination different treatment approaches may bring great opportunities to the new generation of cancer therapy.

References

1. Yuan A, Wu J, Tang X, Zhao L, Xu F, Hu Y (2013) Application of near-infrared dyes for tumor imaging, photothermal, and photodynamic therapies. *J Pharm Sci* 102:6–28
2. Luo S, Zhang E, Su Y, Cheng T, Shi C (2011) A review of NIR dyes in cancer targeting and imaging. *Biomaterials* 32:7127–7138
3. Frenette M, Hatamimoslehabadi M, Bellinger-Buckley S, Laoui S, La J, Bag S, Mallidi S, Hasan T, Bouma B, Yelleswarapu C, Rochford J (2014) Shining light on the dark side of imaging: excited state absorption enhancement of a Bis-styryl BODIPY photoacoustic contrast agent. *J Am Chem Soc* 136:15853–15856
4. Frangioni JV (2003) In vivo near-infrared fluorescence imaging. *Curr Opin Chem Biol* 7:626–634
5. Wang LV, Hu S (2012) Photoacoustic tomography: in vivo imaging from organelles to organs. *Science* 335:1458–1462
6. Sheng Z, Song L, Zheng J, Hu D, He M, Zheng M, Gao G, Gong P, Zhang P, Ma Y, Cai L (2013) Protein-assisted fabrication of nano-reduced graphene oxide for combined in vivo photoacoustic imaging and photothermal therapy. *Biomaterials* 34:5236–5243
7. Sheng Z, Hu D, Xue M, He M, Gong P, Cai L (2013) Indocyanine green nanoparticles for theranostic applications. *Nano-Micro Lett* 5:145–150
8. Mitsunaga M, Nakajima T, Sano K, Kramer-Marek G, Choyke PL, Kobayashi H (2012) Immediate in vivo target-specific cancer cell death after near infrared photoimmunotherapy. *BMC Cancer* 12:345
9. Jiang C, Cheng H, Yuan A, Tang X, Wu J, Hu Y (2014) Hydrophobic IR780 encapsulated in biodegradable human serum albumin nanoparticles for photothermal and photodynamic therapy. *Acta Biomater*. doi:10.1016/j.actbio.2014.11.041
10. Cheng C, He WW, Gong H, Wang C, Chen Q, Cheng ZP, Liu Z (2013) PEGylated micelle nanoparticles encapsulating a non-fluorescent near-infrared organic dye as a safe and highly-effective photothermal agent for in vivo cancer therapy. *Adv Fun Mater* 23:5893–5902

11. Wong BS, Yoong SL, Jagusiak A, Panczyk T, Ho HK, Ang WH, Pastorin G (2013) Carbon nanotubes for delivery of small molecule drugs. *Adv Drug Deliv Rev* 65:1964–2015
12. Wu X, Zhang F, Chen R, Zheng W, Yang X (2014) Recent advances in imaging-guided interventions for prostate cancers. *Cancer Lett* 349:114–119
13. Vahrmeijer AL, Huttemer M, van der Vorst JR, van de Velde CJ, Frangioni JV (2013) Image-guided cancer surgery using near-infrared fluorescence. *Nat Rev Clin Oncol* 10:507–518
14. Rahmathulla G, Recinos PF, Kamian K, Mohammadi AM, Ahluwalia MS, Barnett GH (2014) MRI-guided laser interstitial thermal therapy in neuro-oncology: a review of its current clinical applications. *Oncology* 87:67–82
15. van Dam GM, Themelis G, Crane LM, Harlaar NJ, Pleijhuis RG, Kelder W, Sarantopoulos A, de Jong JS, Arts HJ, van der Zee AG, Bart J, Low PS, Ntziachristos V (2011) Intraoperative tumor-specific fluorescence imaging in ovarian cancer by folate receptor- α targeting: first in-human results. *Nat Med* 17:1315–1319
16. Mohs AM, Mancini MC, Singhal S, Provenzale JM, Leyland-Jones B, Wang MD, Nie S (2010) Hand-held spectroscopic device for in vivo and intraoperative tumor detection: contrast enhancement, detection sensitivity, and tissue penetration. *Anal Chem* 82:9058–9065
17. Madajewski B, Judy BF, Mouchli A, Kapoor V, Holt D, Wang MD, Nie S, Singhal S (2012) Intraoperative near-infrared imaging of surgical wounds after tumor resections can detect residual disease. *Clin Cancer Res* 18:5741–5751
18. Mitsunaga M, Ogawa M, Kosaka N, Rosenblum LT, Choyke PL, Kobayashi H (2011) Cancer cell-selective in vivo near infrared photoimmunotherapy targeting specific membrane molecules. *Nat Med* 17:1685–1691
19. Nakajima T, Sano K, Choyke PL, Kobayashi H (2013) Improving the efficacy of photoimmunotherapy (PIT) using a cocktail of antibody conjugates in a multiple antigen tumor model. *Theranostics* 3:357–365
20. Mitsunaga M, Nakajima T, Sano K, Choyke PL, Kobayashi H (2012) Near-infrared theranostic photoimmunotherapy (PIT): repeated exposure of light enhances the effect of immunoconjugate. *Bioconjug Chem* 23:604–609
21. Nakajima T, Sano K, Mitsunaga M, Choyke PL, Kobayashi H (2012) Real-time monitoring of in vivo acute necrotic cancer cell death induced by near infrared photoimmunotherapy using fluorescence lifetime imaging. *Cancer Res* 72:4622–4628
22. Dorozhkin SV, Epple M (2002) Biological and medical significance of calcium phosphates. *Angew Chem Int Ed Engl* 41:3130–3146
23. Altinoğlu EI, Russin TJ, Kaiser JM, Barth BM, Eklund PC, Kester M, Adair JH (2008) Near-infrared emitting fluorophore-doped calcium phosphate nanoparticles for in vivo imaging of human breast cancer. *ACS Nano* 2:2075–2084
24. Barth BM, Sharma R, Altinoğlu EI, Morgan TT, Shanmugavelandy SS, Kaiser JM, McGovern C, Matters GL, Smith JP, Kester M, Adair JH (2010) Bioconjugation of calcium phosphosilicate composite nanoparticles for selective targeting of human breast and pancreatic cancers in vivo. *ACS Nano* 4:1279–1287
25. Barth BM, Altinoğlu EI, Shanmugavelandy SS, Kaiser JM, Crespo-Gonzalez D, DiVittore NA, McGovern C, Goff TM, Keasey NR, Adair JH, Loughran TP Jr, Claxton DF, Kester M (2011) Targeted indocyanine-green-loaded calcium phosphosilicate nanoparticles for in vivo photodynamic therapy of leukemia. *ACS Nano* 5:5325–5337
26. Yu J, Yaseen MA, Anvari B, Wong MS (2007) Synthesis of near-infrared-absorbing nanoparticle-assembled capsules. *Chem Mater* 19:1277–1284
27. Yu J, Javier D, Yaseen MA, Nitin N, Richards-Kortum R, Anvari B, Wong MS (2010) Self-assembly synthesis, tumor cell targeting, and photothermal capabilities of antibody-coated indocyanine green nanocapsules. *J Am Chem Soc* 132:1929–1938
28. Yaseen MA, Yu J, Jung B, Wong MS, Anvari B (2009) Biodistribution of encapsulated indocyanine green in healthy mice. *Mol Pharm* 6(5):1321–1332

29. Yaseen MA, Yu J, Wong MS, Anvari B (2008) In-vivo fluorescence imaging of mammalian organs using charge-assembled mesocapsule constructs containing indocyanine green. *Opt Express* 16:20577–20587
30. Quan B, Choi K, Kim YH, Kang KW, Chung DS (2012) Near infrared dye indocyanine green doped silica nanoparticles for biological imaging. *Talanta* 99:387–393
31. Sharma P, Bengtsson NE, Walter GA, Sohn HB, Zhou G, Iwakuma N, Zeng H, Grobmyer SR, Scott EW, Moudgil BM (2012) Gadolinium-doped silica nanoparticles encapsulating indocyanine green for near infrared and magnetic resonance imaging. *Small* 8:2856–2868
32. Lee CH, Cheng SH, Wang YJ, Chen YC, Chen NT, Souris J, Chen CT, Mou CY, Yang CS, Lo LW (2009) Near-infrared mesoporous silica nanoparticles for optical imaging: characterization and in vivo biodistribution. *Adv Funct Mater* 19:215–222
33. Cabral H, Matsumoto Y, Mizuno K, Chen Q, Murakami M, Kimura M, Terada Y, Kano MR, Miyazono K, Uesaka M, Nishiyama N, Kataoka K (2011) Accumulation of sub-100 nm polymeric micelles in poorly permeable tumours depends on size. *Nat Nanotechnol* 6:815–823
34. Murakami M, Cabral H, Matsumoto Y, Wu S, Kano MR, Yamori T, Nishiyama N, Kataoka K (2011) Improving drug potency and efficacy by nanocarrier-mediated subcellular targeting. *Sci Transl Med* 3:64ra2
35. Matsumura Y (2011) Preclinical and clinical studies of NK012, an SN-38-incorporating polymeric micelles, which is designed based on EPR effect. *Adv Drug Deliv Rev* 63:184–192
36. Matsumura Y (2008) Poly (amino acid) micelle nanocarriers in preclinical and clinical studies. *Adv Drug Deliv Rev* 60:899–914
37. Nishiyama N, Kataoka K (2006) Current state, achievements, and future prospects of polymeric micelles as nanocarriers for drug and gene delivery. *Pharmacol Ther* 112:630–648
38. Torchilin VP (2007) Micellar nanocarriers: pharmaceutical perspectives. *Pharm Res* 24:1–16
39. Kedar U, Phutane P, Shidhaye S, Kadam V (2010) Advances in polymeric micelles for drug delivery and tumor targeting. *Nanomedicine* 6:714–729
40. Wang R, Xiao R, Zeng Z, Xu L, Wang J (2012) Application of poly(ethylene glycol)-distearylphosphatidylethanolamine (PEG-DSPE) block copolymers and their derivatives as nanomaterials in drug delivery. *Int J Nanomedicine* 7:4185–4198
41. Chiu SJ, Marcucci G, Lee RJ (2006) Efficient delivery of an antisense oligodeoxyribonucleotide formulated in folate receptor-targeted liposomes. *Anticancer Res* 26:1049–1056
42. Yang X, Koh CG, Liu S, Pan X, Santhanam R, Yu B, Peng Y, Pang J, Golan S, Talmon Y, Jin Y, Muthusamy N, Byrd JC, Chan KK, Lee LJ, Marcucci G, Lee RJ (2009) Transferrin receptor-targeted lipid nanoparticles for delivery of an antisense oligodeoxyribonucleotide against Bcl-2. *Mol Pharm* 6:221–230
43. Xiong XB, Huang Y, Lu WL, Zhang X, Zhang H, Nagai T, Zhang Q (2005) Intracellular delivery of doxorubicin with RGD-modified sterically stabilized liposomes for an improved antitumor efficacy: in vitro and in vivo. *J Pharm Sci* 94:1782–1793
44. Allen TM (2002) Ligand-targeted therapeutics in anticancer therapy. *Nat Rev Cancer* 2:750–763
45. Zheng C, Zheng M, Gong P, Jia D, Zhang P, Shi B, Sheng Z, Ma Y, Cai L (2012) Indocyanine green-loaded biodegradable tumor targeting nanoprobes for in vitro and in vivo imaging. *Biomaterials* 33:5603–5609
46. Zheng M, Yue C, Ma Y, Gong P, Zhao P, Zheng C, Sheng Z, Zhang P, Wang Z, Cai L (2013) Single-step assembly of DOX/ICG loaded lipid – polymer nanoparticles for highly effective chemo-photothermal combination therapy. *ACS Nano* 7:2056–2067
47. Zhao P, Zheng M, Yue C, Luo Z, Gong P, Gao G, Sheng Z, Zheng C, Cai L (2014) Improving drug accumulation and photothermal efficacy in tumor depending on size of ICG loaded lipid-polymer nanoparticles. *Biomaterials* 35:6037–6046
48. Zheng X, Zhou F, Wu B, Chen WR, Xing D (2012) Enhanced tumor treatment using bifunctional indocyanine green-containing nanostructure by intratumoral or intravenous injection. *Mol Pharm* 9:514–522

49. Zheng X, Xing D, Zhou F, Wu B, Chen WR (2011) Indocyanine green-containing nanostructure as near infrared dual-functional targeting probes for optical imaging and photothermal therapy. *Mol Pharm* 8:447–456
50. Yokoyama M, Miyauchi M, Yamada N, Okano T, Sakurai Y, Kataoka K, Inoue S (1990) Characterization and anticancer activity of the micelle-forming polymeric anticancer drug adriamycin-conjugated poly(ethylene glycol)-poly(aspartic acid) block copolymer. *Cancer Res* 50:1693–1700
51. Chen H, Xiao L, Anraku Y, Mi P, Liu X, Cabral H, Inoue A, Nomoto T, Kishimura A, Nishiyama N, Kataoka K (2014) Polyion complex vesicles for photoinduced intracellular delivery of amphiphilic photosensitizer. *J Am Chem Soc* 136:157–163
52. Osada K, Christie RJ, Kataoka K (2009) Polymeric micelles from poly(ethylene glycol)-poly(amino acid) block copolymer for drug and gene delivery. *J R Soc Interface* 3:S325–S339
53. Yang H, Mao H, Wan Z, Zhu A, Guo M, Li Y, Li X, Wan J, Yang X, Shuai X, Chen H (2013) Micelles assembled with carbocyanine dyes for theranostic near-infrared fluorescent cancer imaging and photothermal therapy. *Biomaterials* 34:9124–9133
54. Guo M, Mao H, Li Y, Zhu A, He H, Yang H, Wang Y, Tian X, Ge C, Peng Q, Wang X, Yang X, Chen X, Liu G, Chen H (2014) Dual imaging-guided photothermal/photodynamic therapy using micelles. *Biomaterials* 35:4656–4666
55. Wan Z, Mao H, Guo M, Li Y, Zhu A, Yang H, He H, Shen J, Zhou L, Jiang Z, Ge C, Chen X, Yang X, Liu G, Chen H (2014) Highly efficient hierarchical micelles integrating photothermal therapy and singlet oxygen-synergized chemotherapy for cancer eradication. *Theranostics* 4:399–411
56. Zhang L, Zhang R, Somasundaran P (2006) Adsorption of mixtures of nonionic sugar-based surfactants with other surfactants at solid/liquid interfaces II. Adsorption of n-dodecyl-beta-D-maltoside with a cationic surfactant and a nonionic ethoxylated surfactant on solids. *J Colloid Interface Sci* 302:25–31
57. Kirchherr AK, Briel A, Mäder K (2009) Stabilization of indocyanine green by encapsulation within micellar systems. *Mol Pharm* 6:480–491
58. Musacchio T, Laquintana V, Latrofa A, Trapani G, Torchilin VP (2009) PEG-PE micelles loaded with paclitaxel and surface-modified by a PBR-ligand: synergistic anticancer effect. *Mol Pharm* 6:468–479
59. Deng J, Gao N, Wang Y, Yi H, Fang S, Ma Y, Cai L (2012) Self-assembled cationic micelles based on PEG-PLL-PLLeu hybrid polypeptides as highly effective gene vectors. *Biomacromolecules* 13:3795–3804
60. Wu L, Fang S, Shi S, Deng J, Liu B, Cai L (2013) Hybrid polypeptide micelles loading indocyanine green for tumor imaging and photothermal effect study. *Biomacromolecules* 14:3027–3033
61. Pitto-Barry A, Barry NPE (2014) Pluronic® block-copolymers in medicine: from chemical and biological versatility to rationalization and clinical advances. *Polym Chem* 5:3291–3297
62. Kim TH, Chen Y, Mount CW, Gombotz WR, Li X, Pun SH (2010) Evaluation of temperature-sensitive, indocyanine green-encapsulating micelles for noninvasive near-infrared tumor imaging. *Pharm Res* 27:1900–1913
63. Xu RX, Huang J, Xu JS, Sun D, Hinkle GH, Martin EW, Pivoski SP (2009) Fabrication of indocyanine green encapsulated biodegradable microbubbles for structural and functional imaging of cancer. *J Biomed Opt* 14:034020
64. Patel RH, Wadajkar AS, Patel NL, Kavuri VC, Nguyen KT, Liu H (2012) Multifunctionality of indocyanine green-loaded biodegradable nanoparticles for enhanced optical imaging and hyperthermia intervention of cancer. *J Biomed Opt* 17:046003
65. Zhen Z, Tang W, Chen H, Lin X, Todd T, Wang G, Cowger T, Chen X, Xie J (2013) RGD-modified apoferritin nanoparticles for efficient drug delivery to tumors. *ACS Nano* 7:4830–4837
66. Theil EC (1987) Ferritin: structure, gene regulation, and cellular function in animals, plants, and microorganisms. *Annu Rev Biochem* 56:289–315

67. Lin X, Xie J, Niu G, Zhang F, Gao H, Yang M, Quan Q, Aronova MA, Zhang G, Lee S, Leapman R, Chen X (2011) Chimeric ferritin nanocages for multiple function loading and multimodal imaging. *Nano Lett* 11:814–819
68. Liang M, Fan K, Zhou M, Duan D, Zheng J, Yang D, Feng J, Yan X (2014) H-ferritin-nanocaged doxorubicin nanoparticles specifically target and kill tumors with a single-dose injection. *Proc Natl Acad Sci U S A* 111:14900–14905
69. Zhen Z, Tang W, Guo C, Chen H, Lin X, Liu G, Fei B, Chen X, Xu B, Xie J (2013) Ferritin nanocages to encapsulate and deliver photosensitizers for efficient photodynamic therapy against cancer. *ACS Nano* 7:6988–6996
70. Garcia AM, Alarcon E, Muñoz M, Scaiano JC, Edwards AM, Lissi E (2011) Photophysical behaviour and photodynamic activity of zinc phthalocyanines associated to liposomes. *Photochem Photobiol Sci* 10:507–514
71. Huang P, Rong P, Jin A, Yan X, Zhang MG, Lin J, Hu H, Wang Z, Yue X, Li W, Niu G, Zeng W, Wang W, Zhou K, Chen X (2014) Dye-loaded ferritin nanocages for multimodal imaging and photothermal therapy. *Adv Mater* 26:6401–6408
72. Kratz F (2008) Albumin as a drug carrier: design of prodrugs, drug conjugates and nanoparticles. *J Control Release* 132:171–183
73. Kratz F, Elsadek B (2012) Clinical impact of serum proteins on drug delivery. *J Control Release* 161:429–445
74. Kratz F (2014) A clinical update of using albumin as a drug vehicle – a commentary. *J Control Release* 190:331–336
75. Chen Q, Liang C, Wang X, He J, Li Y, Liu Z (2014) An albumin-based theranostic nano-agent for dual-modal imaging guided photothermal therapy to inhibit lymphatic metastasis of cancer post surgery. *Biomaterials* 35:9355–9362
76. Chen Q, Wang C, Zhan Z, He W, Cheng Z, Li Y, Liu Z (2014) Near-infrared dye bound albumin with separated imaging and therapy wavelength channels for imaging-guided photothermal therapy. *Biomaterials* 35:8206–8214
77. Sheng Z, Hu D, Zheng M, Zhao P, Liu H, Gao D, Gong P, Gao G, Zhang P, Ma Y, Cai L (2014) Smart human serum albumin-indocyanine green nanoparticles generated by programmed assembly for dual-modal imaging-guided cancer synergistic phototherapy. *ACS Nano*. doi:10.1021/nn5062386

Part III
Dendrimers and Liposomes
for Theranostics

Chapter 8

Dendrimer-Based Nanodevices as Contrast Agents for MR Imaging Applications

Wenjie Sun, Jingchao Li, Mingwu Shen, and Xiangyang Shi

Abstract Dendrimers possess unique three-dimensional architectures, highly branched macromolecular characteristics, and abundant terminal functional groups. These properties of dendrimers afford their uses as a versatile nanoplatform to design multifunctional nanodevices for various biomedical applications, especially for magnetic resonance (MR) imaging of different biological systems. The periphery of dendrimers can be linked with targeting ligands and imaging agents, while the unique dendrimer interior and surface functionality render their uses to form dendrimer-entrapped metal nanoparticles (NPs) or dendrimer-assembled magnetic iron oxide NPs. The formed dendrimer-based contrast agents can be used for various MR imaging applications, including T_1 -weighted MR, T_2 -weighted MR, MR/computed tomography, MR/fluorescence imaging of blood pool, animal organs, and tumors. In particular, this chapter mainly introduces some recent advances of dendrimer-based contrast agents for MR imaging of cancer.

Keywords Dendrimers • Nanodevices • Contrast agents • MR imaging • Dual-modal imaging

W. Sun • X. Shi (✉)

State Key Laboratory for Modification of Chemical Fibers and Polymer Materials, College of Materials Science and Engineering, Donghua University, Shanghai 201620, People's Republic of China

College of Chemistry, Chemical Engineering and Biotechnology, Donghua University, Shanghai 201620, People's Republic of China
e-mail: xshi@dhu.edu.cn

J. Li • M. Shen (✉)

College of Chemistry, Chemical Engineering and Biotechnology, Donghua University, Shanghai 201620, People's Republic of China
e-mail: mwshen@dhu.edu.cn

8.1 Introduction

Dendrimers are recognized as synthetic macromolecules with unique three-dimensional architectures and highly branched macromolecular characteristics [1–3]. As compared to traditional linear polymers, dendrimers possess many outstanding advantages such as monodispersity, generation-dependent geometry, well-defined composition and architecture, highly branched inner cavity, and plentiful terminal functional groups [2, 4–8]. These properties of dendrimers render their uses as a multifunctional nanoplatform for surface modification or conjugation with targeting ligands and imaging agents, for entrapment of metal nanoparticles (NPs), and for stabilizing or assembling magnetic NPs [9–11] for various biomedical applications, especially in magnetic resonance (MR) imaging of different biological systems [12]. The structures of several commonly used dendrimers are shown in Fig. 8.1 [13].

MR imaging is a powerful, noninvasive imaging technique for disease diagnosis [14–17] due to its attractive advantages, including a nonionizing radiation source, tomographic capabilities, and high spatial resolution between different soft tissues [9, 18–23]. However, one of the major drawbacks of MR imaging is its limited sensitivity and specificity [23, 24]. For high-quality MR imaging applications,

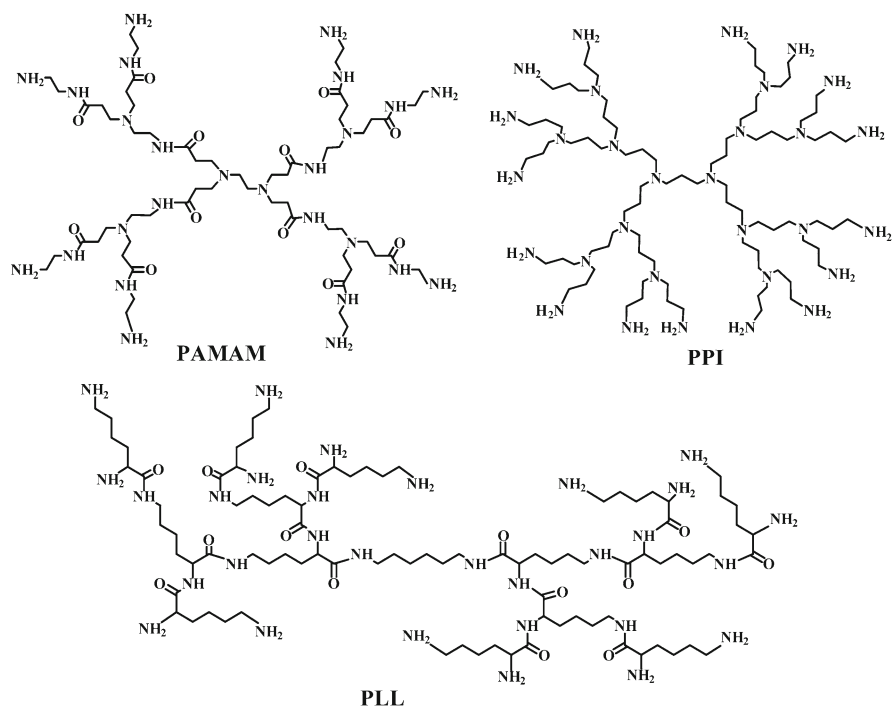


Fig. 8.1 The structures of several commonly used dendrimers (Reproduced with permission from Ref. [13], Copyright 2014 Elsevier)

contrast agents have to be used. The commonly used MR contrast agents can be divided into two types: paramagnetic gadolinium (Gd)- or manganese (Mn)-based T_1 MR imaging contrast agents and superparamagnetic iron oxide NP- or lanthanide ion-based T_2 MR imaging contrast agents [25–30]. For T_1 MR imaging, the low molecular weight (Mw) Gd(III) complexes such as Gd(III)-DTPA (diethylenetriaminepentaacetic acid) or Gd(III)-DOTA (1,4,7,10-tetraazacyclododecane-1,4,7,10-tetraacetic acid) approved by the FDA possess rapid clearance rates from vascular circulation, fast renal excretion, and relatively low relaxivity [31]. For T_2 MR imaging, superparamagnetic iron oxide (IO) NPs have been widely developed as negative contrast agents due to their high relaxivity and biocompatibility [32]. However, these magnetic NPs usually suffer a problem of colloidal instability [33, 34]. Therefore, dendrimer-based nanotechnology has been developed to prepare various T_1 - and T_2 -weighted MR contrast agents that can overcome the above drawbacks.

This chapter mainly highlights some recent advances in dendrimer-based nanodevices as contrast agents for different MR imaging applications. In particular, two types of MR imaging contrast agents including dendrimer-Gd complexes and dendrimer-functionalized iron oxide NPs will be introduced in detail. Moreover, this review also provides a brief survey of several dendrimer-based multifunctional systems for dual-modal MR/CT and MR/fluorescence imaging applications. It should be emphasized that this is not a comprehensive review to cover all aspects of the dendrimer-based MR contrast agents, but rather discusses the key developments of various dendrimer-based nanodevices for MR imaging of different biological systems, in particular MR imaging of cancer.

8.2 Dendrimer-Based Complexes for T_1 -Weighted MR Imaging

Based on the advantages of the well-defined structure and multifunctional surface groups, dendrimers have been widely developed as novel T_1 -positive macromolecular MR contrast agents. Herein, this section presents a brief overview of dendrimer-based complexes (including dendrimer-Gd complexes and dendrimer-Mn complexes) for T_1 MR imaging applications.

8.2.1 Dendrimer-Gd Complexes

8.2.1.1 Dendrimer-Gd Complexes

Poly(amidoamine) (PAMAM) dendrimers have been used to prepare macromolecular Gd complexes. In an earlier work, Wiener et al. [35] first modified the PAMAM dendrimers of different generations with 2-(4-isothiocyanatobenzyl)-6-methyldiethylenetriaminepentaacetic acid (1B4M-DTPA) via a thiourea linkage. Then, Gd(III)

ions were chelated to synthesize the PAMAM-DTPA-Gd nanocomplexes for MR imaging applications. The results showed that the r_1 relaxivity of generation 6 (G6) PAMAM dendrimer-based nanocomplexes was much higher than that of DTPA-Gd complexes, suggesting that the PAMAM-DTPA-Gd nanocomplexes have the potential to be used for MR imaging applications. Afterwards, the Kobayashi group investigated a series of dendrimeric Gd-based MR imaging contrast agents by conjugation of DTPA with PAMAM dendrimers of different generations, followed by Gd(III) chelation. The authors' work shows that dendrimer-Gd complexes can be used as contrast agents for MR imaging of different biosystems, such as functional renal imaging [36], blood pool imaging [37, 38], liver imaging [39], and lymphatic imaging [40]. The different uses of the dendrimer-Gd complexes are largely dependent on the number of the dendrimer generation.

The above dendrimer-Gd nanocomplexes are commonly excreted via the liver or kidneys, thus having decreased plasma concentrations. Additionally, the size of the dendrimer and the surface charge also influence the overall biodistribution of the dendrimeric Gd-based contrast agents [38, 41, 42]. Therefore, some surface modifications of these contrast agents have been explored. For instance, polyethylene glycol (PEG) modification (PEGylation) has been used to render the nanodevices with improved hydrophilicity and reduced recognition by the reticuloendothelial system (RES), resulting in a longer half-life in blood circulation and lower immunogenicity [43, 44]. Therefore, PEGylation of dendrimers has been considered to be a useful strategy to improve the pharmacokinetics of the dendrimeric nanodevices for MR imaging applications [43, 45]. For instance, Kobayashi and coworkers [43] prepared the PEGylated PAMAM dendrimer-Gd complexes by conjugating both PEG and chelator to the terminal groups of dendrimers. This synthesis method is possible to impact the uniformity of the dendrimers. In another work, Kono et al. [46, 47] developed a fully PEGylated dendrimeric MR contrast agent to improve the homogeneity of the device. Their results show that the PEGylation modification is advantageous in lowering the toxicity and improving the retention of the device in the circulation with decreased rates of nonspecific renal and hepatic uptake. In addition, the dendrimer generation and the PEG chain length were found to impact on the relaxivity of the PEGylated PAMAM Gd-DTPA complexes [48]. Shorter PEG chain length and higher dendrimer generation rendered the dendrimer-Gd complexes with higher r_1 relaxivity.

Although dendrimer-Gd nanocomplexes have been well developed for MR imaging applications, their translation to clinical trials has been quite limited due to their potential toxic side effects and the occurrence of nephrogenic systemic fibrosis (NSF) [49]. In order to minimize the toxicity of the Gd ions while maintaining the favorable imaging performance of the dendrimeric nanodevices, biodegradable dendrimers having disulfide bonds in the molecular backbones have been reported to be used for the design of MR contrast agents [50, 51]. Recently, Huang et al. [52] developed a facile method to synthesize size-controllable and biodegradable Gd-complexed dendrimer nanoclusters for MR imaging applications (Fig. 8.2). The biodegradable polydisulfide dendrimer nanoclusters possessed a circulation half-life of >1.6 h in mice and displayed significant contrast enhancement in the

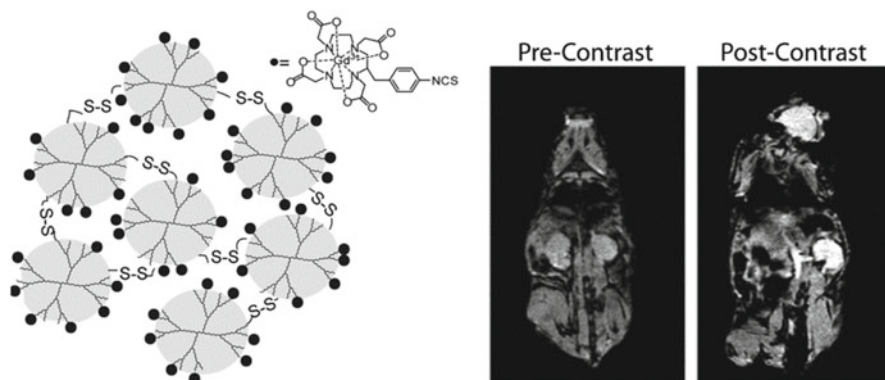


Fig. 8.2 Schematic representation of Gd-labeled polydisulfide dendrimer clusters (DNCs) and corresponding MR images of nu/nu nude mice before and after the tail vein injection of polydisulfide DNCs (Reproduced with permission from Ref. [52], Copyright 2012 Elsevier)

abdominal aorta and kidneys for as long as 4 h. What's more, the dendrimer nanoclusters gradually degraded into smaller components under physiological conditions, which greatly facilitated their renal clearance.

Besides the use of PAMAM dendrimers to construct MR contrast agents, other types of dendrimers such as triazine dendrimers, polypropylenimine (PPI) dendrimers, and peptide dendrimers [53] have also been used for MR imaging applications. Lim and coworkers [54, 55] described a series of MR imaging contrast agents based on monodisperse triazine dendrimers of two different generations (G3 and G5), including four kinds of Gd-based contrast agents, G3-(Gd-DOTA)₂₄, G5-(Gd-DOTA)₉₆, G3-(Gd-DTPA)₂₄, and G5-(Gd-DTPA)₉₆. Two G3 dendrimer-based agents showed a shorter half-life in blood and more rapid renal excretion than the G5 counterparts. In addition, the DOTA-chelated agents, G3-(Gd-DOTA)₂₄ and G5-(Gd-DOTA)₉₆, had better r_1 relaxivity than the corresponding DTPA-chelated ones. Meanwhile, a series of Gd-DTPA-functionalized PPI dendrimers have been also reported [17, 37, 56–58] to be promising MR contrast agents. For example, Kobayashi et al. [37] demonstrate that PPI dendrimer-based MR contrast agents are cleared more rapidly from the body than PAMAM dendrimer-based agents with the same numbers of branches. Langereis et al. [56–58] reported a series of Gd(III) DTPA-based PPI dendrimers employing an isocyanate-activated lysine-based DTPA chelates. These dendrimeric devices had a significantly increased r_1 relaxivity, which is about 4.7 times of the traditional Gd-DTPA complexes.

8.2.1.2 Multifunctional Dendrimer-Gd Complexes for Targeted Tumor MR Imaging

All of the dendrimer-Gd nanocomplexes mentioned above can be used as good positive contrast agents for MR imaging. However, they do not have the high affinity to specific cancer cells, which limits their applications for diagnosis of tumor only

through passive enhanced permeability and retention (EPR) effect [59]. For targeted tumor MR imaging, it is essential to modify specific targeting ligands on the surface of the dendrimer-Gd nanocomplexes [17]. The commonly used targeting ligands that have been conjugated to the surface of dendrimers include monoclonal antibodies [60, 61], peptides [62, 63], folic acid (FA) [9, 64], polysaccharides [65], proteins [66], and oligo-nucleotides [67].

FA is one of the most studied cancer-targeting ligands for targeted MR imaging applications because it has a high affinity to FA receptors (FAR) over-expressed in several human carcinomas [68]. Swanson et al. [64] prepared a FA-targeted dendrimeric MR imaging contrast agent via conjugating FA and Gd-DOTA onto the surface of G5 PAMAM dendrimers. The targeted device of Gd-DOTA-G5-FA displayed significantly higher MR contrast enhancement in the KB (a human epithelial carcinoma cell line) xenografted tumor than the nontargeted device of Gd-DOTA-G5 without FA. What's more, the strong tumor MR signal enhancement of the mice treated with the targeted device was able to remain for 24 h and then slowly decreased from 24 to 48 h, while the tumor MR signal enhancement of the mice treated with the nontargeted device just presented only for 1 h. In another work, Chen et al. [69] reported another FA-targeted MR contrast agent by conjugating FA and Gd-DTPA onto PEG-cored dendrimers with 16 functional hydroxyl groups. The cellular uptake experiments demonstrated that the KB tumor had a significantly enhanced uptake of FA-targeted device than the nontargeted one. In the dynamic contrast-enhanced MR imaging, KB cells showed a delayed contrast washout pattern after injection of the FA-targeted device when compared to the FAR-negative HT-1080 tumor. These studies indicate that FA-modified dendrimeric Gd complexes enable targeted T_1 -weighted MR imaging of FAR-positive tumors.

Peptide ligands [62] can also be linked onto the surface of dendrimers for targeted MR imaging of cancer. Recently, Tan and coworkers [63] synthesized and evaluated a cyclic decapeptide CGLIIQKNEC (CLT1)-targeted MR imaging agent via conjugating Gd-DOTA and the CLT1 peptide onto the surface of G2 and G3 nanoglobular lysine dendrimers with a cubic silsesquioxane core. They found that the CLT1 peptide modification enabled the nanoglobular agents to have greater contrast enhancement in MDA-MB-231-bearing female athymic mice than the corresponding nontargeted agents at 0.03 mmol/kg of Gd. Many other studies also confirmed the advantages to use targeted dendrimeric contrast agents for specific imaging of different types of tumors [70, 71]. Therefore, the targeted dendrimeric Gd-based contrast agents are promising for specific tumor MR imaging.

8.2.2 Dendrimer-Based Mn Complexes

Although Gd-based contrast agents are well-tolerated by a majority of patients, there are increasing reports of the toxic side effects with impaired renal function named NSF. Therefore, non-Gd-based contrast agents have been emerging. Since

Mn^{2+} is another cation that can change the relaxation of water protons, Mn-based complexes have been widely studied among the non-Gd-based contrast agents for MR imaging applications. The Mn-based materials include ionic manganese (MnCl_2) [72], manganese oxides (MnO [27, 73], MnO_2 [74], Mn_3O_4 [26, 75]), chelated manganese [76], polydisulfide Mn complexes [77], and dendrimer-based Mn complexes [78, 79]. In this section, we focus on the dendrimer-based Mn complexes for MR imaging applications.

Bertin et al. [78] evaluated a new dendritic Mn-DTPA complex as a Mn-based MR imaging contrast agent via *in vitro* and *in vivo* studies. In their research, the comparison between the dendritic Gd complex using the same synthetic method and the two commercial MR imaging contrast agents (Gd-DTPA and Mn(II)-dipyridoxal diphosphate (Mn-DPDP)) was made to determine the influence of the paramagnetic ion on the toxicity and relaxivity and the potential application of the dendritic Mn-DTPA complex for brain MR imaging. The authors showed that the dendritic Mn-DTPA complex possessed better r_1 relaxivity than the commercial Mn-DPDP agents and could be used for MR imaging of the neurological diseases such as Alzheimer or Parkinson. In another work, Tan and coworkers [80] also investigated the nanoglobular poly-L-lysine dendrimer-based Mn complexes for tumor MR imaging by conjugating a CLT1 peptide and Mn-DOTA complex onto the surface of G3 dendrimers (Fig. 8.3a). The authors showed that the peptide targeting enabled significant MR signal enhancement in breast tumor-bearing mice at a low dose of Mn (0.03 mmol/kg) when compared to the nontargeted device (Fig. 8.3b). In the authors' following work [81], nanoglobular DOTA-Mn and nanoglobular NOTA-Mn (1, 4, 7-triazacyclononane-1, 4, 7-triacetic acid) complexes were synthesized to investigate the impact of the type of ligand on the relaxivity and tumor contrast enhancement, as well as the influence of the dendrimer generation on the performance of their DOTA-Mn complexes in MR imaging. The authors showed that the r_1 relaxivities of G2, G3, and G4 nanoglobular-based DOTA-Mn complexes were measured to be 3.32, 2.8, and 2.4 $\text{mM}^{-1} \text{s}^{-1}$, respectively, which are much higher than that of free MnCl_2 . The higher-generation dendrimer led to less r_1 relaxivities, probably due to the limited access of water protons to the paramagnetic Mn(II) ions within the ligands modified onto the dense dendrimer terminal groups, and it may be also possible that the DOTA chelates are buried in the G3 or G4 dendrimers and less accessible to solvation as compared to the G2 dendrimer. In addition, the r_1 relaxivity of the G3-NOTA-Mn complex was 3.80 $\text{mM}^{-1} \text{s}^{-1}$, higher than that of the G3-DOTA-Mn complexes due to a bound water molecule in the inner solvation site. The Mn-based nanoglobular agents of different dendrimer generations displayed effective enhanced contrast in the tumor imaging. All these data suggest that dendrimer-Mn complexes might be used as promising non-Gd-based contrast agents for MR imaging.

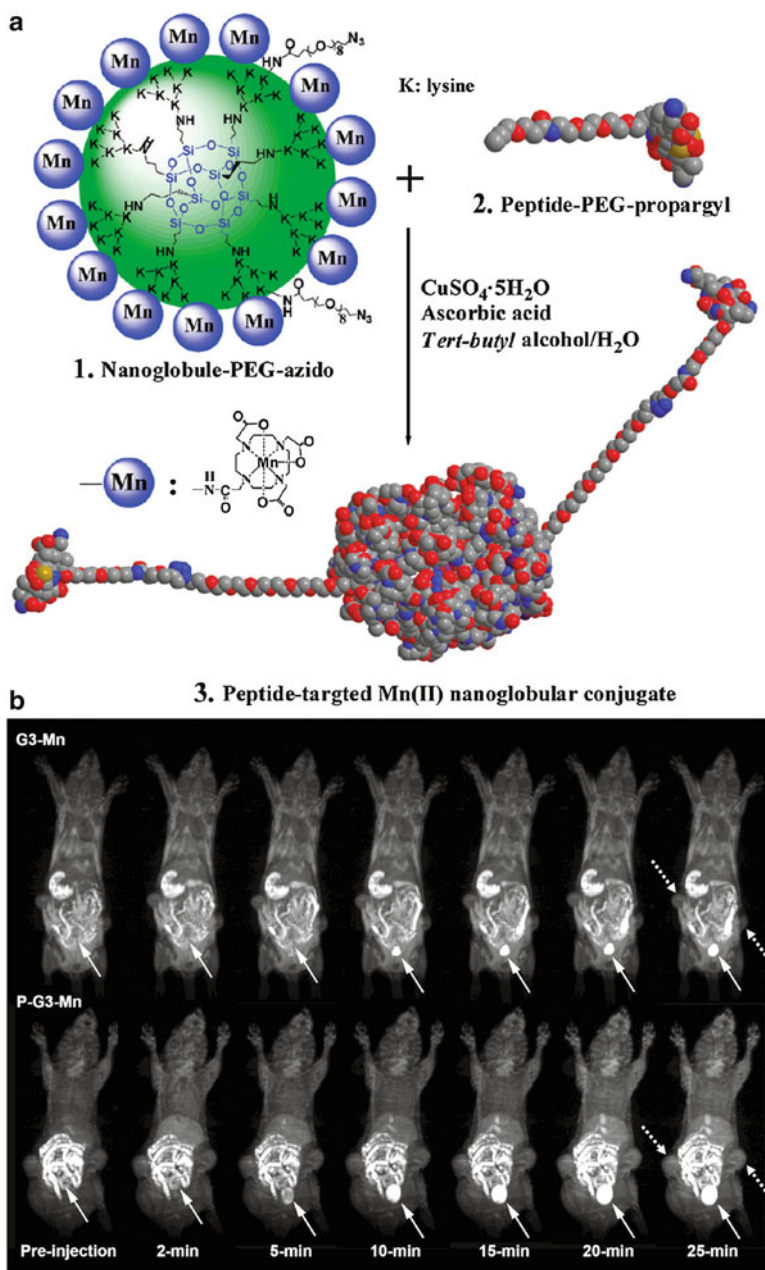


Fig. 8.3 (a) Synthetic scheme of a peptide CLT1-targeted nanoglobular Mn(II)-DOTA conjugate via click chemistry; (b) Representative 3D maximum intensity projection images (T_1 -weighted) of a tumor-bearing mouse injected with G3-DOTA-Mn (G3-Mn) and peptide CLT1-targeted G3-DOTA-Mn (P-G3-Mn) nanoglobular MRI contrast agent at $30 \mu\text{mol-Mn/kg}$ (*solid arrows* show urinary bladder and *dashed arrows* show tumor) (Reproduced with permission from Ref. [80], Copyright 2010 American Chemical Society)

8.3 Dendrimer-Based Iron Oxide Nanoparticles for T₂-Weighted MR Imaging

8.3.1 Dendrimer-Based Iron Oxide Nanoparticles

Besides dendrimer-based Gd or Mn complexes as positive contrast agents for T₁-weighted MR imaging, dendrimers can also be used to modify IO NPs to develop T₂-weighted negative MR imaging contrast agents. Dendrimers can be used as a stabilizer to induce the in situ formation of IO NPs and can be assembled onto preformed IO NPs for MR imaging [28, 82–84] to diagnose diseases or track transplanted cells after the intracellular magnetic labeling. The major difference between dendrimer-stabilized IO NPs and dendrimer-assembled IO NPs is that the former involves the in situ formation of IO NPs in the presence of dendrimers, while the latter involves the assembly of dendrimers or functionalized dendrimers onto preformed IO NPs.

8.3.1.1 Dendrimer-Stabilized IO NPs

Due to the abundant surface functional groups, dendrimers can be used to stabilize the formation of the IO NPs. For example, Strable et al. [82] reported the synthesis of highly water-soluble nanocomposites of ferromagnetic IO NPs using PAMAM dendrimers as stabilizers. In their work, the carboxylated G4.5 PAMAM dendrimers were utilized to stabilize the ferrimagnetic IO NPs under a mild condition. They demonstrate that electrostatic interaction between negatively charged carboxylated PAMAM dendrimers and the positively charged IO NPs plays an important role in the stabilization process. The formed dendrimer-stabilized IO NPs have good colloidal stability and strong effect on the relaxation of water protons, making them promising for MR imaging applications.

Bulte and colleagues [30] used the synthesized magnetodendrimers to label human neural stem cells through a nonspecific membrane adsorption process with subsequent intracellular localization in endosomes. The incubated magnetodendrimer doses as low as 1 mg iron/mL allowed sufficient MR cell contrast without effecting the cell viability and differentiation. The labeled neural stem cells could be easily detected in vivo by MR imaging at least 6 weeks after transplantation. Then the magnetodendrimers were used to track the olfactory ensheathing glia grafted into the rat spinal cord [85] and to detect the murine and human skin stem/progenitor cells [86] by MR imaging. However, one major problem related to the utilized magnetodendrimers is the lack of targeting ligand modifications, limiting their applications in specific MR imaging of different biological systems.

8.3.1.2 Dendrimer-Assembled IO NPs

Beyond the role of stabilizer played by dendrimers in the in situ formation of IO NPs, preformed IO NPs can also be assembled with dendrimers to form dendrimer-assembled NPs. Furthermore, in order to achieve the specific targeted MR imaging of cancer cells in vitro and in vivo, it is necessary to assemble targeting ligand-functionalized dendrimers onto the surface of preformed IO NPs.

In one of our previous studies [28], a group of FA-modified carboxyl-functionalized G3 PAMAM dendrimers were synthesized and then assembled onto the surface of IO NPs synthesized using a controlled coprecipitation of Fe(II) and Fe(III) ions through electrostatic interaction, aiming to achieve specific targeted MR imaging of KB cells overexpressing FAR. Unfortunately, due to the excess peripheral carboxylic groups of the dendrimers, the receptor-mediated endocytosis of IO NPs assembled with FA-modified dendrimers was not facilitated. To render the IO NPs with targeting specificity, Wang et al. assembled a bilayer of negatively charged polystyrene sulfonate sodium salt (PSS) and positively charged G5 dendrimers prefunctionalized with fluorescein isothiocyanate (FI) and FA (G5.NH₂-FI-FA) via electrostatic layer-by-layer (LbL) deposition, followed by acetylation of the remaining dendrimer terminal amines [84]. The formed dendrimer-assembled IO NPs are able to be used for targeted MR imaging of cancer cells overexpressing FAR in vitro, but with limited success in vivo possibly due to the fact that the used PSS polymer is not biocompatible and the bilayers formed via electrostatic assembly may not be sufficiently stable. In a following study, we assembled IO NPs with multilayers of biocompatible poly(glutamic acid) (PGA) and poly(L-lysine) (PLL), followed by assembling with G5.NH₂-FI-FA PAMAM dendrimers [83]. The multilayers were then cross-linked via EDC chemistry, and the remaining dendrimer terminal amines were acetylated. The fabricated shell cross-linked IO (SCIO) NPs were water soluble and stable and displayed good biocompatibility in a given concentration range. After injection of the targeted SCIO-FA or nontargeted SCIO-NonFA NPs into the tumor-bearing mice, the in vivo MR imaging of tumors was performed (Fig. 8.4). We show that after 24 h injection of the SCIO-FA NPs, the tumor MR signal intensity is decreased more significantly than the injection with the nontargeted SCIO-NonFA NPs at the same time point. These data demonstrate that the developed SCIO-FA NPs are able to be used for targeting MR imaging of KB tumor model in vivo.

8.3.2 Dendrimer-Modified Lanthanide T₂ MR Imaging Contrast Agents

In addition to superparamagnetic IO NPs used for T₂-weighted MR imaging, lanthanide ions can also be explored for T₂ MR imaging [87, 88]. In a recent study, Klemm et al. [89] reported the synthesis of dendrimer-based T₂ lanthanide MR imaging

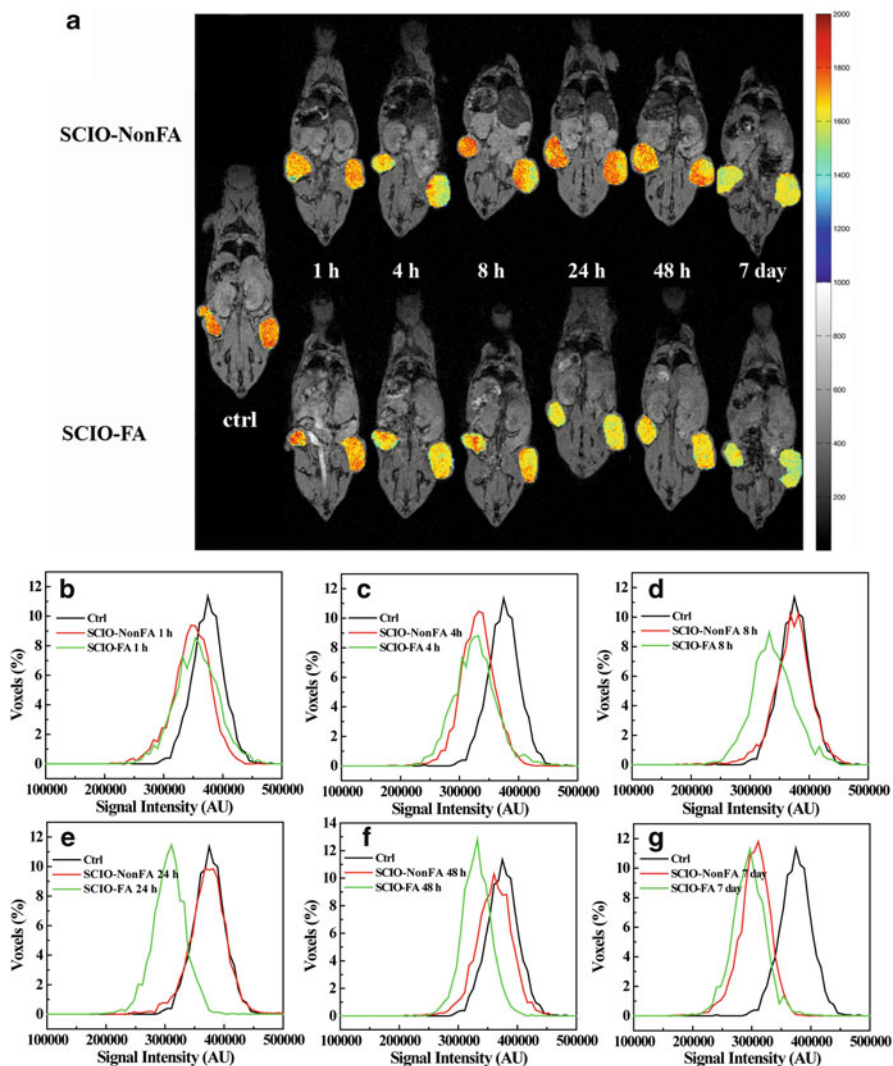


Fig. 8.4 In vivo MR imaging of tumor. In vivo color maps (a) of T₂-weighted MR images of mice implanted with cancer cell line KB cells, at different time points after injection of SCIO-NonFA and SCIO-FA NPs, respectively. The color bar (from red to blue) indicates the MR signal intensity changes from high to low. Comparison of statistically normalized histograms of the voxel intensities (whole tumor) from targeted SCIO-FA (green histogram) and nontargeted SCIO-NonFA (red histogram) NPs at the time points of 1 h (b), 4 h (c), 8 h (d), 24 h (e), 48 h (f), and 7 days (g) (Reproduced with permission from Ref. [83], Copyright 2008 Wiley-VCH Verlag GmbH & Co. KGaA)

probes with good biocompatibility and high r_2 relaxivity. The lanthanide ions were firstly complexed with TREN-bis(1-methyl-3,2-HOPO)-TAM-ethylamine ligand, then the formed complexes were covalently attached to the esteramide (EA) or PLL dendrimer by an amidation reaction. The relaxivity of these dendrimer-based lanthanide complexes can be as high as $374 \text{ mM}^{-1}\text{s}^{-1}$ per dendrimer. The high relaxivities, bioavailability, and low in vitro toxicity render the dendrimer-based lanthanide agents with promising potential to be used for T_2 MR imaging of different biological systems.

8.4 Dendrimer-Based Systems for Dual Modality Imaging

With the rapid development of nanoscience and nanotechnology, various nanodevices have been successfully developed for different molecular imaging applications, including MR imaging, position emission tomography (PET) imaging, computed tomography (CT) imaging, optical imaging, and single photon emission computed tomography (SPECT) imaging. However, each imaging modality possesses its own limitations and weaknesses, and none of them is able to provide complete structural and functional information independently [90]. It is highly desirable to combine other imaging modes with MR imaging to develop various dual-modal contrast agents such as MR/fluorescence [91], MR/PET [92], MR/CT [25, 90], and MR/optical imaging [93].

The unique three-dimensional architectures and abundant terminal groups afford dendrimers with the ability to encapsulate different NPs in their interior or covalently conjugate functional molecules on their surfaces, thereby allowing for generation of various multifunctional nanodevices for the diagnosis applications of different biological systems. Herein, we discuss some recent key developments in the use of dendrimers as a versatile platform for dual-mode MR/CT and MR/fluorescence imaging applications.

8.4.1 Dendrimer-Based Dual-Mode MR/CT Imaging Contrast Agents

Dendrimers have been known to be able to entrap or stabilize some noble metal NPs (Au or Ag) for CT imaging applications [94, 95]. With the ability to conjugate Gd chelator to form dendrimeric Gd-based T_1 MR contrast agents and to conjugate PEG on the dendrimer periphery to improve the pharmacokinetics and biocompatibility of dendrimers [96], it is highly desirable to develop dendrimer-based MR/CT contrast agents for dual-mode accurate diagnosis of different biological systems.

In a recent study, Wen et al. [25] reported a facile approach to synthesizing Gd-loaded dendrimer-entrapped Au NPs (Gd-Au DENPs) for dual-mode MR/CT

imaging applications. In their work, G5 PAMAM dendrimers covalently attached with DOTA and PEG monomethyl ether (*m*PEG) were used as templates to synthesize Au NPs. Followed by sequential chelation of Gd(III) and acetylation of the remaining dendrimer terminal amine groups, multifunctional Gd-Au DENPs were formed and characterized to have a r_1 relaxivity of $1.05 \text{ mM}^{-1}\text{s}^{-1}$ due to the loaded Gd(III) ions and excellent X-ray attenuation property due to the entrapped Au NPs as well as the chelated Gd(III). The formed Gd-Au DENPs enabled MR/CT dual-mode imaging of the heart, liver, kidney, and bladder of rat or mouse within a time frame of 45 min. Likewise, in vivo biodistribution studies reveal that the developed Gd-Au DENPs have a prolonged blood circulation time and can be cleared from the major organs within 24 h.

By taking into consideration the unique structural characteristics of the dendrimers that can also be further functionalized with various targeting ligands (e.g., FA or RGD peptide), Chen et al. [97] reported the synthesis and characterization of FA-targeted multifunctional Au DENPs loaded with Gd(III) for targeted dual-mode MR/CT imaging of tumors. Compared to the study reported by Wen et al. [25], simply modifying PEGylated FA and *m*PEG was able to afford the formation of the FA-targeted Gd-Au DENPs. The formed Gd-Au DENPs-FA displayed reasonable r_1 relaxivity and excellent X-ray attenuation intensity due to the coexistence of Au NPs and Gd(III) ions within the single multifunctional nanodevice (Fig. 8.5a–d). More importantly, the developed dendrimeric nanoprobe can be used for targeted CT and MR imaging of FAR-expressing tumors via FA-mediated targeting pathway (Fig. 8.5e–h).

Besides the formation of T_1 MR/CT dual-mode contrast agents, T_2 MR/CT dual-mode contrast agents can also be constructed via the versatile dendrimer nanotechnology. In our another work, we have shown that Au DENPs are able to be assembled onto preformed IO NPs via an LbL assembly approach [98]. The results of T_2 relaxometry and X-ray attenuation measurements show that the formed Fe_3O_4 @Au nanocomposite particles (NCPs) have a r_2 relaxivity of $71.55 \text{ mM}^{-1}\text{s}^{-1}$ and enhanced X-ray attenuation property. Therefore, the developed Fe_3O_4 @Au NCPs are able to be used as contrast agents for dual-mode T_2 MR imaging and CT imaging of cancer cells in vitro and MR imaging of mouse liver and CT imaging of a subcutaneous tissue in vivo (Fig. 8.6). This study suggests that the developed Fe_3O_4 @Au NCPs may be able to be applied for dual-mode MR/CT imaging of different biological systems.

8.4.2 Dendrimer-Based MR/Fluorescence Dual-Mode Imaging Applications

Various fluorescent dyes such as fluorescein isothiocyanate (FITC) [99], tetramethylrhodamine-5-isothiocyanate (TRITC) [100], Cy5 [101], and Cy5.5 [102] have been utilized for fluorescence imaging. By using dendrimers as a unique

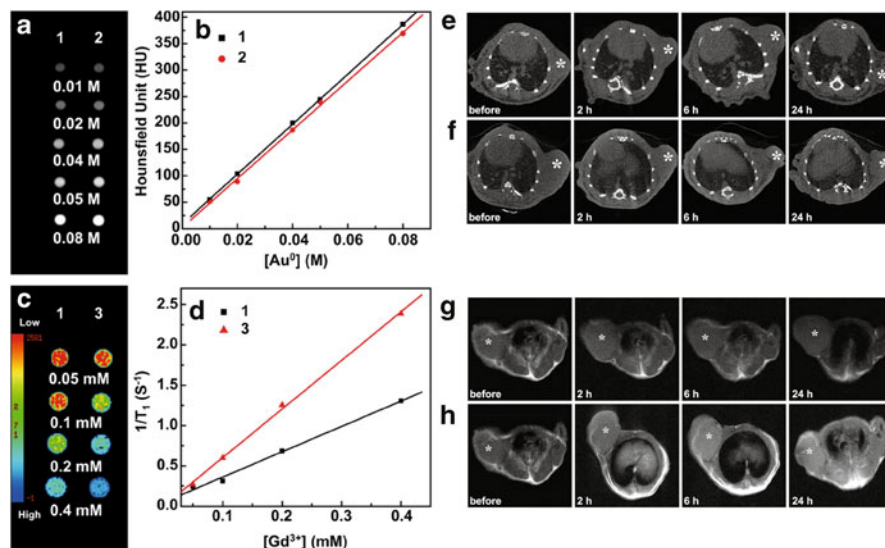


Fig. 8.5 The CT images (a) and X-ray attenuation (HU) (b) of Gd-Au DENPs-FA (1) and Au DENPs-FA (2) at different Au concentrations. c and d show the T_1 MR phantom images and the linear fitting of the inverse T_1 of Gd-Au DENPs-FA (1) and G5-Gd-FA (3) as a function of Gd concentration. Representative transection CT (e, f) and MR (g, h) images of mice bearing transplanted KB tumors after intravenous injection of the nontargeted Gd-Au DENPs (e, g) and targeted Gd-Au DENPs-FA (f, h) at different time points (Reproduced with permission from Ref. [97], Copyright 2013 Elsevier)

platform, both fluorescence dye and MR imaging elements can be coupled to a single nanoparticulate system for dual-mode MR/fluorescence imaging applications.

The dendrimer terminal amines can be used to attach both Gd(III) chelates and fluorescence dye molecules, rendering them with dual-mode MR/fluorescence imaging property. For instance, Brechbiel and coworkers [61] described a biotinylated dendrimer-based imaging agent modified with both rhodamine green and DTPA chelates for targeted MR/fluorescence imaging of ovarian cancer cells. In this work, dendrimers were linked by a disulfide bridge, which could be cleaved and coupled to a maleimide functionalized biotin. The *in vivo* experiment with mice bearing ovarian tumors demonstrates that the dendrimer-based nanodevice can efficiently target and deliver sufficient amounts of chelated Gd(III) and fluorophores to the tumor site, enabling effective dual-mode MR/fluorescence imaging of tumors. In another study, Talanov et al. [103] selected a near-infrared dye Cy5.5 to label the Gd(DTPA)-conjugated G6 PAMAM dendrimers. The use of Cy5.5 dye is quite advantageous over other fluorophores due to the increased imaging penetration through living tissue and reduced background interference. The formed dendrimeric nanodevice is able to be used as a nanoprobe for dual-mode MR/fluorescence imaging of sentinel lymph nodes in mice (Fig. 8.7).

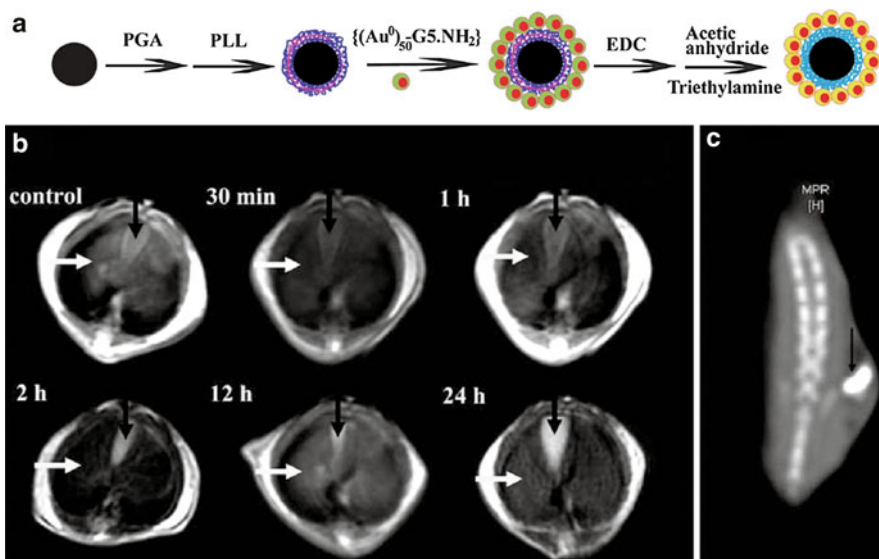


Fig. 8.6 (a) Schematic representation of the fabrication of $\text{Fe}_3\text{O}_4@\text{Au}$ NCPs. (b) T_2 -weighted images of mouse liver before and after intravenous injection of 0.1 mL $\text{Fe}_3\text{O}_4@\text{Au}$ NCPs ($[\text{Fe}] = 8.82 \text{ mg mL}^{-1}$, and $[\text{Au}] = 1.57 \text{ mg mL}^{-1}$). In MR image, the *black arrow* indicates the gallbladder, while the *white arrow* indicates the liver. (c) CT image of a mouse subcutaneously injected with 0.5 mL $\text{Fe}_3\text{O}_4@\text{Au}$ NCPs ($[\text{Fe}] = 8.82 \text{ mg mL}^{-1}$, and $[\text{Au}] = 1.57 \text{ mg mL}^{-1}$) into its back on the right at 5 min post-injection. The *black arrow* points to the injection region (Reproduced with permission from Ref. [98], Copyright 2012 Royal Society of Chemistry)

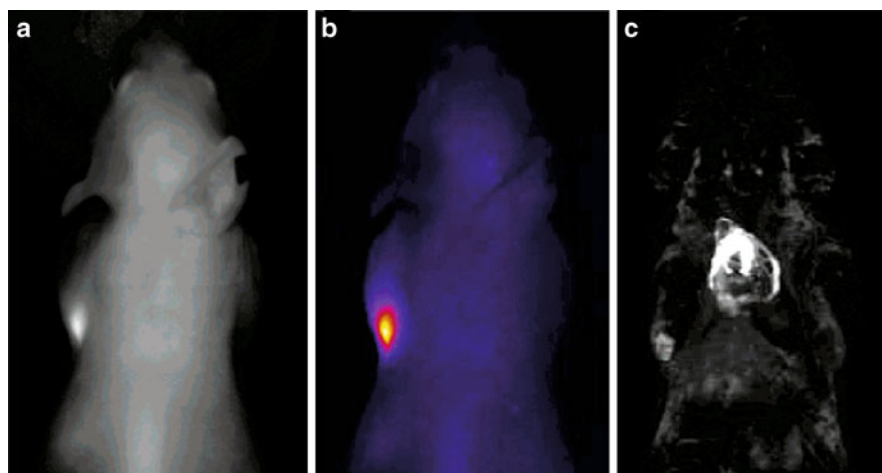


Fig. 8.7 Sentinel lymph node images of a normal mouse. (a) Optical image obtained under simultaneous white light and filtered (615–665 nm) excitation light detected with the emission filter set to 720 nm demonstrating fluorescence in the axillary lymph node of the mouse. (b) Image from (a) shown in false color. (c) Maximum intensity projection calculated from a 3D spoiled gradient echo MR imaging acquired using a GE Signa Excite 3T, which illustrates the injection site in the mammary fat pad, the draining lymphatics, and axillary lymph node depicted in (b) (Reproduced with permission from Ref. [103], Copyright 2006 American Chemical Society)

8.5 Conclusion and Outlooks

This chapter gives a brief literature overview of the recent advances in dendrimer-based nanodevices for T_1 MR, T_2 MR, and dual-modal MR/CT and MR/fluorescence imaging applications. The unique structural characteristics of dendrimers enable their uses as a versatile platform to conjugate Gd or Mn chelator, to link targeting ligands or fluorescent dyes, to entrap noble metal NPs, or to stabilize or assemble IO NPs for MR or dual-mode MR/CT (MR/fluorescence) imaging applications, especially in the imaging of tumors.

Although much effort has been devoted to the development of dendrimer-based nanodevices for MR imaging applications, this area of research still remains largely unexplored. Due to the unique property of dendrimers, other different imaging elements can also be incorporated within or onto the dendrimer platform. In this context, different types of imaging modes can be combined with MR for accurate diagnosis applications. In addition, for targeted imaging applications, the dendrimeric MR contrast agents can be modified with different targeting ligands (vitamins, sugars, peptides, or antibodies), thereby allowing for specific MR imaging of different biological systems. Furthermore, with the ability to conjugate or complex drug molecules, the dendrimeric MR contrast agents can also be modified or be loaded with different drug molecules [104–106], allowing for MR imaging-guided therapy of different biological systems. These challenges are expected to drive an extensive collaboration between scientists from different areas to develop effective multifunctional dendrimer-based MR contrast agents for different biomedical applications.

Acknowledgments This research is financially supported by the National Natural Science Foundation of China (21273032), the Sino-German Center for Research Promotion (GZ899), the Ph.D. Programs Foundation of Ministry of Education of China (20130075110004), and the Program for Professor of Special Appointment (Eastern Scholar) at Shanghai Institutions of High Learning.

References

1. Helms B, Meijer E (2006) Dendrimers at work. *Science* 313(5789):929–930
2. Tomalia D, Baker H, Dewald J, Hall M, Kallos G, Martin S, Roeck J, Ryder J, Smith P (1985) A new class of polymers: starburst-dendritic macromolecules. *Polym J* 17(1):117–132
3. Tomalia DA (2004) Birth of a new macromolecular architecture: dendrimers as quantized building blocks for nanoscale synthetic organic chemistry. *Aldrichimica Acta* 37(2):39–57
4. Cheng Y, Zhao L, Li Y, Xu T (2011) Design of biocompatible dendrimers for cancer diagnosis and therapy: current status and future perspectives. *Chem Soc Rev* 40(5):2673–2703
5. Esfand R, Tomalia DA (2001) Poly (amidoamine)(PAMAM) dendrimers: from biomimicry to drug delivery and biomedical applications. *Drug Discov Today* 6(8):427–436
6. Kannaiyan D, Imae T (2009) pH-dependent encapsulation of pyrene in PPI-core: PAMAM-shell dendrimers. *Langmuir* 25(9):5282–5285
7. Karatasos K, Adolf D, Davies G (2001) Statics and dynamics of model dendrimers as studied by molecular dynamics simulations. *J Chem Phys* 115(11):5310–5318

8. Sadekar S, Ghandehari H (2012) Transepithelial transport and toxicity of PAMAM dendrimers: implications for oral drug delivery. *Adv Drug Deliv Rev* 64(6):571–588
9. Zhang WL, Li N, Huang J, Yu JH, Wang DX, Li YP, Liu SY (2010) Gadolinium-conjugated FA-PEG-PAMAM-COOH nanoparticles as potential tumor-targeted circulation-prolonged macromolecular MRI contrast agents. *J Appl Polym Sci* 118(3):1805–1814
10. Wen S, Liu H, Cai H, Shen M, Shi X (2013) Targeted and pH-responsive delivery of doxorubicin to cancer cells using multifunctional dendrimer-modified multi-walled carbon nanotubes. *Adv Healthcare Mater* 2(9):1267–1276
11. Shi X, Wang S, Meshinchi S, Van Antwerp ME, Bi X, Lee I, Baker JR (2007) Dendrimer-entrapped gold nanoparticles as a platform for cancer-cell targeting and imaging. *Small* 3(7):1245–1252
12. Longmire MR, Ogawa M, Choyke PL, Kobayashi H (2014) Dendrimers as high relaxivity MR contrast agents. *Wiley Interdiscip Rev Nanomed Nanobiotechnol* 6(2):155–162
13. Qiao Z, Shi X (2015) Dendrimer-based molecular imaging contrast agents. *Prog Polym* 44:1–27
14. Laurent S, Forge D, Port M, Roch A, Robic C, Vander Elst L, Muller RN (2008) Magnetic iron oxide nanoparticles: synthesis, stabilization, vectorization, physicochemical characterizations, and biological applications. *Chem Rev* 108(6):2064–2110
15. Schiffmann R, van der Knaap MS (2009) Invited article: an MRI-based approach to the diagnosis of white matter disorders. *Neurology* 72(8):750–759
16. Serres S, Soto MS, Hamilton A, McAteer MA, Carbonell WS, Robson MD, Ansorge O, Khrapitchev A, Bristow C, Balathasan L (2012) Molecular MRI enables early and sensitive detection of brain metastases. *Proc Natl Acad Sci* 109(17):6674–6679
17. Langereis S, Dirksen A, Hackeng TM, van Genderen MH, Meijer E (2007) Dendrimers and magnetic resonance imaging. *New J Chem* 31(7):1152–1160
18. Cai H, An X, Cui J, Li J, Wen S, Li K, Shen M, Zheng L, Zhang G, Shi X (2013) Facile hydrothermal synthesis and surface functionalization of polyethyleneimine-coated iron oxide nanoparticles for biomedical applications. *ACS Appl Mater Interfaces* 5(5):1722–1731
19. Alexiou C, Jurgons R, Seliger C, Iro H (2006) Medical applications of magnetic nanoparticles. *J Nanosci Nanotechnol* 6(9–10):2762–2768
20. Na HB, Song IC, Hyeon T (2009) Inorganic nanoparticles for MRI contrast agents. *Adv Mater* 21(21):2133–2148
21. Sosnovik DE, Weissleder R (2007) Emerging concepts in molecular MRI. *Curr Opin Biotechnol* 18(1):4–10
22. Nune SK, Gunda P, Thallapally PK, Lin Y-Y, Laird Forrest M, Berkland CJ (2009) Nanoparticles for biomedical imaging. *Expert Opin Drug Deliv* 6(11):1175–1194
23. Mahajan S, Koul V, Choudhary V, Shishodia G, Bharti AC (2013) Preparation and in vitro evaluation of folate-receptor-targeted SPION-polymer micelle hybrids for MRI contrast enhancement in cancer imaging. *Nanotechnology* 24(1):015603
24. Hardie AD, Naik M, Hecht EM, Chandarana H, Mannelli L, Babb JS, Taouli B (2010) Diagnosis of liver metastases: value of diffusion-weighted MRI compared with gadolinium-enhanced MRI. *Eur Radiol* 20(6):1431–1441
25. Wen S, Li K, Cai H, Chen Q, Shen M, Huang Y, Peng C, Hou W, Zhu M, Zhang G (2013) Multifunctional dendrimer-entrapped gold nanoparticles for dual mode CT/MR imaging applications. *Biomaterials* 34(5):1570–1580
26. Yang H, Zhuang Y, Hu H, Du X, Zhang C, Shi X, Wu H, Yang S (2010) Silica-coated manganese oxide nanoparticles as a platform for targeted magnetic resonance and fluorescence imaging of cancer cells. *Adv Funct Mater* 20(11):1733–1741
27. Na HB, Lee JH, An K, Park YI, Park M, Lee IS, Nam DH, Kim ST, Kim SH, Kim SW (2007) Development of a T₁ contrast agent for magnetic resonance imaging using MnO nanoparticles. *Angew Chem* 119(28):5493–5497
28. Shi X, Thomas TP, Myc LA, Kotlyar A, Baker JR Jr (2007) Synthesis, characterization, and intracellular uptake of carboxyl-terminated poly (amidoamine) dendrimer-stabilized iron oxide nanoparticles. *Phys Chem Chem Phys* 9(42):5712–5720

29. Yang H, Zhang C, Shi X, Hu H, Du X, Fang Y, Ma Y, Wu H, Yang S (2010) Water-soluble superparamagnetic manganese ferrite nanoparticles for magnetic resonance imaging. *Biomaterials* 31(13):3667–3673
30. Bulte JW, Kraitchman DL (2004) Iron oxide MR contrast agents for molecular and cellular imaging. *NMR Biomed* 17(7):484–499
31. Zhu D, Liu F, Ma L, Liu D, Wang Z (2013) Nanoparticle-based systems for T₁-weighted magnetic resonance imaging contrast agents. *Int J Mol Sci* 14(5):10591–10607
32. Ge S, Shi X, Sun K, Li C, Uher C, Baker JR Jr, Banaszak Holl MM, Orr BG (2009) Facile hydrothermal synthesis of iron oxide nanoparticles with tunable magnetic properties. *J Phys Chem C* 113(31):13593–13599
33. Li J, He Y, Sun W, Luo Y, Cai H, Pan Y, Shen M, Xia J, Shi X (2014) Hyaluronic acid-modified hydrothermally synthesized iron oxide nanoparticles for targeted tumor MR imaging. *Biomaterials* 35(11):3666–3677
34. Li J, Zheng L, Cai H, Sun W, Shen M, Zhang G, Shi X (2013) Polyethyleneimine-mediated synthesis of folic acid-targeted iron oxide nanoparticles for in vivo tumor MR imaging. *Biomaterials* 34(33):8382–8392
35. Wiener E, Brechbiel M, Brothers H, Magin R, Gansow O, Tomalia D, Lauterbur P (1994) Dendrimer-based metal chelates: a new class of magnetic resonance imaging contrast agents. *Magn Reson Med* 31(1):1–8
36. Kobayashi H, Jo SK, Kawamoto S, Yasuda H, Hu X, Knopp MV, Brechbiel MW, Choyke PL, Star RA (2004) Polyamine dendrimer-based MRI contrast agents for functional kidney imaging to diagnose acute renal failure. *J Magn Reson Imaging* 20(3):512–518
37. Kobayashi H, Kawamoto S, Jo S-K, Bryant HL, Brechbiel MW, Star RA (2003) Macromolecular MRI contrast agents with small dendrimers: pharmacokinetic differences between sizes and cores. *Bioconjugate Chem* 14(2):388–394
38. Kobayashi H, Brechbiel MW (2005) Nano-sized MRI contrast agents with dendrimer cores. *Adv Drug Deliv Rev* 57(15):2271–2286
39. Kobayashi H, Saga T, Kawamoto S, Sato N, Hiraga A, Ishimori T, Konishi J, Togashi K, Brechbiel MW (2001) Dynamic micro-magnetic resonance imaging of liver micrometastasis in mice with a novel liver macromolecular magnetic resonance contrast agent DAB-Am64-(1B4M-Gd)₆₄. *Cancer Res* 61(13):4966–4970
40. Kobayashi H, Kawamoto S, Choyke PL, Sato N, Knopp MV, Star RA, Waldmann TA, Tagaya Y, Brechbiel MW (2003) Comparison of dendrimer-based macromolecular contrast agents for dynamic micro-magnetic resonance lymphangiography. *Magn Reson Med* 50(4):758–766
41. Longmire M, Choyke PL, Kobayashi H (2008) Dendrimer-based contrast agents for molecular imaging. *Curr Top Med Chem* 8(14):1180–1186
42. Sena LM, Fishman SJ, Jenkins KJ, Xu H, Brechbiel MW, Regino CA, Kosaka N, Bernardo M, Choyke PL, Kobayashi H (2010) Magnetic resonance lymphangiography with a nano-sized gadolinium-labeled dendrimer in small and large animal models. *Nanomedicine* 5(8):1183–1191
43. Kobayashi H, Kawamoto S, Saga T, Sato N, Hiraga A, Ishimori T, Konishi J, Togashi K, Brechbiel MW (2001) Positive effects of polyethylene glycol conjugation to generation-4 polyamidoamine dendrimers as macromolecular MR contrast agents. *Magn Reson Med* 46(4):781–788
44. He X-H, Shaw P-C, Tam S-C (1999) Reducing the immunogenicity and improving the in vivo activity of trichosanthin by site-directed pegylation. *Life Sci* 65(4):355–368
45. Margerum LD, Campion BK, Koo M, Shargill N, Lai J-J, Marumoto A, Christian Sontum P (1997) Gadolinium (III) DO3A macrocycles and polyethylene glycol coupled to dendrimers effect of molecular weight on physical and biological properties of macromolecular magnetic resonance imaging contrast agents. *J Alloys Compd* 249(1):185–190
46. Kono K, Kojima C, Hayashi N, Nishisaka E, Kiura K, Watarai S, Harada A (2008) Preparation and cytotoxic activity of poly (ethylene glycol)-modified poly (amidoamine) dendrimers bearing adriamycin. *Biomaterials* 29(11):1664–1675

47. Haba Y, Harada A, Takagishi T, Kono K (2005) Synthesis of biocompatible dendrimers with a peripheral network formed by linking of polymerizable groups. *Polymer* 46(6):1813–1820
48. Kojima C, Turkbey B, Ogawa M, Bernardo M, Regino CA, Bryant LH Jr, Choyke PL, Kono K, Kobayashi H (2011) Dendrimer-based MRI contrast agents: the effects of PEGylation on relaxivity and pharmacokinetics. *Nanomed-Nanotechnol Biol Med* 7(6):1001–1008
49. Kuo PH, Kanal E, Abu-Alfa AK, Cowper SE (2007) Gadolinium-based MR contrast agents and nephrogenic systemic fibrosis. *Radiology* 242(3):647–649
50. Lu Z-R, Mohs AM, Zong Y, Feng Y (2006) Polydisulfide Gd (III) chelates as biodegradable macromolecular magnetic resonance imaging contrast agents. *Int J Nanomed* 1(1):31–40
51. Lu ZR, Wu X (2010) Polydisulfide-based biodegradable macromolecular magnetic resonance imaging contrast agents. *Isr J Chem* 50(2):220–232
52. Huang C-H, Nwe K, Al Zaki A, Brechbiel MW, Tsourkas A (2012) Biodegradable polydisulfide dendrimer nanoclusters as MRI contrast agents. *ACS Nano* 6(11):9416–9424
53. Luo K, Liu G, She W, Wang Q, Wang G, He B, Ai H, Gong Q, Song B, Gu Z (2011) Gadolinium-labeled peptide dendrimers with controlled structures as potential magnetic resonance imaging contrast agents. *Biomaterials* 32(31):7951–7960
54. Lim J, Turkbey B, Bernardo M, Bryant LH Jr, Garzoni M, Pavan GM, Nakajima T, Choyke PL, Simanek EE, Kobayashi H (2012) Gadolinium MRI contrast agents based on triazine dendrimers: relaxivity and in vivo pharmacokinetics. *Bioconjugate Chem* 23(11):2291–2299
55. Lim J, Guo Y, Rostollan CL, Stanfield J, Hsieh J-T, Sun X, Simanek EE (2008) The role of the size and number of polyethylene glycol chains in the biodistribution and tumor localization of triazine dendrimers. *Mol Pharmaceut* 5(4):540–547
56. Langereis S, De Lussanet QG, Van Genderen MH, Backes WH, Meijer E (2004) Multivalent contrast agents based on gadolinium-diethylenetriaminepentaacetic acid-terminated poly(propylene imine) dendrimers for magnetic resonance imaging. *Macromolecules* 37(9):3084–3091
57. Langereis S, de Lussanet QG, van Genderen MH, Meijer E, Beets-Tan RG, Griffioen AW, van Engelshoven J, Backes WH (2006) Evaluation of Gd (III) DTPA-terminated poly(propylene imine) dendrimers as contrast agents for MR imaging. *NMR Biomed* 19(1):133–141
58. de Lussanet QG, Langereis S, Beets-Tan RG, van Genderen MH, Griffioen AW, van Engelshoven JM, Backes WH (2005) Dynamic contrast-enhanced MR imaging kinetic parameters and molecular weight of dendritic contrast agents in tumor angiogenesis in mice. *Radiology* 235(1):65–72
59. Artemov D (2003) Molecular magnetic resonance imaging with targeted contrast agents. *J Cell Biochem* 90(3):518–524
60. Kobayashi H, Sato N, Saga T, Nakamoto Y, Ishimori T, Toyama S, Togashi K, Konishi J, Brechbiel MW (2000) Monoclonal antibody-dendrimer conjugates enable radiolabeling of antibody with markedly high specific activity with minimal loss of immunoreactivity. *Eur J Nucl Med* 27(9):1334–1339
61. Xu H, Regino CA, Koyama Y, Hama Y, Gunn AJ, Bernardo M, Kobayashi H, Choyke PL, Brechbiel MW (2007) Preparation and preliminary evaluation of a biotin-targeted, lectin-targeted dendrimer-based probe for dual-modality magnetic resonance and fluorescence imaging. *Bioconjugate Chem* 18(5):1474–1482
62. Han L, Li J, Huang S, Huang R, Liu S, Hu X, Yi P, Shan D, Wang X, Lei H (2011) Peptide-conjugated polyamidoamine dendrimer as a nanoscale tumor-targeted T₁ magnetic resonance imaging contrast agent. *Biomaterials* 32(11):2989–2998
63. Tan M, Wu X, Jeong E-K, Chen Q, Lu Z-R (2010) Peptide-targeted nanoglobular Gd-DOTA monoamide conjugates for magnetic resonance cancer molecular imaging. *Biomacromolecules* 11(3):754–761
64. Swanson SD, Kukowska-Latallo JF, Patri AK, Chen C, Ge S, Cao Z, Kotlyar A, East AT, Baker JR (2008) Targeted gadolinium-loaded dendrimer nanoparticles for tumor-specific magnetic resonance contrast enhancement. *Int J Nanomed* 3(2):201–210

65. Wolfenden ML, Cloninger MJ (2005) Mannose/glucose-functionalized dendrimers to investigate the predictable tunability of multivalent interactions. *J Am Chem Soc* 127(35):12168–12169
66. van Baal I, Malda H, Synowsky SA, van Dongen JL, Hackeng TM, Merckx M, Meijer E (2005) Multivalent peptide and protein dendrimers using native chemical ligation. *Angew Chem Int Ed* 44(32):5052–5057
67. Choi Y, Mecke A, Orr BG, Banaszak Holl MM, Baker JR (2004) DNA-directed synthesis of generation 7 and 5 PAMAM dendrimer nanoclusters. *Nano Lett* 4(3):391–397
68. Antony AC (1992) The biological chemistry of folate receptors. *Blood* 79(11):2807–2820
69. Chen W-T, Thirumalai D, Shih TT-F, Chen R-C, Tu S-Y, Lin C-I, Yang P-C (2010) Dynamic contrast-enhanced folate-receptor-targeted MR imaging using a Gd-loaded PEG-dendrimer-folate conjugate in a mouse xenograft tumor model. *Mol Imaging Biol* 12(2):145–154
70. Kobayashi H, Kawamoto S, Saga T, Sato N, Ishimori T, Konishi J, Ono K, Togashi K, Brechbiel MW (2001) Avidin-dendrimer-(1B4M-Gd) 254: a tumor-targeting therapeutic agent for gadolinium neutron capture therapy of intraperitoneal disseminated tumor which can be monitored by MRI. *Bioconjugate Chem* 12(4):587–593
71. Park J, Lee JJ, Jung JC, Yu DY, Oh C, Ha S, Kim TJ, Chang Y (2008) Gd-DOTA conjugate of RGD as a potential tumor-targeting MRI contrast agent. *ChemBioChem* 9(17):2811–2813
72. Lee JH, Silva AC, Merkle H, Koretsky AP (2005) Manganese-enhanced magnetic resonance imaging of mouse brain after systemic administration of $MnCl_2$: dose-dependent and temporal evolution of T_1 contrast. *Magn Reson Med* 53(3):640–648
73. Shin J, Anisur RM, Ko MK, Im GH, Lee JH, Lee IS (2009) Hollow manganese oxide nanoparticles as multifunctional agents for magnetic resonance imaging and drug delivery. *Angew Chem Int Ed* 48(2):321–324
74. Zhao Z, Fan H, Zhou G, Bai H, Liang H, Wang R, Zhang X, Tan W (2014) Activatable fluorescence/MRI bimodal platform for tumor cell imaging *via* MnO_2 nanosheet-aptamer nanoprobe. *J Am Chem Soc* 136(32):11220–11223
75. Hu H, Dai A, Sun J, Li X, Gao F, Wu L, Fang Y, Yang H, An L, Wu H (2013) Aptamer-conjugated $Mn_3O_4@SiO_2$ core-shell nanoprobes for targeted magnetic resonance imaging. *Nanoscale* 5(21):10447–10454
76. Pan D, Schmieder AH, Wickline SA, Lanza GM (2011) Manganese-based MRI contrast agents: past, present, and future. *Tetrahedron* 67(44):8431–8444
77. Ye Z, Jeong EK, Wu X, Tan M, Yin S, Lu ZR (2012) Polydisulfide manganese (II) complexes as non-gadolinium biodegradable macromolecular MRI contrast agents. *J Magn Reson Imaging* 35(3):737–744
78. Bertin A, Steibel J, Michou-Gallani A-I, Gallani J-L, Felder-Flesch D (2009) Development of a dendritic manganese-enhanced magnetic resonance imaging (MEMRI) contrast agent: synthesis, toxicity (in vitro) and relaxivity (in vitro, in vivo) studies. *Bioconjugate Chem* 20(4):760–767
79. Nguyen TH, Bryant H, Shapsa A, Street H, Mani V, Fayad ZA, Frank JA, Tsimikas S, Briley-Saebo KC (2015) Manganese G8 dendrimers targeted to oxidation-specific epitopes: In vivo MR imaging of atherosclerosis. *J Magn Reson Imaging* 41(3):797–805
80. Tan M, Wu X, Jeong E-K, Chen Q, Parker DL, Lu Z-R (2010) An effective targeted nanoglobular manganese (II) chelate conjugate for magnetic resonance molecular imaging of tumor extracellular matrix. *Mol Pharmaceut* 7(4):936–943
81. Tan M, Ye Z, Jeong E-K, Wu X, Parker DL, Lu Z-R (2011) Synthesis and evaluation of nanoglobular macrocyclic Mn (II) chelate conjugates as non-gadolinium (III) MRI contrast agents. *Bioconjugate Chem* 22(5):931–937
82. Strable E, Bulte JWM, Moskowitz B, Vivekanandan K, Allen M, Douglas T (2001) Synthesis and characterization of soluble iron oxide-dendrimer composites. *Chem Mater* 13(6):2201–2209
83. Shi X, Wang SH, Swanson SD, Ge S, Cao Z, Van Antwerp ME, Landmark KJ, Baker JR Jr (2008) Dendrimer-functionalized shell-crosslinked iron oxide nanoparticles for in-vivo magnetic resonance imaging of tumors. *Adv Mater* 20(9):1671–1678

84. Wang SH, Shi X, Van Antwerp M, Cao Z, Swanson SD, Bi X, Baker JR Jr (2007) Dendrimer-functionalized iron oxide nanoparticles for specific targeting and imaging of cancer cells. *Adv Funct Mater* 17(16):3043–3050
85. Lee IH, Bulte JWM, Schweinhardt P, Douglas T, Trifunovski A, Hofstetter C, Olson L, Spenger C (2004) *In vivo* magnetic resonance tracking of olfactory ensheathing glia grafted into the rat spinal cord. *Exp Neurol* 187(2):509–516
86. Tunci P, Bulte JWM, Bruzzone MG, Poliani PL, Cajola L, Grisoli M, Douglas T, Finocchiaro G (2006) Brain engraftment and therapeutic potential of stem/progenitor cells derived from mouse skin. *J Gene Med* 8(4):506–513
87. Aime S, Crich SG, Gianolio E, Giovenzana GB, Tei L, Terreno E (2006) High sensitivity lanthanide(III) based probes for MR-medical imaging. *Coord Chem Rev* 250(11–12):1562–1579
88. Ferrauto G, Castelli DD, Di Gregorio E, Langereis S, Burdinski D, Grull H, Terreno E, Aime S (2014) Lanthanide-loaded erythrocytes as highly sensitive chemical exchange saturation transfer MRI contrast agents. *J Am Chem Soc* 136(2):638–641
89. Klemm PJ, Floyd WC III, Andolina CM, Frechet JMJ, Raymond KN (2012) Conjugation to biocompatible dendrimers increases lanthanide T_2 relaxivity of hydroxypyridinone complexes for magnetic resonance imaging. *Eur J Inorg Chem* 12:2108–2114
90. Li J, Zheng L, Cai H, Sun W, Shen M, Zhang G, Shi X (2013) Facile one-pot synthesis of Fe_3O_4 @Au composite nanoparticles for dual-mode MR/CT imaging applications. *ACS Appl Mater Interfaces* 5(20):10357–10366
91. Jiang L, Zhou Q, Mu K, Xie H, Zhu Y, Zhu W, Zhao Y, Xu H, Yang X (2013) pH/temperature sensitive magnetic nanogels conjugated with Cy5.5-labeled lactoferrin for MR and fluorescence imaging of glioma in rats. *Biomaterials* 34(30):7418–7428
92. Lee J, Lee TS, Ryu J, Hong S, Kang M, Im K, Kang JH, Lim SM, Park S, Song R (2013) RGD peptide-conjugated multimodal NaGdF_4 : $\text{Yb}^{3+}/\text{Er}^{3+}$ nanophosphors for upconversion luminescence, MR, and PET imaging of tumor angiogenesis. *J Nucl Med* 54(1):96–103
93. Kryza D, Taleb J, Janier M, Marmuse L, Miladi I, Bonazza P, Louis C, Perriat P, Roux S, Tillement O (2011) Biodistribution study of nanometric hybrid gadolinium oxide particles as a multimodal SPECT/MR/optical imaging and theragnostic agent. *Bioconjugate Chem* 22(6):1145–1152
94. Liu H, Wang H, Guo R, Cao X, Zhao J, Luo Y, Shen M, Zhang G, Shi X (2010) Size-controlled synthesis of dendrimer-stabilized silver nanoparticles for X-ray computed tomography imaging applications. *Polym Chem* 1(10):1677–1683
95. Liu H, Xu Y, Wen S, Zhu J, Zheng L, Shen M, Zhao J, Zhang G, Shi X (2013) Facile hydrothermal synthesis of low generation dendrimer-stabilized gold nanoparticles for *in vivo* computed tomography imaging applications. *Polym Chem* 4(6):1788–1795
96. Peng C, Zheng L, Chen Q, Shen M, Guo R, Wang H, Cao X, Zhang G, Shi X (2012) PEGylated dendrimer-entrapped gold nanoparticles for *in vivo* blood pool and tumor imaging by computed tomography. *Biomaterials* 33(4):1107–1119
97. Chen Q, Li K, Wen S, Liu H, Peng C, Cai H, Shen M, Zhang G, Shi X (2013) Targeted CT/MR dual mode imaging of tumors using multifunctional dendrimer-entrapped gold nanoparticles. *Biomaterials* 34(21):5200–5209
98. Cai H, Li K, Shen M, Wen S, Luo Y, Peng C, Zhang G, Shi X (2012) Facile assembly of Fe_3O_4 @Au nanocomposite particles for dual mode magnetic resonance and computed tomography imaging applications. *J Mater Chem* 22(30):15110–15120
99. Feng J, Chang D, Wang Z, Shen B, Yang J, Jiang Y, Ju S, He N (2014) A FITC-doped silica coated gold nanocomposite for both *in vivo* X-ray CT and fluorescence dual modal imaging. *RSC Adv* 4(94):51950–51959
100. Karreman MA, Agronskaia AV, van Donselaar EG, Vocking K, Fereidouni F, Humbel BM, Verrips CT, Verkleij AJ, Gerritsen HC (2012) Optimizing immuno-labeling for correlative fluorescence and electron microscopy on a single specimen. *J Struct Biol* 180(2):382–386
101. Juette MF, Terry DS, Wasserman MR, Zhou Z, Altman RB, Zheng Q, Blanchard SC (2014) The bright future of single-molecule fluorescence imaging. *Curr Opin Chem Biol* 20:103–111

102. Lingyu J, Qing Z, Ketao M, Hui X, Yanhong Z, Wenzhen Z, Yanbing Z, Huibi X, Xiangliang Y (2013) pH/temperature sensitive magnetic nanogels conjugated with Cy5.5-labeled lactoferrin for MR and fluorescence imaging of glioma in rats. *Biomaterials* 34(30):7418–7428
103. Talanov VS, Regino CA, Kobayashi H, Bernardo M, Choyke PL, Brechbiel MW (2006) Dendrimer-based nanoprobe for dual modality magnetic resonance and fluorescence imaging. *Nano Lett* 6(7):1459–1463
104. Caminade A-M, Turrin C-O (2014) Dendrimers for drug delivery. *J Mater Chem B* 2(26):4055–4066
105. Fu F, Wu Y, Zhu J, Wen S, Shen M, Shi X (2014) Multifunctional lactobionic acid-modified dendrimers for targeted drug delivery to liver cancer cells: Investigating the role played by PEG spacer. *ACS Appl Mater Interfaces* 6(18):16416–16425
106. Zhu J, Shi X (2013) Dendrimer-based nanodevices for targeted drug delivery applications. *J Mater Chem B* 1(34):4199–4211

Chapter 9

Functional Dendritic Polymer-Based Nanoscale Vehicles for Imaging-Guided Cancer Therapy

Yanhong Zhang, Kui Luo, and Zhongwei Gu

Abstract The quest for highly efficient and accurate diagnosis and specific therapy approaches has become the key factor for successful cancer treatment. Over recent decades, with the advancements in the fields of nanotechnology and biomaterials, functional nanomaterials have been developed as nanocarriers for cancer diagnosis and therapy. Unlike the traditional low-molecular-weight imaging probes and therapeutic agents, early clinical results showed that nanocarriers with imaging and therapeutic agents could result in increased accumulation in tumor, increased signal intensity, enhanced anticancer efficacy, and reduced side effects owing to the passive targeting features of nanoparticles via enhanced permeability and retention (EPR) effect. Recently, new nanomedicine enables the incorporation of imaging agents and anticancer agents in one system, namely, theranostic nanomedicine, which combines both therapeutic and diagnostic capabilities in a single entity for personalized medicine. Those novel nanosystems for cancer theranostics are emergent and have promising applications in concurrent molecular imaging of biomarkers, delivery of anticancer drugs, monitoring of nanosystems' behaviors in vivo, simultaneous monitoring of the disease progression, and guidance of therapeutic outcomes. Biodegradable polymer-based theranostic nanosystems have demonstrated great potential clinical impact for the foreseeable future, due to their good biocompatibility and flexible chemistry. Dendritic polymers are a class of well-defined macromolecules with branching units, precise structures, low polydispersity, controllable nanoscale size, as well as highly adaptable and flexible surface chemistry. These unique features have proposed dendritic polymers as nanoscale imaging agents, drug delivery systems, and theranostic nanosystems for cancer treatment. This chapter highlights the advantages of dendritic polymer-based theranostic nanosystems and the emergent concept of theranostics for the safe and effective tumor treatment in the next generation nanomedicine. The novel developments of dendritic polymer-based theranostic nanosystems described here provide great potential to achieve better cancer therapeutic.

Y. Zhang • K. Luo (✉) • Z. Gu
National Engineering Research Center for Biomaterials, Sichuan University,
Chengdu 610064, China
e-mail: luokui@scu.edu.cn

Keywords Cancer therapy • Cancer diagnosis • Dendritic polymers • Nanoparticles • Theranostic • Biosafety

9.1 Introduction

Successful cancer treatment depends on accurate diagnostics and efficient therapy. Current diagnostic techniques, including magnetic resonance imaging (MRI), radionuclide-based imaging, computed tomography (CT), ultrasound, and optical imaging (bioluminescence and fluorescence), offer opportunities that disease can be detected earlier and consequently guide when and where the therapy can be most effective. Additionally, both biological response and therapeutic efficacy following treatment can be monitored. However, currently, most of the bioimaging probes used in the clinic are those with low molecular weight. This largely hampers their applications due to the characteristics, such as poor selectivity, high doses leading to toxicity, instability, short detention time, and lack of the ability to modify themselves [1]. On the other hand, cancer therapy requests for high efficacy and good biosafety. Conventional chemotherapeutic agents are used in the treatment of many cancers. However, there remain some challenges for those agents, including poor water solubility, nonspecific biodistribution and cytotoxicity, unfavorable pharmacokinetics, and drug resistance, resulting in low therapeutic index along with numerous systemic toxicities [2]. Hence, the quest for highly efficient and safe imaging probes and therapeutic and functional agents is a significant factor for cancer treatments.

Medical nanoparticles demonstrate promise as creative and innovative technology for cancer diagnosis and therapy [2, 3], as nanoparticles for delivery small molecular agents have multiple advantages, such as improved solubility, extended half-life, improved pharmacokinetics, reduced toxicity, passively targeting tumors via the EPR effect, and active cellular uptake. Moreover, the presence of functional groups allows the modification of the bioimaging agents and therapeutic carriers and then promotes the specificity and biological activity. Many nanotechnologies, including polymers [4, 5], liposomes [6], metallic nanoparticles [7], carbon nanotubes [8], and quantum dots [9], are examples of the nanoplatform that can be utilized as multifunctional formulations for cancer treatment. Among these carriers, natural and synthetic polymer-based nanoscale systems fabricated from polyethylene glycol (PEG) [10], polyglutamic acid (PGA) [11], polysaccharides [12], *N*-(2-hydroxypropyl)methacrylamide (HPMA) copolymer [13], and dendritic polymers [14], have been widely proved to be targeting nanoscale vehicles for cancer treatment.

Dendritic polymers [15], including dendrimers [14, 16–18], dendron [19], dendron-grafted polymers [20], and hyperbranched macromolecules [21–23], which are characterized by a three-dimensional highly branched structure and a large number of terminal groups, have been investigated as optimal candidates for

agent delivery [24, 25]. In 1985, Tomalia et al. successfully synthesized the first poly(amidoamine) (PAMAM) dendrimer [26]. Dendritic polymers with nanoscale sizes, including PAMAM and poly(propyleneimine) (PPI) dendrimers and their derivatives [27], peptide dendron and dendrimers synthesized from amino acids [28], non-biodegradable dendrimers prepared via click chemistry, dendronized polymers grafted with low-generation dendron, low-generation dendron or dendrimers functionalized with linear polymers, and branched polymers with similar structure of dendrimer prepared via polymerization, have been investigated as nanoscale vehicles, such as imaging probes for cancer diagnosis [29–31] and drug/gene/protein/siRNA delivery systems [27, 32–34]. Those nanomedicines based on dendritic polymers have showed unique features owing to their precise nanostructures and highly adaptable and flexible surface chemistry [35–37]. It is noted that the highly branched, multivalent surface and rich surface groups make them optimal candidates for a variety of functionalization for cancer treatment [38–40], for example, drug conjugation, cancer-targeting moiety attachment, and imaging probes label. Additionally, the dendritic polymers with adjustable cavities can be employed to directly encapsulate small agents that will release in cancer cells [41]. Compared with linear polymeric vehicles, the highly branched dendritic polymers, owing to their multivalent architectures and rich functional groups, show increased solubility, very low intrinsic viscosities, and significantly higher efficient cellular uptake than that of linear polymeric drug delivery systems via the “cluster effects,” such as PEG [42] and *N*-(2-hydroxypropyl)methacrylamide (HPMA)-based vehicles [43, 44]. Moreover, the dendritic vehicles with optimal nanoscale sizes have resulted in longer blood circulation time and significantly increased accumulation of agents into tumor. Those attractive features propose dendritic polymers as potential vehicles for cancer treatment [45].

In the conventional cancer treatment, the imaging probes and therapeutic agents are administrated separately, leading to higher cost and reduplicate suffering of patients. In an attempt to overcome those shortcomings, the concept theranostics originally coined by Picard in 2002 [46], which integrates diagnostic imaging moieties and therapeutic agents into a single platform [47]. Compared with the traditional separate administration, theranostics combining diagnosis and therapy into one dosage have the possibility to realize biodistribution and tumor targeting for both imaging and therapeutic agents. Additionally, theranostic technology is able to monitor and tune the therapy at the same time according to the disease progresses, providing individual treatment options according to therapeutic window, resulting in improved prognoses as the seamless integration of diagnosis, therapy, follow-up, and different therapeutic modalities. Recently, various nanomaterials, including carbon nanotubes [48]; magnetic nanomaterials [49]; quantum dots [50]; mesoporous silica [51, 52]; surface-enhanced Raman scattering silver/gold, nano/microbubbles, and protein [53]; liposomes [54]; and polymers [55], have been utilized as multifunctional formulations for cancer theranostics.

The functional and multivalent dendritic polymers, thanks to their structural features and good biosafety, have demonstrated the unique potential as targeting nanoscale drug/imaging probe delivery and theranostic delivery systems based on

the EPR effect (passive targeting) and high active-targeting efficacy [15]. In this chapter, we will focus on the characteristics of dendritic polymeric systems, as well as their applications in theranostic-based strategies for cancer treatments. Finally, the limitations and future challenges will be addressed.

9.2 Dendritic Architectures

Dendritic polymers are highly branched macromolecules which have a uniform three-dimensional architecture [15, 56]. Due to the attractive properties like topological features, adequate internal cavities, and rich terminal functional groups, dendritic polymers have demonstrated potential to be novel scaffolds in nanomedicine [56–58]. The existing dendritic polymeric system generally contains the following seven subclasses according to their topological structures: (a) dendrimers, (b) linear-dendritic hybrids, (c) dendritic-dendritic block polymers, (d) dendronized polymers, (e) hyperbranched polymers, (f) multiarm star polymers, and (g) hypergrafted polymers [59]. The first four subclasses show high-regularity structures, while the latter three exhibit a random branched structure. Furthermore, these different kinds of dendritic polymers have unique architectures, outstanding morphologies, and specific functions.

As contrasted with conventional linear polymers, dendritic polymers exhibit distinct physicochemical and biological properties [58]. Dendritic architecture possesses monodisperse nature, showing little molecular entanglement or interpenetrating structures [60]. In addition, this kind of architecture also demonstrates features including low viscosity and high solubility. Among these, multivalency and functional groups attached to the polymeric scaffold play a vital role in determining the material properties. For instance, polyamidoamine (PAMAM) dendrimers, the highly symmetrical, highly branched, and monodisperse polymers with functional groups in an activated form, can be utilized to deliver antigen peptides to dendritic cells (DCs). The large number of functional groups of dendritic polymers provides a powerful tool to improve their effects. Simultaneously, the surface modification owing to abundant terminal functional groups can decrease the toxicity. PAMAM dendrimer was chemically modified with biocompatible PEG chains resulted in better biocompatibility than non-PEGylated one. Therefore, currently, the dendritic polymers have been functionalized to meet the need of vehicles with high efficacy and good biosafety for cancer diagnosis and therapy.

9.3 Dendritic Polymer-Based Imaging Probes for Cancer Diagnosis

Bioimaging is a hot area of research to explore specific molecular pathways in living animals or humans. Up to now, various bioimaging techniques, such as optical imaging, MRI, nuclear tomographic imaging, multimodal imaging technologies,

and so on, have been developed and applied in cancer diagnosis. These powerful techniques can visualize the complicated biological processes in vivo through exquisite bioimaging probes with advanced modalities and can locate in tumor tissue/cell, showing the potential to apply to cancer therapy, playing an important role in simultaneous diagnosis and therapy. Most of the probes currently used in clinic are low-molecular-weight compounds; therefore, some limitations like instability, non-specificity, insensitivity, toxicity, and short plasma half-life, might hamper their applications.

Various bioimaging probes have been developed in order to enhance their sensitivity, improve selective ability, and prolong detection time. Especially, dendritic polymers would provide tunable structures and enable multifunctional modification [17, 61]. Firstly, they have a large number of chemical groups and can be modified with small molecular imaging probes and other functions [62, 63]. Then, their detection time can be largely tuned based on their physicochemical properties. Most important is that both of contrast agents and therapy agents can be integrated simultaneously either in the interior cavities or on the surfaces, achieving cancer theranostics [64].

Functional dendritic polymers can be employed as imaging probes. Especially, the low-generation dendrimers or dendrons are functionalized with imaging probes and targeting moieties [65, 66], as the dendritic polymers with low molecular weight can be cleared from body, resulting in good biosafety [67]. The dendritic polymers with precise and tunable nanoscopic sizes may be excellent candidates as multivalent MRI probes. We firstly reported a series of novel Gd-based multifunctional peptide dendritic probes ranging of generations 2, 3, and 4 were designed and prepared as liver MRI probes, and the molecular structures of those dendritic MRI agents functionalized with multiple galactosyl moieties were controlled structures via organic chemistry, as shown in Fig. 9.1, resulting in a single molecular weight [65, 66]. These peptide dendritic MRI agents showed improved r_1 value in the range of 6.4–12.6 mM⁻¹·S⁻¹, which was up to threefold increase compared with clinical agent Gd-DTPA. Additionally, compared with clinical agents and nontargeting dendritic agents, these dendritic agents functionalized with multiple galactosyl moieties showed much higher cell uptake as demonstrated in T_1 -weighted scans in vitro and much better signal intensity (SI) enhancement in mouse liver in vivo, especially at 60 min postinjection. Therefore, the dendritic agents functionalized with galactosyl moieties may be utilized as targeting MRI agents for liver cancer diagnosis. Unlike amine-terminated dendrimers, such as PPI and PAMAM, which might present hemolytic effects, the peptide dendritic agents are prepared from amino acids, showing good biocompatibility through in vitro MTT cell proliferation assay and in vivo toxicity studies [68]. Since the peptide branching units have biodegradable property. Our and other groups' previously studies showed that the longitudinal relaxivities and system circulation of dendritic-based Gd(III) chelates were molecular weight dependent, and increasing the number of generations was a method to improve their sensitivity [29, 69]. Moreover, the high-generation ones showed higher drug/imaging moieties encapsulation capability and could assemble into nanoparticles suitable for tumor passive targeting. However, due to the steric hindrance, it's not easy to acquire high-generation dendrimers. For most of the den-

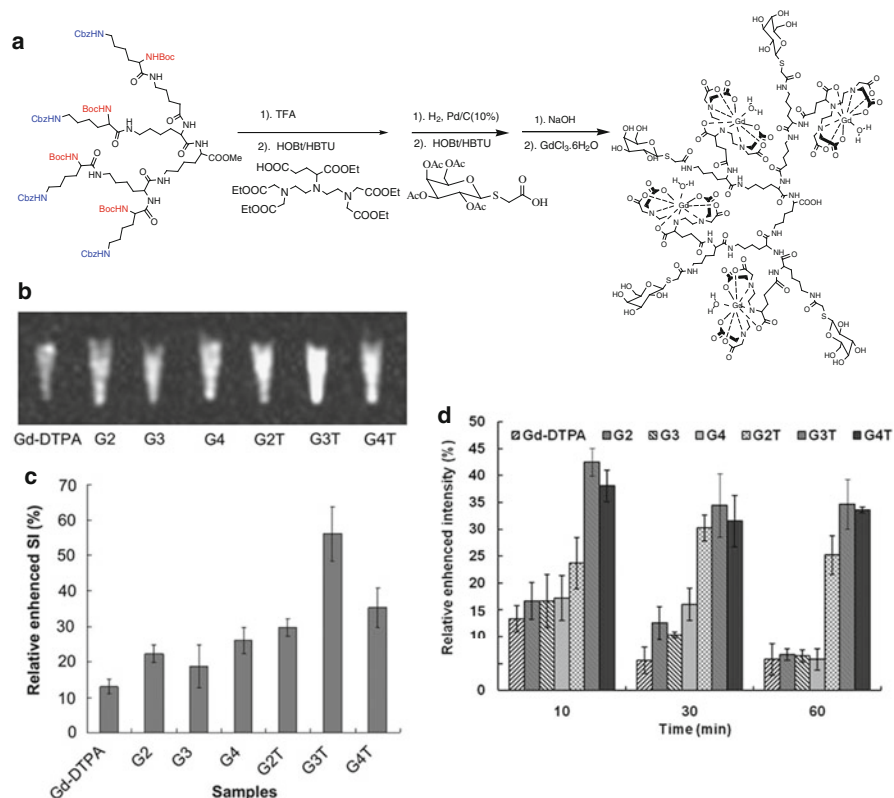


Fig. 9.1 The synthesis route of Gd(III)-dendritic probe G3T with four Gd-DTPA labels and four galactosyl moieties (a). In vitro MRI study on HepG2 cells and in vivo studies showed that the targeting dendritic probe (G2T, G3T, and G4T) resulted in relative enhanced signal intensity (SI) in cells at 4 h post-incubation (b) MR images and (c) enhanced in vivo SI (d) (Reprinted from reference [65], Copyright (2011), with permission from Elsevier)

dritic polymers, such as PAMAM and PPI dendrimers, the size is below 10 nm, and the high-generation ones also lead to potential toxicity, as the non-biodegradable branch units [70, 71]. Although the emergence of click chemistry provides an alternative strategy to prepare high-generation peptide dendritic polymers, the cytotoxicity is still observed when the generation is over five and molecular weight is over 20 kDa [68]. That is due to their slow degradation.

Recently, biodegradable dendritic polymers, such as dendrimers and dendrons with low molecular weight, are functionalized with linear polymers, and the new dendritic ones with much higher molecular weight showed significantly increased EPR effects and long blood circulation time in vivo. Among the polymers, polyethylene glycol (PEG), as a component that can decrease nonspecific interactions of dendrimers with others in the blood, is introduced to extend retention time and eliminate the naked dendritic scaffold drawbacks of hemolytic toxicity (especially

for cationic ones), uncontrolled drug burst release, etc. When the six-generation and melamine dendrimers were functionalized with amine, guanidine, carboxylate, sulfonate, phosphonate, and PEG, the hemolytic and cytotoxicity studies showed that the cationic dendritic polymers were more cytotoxic and hemolytic than PEGylated ones. Moreover, the PEGylated dendritic polymers resulted in no toxicity, lethality, and abnormalities in blood chemistry [72, 73]. Margerum et al. functionalized PAMAM dendrimers (G2 and G3) with PEG and the macrocycle 1-(4-isothiocyanatobenzyl)amido-4,7,10-triacetic acid-tetraazacyclododecane (DO3A-bz-NCS) was conjugated to the dendritic scaffold, followed by chelation with gadolinium ion (Gd^{3+}), resulting in water-soluble, monodisperse, and dendritic MRI contrast agents [74]. It is notable that the lower molecule agent (MW: 22 kDa) showed lower blood elimination half-life of 11 min, and the higher molecule ones (MW: 61.8 kDa) increased the blood elimination half-life to 115 min, indicating the number of PEG influenced the features of the MRI agents. Based on the above observations, we reported the Gd(III)-based peptide dendritic polymer and PEGylated dendritic one with highly controlled structures and single molecular weights and their potential use as MRI contrast agents [69]. These three-generation dendritic agents showed no obvious cytotoxicity, indicating the scaffold could be degraded to segments with much lower molecular weights. Our study demonstrated the PEGylated dendritic formulations resulted in significantly improved r_1 value of $39.2 \text{ Gd(III) mM}^{-1} \text{ s}^{-1}$, which was over ninefold increase in T_1 relaxivity compared with clinical agent of Gd-DTPA [69]. Compared with the non-PEGylated dendritic agents and clinical agent of DTPA-Gd, in vivo studies have shown that the mPEGylated agent resulted in much higher SI enhancement in mouse kidney at 60 min postinjection, as the observed 54.8 % relatively enhanced SI. Additionally, for the mPEGylated dendritic agent, much higher accumulation of gadolinium in the liver and kidney was also detected, and much higher Gd(III) concentration in blood with $38 \mu\text{g Gd(III)/g blood}$ at 1 h postinjection was also observed, indicating much longer blood circulation time. Finally, the Gd(III) concentration in blood also decreased for all the dendritic agents, indicating the Gd(III) could be cleared from the body and the dendritic agents have potential good biosafety [69]. That is attributed to the biodegradability of peptide dendritic structures [75]. These findings indicate that the PEGylated peptide dendritic polymers can be employed as imaging probes and drug delivery systems for cancer treatment, because of the long blood circulation and biodegradable features.

In order to prevent the removal of nanoparticles by the mononuclear phagocyte system (MPS), PEG not only has been employed to functionalize dendrimer, dendron, and inorganic imaging nanoparticles but also has provided the possibility to fabricate PEG-based hyperbranched polymers [76, 77]. The introduction of a branched architecture simultaneously provides multiple functionalities of both imaging and targeting. Targeting ligand, folate, endows this platform with the capability for cellular targeting. Furthermore, the structures and molecular weights can be controlled via reversible addition-fragmentation chain transfer (RAFT) polymerization [78], and the size of the polymeric particles plays a significant role in their subsequent behavior in vivo [79]. The results in confocal and FACS clearly showed

that groups conjugated with folic acid on the polymer demonstrate increasing rate and degree of molecular import into cells, while cells in unconjugated one show very little uptake of polymer. Finally, the competitive binding assay suggests that internalization takes place via the folate receptor. Both MR and optical images indicate a clear signal of the folate-conjugated and unconjugated imaging agents in major organs [30, 80], suggesting the intrinsic sensitivity and complementarity of these multimodal imaging probes. However, obvious signal of the tumor is only detected in folate-conjugated groups, showing that the decoration of folate increases the capability of tumor targeting.

In order to overcome the drawbacks of dendrimers or dendron with small nanoscale size, recently dendronization strategy has been employed to prepare dendritic polymer-based nanoparticles with larger sizes and well-defined molecular objects via connecting low-generation dendron to polymeric scaffold [81, 82], in which the linear polymer was designed as a polyfunctional and polydisperse core, and the new polymers with dendritic architectures were referred as “dendronized polymers” [83, 84]. Once the dendritic polymers have been functionalized with hydrophobic and hydrophilic moieties, the amphiphilic dendronized polymers can self-assemble into nanoparticles possessing the advantages of dendrimer and linear polymer [85, 86]. The dendronization and self-assembly strategy can address the synthetic challenges associated with preparation of functionalized dendrimer- or dendron-based nanoparticles with desired sizes. Bai and coworkers reported water-soluble dendronized polyfluorenes, and the dendritic polyfluorenes prepared via dendronization exhibited a quite high quantum yield in water, providing potential as fluorescent probes for cancer or cancer cell diagnosis [87].

Although the introduction of nanomaterials has dealt with a few challenges in imaging, there are still some fundamental drawbacks of imaging technologies. For instance, MRI generates high spatial resolution but is often hindered by poor sensitivity. Optical imaging has high sensitivity with low cost; however, it suffers from autofluorescence and absorption by tissues. Positron emission tomography (PET) shows high detection efficiency and excellent tissue penetration but causes radiation for the patients. In this case, the combination of strengths of one imaging modality with a complementary modality has come to the fore. For example, Wen et al. designed and synthesized multifunctional gadolinium-loaded dendrimer-entrapped gold nanoparticles (Gd-Au DENPs) for dual-mode CT/MR imaging applications [88, 89]. From the results of T1 relaxometry and X-ray attenuation measurements, it is demonstrated that the formed Gd-Au DENPs achieved a r_1 relaxivity of $1.05 \text{ mM}^{-1}\cdot\text{s}^{-1}$ and enhanced X-ray attenuation property, which contributed to loaded Gd(III) ions as well as AuNPs. The in vivo biodistribution studies revealed that the Gd-Au DENPs gained a prolonged circulation time and were able to be cleared from the major organs within 24 h. More importantly, Gd-Au DENPs were colloidally stable and there was no significant toxicity even when the Au concentration increases to $50 \text{ }\mu\text{M}$. Recently, Rolfe et al. described a dendritic polymer for multimodal imaging. And it is the first time to combine exceptional spatial and anatomical resolution $^{19}\text{F}/^1\text{H}$ magnetic resonance imaging with highly sensitive fluorescence imaging [90].

9.4 Dendritic Polymer-Based Drug Delivery Systems for Cancer Therapy

Dendritic polymers have been investigated as nanoscale vehicles for carrying anti-cancer drugs for cancer therapy, which is based on the characteristics in tumor cell/tissue. For instance, the endothelial lining of the blood vessel wall is more permeable than normal state, leading to the selective higher accumulation of dendritic macromolecules in tumors, which is known as EPR effect or named passive targeting. Furthermore, tumor and its related tissues often overexpress specific receptors, antigens, or integrins, such as $\alpha_v\beta_3$, providing different ways to prepare drug delivery vehicles, as the dendritic drug delivery systems are functionalized with tumor-targeting moieties, resulting in active targeting. Currently, most anticancer drugs suffer from some challenges, including poor water solubility, nonspecific cytotoxicity, and unfavorable pharmacokinetics, which lead to low therapeutic index and high side effects. To overcome these shortcomings, functional dendritic polymers are designed and utilized as carriers for drug delivery. Compared with linear polymers, the dendritic ones are hyperbranched and globular macromolecules with a multivalent surface and interior shells, making them interesting candidates for the application as delivery systems for cancer therapy.

For dendritic polymer-based delivery systems for cancer therapy, the active anti-cancer pharmaceutical agents follow two different mechanisms. First is that these agents can be encapsulated into the internal supramolecular voids of dendritic polymers via physical incorporation based on host-guest chemistry. Physical incorporation has some straightforward advantages. It provides a rapid and simple preparation method without adverse effect on the structures of drugs and their pharmacological bioactivity. Moreover, the encapsulation of drug in the dendritic voids protects labile molecules from degradation and also solves solubility problem associated with hydrophobic compounds. The pioneered application of dendritic polymers with a unique chemical architecture and multivalent periphery as a candidate for drug delivery in cancer therapy is the so-called “dendritic box”-type architecture. In 1982, initial studies by Maciejewski have shown the use of egg shell-like architectures for the non-covalently entrapment of guest molecules in polymers. Until now, several types of dendritic polymers, such as dendrimer, hyperbranched polyethylenimines, polyglycerols [91], and polyesters [92, 93], have been investigated for the encapsulation of drugs. For example, Ye et al. investigated the carboxylate functionalized hyperbranched polyglycerols (HPGs), and their capacity to bind cisplatin, controllably release drug as well as inhibit proliferation of KU-7-luc bladder cancer cells. Carboxylates with different densities were conjugated to HPGs, resulting in HPG-C_{8/10}-MePEG_{6,5}-COOH₁₁₃ and HPG-C_{8/10}-MePEG_{6,5}-COOH₃₄₈ [91]. Both carboxylated HPGs showed a hydrodynamic diameter ranging from 5 to 10 nm and demonstrated good biocompatibility as well as effective inhibition of KU-7-luc bladder cancer cells. Meanwhile, they found that different levels of carboxylate had an effect on their behaviors of cisplatin loading and drug release. HPG-C_{8/10}-MePEG_{6,5}-COOH₁₁₃ bound up to 10 % w/w cisplatin and released drug at the

same rate over 7 days. In contrast, HPG-C_{8/10}-MePEG_{6.5}-COOH₃₄₈ bound up to 20 % w/w drug and indicated a significantly slower release than HPG-C_{8/10}-MePEG_{6.5}-COOH₁₁₃ at pH 6.0 and pH 7.4. In addition to direct entrapment of small-molecule drugs within the inner nanocavities of dendritic polymers, the self-assembly of polymers also allows drugs to be encapsulated into the void spaces. Zou et al. discovered the amphiphilic, modified hyperbranched aliphatic polyester Boltorn™ H20 (H20) was suitable to be designed as a controlled drug delivery system [92]. Biodegradable H20 is a spherical molecule with hydroxyl groups, allowing modification for other polymers, establishing an amphiphilic hyperbranched polyester. And this amphiphilic H20-AM was obtained through the introduction of succinic anhydride and glycidyl methacrylate. Besides, it could self-assemble into nanoparticles in aqueous solution, encapsulating daidzein. The DLS study showed the average particle size was 39.4 nm, and size distribution was relatively low. As for the behavior of drug release, nanoparticles degraded in a random one-by-one manner in the presence of the enzyme lipase PS and sustained several days, leading to a novel controlled drug release system.

Besides encapsulation of anticancer agents, chemical conjugation is another approach to develop dendritic polymers in cancer therapy. Anticancer drugs which are covalently conjugated to dendritic scaffold can achieve increased drug loading, controlled and selective drug release, and enhanced biosafety. Recently, environmentally responsive dendritic conjugates are reported to explore the drug release features and their potential as an anticancer platform. We have reported that the functionalization of pH sensitiveness and cellular targeting is a promising strategy to fabricate drug delivery systems with high efficiency, high selectivity, and low toxicity. We designed and prepared a poly(L-glutamic acid) dendrimer-based drug delivery system with both pH sensitive and functionalized with targeting moiety of biotin. The nanocubic polyhedral oligomeric silsesquioxane (POSS) was utilized as core, and the anticancer drug DOX was conjugated to the dendrimer via pH-sensitive hydrazine bonds. The low-generation dendrimer-based conjugate could self-assemble into nanoscale carrier with size around 50 nm confirmed via DLS and TEM. The nanoscale carrier demonstrated much higher drug release rates at pH 5.0 than those at pH 7.0 owing to the acid-sensitive hydrazine bonds. We proposed that the selectively cellular uptake of the biotin functionalized nanoscale carrier was mainly via receptor-mediated endocytosis, which was proved by cellular internalization study. The pH-sensitive dendrimer-based conjugate could be internalized in mice breast cancer 4T1 cells efficiently and resulting in close IC₅₀ values compared with that of free DOX. However, compared with the free drug, although slightly increased in vivo anticancer efficacy was observed in mice xenograft breast cancer models, the results demonstrated that it was still not satisfied. That was attributed to the low tumor accumulation mediated by low-generation dendrimer. Therefore, increasing generation and surface modification can be utilized to gain longer retention time and higher antitumor efficacy. However, increasing generation is not easy due to the steric hindrance and may cause side effects.

In order to achieve high tumor accumulation and ensure safety, polyethylene glycol (PEG), which can extend blood circulation in blood, is used to modify the

surface of dendrimers with low molecular weight and generation. We described the mPEGylated peptide dendron-doxorubicin conjugates based pH-responsive nanoparticles for cancer therapy, whereas the generation of the dendron was generation three (G3) [94]. DLS, SEM, and TEM studies revealed that the amphiphilic dendron-DOX conjugating with features of block polymers could self-assemble into nanoparticles, with neutral charged surface and diameter around 80 nm, showing globular morphology. Compared with normal physiological conditions, DOX release from the particles was much faster at pH 5.0, which imitated the tumor conditions, indicating pH-sensitive drug release owing to the cleavage of the hydrazone bonds. In terms of in vitro cytotoxicity, nanoparticles were shown to effectively kill breast tumor cell 4T1. Additionally, the nanoparticle produced excellent antitumor effects and induced apoptosis on the 4T1 breast tumor model, while DOX only showed moderate efficacy. In vivo toxicity evaluation demonstrated that drug-free dendron and drug-loading nanoparticles have had no significant systematic toxicity. Thus, the functionalized peptide dendron-DOX conjugate-based pH-responsive nanoparticles have the potential to be safe and efficient drug delivery systems for cancer therapy. It is notable that both environment-responsive linker (bone) and PEGylation are important to dendritic drug delivery systems. For example, Duncan and coworkers reported PAMAM dendrimer-based Pt-loaded dendritic systems where the cisplatin (Pt) was coupled with the dendrimer via an ester linkage and the Pt content was 20–25 wt.%, resulting in high aqueous solubility and stability (tenfold higher aqueous solubility compared with free Pt) [95]. However, although this dendritic drug delivery system showed insignificant toxicity toward all tested cancer cells lines, too slow drug release was also observed and the great stability (<1 % Pt release) upon incubation in PBS (pH 7.4) and citrate buffers (pH 5.5) at 37 °C for 72 h, indicating low anticancer efficacy in vivo. Therefore, to enhance the drug release rate as well as stability in circulation system, the drug can be covalently attached to dendritic scaffold via environmentally sensitive linker or bone. We also reported PEGylated dendritic diaminocyclohexyl-platinum (II) (dendrimer-DACHPt) conjugates, whereas the generation of the dendrimer was also generation three (G3). That dendritic conjugate were investigated as pH-sensitive drug delivery vehicles where the drug DACHPt with the same structure as oxaliplatin was linked to mPEGylated dendrimer by *N,O*-chelate coordination [96]. Carboxyl groups and alkynyl groups were employed to modify the periphery of the dendrimer, and azido mPEG chains were conjugated via a Cu(I)-catalyzed alkyne-azide click cycloaddition (CuAAC). Dendrimers with different mPEG chains, mPEG(750)-dendrimer-DACHPt and mPEG(2k)-dendrimer-DACHPt, were synthesized to investigate the behaviors of them in cancer therapy. This is necessary for investigating the drug release characteristics. After the 48 h incubation at pH 7.4 and 5.0, drug release results showed that both the mPEG(750)-dendrimer-DACHPt and mPEG(2k)-dendrimer-DACHPt were relatively stable at pH 7.4 and achieved a faster release in acetate buffer (pH 5.0) by 48 h, indicating good stability in circulation and relatively rapid release in endosome. This phenomenon was caused by pH-induced transformation of *N,O* chelate. The results from biodistribution studies demonstrated the platinum levels of oxaliplatin® measured in blood were much lower than conjugates

groups over the test time. Simultaneously, the platinum level in tumor tissue of oxaliplatin[®] was also much lower than conjugate groups and sharply decreased at 36 h postinjection, while the dendritic conjugates showed no significant decrease. Meanwhile, the *in vivo* anticancer efficacy was observed, and the dendrimer-DACHPt conjugates achieved obviously better suppression of tumor growth than oxaliplatin[®] at equal doses in an SKOV-3 human ovarian cancer xenograft. Those studies and results indicated that the high accumulation and significantly increased anticancer efficacy can be achieved via the PEGylation and chemical conjugation.

In addition to PEGylation, dendronization strategy has been used to prepare dendritic polymers with high molecular weight and biodegradable features, and the dendritic drug delivery systems are able to carry drug to tumor with high efficacy. The new polymers with dendritic architecture were referred to as “dendronized polymers” [83, 84]. By optimization of the structures, some amphiphilic dendronized polymers can self-assemble into nanoparticles via combination of the advantages of dendrimer and linear polymer [85, 86], resulting in nanoparticles with desired sizes suitable for cancer treatment. We have reported the preparation and characterization of dendronized heparin-DOX conjugate and its self-assembled nanoparticles as pH-sensitive drug delivery vehicles for breast tumor therapy, as shown in Fig. 9.2 [20]. The low-generation peptide dendron (G2) was conjugated to heparin via click reaction, and the drug DOX was conjugated to the hydrophobic dendron through pH-sensitive hydrazone bond. The prepared amphiphilic dendronized polymer self-assembled into compact nanoparticle with negatively charged surface and size of 80–100 nm, which were determined by DLS and TEM studies. That dendronized heparin-DOX conjugate-based nanoscale vehicle demonstrated pH-sensitive drug release features and significantly increased antitumor activity, high anti-angiogenesis effects, and induced apoptosis on the 4T1 breast tumor model. Because the heparin is non-cytotoxic, biodegradable, rich in animal tissues, and water soluble and of its application as an anticoagulant drug due to its ability to accelerate the rate at which antithrombin inhibits serine proteases in the blood coagulation cascade [97, 98], the dendronized heparin-DOX conjugate-based nanoscale vehicle also resulted in no significant toxicity to healthy organs of both tumor-bearing and healthy mice. Therefore, the dendronization and self-assembly can overcome the synthetic challenges associated with preparation of dendritic polymer-based nanoparticles with satisfied sizes for tumor passive targeting.

9.5 Dendritic Polymer-Based Nanosystems for Cancer Therapy Guided by Imaging

At the intersection between diagnosis and therapeutic, focus has been put on integrating the above-described approaches into a single formulation, termed as “theranostics,” providing a novel method for cancer treatment. Theranostic is related to but different from traditional diagnosis and treatment. It is committed to a

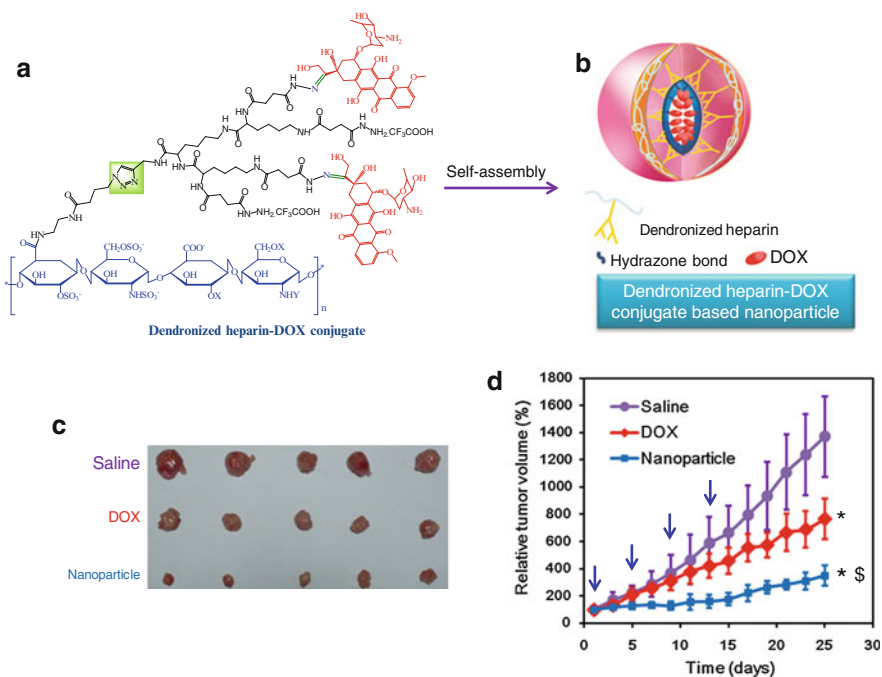


Fig. 9.2 Structures of dendronized heparin-DOX conjugate (a) and the illustration of dendronized heparin-DOX conjugate self-assembled into nanoparticles (b). The dendronized polymer-based nanoparticles resulted in higher in vivo 4T1-tumor growth inhibition (c, d) (Reprinted from reference [20], Copyright 2013, with permission from Elsevier)

comprehensive and precise diagnostic, as well as various treatment options that are suitable for patients. Moreover, theranostics can provide valuable real-time monitoring of agent delivery, agent release, and therapeutic outcomes following treatments. The nanoparticles, owing to exquisite nanostructures and huge surface area to volume ratios, may offer opportunities to develop theranostic platforms that can simultaneously monitor and treat disease in a single platform. Besides, nanoparticles can be functionalized via chemical conjugation or physical encapsulation to accommodate the different requirements of theranostic systems. Meanwhile, nanostructures have the ability to target tumors via passive accumulation or active-targeting approaches. Up to now, several nanoparticle vehicles, such as dendritic polymers [99], silica nanoparticles [51, 52], magnetic nanoparticles [100], gold nanomaterials [101, 102], carbon nanomaterials [48, 103], and protein-based nanomaterials, have been explored in theranostics for cancer [104, 105]. Functional dendritic polymers, as one of the excellent nanoscale carriers, provide numerous functional groups and adequate spatial cavities for imaging and therapeutic components while maintaining good solubility and biocompatibility. All their unique properties make them promising candidates for cancer theranostic.

Currently, representative investigated imaging modalities are X-ray computed tomography (XCT), MRI, ultrasound imaging (UI), optical imaging (OI), and nuclear imaging (NI), which have been applied to view the human body in order to diagnose, monitor, or treat the tumors. Each type of modality has its advantages and drawbacks and provides different information about the area of interest being diagnosed or treated. For the functional nanomaterials for cancer theranostics, selection of an appropriate imaging modality is highly dependent on the biochemical process which is expected to visualize and the type of imaging data that is needed to be obtained. To dendritic polymer-based theranostics nanocarriers, the representative imaging modalities are OI (including DOX for fluorescence, photodynamic therapy) and MRI (including Gd^{3+} -labeled carriers and magnetic hybrid nanoparticles).

9.5.1 Near-Infrared-Based Dendritic Nanosystems

Optical imaging is widely used as a biomedical imaging modality for preclinical research due to the attractive features, including low cost, good spatial resolution, and high sensitivity. To the anticancer agents without imaging property, the biodistribution of dendritic theranostic nanosystems in vivo can be guided by NIR imaging, and the imaging probes include fluorescein isothiocyanate (FITC), Cy5, and Cy5.5. Meanwhile, the interaction with cells and their cellular entry can be visualized by flow cytometry, confocal microscopy, and UV/visible spectroscopy [35, 106]. Backer et al. reported the NIR dye Cy5-labeled and boronated PAMAM dendrimers (VEGF-BD/Cy5) and the dendrimer without VEGF (BD/Cy5) for boron neutron capture therapy (BNCT) [107]. The generation 5 dendrimers were modified with vascular endothelial growth factors (VEGF). For in vivo analysis, NIR fluorescent imaging was employed to study their biodistribution, uptake in tumor-bearing mice, and monitor the in vivo activities in 4T1 mouse breast carcinoma, resulting in selective accumulation of VEGF-BD/Cy5. The NIR dye Cy5-labeled dendritic vehicle (VEGF-BD/Cy5) was therefore potential to be theranostic vehicle for BNCT of tumor neovasculature.

The in vivo increased anticancer efficacy and accumulation in tumor can be mediated by multifunctional dendritic polymer-based theranostic systems, where the theranostic nanosystems are functionalized with active-targeting moieties and imaging probe FITC. For example, the cationic PAMAM dendrimers were partly neutralized through partial acetylation, providing enhanced solubility and preventing protein adsorption and nonspecific targeting interactions in vivo, as the surface amino groups were protected. On the other hand, the acetylated dendrimers were further conjugated with imaging probe FITC, targeting moiety folic acid (FA) and chemotherapeutic drug paclitaxel, resulting in cancer-targeting theranostic nanosystems. These multifunctional theranostic nanosystems have been investigated as targeting drug delivery systems, and their in vitro targeting to cancer cells can be guided by fluorescence imaging [108]. It is also reported that the acetylated PAMAM

dendrimers were further functionalized with the targeting moiety biotin and imaging probe FITC. The targeting drug delivery was achieved and monitored by flow cytometry and confocal microscopy, showing that the theranostic nanosystems functionalized with biotin exhibited much higher cellular uptake into HeLa cells than that without biotin [109]. Choi et al. reported the cationic G5 PAMAM dendrimer functionalized with FITC and FA as theranostic gene delivery vectors for cancer treatment. The theranostic nanosystems could self-assemble with complementary DNA oligonucleotides (5'-phosphate-modified 34-base-long oligonucleotides), and the pDNA was protected. The novel nanoscale systems lead to gene delivery systems with "cluster effects" feature that targeted cancer cells that overexpressed the high-affinity folate receptor, which was monitored by fluorescence imaging. In vitro studies of the nanoparticles loading pDNA showed specific binding to KB cells [110]. Those studies and results indicated that functional dendrimers with targeting moieties and imaging probe of FITC could be employed as theranostic nanosystems for gene and drug delivery systems.

Recently, dendronization strategy also showed possibility for theranostic nanosystems combining drugs delivery and fluorescence imaging. Recently, fluorescent materials with molecular imaging functionality are designed as biomaterials studied in biology and pathophysiology. Among those materials, water-soluble dendronized polyfluorenes have been reported as their extremely high fluorescence quantum yield in aqueous media [111]. Liu and coworkers reported hyperbranched polyfluorene with ionic groups for the fluorescence imaging of cancer diagnosis [112]. PEGylation was employed to functionalize the fluorescent polymers for drug delivery, which might be suitable for different drugs. Bai et al. reported novel dendronized fluorescent polyfluorenes were prepared from hydrophilic monomers and hydrophobic comonomers by polymerization [87]. These dendronized polymers were water soluble and showed differential cellular uptake and strong fluorescence. Once loaded with anticancer drugs, the dendronized fluorescent polyfluorenes might be suitable for cancer theranostics.

Therefore, fluorescence imaging based theranostics plays an important part in real-time monitoring of drug distribution and assessment of therapy in preclinical research. Ornelas and coworkers designed a dendrimer-based building block for theranostics [99]. The Janus-like dendrimer system was formed by combining 2 separately synthesized dendrons, consisting of 9 azide termini, 9 amine termini, and 54 terminal acid groups. A near-infrared (NIR) cyanine dye was employed by reacting with the nine amine termini to provide optical imaging. Besides, this system showed no toxicity toward T98G human cells. The synthetic strategy reported in this study might offer an effective way for theranostics. Santra et al. synthesized a water-soluble, hyperbranched polyhydroxyl (HBPH) nanoparticle which simultaneously encapsulated the near-infrared dye indocyanine green (ICG) for imaging and cytochrome *c* (Cyt *c*) as a therapeutic agent [113]. The presence of amphiphilic pockets inside the three-dimensional hyperbranched structures played an important role in encapsulation of above functional cargos. It was reported that the introduction of folic acid developed a targeted transmembrane carrier, and the Cyt *c*-encapsulating HBPH nanoparticles could deliver this functional apoptosis-initiating

protein to folate-receptor-positive cancer cells, followed by apoptotic response and programmed cell death, like fluorescent dyes and a protein. Moreover, confocal microscopy was utilized to optically confirm the intracellular release of Cyt *c* and cell apoptosis. The results indicated that there was an enhanced fluorescence in the cytoplasm when the folate nanoparticles were incubated with lung cancer cells (A549) which express the folate receptor, while there was no significant fluorescence in MCF 7 cells which did not express the folate receptor. Interestingly, after being preincubated with free folic acid, the folate nanoparticles showed minimal internalization in the same A549 cells. Moreover, phenomena involved dramatic cellular morphological changes and cell death were observed when the cells were incubated with the Cyt *c*-encapsulating HBPH nanoparticles. In conclusion, this novel HBPH nanoparticle-based targeted release system might have great potential for use in theranostics.

Besides fluorescent dyes, doxorubicin (DOX), as one of the mostly utilized anticancer pharmaceuticals, has been widely investigated not only for its anticancer effect but also for its autofluorescence, which makes it an unordinary candidate for theranostic. DOX can be conjugated with or encapsulated into dendritic polymers to work its therapeutic effects. Additionally, the fluorescence of DOX can be directly measured without additional probes. Based on the autofluorescence of DOX, the mechanistic studies, including cell uptake and internalization, were carried out in the absence of other imaging probes. Additionally, the effect of PEGylation degree on the tumor-targeting efficiency of the dendritic conjugates in SKOV-3 tumor models was also visualized by *in vivo* fluorescence imaging. In recent years, we focus on this kind of theranostic system and try to improve its functions. We reported an amphiphilic peptide dendritic copolymer-DOX nanoscale conjugate that prepared via two-step highly efficient click reaction as an anticancer agent. The introduction of the glycyphenylalanylleucylglycine tetrapeptide spacer (Gly-Phe-Leu-Gly, GFLG), which is a sensitive cathepsin B, a lysosomal cysteine protease overexpressed in many tumor cells and tumor endothelial cells, allowed enzyme-responsive release of DOX. Moreover, the autofluorescence of DOX provided information about the delivery of anticancer drugs, leading to the further understanding of the anticancer action principle. We demonstrated the dendron-GFLG-DOX conjugate could self-assemble into compact nanoparticles with negatively charged surface through DLS and TEM studies, as shown in Fig. 9.3 [114]. The drug release tests showed this conjugate possessed enzyme-responsive drug release features while it was stable under normal conditions. Simultaneously, the fluorescence of DOX was used directly to measure cellular uptake without other markers. CLSM images indicated designed nanoparticles could be uptaken by cancer cells, leading to potential anticancer efficacy. The *ex vivo* fluorescent image also indicated accumulation and long-time retention of nanoparticles within tumors, showing therapeutic outcomes following treatments. Consequently, the nanoparticles substantially enhanced anti-tumor efficacy compared with the free DOX both *in vitro* and *in vivo*. Furthermore, through body weight shifts, the nanoparticles decreased DOX-induced systemic toxicities. Histological analysis of organs further indicated free DOX-induced cardiotoxicity, while nanoparticles showed good biosafety [115]. Therefore, the

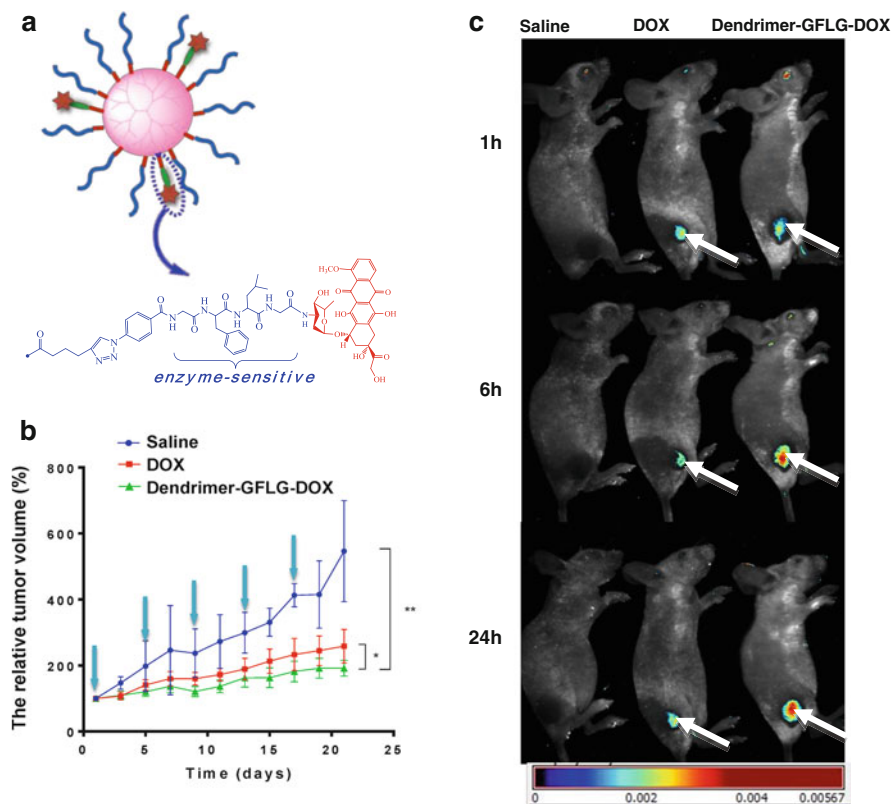


Fig. 9.3 Molecular structure of dendrimer-GFLG-DOX conjugate (a) and that conjugate assembled to nanoparticles. Comparison of the tumor inhibition effect of dendrimer-GFLG-DOX versus free-drug DOX and saline in the human ovarian tumor SKOV-3 model conjugate demonstrated significant enhanced tumor inhibition at equal dose (b). The in vivo biodistribution of DOX and the conjugate was measured by fluorescent imaging in nude mice bearing SKOV-3 tumor (1 h, 6 h, 24 h) after injection through caudal vein (c) (Reprinted from reference [114], Copyright 2014, with permission from The Royal Society of Chemistry)

dendron-GFLG-DOX conjugate-based nanoparticle served as a potential theranostic vehicle for cancer. Extensive investigation has been performed by us. Recently, we described the preparation of enzyme-sensitive mPEGylated peptide dendrimer-doxorubicin conjugate and its potential as theranostic platform for breast tumor [114]. On one hand, DOX acted as an antitumor drug. On the other hand, it provided a real-time monitoring of its own delivery. From the in vivo fluorescent imaging study, dendrimer-DOX conjugate-based nanoparticles had the ability to rapidly accumulate at tumor site via EPR effect due to the appropriate nanoscale size, showing increasing signals in tumor and reached a maximum at 24 h. In contrast, free DOX only had a modest signal and was barely changed. All these in vivo imaging results suggested the delivery and aggregation of DOX and might provide a useful strategy for design of dendritic polymer as a safe and effective theranostic scaffold.

9.5.2 Dendritic Theranostic Nanosystems for Photodynamic Therapy

Photodynamic therapy (PDT) has emerged as one of the important and well-recognized clinical therapeutic strategies to cancer and other diseases therapy, as its great advances have been observed in recent years, which involves three elements: a photosensitizer, light, and oxygen [116]. Compared with chemotherapy and radiotherapy, the PDT for cancer therapy has showed some advantages, as their relative specificity and selectivity of PDT with low side effects. Additionally, photosensitizing drugs have been known and applied in medicine for several thousand years, and some agents, including porphyrins, their derivatives, and porphyrin-inducing drugs, are the most commonly utilized photosensitizers [117]. Similar to the other small-molecule drugs, porphyrins and their derivatives showed some shortcomings. Therefore, biodegradable polymeric nanoparticles have been designed for PDT to enhance their accumulation into tumors and control drug release from as early as 1990, and the first report is hematoporphyrin adsorbed in polyalkylcyanoacrylate nanoparticles [118]. Moreover, the outstanding near-infrared (NIR) optical properties of PDT agents, including porphyrins and their derivatives, provide possibility of their nanoscale systems for cancer theranostic and visualization of malignant tissue by fluorescence imaging (Fig. 9.4) [119].

Dendritic polymers, such as dendrimers, have been designed to carrier PDT agents for cancer PDT [120]. Firstly, owing to the internal cavities of structural features, dendrimers have been employed to encapsulate PDT agents. For example, the high-generation dendrimers were functionalized with phloroglucinol and succinic acid, and the resulted water-soluble, anionic surface and biocompatible dendritic polymers were utilized to load hydrophobic PDT agent of protoporphyrin IX (PpIX) [121]. The cytotoxicity of those theranostics nanosystems on dalton lymphoma ascites (DLA) cancer cell lines upon visible light treatment showed much higher cytotoxic reactive oxygen species (ROS) than those of free PpIX and its free-drug carriers. Kono et al. modified the PAMAM and PPI dendrimers via

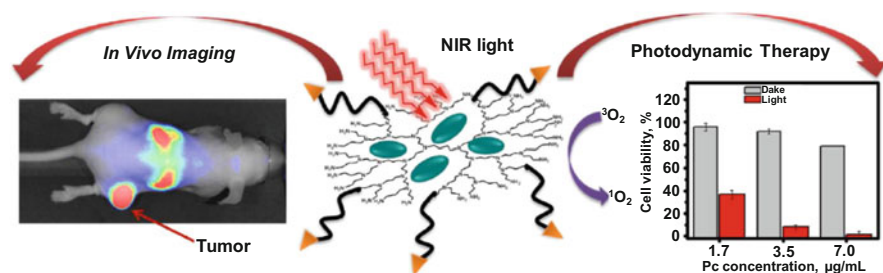


Fig 9.4 The illustration of tumor-targeting dendritic polymer-based theranostic nanosystems for cancer photodynamic therapy and their in vivo cancer theranosis and the relative intracellular ROS levels in A2780/AD cells incubated with theranostic dendritic nanocarriers (Image is adapted with permission from reference [119], Copyright 2013, American Chemical Society)

PEGylation, resulting in PEG-PAMAM and PEG-PPI to carry photosensitizers rose bengal (RB) and PpIX for PDT. It was found that PEG-PPI-loaded PpIX demonstrated higher cytotoxicity in vitro upon visible light treatment, compared with free PpIX, suggesting that PEGylated cationic dendrimers were promising vehicles for PDT [122]. Additionally, PEGylated PPI dendrimer functionalized with luteinizing hormone-releasing hormone (LHRH) peptide also showed efficient delivery phthalocyanines (Pc, as one photosensitizer) [119]. The theranostic nanosystems demonstrated subcellular localization in vitro, and their organ distribution in vivo was determined via the intrinsic fluorescence properties of phthalocyanine [119].

9.5.3 *Magnetic Resonance Imaging-Based Dendritic Nanosystems*

Magnetic resonance imaging (MRI) has been one of the most promising multifunctional imaging techniques, since it possesses advantages such as noninvasiveness, high spatial resolution, and relatively deep penetration toward soft tissue. Nowadays, MRI-based theranostic platform has been extensively investigated, as it is much more sensitive than X-ray technologies for soft tissues in human body. However, to MRI-based theranostic nanosystems for cancer treatment, some challenges still remain and the future exploration of paramagnetic MRI theranostic nanosystems might meet the following requirements: (1) the MRI probes and anticancer drugs should be conjugated or loaded into a single scaffold; (2) they should specifically target tumors; (3) the relaxivity r_1 should be high and the MRI probes should be at low doses; (4) the intravascular duration should be long enough; (5) the excretion time should be suitable; (6) the drugs and MRI probes should be released from the carriers to meet the requirement of biosafety.

Gadolinium(III) chelates have been proved as the most commonly used T_1 MRI contrast agents in clinical application, due to their ability to provide a positive image contrast. Some nanoscale systems labeled with gadolinium(III) chelates, such as Gd-DTPA and Gd-DOTA, have demonstrated to increase the longitudinal relaxation rates of surrounding water protons and have much higher positive single intensity, resulting in the possibility as novel nanoscale MRI contrast agents for cancer diagnosis. When both anticancer agents and gadolinium(III) chelates are conjugated or loaded to nanoscale vehicles, theranostic nanosystems are obtained for cancer treatment and the possibility to guide their biodistribution and tumor targeting for both imaging and therapeutic agents can be achieved by MRI. Tomalia et al. have reported the dendritic polymers can be used as multipurpose theranostic nanosystems for anticancer drug delivery and diagnostic MRI contrast agents [17]. K. Kono and coworkers have proposed some multifunctional liposomes based on temperature-sensitive copoly(EOEOVE-block-ODVE) and PAMAM dendrimers functionalized Gd chelate. The liposomes have temperature-responsive drug release features and MR imaging functions. The anticancer drug DOX was then successfully been

encapsulated into the liposomes, giving dendritic polymer-based theranostic liposomes, which were capable of retaining the therapeutic agent within their interior at physiological temperatures and releasing the drug at temperatures above 40 °C. The *in vivo* accumulation processes of the theranostic liposomes were guided via MR imaging, suggesting the size of liposome affected their accumulation efficiency in tumors [123]. Those results provide some references for designing dendritic polymer-based liposomes for cancer treatment via optimization of the molecular structures.

Recently, Li et al. have successfully synthesized amphiphilic multiarm star block copolymer-based unimolecular for simultaneously cancer-targeted drug delivery and MR imaging [124]. This copolymer-based unimolecular micelle, H40-PCL-b-P(OEGMA-Gd-FA), was composed of the following parts: (a) core, a fourth-generation hyperbranched polyester (Boltorn H40); (b) inner layer, a hydrophobic poly(3-caprolactone) (PCL); and (c) hydrophilic outer corona, a hydrophilic poly(oligo(ethylene glycol) monomethyl ether methacrylate) (POEGMA) which was conjugated with MRI contrast agent DOTA-Gd (Gd) and targeting group folic acid (FA). Anticancer drug paclitaxel was encapsulated within the hydrophobic core and achieved controlled release of up to 80 % loaded drug over ~120 h. In addition, the employment of targeting moieties (FA) considerably enhanced *in vitro* cytotoxicity with ~23 % of cell viability at a polymer concentration of 80 mg/mL, which suggested improved anticancer efficacy. From the results of *in vitro* MRI experiments, it indicated that the value of T1 relaxivity ($18.14 \text{ s}^{-1} \text{ mM}^{-1}$) in unimolecular micelles group was much higher than that in the small-molecule counterpart ($3.12 \text{ s}^{-1} \text{ mM}^{-1}$). Furthermore, *in vivo* MR imaging experiments in rats revealed markedly positive contrast enhancement, and relatively long blood circulation, demonstrating this copolymer-based unimolecular micelle could serve as a potential theranostic system for cancer. More recently, another good example employing dendritic polymer as a potential theranostic has been reported by Ardana et al. They synthesized functional hyperbranched polymers (HBPs), which contained an imaging modality (^{19}F MRI) and carried therapeutic genes at the same time [125]. The in-depth analyses of the molecular structure, including 1D and 2D NMR and UV/vis, were performed to explore whether the diagnostic and therapeutic agents were complementary and played their respective roles. The optimized routes for conjugation of biomolecules utilizing the RAFT end group were also identified and did not show significant effect on the molecular integrity.

In addition to gadolinium(III) chelate-based nanoscale systems, superparamagnetic nanomaterials, such as ZnFe_2O_4 , NiFe_2O_4 , MnFe_2O_4 , CoFe_2O_4 , and Fe_3O_4 , have been reported as a kind of important magnetic materials with zero coercive force, residual magnetism, and high saturation magnetization. Multifunctional superparamagnetic nanoparticles, owing to their biocompatibility, can also be applied in the therapy of cancers, such as drug delivery, gene delivery, PDT, and PTT, which have attracted ever-increasing attention due to their unique physical characteristics and the capability of targeting cancer. Kim et al. reported iron oxide-based magnetically targeted drug delivery, whereas the biodegradable PLGA polymer was employed to encapsulate the inorganic nanoparticles and drug DOX. The

synergetic targeting efficiency was enhanced via the magnetic guiding of the inorganic-organic hybrid [126].

Among the superparamagnetic nanomaterials, the monodisperse magnetic nanoparticles, such as superparamagnetic iron oxide (SPIO), have been employed for the cancer theranostics [127–129]. Dendritic polymers, such as dendrimers and dendrons, have been utilized to functionalize the SPIO to improve the hydrophilic and biocompatibility [130–132]. Two strategies, including encapsulation and surface modification, were employed to synthesize dendritic polymer/SPIO nanoparticle hybrids for cancer diagnosis and therapy. Firstly, the unique structural feature of dendritic polymers, such as the cavity, allows them to be employed as templates to encapsulate or assemble SPIO, giving various water-soluble nanoscale vehicles. Additionally, the rich surface chemistry of the dendrimers or dendrons provides possibility to carry out surface functionalization with tumor-targeting moieties and hydrophilic polymers, such as PEG, resulting in nanosystems with good colloidal stability [133, 134]. It is notable that the nanosystems can load not only SPIO but also the anticancer drugs, giving novel theranostic nanosystems for cancer treatment. Secondly, tunable surface chemistry of SPIO allows their surface modification via conjugation chemistry [135, 136]. After conjugation, the dendronized nanoparticles are stable in water and can be further employed as imaging probes, drug/gene delivery vehicles, or theranostic nanocarriers [132, 137, 138].

9.6 Conclusion

In this chapter, we have highlighted the typical dendritic polymer-based nanosystems with multifunctional structures and components for tumor diagnosis and therapy guided by imaging. Dendritic polymers have showed several advantages over conventional polymers, including the fact that they are well-defined molecules and have controlled nanoscale size and flexible chemistry. The advantages allow these nanostructures to be used as ideal vehicles for both passive and active-targeting drug delivery and as diagnostic agents for cancer treatments. Dendritic polymer-based nanosystems have achieved a number of encouraging applications, and some are in the final stages of human clinical testing in the US FDA approval process [139, 140]. It is notable that dendritic polymer-based theranostic nanoystems for tumor-targeting theranosis have provided multifunctions through the combination of the diagnosis and therapy into one scaffold and one dosage, enabling the monitoring and adjustment of the therapy during the disease progression. Up to today, dendritic polymer-based theranostic nanoystems can directly reflect the therapeutic outcomes and the behaviors of the nanosystems in vivo, such as biodegradability, biodistribution, and accumulation in tumors. However, the studies of the dendritic polymer-based nanosystems for tumor diagnosis, therapy, and targeting theranostic are still in its infancy and nanosystems have yet to be clinically used in the world. Due to some inherent problems, such as the vulnerability and stability issues, biodegradability and biosafety during scale-up production have not been addressed.

Much effort is required for systematic research of the safety issue, efficiency of drug delivery, and diagnosis before these theranostic nanosystems reach the clinical trials, which can be achieved via optimizing the dendritic structures. Overall, the multifunctional dendritic polymer-based nanosystems have the potential to be developed a general platform for cancer therapy guided by imaging.

References

1. Aggarwal P, Hall JB, McLeland CB, Dobrovolskaia MA, McNeil SE (2009) Nanoparticle interaction with plasma proteins as it relates to particle biodistribution, biocompatibility and therapeutic efficacy. *Adv Drug Deliv Rev* 61:428–437
2. Peer D, Karp JM, Hong S, Farokhzad OC, Margalit R, Langer R (2007) Nanocarriers as an emerging platform for cancer therapy. *Nat Nanotechnol* 2:751–760
3. Cho K, Wang X, Nie S, Shin DM (2008) Therapeutic nanoparticles for drug delivery in cancer. *Clin Cancer Res* 14:1310–1316
4. Yang Y, Pan D, Luo K, Li L, Gu Z (2013) Biodegradable and amphiphilic block copolymer–doxorubicin conjugate as polymeric nanoscale drug delivery vehicle for breast cancer therapy. *Biomaterials* 34:8430–8443
5. Soppimath KS, Aminabhavi TM, Kulkarni AR, Ruzdzinski WE (2001) Biodegradable polymeric nanoparticles as drug delivery devices. *J Control Release* 70:1–20
6. Kroon J, Metselaar JM, Storm G, van der Pluijm G (2014) Liposomal nanomedicines in the treatment of prostate cancer. *Cancer Treat Rev* 40:578–584
7. Huang X, Jain PK, El-Sayed IH, El-Sayed MA (2007) Gold nanoparticles: interesting optical properties and recent applications in cancer diagnostics and therapy. *Futur Med* 2:681–693
8. Kam NWS, O’Connell M, Wisdom JA, Dai H (2005) Carbon nanotubes as multifunctional biological transporters and near-infrared agents for selective cancer cell destruction. *Proc Natl Acad Sci U S A* 102:11600–11605
9. Gao X, Cui Y, Levenson RM, Chung LW, Nie S (2004) In vivo cancer targeting and imaging with semiconductor quantum dots. *Nat Biotechnol* 22:969–976
10. Vicent MJ, Greco F, Nicholson RI, Paul A, Griffiths PC, Duncan R (2005) Polymer therapeutics designed for a combination therapy of hormone-dependent cancer. *Angew Chem* 117:4129–4134
11. Li C, Yu D-F, Newman RA, Cabral F, Stephens LC, Hunter N, Milas L, Wallace S (1998) Complete regression of well-established tumors using a novel water-soluble poly (L-glutamic acid)-paclitaxel conjugate. *Cancer Res* 58:2404–2409
12. Hreczuk-Hirst D, Chicco D, German L, Duncan R (2001) Dextrins as potential carriers for drug targeting: tailored rates of dextrin degradation by introduction of pendant groups. *Int J Pharm* 230:57–66
13. Duncan R (2006) Polymer conjugates as anticancer nanomedicines. *Nat Rev Cancer* 6:688–701
14. Gillies ER, Frechet JM (2005) Dendrimers and dendritic polymers in drug delivery. *Drug Discov Today* 10:35–43
15. Patri AK, Majoros IJ, Baker JR (2002) Dendritic polymer macromolecular carriers for drug delivery. *Curr Opin Chem Biol* 6:466–471
16. Liu M, Fréchet JM (1999) Designing dendrimers for drug delivery. *Pharm Sci Technol Today* 2:393–401
17. Tomalia D, Reyna L, Svenson S (2007) Dendrimers as multi-purpose nanodevices for oncology drug delivery and diagnostic imaging. *Biochem Soc Trans* 35:61
18. Svenson S (2009) Dendrimers as versatile platform in drug delivery applications. *Eur J Pharm Biopharm* 71:445–462

19. Berna M, Dalzoppo D, Pasut G, Manunta M, Izzo L, Jones AT, Duncan R, Veronese FM (2006) Novel monodisperse PEG-dendrons as new tools for targeted drug delivery: synthesis, characterization and cellular uptake. *Biomacromolecules* 7:146–153
20. She W, Li N, Luo K, Guo C, Wang G, Geng Y, Gu Z (2013) Dendronized heparin – doxorubicin conjugate based nanoparticle as pH-responsive drug delivery system for cancer therapy. *Biomaterials* 34:2252–2264
21. Mo B, Liu H, Zhou X, Zhao Y (2015) Facile synthesis of photolabile dendritic-unit-bridged hyperbranched graft copolymers for stimuli-triggered topological transition and controlled release of Nile red. *Polym Chem* 6:3489–3501
22. Liu J, Pang Y, Huang W, Zhu X, Zhou Y, Yan D (2010) Self-assembly of phospholipid-analogous hyperbranched polymers nanomicelles for drug delivery. *Biomaterials* 31:1334–1341
23. Paleos CM, Tsiourvas D, Sideratou Z, Tziveleka L-A (2010) Drug delivery using multifunctional dendrimers and hyperbranched polymers. *Expert Opin Drug Deliv* 7:1387–1398
24. Fischer M, Vögtle F (1999) Dendrimers: from design to application—a progress report. *Angew Chem Int Ed* 38:884–905
25. Bosman A, Janssen H, Meijer E (1999) About dendrimers: structure, physical properties, and applications. *Chem Rev* 99:1665–1688
26. Tomalia D, Baker H, Dewald J, Hall M, Kallos G, Martin S, Roeck J, Ryder J, Smith P (1985) A new class of polymers: starburst-dendritic macromolecules. *Polym J* 17:117–132
27. Esfand R, Tomalia DA (2001) Poly(amidoamine)(PAMAM) dendrimers: from biomimicry to drug delivery and biomedical applications. *Drug Discov Today* 6:427–436
28. Darbre T, Reymond J-L (2006) Peptide dendrimers as artificial enzymes, receptors, and drug-delivery agents. *Acc Chem Res* 39:925–934
29. Kobayashi H, Brechbiel MW (2005) Nano-sized MRI contrast agents with dendrimer cores. *Adv Drug Deliv Rev* 57:2271–2286
30. Konda SD, Aref M, Wang S, Brechbiel M, Wiener EC (2001) Specific targeting of folate-dendrimer MRI contrast agents to the high affinity folate receptor expressed in ovarian tumor xenografts. *Magn Reson Mater Phys Biol Med* 12:104–113
31. Kobayashi H, Brechbiel MW (2004) Dendrimer-based nanosized MRI contrast agents. *Curr Pharm Biotechnol* 5:539–549
32. Patri AK, Kukowska-Latallo JF, Baker JR Jr (2005) Targeted drug delivery with dendrimers: comparison of the release kinetics of covalently conjugated drug and non-covalent drug inclusion complex. *Adv Drug Deliv Rev* 57:2203–2214
33. Tang MX, Redemann CT, Szoka FC (1996) In vitro gene delivery by degraded polyamidoamine dendrimers. *Bioconjug Chem* 7:703–714
34. Dufès C, Uchegbu IF, Schätzlein AG (2005) Dendrimers in gene delivery. *Adv Drug Deliv Rev* 57:2177–2202
35. Kolhe P, Khandare J, Pillai O, Kannan S, Lieh-Lai M, Kannan RM (2006) Preparation, cellular transport, and activity of polyamidoamine-based dendritic nanodevices with a high drug payload. *Biomaterials* 27:660–669
36. Han L, Huang R, Li J, Liu S, Huang S, Jiang C (2011) Plasmid pORF-hTRAIL and doxorubicin co-delivery targeting to tumor using peptide-conjugated polyamidoamine dendrimer. *Biomaterials* 32:1242–1252
37. Hu J, Su Y, Zhang H, Xu T, Cheng Y (2011) Design of interior-functionalized fully acetylated dendrimers for anticancer drug delivery. *Biomaterials* 32:9950–9959
38. D’Emanuele A, Attwood D (2005) Dendrimer–drug interactions. *Adv Drug Deliv Rev* 57:2147–2162
39. Kannan RM, Nance E, Kannan S, Tomalia DA (2014) Emerging concepts in dendrimer-based nanomedicine: from design principles to clinical applications. *J Intern Med* 276:579–617
40. Shah ND, Parekh HS, Steptoe RJ (2014) Asymmetric peptide dendrimers are effective linkers for antibody-mediated delivery of diverse payloads to B cells in vitro and in vivo. *Pharm Res* 31:3150–3160

41. Medina SH, El-Sayed ME (2009) Dendrimers as carriers for delivery of chemotherapeutic agents. *Chem Rev* 109:3141
42. Khandare JJ, Jayant S, Singh A, Chandna P, Wang Y, Vorsa N, Minko T (2006) Dendrimer versus linear conjugate: influence of polymeric architecture on the delivery and anticancer effect of paclitaxel. *Bioconjug Chem* 17:1464–1472
43. Kopeček J, Kopečková P, Minko T, Lu Z-R, Peterson C (2001) Water soluble polymers in tumor targeted delivery. *J Control Release* 74:147–158
44. Kopeček J, Kopečková P, Minko T, Lu Z-R (2000) HPMA copolymer–anticancer drug conjugates: design, activity, and mechanism of action. *Eur J Pharm Biopharm* 50:61–81
45. Tekade RK, Kumar PV, Jain NK (2008) Dendrimers in oncology: an expanding horizon. *Chem Rev* 109:49–87
46. Picard FJ, Bergeron MG (2002) Rapid molecular theranostics in infectious diseases. *Drug Discov Today* 7:1092–1101
47. Baum RP, Kulkarni HR (2012) Theranostics: from molecular imaging using Ga-68 labeled tracers and PET/CT to personalized radionuclide therapy—the Bad Berka experience. *Theranostics* 2:437
48. Mashal A, Sitharaman B, Li X, Avti PK, Sahakian AV, Booske JH, Hagness SC (2010) Toward carbon-nanotube-based theranostic agents for microwave detection and treatment of breast cancer: enhanced dielectric and heating response of tissue-mimicking materials. *Biomed Eng IEEE Trans* 57:1831–1834
49. Ho D, Sun X, Sun S (2011) Monodisperse magnetic nanoparticles for theranostic applications. *Acc Chem Res* 44:875–882
50. Singh SP (2011) Multifunctional magnetic quantum dots for cancer theranostics. *J Biomed Nanotechnol* 7:95–97
51. Lee JE, Lee N, Kim T, Kim J, Hyeon T (2011) Multifunctional mesoporous silica nanocomposite nanoparticles for theranostic applications. *Acc Chem Res* 44:893–902
52. Cheng S-H, Lee C-H, Yang C-S, Tseng F-G, Mou C-Y, Lo L-W (2009) Mesoporous silica nanoparticles functionalized with an oxygen-sensing probe for cell photodynamic therapy: potential cancer theranostics. *J Mater Chem* 19:1252–1257
53. Han X-J, Sun L-F, Nishiyama Y, Feng B, Michiue H, Seno M, Matsui H, Tomizawa K (2013) Theranostic protein targeting ErbB2 for bioluminescence imaging and therapy for cancer. *PLoS One* 8:e75288
54. Al-Jamal WT, Kostarelos K (2011) Liposomes: from a clinically established drug delivery system to a nanoparticle platform for theranostic nanomedicine. *Acc Chem Res* 44:1094–1104
55. Krasia-Christoforou T, Georgiou TK (2013) Polymeric theranostics: using polymer-based systems for simultaneous imaging and therapy. *J Mater Chem B* 1:3002–3025
56. Khandare J, Calderón M, Dagia NM, Haag R (2012) Multifunctional dendritic polymers in nanomedicine: opportunities and challenges. *Chem Soc Rev* 41:2824–2848
57. Calderón M, Quadir MA, Strumia M, Haag R (2010) Functional dendritic polymer architectures as stimuli-responsive nanocarriers. *Biochimie* 92:1242–1251
58. Quadir MA, Haag R (2012) Biofunctional nanosystems based on dendritic polymers. *J Control Release* 161:484–495
59. Dong R, Zhou Y, Zhu X (2014) Supramolecular dendritic polymers: from synthesis to applications. *Acc Chem Res* 47:2006–2016
60. Tomalia DA, Christensen JB, Boas U (2012) Dendrimers, dendrons, and dendritic polymers: discovery, applications, and the future. Cambridge University Press, New York
61. Almutairi A, Rossin R, Shokeen M, Hagooly A, Ananth A, Capoccia B, Guillaudeu S, Abendschein D, Anderson CJ, Welch MJ (2009) Biodegradable dendritic positron-emitting nanoprobes for the noninvasive imaging of angiogenesis. *Proc Natl Acad Sci* 106:685–690
62. Almutairi A, Guillaudeu SJ, Berezin MY, Achilefu S, Fréchet JM (2008) Biodegradable pH-sensing dendritic nanoprobes for near-infrared fluorescence lifetime and intensity imaging. *J Am Chem Soc* 130:444–445

63. Menjoge AR, Kannan RM, Tomalia DA (2010) Dendrimer-based drug and imaging conjugates: design considerations for nanomedical applications. *Drug Discov Today* 15:171–185
64. Reichert S, Calderón M, Licha K, Haag R (2012) Multivalent dendritic architectures for theranostics. In: Swami A, Shi J, Gadde S, Votruba AR, Kolishetti N, Farokhzad O (eds) *Multifunctional nanoparticles for drug delivery applications*. Springer, New York, pp 315–344
65. Luo K, Liu G, He B, Wu Y, Gong Q, Song B, Ai H, Gu Z (2011) Multifunctional gadolinium-based dendritic macromolecules as liver targeting imaging probes. *Biomaterials* 32:2575–2585
66. Luo K, Liu G, Zhang X, She W, He B, Nie Y, Li L, Wu Y, Zhang Z, Gong Q (2009) Functional L-lysine dendritic macromolecules as liver-imaging probes. *Macromol Biosci* 9:1227–1236
67. Luo K, Li C, Wang G, Nie Y, He B, Wu Y, Gu Z (2011) Peptide dendrimers as efficient and biocompatible gene delivery vectors: synthesis and in vitro characterization. *J Control Release* 155:77–87
68. Luo K, Li C, Li L, She W, Wang G, Gu Z (2012) Arginine functionalized peptide dendrimers as potential gene delivery vehicles. *Biomaterials* 33:4917–4927
69. Luo K, Liu G, She W, Wang Q, Wang G, He B, Ai H, Gong Q, Song B, Gu Z (2011) Gadolinium-labeled peptide dendrimers with controlled structures as potential magnetic resonance imaging contrast agents. *Biomaterials* 32:7951–7960
70. Jain K, Kesharwani P, Gupta U, Jain N (2010) Dendrimer toxicity: let's meet the challenge. *Int J Pharm* 394:122–142
71. Duncan R, Izzo L (2005) Dendrimer biocompatibility and toxicity. *Adv Drug Deliv Rev* 57:2215–2237
72. Chen H-T, Neerman MF, Parrish AR, Simanek EE (2004) Cytotoxicity, hemolysis, and acute in vivo toxicity of dendrimers based on melamine, candidate vehicles for drug delivery. *J Am Chem Soc* 126:10044–10048
73. Kojima C, Kono K, Maruyama K, Takagishi T (2000) Synthesis of polyamidoamine dendrimers having poly (ethylene glycol) grafts and their ability to encapsulate anticancer drugs. *Bioconjug Chem* 11:910–917
74. Margerum LD, Campion BK, Koo M, Shargill N, Lai J-J, Marumoto A, Sontum PC (1997) Gadolinium(III) DO₃A macrocycles and polyethylene glycol coupled to dendrimers effect of molecular weight on physical and biological properties of macromolecular magnetic resonance imaging contrast agents. *J Alloys Compd* 249:185–190
75. Boyd BJ, Kaminskas LM, Karellas P, Krippner G, Lessene R, Porter CJ (2006) Cationic poly-L-lysine dendrimers: pharmacokinetics, biodistribution, and evidence for metabolism and bioresorption after intravenous administration to rats. *Mol Pharm* 3:614–627
76. Dong Y, Gunning P, Cao H, Mathew A, Newland B, Saeed AO, Magnusson JP, Alexander C, Tai H, Pandit A (2010) Dual stimuli responsive PEG based hyperbranched polymers. *Polym Chem* 1:827–830
77. Dong Y, Saeed AO, Hassan W, Keigher C, Zheng Y, Tai H, Pandit A, Wang W (2012) “One-step” preparation of thiol-Ene clickable PEG-based thermoresponsive hyperbranched copolymer for in situ crosslinking hybrid hydrogel. *Macromol Rapid Commun* 33:120–126
78. Liu B, Kazlauciusas A, Guthrie JT, Perrier S (2005) One-pot hyperbranched polymer synthesis mediated by reversible addition fragmentation chain transfer (RAFT) polymerization. *Macromolecules* 38:2131–2136
79. Zargar A, Chang K, Taite LJ, Schork FJ (2011) Mathematical modeling of hyperbranched water-soluble polymers with applications in drug delivery. *Macromol React Eng* 5:373–384
80. Sonvico F, Mornet S, Vasseur S, Dubernet C, Jaillard D, Degrouard J, Hoebeke J, Duguet E, Colombo P, Couvreur P (2005) Folate-conjugated iron oxide nanoparticles for solid tumor targeting as potential specific magnetic hyperthermia mediators: synthesis, physicochemical characterization, and in vitro experiments. *Bioconjug Chem* 16:1181–1188
81. Frauenrath H (2005) Dendronized polymers-building a new bridge from molecules to nanoscopic objects. *Prog Polym Sci* 30:325–384

82. Schlüter AD, Rabe JP (2000) Dendronized polymers: synthesis, characterization, assembly at interfaces, and manipulation. *Angew Chem Int Ed* 39:864–883
83. Gao M, Jia X, Kuang G, Li Y, Liang D, Wei Y (2009) Thermo- and pH-responsive dendronized copolymers of styrene and maleic anhydride pendant with poly (amidoamine) dendrons as side groups. *Macromolecules* 42:4273–4281
84. Laurent BA, Grayson SM (2011) Synthesis of cyclic dendronized polymers via divergent “graft-from” and convergent click “graft-to” routes: preparation of modular toroidal macromolecules. *J Am Chem Soc* 133:13421–13429
85. Rudick JG, Percec V (2008) Induced helical backbone conformations of self-organizable dendronized polymers. *Acc Chem Res* 41:1641–1652
86. Percec V, Rudick JG, Peterca M, Heiney PA (2008) Nanomechanical function from self-organizable dendronized helical polyphenylacetylenes. *J Am Chem Soc* 130:7503–7508
87. Bai L, Li W, Chen J, Bo F, Gao B, Liu H, Li J, Wu Y, Ba X (2013) Water-soluble fluorescent probes based on dendronized polyfluorenes for cell imaging. *Macromol Rapid Commun* 34:539–547
88. Wen S, Li K, Cai H, Chen Q, Shen M, Huang Y, Peng C, Hou W, Zhu M, Zhang G (2013) Multifunctional dendrimer-entrapped gold nanoparticles for dual mode CT/MR imaging applications. *Biomaterials* 34:1570–1580
89. Chen Q, Wang H, Liu H, Wen S, Peng C, Shen M, Zhang G, Shi X (2015) Multifunctional dendrimer-entrapped gold nanoparticles modified with RGD peptide for targeted computed tomography/magnetic resonance dual-modal imaging of tumors. *Anal Chem* 87:3949–3956
90. Rolfe BE, Blakey I, Squires O, Peng H, Boase NR, Alexander C, Parsons PG, Boyle GM, Whittaker AK, Thurecht KJ (2014) Multimodal polymer nanoparticles with combined 19F magnetic resonance and optical detection for tunable, targeted, multimodal imaging in vivo. *J Am Chem Soc* 136:2413–2419
91. Ye L, Letchford K, Heller M, Liggins R, Guan D, Kizhakkedathu JN, Brooks DE, Jackson JK, Burt HM (2010) Synthesis and characterization of carboxylic acid conjugated, hydrophobically derivatized, hyperbranched polyglycerols as nanoparticulate drug carriers for cisplatin. *Biomacromolecules* 12:145–155
92. Zou J, Shi W, Wang J, Bo J (2005) Encapsulation and controlled release of a hydrophobic drug using a novel nanoparticle-forming hyperbranched polyester. *Macromol Biosci* 5:662–668
93. Radowski MR, Shukla A, von Berlepsch H, Böttcher C, Pickaert G, Rehage H, Haag R (2007) Supramolecular aggregates of dendritic multishell architectures as universal nanocarriers. *Angew Chem Int Ed* 46:1265–1269
94. Li N, Li N, Yi Q, Luo K, Guo C, Pan D, Gu Z (2014) Amphiphilic peptide dendritic copolymer-doxorubicin nanoscale conjugate self-assembled to enzyme-responsive anticancer agent. *Biomaterials* 35:9529–9545
95. Malik N, Evagorou EG, Duncan R (1999) Dendrimer-platinate: a novel approach to cancer chemotherapy. *Anticancer Drugs* 10:767–776
96. Pan D, Guo C, Luo K, Yi Q, Gu Z (2014) PEGylated dendritic diaminocyclohexyl-platinum (II) conjugates as pH-responsive drug delivery vehicles with enhanced tumor accumulation and antitumor efficacy. *Biomaterials* 35:10080–10092
97. Park JW, Jeon OC, Kim SK, Al-Hilal TA, Jin SJ, Moon HT, Yang VC, Kim SY, Byun Y (2010) High antiangiogenic and low anticoagulant efficacy of orally active low molecular weight heparin derivatives. *J Control Release* 148:317–326
98. Tang DW, Yu SH, Ho YC, Mi FL, Kuo PL, Sung HW (2010) Heparinized chitosan/poly(γ -glutamic acid) nanoparticles for multi-functional delivery of fibroblast growth factor and heparin. *Biomaterials* 31:9320–9332
99. Ornelas C, Pennell R, Liebes LF, Weck M (2011) Construction of a well-defined multifunctional dendrimer for theranostics. *Org Lett* 13:976–979

100. Quan Q, Xie J, Gao H, Yang M, Zhang F, Liu G, Lin X, Wang A, Eden HS, Lee S (2011) HSA coated iron oxide nanoparticles as drug delivery vehicles for cancer therapy. *Mol Pharm* 8:1669–1676
101. Chen J, Yang M, Zhang Q, Cho EC, Cobley CM, Kim C, Glaus C, Wang LV, Welch MJ, Xia Y (2010) Gold nanocages: a novel class of multifunctional nanomaterials for theranostic applications. *Adv Funct Mater* 20:3684–3694
102. Xia Y, Li W, Cobley CM, Chen J, Xia X, Zhang Q, Yang M, Cho EC, Brown PK (2011) Gold nanocages: from synthesis to theranostic applications. *Acc Chem Res* 44:914–924
103. Liu Z, Liang X-J (2012) Nano-carbons as theranostics. *Theranostics* 2:235–237
104. Sheng Z, Song L, Zheng J, Hu D, He M, Zheng M, Gao G, Gong P, Zhang P, Ma Y (2013) Protein-assisted fabrication of nano-reduced graphene oxide for combined in vivo photoacoustic imaging and photothermal therapy. *Biomaterials* 34:5236–5243
105. Chen X, Gambhir SS, Cheon J (2011) Theranostic nanomedicine. *Acc Chem Res* 44:841–841
106. Kolhe P, Misra E, Kannan RM, Kannan S, Lieh-Lai M (2003) Drug complexation, in vitro release and cellular entry of dendrimers and hyperbranched polymers. *Int J Pharm* 259:143–160
107. Backer MV, Gaynutdinov TI, Patel V, Bandyopadhyaya AK, Thirumamagal B, Tjarks W, Barth RF, Claffey K, Backer JM (2005) Vascular endothelial growth factor selectively targets boronated dendrimers to tumor vasculature. *Mol Cancer Ther* 4:1423–1429
108. Majoros IJ, Myc A, Thomas T, Mehta CB, Baker JR (2006) PAMAM dendrimer-based multifunctional conjugate for cancer therapy: synthesis, characterization, and functionality. *Biomacromolecules* 7:572–579
109. Yang W, Cheng Y, Xu T, Wang X (2009) Wen L-p: Targeting cancer cells with biotin–dendrimer conjugates. *Eur J Med Chem* 44:862–868
110. Choi Y, Thomas T, Kotlyar A, Islam MT, Baker JR Jr (2005) Synthesis and functional evaluation of DNA-assembled polyamidoamine dendrimer clusters for cancer cell-specific targeting. *Chem Biol* 12:35–43
111. Zhu B, Han Y, Sun M, Bo Z (2007) Water-soluble dendronized polyfluorenes with an extremely high quantum yield in water. *Macromolecules* 40:4494–4500
112. Wang G, Pu K-Y, Zhang X, Li K, Wang L, Cai L, Ding D, Lai Y-H, Liu B (2011) Star-shaped glycosylated conjugated oligomer for two-photon fluorescence imaging of live cells. *Chem Mater* 23:4428–4434
113. Santra S, Kaittanis C, Perez JM (2010) Cytochrome C encapsulating theranostic nanoparticles: a novel bifunctional system for targeted delivery of therapeutic membrane-impermeable proteins to tumors and imaging of cancer therapy. *Mol Pharm* 7:1209–1222
114. Zhang C, Pan D, Luo K, Li N, Guo C, Zheng X, Gu Z (2014) Dendrimer-doxorubicin conjugate as enzyme-sensitive and polymeric nanoscale drug delivery vehicle for ovarian cancer therapy. *Polym Chem* 5:5227–5235
115. Zhang C, Pan D, Luo K, She W, Guo C, Yang Y, Gu Z (2014) Peptide dendrimer–doxorubicin conjugate-based nanoparticle as an enzyme-responsive drug delivery system for cancer therapy. *Adv Healthc Mater* 8:1299–1308
116. Chatterjee DK, Fong LS, Zhang Y (2008) Nanoparticles in photodynamic therapy: an emerging paradigm. *Adv Drug Deliv Rev* 60:1627–1637
117. Zhang Y, Lovell JF (2012) Porphyrins as theranostic agents from prehistoric to modern times. *Theranostics* 2:905
118. Bresseur N, Brault D, Couvreur P (1991) Adsorption of hematoporphyrin onto polyalkylcyanoacrylate nanoparticles: carrier capacity and drug release. *Int J Pharm* 70:129–135
119. Taratula O, Schumann C, Naleway MA, Pang AJ, Chon KJ, Taratula O (2013) A multifunctional theranostic platform based on phthalocyanine-loaded dendrimer for image-guided drug delivery and photodynamic therapy. *Mol Pharm* 10:3946–3958

120. Ideta R, Tasaka F, Jang W-D, Nishiyama N, Zhang G-D, Harada A, Yanagi Y, Tamaki Y, Aida T, Kataoka K (2005) Nanotechnology-based photodynamic therapy for neovascular disease using a supramolecular nanocarrier loaded with a dendritic photosensitizer. *Nano Lett* 5:2426–2431
121. Kumar MS, Babu A, Murugesan R, Jeyasubramanian K (2012) Novel water soluble dendrimer nanocarrier for enhanced photodynamic efficacy of protoporphyrin IX. *Nano Biomed Eng* 4:132–138
122. Kojima C, Toi Y, Harada A, Kono K (2007) Preparation of poly (ethylene glycol)-attached dendrimers encapsulating photosensitizers for application to photodynamic therapy. *Bioconjug Chem* 18:663–670
123. Kono K, Nakashima S, Kokuryo D, Aoki I, Shimamoto H, Aoshima S, Maruyama K, Yuba E, Kojima C, Harada A (2011) Multi-functional liposomes having temperature-triggered release and magnetic resonance imaging for tumor-specific chemotherapy. *Biomaterials* 32:1387–1395
124. Li X, Qian Y, Liu T, Hu X, Zhang G, You Y, Liu S (2011) Amphiphilic multiarm star block copolymer-based multifunctional unimolecular micelles for cancer targeted drug delivery and MR imaging. *Biomaterials* 32:6595–6605
125. Ardana A, Whittaker AK, Thurecht KJ (2014) PEG-based hyperbranched polymer theranostics: optimizing chemistries for improved bioconjugation. *Macromolecules* 47:5211–5219
126. Kim J, Lee JE, Lee SH, Yu JH, Lee JH, Park TG, Hyeon T (2008) Designed fabrication of a multifunctional polymer nanomedical platform for simultaneous cancer-targeted imaging and magnetically guided drug delivery. *Adv Mater* 20:478–483
127. Santhosh PB, Ulrich NP (2013) Multifunctional superparamagnetic iron oxide nanoparticles: promising tools in cancer theranostics. *Cancer Lett* 336:8–17
128. Smejkalova D, Nešporová K, Huerta-Angeles G, Syrovátka J, Jiráček D, Gálisová A, Velebný V (2014) Selective in vitro anticancer effect of superparamagnetic iron oxide nanoparticles loaded in hyaluronan polymeric micelles. *Biomacromolecules* 15:4012–4020
129. Xie J, Jon S (2012) Magnetic nanoparticle-based theranostics. *Theranostics* 2:122–124
130. Martin AL, Bernas LM, Rutt BK, Foster PJ, Gillies ER (2008) Enhanced cell uptake of superparamagnetic iron oxide nanoparticles functionalized with dendritic guanidines. *Bioconjug Chem* 19:2375–2384
131. Lamanna G, Kueny-Stotz M, Mamlouk-Chaouachi H, Ghobril C, Basly B, Bertin A, Miladi I, Billotey C, Pourroy G, Bégin-Colin S (2011) Dendronized iron oxide nanoparticles for multimodal imaging. *Biomaterials* 32:8562–8573
132. Basly B, Felder-Flesch D, Perriat P, Pourroy G, Bégin-Colin S (2011) Properties and suspension stability of dendronized iron oxide nanoparticles for MRI applications. *Contrast Media Mol Imaging* 6:132–138
133. Shen M, Shi X (2010) Dendrimer-based organic/inorganic hybrid nanoparticles in biomedical applications. *Nanoscale* 2:1596–1610
134. Canilho N, Kasëmi E, Schlüter AD, Ruokolainen J, Mezzenga R (2007) Real space imaging and molecular packing of dendronized polymer-lipid supramolecular complexes. *Macromolecules* 40:7609–7616
135. Abu-Reziq R, Alper H, Wang D, Post ML (2006) Metal supported on dendronized magnetic nanoparticles: highly selective hydroformylation catalysts. *J Am Chem Soc* 128:5279–5282
136. Pan B-F, Gao F, Ao L-M (2005) Investigation of interactions between dendrimer-coated magnetite nanoparticles and bovine serum albumin. *J Magn Magn Mater* 293:252–258
137. Zhu R, Jiang W, Pu Y, Luo K, Wu Y, He B, Gu Z (2011) Functionalization of magnetic nanoparticles with peptide dendrimers. *J Mater Chem* 21:5464–5474
138. Walter A, Billotey C, Garofalo A, Ulhaq-Bouillet C, Lefèvre C, Taleb J, Laurent S, Vander Elst L, Muller RN, Lartigau L (2014) Mastering the shape and composition of dendronized iron oxide nanoparticles to tailor magnetic resonance imaging and hyperthermia. *Chem Mater* 26:5252–5264

139. Jiang Y-H, Emau P, Cairns JS, Flanary L, Morton WR, McCarthy TD, Tsai C-C (2005) SPL7013 gel as a topical microbicide for prevention of vaginal transmission of SHIV89. 6P in macaques. *AIDS Res Hum Retrovir* 21:207–213
140. McCarthy TD, Karellas P, Henderson SA, Giannis M, O'Keefe DF, Heery G, Paull JR, Matthews BR, Holan G (2005) Dendrimers as drugs: discovery and preclinical and clinical development of dendrimer-based microbicides for HIV and STI prevention. *Mol Pharm* 2:312–318

Chapter 10

Multifunctional Liposomes for Imaging-Guided Therapy

Xiuli Yue and Zhifei Dai

Abstract Liposomes has enjoyed an explosive development in nanomedicine due to the exciting feature of easy combinations of diagnostic and/or therapeutic agents into a single agent. A variety of multifunctional liposomes have been developed by loading various therapeutic agents (e.g., radionuclides, doxorubicin, paclitaxel, siRNA, DNA) and imaging contrast agents (e.g., radionuclides, quantum dots, Gd complex, and Fe_3O_4). Each component would operate a different function, such as molecular targeting, contrast-enhanced imaging (e.g., nuclear, fluorescence, magnetic resonance, CT, photoacoustic, and ultrasound), and therapy (e.g., chemotherapy, photothermal therapy, photodynamic therapy, gene therapy, or combined therapy). Moreover, the surface of liposomes can be easily modified with ligands for targeting delivery to the diseased sites. In addition, the multimodality imaging functionalization of therapeutic drug carrying liposomes is of particular interest for personalized monitoring of the in vivo tumor targeting and pharmacokinetics of liposomal therapeutic agents, predicting therapy outcome, and gaining a better understanding of the prognosis-associated disease status by combining the advantageous information from each imaging modality. Therefore, multifunctional liposomes can serve as a theranostic nanomedicine for noninvasive imaging diagnosis, real-time imaging guidance, and remote-controlled therapeutics, especially imaging-guided therapeutics, enabling personalized detection and treatment of diseases with high efficacy. However, liposomes still have not attained their full potential because of insufficient stability. Recently, a hybrid liposomal cerasome with high stability has been developed to overcome general problems associated with current liposome technology. The present chapter first highlights some of the key advances of theranostic liposomes for imaging-guided therapy as a tool in personalized medicine.

X. Yue

School of Municipal and Environmental Engineering, Harbin Institute of Technology, Harbin 150001, China

Z. Dai (✉)

Department of Biomedical Engineering, College of Engineering, Peking University, Beijing, China

e-mail: zhifei.dai@pku.edu.cn; <http://bme.pku.edu.cn/~daizhifei>

Keywords Liposomes • Cerasomes • Drug delivery • Contrast-enhanced imaging • Nanotheranostic agent

10.1 Introduction

The molecular and diagnostic imaging has attracted wide research interests in the treatment planning of a variety of diseases and especially in cancer therapy [1–3]. Noninvasive diagnostic imaging techniques, such as magnetic resonance (MR), computed tomography (CT), ultrasound (US), positron emission tomography (PET), and single photon emission computed tomography (SPECT), serve as powerful tools for clinical diagnosis, disease status monitoring, and treatment evaluation. According to the tissue contrast or function mechanisms, each imaging modality owns a specific sensitivity, spatiotemporal resolution relating to diseases, and physiological or biological procedures [4–6]. Multimodal imaging modality may combine their advantages and counterbalance the disadvantages of individual imaging modalities so the employment of multimodal imaging technique opens a new way to improve disease diagnosis and treatment evaluation [7]. Besides the instrument innovation, multimodality imaging techniques require the development of new imaging tracers and probes [8, 9].

The employment of a single platform integrating multiple contrast agents to empower multimodal imaging of diseases and/or treatment response is advantageous over a single functional contrast agent, as each contrast agent in the platform may supply reciprocal information for the other imaging modalities. In recent years, theranostics as a treatment integrating a diagnostic imaging tool for decision-making in the consequently targeted therapy has recently drawn considerable attention [10]. One of the most exciting features of nanoparticle for the drug delivery applications is the capability to increase the stability, and improve pharmacokinetics and biodistribution of large amount of therapeutic and diagnostic agents, conducting to more efficient drug administration or better therapeutic efficiency with reduced side effects [11]. Accordingly, multifunctional nanoparticles can be excellent drug delivery systems to achieve this aim, contributing to a more individualized cancer treatment strategy by boosting effective drug delivery through imaging guidance and treatment response monitoring [12]. Theranostic nanotechnologies can offer unique characteristics and novel strategies to guide, evaluate, and personalize treatment in real time [13].

Liposomes, unilamellar lipid bilayer nanoparticles with an aqueous core domain which may entrap both lipophilic and hydrophilic species, have attracted considerable attention for controlled or targeted release of various drugs and diagnostic agents due to their unique properties [14, 15]. Liposomes not only can accumulate passively in cancerous tissues by infiltration across abnormal leaky tumor vasculature called as the enhanced permeability and retention effect but also accumulate actively in cancerous tissues by targeting tumor cell or targeting tumor angiogenic

marker specifically. A variety of functional molecules can be easily entrapped in the interior of liposomes, inserted in the liposomal bilayer, or coupled on the bilayer membrane surface so liposomes can be fabricated to serve as a powerful platform with the multimodal theranostic capability [16, 17].

Although lots of liposomal pharmaceuticals have received FDA approval for clinical cancer therapy or are under trials, liposomes still have not attained their full potential due to their insufficient morphological stability [18]. Depending on their composition, the final liposome formulations may suffer from short shelf-lives partly due to chemical and physical instability. The insufficient stability of the liposomes could lead to their rapid clearance from circulation, often before reaching their target. Grafting polyethylene glycol (PEG) onto liposomes has demonstrated to reduce strongly the uptake by mononuclear phagocyte system (MPS), prolong blood circulation, and thus improve distribution in perfused tissues [19]. Yet, the liposomes containing PEGylated phospholipids may lead to skin toxicity generally known as “hand-foot syndrome” [20, 21]. In addition, the presence of PEG large molecules on the liposomal surface may reduce the interactions of liposomes with cells and hinder entry of liposomes into the tumor tissue.

Recently, a type of organic-inorganic nanohybrid cerasome was developed through a combination of sol-gel reactions and self-assembly of molecularly designed lipidic organoalkoxysilane to form liposomal bilayer structure covering an atomic layer of inorganic polyorganosiloxane networks on its surface [22]. The siloxane surface adds remarkably high mechanical stability and heat resistance compared with conventional liposome, providing a simple and widely applicable tool to overcome general problems associated with current liposome technology. As a new drug delivery system, its unique advantages give wide applicability to the cerasomes in roles as gene carriers [23], drug delivery systems [24], and other biomedical applications.

10.2 Liposome Properties in Theranostic Design

10.2.1 Design of Passively Targeting Theranostic Liposomes

Due to rapid and uncontrollable tumor growth with a contributive effect from the inflammation condition within the tissue, cancerous tissues have been proved to be leaky blood vessels with gaps up to 700 nm between the endothelial cell layers, forcing nanoparticles out of blood vessels into the extracellular space within the diseased tissue [25, 26]. Such effect is called as the enhanced permeability and retention (EPR) effect [4]. The nontargeted or passive tumor targeting is often attributed to the EPR effect. Liposomes with the diameter hundred times less than red blood cells is able to infiltrate through fenestrated cellular barriers because of the insufficient lymphatic drainage in cancerous tissue and the pressure difference between the blood stream and the interstitial space [26]. Significant heterogeneity in

the EPR-based accumulation has been observed in different types of cancers. The EPR effect is evaluated to be strong in Kaposi's sarcoma and weak in lung, breast, and colon cancer. Nevertheless, more investigations on the EPR effect are required to wholly identify the heterogeneity within tumor accumulation in various cancers.

In order to control biodistribution of liposome to reach a high extent of cancerous accumulation, it is essential to take account of several essential issues on the design and preparation of passively targeted liposomes, such as lipid composition, content of cholesterol and PEG-lipid, surface chemistry characteristics, particle diameter, and shape. One of the most effective attempts was to manipulate chemical composition of lipid membrane in order for the modification of bilayer fluidity. Cholesterol is usually introduced into the lipid bilayer membrane to prevent encapsulated drugs leaking during systemic circulation and reduce blood protein adsorption. Damen et al. reported that introduced cholesterol may cause increased phospholipids packing in the lipid bilayer, leading to a reduction of phospholipids transfer to HDL [27]. Senior et al. showed that liposomes obtained from phosphatidylcholine (PC) with saturated fatty acyl chains or from sphingomyelin are more stable in the blood than liposomes prepared from PC with unsaturated fatty acyl chains [28]. In most clinical investigations, more than 30 mol% cholesterol was used to prepare radiolabeled liposomes for cancer imaging. While designing a drug delivery system, it is required to achieve triggered drug release from liposomes or passive diffusion at the target area in order to achieve a therapeutic effect. On the contrary, the radionuclide leakage during systemic circulation may conduce to misinterpret biodistribution of liposomes so it is strongly required to entirely retain the loaded radionuclide inside liposomes for diagnostic imaging applications.

Physical and chemical stability of liposome formulations can be improved greatly by optimizing the size distribution, pH and ionic strength, as well as the addition of antioxidants and chelating agents. However, biological stability of liposomes depends on the presence of agents that interact with liposomes upon application to the subject. Upon intravenous injection, liposomes can be quickly captured by the MPS and eliminated during blood circulation [29]. The main limitation to employ liposomes as drug delivery systems is effective uptake of liposomes by the macrophages and the subsequent removal from blood circulation when the target sites are beyond the MPS. The MPS can distinguish the liposomes themselves but distinguish selected serum proteins (opsonins). Binding of opsonins on the surface of the liposomes results in removal of liposomes during blood circulation, in particular for non-PEGylated liposomes [30]. Because the spleen and liver have high concentration of macrophages which are from the bone marrow and hepatocytes, the spleen and liver are mainly responsible for liposome clearance in blood [31, 32]. Moreover, liposomes may interact with some high-density lipoproteins (HDL) and low-density lipoproteins (LDL) lipoproteins in the blood. Such interaction can include enzymatic hydrolysis and lipid exchange, eventually resulting in liposome disintegration and the fast release of the loaded drug into the plasma [33]. The physicochemical properties of liposomes (e.g., particle size, net surface charge, fluidity, hydrophobicity, and packing of the lipid bilayers) have effect on the type of proteins binding to them [34, 35]. Problems with the colloidal instability of liposomes can be resolved simply by increasing the charge on the liposomes and/or

decreasing the ionic strength of the medium. Additionally, the presence of inert surface groups also reduces liposome interactions with macromolecules and thus stabilizes these particles.

Surface modification of liposomes with PEG and other hydrophilic polymers may reduce interaction between liposome and RES and lipoproteins, leading to an increase of the liposome half-life time in blood [36]. The first strategy studied was the preparation of liposomes mimicking the erythrocyte membrane by modifying liposome surface with gangliosides and sialic acid derivatives, such as monosialoganglioside (GM1) [37]. Unlike GM1, molecular weight and structure of PEG molecules may be easily adapted specifically. Surface modification of liposomes with PEG can be achieved by physically adsorbing the polymer onto the surface of the vesicles, by incorporating the PEG-lipid conjugate during liposome preparation, or by covalently attaching reactive groups onto the surface of preformed liposomes. The lifetime in blood circulation can more or less be modulated by altering the PEGylation degree of liposomes. Usually, the higher PEGylation degree of liposomes leads to longer blood circulation half-life, hence higher infiltration into the cancerous tissue [38]. It can be helpful to drug delivery functions, but it is not optimum for the radiolabeled liposomes to be used as diagnostic imaging contrast agents. In such situation, clearance of background signal of the diagnostic liposomes from the blood can lead to general improvement of imaging quality. In order to optimize images and reduce the background signal from the blood, a compromise should be reached between circulation time and cancerous accumulation.

The size of liposomes has an effect on the drug-loading content, stability, and capability. It was found that loading efficiency of liposomes increases with increasing size, while the liposome stability decreases with increasing size above an optimal 80–200 nm range and ability to extravasate decreases with increasing size. So, its size range is a compromise. The administered liposome dose can have an effect on opsonization, biodistribution, and RES clearance to some extent. In addition, the particle size of liposomes is a key factor for *in vivo* applications to prevent opsonization and RES recognition. Compared with smaller liposomes of similar compositions, larger liposomes can be rapidly removed from the blood circulation [39]. Smaller liposomes own a longer half-life time than larger liposomes (500–5,000 nm). It indicates that phagocytes can recognize the difference in the sizes between foreign particles. A few strategies have been introduced to adapt liposome size and charge in order to reduce MPS uptake. Nevertheless, the clearance rates of PEGylated liposomes are comparatively callous to the particle size ranging from 50 to 250 nm [37, 39].

10.2.2 Design of Actively Targeting Theranostic Liposomes

Despite the passive targeting via EPR effect, an active tumor targeting has been suggested to further boost cancerous accumulation and cellular uptake of liposomes [4]. By modifying the liposome surface using targeting ligands to overexpressed

receptors on cancer cells or extremely expressed biomarkers on the endothelium of tumorous vasculature, the tumor targeting of liposomes can be potentially improved [40]. A variety of targeting ligands have been used for the surface modification of liposomes, such as monoclonal antibodies, antibody fragments, aptamers, peptides, folic acid, and carbohydrates [41]. So far, active targeting methodologies of tumor cells and tissues have used targeting ligands for lots of receptors, e.g., folate, integrin, transferrin, somatostatin, epidermal growth factor (EGFR), membrane matrix metalloprotease, vasoactive intestinal peptide receptors (VIP-R), and nucleosome-specific monoclonal antibody 2C5. After intravenous injection of 2C5-modified ^{111}In -labeled liposomes into tumor-bearing mice, biodistribution was visualized through gamma-imaging studies [42]. It was clearly shown by the data and images that high tumor accumulation was achieved by using 2C5-modified ^{111}In -labeled liposomes in comparison with nontargeted controls (Fig. 10.1) [43]. By using PEGylated ^{64}Cu -liposomes outfitted with octreotate (TATE) which can actively target the overexpressed receptors on neuroendocrine tumors, PET imaging exhibited

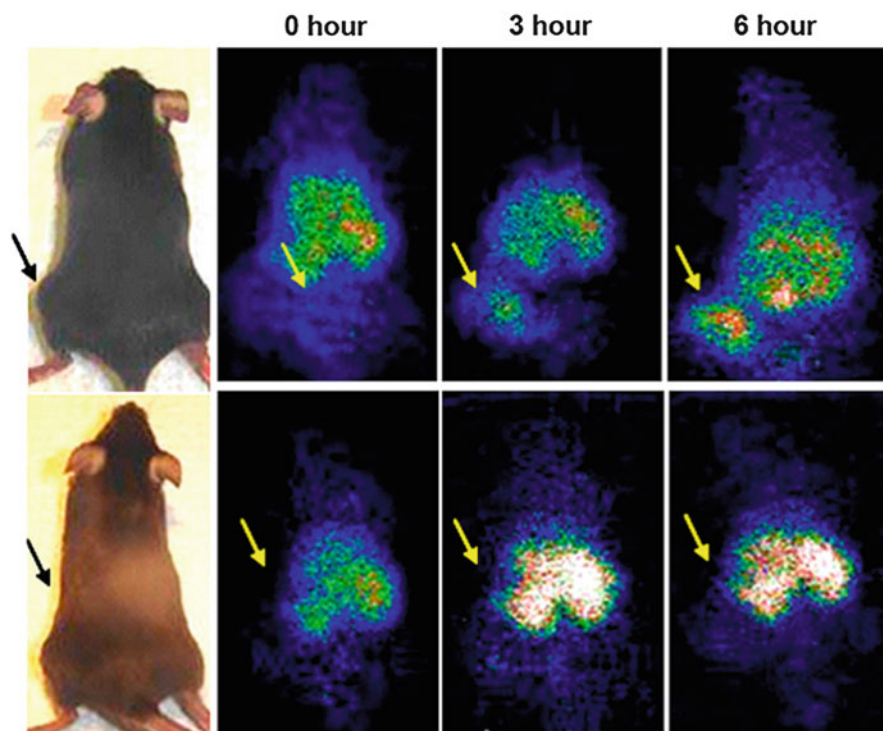


Fig. 10.1 Whole body imaging of Lewis lung carcinoma tumor-bearing mice at different time points after the injection of ^{111}In -labeled PEGylated liposomes. *Upper row*, 2C5-modified liposomes; *bottom row*, control unmodified liposome. *Arrows* indicate tumor locations. Notice the much faster accumulation of antibody-targeted liposomes in the tumor (Reprinted with the permission from Ref. [43]. Copyright 2007 Springer)

higher tumor-to-muscle (T/M) ratio (12.7 ± 1.0) in a xenograft mice model than the control liposomes without TATE (8.9 ± 0.9) [44].

While the active targeting strategy is employed to increase the imaging agent concentration in diseased tissue relatively to healthy organs and tissue, it is not clear how much tumor accumulation or cellular uptake of theranostic liposomes can be improved by the use of targeting ligands compared to the EPR-based passive targeting in solid tumor accumulation. Different studies may get contradictory result. Some of the investigations have demonstrated that active targeting ligands can enhance the tumor accumulation of liposomes [42, 45], while other investigations show that the targeting ligand-modified nanoparticles have a cancer accumulation and biodistribution similar to the unmodified nanoparticles [46]. Liposomes may have a high degree of accumulation due to the EPR effect in some cancer types, while ineffectual in other cancers. In the latter, modifying liposomes with targeting ligands may have great effect on the improvement of the tumor accumulation. In addition, the relevance of targeting optimization in mouse xenograft models has not been apparent yet to human cancers. Nevertheless, the active targeting of liposomes could be less efficient in xenograft models than in humans. More investigations in clinic employing the actively targeted radiolabeled liposomes are thus required to offer more details on how the actively targeted liposomes could be applied for diagnostic and therapeutic clinical applications.

10.3 MRI-Guided Drug Delivery Using Thermosensitive Liposomes and HIFU

10.3.1 Thermosensitive Liposomes

Chemotherapy is one of the most common treatment modalities of a variety of cancers. However, one of the main drawbacks of this therapy is that the most frequently used anticancer drugs are not specifically toxic to cancer cells and are toxic to the surrounding normal tissues. The low selectivity of the anticancer drugs to the cancer cells often causes undesirable side effects that limit dose and therapeutic window. In addition, the efficacy of free chemotherapeutic agents is also hampered by multi-drug resistance. To resolve these problems, a variety of drug nanocarriers that are triggered by stimuli (i.e., temperature, pH, enzyme, and light) have been fabricated to enhance accumulation in tumor tissues and cells, reduce systemic toxicity, and increase maximum tolerated dosages [47–50]. Through passive targeting mechanisms effect, and active targeting with specific antibodies or other ligands, drug nanocarriers can accumulate in tumors [51]. Among the stimuli-responsive drug delivery systems, temperature triggering is advantageous due to the controllability of the temperature at the desired location and time by applying an external biomedical device such as near-infrared light [52], radio frequency [53], microwave [54], and high intensity focused ultrasound (HIFU) [55, 56].

The thermal-sensitive liposome (the low temperature-sensitive liposome, LTSL) responds at clinically attainable hyperthermic temperatures releasing its entrapped drugs at the phase transition temperature (T_m) of the lipid bilayer in a matter of seconds as it passes through the microvasculature of a warmed tumor [57] (Fig. 10.2). The LTSL consists of a judicious combination of three lipid components, each with a specific function and each affecting specific material properties, including a sharp thermal transition and a rapid onset of membrane permeability to small ions, drugs, and small dextran polymers. At T_m , the lipid membrane changes its structure as it transfers from a gel to the liquid-crystalline phase [58]. Liposomal membranes in the liquid-crystalline phase are more permeable to water and drugs in comparison with the gel phase. At the T_m , the permeability of the liposomal bilayer membrane raises by several orders of magnitude, hence leading to the release of the liposome-loaded drugs. The amount of released drug was found to be the highest at T_m [59]. Nonetheless, the obvious drug release was observed already at 1–2° below T_m because of the existence of domain structures (i.e., grain boundaries) within the liposomal membranes.

In a pioneering work, Yatvin et al. investigated thermosensitive liposomes consisted of 1,2-dipalmitoyl-*sn*-glycerophosphocholine (DPPC, $T_m=41.5$ °C) [60] and 1,2-distearoyl-*sn*-glycerophosphocholine (DSPC, $T_m=54.9$ °C) [61] for thermally triggered release of neomycin and methotrexate. However, temperature-sensitive DPPC liposomes showed relatively low drug release kinetics without quantitative drug release at T_m [62]. The introduction of *lyso*-phospholipids (such as monopalmitoylphosphatidylcholine, MSPC) in the DPPC-based vesicles shows a remark-

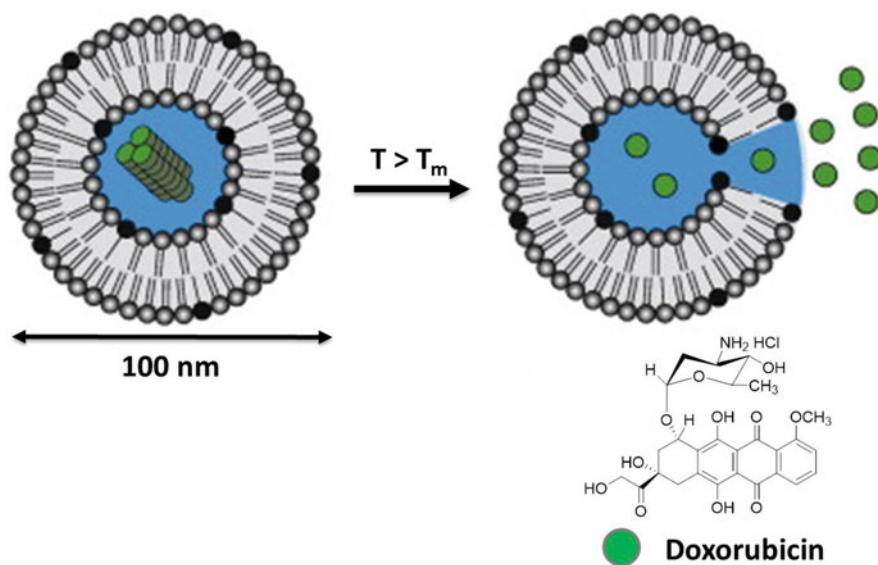


Fig. 10.2 Schematic representation of heat-triggered doxorubicin release from a thermal-sensitive liposome (Reprinted from ref. [57]. Copyright 2012, with permission from Elsevier)

able influence on the performance of the liposomal bilayer. Needham et al. developed *lyso*-PC-based LTSL for localized delivery of doxorubicin in combination with mild hyperthermia (41–42 °C) [63]. The experiments showed that the incorporation of *lyso*-PC resulted in quantitative doxorubicin release within a few seconds responding to mild hyperthermia compared with pure DPPC/DSPC-based thermosensitive liposomes [62]. The production of transient cavities and instability along the liposomal grain boundaries caused the rapid release of doxorubicin at T_m [64]. It is supposed that such cavities have thermodynamical stability in the existence of *lyso*-PC and PEGylated phospholipids [65].

In the recent research work, Needham et al. explored the effect of bilayer-concentration changes involving the lysolipid and the presence or absence of DSPE-PEG2000 on both the lipid transition temperature and the drug release [66]. The incorporation of 4 mol% DSPE-PEG2000 raises T_m by about 1 °C, while the inclusion of 5.0, 9.7, 12.7, and 18.0 mol% MSPC causes a slight decrease of T_m . In the absence of MSPC, almost no encapsulated doxorubicin-citrate was released. As the content of MSPC in the lipid mixture increased from 5.0 % to 9.3 mol% MSPC, initial doxorubicin release rates increased, with 8.5 and 9.3 mol% MSPC formulations giving 80 % of encapsulated drug released in 4 and 3 min, respectively. The incorporation of PEGylated lipid is found to be essential in order for the lysolipid-induced permeability to reach these very fast times. PEG-lipid included in a DPPC-DSPC mixture can alone enhance the permeability. Lysolipid could induce the formation of the pores, while the PEG-lipid could stabilize them and keep them open during the melting process. Lysolipids and PEG-lipids which might accumulate at the grain boundary defects are supported indirectly by observations by Ickenstein et al. [67]. The formation of lasting nanopores in lipid bilayers initially requires the presence (from the solid-phase structure) of grain boundary defects at the DPPC transition. The permeabilizing component(s) can either be a pore forming lysolipid/surfactant plus a PEG-lipid or can be generated by a PEG-surfactant incorporated at 4–5 mol%.

Lindner et al. explored another type of thermosensitive liposomes based on phosphatidylglyceroglycerol analogues [68]. It was shown that the temperature-sensitive liposomes composed of DPPC/DSPC/DPPGOG (DPPGOG = dipalmitoyl-*sn*-glycero-3-phosphoglyceroglycerol) displayed an increased serum stability at 37 °C. In addition, the DPPGOG-based liposomes exhibited a prolonged blood circulation time, resulting in higher plasma levels of doxorubicin in comparison with other thermosensitive liposomal formulations [68]. The size effect on the TSLs drug release profiles was also investigated. It was found that PEGylated LTSLs of 140 nm were more stable than liposomes of 120 nm, whereas the TSLs based on DPPGOG had similar doxorubicin release behavior for liposomes in the range of 120 and 160 nm [69]. It indicated that we can tune the drug release behavior and the circulation time of TSLs by varying the membrane composition and the size of the TSLs nanocarrier.

Preclinical experiments with the doxorubicin-loaded LTSLs combined with regional hyperthermia improved greatly the efficacy of thermally triggered drug delivery [70]. But, the main disadvantage of the *lyso*-PC-based LTSLs is the rapid

drug leakage at body temperature, and 30 % doxorubicin is released within 30 s [71]. In order to resolve this problem, Park et al. developed a novel thermosensitive liposome (STL) composed of DPPC, DSPE-PEG-2000, cholesterol, and a fatty acid conjugated elastin-like polypeptide (ELP). The STL exhibited better stability than conventional LTSL-lysolipid-based temperature-sensitive liposomes at 37 °C in the presence of serum [72]. There was rapid release of doxorubicin in the range of 39–42 °C (≥ 95 % release at 42 °C within 10 s).

10.3.2 Temperature-Triggered Local Drug Delivery Using MRI-Guided HIFU

Localized hyperthermia as required to trigger drug release from LTSLs can be achieved by employing various methods including radiofrequency electric current, microwaves, laser, as well as HIFU [57]. Among these heating methods, HIFU takes a unique advantage in terms of controlled, noninvasive heating of precisely targeted tissues [73]. HIFU has been applied to treat deep-seated tissues noninvasively by depositing focused ultrasound with a high acoustic intensity in the focal volume, resulting in local heating or a strong mechanical stimulus [74]. The mechanical stimulus induced by ultrasound irradiation can enhance drug infiltration across the blood vessel into the interstitial space. Thus, it is very interesting to trigger delivery of hydrophilic and cell-impermeable drugs (e.g., siRNA, pDNA) across biological membrane barriers by pressure-mediated drug delivery. HIFU has been employed to transport a lethal thermal dose for thermal ablation of tissues by elevating rapidly to temperatures of 60 °C since the 1940s [75]. In addition, HIFU has been widely used to noninvasively treat malignancies, where relatively long, continuous exposures are utilized, to produce the required high temperature elevations for thermal ablation and direct tumor destruction [76]. If, however, shorter pulses are given together with relatively short duty cycles, this will reduce the temporal average intensities and generation of heat, allowing for transient nonlethal temperature elevations of only 4–5 °C [77], where interactions of ultrasound energy with exposed tissue will be primarily nonthermal. Such exposures have been applied to noninvasively enhance local delivery of various therapeutic agents into different tissue types, improving their therapeutic efficacy [78].

The combination of LTSL with HIFU allows for noninvasive targeting of drug delivery. Dromi et al. utilized ThermoDox[®] (Celsion Corp.), a *lyso*-PC temperature-sensitive liposomal doxorubicin formulation (2 mg drug/kg) in combination with pulsed HIFU for thermal-sensitive drug delivery [79]. Before the *in vivo* experiment, temperature elevation upon HIFU irradiation was calibrated with a thermocouple. HIFU-triggered thermal ablation was carried out either directly or 24 h after the LTSLs injection. It was found that HIFU-induced hyperthermia directly after the LTSLs injection conducted to higher drug concentration in the tumor than the control experiment with no hyperthermia. No additional increase of the drug concentration could be detected in the tumor when HIFU-triggered heating

was done 24 h after the LTSLs injection, indicating the LTSL clearance from the blood circulation within 24 h and/or drug release from the LTSL at body temperatures. The doxorubicin content in the LTSL groups increased significantly from 0 to 24 h, but the doxorubicin concentration at tumor sites remained to be obviously lower than that of the HIFU-combined LTSL group immediately after the LTSLs injection. As a result, the HIFU treatment directly after LTSLs injection led to a significant tumor growth inhibition in comparison with all control groups. In this *in vivo* thermal ablation, no real-time temperature determinations were carried out, so the real tumor temperature was not clear. Nevertheless, the temperature mapping based on magnetic resonance (MR) has been set up for MR-guided HIFU (MR-HIFU) ablation process, allowing for temperature readout of the treated tissue on near real time [57].

In the recent years, the temperature-induced localized drug delivery has been expanded to MR image-guided drug delivery by the simultaneous loading of therapeutic agents and MRI contrast agent inside LTSLs. The proof-of-concept investigations have been explored by utilizing MR imaging and MR-guided HIFU combined with paramagnetic LTSLs in a preclinical setting [80]. MR-HIFU is very promising for noninvasive, localized, and controlled hyperthermia. The integration of MR-HIFU treatments with LTSLs would cause revolutionization in the field of personalization medicine relating to identifying tumor location and size, monitoring treatment procedure, and noninvasive temperature mapping [81]. By accurately calculating the temperature variations from the MR phase images, MR can offer spatiotemporal temperature feedback to the HIFU control unit. Electronic beam steering employing a phased array ultrasound transducer combined with near real-time MRI temperature mapping makes it possible to heat larger volumes of tumor tissue in a rapid controllable volumetric manner [82]. For the employment of MR-HIFU technology platform to temperature-sensitive drug delivery in a preclinical setting, it is very important to precisely control the temperature in a narrow window of 41–42 °C since vascular shutdown can happen above 43 °C [83]. And the HIFU technology must be adjusted to heat homogeneously the tumor tissue over 30–60 min at 41–42 °C, necessitating a powerful temperature feedback to resolve problems, such as patient motion and magnetic field drift.

The MR-HIFU provides volumetric beam steering so the whole rat tumor can be involved in a treatment. The MR temperature mapping can be an input for a binary feedback control algorithm to the phased array ultrasound transducer to keep moderate thermal ablation over 30 min with interleaved T_1 mapping of the cancerous tissue to trace release of the MRI contrast agents from the ITSLs [57]. Grüll and his team used a combination of MRI and HIFU technologies together with LTSLs containing Gd complex of [Gd(HPDO3A)(H₂O)] as T_1 contrast agent and doxorubicin for local drug delivery [84]. The LTSLs, injected at a dose of 5 mg doxorubicin/kg into the bloodstream, transport the drug around the body and to the tumor. The latter is mildly heated using a focused ultrasound beam, causing the LTSLs in the tumor to release their drug payload. Simultaneous MR imaging is used to locate the tumor, measure local tissue temperature, and guide the ultrasound heating. The release of the contrast agent can be monitored with MRI, allowing correlated measurements

and visualizations of drug uptake in the tumor and surrounding tissue. The release of the MRI contrast agent from the TSL can be proven by a decrease in T_1 in the MR images across the tumor for the HIFU-treated tumors, while the T_1 merely reduced, minimally employing the paramagnetic TSLs in non-heated tumors [84]. The HIFU-mediated drug delivery guided by MRI exhibited obvious increase of drug concentrations inside the target tissue. It may provide a novel minimally invasive and local cancer treatment option in near future. Negussie et al. evaluated the in vitro doxorubicin release kinetic of imageable *lyso*-PC-based temperature-sensitive liposomes (iTSLs) and thermosensitive drug delivery guided by MRI, utilizing a clinical MR-HIFU system in rabbits bearing a VX2 tumors [80]. Their preliminary study showed MRI signal intensity increase after injection of iTSL, followed by further increases after each 10-min hyperthermia treatment.

Grüll et al. further investigated the blood kinetics and biodistribution of the ^{111}In -labeled LTSLs co-encapsulating doxorubicin and T_1 contrast agent of $[\text{Gd}(\text{HPDO3A})(\text{H}_2\text{O})]$ in rats using SPECT/CT imaging [85]. In addition, the effect of local MR-HIFU-mediated hyperthermia of the tumor on the biodistribution of the LTSLs, doxorubicin, and T_1 contrast agent was explored in detail. It was shown that the radiolabeled TSLs co-encapsulating doxorubicin and T_1 contrast agent had a long blood circulation time of the liposomal carrier and premature release of the drug and the MRI contrast agent at physiological temperatures in Fisher rats. The SPECT/CT images and biodistribution studies demonstrated high uptake of the LTSLs in the spleen and the liver for both the HIFU-treated and nontreated rats. HIFU-mediated hyperthermia of the tumor had a 4.4-fold higher uptake of the ^{111}In -labeled LTSLs in the tumor ($t=48$ h) than the control experiments with no HIFU treatment. Moreover, the doxorubicin concentration was increased by a factor 7.9 upon the HIFU treatment. This increased accumulation of the LTSLs encapsulating doxorubicin at longer time points can play a key role on the therapeutic outcome of MR-HIFU-mediated drug delivery. These fundamental insights on the effect of HIFU on the biodistribution of LTSLs and their encapsulating doxorubicin and T_1 contrast agent are important for clinical translation of MR-HIFU-mediated drug delivery.

10.4 Radiolabeled Liposomes for Combining Imaging and Therapy

10.4.1 Nuclear Imaging Techniques

Positron emission tomography (PET) imaging has been the fastest developing diagnostic imaging modality because of its quantitative feature and high sensitivity, and PET is now a contemporary tool for diagnostics and treatments of cancer. The gamma rays-based single photon emission computed tomography (SPECT) remains to be the most broadly applied nuclear imaging modality because of the large amount of scanners in clinic around the globe. Compared with PET, the SPECT technique takes an advantage: the radioisotopes are usually more long-lived, and the

resolution of image is better than for PET. SPECT imaging requires single photon emitting radionuclides, such as ^{67}Ga , ^{111}In , ^{123}I , ^{186}Re , $^{99\text{m}}\text{Tc}$, and ^{201}Tl , whereas PET imaging needs positron-emitting radionuclides, such as ^{11}C , ^{61}Cu , ^{62}Cu , ^{64}Cu , ^{18}F , ^{68}Ga , ^{124}I , ^{13}N , ^{15}O , ^{82}Rb , and ^{89}Zr . In vivo imaging using radiopharmaceuticals plays a key role in diagnosis and therapy of diseases, as well as drug development. Even though many excellent radiopharmaceuticals are commercially available, developing novel agents and other radionuclides for PET and SPECT imaging still attracts tremendous research and industry interests currently [4].

Nuclear imaging techniques, particularly PET imaging, have the advantage to monitor radionuclides at trace level, in which the employed doses show no pharmacological effects. So, the PET and SPECT imaging techniques play an important role in drug development and discovery, screen, and identification of novel drug candidates. Radiolabeled liposomes may be monitored at trace level by tracking photons emitted directly with SPECT imaging technique or tracing positron annihilation using PET imaging technique of the radionuclide decaying. The first liposomal radiotracer (^{111}In -loaded liposome) was developed in the early 1980s and used widely for in vivo tumor diagnosis in γ -ray camera scintigraphy [86]. The ^{111}In -loaded liposomes got success in clinical trials for visualizing several tumors by using nuclear imaging technique [87]. By employing lipophilic chelators and ionophores applied for the SPECT imaging, single photon emitting radionuclides have been successfully encapsulated into the preformed liposomes by using remote loading method [88]. PET shows a better detection sensitivity than SPECT, and the radiotracer of concentrations as low as 10^{-12} M can be visualized using PET imaging technique [89]. Nevertheless, it is a big challenge to load and label radiopharmaceuticals for PET imaging. So far, very few liposomal strategies have been reported for entrapping the PET used positron-emitting radionuclides [90].

Liposomes have been widely used as vehicles to load and deliver diagnostic imaging agents and therapeutic compounds, but no liposomal radiopharmaceuticals have been approved and available in the market for diagnostic nuclear imaging applications. Several liposomal radiopharmaceuticals with different radionuclide were studied in vivo; however, merely the single photon emitting radionuclides, ^{111}In and $^{99\text{m}}\text{Tc}$, were applied for clinical studies of inflammation and infection [91] and cancers [92] with SPECT imaging. No clinical trials have been reported on liposomal radiopharmaceuticals used for PET diagnostic imaging. Nevertheless, liposomal radiopharmaceuticals show a few promising future PET diagnostic imaging applications since their high detecting sensitivity provides us an opportunity to compare quantitatively liposomal drug candidates. Moreover, the employment of liposomal radiopharmaceuticals enables to track the biodistribution of a liposomal drug in cancer patients, which can additionally be essential for other therapeutic techniques, such as anti-angiogenic agents and radiation therapy [93]. This preclinical study of nuclear imaging can hopefully give us more details on how liposomal methodology may be applied for diagnosis and therapy of diseases. Due to the variety of liposome design and preparations, radiolabeled liposomes could be conveniently engineered to be theranostic nanomedicine for simultaneous therapeutic and diagnostic imaging applications, and such liposomal methodology enables to integrate diagnostic imaging and treatment for personalized medicine. PET imaging

permits to analyze directly the radioactivity isolated specifically in a region of interest (ROI), thus to quantitatively determine biodistribution according to the pixel intensity differences. Due to the limitation of employing SPECT imaging in comparison with PET imaging, we have a pressing need for the development of liposomal radiopharmaceuticals of PET imaging for preclinical and clinical investigations.

10.4.2 Labeling Liposomes with Radionuclide

To date, various strategies have been presented for labeling liposomes with radionuclides. In order to use liposomes as radionuclide carriers for imaging and diagnostic application, the labeling technique should meet the following important features [4]: (1) facile and quick fabrication at room temperature, (2) high drug-loading content, (3) easily available radionuclides with excellent imaging capability, and (4) good radiolabeling stability [94]. The techniques for incorporating radionuclides into liposomes for *in vivo* imaging using SPECT and PET may be generally categorized into four strategies: (1) passive entrapping [95], (2) membrane labeling [96], (3) surface chelation [97], and (4) remote loading [88]. No labeling and loading technique is perfect, and each approach has its advantage and limitation.

Passive entrapping of the radionuclide inside liposomes is carried out during the liposome production. The drug-loading content is usually less than 10 % for 100 nm liposomes, so this technique is scarcely employed. In the membrane labeling method, the radionuclide is coupled to the surface of liposomes or incorporated within the liposomal bilayer. The radionuclides may be coupled to either as-prepared liposomes or a lipid which is used to formulate the liposomes. In this technique, the insufficient stability of liposome radiolabeling is a risk, which may lead to loss of radioactivity from the liposomes *in vivo*. As a result, the diagnostic image quality may be reduced, conducting to an inaccurate estimation of the liposome biodistribution.

The approaches of surface chelation and remote loading may be applied for the prepared liposomes. Because of the high loading content and radionuclide retention, such two approaches are the most widely applied. Surface chelation of the prepared liposomes is carried out by introducing the conjugates of lipid chelator binding the radionuclides into the liposomal membrane during the liposome formation. The labeling efficiency is usually as high as 90 % in this method. The radionuclides are conjugated to the liposome surface, so the radionuclide is easily exposed to plasma proteins during systemic circulation. It may lead to the radionuclide release from liposomes. Therefore, the *in vivo* stability of surface-chelated liposomes highly depends on the binding constant of radionuclide/chelator.

In the remote loading approach, the radionuclide is actively loaded inside the aqueous core domain of liposomes, in which lipophilic chelators and ionophores can ship the radionuclide across the prepared liposome membrane, and the radionuclide can be delivered to a pre-entrapped chelator. The radionuclides are concentrated in the core aqueous domain of the liposomes, giving high drug entrapping efficiency (>90 %) and the greatest *in vivo* stability because liposomal membrane

can prevent the radionuclide exchange with the biological environment [98]. Petersen et al. developed the ^{64}Cu PEGylated liposomes by remote loading of ^{64}Cu into the prepared PEGylated liposomes with DOTA as the entrapped copper chelator and the 2-hydroxyquinoline chelator to ship the copper across the lipid bilayer membrane. A very high loading efficiency (>95 %) was obtained by this labeling method. The imaging capability of the ^{64}Cu liposome with PEG brush was evaluated with a HT29 colon adenocarcinoma xenograft model in tumor-bearing mice. The high-quality images in Fig. 10.3 demonstrate the potential of using ^{64}Cu -liposomes in PET/CT imaging [99]. It is very clear that long-circulating PEGylated ^{64}Cu -liposomes accumulate selectively in cancerous tissue because of EPR effect (Fig. 10.3c, d). The high resolution and better sensitivity of PET will allow for

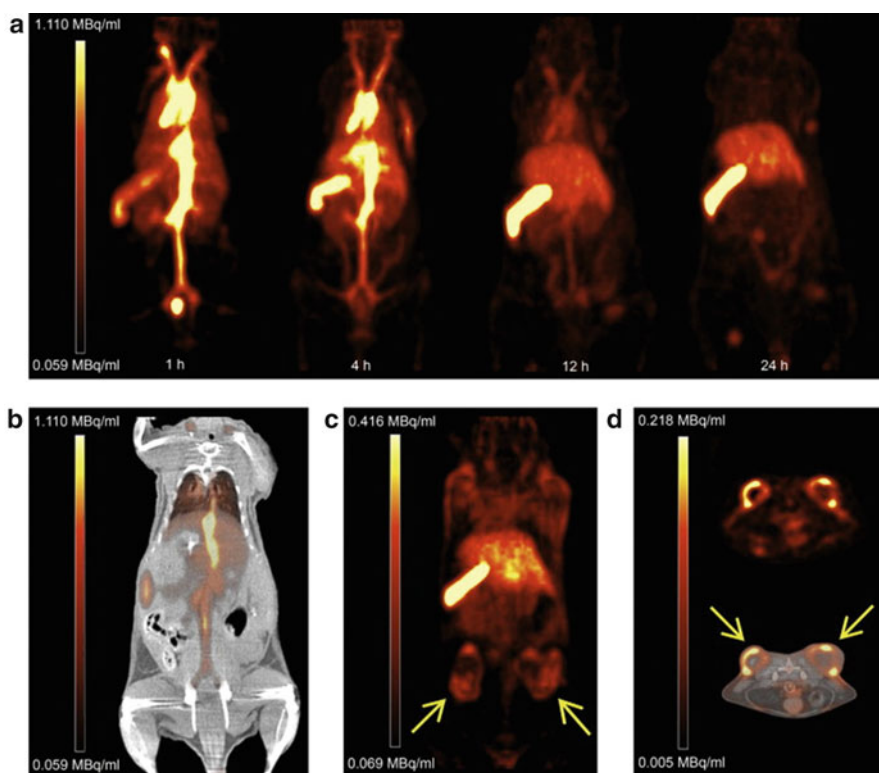


Fig. 10.3 PET/CT images of ^{64}Cu -liposomes distribution in normal and tumor-bearing mice. (a) Coronal PET images 1, 4, 12, and 24 h postinjection of ^{64}Cu -liposomes into a normal mouse. (b) Coronal PET/CT-fusion image 4 h postinjection of ^{64}Cu -liposomes into a normal mouse. (c) Coronal PET image 24 h postinjection of ^{64}Cu -liposomes into a mouse bearing colon adenocarcinoma (HT29; marked with *arrows*) on right and left flank. (d) Axial PET image (*top*) and axial PET/CT-fusion (*bottom*) images 24 h postinjection of ^{64}Cu -liposomes into a mouse bearing colon adenocarcinoma (HT29; marked with *arrows*) on *right* and *left* flank (Reprinted from Ref. [99], Copyright 2011, with permission from Elsevier)

detection of small and malignant tumors with significantly lower radioactivity dose to the patient compared to SPECT imaging [99].

The radionuclides remote loading with the prepared liposomes may be categorized into three approaches [4]: (1) a lipophilic chelator is used to transport the radionuclide across the liposomal bilayer into the internal aqueous compartment, inside which the radionuclide can chelate with a loaded metal chelator and gets encapsulated. For example, ^{67}Ga and ^{111}In can be loaded into the prepared liposomes encapsulating the chelator of nitrilotriacetic acid (NTA) [100] or the chelator of deferoxamine (DF) [101]. In this method, 8-hydroxyquinoline (oxine) can be utilized as lipophilic chelator for the transportation of ^{67}Ga (or ^{111}In) across the liposomal bilayer in the form of radionuclide/lipophilic chelator, from which ^{67}Ga (or ^{111}In) can be captured by the encapsulated NTA or DF. (2) An ionophore is incorporated in the liposome bilayer to make a hydrophilic pore, which ensures metal ions and/or radionuclides to go through the bilayer membrane. The A23187 ionophore has been successfully introduced into liposomal bilayer membranes to ship external $^{111}\text{InCl}_3$ across the bilayer membrane, in which the radionuclide can be captured by interacting with entrapped NTA chelators. (3) The lipophilic chelator *N,N*-bis(2-mercaptoethyl)-*N',N'*-diethylethylenediamine (BMEDA) has been successfully applied for liposomes labeling with $^{99\text{m}}\text{Tc}$ radionuclides by a pH gradient technique [102].

10.4.3 Quality Control of Radiolabeled Liposomes

A variety of quality control (QC) tests should be carried out on every single radiopharmaceutical batch produced for human injection to reach the acceptable tracer quality [4]. In order to comply with quality requirements, specifications have to be carefully considered during the development and in the production process. Because of the radioactive decay, the time between the production and the administration into patients can be insufficient to satisfy all the normal pharmaceutical QC requirements so radiopharmaceuticals have to be manufactured within strict time limits. Therefore, during the development process, the time to analyze every QC is a key parameter. After the radioactive labeling process, dependable QC tests are often required to be finished within 30–60 min. The production procedure of a liposomal radiopharmaceutical usually include two individual preparation steps: one is a non-radioactive process to prepare liposomes and the other is a radioactive process to produce the radiolabeled liposomes for injection. At each preparation step during manufacturing a liposomal radiopharmaceutical, specifications should be considered and QC tests should be carried out.

A number of parameters are required to be measured for the characterization of the liposomal radiopharmaceutical quality. For nonradioactive liposomes, some of the recommended specifications include physiochemical tests (surface charge, particle morphology and size, phase transition temperature, osmotic properties, etc.), identification of the entrapped and un-entrapped active species, degraded lipid

products, quantification of the components of lipids, in vitro stability test/shelf-life, and endotoxin and sterility tests. For human injectable liposomal radiopharmaceuticals [103], some QC tests, such as pH and appearance, physiochemical and biological tests, identity and purity of radionuclide, radiotracer purity and identity, radiotracer stability, and endotoxin and sterility tests, are highly recommended.

A variety of radiopharmaceuticals have to be fabricated prior to use, e.g., by liposomes remote loading due to short half-lives, but the stability concerns remain to be slow-decaying isotopes which can be longer stored because of possible radiolysis. Thus, suitable parameters must be established and documented to evaluate the stability of the liposomal radiopharmaceutical under certain storage conditions [104]. Hence, a stability test must be carried out in the possible harshest conditions. Radiochemical impurities may originate from a deficient chelation or loading in the labeling and loading process of the prepared liposomes because of uncompleted and side reactions, radiolysis, unsought lipophilic chelators, or ionophores content for the radionuclide binding [103]. The retention time (R_T) of the radiopharmaceutical liposomes is often used for radiochemical identification of a liposomal radiopharmaceutical by comparing with the R_T of a standard non-radiolabeled liposome by using analytical HPLC and size exclusion chromatography.

10.4.4 Liposomal Radiopharmaceuticals for Cancer Imaging and Therapy

Molecular imaging permits a noninvasive readout to provide information which was merely possible by biopsies and pathological evaluation in the past, so it can be an essential technique for diagnosis, monitoring, and treatment evaluation. In the recent decade, many radiopharmaceuticals have been explored for diagnosis, characterizing the tumor microenvironment, guiding treatments, and evaluating therapeutic efficacy [105]. Because of their sensitivity to phenotypical characteristics and specific tumor microenvironmental conditions, novel radiopharmaceuticals can target cancer tissue. People pay more attention to develop diagnostic strategies to include imaging contrast agents for novel molecular targets and further understand how the combinations of imaging contrast agent may provide more knowledge on tumorous heterogeneities. It aims at localization and staging of the cancer and assistance to select the optimal treatment strategies. For this concern, liposomal radiopharmaceuticals targeting tumors can possibly have appealing imaging characteristics and may be a supplementation to existing imaging contrast agents due to its different accumulation mechanisms from the existent agents. The liposomes targeting tumors have been extensively tested in preclinical evaluation to deliver anticancer agents, such as HER2, transferrin, integrin, and galectin-1 and interleukin 13 receptor-targeted liposomes [106]. Moreover, the tumor angiogenic vasculature has been widely explored as a target to deliver vascular disrupting and therapeutic agents. The targeting tractability of radiopharmaceutical liposomes can

supply additional biological insight to the invasive procedure-based biopsies [107]. In addition, liposomal radiopharmaceuticals can be used for the guidance of personalized treatments by classifying patients in accordance with radiopharmaceutical binding levels of the specific biomarkers or interesting targets. Mucus barriers lining mucosal epithelia may reduce the effectiveness of nanocarrier-based mucosal drug delivery and imaging. Yu et al. developed liposome-based mucus-penetrating particles (MPP) capable of loading hydrophilic agents, e.g., the diaCEST MRI contrast agent barbituric acid (BA) [108]. It was found that noninvasive diaCEST MRI illustrated uniform vaginal coverage and longer retention of BA-loaded 7 mol%-PEG liposomes compared to unencapsulated BA, showing promise for drug delivery and imaging at mucosal surfaces. Nanohybrid liposomes coated with amphiphilic hyaluronic acid-ceramide (HACE) was fabricated for targeted delivery of anticancer drug and *in vivo* cancer imaging. Nanohybrid liposomes including doxorubicin and Magnevist, a contrast agent for magnetic resonance (MR) imaging, with 120–130 nm mean diameter and a narrow size distribution, were developed. DOX release from the developed formulation was improved at acidic pH (pH 5.5 and 6.8) versus physiological pH (pH 7.4). Cytotoxicity induced by the blank plain liposome was reduced by coating the outer surface of the nanohybrid liposome with HACE. Cellular uptake of doxorubicin from the nanohybrid liposome was enhanced by HA and CD44 receptor interaction versus the plain liposome. *In vivo* contrast-enhancing effects revealed that the nanohybrid liposome can be used as a tumor targeting MR imaging probe for cancer diagnosis. In a pharmacokinetic study in rats, *in vivo* clearance of doxorubicin was decreased in the order doxorubicin solution, plain liposome (F2), and nanohybrid liposome (F3), indicating prolonged circulation of the drug in the blood stream and improved therapeutic efficacy of the nanohybrid liposome (F3). Based on these findings, the nanohybrid liposomal system may be a useful candidate for real-time cancer diagnosis and therapy [109].

Multimodal imaging provides more efficient and accurate diagnosis of various diseases, so a variety of multimodal imaging probes have been synthesized and tested as new contrasting agents [8]. As a multimodal imaging platform, liposomes have many attractive characteristics, such as a well-established preparation method, easy size control, easy surface modification, large loading capacity, and excellent *in vivo* stability [110]. Kim et al. developed a trimodal liposome for optical, nuclear, and MR tumor imaging [111]. The authors synthesized a new bimodal radioactive tracer of hexadecyl-4- ^{124}I iodobenzoate (^{124}I HIB) that emits both luminescence and nuclear signals. Then, a trimodal liposome was prepared by one-pot formulation of phosphatidylcholine, cholesterol, PEGylated lipid, lipophilic gadolinium complex, and the radiolabeled ^{124}I HIB. Fast clearance of the radiotracer from reticuloendothelial systems enables vivid tumor imaging with high tumor-to-background ratio (Fig. 10.4) [111]. Li et al. fabricated a multifunctional theranostic liposomal drug delivery system integrating multimodality MR, near-infrared (NIR) fluorescent and nuclear imaging of liposomal drug delivery, and therapy monitoring and prediction [112]. The premanufactured liposomes consist of 1,2-distearoyl-sn-glycero-3-phosphocholine (DSPC), cholesterol, lipophilic gadolinium complex,

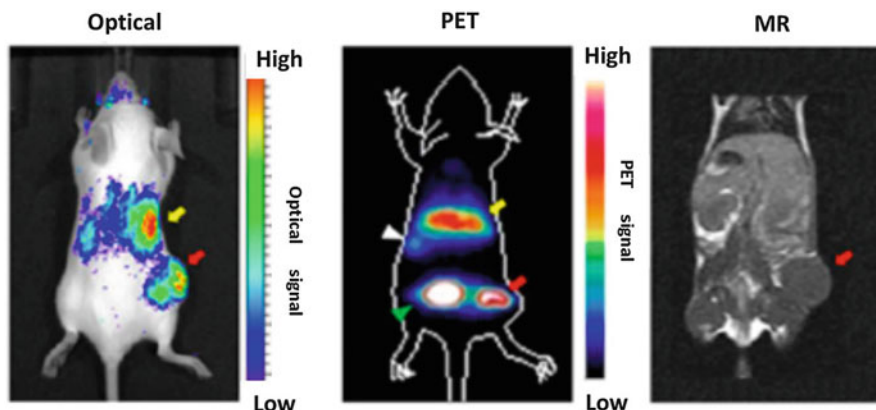


Fig. 10.4 Typical optical luminescence, PET and MR image of CT26 tumor-bearing mouse at 4 h postinjection of [^{124}I]HIB-Gd-liposome ($n=3$) (Reprinted with the permission from Ref. [111]. Copyright 2014 American Chemical Society)

and DOTA-DSPE with the molar ratio of 39:35:25:1. A lipidized NIR fluorescent tracer of IRDye-DSPE was inserted into the premanufactured liposomes. After loading doxorubicin, the multifunctional liposomes were stably radiolabeled with $^{99\text{m}}\text{Tc}$ or ^{64}Cu for SPECT or PET imaging, respectively. MR, NIR fluorescent, SPECT, and PET images clearly displayed either the high intratumoral retention or distribution of the multifunctional liposomes. This multifunctional liposome-carrying drug has great potential for disease theranostics, allowing noninvasive multimodality NIR fluorescent, MR, SPECT, and PET imaging of their in vivo behavior and capitalizing on the inherent advantages of each modality [112].

In a word, liposomal radiopharmaceuticals for nuclear imaging have been demonstrated to be extremely sensitive imaging agents which may be hopefully applied clinically. Especially, the agents for PET imaging are expected to be essential in the near future to quantify and optimize liposome-based drug delivery systems during personalized treatments. Liposomal radiopharmaceuticals can operate as a tool for individualization and optimization of cancer therapy because of the capability to predict the biodistribution of liposomal drug delivery systems [4].

10.5 Nanohybrid Liposomal Cerasome for Theranostics

10.5.1 Preparation and Properties of Cerasomes

Similar to liposomes, cerasomes are spherical vesicles with the lipid bilayer membrane around 4 nm in thickness. The fabrication procedure of cerasomes is analogous to that of the liposomes prepared from phospholipids. Conventional liposomes

consist of phospholipids, but cholesterol is often included as a constituent to improve the rigidity of the bilayer membrane and enhance the stability of the bilayer in the presence of biological fluids. In contrast, no cholesterol is needed for the fabrication of cerasomes. Based on the concept of the critical packing parameters for lipid assemblies, cerasome-forming lipids (CFLs) are designed and synthesized to have triethoxysilane headgroups and hydrophobic alkyl chains, which are linked by a connector part, e.g., oligopeptide moieties [22–24]. Upon hydrolysis of the triethoxysilyl groups, the CFLs become amphiphilic to self-assemble lipid bilayer in aqueous solution. Cerasomes were produced by direct dispersion of CFLs in aqueous solution using vortex-mixing, leading to the formation of a liposome which self-rigidifies via in situ sol-gel processes ($\text{Si-OCH}_3\text{CH}_2 + \text{H}_2\text{O} \rightarrow \text{Si-OH} + \text{CH}_3\text{CH}_2\text{OH}$ followed by $2\text{Si-OH} \rightarrow \text{Si-O-Si} + \text{H}_2\text{O}$) on the surface [22]. Moreover, siloxane network spontaneously develops via the condensation among the silanol groups on the relatively hydrophobic membrane surface. Generally, the size of the multilamellar cerasomes is in the range of sub-micrometers. Upon ultrasonication of the aqueous dispersion of cerasomes using a probe-type sonicator above the phase transition temperature of the lipids, the multilamellar vesicles (MLVs) converted into the corresponding single unilamellar vesicles (SUVs) with a diameter less than 200 nm.

The conventional liposome formulation has insufficient stability. A typical phenomenon of the increase in particle size is often observed during the formulation processing storage due to the aggregation or the fusion of unstable liposomes. It generally conduces to rapid uptake by the reticuloendothelial system followed by rapid clearance and a short half-life. Thus, controlling and maintaining liposomes at small and uniform sizes are essential in producing a viable pharmaceutical product. Nevertheless, the solution of cerasomes could be stored at 4 °C for several months with almost no change in particle size, indicating no aggregation or fusion of cerasomes [20]. In addition, cerasomes show remarkably high stability towards surfactant solubilization, acidic treatment. The siloxane network covering lipid bilayer is viewed as a protection towards all factors susceptible to destabilize bare liposomes. The silicalike layer of cerasomes greatly reduces liposome fusion, resulting in a substantial increase in their long-term stability [20, 22].

In order to develop cerasomes for biomedical applications, the biocompatibility of cerasomes with an average diameter of 153.7 ± 8.0 nm was evaluated with the silica nanoparticles prepared with an average diameter of 153.2 ± 7.3 nm as control [113]. It was found that cerasomes were internalized through nonspecific or clathrin-related endocytosis and affected different aspects of cell functions to a smaller extent than silica nanoparticles of the similar size, including cell proliferation, cell cycle, cell apoptosis, endogenous reactive oxygen species (ROS) level, and intercellular adhesion molecule-1 (ICAM-1) expression. The introduction of lipid bilayer membrane architecture into cerasomes boosts the biocompatibility. Cerasome's biocompatibility compares traditional liposome but better than silica nanoparticles, indicating great potential for drug and gene delivery applications [24].

10.5.2 Cerasomes as Drug/Gene Carriers

It is different from traditional liposomes that cerasomes can encapsulate not only both hydrophobic and hydrophilic molecules but also amphiphilic molecules. In order to investigate the effect of lipid structure on the release behavior of cerasomes, a series of new cerasome-forming lipids (A, B, C, and D) were designed and synthesized with different numbers of triethoxysilyl headgroups and alkyl chains covalently attached to each other via glycerol or pentaerythritol linkers (Fig. 10.5a) [114]. The *in vitro* paclitaxel (PTX) released from cerasome A, B, C, and D were examined over an experimental time period of 96 h. As seen in Fig. 10.5b, four types of cerasomes exhibited similar release profiles. No initial burst release was observed due to their high stability. But their PTX release rates from the cerasomes were much different and remarkably influenced by the molecular structure of the cerasome-forming lipids. From cerasome A to cerasome C, the release rate decreased with increasing number of triethoxysilane headgroups in the cerasome-forming lipids. Within 100 h, the total release amount of PTX reached to 36 %, 24 %, and 18 % for cerasome A, B, and C, respectively. The formation of siloxane bonds conducted to a silicalike surface of cerasomes with high degree of polymerization. The density of siloxane networks increased as the number of triethoxysilane headgroups in the cerasome-forming lipids increased. The slower release rate was attributed to the higher density of siloxane networks, which could block the drug release channels. Both cerasome A and D had one triethoxysilane headgroup in their corresponding lipids, but cerasome A had a higher release rate than cerasome D because of the difference in the chemical structure of the cerasome-forming lipids. The existence of one more alkyl chain in lipid D may make the cerasome bilayer more compacted, and the hydrophobic interaction between the lipid bilayer and PTX stronger. This resulted in a lower release rate from cerasome D. Therefore, the structure of cerasome-forming lipids also plays an important role in modulating the drug release behavior. It provides us an opportunity to control the drug release rates from

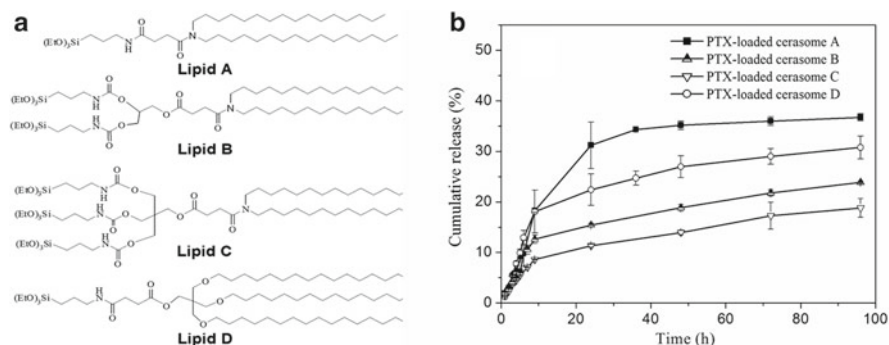


Fig. 10.5 (a) Chemical structures of four cerasome-forming lipid A, B, C, and D. (b) Cumulative release of PTX from cerasome A–D as a function of time (Reprinted with the permission from Ref. [114]. Copyright 2013 Wiley)

cerasomes by adjusting the number of triethoxysilane headgroup and alkyl chains in the cerasome-forming lipids.

It is very interesting that the magnitude of the initial burst and the rate of the sustained release of doxorubicin from cerasomes can be conveniently modulated by incorporating dipalmitoylphosphatidylglycerol (DPPG) into cerasomes and altering the ratios of cerasome-forming lipid A and DPPG [115, 116]. As shown in Fig. 10.6, $32.2 \pm 1.8 \%$, $41.4 \pm 1.9 \%$, $55.7 \pm 2.7 \%$, $66.7 \pm 3.0 \%$, and $75.8 \pm 2.0 \%$ doxorubicin were released from cerasomes incorporating 0 %, 10 %, 30 %, 50 %, and 80 % DPPG in the first 10 h, respectively. Clearly, the initial burst release of doxorubicin from cerasomes increased with increasing the DPPG content, indicating that DOX interacts more strongly with hydrolyzed CFLs than DPPG. An increase in the DPPG content weakened interactions between drug carrier in cerasomes. Thus, more encapsulated doxorubicin molecules existing in the molecularly dispersed state were available for the initial burst release. As the DPPG content increased, the sustained release of doxorubicin from cerasomes following the initial burst also slightly increased. As a result, the cumulative release of doxorubicin from cerasomes incorporating 0 %, 10 %, 30 %, 50 %, and 80 % DPPG was $55.2 \pm 1.5 \%$, $65.7 \pm 5.0 \%$, $85.0 \pm 2.9 \%$, $93.2 \pm 2.1 \%$, and $97.6 \pm 1.3 \%$ doxorubicin in 57 h, respectively (Fig. 10.6). Due to the difference in the development of siloxane networks in the mixed cerasomes, the degree of polymerization of siloxane networks decreases as the proportion of DPPG increases; hence, the release rate increases. Consequently, both the initial burst and subsequent sustained release can be modu-

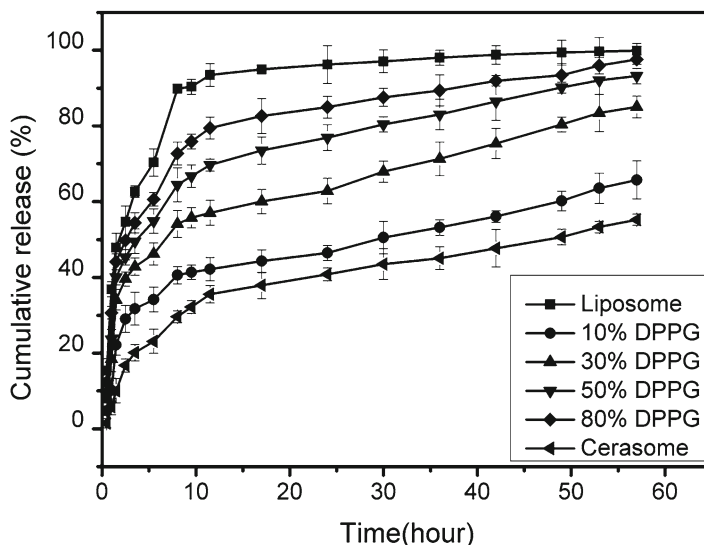


Fig. 10.6 Influences of vesicle composition on the sustained release of *doxorubicin* from DPPG-cerasomes. ■ Liposomes, ◆ 80 % DPPG, ▼ 50 % DPPG, ▲ 30 % DPPG, ● 10 % DPPG, ◀ cerasomes. Data shown as mean \pm SD, $n=5$ (Reprinted from Ref. [115], Copyright 2012, with permission from Elsevier)

lated by alteration in vesicle composition to achieve a wide range of release profiles. Therefore, the incorporation of DPPG into cerasome offers a new mechanism to modulate the release profiles of doxorubicin from cerasomes.

An ideal drug nanocarrier should be stable enough during systemic circulation and rapidly release high concentrations of active drug after reaching targeted region, but it is often difficult to be achieved since these two elements are apparently different. With the aim to develop a drug delivery system which is stable enough to minimize drug leakage during blood circulation and mediates a rapid drug release, Dai et al. developed HIFU and temperature-sensitive cerasomes (HTSCs) from a cerasome-forming lipid A by introducing thermosensitive liposome-forming lipids of 1,2-dipalmitoyl-sn-glycero-3-phosphocholine (DPPC), MSPC, and 1,2-distearoyl-sn-glycero-3-phosphoethanolamine-N-PEG2000 (DSPE-PEG2000) into the cerasomes [117]. The HTSCs showed spherical shape with an average diameter around 200 nm. Both hydrophilic and lipophilic drugs can be efficiently loaded into HTSCs. In addition, the release rate of HTSCs could be conveniently modulated by varying the molar ratios of CFL to DPPC. The drug-loaded HTSCs exhibited much longer blood circulation time (half-life $>8.50 \pm 1.49$ h) than conventional LTSL (0.92 ± 0.17 h). An *in vitro* study showed that the drug-loaded HTSCs were highly stable at 37 °C and gave a burst release at 42 °C, capable to act synergistically against tumors. More than 90 % hydrophilic drugs could be released from the HTSCs with a proportion of 43.25 % of CFL in 1 min at an elevated temperature of 42 °C generated by HIFU exposure. The *in vivo* studies demonstrated that the tumor growth of the adenocarcinoma (MDA-MB-231)-bearing mice could be significantly inhibited after intravenous injection of doxorubicin-loaded HTSCs at 5 mg doxorubicin/kg, followed by double HIFU irradiation. Therefore, the drug-loaded HTSCs combined with HIFU hold great potential for efficient localized chemotherapy of cancer by delivering high concentration of chemotherapy drugs directly to the tumor, achieve maximum therapeutic efficacy and minimal side effects, and avoid the damage to the healthy tissues caused by systemic administration of drugs.

Cationic liposomes have been widely used as transfection agents in gene delivery by binding DNAs and RNAs electrostatically to give lipoplexes which are taken in the cells via endocytosis to ultimately result in expression of the encoded gene [89, 90]. Nevertheless, the bilayer-keeping forces are not very strong, and liposomes are not so rigid or robust. Liposomes may easily undergo fusion as induced by hydrophobic species and/or simple ions. Therefore, the surface-rigidified cerasomes were applied as a gene carrier [23]. It is proved that cerasomes are neither fused nor cross-linked when bound to siRNA (short duplex RNA) but not to plasmid DNA which induces cross-linking [118]. To provide a solution to many of the limitations associated with current delivery platforms of siRNA, PEGylated cationic cerasomes (PCCs) were fabricated by doping a cationic lipid hydroxyl group liposomal nanohybrid cerasomes. It was found that the PEGylation of the cationic cerasome could protect the cerasome nanoparticles from agglomeration and macrophage capture, reduce protein absorption, consequently prolong the blood-circulating time, and enhance the siRNA delivery efficiency [119]. Moreover, incorporation of the cat-

ionic lipid containing hydroxyl group further facilitates endosome release. Upon systemic administration, PCCs were found to be effectively delivered into the liver and preferential uptake hepatocytes in mice, thereby leading to high siRNA gene-silencing activity, suggesting potential therapeutic applications of PCCs-mediated delivery of siRNA for liver diseases. Therefore, such cerasome strategy thus provides a simple and widely applicable tool to resolve common problems relating to present liposome-based drug and gene delivery. It is anticipated that cerasomes can be a promising candidate as drug/gene carrier with more sophisticated and smarter controlled release behavior.

10.5.3 Loading Functional Nanoparticles into Cerasomes for Theranostics

Although many successes have been achieved with magnetic liposomes, there are still a few challenges in the design of magnetic liposomes that are stable and long-circulating in vivo, but may be destabilized in a controlled fashion to facilitate drug release at the target site. Suffering from the classical issue of instability associated with lipid bilayers, the morphology of magnetic liposomes often changes significantly with magnetic nanoparticles and lipid concentrations. Magnetic liposomes generally exhibit a short circulation half-life after intravenous administration since they are prone to form aggregates and fuse to form larger vesicles in suspension, which may result in inclusion leakage. Therefore, it is of importance to develop more stable magnetic liposomes.

To overcome general problems about current magnetic liposome technology, magnetic cerasomes combining the advantages of both cerasome carriers and magnetic nanoparticles were developed recently. In addition, it was found that both doxorubicin and hydrophobic Fe_3O_4 nanoparticles can be loaded into the aqueous interior of cerasomes via facile one-step construction [120] (Fig. 10.7). A possible explanation is that the hydrophobic Fe_3O_4 NPs can be trapped inside the aqueous core of cerasomes through the formation of an intermediate Fe_3O_4 -micelle complex. It was reported that the loading of hydrophobic Fe_3O_4 nanoparticles with phospholipids in water lead to the formation of Fe_3O_4 -micelle complex [121, 122] or Fe_3O_4 -liposome complex [123]. In the Fe_3O_4 -micelle complex state, Fe_3O_4 nanoparticle is covered by a lipid monolayer, while in the Fe_3O_4 -liposome state, Fe_3O_4 nanoparticle presents in the lipid bilayer of liposomes. The cerasome bilayer is about 4 nm thick, so the hydrophobic Fe_3O_4 nanoparticles larger than 5 nm cannot stay in the lipid bilayer due to a high energy penalty. Hence, the hydrophobic Fe_3O_4 surface should be completely covered by the lipid monolayer, leading to the formation of Fe_3O_4 -micelle complex.

The encapsulation efficiency of doxorubicin was found to increase with decreasing ratios of Fe/C, which was evaluated to be $21.7 \pm 5.4\%$ at the Fe/C ratio of 10:1 and $51.6 \pm 5.9\%$ at the Fe/C ratio of 0:10, respectively. Most importantly, the Fe_3O_4

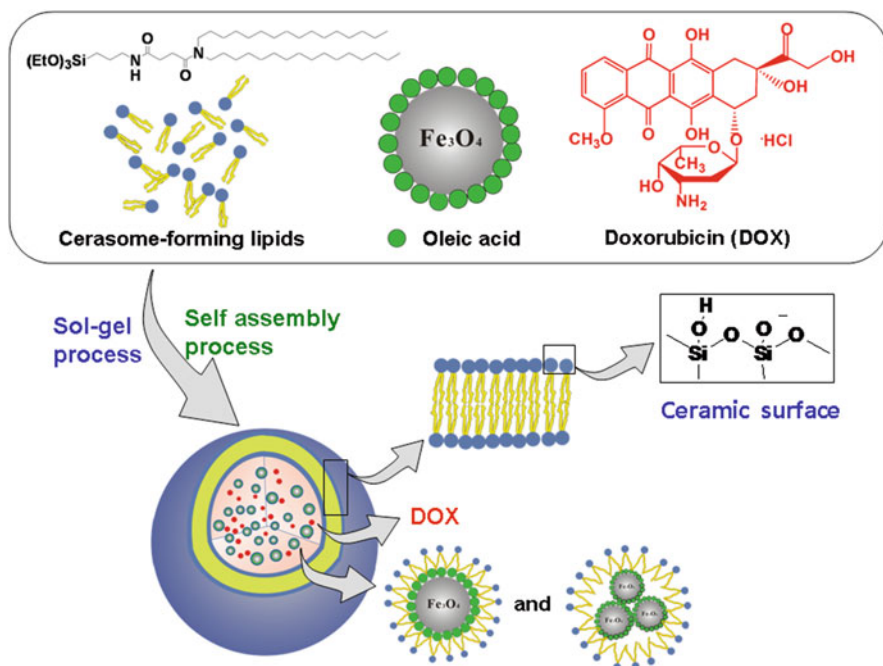


Fig. 10.7 Schematic illustration of DOX-loaded magnetic cerasomes (Reprinted from Ref. [120], Copyright 2012, with permission from Elsevier)

loading content reached a maximum (approximately 0.69 mg/mL) at a Fe/C molar ratio of 4:1. In addition, at a Fe/C molar ratio of 4:1, we could obtain a good drug-loading content of $3.2 \pm 1.3\%$ and a high encapsulation efficiency of $43.4 \pm 4.7\%$, which is close to the highest value of $51.6 \pm 5.9\%$ at the Fe/C ratio of 0:10. Therefore, the Fe/C molar ratio of 4:1 was used for the fabrication of the doxorubicin-loaded magnetic cerasomes in further studies [120].

Superparamagnetism is of importance in drug delivery. The doxorubicin-loaded magnetic cerasomes showed fast response to the external magnetic field and could be redispersed quickly with a slight shake after removal of the magnetic field. The two saturation magnetization curves measured at 300 K showed no hysteresis loop, which means that both Fe₃O₄ nanoparticles and the drug-loaded magnetic cerasomes possess strong superparamagnetism. The saturation magnetization value (M_s) of the doxorubicin-loaded magnetic cerasomes was 25.95 emu g^{-1} . It is lower than that of Fe₃O₄ nanoparticles (69.65 emu g^{-1}) due to the overall reduction in the total ferrite content in cerasomes. It should be noted that the doxorubicin-loaded magnetic cerasomes still show high magnetization, ensuring its application for MR imaging, magnetic targeting, and separation as a drug carrier.

The dose of drug required to achieve clinically effective cytotoxicity in tumors often causes severe damage to normal tissues. Light-triggered drug release is an attractive strategy for the spatiotemporal control of drug delivery, which may allow

for precise, on-demand drug delivery within individual cells *in vitro* to enable precise treatment of cancer *in vivo*. Gold nanoshell mediates strong surface heat flux upon absorption of near-infrared (NIR) light, thus is an excellent candidate for NIR light-triggered release of drug from nanocarriers as well as photothermal treatment agent. In combination with gold nanoshells, liposomes have been shown to be able to thermally control the release of encapsulated agents. The permeability of liposomes is greatly enhanced around the liposomal membrane melting temperature (T_m), which depends on the lipid composition [124]. Upon heating the liposomal membrane above, T_m drug can thus be released. The double long-strand alkane-based liposomes have T_m typically close to body temperature, which results in drug leakage during circulation in human system. By choosing a T_m far above body temperature, leakage during circulation can be much more minimized [125]. Moreover, the gold nanoshell-coated liposomes may go through a melting and fusion process due to the insufficient stability of traditional liposomes, leading to the formation of large gold aggregates, so the contents in liposomes usually exhibit a one-time release profile instead of multiple release kinetics [126]. Therefore, the doxorubicin-loaded magnetic cerasomes coated with gold nanoshell were developed by loading both hydrophobic doxorubicin and Fe_3O_4 nanoparticles into the cholesteryl succinyl silane-based cerasomes, followed by the formation of gold nanoshell around cerasome surface to combine MR imaging, magnetic field-guided drug delivery, light-triggered drug release, and photothermal therapy [127].

Compared with conventional systems, such as liposomes, such drug-loaded magnetic cerasomes with gold nanoshell take more advantages for potential clinical applications as follows: (1) Minimize the drug leakage during systemic circulation because cholesteryl molecule as the hydrophobic part has a melting temperature as high as 150 °C. (2) Realize multiple release kinetics rather than one-time release profile due to the remarkably high mechanical stability and heat resistance compared to traditional liposomes. (3) Improve drug encapsulation efficiency and loading content because of the full hydrophobic interior of cerasomes. (4) Identify the location and size of tumors, evaluate the therapeutic efficacy, and address the drug amount accumulated in the tumor through contrast-enhanced MR imaging. (5) Significantly improve the cancer cell killing capability, greatly increase the selectivity, and potentially overcome resistance to chemotherapeutic agents by the combined photothermal therapy, chemotherapy, magnetic field-guided drug delivery, and MR imaging. In a word, this new multifunctional platform combines all functions within a single agent to yield substantial promise for highly efficient anticancer treatment.

High-quality water-soluble quantum dots have attracted intensive research interests for biomedical application. Quantum dots can be prepared directly in water but often have narrow available size ranges and wide size distribution, resulting in wide full width at half maximum of the emission spectrum. In contrast, quantum dots produced from high temperature organic solvent synthetic strategies are monodisperse with very wide emission color ranging from ultraviolet to near infrared (300–2500 nm). However, these quantum dots synthesized in organic solvents are water insoluble. Thus, how to make the high-quality hydrophobic quantum dots water

soluble is a big challenge. In order to overcome general problems associated with current hydrophobic quantum dots, a one-pot strategy was developed for the encapsulation of hydrophobic quantum dots into cerasome [128]. This “all-in-one” procedure for simultaneous synthesis, encapsulation, and solubilization of high-quality quantum dots is based on the use of dihexadecylamine and 3-isocyanatopropyltriethoxysilane. Upon sonication in water, the condensation of dihexadecylamine and 3-isocyanatopropyltriethoxysilane leads to the formation of a cerasome-forming lipid of the urea, which spontaneously encapsulates and solubilizes the hydrophobic quantum dots by self-assembly and sol-gel process without the use of any additional materials or steps. After encapsulation into cerasome, quantum dots become well dispersed in aqueous solution. Such water-soluble quantum dots cerasomes show a good photostability and keep the luminescence property of the original hydrophobic quantum dots.

10.5.4 Cerasomal Porphyrin for Photodynamic Theranostics of Cancer

Due to the flexibility to accommodate photosensitizers with variable physicochemical properties, liposomes have come into focus as a valuable carrier and delivery system for the improvement of the efficacy and safety of photodynamic therapy (PDT) [129]. However, a lipid exchange between the liposomes and lipoproteins may result in an irreversible disintegration of the liposome, hence the release of photosensitizers in the bloodstream. Unlike conventional chemotherapy, the release of the photosensitizer drugs is not a prerequisite for PDT action, so this premature release may reduce efficacy of treatment [130]. Porphyrin and its derivatives are the most used photosensitizers for photodynamic diagnosis and therapy. Dai et al. designed and synthesized a conjugate of porphyrin-organoalkoxysilylated lipid (PORSIL) with dual triethoxysilyl heads, a hydrophobic double-chain segment, a porphyrin moiety, and a connector unit among them, which was used to fabricate porphyrin-conjugated cerasomes for the first time by sol-gel reaction and self-assembly process (Fig. 10.8) [131, 132]. The average diameter of this porphyrin cerasome was evaluated to be 70 ± 13 nm. The covalent attachment of porphyrin to cerasomes resulted in the drug-loading content of 33.46 %, significantly higher than the physically entrapping cerasomes or liposomes (generally less than 10 %). In addition, the premature release of photosensitizers can be avoided during systemic circulation.

The shape of the absorption spectrum of porphyrin-conjugated cerasomes is quite similar to that of the solution-phase PORSIL lipid, suggesting that no aggregation of porphyrin molecules occurs in the nanoparticles. Both Soret and Q bands of porphyrin moieties exhibit bathochromic shift of 3 nm due to an alternative arranging mode of porphyrin group and alkyl chains. The existence of double-alkyl chains sterically hinders porphyrin moieties' approaching each other, which is highly

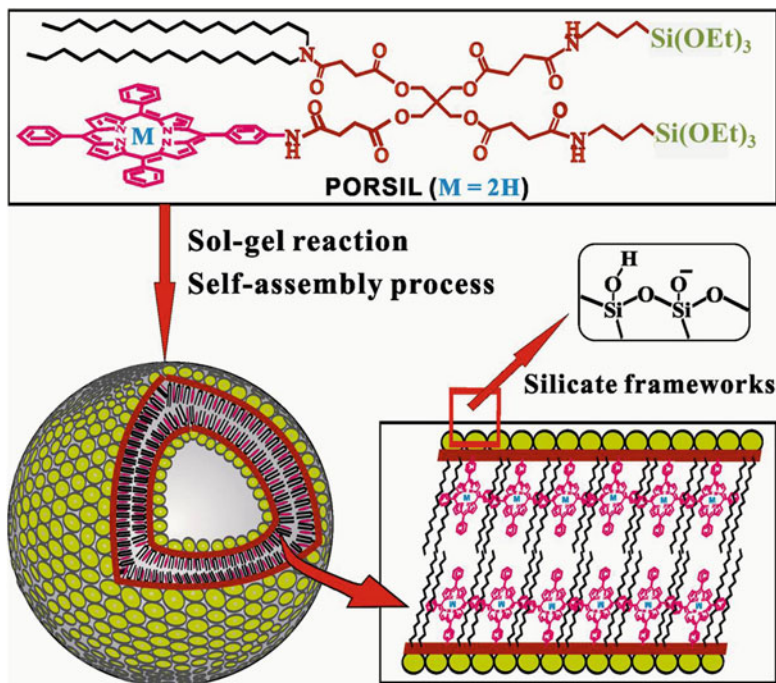


Fig. 10.8 Schematic illustration for the formation of porphyrin-conjugated cerasome from a PORASIL lipid (Reprinted from Ref. [131], Copyright 2014, with permission from Wiley)

effective for preparing photofunctional cerasomes to load porphyrin photosensitizer without causing its aggregation. It was found that the presence of the double-alkyl chains avoided significant fluorescence self-quenching in such porphyrin-conjugated cerasomes. Confocal laser scanning microscopy (CLSM) showed that the porphyrin-conjugated cerasomes were highly fluorescent and were clearly observed inside the cells as red spots distributing in the cytoplasm. In addition, the conjugation of porphyrin to cerasomes improved significantly the $^1\text{O}_2$ generation. Significant phototoxic effect on the cultured cells was observed after treatment of HeLa cells with various concentrations of the porphyrin-conjugated cerasomes followed by subsequent irradiation with the light (400–700 nm). In addition, no obvious dark toxicity was seen.

The blood circulation dynamics of the porphyrin-conjugated cerasomes was investigated in comparison with the porphyrin-loaded liposomes. The decrease in the blood fluorescence intensity of the porphyrin-conjugated cerasomes was only 33.5 % after intravenous injection for 24 h, showing dramatically prolonged and slow clearance kinetics. On the contrary, the blood fluorescence intensity of the porphyrin-loaded liposomes decreased to 30 % at 6 h, and almost no fluorescence was observed at 24 h, exhibiting rapid clearance kinetics. It provided a strong evi-

dence that the porphyrin-conjugated cerasomes can maintain a long circulation without PEG chains.

In a word, the covalent linkage of porphyrins can prevent cerasomes from releasing photosensitizers during systemic circulation and thus enhance the outcome of PDT. The orderly arranging mode of porphyrins in the lipid bilayer improves the efficacy of singlet oxygen production even at an extremely high number of porphyrins, effectively prevent fluorescence loss of porphyrins, and permitting a powerful tool for *in vivo* imaging, photodynamic diagnosis, and therapy. The capability to encapsulate chemotherapeutic drugs into the internal aqueous core of the porphyrin-conjugated cerasomes enables to develop a drug-carrier system for the synergistic combination of chemotherapy and PDT for the treatment of cancer. The porphyrin-conjugated cerasomes have shown an avid uptake by malignant cells and cellular phototoxicity under irradiation. There is no doubt that the dual-function nature of the porphyrin-conjugated cerasomes will play an important role in future clinical photodynamic theranostics.

10.6 Conclusions and Perspectives

In the last decades, liposomes have been shown to act as a universal drug delivery system, confirmed by the use for noninvasive imaging diagnosis, real-time imaging guidance, and remote-controlled therapeutics, especially imaging-guided therapeutics, enabling personalized detection and treatment of diseases with high efficacy. The combination of the favorable biodistribution of liposomes to tumors and their microenvironments, as well as their prominent imaging contrast properties, offers the exciting possibility of the simultaneous delivery and detection of therapeutic agents *in vivo*. Overall, we believe that theranostic liposomes with superior properties constitutes a major advance in the application of nanotechnologies in medicine and has opened up new ways for the diagnosis and treatment of important human diseases such as cancer. Theranostic liposomes may further operate as a strategy to individualize schedule and level of patient dosages and to evaluate therapeutic efficacy at an early stage, ensuring personalized suitable changes in treatment strategies, probably leading to an improvement in the survival prognosis for cancer patients. These encouraging results point to a clinical translation in near future, offering a new minimally invasive and local treatment option in cancer. Especially, nanohybrid liposomal cerasomes will soon begin to reach their full potential as an important class of theranostic nanoagents and will contribute to significant advances in the treatment of many classes of diseases due to the unique features of cerasomes including higher stability than conventional liposomes and lower rigidity and density than competing silica nanoparticles. All these efforts will of course require interdisciplinary collaborations of chemists, physicists, biologists, and materials scientists.

Acknowledgments This research was financially supported by State Key Program of National Natural Science of China (No. 81230036), National Natural Science Foundation of China (No. 21273014), and National Natural Science Foundation for Distinguished Young Scholars (No. 81225011).

References

1. Daniel JAM, John MH, Robert JH et al (2007) Molecular imaging techniques in body imaging. *Radiology* 245(2):333–356. doi:[10.1148/radiol.2452061117](https://doi.org/10.1148/radiol.2452061117)
2. Khullar O, Frangioni JV, Grinstaff M et al (2009) Image-guided sentinel lymph node mapping and nanotechnology-based nodal treatment in lung cancer using invisible near-infrared fluorescent light. *Semin Thorac Cardiovasc Surg* 21(4):309–315. doi:[10.1053/j.semtcvs.2009.11.009](https://doi.org/10.1053/j.semtcvs.2009.11.009)
3. Troyan SL, Kianzad V, Gibbs-Strauss SL et al (2009) The FLARE intraoperative near-infrared fluorescence imaging system: a first-in-human clinical trial in breast cancer sentinel lymph node mapping. *Ann Surg Oncol* 16(10):2943–2952. doi:[10.1245/s10434-009-0594-2](https://doi.org/10.1245/s10434-009-0594-2)
4. Petersen AL, Hansen AE, Gabizon A et al (2012) Liposome imaging agents in personalized medicine. *Adv Drug Deliv Rev* 64:1417–1435. doi:[10.1016/j.addr.2012.09.003](https://doi.org/10.1016/j.addr.2012.09.003)
5. Lanza GM, Winter PM, Caruthers SD et al (2004) Magnetic resonance molecular imaging with nanoparticles. *J Nucl Cardiol* 11(6):733–743. doi:[10.1016/j.nuclcard.2004.09.002](https://doi.org/10.1016/j.nuclcard.2004.09.002)
6. Blasberg RG, Gelovani J (2002) Molecular-genetic imaging: a nuclear medicine-based perspective. *Mol Imaging* 1(3):280–300
7. Martí-Bonmatí L, Sopena R, Bartumeus P et al (2010) Multimodality imaging techniques. *Contrast Media Mol Imaging* 5(4):180–189. doi:[10.1002/cmimi.393](https://doi.org/10.1002/cmimi.393)
8. Louie A (2010) Multimodality imaging probes: design and challenges. *Chem Rev* 110(5):3146–3195. doi:[10.1021/cr9003538](https://doi.org/10.1021/cr9003538)
9. Jennings LE, Long NJ (2009) ‘Two is better than one’ probes for dual-modality molecular imaging. *Chem Commun (Camb)* 24:3511–3524. doi:[10.1039/b821903f](https://doi.org/10.1039/b821903f)
10. Lammers T, Kiessling F, Hennink WE et al (2010) Nanotheranostics and image-guided drug delivery: current concepts and future directions. *Mol Pharm* 7(6):1899–1912. doi:[10.1021/mp100228v](https://doi.org/10.1021/mp100228v)
11. Buse J, El-Aneed A (2010) Properties, engineering and applications of lipid-based nanoparticle drug-delivery systems: current research and advances. *Nanomedicine* 5(8):1237–1260. doi:[10.2217/nnm.10.107](https://doi.org/10.2217/nnm.10.107)
12. Koning GA, Krijger GC (2007) Targeted multifunctional lipid-based nanocarriers for image-guided drug delivery. *Anticancer Agents Med Chem* 7(4):425–440
13. Lammers T, Aime S, Hennink WE et al (2011) Theranostic nanomedicine. *Acc Chem Res* 44(10):1029–1038. doi:[10.1021/ar200019c](https://doi.org/10.1021/ar200019c)
14. Gabizon AA (2007) Applications of liposomal drug delivery systems to cancer therapy. In: Amiji MM (ed) *Nanotechnology for cancer therapy*, 1st edn. CRC Press, Boca Raton, pp 595–611
15. Elbayoumi TA, Torchilin VP (2010) Current trends in liposome research. *Methods Mol Biol* 605:1–27. doi:[10.1007/978-1-60327-360-2_1](https://doi.org/10.1007/978-1-60327-360-2_1)
16. Bao A, Goinsc B, Klipper R et al (2004) Direct ^{99m}Tc labeling of pegylated liposomal doxorubicin (Doxil) for pharmacokinetic and non-invasive imaging studies. *J Pharmacol Exp Ther* 308(2):419–425. doi:[10.1124/jpet.103.059535](https://doi.org/10.1124/jpet.103.059535)
17. Madaswamy MS, Si-Shen F (2013) Theranostic liposomes for cancer diagnosis and treatment: current development and pre-clinical success. *Expert Opin Drug Deliv* 10(2):151–155. doi:[10.1517/17425247.2013.729576](https://doi.org/10.1517/17425247.2013.729576)
18. Puri A, Loomis K, Smith B et al (2009) Lipid-based nanoparticles as pharmaceutical drug carriers: from concepts to clinic. *Crit Rev Ther Drug Carrier Syst* 26(6):523–580

19. Allen T, Hansen C, Martin F et al (1991) Liposomes containing synthetic lipid derivatives of poly(ethylene glycol) show prolonged circulation half-lives in vivo. *Biochim Biophys Acta* 1066(1):29–36
20. Zhong C, Yan M, Xiuli Y et al (2010) Stabilized liposomal nano hybrid cerasomes for drug delivery applications. *Chem Commun* 46(29):5265–5267. doi:[10.1039/b926367e](https://doi.org/10.1039/b926367e)
21. Gordon KB, Tajuddin A, Guitart J et al (1995) Hand-foot syndrome-associated with liposome-encapsulated doxorubicin therapy. *Cancer* 75(8):2169–2173. doi:[10.1002/1097-0142\(19950415\)75:8<2169::AID-CNCR2820750822>3.0.CO;2-H](https://doi.org/10.1002/1097-0142(19950415)75:8<2169::AID-CNCR2820750822>3.0.CO;2-H)
22. Katagiri K, Hashizume M, Ariga K et al (2007) Preparation and characterization of a novel organic-inorganic nano hybrid “cerasome” formed with a liposomal membrane and silicate surface. *Chem Eur J* 13(18):5272–5281. doi:[10.1002/chem.200700175](https://doi.org/10.1002/chem.200700175)
23. Matsui K, Sando S, Sera T et al (2006) Cerasome as an infusible, cell-friendly, and serum-compatible transfection agent in a viral size. *J Am Chem Soc* 128(10):3114–3115. doi:[10.1021/ja058016](https://doi.org/10.1021/ja058016)
24. Yue XL, Dai ZF (2014) Recent advances in liposomal nano hybrid cerasomes as promising drug nanocarriers. *Adv Colloid Interf* 207(S1):32–42. doi:[10.1016/j.cis.2013.11.014](https://doi.org/10.1016/j.cis.2013.11.014)
25. Thomas LA, Simon SJ, Kent J (2005) Advanced strategies in liposomal cancer therapy: problems and prospects of active and tumor specific drug release. *Prog Lipid Res* 44(1):68–97. doi:[10.1016/j.plipres.2004.12.001](https://doi.org/10.1016/j.plipres.2004.12.001)
26. Kaasgaard T, Andresen TL (2010) Liposomal cancer therapy: exploiting tumor characteristics. *Expert Opin Drug Deliv* 7(2):225–243. doi:[10.1517/17425240903427940](https://doi.org/10.1517/17425240903427940)
27. Damen J, Regts J, Scherphof G (1981) Transfer and exchange of phospholipid between small unilamellar liposomes and rat plasma high-density lipoproteins: dependence on cholesterol and phospholipid composition. *Biochim Biophys Acta* 665(3):538–545. doi:[10.1016/0005-2760\(81\)90268-X](https://doi.org/10.1016/0005-2760(81)90268-X)
28. Senior J, Gregoriadis G (1982) Is half-life of circulating liposomes determined by changes in their permeability? *FEBS Lett* 145(1):109–114. doi:[10.1016/0014-5793\(82\)81216-7](https://doi.org/10.1016/0014-5793(82)81216-7)
29. Scherphof GL (1985) Uptake and intracellular processing of targeted and nontargeted liposomes by rat Kupffer cells in vivo and in vitro. *Ann N Y Acad Sci* 446:368–384. doi:[10.1111/j.1749-6632.1985.tb18414.x](https://doi.org/10.1111/j.1749-6632.1985.tb18414.x)
30. Woodle MC, Lasic DD (1992) Sterically stabilized liposomes. *Biochim Biophys Acta* 1113(2):171–199
31. Gregoriadis G (1976) The carrier potential of liposomes in biology and medicine. *N Engl J Med* 295(14):765–770
32. Senior JH (1987) Fate and behavior of liposomes in vivo – a review of controlling factors. *Crit Rev Ther Drug Carrier Syst* 3(2):123–193
33. Fugman D, Shirak K, Jackson R et al (1984) Lipoprotein lipase-A2-catalyzed and phospholipase-A2-catalyzed hydrolysis of phospholipid-vesicles with an encapsulated fluorescent dye – effects of apolipoproteins. *Biochim Biophys Acta* 795(2):191–195
34. Chonn A, Semple SC, Cullis PR (1995) Beta 2-glycoprotein I is a major protein associated with very rapidly cleared liposomes in vivo, suggesting a significant role in the immune clearance of “non-self” particles. *J Biol Chem* 270(43):25845–25849
35. Oja CDM, Semple SC, Chonn A et al (1996) Influence of dose on liposome clearance: critical role of blood proteins. *Biochim Biophys Acta* 1281(1):31–37
36. Papahadjopoulos D, Allen TM, Gabizon A et al (1991) Sterically stabilized liposomes – improvements in pharmacokinetics and antitumor therapeutic efficacy. *Proc Natl Acad Sci U S A* 88(24):11460–11464
37. Liu D, Mori A, Huang L (1992) Role of liposome size and res blockade in controlling biodistribution and tumor uptake of Gm1-containing liposomes. *Biochim Biophys Acta* 1104(1):95–101
38. Gabizon A (2001) Stealth liposomes and tumor targeting: one step further in the quest for the magic bullet. *Clin Cancer Res* 7(2):223–225
39. Allen TM, Stuart D (1998) Liposome pharmacokinetics. Classical, sterically stabilized, cationic liposomes and immunoliposomes. In: Janoff A (ed) *Liposomes: rational design*, 1st edn. Marcel Dekker, New York, pp 63–87

40. Danhier F, Feron O, Preat V (2010) To exploit the tumor microenvironment: passive and active tumor targeting of nanocarriers for anti-cancer drug delivery. *J Control Release* 148(2):135–146. doi:[10.1016/j.jconrel.2010.08.027](https://doi.org/10.1016/j.jconrel.2010.08.027)
41. Kievit FM, Miqin Z (2011) Cancer nanotheranostics: improving imaging and therapy by targeted delivery across biological barriers. *Adv Mater* 23(36):H217–H247. doi:[10.1002/adma.201102313](https://doi.org/10.1002/adma.201102313)
42. Elbayoumi TA, Torchilin VP (2006) Enhanced accumulation of long-circulating liposomes modified with the nucleosome-specific monoclonal antibody 2C5 in various tumours in mice: Gamma-imaging studies. *Eur J Nucl Med Mol Imaging* 33(10):1196–1205
43. Torchilin VP (2007) Targeted pharmaceutical nanocarriers for cancer therapy and imaging. *AAPS J* 9(2):E128–E147
44. Petersen AL, Binderup T, Jølcck RI (2012) Positron emission tomography evaluation of somatostatin receptor targeted ^{64}Cu -TATE-liposomes in a human neuroendocrine carcinoma mouse model. *J Control Release* 160(2):254–263. doi:[10.1016/j.jconrel.2011.12.038](https://doi.org/10.1016/j.jconrel.2011.12.038)
45. Erdogan S, Roby A, Torchilin VP (2006) Enhanced tumor visualization by gamma-scintigraphy with ^{111}In -labeled polychelating-polymer-containing immunoliposomes. *Mol Pharm* 3(5):525–530
46. Bartlett DW, Su H, Hildebrandt IJ (2007) Impact of tumor-specific targeting on the biodistribution and efficacy of siRNA nanoparticles measured by multimodality in vivo imaging. *Proc Natl Acad Sci U S A* 104(39):15549–15554
47. Allen TM, Cullis PR (2004) Drug delivery systems: entering the mainstream. *Science* 303(5665):1818–1822
48. Liang XL, Yue XL, Dai ZF et al (2011) Photoresponsive liposomal nanohybrid cerasomes. *Chem Commun (Camb)* 47(16):4751–4753. doi:[10.1039/c1cc00063b](https://doi.org/10.1039/c1cc00063b)
49. Weinstein JN, Magin RL, Yatvin MB et al (1979) Liposomes and local hyperthermia: selective delivery of methotrexate to heated tumors. *Sciences* 204(4389):188–191
50. Alvarez-Lorenzo C, Bromberg L, Concheiro A (2009) Light-sensitive intelligent drug delivery systems. *Photochem Photobiol* 85(4):848–860. doi:[10.1111/j.1751-1097.2008.00530.x](https://doi.org/10.1111/j.1751-1097.2008.00530.x)
51. Yu B, Tai HC, Xue W et al (2010) Receptor targeted nanocarriers for therapeutic delivery to cancer. *Mol Membr Biol* 27(7):286–298. doi:[10.3109/09687688.2010.521200](https://doi.org/10.3109/09687688.2010.521200)
52. Carpentier A, Chauvet D, Reina V (2012) MR-guided Laser-Induced Thermal Therapy (LITT) for recurrent glioblastomas. *Lasers Surg Med* 44(5):361–368. doi:[10.1002/lsm.22025](https://doi.org/10.1002/lsm.22025)
53. Fatehi D, van der Zee J, de Bruijne M et al (2007) RF-power and temperature data analysis of 444 patients with primary cervical cancer: deep hyperthermia using the sigma-60 applicator is reproducible. *Int J Hyperthermia* 23(8):623–643
54. Johnson JE, Neuman DG, Maccarini PF et al (2006) Evaluation of a dual-arm Archimedean spiral array formicrowave hyperthermia. *Int J Hyperthermia* 22(6):475–490
55. Salomir R, Palussiere J, Vimeux FC et al (2000) Local hyperthermia with MR-guided focused ultrasound: spiral trajectory of the focal point optimized for temperature uniformity in the target region. *J Magn Reson Imaging* 12(4):571–583
56. Hamano N, Negishi Y, Takatori K et al (2014) Combination of bubble liposomes and High-Intensity Focused Ultrasound (HIFU) enhanced antitumor effect by tumor ablation. *Biol Pharm Bull* 37(1):174–177
57. Grilla H, Langereis S (2012) Hyperthermia-triggered drug delivery from temperature-sensitive liposomes using MRI-guided high intensity focused ultrasound. *J Control Release* 161(2):317–327. doi:[10.1016/j.jconrel.2012.04.041](https://doi.org/10.1016/j.jconrel.2012.04.041)
58. Evans E, Needham D (1987) Physical-properties of surfactant bilayer-membranes—thermal transitions, elasticity, rigidity, cohesion, and colloidal interactions. *J Phys Chem* 91(16):4219–4228. doi:[10.1021/j100300a003](https://doi.org/10.1021/j100300a003)
59. Cruzeiro-Hansson L, Mouritsen OG (1988) Passive ion permeability of lipid membranes modeled via lipid domain interfacial area. *Biochim Biophys Acta* 944(1):63–72
60. Ruocco MJ, Siminovitch DJ, Griffin RG (1985) Comparative study of the gel phases of ether-linked and ester-linked phosphatidylcholines. *Biochemistry (Mosc)* 24(10):2406–2411

61. Mabrey S, Sturtevant JM (1976) Investigation of phase-transitions of lipids and lipid mixtures by high sensitivity differential scanning calorimetry. *Proc Natl Acad Sci U S A* 73(11):3862–3866
62. Bratton DL, Harris RA, Clay KL et al (1988) Effects of platelet activating factor and related lipids on phase-transition of dipalmitoylphosphatidylcholine. *Biochim Biophys Acta* 941(1):76–82
63. Needham D, Dewhirst MW (2001) The development and testing of a new temperature-sensitive drug delivery system for the treatment of solid tumors. *Adv Drug Deliv Rev* 53(2):285–305
64. Chelsea D, Landon CD, Park JY et al (2011) Nanoscale drug delivery and hyperthermia: the materials design and preclinical and clinical testing of low temperature-sensitive liposomes used in combination with mild hyperthermia in the treatment of local cancer. *Open Nanomedicine J* 3:38–64
65. Banno B, Ickenstein LM, Chiu GNC et al (2009) The functional roles of poly(ethylene glycol)-lipid and lysolipid in the drug retention and release from lysolipid-containing thermosensitive liposomes in vitro and in vivo. *J Pharm Sci* 99(5):2295–2308. doi:[10.1002/jps.21988](https://doi.org/10.1002/jps.21988)
66. Needham D, Park JY, Wright AM et al (2013) Materials characterization of the low temperature sensitive liposome (LTSL): effects of the lipid composition (lysolipid and DSPE-PEG2000) on the thermal transition and release of doxorubicin. *Faraday Discuss* 161:515–534. doi:[10.1039/c2fd20111a](https://doi.org/10.1039/c2fd20111a)
67. Ickenstein LM, Arfvidsson MC, Needham D et al (2003) Disc formation in cholesterol-free liposomes during phase transition. *Biochim Biophys Acta* 1614(2):135–138
68. Lindner LH, Eichhorn ME, Eibl H et al (2004) Novel temperature-sensitive liposomes with prolonged circulation time. *Clin Cancer Res* 10(6):2168–2178. doi:[10.1158/1078-0432](https://doi.org/10.1158/1078-0432)
69. Hossann M, Wang TT, Wiggenshorn M et al (2010) Size of thermosensitive liposomes influences content release. *J Control Release* 147(3):436–443. doi:[10.1016/j.jconrel.2010.08.013](https://doi.org/10.1016/j.jconrel.2010.08.013)
70. Needham D, Dewhirst MW (2001) The development and testing of a new temperature-sensitive drug delivery system for the treatment of solid tumors. *Adv Drug Deliv Rev* 53(3):285–305. doi:[10.1016/S0169-409X\(01\)00233-2](https://doi.org/10.1016/S0169-409X(01)00233-2)
71. Gasselhuber A, Dreher MR, Negussie A et al (2010) Mathematical spatio-temporal model of drug delivery from low temperature sensitive liposomes during radiofrequency tumour ablation. *Int J Hyperthermia* 26(5):499–513. doi:[10.3109/02656731003623590](https://doi.org/10.3109/02656731003623590)
72. Park SM, Kim MS, Park SJ et al (2013) Novel temperature-triggered liposome with high stability: formulation, in vitro evaluation, and in vivo study combined with high-intensity focused ultrasound (HIFU). *J Control Release* 170(3):373–379. doi:[10.1016/j.jconrel.2013.06.003](https://doi.org/10.1016/j.jconrel.2013.06.003)
73. Ter Haar G, Coussios C (2007) High intensity focused ultrasound: physical principles and devices. *Int J Hyperthermia* 23(2):89–104. doi:[10.1080/02656730601186138](https://doi.org/10.1080/02656730601186138)
74. Tempany CMC, McDannold NJ, Hynynen K et al (2011) Focused ultrasound surgery in oncology: overview and principles. *Radiology* 259(1):39–56. doi:[10.1148/radiol.11100155](https://doi.org/10.1148/radiol.11100155)
75. McDannold NJ, King RL, Jolesz FA et al (2000) Usefulness of MR imaging-derived thermometry and dosimetry in determining the threshold for tissue damage induced by thermal surgery in rabbits. *Radiology* 216(2):517–523, doi:<http://dx.doi.org/10.1148/radiology.216.2.r00au42517>
76. Kennedy JE (2005) High-intensity focused ultrasound in the treatment of solid tumours. *Nat Rev Cancer* 5(4):321–327. doi:[10.1038/nrc1591](https://doi.org/10.1038/nrc1591)
77. Miller DL, Song JM (2003) Tumor growth reduction and DNA transfer by cavitation-enhanced high-intensity focused ultrasound in vivo. *Ultrasound Med Biol* 29(6):887–893. doi:[10.1016/S0301-5629\(03\)00031-0](https://doi.org/10.1016/S0301-5629(03)00031-0)
78. Frenkel V, Etherington A, Greene M et al (2006) Delivery of liposomal doxorubicin (Doxil) in a breast cancer tumor model: investigation of potential enhancement by pulsed-high intensity focused ultrasound exposure. *Acad Radiol* 13(4):469–479. doi:[10.1016/j.acra.2005.08.024](https://doi.org/10.1016/j.acra.2005.08.024)

79. Dromi S, Frenkel V, Luk A et al (2007) Pulsed-high intensity focused ultrasound and low temperature-sensitive liposomes for enhanced targeted drug delivery and antitumor effect. *Clin Cancer Res* 13(9):2722–2727. doi:[10.1158/1078-0432.CCR-06-2443](https://doi.org/10.1158/1078-0432.CCR-06-2443)
80. Negussie AH, Yarmolenko PS, Partanen A et al (2011) Formulation and characterisation of magnetic resonance imageable thermally sensitive liposomes for use with magnetic resonance-guided high intensity focused ultrasound. *Int J Hyperthermia* 27(2):140–155. doi:[10.3109/02656736.2010.528140](https://doi.org/10.3109/02656736.2010.528140)
81. Cline HE, Hynynen K, Hardy CJ et al (1994) MR temperature mapping of focused ultrasound surgery. *Magn Reson Med* 31(6):628–636. doi:[10.1002/mrm.1910310608](https://doi.org/10.1002/mrm.1910310608)
82. Voogt MJ, Trillaud H, Kim YS et al (2012) Volumetric feedback ablation of uterine fibroids using magnetic resonance-guided high intensity focused ultrasound therapy. *Eur Radiol* 22(2):411–417. doi:[10.1007/s00330-011-2262-8](https://doi.org/10.1007/s00330-011-2262-8)
83. Hildebrandt B, Wust P, Ahlers O et al (2002) The cellular and molecular basis of hyperthermia. *Crit Rev Oncol Hematol* 43(1):33–56. doi:[10.1016/S1040-8428\(01\)00179-2](https://doi.org/10.1016/S1040-8428(01)00179-2)
84. de Smet M, Heijman E, Langereis S et al (2011) Magnetic resonance imaging of high intensity focused ultrasound mediated drug delivery from temperature-sensitive liposomes: an in vivo proof-of-concept study. *J Control Release* 150(1):102–110. doi:[10.1016/j.jconrel.2010.10.036](https://doi.org/10.1016/j.jconrel.2010.10.036)
85. de Smet M, Langereis S, van den Bosch S et al (2013) SPECT/CT imaging of temperature-sensitive liposomes for MR-image guided drug delivery with high intensity focused ultrasound. *J Control Release* 169(1-2):82–90. doi:[10.1016/j.jconrel.2013.04.005](https://doi.org/10.1016/j.jconrel.2013.04.005)
86. Proffitt RT, Williams LE, Presant CA et al (1983) Tumor-imaging potential of liposomes loaded with In-111-NTA: biodistribution in mice. *J Nucl Med* 24(1):45–51
87. Presant CA, Turner AF, Proffitt RT (1994) Potential for improvement in clinical decision-making: tumor imaging with In-111 labeled liposomes results of a phase II-III study. *J Liposome Res* 4(2):985–1008. doi:[10.3109/08982109409018615](https://doi.org/10.3109/08982109409018615)
88. Awasthi VD, Goins B, Klipper R et al (1998) Dual radiolabeled liposomes: biodistribution studies and localization of focal sites of infection in rats. *Nucl Med Biol* 25(2):155–160. doi:[10.1016/S0969-8051\(97\)00162-5](https://doi.org/10.1016/S0969-8051(97)00162-5)
89. Gambhir SS, Herschman HR, Cherry SR et al (2000) Imaging transgene expression with radionuclide imaging technologies. *Neoplasia* 2(1-2):118–138. doi:[10.1038/sj.neo.7900083](https://doi.org/10.1038/sj.neo.7900083)
90. Marik J, Tartis MS, Zhang H et al (2007) Long-circulating liposomes radiolabeled with [¹⁸F]fluorodipalmitin ([¹⁸F]FDP). *Nucl Med Biol* 34(2):165–171. doi:[10.1016/j.nucmedbio.2006.12.004](https://doi.org/10.1016/j.nucmedbio.2006.12.004)
91. Dams ETM, Oyen WJG, Boerman OC et al (2000) ^{99m}Tc-PEG liposomes for the scintigraphic detection of infection and inflammation clinical evaluation. *J Nucl Med* 41(4):622–630
92. Presant CA, Blayney D, Proffitt RT et al (1990) Preliminary report: imaging of Kaposi sarcoma and lymphoma in AIDS with indium-111-labelled liposomes. *Lancet* 335(8701):1307–1309. doi:[10.1016/0140-6736\(90\)91188-G](https://doi.org/10.1016/0140-6736(90)91188-G)
93. Goins BA (2008) Radiolabeled lipid nanoparticles for diagnostic imaging. *Expert Opin Med Diagn* 2(7):853–873. doi:[10.1517/17530059.2.7.853](https://doi.org/10.1517/17530059.2.7.853)
94. Phillips WT (1999) Delivery of gamma-imaging agents by liposomes. *Adv Drug Deliv Rev* 37(1-3):13–32. doi:[10.1016/S0169-409X\(98\)00108-2](https://doi.org/10.1016/S0169-409X(98)00108-2)
95. Holmberg E, Maruyama K, Litzinger DC et al (1989) Highly efficient immunoliposomes prepared with a method which is compatible with various lipid compositions. *Biochem Biophys Res Commun* 165(3):1272–1278. doi:[10.1016/0006-291X\(89\)92740-X](https://doi.org/10.1016/0006-291X(89)92740-X)
96. Morgan JR, Williams KE, Davies RL et al (1981) Localisation of experimental staphylococcal abscesses by ^{99m}Tc-technetium-labelled liposomes. *J Med Microbiol* 14(2):213–217. doi:[10.1099/00222615-14-2-213](https://doi.org/10.1099/00222615-14-2-213)
97. Laverman P, Dams ETM, Oyen WJG et al (1999) A novel method to label liposomes with Tc-99m by the hydrazino nicotinyl derivative. *J Nucl Med* 40(1):192–197
98. Goins BA, Phillips WT (2001) The use of scintigraphic imaging as a tool in the development of liposome formulations. *Prog Lipid Res* 40(1-2):95–123. doi:[10.1016/S0163-7827\(00\)00014-X](https://doi.org/10.1016/S0163-7827(00)00014-X)

99. Petersen AL, Binderup T, Rasmussen P et al (2011) ^{64}Cu loaded liposomes as positron emission tomography imaging agents. *Biomaterials* 32(9):2334–2341. doi:[10.1016/j.biomaterials.2010.11.059](https://doi.org/10.1016/j.biomaterials.2010.11.059)
100. Beaumier PL, Hwang KJ (1982) An efficient method for loading indium-111 into liposomes using acetylacetone. *J Nucl Med* 23(9):810–815
101. Gabizon A, Huberty J, Straubinger RM et al (1988) An improved method for in vivo tracing and imaging of liposomes using a gallium 67–deferoxamine complex. *J Liposome Res* 1(1):123–135. doi:[10.3109/08982108809035986](https://doi.org/10.3109/08982108809035986)
102. Bao AD, Goins B, Klipper R et al (2004) Direct Tc-99m labeling of pegylated liposomal doxorubicin (Doxil) for pharmacokinetic and non-invasive imaging studies. *J Pharmacol Exp Ther* 308(2):419–425. doi:[10.1124/jpet.103.059535](https://doi.org/10.1124/jpet.103.059535)
103. Vallabhajosula S (2009) *Molecular imaging: radiopharmaceuticals for PET and SPECT*, 1st edn. Springer, New York
104. Food and Drug Administration, U.S. FDA's Guidance (2011) PET drugs – current good manufacturing practice (cGMP). Washington, DC. <http://www.fda.gov>
105. Willmann JK, van Bruggen N, Dinkelborg LM et al (2008) Molecular imaging in drug development. *Nat Rev Drug Discov* 7(7):591–607. doi:[10.1038/nrd2290](https://doi.org/10.1038/nrd2290)
106. Gedda L, Fondell A, Lundqvist H et al (2012) Experimental radionuclide therapy of HER2-expressing xenografts using two-step targeting nucleosome particles. *J Nucl Med* 53(3):480–487. doi:[10.2967/jnumed.111.096891](https://doi.org/10.2967/jnumed.111.096891)
107. Diamandis M, White NMA, Yousef GM (2010) Personalized medicine: marking a new epoch in cancer patient management. *Mol Cancer Res* 8(9):1175–1187. doi:[10.1158/1541-7786.MCR-10-0264](https://doi.org/10.1158/1541-7786.MCR-10-0264)
108. Yu T, Chan K W Y, Anonuevo A et al (2015) Liposome-based mucus-penetrating particles (MPP) for mucosal theranostics: demonstration of diamagnetic chemical exchange saturation transfer (diaCEST) magnetic resonance imaging (MRI). *Nanomedicine-Nanotechnol Biol Med* 1(2):401–405. doi:[10.1016/j.nano.2014.09.019](https://doi.org/10.1016/j.nano.2014.09.019)
109. Park JH, Cho HJ, Yoon HY (2014) Hyaluronic acid derivative-coated nanohybrid liposomes for cancer imaging and drug delivery. *J Control Release* 174:98–108. doi:[10.1016/j.jconrel.2013.11.016](https://doi.org/10.1016/j.jconrel.2013.11.016)
110. Mulder WJM, Strijkers GJ, van Tilborg GAF et al (2009) Nanoparticulate assemblies of amphiphiles and diagnostically active materials for multimodality imaging. *Acc Chem Res* 42(7):904–914. doi:[10.1021/ar800223c](https://doi.org/10.1021/ar800223c)
111. Kim J, Pandya DN, Lee W et al (2014) Vivid tumor imaging utilizing liposome-carried bimodal radiotracer. *ACS Med Chem Lett* 5(4):390–394. doi:[10.1021/ml400513g](https://doi.org/10.1021/ml400513g)
112. Li SH, Goins B, Zhang LJ et al (2012) Novel multifunctional theranostic liposome drug delivery system: construction, characterization, and multimodality MR, near-infrared fluorescent, and nuclear imaging. *Bioconjug Chem* 23(6):1322–1332. doi:[10.1021/bc300175d](https://doi.org/10.1021/bc300175d)
113. Ma Y, Dai ZF, Gao YG et al (2011) Liposomal architecture boosts biocompatibility of nanohybrid cerasomes. *Nanotoxicology* 5(4):622–635. doi:[10.3109/17435390.2010.546950](https://doi.org/10.3109/17435390.2010.546950)
114. Liang XL, Li XD, Jing LJ et al (2013) Design and synthesis of lipidic organoalkoxysilane for self-assembly of liposomal nanohybrid cerasomes with controlled drug release properties. *Chem Eur J* 19(47):16113–16121. doi:[10.1002/chem.201302518](https://doi.org/10.1002/chem.201302518)
115. Jin YS, Yue XL, Zhang QY et al (2012) Cerasomal doxorubicin with long-term storage stability and controllable sustained release. *Acta Biomater* 8(9):3372–3380. doi:[10.1016/j.actbio.2012.05.022](https://doi.org/10.1016/j.actbio.2012.05.022)
116. Cao Z, Yue XL, Jin YS et al (2012) Modulation of release of paclitaxel from composite cerasomes. *Colloids Surf B Biointerfaces* 98:97–104. doi:[10.1016/j.colsurfb.2012.05.001](https://doi.org/10.1016/j.colsurfb.2012.05.001)
117. Liang XL, Gao J, Jiang LD et al (2015) Nanohybrid liposomal cerasomes with good physiological stability and rapid temperature responsiveness for HIFU triggered local chemotherapy of cancer. *ACS Nano* 9(2):1280–1293. doi:[10.1021/nm507482w](https://doi.org/10.1021/nm507482w)
118. Matsui K, Sasaki Y, Komatsu T et al (2007) RNAi gene silencing using cerasome as a viral-size siRNA-carrier free from fusion and cross-linking. *Bioorg Med Chem Lett* 17(14):3935–3938. doi:[10.1016/j.bmcl.2007.04.097](https://doi.org/10.1016/j.bmcl.2007.04.097)

119. Li YY, Zheng SQ, Liang XL et al (2014) Doping hydroxylated cationic lipid into PEGylated cerasome boosts in vivo siRNA transfection efficacy. *Bioconjug Chem* 25(11):2055–2066. doi:[10.1021/bc500414e](https://doi.org/10.1021/bc500414e)
120. Cao Z, Yue XL, Li XD et al (2013) Stabilized magnetic cerasomes for drug delivery. *Langmuir* 29(48):14976–14983. doi:[10.1021/la401965a](https://doi.org/10.1021/la401965a)
121. van Tilborg GAF, Mulder WJM, Deckers N et al (2006) Annexin A5-functionalized bimodal lipid-based contrast agents for the detection of apoptosis. *Bioconjug Chem* 17(3):741–749. doi:[10.1021/bc0600259](https://doi.org/10.1021/bc0600259)
122. Giri J, Thakurta SG, Bellare J et al (2005) Preparation and characterization of phospholipid stabilized uniform sized magnetite nanoparticles. *J Magn Magn Mater* 293(1):62–68. doi:[10.1016/j.jmmm.2005.01.044](https://doi.org/10.1016/j.jmmm.2005.01.044)
123. Kuznetsov AA, Filippov VI, Alyautdin RN et al (2001) Application of magnetic liposomes for magnetically guided transport of muscle relaxants and anti-cancer photodynamic drugs. *J Magn Magn Mater* 225(1-2):95–100. doi:[10.1016/S0304-8853\(00\)01235-X](https://doi.org/10.1016/S0304-8853(00)01235-X)
124. Needham D, Anyarambhatla G, Kong G et al (2000) A new temperature-sensitive liposome for use with mild hyperthermia: characterization and testing in a human tumor xenograft model. *Cancer Res* 60(5):1197–1201
125. Amstad E, Kohlbrecher J, Muller E et al (2009) Triggered release from liposomes through magnetic actuation of iron oxide nanoparticle containing membranes. *Nano Lett* 11(4):1664–1670. doi:[10.1021/nl2001499](https://doi.org/10.1021/nl2001499)
126. Jin YD, Gao XH (2009) Spectrally tunable leakage-free gold nanocontainers. *J Am Chem Soc* 131(49):17774–17776. doi:[10.1021/ja9076765](https://doi.org/10.1021/ja9076765)
127. Ma Y, Liang XL, Tong S et al (2013) Gold nanoshelled nanomicelles for potential MRI imaging, light-triggered drug release and photothermal therapy. *Adv Funct Mater* 23(7):815–822. doi:[10.1002/adfm.201201663](https://doi.org/10.1002/adfm.201201663)
128. Li SZ, Ma Y, Yue XL (2010) Encapsulation of quantum dots inside liposomal hybrid cerasome using a one-pot procedure. *J Dispers Sci Technol* 31(12):1727–1731. doi:[10.1080/01932690903542842](https://doi.org/10.1080/01932690903542842)
129. Derycke ASL, de Witte PAM (2004) Liposomes for photodynamic therapy. *Adv Drug Deliv Rev* 56(1):17–30. doi:[10.1016/j.addr.2003.07.014](https://doi.org/10.1016/j.addr.2003.07.014)
130. Roy I, Ohulchanskyy TY, Pudavar HE et al (2003) Ceramic-based nanoparticles entrapping water-insoluble photosensitizing anticancer drugs: a novel drug-carrier system for photodynamic therapy. *J Am Chem Soc* 125(26):7860–7865. doi:[10.1021/ja0343095](https://doi.org/10.1021/ja0343095)
131. Liang XL, Li XD, Yue XL et al (2011) Conjugation of porphyrin to nanohybrid cerasomes for photodynamic therapy of cancer. *Angew Chem Int Ed* 50(49):11622–11627. doi:[10.1002/anie.201103557](https://doi.org/10.1002/anie.201103557)
132. Liang XL, Li XD, Jing LJ et al (2014) Theranostic porphyrin dyad nanoparticles for magnetic resonance imaging guided photodynamic therapy. *Biomaterials* 35(24):6379–6388. doi:[10.1016/j.biomaterials.2014.04.094](https://doi.org/10.1016/j.biomaterials.2014.04.094)